

Some parts of this thesis may have been removed for copyright restrictions.

If you have discovered material in AURA which is unlawful e.g. breaches copyright, (either yours or that of a third party) or any other law, including but not limited to those relating to patent, trademark, confidentiality, data protection, obscenity, defamation, libel, then please read our [Takedown Policy](#) and [contact the service](#) immediately

INTERACTION BETWEEN FOUNDATIONS AND STRUCTURES

Md. AZADUR RAHMAN BSc Eng, MSc

A THESIS SUBMITTED FOR THE DEGREE OF
DOCTOR OF PHILOSOPHY

DEPARTMENT OF CIVIL ENGINEERING
THE UNIVERSITY OF ASTON IN BIRMINGHAM

OCTOBER 1978

INTERACTION BETWEEN FOUNDATIONS AND STRUCTURES

Md. AZADUR RAHMAN

A THESIS SUBMITTED FOR THE DEGREE OF DOCTOR OF PHILOSOPHY

1978

SUMMARY

The thesis considers the interaction between complete structures and their supporting soil. The finite element method is applied and computer programs are developed for the three dimensional non-linear analysis of the superstructure, the foundation and the soil as an integral system. The non-linear properties of the soil are determined from triaxial tests and represented by a set of graphs of octahedral shear stress and strain. These are mathematically formulated in terms of the cubic spline functions and followed by an incremental analysis technique. When the long-term settlements of soils such as clay are given by Terzaghi's consolidation theory, an iterative method of analysis is proposed. Tensile separations at the foundation-soil interface and within the soil mass are represented by incorporating dummy joints in the mesh and activating them to introduce a physical crack.

The data preparation for the computer programs is largely automated so that they can be used with a minimum of manual effort and without a knowledge of the details of the analytical method. Two methods of the construction of the overall stiffness matrix which require little or no core storage are presented. Economy in the computer time is achieved by formulating the element stiffness matrices in terms of explicit expressions. A comparison of the cost of the analysis and the size of the problem is presented.

The results of a series of experiments on the models of two space frames, a box culvert and a tall structure resting on a bed of sand are reported and compared with the analytical results. Two large practical structures and their supporting soil are analysed and their interactive behaviours are investigated.

Key words: Interaction, finite elements, non-linearity, cracks, large structures.

ACKNOWLEDGEMENT

The author is grateful to his supervisor Professor K I Majid for his invaluable advice and guidance throughout the course of this research. Thanks are due to the staff of the computer centres of the Universities of Aston, Manchester and Birmingham, particularly Dr P D Mallinson and Mr R Pearce, for their co-operation and technical advice. Mention must also be made of Messrs D J Blackburn and T Reilly for their participation in one of the model experiments. The author is grateful to Mr S M Wagstaff and his colleagues in the departmental laboratories and workshops for their help during the experimental work. Thanks are also due to Messrs D E A Hussein and M M El-Gusbi for helping with the tracing of the diagrams and to Miss B M Ingram for typing the thesis.

The author is indebted to his wife Najma for her encouragement and forbearance.

CONTENTS

SUMMARY

ACKNOWLEDGEMENT

CONTENTS

NOTATIONS

FLOWCHART SYMBOLS

	Page Number
CHAPTER 1 INTRODUCTION	
1.1 Introduction	1
1.2 A review of interaction methods	3
1.2.1 Simple soil models	3
1.2.2 Simplified interactive analysis	6
1.2.3 The use of finite elements in interactive analysis	9
1.3 Essential features of structure-soil interaction	13
1.4 Assumptions and limitations of the proposed approach	15
1.5 The finite element method	16
1.5.1 Formulation of a finite element	18
1.5.2 Convergence criteria	22
1.6 Scope of the work	24
CHAPTER 2 REPRESENTATION OF THE NON-LINEAR PROPERTIES BY SPLINE FUNCTIONS	
2.1 Introduction	29
2.2 Representation of three dimensional soil properties	30
2.2.1 The octahedral components	31
2.3 Representation of triaxial test results in terms of the octahedral components	34
2.4 Mathematical formulation of the $\tau_{oct}-\gamma_{oct}$ curves	35
2.5 The theory of splines	36
2.6 The cubic spline function	38
2.6.1 Formulation of the cubic spline function	38
2.7 Application of the cubic spline function to describe $\tau_{oct}-\gamma_{oct}$ curves of sand	46

		Page Number
2.8	Comparison of the spline and the hyperbolic representations	48
2.9	Some analogies of the spline interpolation	48
CHAPTER 3 THE NON-LINEAR ANALYSIS OF SOIL		
3.1	Introduction	50
3.2	A solid element	50
3.2.1	Selection of the solid element	50
3.2.2	Stiffness formulation of the rectangular parallelepiped element	53
3.2.3	Calculation of the strains and the stresses in the solid element	64
3.2.4	Calculation of the principal stresses	66
3.3	Non-linear analysis technique	69
3.3.1	Introduction	69
3.3.2	Non-linear finite element analysis	69
3.3.3	The incremental method	72
CHAPTER 4 TENSION SEPARATION AND CRACK PROPAGATION		
4.1	Introduction	76
4.2	Analytical representation of cracks	77
4.3	Development of a tension separation method	80
4.3.1	Method of introducing a separation	80
4.3.2	Criterion for the development of a crack	83
4.3.3	Classification of crack types	86
4.4	Closure of cracks	89
4.5	Procedure of a crack propagation analysis	89
4.6	An example on crack propagation	90
CHAPTER 5 ANALYSIS OF STRUCTURES RESTING ON CLAY		
5.1	Introduction	92
5.2	Settlement calculation in clay	92
5.3	Representation of the non-linear properties of clay	94
5.4	Finite element interaction analysis of the structure and the clay	95
5.5	Tension separation in clay	97
5.6	Examples of the analysis of structures resting on clay	98

	Page Number
5.6.1 Four-bay plane frame	98
5.6.2 Results of the plane frame example	100
5.6.2.1 The influence of Poisson's ratio	100
5.6.2.2 Comparison of the results	101
5.6.3 Analysis of the plane frame resting on a non-linear clay	107
5.6.4 Analysis of a single-bay space frame	108
CHAPTER 6 THE FINITE ELEMENT COMPUTER PROGRAMS	
6.1 Introduction	110
6.2 The finite elements used	110
6.3 The computer programs	112
6.4 Storage of the stiffness matrix	112
6.5 Construction of the stiffness matrix	113
6.5.1 The method of joint groups	115
6.5.1.1 Development of the method	115
6.5.1.2 Computer implementation of the method	115
6.5.2 Construction of \underline{K} by joints	120
6.6 Solution of the simultaneous equations	121
6.6.1 Preparation	121
6.6.2 The solution routine	123
6.7 The use of spline functions	126
6.8 Computer implementation of the crack propagation method	127
6.8.1 Description of subroutine SEPRTN	129
6.9 Automatic data generation	130
6.10 The structure of the computer programs	134
6.11 Use of the core store	136
6.12 Tests on the computer programs	137
6.12.1 Tests of accuracy	137
6.12.2 Computer time	137
6.12.3 Commercial cost	139
6.13 Conclusion	140
CHAPTER 7 MODEL EXPERIMENTS	
7.1 Introduction	141
7.2 Various tests performed	142
7.2.1 Test series A - single-bay space frame model	142

		Page Number
7.2.2	Test series B - box culvert model	144
7.2.3	Test series C - a tall structure	145
7.2.4	Test series D - three-bay space frame	147
7.3	Mechanical properties of the structure material	148
7.4	Properties of the dry sand	149
7.4.1	Determination of the stress-strain properties of the sand	149
7.4.2	The triaxial apparatus	150
7.4.3	Calibrations	153
7.4.4	Preparation of the sample	155
7.4.5	Experimental procedure	156
7.4.6	Calculations	159
7.4.7	Results of the triaxial tests	161
7.4.8	Calculation of Poisson's ratio	163
7.5	The test rig	164
7.5.1	Sand bed and deposition apparatus	165
7.5.2	The reaction frame	166
7.5.3	Standardization of the sand deposition method	167
7.6	The loading systems	168
7.6.1	Loading device for test series A, C and D	169
7.6.2	Loading device for test series B	170
7.7	Experimental procedure	171
7.7.1	Preparation of the sand bed	171
7.7.2	The test procedure	173
CHAPTER 8 COMPARISON OF EXPERIMENTAL AND THEORETICAL RESULTS		
8.1	Introduction	176
8.2	Finite element analysis of the models	176
8.2.1	Model A : a space frame	177
8.2.2	Model B : a box culvert	178
8.2.3	Model C : a tall structure	179
8.2.4	Model D : a three-bay space frame	180
8.3	Results of model A - single-bay space frame	180
8.3.1	Experimental calculations	180

		Page Number
8.3.2	Deflections and settlements of the structure	181
8.3.3	Bending moments	184
8.3.4	Stresses in the soil	186
8.4	Results of model B - the box culvert	186
8.4.1	Deflections	186
8.4.2	Tension separation	189
8.4.3	Bending moments	191
8.4.4	Stresses in the soil	194
8.5	Results of model C - tall structure	197
8.5.1	Deflections	197
8.5.2	Bending moments	200
8.5.3	Stresses in the soil	202
8.6	Results of model D - three-bay frame	203
8.6.1	Deflections and settlements	203
8.6.2	Bending moments	206
8.6.3	Stresses in the soil	207
CHAPTER 9 INTERACTIVE BEHAVIOUR OF PRACTICAL STRUCTURES		
9.1	Introduction	208
9.2	A silo complex	208
9.2.1	Description of the silo structure	209
9.2.2	Description of the supporting soil	209
9.2.3	Finite element idealization of the problem	210
9.2.4	The analysis of the silos	213
9.2.5	Results of the analysis	214
9.2.5.1	Deflections and settlements	214
9.2.5.2	Bending moments	220
9.2.5.3	Stresses in the soil	225
9.2.6	Conclusion	226
9.3	Analysis of a 50-storey space structure	227
9.3.1	Loads on the structure	229
9.3.2	The finite element analysis	229
9.3.3	Results of the analyses	232
9.3.3.1	The deflections of the structure and the raft	232
9.3.3.2	The bending moments	235

	Page Number
9.3.3.3 Stresses under the structure	238
CHAPTER 10 CONCLUSIONS AND SUGGESTIONS FOR FURTHER WORK	241
APPENDIX I Listing of the spline formulation program	
APPENDIX II The finite elements	
APPENDIX III Arrays and variables in programs described in chapter 6	
REFERENCES	

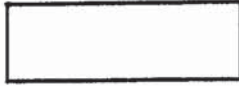
NOTATIONS

A	Anisotropy ratio
\underline{A}	Matrix defining the strain at a point in a finite element containing terms of the co-ordinates
a, b, c	Dimensions of the solid finite element
\underline{B}	Strain matrix
b_{ij}	An element of strain matrix \underline{B}
\underline{C}	Matrix of element dimensions defining the nodal displacements
c'	Apparent cohesion of soil
\underline{D}	Material properties matrix
E	Young's modulus of elasticity
e	Eccentricity of an applied load
e_x, e_z	Eccentricities in x and z directions
G	Shear modulus
\underline{H}	Co-ordinate transformation matrix
I	Second moment of area
J_1, J_2, J_3	The stress invariants
K	Bulk modulus
\underline{K}	Overall stiffness matrix
\underline{k}	Element stiffness matrix
$\{\underline{L}\}$	Load vector
l, m, n	Direction cosines
M	Compression modulus of triaxial sample membrane
M_x, M_y, M_z	Moments about x, y and z axes
m_v	Coefficient of volume compressibility of clay
\underline{N}	Displacement function matrix
$\{p\}$	Nodal forces of an element

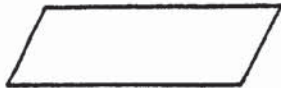
p, q, r	Local co-ordinate axes of an element
R	Stress ratio at failure in a triaxial test
$S(x)$	A spline function
$s(x)$	A natural spline function
$\{\underline{U}\}$	Displacement vector at a point
u, v, w	x, y, z components of displacement
$\{\underline{X}\}$	Overall displacement vector
x, y, z	Global co-ordinate axes
$\{\underline{\alpha}\}$	Vector of constants defining the displacement function
γ_{oct}	Octahedral shear strain
γ_w	Unit weight of water
$\gamma_{xy}, \gamma_{yz}, \gamma_{xz}$	Shear strains
ΔS	An increment of settlement
$\{\underline{\delta}\}$	Vector of element nodal displacements
$\delta_x, \delta_y, \delta_z$	Translations in x, y and z directions
δP	An increment of the load
δP^*	Increment of load necessary to initiate a crack
$\{\underline{\epsilon}\}$	Vector of the components of strain at a point
ϵ_{oct}	Octahedral normal strain
ϵ_v	Volumetric strain
$\epsilon_x, \epsilon_y, \epsilon_z$	Normal strains in x, y and z directions.
$\epsilon_1, \epsilon_2, \epsilon_3$	Major, intermediate and minor principal strains
η	Porosity
$\theta_x, \theta_y, \theta_z$	Rotations about x, y and z axes
ν	Poisson's ratio
$\{\underline{\sigma}\}$	Vector of the components of stress at a point
σ_c	Cell pressure in triaxial test

σ_{oct}	Octahedral normal stress
σ_{octi}	Initial octahedral normal stress due to the body forces
σ_t	Tensile stress necessary to be developed to initiate a crack
$\sigma_x, \sigma_y, \sigma_z$	Normal stresses in x, y and z directions
$\sigma_1, \sigma_2, \sigma_3$	Major, intermediate and minor principal stresses
τ_{oct}	Octahedral shear stress
$\tau_{xy}, \tau_{yz}, \tau_{xz}$	Shear stresses
ϕ	Second derivative of the spline function
ϕ'	Apparent angle of internal friction

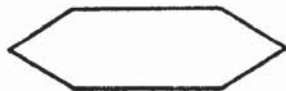
FLOWCHART SYMBOLS



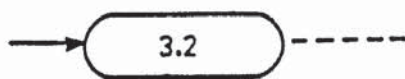
Process definition



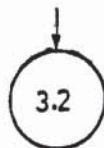
Input/Output



Decision and conditional branch



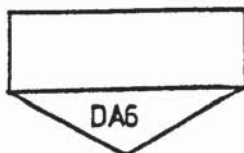
Terminal point with number - first digit indicates sheet number and second digit indicates block number



Connector - transfer to terminal number indicated



Comment annotation



Transfer to or from a direct access backing store with unit number indicated



Flow lines

CHAPTER 1

INTRODUCTION

1.1 INTRODUCTION

A structure and its supporting soil always form an integral unit. A study of the interaction between the two leads to a better understanding of the behaviour of both. Traditionally, however, these two components have been isolated and treated separately. In this manner, any interaction that may take place between the two has been overlooked. While such an approach is irrational and often incorrect, it sometimes produces a "safe" design. This is achieved by limiting the movements of the foundation to a low value, which results in an uneconomical design.

Meyerhof (1947) appreciated the interaction of building frames with their supporting soil and suggested the inclusion of structural rigidity when calculating settlement of their supports. A growing interest has since been shown in this field which has become increasingly important with the necessity of building cheaper and more complex structures on less favourable grounds. It has also become possible because the modern approach to structural analysis and the existence of computer have brought such an approach within the reach of the engineer. Two committees were formed by the Institution of the Structural Engineers who published their reports in 1974 (Littlejohn and MacLeod) and in 1978 (Thorburn). Both these reports recommended research into analytical methods of solving the structure-soil interaction. It is considered that the effect of the interaction is to redistribute the forces and the bending moments in the structure. Thorburn (1978) in his foreward to the report

stated that the engineer is faced with a choice between the following two actions:

- (1) To avoid the interactive forces by realizing a perfectly unyielding ground, or
- (2) To include these forces in the structural design.

An unyielding support does not exist, while the interactive analysis permits the structure to be designed to carry the redistributed forces and moments. This results either in a more realistic design or a more economical one or both.

It should be pointed out that the purpose of an interactive study is not to select a foundation which is more suitable for a given soil condition. The purpose is to find out the manner in which the structure and the soil influence one another, whichever type of foundation is used. Only after such a study it is possible to select a suitable foundation.

The methods of interactive analysis available to date are inadequate and oversimplified. For this reason one aim of this thesis is to produce an improved approach to this problem. The limitations of classical mathematics in analysing this complex problem are overcome by discretization and the application of numerical techniques. Another aim of this thesis is to make the approach efficient to the extent that large present day engineering structures can be analysed economically. Any method that can not deal with large problems is of a limited use. Several large engineering problems are considered in this thesis. This is done for three reasons:

- (1) To demonstrate the capacity and the capabilities of the present approach.

(2) To carry out a study into the behaviour of these structures which are hitherto unknown.

(3) To find out the actual cost of analysing such large problems.

1.2 A REVIEW OF INTERACTION METHODS

While the need for an interactive analysis is appreciated, few exhaustive methods are available. Most of these simplify the behaviour of the structure or the soil and give insufficient or inaccurate results. 42 years after the production of the first computer, the die hard traditional concept still persists. This approaches the problem as a two-phase system. The structure is one and the soil is the other. Attempts are then made to account for the interaction between these two phases by some simplified approach. Either the soil is analysed, with the structure being represented by an artificial model, or the structure is supported by a fictitious soil. An example of the model used for the structure is the equivalent raft by Meyerhof (1953). This will be described in detail later in the chapter. The relative complexity of the soil behaviour has lead to more drastic simplifications of the various soil models that have been proposed. Some of these are described below.

1.2.1 Simple soil models

The soil models can be classified into two groups. These are either mechanical or mathematical. The simplest and the most widely used mechanical model is the Winkler spring. The soil is replaced by a series of discrete springs giving rise to a linear relationship between the vertical pressure and the vertical deflection of a point on the surface of the soil. Hetenyi (1946) gave analytical

solutions for a beam resting on such a foundation. This simple spring has been modified by many authors to extend its applicability. Galletly (1959) described a modification of the Winkler foundation by assuming a linear relationship between the moment and the angle of rotation in addition to that between the vertical pressure and the vertical deflection. Morris (1966) used visco-elastic Kelvin spring-dashpots coupled with elastic springs to represent the foundation and analysed an orthogonal space frame resting on it. Tsai and Westmann (1967) introduced a modified Winkler spring foundation with different elastic properties in tension and in compression.

As the Winkler foundation consists of a series of unconnected springs, it deflects only directly under the loaded area and is not affected outside this area. This is in contrast to the continuous deflection profile of the surface of most soils. Hetenyi (1950) introduced such continuity in the Winkler spring by an embedded beam connecting the various springs. Fletcher and Hermann (1971) adopted a similar concept and modified the pressure-deflection relationship of the Winkler foundation by including higher derivative terms of the deflection. Reissner (1958) introduced a visco-elastic Winkler foundation which had shear continuity between the springs. Pister and Williams (1960) extended Reissner's model by including the horizontal displacements at the surface of the foundation. Kerr (1961) described a shear connected spring-dashpot model to represent a visco-elastic foundation with lateral continuity. An account of the other foundation models has been given by Kerr (1964). These include linear springs connected by a stretched membrane and linear springs connected by incompressible shear connectors.

The spring models are simple and therefore attractive. However, it is sometimes difficult to correlate the soil properties with the spring constants. This has led to the development of empirical or mathematical models of the soil. The most commonly used is the hypothesis that the soil behaves as an elastic, isotropic, homogeneous and semi-infinite continuum. The mathematical solution of this continuum is based on the classical Boussinesq problem of a point load on the surface of a semi-infinite body. Solutions for various cases of uniform and linearly varying loaded areas on a semi-infinite continuum are available in the literature, Love (1929), Newmark (1942), Poulos (1967a), Giroud (1968) and Poulos and Davis (1974). Gorbunov-Posadov and Serebrjanyi (1961) analysed rectangular slabs resting on an elastic continuum. The solution for a moment loading on a rigid plate resting on a semi-infinite continuum has been given by Lee (1963). The assumption of homogeneity of the continuum in these solutions is not adequate for many soils. Gibson (1967) and Gibson and Sills (1971) gave solutions for a non-homogeneous elastic continuum for two-dimensional problems.

Many soils have only a limited depth and are supported by rigid rock. They also occur in layers of limited depths. Therefore, they cannot be treated as a semi-infinite continuum. Such soils have been assumed to behave as elastic homogeneous layers. The solutions for a perfectly flexible distributed loading on layered soils have been given by Burmister (1945, 1956), Sovinc (1961) and Poulos (1967b). Milovic and Tournier (1974), on the other hand, analysed an elastic layer with a perfectly rigid loaded area on its surface. The intermediate case of a semi-rigid plate on an elastic

layer of soil has been investigated by Pickett and McCormick (1951).

The inclusion of structural rigidity gives rise to mathematical difficulties in the continuum representation of the soil. This has lead to the development of simplified continuum representations, including the use of the lattice analogy to represent the continuum by Hrenikoff (1941), McHenry (1943) and McCormick (1963). Vlasov and Leontiev (1966) used the variational approach to obtain the solution of an elastic continuum with certain restrictions imposed on its possible deformations. Kameswara Rao, Das and Anandakrishnan (1971) extended the applicability of Vlasov's foundation by including the horizontal displacements of the foundation.

1.2.2 Simplified interactive analysis

Simplified methods of interactive analysis with the soil represented by one of the models described above have been proposed by some investigators. One variation of this is the use of the semi-infinite elastic continuum theory for calculating the stresses in the soil and the use of the soil mechanics data to compute the settlements. In fact this is the conventional method of calculating the ground settlements used in a non-interactive analysis.

Zbirohowski-Koscia and Gunasekera (1970) used this method and the Ritz variational approach to analyse a semi-rigid raft resting on the ground. The influence of the superstructure was not considered. Grasshof (1957), on the other hand, analysed a combined footing resting on a semi-infinite elastic continuum with the structure assumed to be either perfectly rigid or perfectly flexible.

The behaviour of a raft or a footing is influenced by the structure it supports. An interactive analysis must consider this influence. Lee and Harrison (1970) and Seetharamulu and Kumar (1973)

analysed a framed structure supported on soil. The soil was represented by a Winkler spring bed and the foundation was treated as a beam on an elastic foundation. Lee and Brown (1972) performed a similar analysis with the soil being assumed to be an elastic semi-infinite continuum. They compared the resulting bending moments with those obtained by using a Winkler soil model. A large variation between the two was found for a multi-bay frame, showing the effect of lateral continuity of the foundation.

Meyerhof (1946) used an empirical pressure-settlement relationship of the soil under the footings of a framed structure. He calculated the settlements of the footings by a semi-graphical method. The structural rigidity was accounted for in the settlement equations by considering the slope and deflection of the structural members. However, the interaction of the different zones of the soil under each footing was neglected. A simplified method of considering the structural rigidity has also been proposed by Meyerhof (1953). The complete structure and the foundation were represented by an equivalent raft. The flexural rigidity of the equivalent raft was obtained as the sum of the flexural rigidities of the framed structure and the foundation. The settlement of this raft was calculated by assuming the soil to be an elastic semi-infinite continuum. The contact pressure distribution under the raft was taken from the solutions obtained by Borowicka (1936, 1938). The redistributed bending moments in the frame were obtained by a separate analysis of the structure subjected to the computed settlements of its bases. Sommer (1965) used a similar method of combining the flexural rigidities of the structure and the foundation. In addition to the settlements, the bending moments in the foundation

were also obtained. The equivalent raft method of considering the structural rigidity in settlement calculations has also been endorsed by an ACI committee, De Simone (1966).

Chamecki (1956) proposed a method for calculating the settlements of structural supports in which the rigidity of the structure was considered in terms of some load transfer coefficients. These coefficients corresponded to the influence lines of the support reactions for unit settlements and could be calculated from the elastic constants of the structural members. The stresses in the soil were calculated from Newmark's charts assuming the soil to be a Boussinesq continuum. The settlements were then calculated from the void ratio - log of pressure relationship of the soil. A process of iteration was necessary to obtain a convergent set of settlements and support reactions. Larnach (1970) employed a similar method of settlement calculation to account for the interaction of the structure and the soil. This utilized Terzaghi's (1943) one dimensional consolidation theory to calculate the settlements of the soil with the stresses being calculated from Boussinesq's semi-infinite continuum solutions. The procedure was programmed on a computer and therefore structures with more complicated geometry than Chamecki's could be analysed. Chamecki (1969) extended the above method to include the visco-elastic material behaviour of reinforced concrete structures.

Larnach and Wood (1972) generalized the above method by using the matrix displacement method to analyse the structure. They also considered the progressive time-dependent settlements of the soil. For the purpose of calculating the soil stresses, this was assumed to be an elastic semi-infinite continuum. The progressive settlements

of the soil were calculated from a finite difference solution of the Terzaghi-Rendulic one dimensional pore pressure dissipation equation. The stiffness matrix of the structure was modified to include the terms corresponding to the support settlements. An incremental analysis technique allowed the non-linear soil characteristics to be included in the analysis.

Komornik and Mazurik (1974) also considered the time-dependent settlement characteristics of the soil and analysed a structure interacting with such a soil. The saturated clay under the discrete structural supports were considered to act independently of the neighbouring soil with a one dimensional consolidation settlement.

1.2.3 The use of finite elements in interactive analysis

All the methods of interactive analysis described above are based on some simplifying assumptions. These methods do not analyse a complete structure and the soil as an integral system or as they are in reality. Only the vertical settlements of the structural supports are calculated while their effects on the structure are estimated by a separate analysis. With the development of numerical techniques such as the finite element method, such simplifications are no longer necessary.

Cheung and Zienkiewicz (1965) presented a finite element method for the analysis of slabs and tanks resting on an elastic foundation. The foundation was included in the analysis by adding its stiffness coefficients, at nodes connected to the structure, to the stiffness matrix of the structural elements. These stiffness coefficients were obtained by assuming the foundation to be either a bed of Winkler's springs or a semi-infinite elastic continuum. This assumption gave explicit pressure-displacement relationships

at the plate-foundation boundary nodes. Only the vertical settlements of these nodes were considered and the tension separations at the boundaries were neglected. These and the assumption that the soil is elastic are untrue. Chung and Nag (1968) extended the above method by including the horizontal contact pressure and vertical tension separation at the plate-soil boundary. The soil was again assumed to be a semi-infinite elastic continuum and was represented in the analysis by explicit stiffness coefficients of the plate-soil interface nodes.

In both the above analyses the soil behaviour was simplified to that of a series of springs or of an elastic homogeneous continuum. Smith (1970), on the other hand, used triangular axisymmetric finite elements to represent the soil to analyse a circular plate resting on it. The soil behaviour was assumed to be elastic, but inhomogeneity of the soil was accounted for by using different values of the modulus of elasticity for different elements.

Most soils exhibit a non-linear stress-strain behaviour. The assumption of linear elasticity for the soil can therefore lead to large errors in the interactive analysis. Majid and Craig (1972) used an incremental technique to perform an interactive analysis with a soil showing non-linear properties. Only two dimensional problems were considered with the structure being represented by plane frame members and the soil by plane strain rectangular and triangular finite elements. Girija Vallabhan and Jain (1972) also used two dimensional triangular finite elements to represent a concrete navigation lock structure and the surrounding soil. A direct iteration method of analysis to take care of the non-linear material properties was employed.

Finite element interaction analysis assuming a two-dimensional behaviour is of a limited applicability. In most practical cases the stresses in the soil disperse in three dimensions. Ruser and Dawkins (1972) analysed the problem of a rigid pile and the surrounding soil by using three dimensional hexahedral finite elements. The non-linear properties of the soil were taken care of by employing a direct iteration scheme of analysis. Tensile failure in the soil elements was simulated by reducing the shear modulus of the soil element where it occurred. The flexibility of the structure was not accounted for and only an analysis of the soil loaded by a rigid body was performed.

King and Chandrasekaran(1974) described a method for analysing a multi-storey space frame on a raft foundation supported by a non-homogeneous soil. The structure was preliminarily analysed assuming fixed supports. This yielded a fixed end load vector at the support points on the raft. In addition, a 'boundary stiffness matrix' was evaluated to represent the response of the structure to the movements of the raft. The soil was represented by three dimensional finite elements with variable properties to account for the non-homogeneity. Its response to the raft movements was evaluated as a 'foundation support stiffness matrix'. The raft was analysed under the external constraints of this matrix and the boundary stiffness matrix of the structure, with the fixed end loads of the structure applied to it. The displacements of the column-raft junctions were then applied on the structure together with the external loads. The structure was reanalysed to obtain the forces and the bending moments in its members. The method is exhaustive and can consider a wide variety of structures and soil. However, the two components were not

treated as an integral unit and the influence of one on the other was considered in several separate analyses.

Cunnell (1974) and Majid and Cunnell (1976) proposed a three dimensional finite element interaction analysis method in which the non-linear stress-strain property of the soil was followed. The structure, the foundation and the soil were represented by suitable three dimensional finite elements and analysed as an integral system. Several simplifying assumptions were made regarding the soil behaviour. These included a hyperbolic representation of the non-linear stress-strain curves for the soil. This resulted in a bad correlation between the theoretical and the experimental load-deflection curves of the model structures studied by them. Furthermore, the soil was assumed to possess the same properties in tension as in compression. Thus the separations in the soil mass as well as the soil-foundation interface due to the development of tensile stresses in these zones were ignored. This is unrealistic, as such separations cause non-linearity and discontinuities in the load-deflection curves and the load-bending moment relationships. Above all, Majid and Cunnell were only successful to analyse simple structures with a limited number of degrees of freedom. This is because they used the computationally expensive isoparametric hexahedral solid elements to represent the soil. The techniques of constructing the overall stiffness matrix and solving the simultaneous equations were also very inefficient. For these reasons, their approach could not successfully be applied to analyse engineering structures of any significance.

1.3 ESSENTIAL FEATURES OF STRUCTURE-SOIL INTERACTION

A realistic interaction problem has the following features:

- (1) The problem is three dimensional. Even for an isolated plane frame resting on the ground, the stresses disperse in all three directions. A two dimensional idealization of the problem is therefore unrealistic. The three dimensional nature of the problem must not be avoided.
- (2) The mechanical behaviour of the soil is non-linear. A linear elastic approach oversimplifies the problem. The errors involved in assuming a linear behaviour for the soil was demonstrated by Majid and Cunnell (1976). A realistic analysis must also adopt an acceptable stress-strain representation.
- (3) Soil is heterogeneous. Its properties vary with depth and laterally. The assumption of a homogeneous continuum to represent the soil is not true. The non-homogeneous nature of the soil must therefore be considered in an interactive approach.
- (4) The mechanical behaviour of the soil is dictated by its initial state of stress which is caused by the body forces. Thus the stiffness and the strength of the soil increase with depth.
- (5) The soil is weak in tension. Local tensile stresses create tensile failure zones. This results in a complete redistribution of stresses within the soil and the structure. It makes the soil more flexible which in turn alters its mechanical behaviour. An interaction analysis must cater for this fact.
- (6) Tensile stresses can also develop at the interface of the structure and the soil. The foundation and the soil are thus separated. This also results in a redistribution of stresses everywhere. Such separations must not be overlooked.

(7) The distribution of the contact pressure under the foundation is complex. A real foundation is subject to vertical loads, horizontal loads as well as moments. As a result, the foundation not just settles but rotates and moves sideways. Assuming a simple pressure distribution is unacceptable. A realistic analysis must not assume any specific pressure distribution. The evaluation of the actual distribution must be an outcome of such an analysis.

(8) As was stated, the junctions of the structure and the soil settle vertically, move horizontally and rotate. The base rotations are responsible for a significant redistribution of bending moments in the structure. It will be shown in chapter 8 how a symmetrical structure loaded symmetrically suffer a redistribution of bending moments due to the rotations of its bases. The horizontal translations cause redistribution of column bending moments and are very significant in sway frames.

(9) The method of analysis must be able to consider the complete structure, the foundation and the soil as an integral system. A mere analysis of the foundation with or without a simplified representation of the structure is inadequate. Various components of the structure exhibit different behaviour at different stages of the loading process.

(10) Engineering structures are often irregular, complex and large. An interaction method should be flexible, capable of including irregularities that are obvious at the beginning of the analysis or may develop later. It should be versatile so that it can tackle different structures with varying soil conditions. The method must be economical in the use of computer time and available computer storage so that these expensive factors do not become an obstacle

in treating large structures. An interactive method should also be economical to the engineer who is often sceptical about the financial advantages of the elaborations involved.

It should be stated in no uncertain terms that the interaction problem is neither limited to the field of soil mechanics nor to that of structural analysis. It is much wider than both and include numerical methods. Without these numerical techniques it is not possible to cover all the above aspects cheaply. One purpose of this thesis is to consider each of these and develop methods of tackling them in an exhaustive yet economical way. The resulting mathematical and programming problems are complex but need not be grasped by the user fully. The finite element method is particularly suitable in this field and is adopted here. The structure, the foundation and the soil are represented by an assemblage of suitable finite elements and analysed as one complete system. This scheme of analysis is logical and allows for the inclusion of all the essential features of an interactive problem in an adequate manner. The soil involved is non-linear and the use of spline functions becomes necessary to cope with its representation.

1.4 ASSUMPTIONS AND LIMITATIONS OF THE PROPOSED APPROACH

The proposed finite element interaction analysis approach takes the following assumptions:

- (1) The soil is isotropic. While it is possible to include anisotropic material properties in a finite element analysis, their exact extent in soils is unknown.
- (2) Soil behaviour can be represented sufficiently accurately by available laboratory and field test results.

(3) While the material non-linearity of the soil is catered for, the geometric non-linearity due to large deformations is excluded. This is adequate for working load conditions as large deformations are usually associated with failure states.

(4) Time-dependent deformations of the soil are excluded from the present approach. However, the long term consolidation settlements of clay are treated.

(5) The structural elements are assumed to be elastic. This is realistic because under working stress conditions they are designed to remain so. The possible material yielding due to the redistribution of the forces and the moments is not considered. The non-linearity due to the effects of axial forces in prismatic members is also neglected.

(6) The interaction is considered for static loads only. The dynamic effects of earthquake and wind forces are not included.

1.5 THE FINITE ELEMENT METHOD

The limitations of classical mathematics in solving continuum problems have lead to the development of two categories of discretization techniques. In the first, the differential equations governing the continuum are formed directly and solved by a mathematical discretization method, such as the finite difference approximations. The second method is based on a physical division of the continuum into finite elements. This method has become particularly popular among the engineers because of the more physical nature of the discretization. The advantage of the method lies in the fact that the steps of the analysis of a continuum are analogous to those for a discrete structure with well defined beam and column

components interconnected only at the joints. The steps in the finite element approximation of a continuum are summarized below after Zienkiewicz (1977). The continuum is divided by imaginary lines or surfaces into a number of finite elements. These are assumed to be interconnected at a discrete number of nodes situated on their boundaries. In the stiffness approach, the displacements of these nodes are the basic unknowns. A set of functions is chosen to describe the internal displacements of the element in terms of the nodal displacements. The internal strains are also expressed in terms of the nodal displacements by using the displacement functions. The state of stress is defined by these and any initial strains. The concentrated forces at the nodes are determined by the equilibrium of the boundary stresses and the distributed loads. This gives the characteristic stiffness relationship of the continuum.

The application of the finite element method requires the use of a digital computer to carry out the numerical processes. The steps in the finite element analysis of a complete structure and its supporting soil are described below.

(a) The structure, the foundation and the soil are idealized as an assemblage of a number of elements. While some structures are composed of discrete well defined components, the soil is always a three dimensional continuum.

(b) The element displacement functions are chosen to specify the pattern in which the elements deform. On the basis of these the element stiffness matrices relating the element nodal forces to the element nodal displacements are evaluated. The stiffness matrices are formulated in such a way that the strain-dependent non-linear properties of the element materials can be catered for economically.

(c) The element stiffness matrices are superimposed to develop the overall stiffness matrix of the structure, the foundation and the soil.

(d) The joint displacements of the complete system are obtained by solving a set of linear simultaneous equations governing the equilibrium conditions at the nodes. This takes the form:

$$\{\underline{L}\} = \underline{K} \{\underline{X}\}$$

where $\{\underline{L}\}$ is the vector of applied loads at the joints, \underline{K} is the overall stiffness matrix and $\{\underline{X}\}$ is the vector of unknown joint displacements.

(e) The joint displacements are used to calculate the other required values such as the strains, the stresses, the forces and the bending moments at various points in the system.

The accuracy of the finite element method depends on the fineness and the accuracy of the discretization of the continuum. The process of the analysis of the discrete system is exact. Therefore each element of the mesh should be chosen carefully to represent the various components of the continuous structure-soil system closely. The general procedure for the formulation of a finite element is summarized in the following sub-section.

1.5.1 Formulation of a finite element

The formulation of a finite element implies the operation of obtaining the element stiffness matrix \underline{k} required in step (b) of the analysis. It also means the calculations of the strains, the stresses etc. at a point in the element from the nodal displacements, as mentioned in (e).

For a typical element the displacements $\{\underline{U}\}$ at a point can be

expressed as a function of the co-ordinates of that point. Such displacement functions are generally expressed as:

$$\{\underline{U}\} = \underline{N} \{\underline{\alpha}\} \quad 1.1$$

where the components of \underline{N} are prescribed functions of the co-ordinates and called the displacement functions and $\{\underline{\alpha}\}$ is a column vector containing constant terms which can be expressed in terms of the nodal displacements $\{\underline{\delta}\}$. Thus:

$$\{\underline{\delta}\} = \underline{C} \{\underline{\alpha}\}$$

$$\text{and} \quad \{\underline{\alpha}\} = \underline{C}^{-1} \{\underline{\delta}\} \quad 1.2$$

in which \underline{C}^{-1} is a matrix containing the constant terms of the element dimensions. It may be noted here that the displacements $\{\underline{U}\}$ at a point in the element can be expressed in terms of the nodal displacements $\{\underline{\delta}\}$ by substituting for $\{\underline{\alpha}\}$ from equation (1.2) into equation (1.1). Thus:

$$\{\underline{U}\} = \underline{N} \underline{C}^{-1} \{\underline{\delta}\}$$

The strain-displacement relationship for a point in the element gives:

$$\{\underline{\epsilon}\} = \nabla \{\underline{U}\}$$

where $\{\underline{\epsilon}\}$ contains the components of strain and ∇ is a linear operator. By performing the partial differentiations of the displacements in equation (1.1),

$$\{\underline{\epsilon}\} = \underline{A} \{\underline{\alpha}\} \quad 1.3$$

where \underline{A} is a matrix containing the terms of the co-ordinates of

the point. Substituting for $\{\alpha\}$ from equation (1.2) into equation (1.3),

$$\{\underline{\epsilon}\} = \underline{A} \underline{C}^{-1} \{\underline{\delta}\} = \underline{B} \{\underline{\delta}\} \quad 1.4$$

The matrix \underline{B} relates the strain within the element to the nodal displacements and is sometimes called the element strain matrix. Using the stress-strain relationships given by the generalized Hooke's laws, the components of stress $\{\underline{\sigma}\}$ are:

$$\{\underline{\sigma}\} = \underline{D} \{\underline{\epsilon}\} \quad 1.5$$

where \underline{D} is the matrix of the elastic properties of the material.

The stiffness matrix of the element, \underline{k} , relates the nodal forces to the nodal displacements by making the nodal forces statically equivalent to the boundary stresses. This is achieved by imposing an arbitrary virtual displacement at the nodes and equating the external and the internal work done by the various forces and stresses during the displacement. Let such virtual nodal displacements be $\{\delta^*\}$. This produces virtual strains $\{\epsilon^*\}$ at a point within the element. By equation (1.4) the virtual strains are:

$$\{\underline{\epsilon}^*\} = \underline{B} \{\underline{\delta}^*\} \quad 1.6$$

The total virtual strain energy in the element is therefore given by:

$$\int_{\text{volume}} \{\underline{\epsilon}^*\}^T \{\underline{\sigma}\} dV$$

Substituting for $\{\underline{\epsilon}^*\}$ and $\{\underline{\sigma}\}$ from equations (1.6) and (1.5) respectively, the total virtual strain energy becomes:

$$\int_V (\underline{B} \{\underline{\delta^*}\})^T \underline{D} \{\underline{\epsilon}\} dV$$

Substituting for $\{\underline{\epsilon}\}$ from equation (1.4), virtual strain energy

$$\begin{aligned} &= \int_V (\underline{B} \{\underline{\delta^*}\})^T \underline{D} \underline{B} \{\underline{\delta}\} dV \\ &= \int_V \{\underline{\delta^*}\}^T \underline{B}^T \underline{D} \underline{B} \{\underline{\delta}\} dV \end{aligned} \quad 1.7$$

In this equation $\{\underline{\delta^*}\}$ and $\{\underline{\delta}\}$ contain virtual and real nodal displacements which are constant for the element. Therefore, these two vectors can be taken out of the integration sign and equation (1.7) can be written as:

$$\text{Virtual strain energy} = \{\underline{\delta^*}\}^T \left(\int \underline{B}^T \underline{D} \underline{B} dV \right) \{\underline{\delta}\} \quad 1.8$$

The external virtual work done by the real nodal forces $\{\underline{p}\}$ in undergoing the virtual nodal displacements $\{\underline{\delta^*}\}$ is given by:

$$\text{external work done} = \{\underline{\delta^*}\}^T \{\underline{p}\} \quad 1.9$$

The stiffness matrix \underline{k} relates $\{\underline{p}\}$ to the real nodal displacements $\{\underline{\delta}\}$ as

$$\{\underline{p}\} = \underline{k} \{\underline{\delta}\}$$

Substituting for $\{\underline{p}\}$ in equation (1.9),

$$\text{external work done} = \{\underline{\delta^*}\}^T \underline{k} \{\underline{\delta}\} \quad 1.10$$

Equating the external work done given by equation (1.10) and the virtual strain energy given by equation (1.8),

$$\{\underline{\delta^*}\}^T \underline{k} \{\underline{\delta}\} = \{\underline{\delta^*}\}^T \left(\int_V \underline{B}^T \underline{D} \underline{B} dV \right) \{\underline{\delta}\}$$

This equality holds for any arbitrary set of $\{\underline{\delta^*}\}$ and $\{\underline{\delta}\}$. Therefore, the following equality must also exist:

$$\underline{k} = \int_V \underline{B}^T \underline{D} \underline{B} dV \quad 1.11$$

Equation (1.11) explicitly defines the stiffness matrix of an element and is derived with respect to a local set of co-ordinates. Generally the overall global co-ordinate axes do not coincide with the local axes of all the elements. A transformation of co-ordinates is therefore necessary, to express the element stiffness matrix in terms of the global co-ordinates, before the overall stiffness matrix can be assembled. This is achieved by defining a transformation matrix \underline{H} which contains the direction cosines of the local co-ordinates with respect to the global axes. The matrix \underline{H} is of the same order as the element stiffness matrix \underline{k} . The transformed stiffness matrix \underline{K} is given by:

$$\underline{K} = \underline{H}^T \underline{k} \underline{H}$$

and thus $\{\underline{L}\} = \underline{K} \{\underline{X}\}$

where $\{\underline{L}\}$ and $\{\underline{X}\}$ are joint loads and displacements in the global system.

1.5.2 Convergence criteria

In the above formulation of a finite element, the basic unknown parameters were selected to be the displacements. The variation of the displacements within the element was defined by the displacement function of equation (1.1). To ensure a close approximation to the exact result the displacement function must satisfy certain conditions of convergence. These are stated below.

(i) The displacement function and its derivatives should be continuous within the element. The order of derivatives upto which the function has to be continuous is decided by the nature of the problem.

(ii) The displacement function should not permit straining in the element when the nodal displacements are caused by rigid body translations and rotations. This means that the strain energy in the element must not change due to the rigid body displacements.

(iii) The displacement function should allow for all states of constant strain, if the nodal displacements are compatible with a constant strain condition within the element.

(iv) The displacement function should satisfy internal compatibility within the element. It should also maintain compatibility of displacements between adjacent elements at the nodes and along the boundaries. When the displacement function for a finite element satisfies all the above conditions, the element is conforming.

1.6 SCOPE OF THE WORK

The essential features of the problem of interaction between a structure and the supporting soil were listed in section 1.3. It was decided to use the finite element method to consider these factors. This, however, necessitated the modification of the technique in several ways.

Laboratory tests on a soil specimen were performed to obtain a set of non-linear stress-strain curves. These represented the behaviour of the soil for various states of initial stresses. To follow the non-linear properties of the soil in the analysis a functional representation of these curves was necessary. Chapter 2 presents the development of such a functional representation. The behaviour of the soil is first represented in terms of the octahedral shear stress and strain for a given initial octahedral normal stress. Since the latter is equal to the cell pressure in a conventional triaxial test, the soil properties were obtained uniquely by performing a series of tests with different cell pressures. Each of these was then represented mathematically using the spline functions. These functions are superior to other mathematical representations and give a better correlation between the theory and the experiment. Results obtained by Cunnell (1974) using a hyperbolic idealization of the stress-strain curves showed that the load-deflection graphs obtained did not fully agree with experiments. A listing of the computer program which carried out these spline formulations for a set of curves is given in Appendix I.

The three dimensional finite element discretization of the soil introduces a large number of degrees of freedom. The element

used should therefore be formulated in an economical manner. To ensure this, the stiffness matrix of the element must be derived explicitly so that no computer time is wasted in formulating this matrix for each element in turn. A rectangular parallelepiped solid element was thus selected and its stiffness matrix is derived explicitly in chapter 3.

A linear analysis is not sufficient to cover the non-linear behaviour of the soil. It was therefore decided to adopt a non-linear incremental approach. In this approach the total applied load is divided into a number of small increments and the system is analysed repeatedly with these incremental loads. The displacements, the strains, the stresses etc. at various points are successively accumulated. The material properties of the soil are altered to correspond to the current level of stresses. This gives an updated stiffness matrix in each increment. Thus the stress-strain curves are followed closely as the applied loads are increased. In this manner the complete load-deflection history of the structure and the soil is traced upto the final stage of loading. This approach is described in chapter 3.

It was pointed out that the soil is weak in tension. This results in local tensile failure zones in the form of cracks, cavities and separations. The boundary between the soil and the foundation is unable to carry tensile stresses. This results in the separation of the structure from the soil wherever these stresses develop. Such separations cause a redistribution of stresses within the system and aggravate its non-linear behaviour. A method of representing these cracks and separations is developed in chapter 4. This method is general and can represent a wide variety of cases.

A crack is physically introduced by separating the elements surrounding it. The method used calculates the crack widths and follows the propagation of cracks as the loads are increased. The method also detects and closes a crack whenever this takes place.

The incremental method of analysis developed in chapter 3 follows the non-linear stress-strain properties of the soil by using the spline functions developed in chapter 2. This is done when the three dimensional soil properties can be obtained explicitly by field or laboratory tests. In the more conventional soil test techniques such explicit curves are not obtained. This is specially true for clay where a one dimensional consolidation test is used to predict the long term settlements. However, in such a scheme the three dimensional nature of the problem and the effect of Poisson's ratio are often ignored. A method of finite element interaction analysis, in which the three dimensional soil properties are evaluated from such a consolidation test, is developed in chapter 5. The dependency of the soil behaviour on the state of stress is also included in the analysis. Here an iterative technique is used.

Chapter 6 describes the computer programs developed for various aspects of the analysis. A complete structure analysed with its foundation and the soil requires the use of various elements. The structure is represented by an assembly of space members and rectangular plates in bending and/or shear. These elements are described in Appendix II. The general computing method for the analysis of a large finite element mesh is developed in chapter 6. The storage and the execution time problems associated with the computer analysis of such problems are solved. Two methods of constructing and storing the overall stiffness matrix are developed. An economical method of

solving the simultaneous equations governing a large finite element problem is also presented. The efficiency of the method in terms of the cost of the analysis is examined.

The accuracy of a method must be assessed before it can be applied to large problems. In the absence of adequate laboratory or field observations, a series of laboratory experiments were undertaken. These were performed on structural models resting on sand of controlled density. The models tested were:

- (a) A single-bay space frame model originally tested by Cunnell (1974) to obtain load-deflection diagrams: The tests were repeated with measurements of bending moments by means of electrical resistance strain gauges. The tests furnished load-deflection and load-bending moment diagrams which were compared with analytical results.
- (b) A twin-chambered box culvert model partially buried in sand: It was tested under vertical point loads with various eccentricities which provided a complete picture of the behaviour of such structures as a vehicle travels along them.
- (c) A tall structure with a latticed foundation which resembled an oil platform: This experiment provided the data for a slender structure with a high ratio of height to base area.
- (d) A three-bay space frame model: Two types of foundation were used for this model. The first consisted of separate pads under the columns and the second was a pair of strip footings. Several tests were performed for various positions of a point load on the structure. They allowed the study of the influence of the foundation stiffness on the behaviour of a structure with a low height to span ratio.

In all the tests, the readings of displacements and strains were obtained by using a number of dial and strain gauges. The

tests involved the modification of an existing test rig which was capable of producing a uniform bed of dry sand repeatedly. The loading system was designed to suit each of the different models. It was necessary also to measure the mechanical properties required to describe the non-linear response of the sand in the test bed. A series of triaxial tests was carried out on the sand at the porosity prevailing in the test bed for various confining pressures. The cell pressure range used was particularly low to conform with the confining pressures expected in the test bed. An account of the experimental work is given in chapter 7.

The results of the experiments with the model structures are presented in chapter 8. These are compared to the results obtained analytically. Particular emphasis is placed on the interactive behaviour of the structure with the soil rather than on the behaviour of the sand. The effects of the base movements and the role of the structure-soil interaction for the models are critically examined.

The agreement between the experimental and the analytical results of the models lead to the application of the method to large problems. A silo complex resting on a chalk foundation and a fifty-storey framed space structure with shear walls resting on clay were selected for this purpose. These are described in chapter 9 together with a critical assessment of their behaviour. It is shown that by the method developed in this thesis, such large and complex problems can be dealt with.

CHAPTER 2

REPRESENTATION OF THE NON-LINEAR PROPERTIES BY SPLINE FUNCTIONS

2.1 INTRODUCTION

Soil - structure interaction analysis based on a single and linear stress-strain function, with constant E and ν , is considered unsatisfactory and often unacceptable. This is because the properties of soil, if at all definable, not only vary in three dimensions but vary non-linearly. The analysis of a structure resting on soil should, therefore, give a non-linear load-deflection curve. For this reason, such an analysis must take account of the non-linear properties of the soil.

Furthermore, results obtained from testing a soil sample does not always produce a smooth stress-strain graph. Such a graph is often discontinuous at random points along it. To avoid these facts and to linearise the soil properties oversimplify the problem.

The analysis of a structure resting on soil by the finite element method, on the other hand, requires an explicit representation of the soil properties. At each stage of loading, properties like E , ν and G , may be non-linear, but should be kept uniquely defined. This is because the stiffness matrix of the individual elements must be constructed explicitly before the analysis can proceed.

It is, therefore, necessary to convert the sample test results to smooth and representative functions. These functions should be sufficiently accurate so that the finite element analysis at least gives acceptable results. This is particularly needed when an incremental analysis is carried out and the soil properties are defined by more than one graph. Discontinuities in these graphs

can lead to incorrect results thus spoiling an expensive analysis. In this chapter a method to represent the non-linear and discontinuous soil behaviour is presented. This makes use of the highly efficient "spline" functions. While the mathematics involved in the derivation of these functions is advanced, they are originated from the draughtman's spline, which is a strip used to draw smooth graphs of variable curvature. The application of these functions to soil representation need not be difficult. Their derivation here is presented in simple terms for clarity.

2.2 REPRESENTATION OF THREE DIMENSIONAL SOIL PROPERTIES

In a general three dimensional condition, most soils undergo shear dilation accompanied by elastic strains. Utilization of stress dilatancy laws to predict such behaviour is possible. The associated mathematical problem, however, makes it unsuitable for practical purposes.

A non-linear elasticity model has been used successfully by many authors including Cunnell (1974), Girija Vallabhan and Jain (1972) and Ruser and Dawkins (1972). The dependency of the state of stress on time and on the history of loading is excluded in this approach. The state of stress is thus assumed to be a function of the state of strain only.

Such a method is also utilized here. The essence of the approach is that the stress-strain relationship is assumed to consist of a series of elastic steps. The laws of elasticity are, therefore, applicable in each of these steps. The formulation of the laws of elasticity in a three dimensional state is facilitated by the use of the octahedral stress components. For the sake of clarity and completeness, the octahedral components of stress and strain are

derived in the following sub-section.

2.2.1 The octahedral components

The general state of stress at a point may be described either by six components of stresses in orthogonal directions or by three principal stresses and their direction cosines. In figure (2.1) x , y and z are an arbitrary set of orthogonal axes and ABC is a plane whose normal has direction cosines l , m and n with respect to these axes. If X , Y and Z are the components of stress on ABC along x , y and z respectively the equilibrium equations for the tetrahedron in figure (2.1) can be written as

$$\begin{bmatrix} \sigma_x & \tau_{xy} & \tau_{xz} \\ \tau_{xy} & \sigma_y & \tau_{yz} \\ \tau_{xz} & \tau_{yz} & \sigma_z \end{bmatrix} \begin{bmatrix} l \\ m \\ n \end{bmatrix} = \begin{bmatrix} X \\ Y \\ Z \end{bmatrix} \quad 2.1$$

where the stress notations are as shown in the figure. If N is the resultant stress on plane ABC and σ_{oct} and τ_{oct} are its normal and shear components, then from equation (2.1),

$$\begin{aligned} \sigma_{oct} = Xl + Ym + Zn &= \sigma_x l^2 + \sigma_y m^2 + \sigma_z n^2 + 2\tau_{xy} lm + 2\tau_{yz} mn \\ &+ 2\tau_{xz} ln \end{aligned} \quad 2.2$$

$$\text{and } \tau_{oct} = (N^2 - \sigma_{oct}^2)^{\frac{1}{2}} \quad 2.3$$

$$\text{where } N^2 = X^2 + Y^2 + Z^2$$

Now, if the x , y , z axes are chosen to coincide with the principal axes, so that

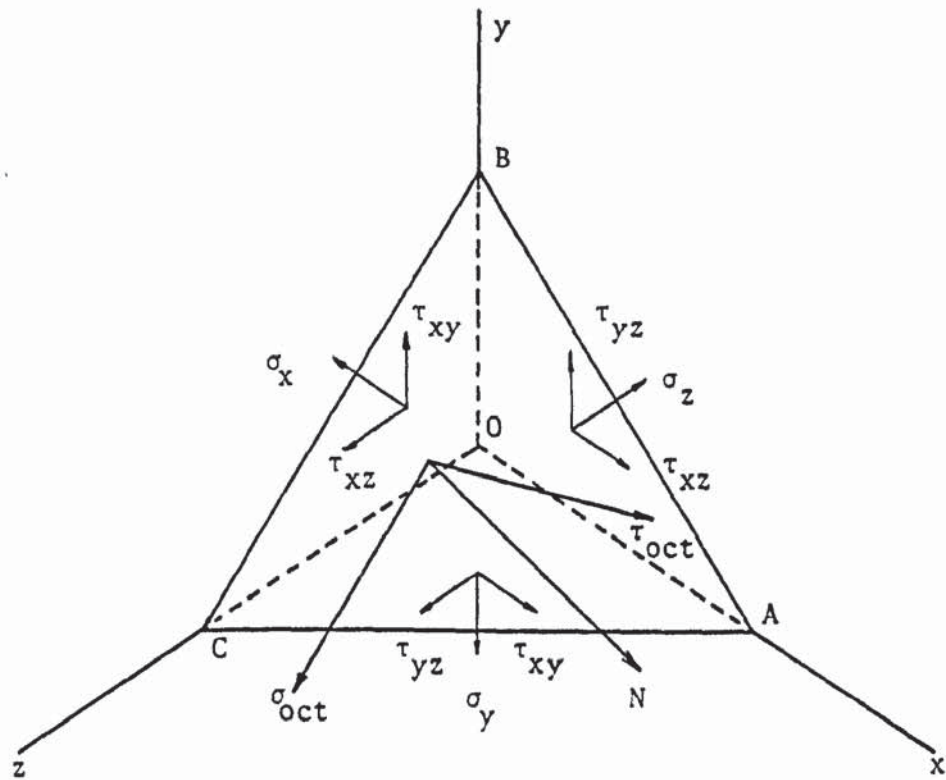


FIGURE 2.1 GENERAL THREE DIMENSIONAL STATE OF STRESS AT A POINT

Sign Convention : The computer programs developed in this thesis use the right hand screw rule, but the soil stresses presented in diagrams in this thesis consider that compressive stresses and strain are positive.

$$\sigma_1 = \sigma_x, \sigma_2 = \sigma_y, \sigma_3 = \sigma_z, \text{ and } \tau_{xy} = \tau_{yz} = \tau_{xz} = 0$$

where σ_1, σ_2 and σ_3 are the principal stresses,

equations (2.2) and (2.3) can be written as

$$\sigma_{\text{oct}} = \sigma_1 \ell^2 + \sigma_2 m^2 + \sigma_3 n^2 \quad 2.4$$

$$\text{and } \tau_{\text{oct}} = [\sigma_1^2 \ell^2 + \sigma_2^2 m^2 + \sigma_3^2 n^2 - (\sigma_1 \ell^2 + \sigma_2 m^2 + \sigma_3 n^2)^2]^{\frac{1}{2}} \quad 2.5$$

where ℓ, m and n are now the direction cosines of the normal to the plane ABC with respect to the principal axes.

If the plane ABC is so chosen that $OA = OB = OC$, such that $\ell = m = n = \frac{1}{\sqrt{3}}$, equations (2.4) and (2.5) reduce to

$$\sigma_{\text{oct}} = \frac{\sigma_1 + \sigma_2 + \sigma_3}{3} = \frac{J_1}{3} \quad 2.6$$

$$\begin{aligned} \text{and } \tau_{\text{oct}} &= \frac{1}{3}[(\sigma_1 - \sigma_2)^2 + (\sigma_2 - \sigma_3)^2 + (\sigma_3 - \sigma_1)^2]^{\frac{1}{2}} \\ &= \frac{1}{3}(2J_1^2 - 6J_2)^{\frac{1}{2}} \end{aligned} \quad 2.7$$

where J_1 and J_2 are the first and the second stress invariants respectively. Such a plane ABC is called an octahedral plane, because it forms one face of a regular octahedron with vertices on the principal axes. The stresses σ_{oct} and τ_{oct} are termed the octahedral normal and the octahedral shear stresses respectively.

Expanding the stress invariants in terms of the general cartesian components of stresses, equations (2.6) and (2.7) can be written as

$$\sigma_{\text{oct}} = \frac{J_1}{3} = \frac{\sigma_x + \sigma_y + \sigma_z}{3} \quad 2.8$$

$$\text{and } \tau_{\text{oct}} = \frac{1}{3}(2J_1^2 - 6J_2)^{\frac{1}{2}}$$

$$= \frac{1}{3}[(\sigma_x - \sigma_y)^2 + (\sigma_y - \sigma_z)^2 + (\sigma_z - \sigma_x)^2 + 6(\tau_{xy}^2 + \tau_{yz}^2 + \tau_{xz}^2)]^{\frac{1}{2}} \quad 2.9$$

Girija Vallabhan and Jain (1972) have shown that the general state of stress at a point can be divided into a hydrostatic component, responsible for the change in volume, and a deviatoric component, responsible for the change in shape of the body. The octahedral normal and shear stress components give a measure of these two components, thereby defining completely the general state of stress.

The strain components corresponding to the octahedral stresses may be written as:

$$\epsilon_{\text{oct}} = \frac{\epsilon_1 + \epsilon_2 + \epsilon_3}{3} = \frac{\epsilon_x + \epsilon_y + \epsilon_z}{3} \quad 2.10$$

$$\text{and } \gamma_{\text{oct}} = \frac{2}{3}[(\epsilon_1 - \epsilon_2)^2 + (\epsilon_2 - \epsilon_3)^2 + (\epsilon_3 - \epsilon_1)^2]^{\frac{1}{2}} \quad 2.11a$$

in terms of the principal strains,

$$\text{and } \gamma_{\text{oct}} = \frac{2}{3}[(\epsilon_x - \epsilon_y)^2 + (\epsilon_y - \epsilon_z)^2 + (\epsilon_z - \epsilon_x)^2 + \frac{3}{2}(\gamma_{xy}^2 + \gamma_{yz}^2 + \gamma_{xz}^2)]^{\frac{1}{2}} \quad 2.11b$$

in terms of the general Cartesian strains.

The bulk modulus K , the ratio of mean stress to volumetric strain, and the shear modulus G can be written in terms of the octahedral stresses and strains as

$$K = \frac{\sigma_{\text{oct}}}{3 \epsilon_{\text{oct}}} = \frac{\sigma_{\text{oct}}}{\epsilon_v}, \text{ where } \epsilon_v \text{ is the volumetric strain,}$$

and
$$G = \frac{d \tau_{oct}}{d \gamma_{oct}}$$

The octahedral stress approach described above has been used successfully by Girija Vallabhan and Reese (1968), to describe stress-deformation behaviour of soils, and by Cunnell (1974) and Girija Vallabhan and Jain (1972), to perform finite element analyses of soils in conjunction with triaxial test results.

2.3 REPRESENTATION OF TRIAXIAL TEST RESULTS IN TERMS OF THE OCTAHEDRAL COMPONENTS

The most ideal way of representing the properties of soil is, of course, the determination of all the octahedral parameters under arbitrary conditions by laboratory tests. While it is possible to do so by using sophisticated and expensive testing, the triaxial test results can be utilized to develop the octahedral parameters. The effect of ignoring the intermediate principal stress in the triaxial test, on the final results of the analysis, is not alarming, Girija Vallabhan and Jain (1972). Substituting σ_3 for σ_2 and ϵ_3 for ϵ_2 in equations (2.6), (2.7), (2.10) and (2.11), the octahedral components can be derived from the triaxial test results. Thus:

$$\sigma_{oct} = (\sigma_1 + 2\sigma_3)/3 \quad 2.12$$

$$\tau_{oct} = \frac{\sqrt{2}}{3} (\sigma_1 - \sigma_3) \quad 2.13$$

$$\epsilon_{oct} = (\epsilon_1 + 2\epsilon_3)/3 = \epsilon_v/3 \quad 2.14$$

$$\gamma_{oct} = \frac{2\sqrt{2}}{3} (\epsilon_1 - \epsilon_3) = \frac{\sqrt{2}}{3} (3\epsilon_1 - \epsilon_v) \quad 2.15$$

A series of triaxial tests was performed on a dry sand. This will be described in chapter 7. The results of the tests are

presented in octahedral form in figure (2.2). Each curve in this figure correspond to a different cell pressure in the test, which is equal to the initial octahedral normal stress, σ_{octi} . It is noticed that the curves are highly non-linear throughout their entire range.

2.4 MATHEMATICAL FORMULATION OF THE $\tau_{oct} - \gamma_{oct}$ CURVES

Having obtained the non-linear stress-strain response of the soil as given by figure (2.2), it is now necessary to incorporate this information in the non-linear finite element analysis. One possible method is to use a digital scheme by supplying a number of pairs of co-ordinates of the curves and performing suitable numerical differentiations to obtain the shear modulus at any point. A more convenient method is to represent the curve by a mathematical function. Hyperbola and some variations of the hyperbola have been very popular in the past for this purpose. These have been used by Kondner (1963), Kondner and Zelasko (1963a, b), Duncan and Chang (1970), Domaschuk and Wade (1969) and Cunnell (1974). This last investigator formulated the $\tau_{oct} - \gamma_{oct}$ curves by the relationship

$$\tau_{oct} = \frac{\gamma_{oct}}{a + b \gamma_{oct}} \quad 2.16$$

where a and b are constants. Although this equation is simple and straight forward, in which the constants a and b have some physical significance, it is unable to represent the curves of figure (2.2) sufficiently closely over the entire range. Cunnell's work showed that a hyperbolic representation under estimates the initial deflections of a structure resting on soil, while it over-

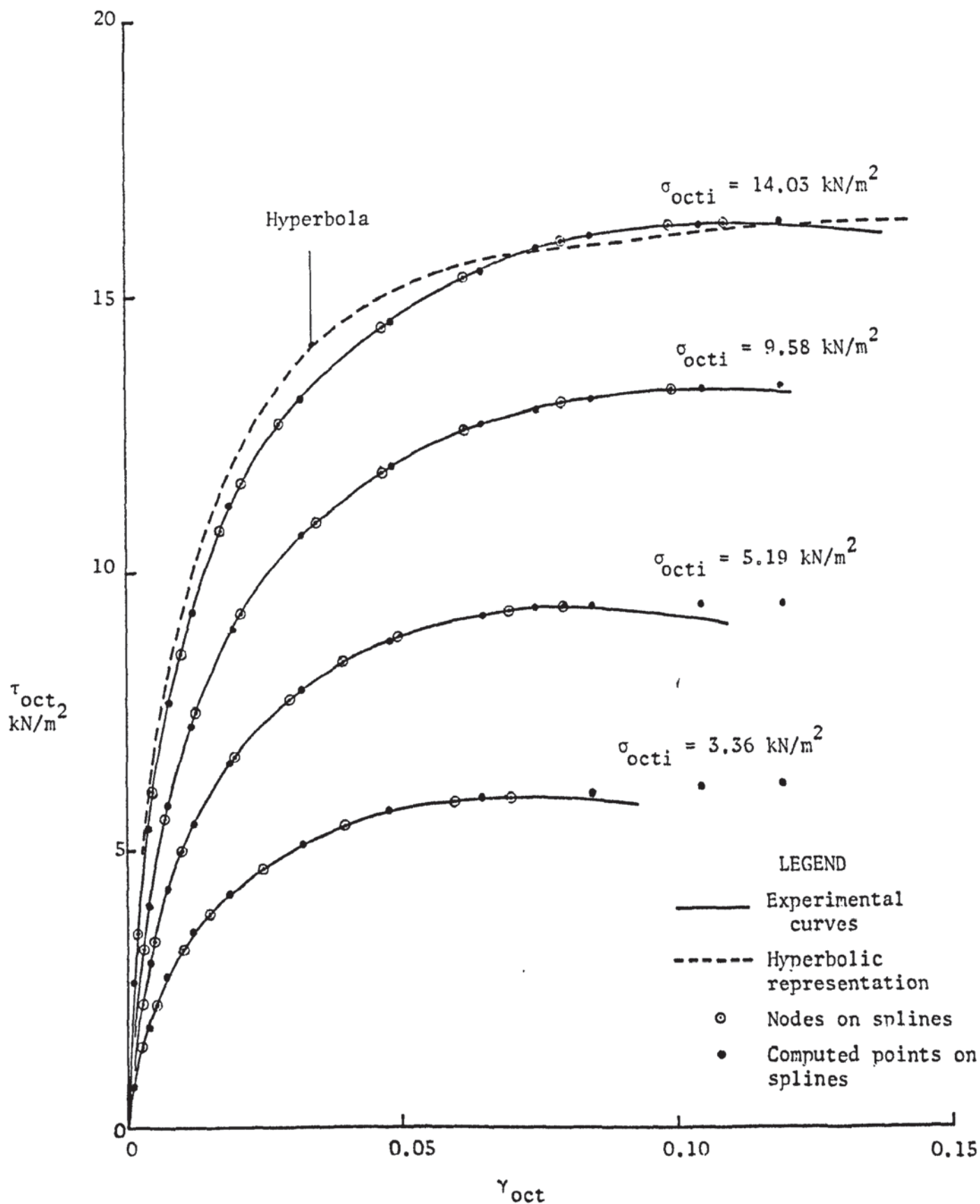


FIGURE 2.2 EXPERIMENTAL $\tau_{oct} - \gamma_{oct}$ CURVES OF SAND WITH THEORETICAL REPRESENTATIONS

estimates it at later stages.

In fact, there can probably be no single polynomial or functional representation of such arbitrary curves over their entire length. The approach suggested here is, therefore, to divide the curve into a number of segments and to obtain a separate functional representation for each of them, so that certain conditions of continuity are satisfied at the joints. The conditions are:

(a) that the two functions representing the segments to the left and to the right of a joint must give the same value of the ordinate at the joint, and (b) that the functions must have the same derivatives at the joint. Such functions are known as "spline" functions. In the following sections the theory of spline functions will be described and a spline representation of the curves in figure (2.2) will be developed.

2.5 THE THEORY OF SPLINES

A spline function $y = f(x)$ has the following powerful properties:

(1) It interpolates between n given points (x_1, y_1) , (x_2, y_2) (x_n, y_n) in which x varies between a and b . Thus

$$a \leq x_1 < x_2 \dots\dots\dots < x_{n-1} < x_n \leq b \quad 2.17$$

The intervals $(x_i - x_{i-1})$ and $(x_{i+1} - x_i)$ need not be equal.

The points (x_i, y_i) are called the nodes of the spline function.

These are the specified data points which are obtained beforehand, from experiments for instance.

(2) The function $f(x)$ overcomes discontinuities in the interpolation between any two intervals x_{i-1} , x_i and x_{i+1} because it has continuous derivatives upto order k , where k is more than 1

but less than n . Thus not only it ensures that the value of y is satisfied at the nodes but also it satisfies the slopes of $f(x)$ at these nodes and in fact its higher derivatives. Notice that between the nodes, the function can be highly non-linear.

(3) The function ensures the accuracy of the interpolation by minimizing the integral

$$I = \int_a^b [f^k(x)]^2 dx \quad 2.18$$

Here $f^k(x)$ is the derivative of $f(x)$ k times.

A spline function or spline is often denoted by $S(x)$. This notation is also adopted here. From now on, h , i and j are three successive nodes of the spline, thus

$$h = i - 1, \quad j = i + 1$$

2.19

and $x_h < x_i < x_j$

In any interval x_i to x_j , $S(x)$ is a piecewise function. It is a polynomial whose degree is either less than $2k-1$ or equal to it. Generally, there will be a different polynomial in each interval. Nonetheless, the two polynomials that represent $S(x)$ to the left and to the right of a node (x_i, y_i) have the same ordinates. They also have the same derivatives of order 1, 2, upto $(2k-2)$. In this manner the polynomial arcs join smoothly at the data points.

The two properties that characterize a spline function $S(x)$ of degree m with nodes at

$$x_1 < x_2 < x_3 \dots \dots \dots x_n$$

are:

(i) In any interval $(x_i \text{ to } x_j)$, with $i = 1, 2 \dots \dots, n-1$ and

$j = 2, 3, \dots, n$, the spline $S(x)$ is described by a polynomial of a maximum degree m . This polynomial continues from $-\infty$ to x_1 on one side and from x_n to $+\infty$ on the other.

(ii) $S(x)$ and its derivatives of all orders upto $(m - 1)$ are continuous in the interval $-\infty$ to $+\infty$. Continuity of the derivatives upto the order $(m - 1)$ is sufficient to ensure a smooth fit at the nodes. Continuity of the derivatives of order m also, means a simple single polynomial.

A "natural" spline function is a spline of odd degree $(2k - 1)$, which reduces to a polynomial of degree $(k - 1)$ in each of the intervals $(-\infty$ to $x_1)$ and $(x_n$ to $+\infty)$. In general these two polynomials will be different. From now on, a natural spline function will be denoted by $s(x)$. In mathematics, the smooth interpolation and the good approximating properties of the natural spline functions have been demonstrated by Greville (1967) and Ahlberg et al (1967). In the following sections a natural spline function of the third degree will be described and utilized to represent $\tau_{\text{oct}} - \gamma_{\text{oct}}$ curves of sand.

2.6 THE CUBIC SPLINE FUNCTION

A cubic spline $s(x)$ is a natural spline in which $k = 2$ and thus the degree of the function, $2k - 1$, is 3. Thus in the interval x_i to x_j , with $i = 1, 2, \dots, n - 1$ and $j = 2, 3, \dots, n$, $s(x)$ is a polynomial of the third degree at most. Outside this range, that is from $-\infty$ to x_1 and from x_n to $+\infty$, the spline reduces to a straight line because $k - 1$ is equal to 1.

2.6.1 Formulation of the cubic spline function

The first requirement for a successful spline interpolation

through a given set of points (x_i, y_i) , with $i = 1, 2, \dots, n$, is to force the function $s(x)$ to pass through the nodes (x_i, y_i) . Thus $s(x_i)$ becomes exactly equal to the ordinates y_i for all values of i . This means that the values of the spline at the boundary points, defined by x_i and x_j , are known. Furthermore, it is also known that, for a cubic spline, the second derivative, ϕ , is linear between the nodes at i and j . The values of ϕ_i and ϕ_j , however, are yet unknown and later on in this chapter a method will be given for finding them. Here, we derive a cubic spline function for the interval x_i to x_j , which will be in terms of the nodal values y_i, y_j and the second derivatives ϕ_i and ϕ_j . The linear variation of ϕ between the nodes i and j is shown in figure (2.3). Between the intervals $-\infty$ to x_1 and x_n to $+\infty$, the cubic spline reduces to a straight line. Thus $\phi_1 = \phi_n = 0$, which means that the second derivative of the spline vanishes outside the range under consideration.

From figure (2.3), it is evident that a linear interpolation can be performed between ϕ_i and ϕ_j to obtain ϕ at any intermediate point. Thus,

$$\phi = s''(x) = \phi_i + (\phi_j - \phi_i) \frac{x - x_i}{x_j - x_i} \quad 2.20$$

where the primes denote the order of the derivatives and

$x_i < x < x_j$. Writing $t_j = x_j - x_i$ and rearranging equation (2.20),

$$s''(x) = \frac{x_j - x}{t_j} \phi_i + \frac{x - x_i}{t_j} \phi_j \quad 2.21$$

Solving this differential equation by integrating equation (2.21) twice with respect to x , the expression for the spline function is obtained as:

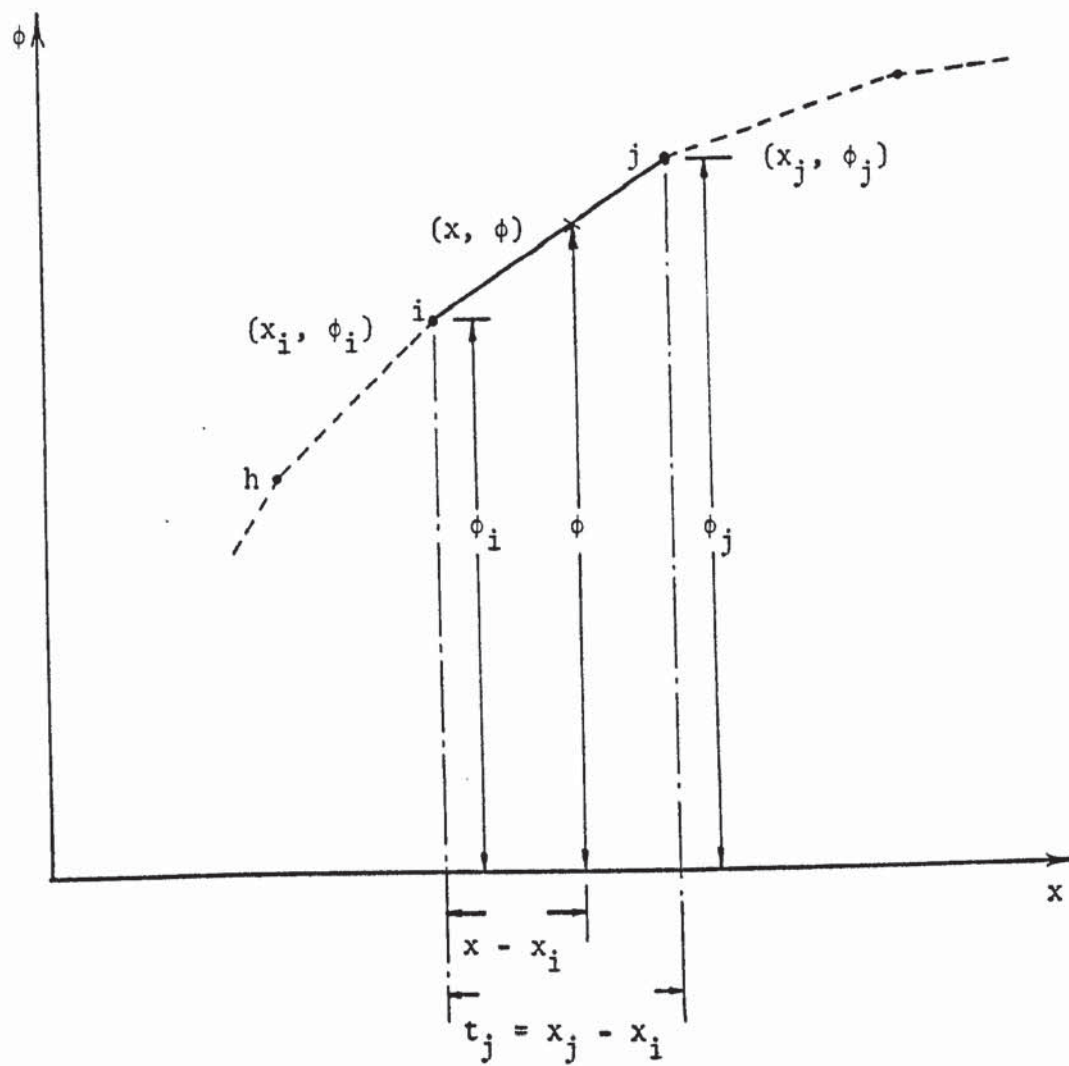


FIGURE 2.3 LINEAR VARIATION OF THE SECOND DERIVATIVE
 ϕ BETWEEN NODES i and j

$$s(x) = \frac{(x_j - x)^3}{6t_j} \phi_i + \frac{(x - x_i)^3}{6t_j} \phi_j + Ax + B \quad 2.22$$

where A and B are the constants of the integration. To evaluate these, the boundary conditions are utilized. These are:

at $x = x_i$, $s(x_i) = y_i$

and at $x = x_j$, $s(x_j) = y_j$,

where y_i and y_j are the known ordinates at the nodes. Therefore, equation (2.22) gives:

(1) At i, where $x = x_i$, and therefore,

$$x_j - x = t_j, \text{ while } x - x_i = 0,$$

$$y_i = \frac{t_j^2}{6} \phi_i + A x_i + B \quad 2.23a$$

(2) At j, where $x = x_j$, and therefore,

$$x_j - x = 0, \text{ while } x - x_i = t_j$$

$$y_j = \frac{t_j^2}{6} \phi_j + A x_j + B \quad 2.23b$$

Solving equations (2.23), the constants A and B are obtained as,

$$A = \frac{y_j - y_i}{t_j} - \frac{t_j}{6} (\phi_j - \phi_i)$$

and
$$B = y_i - \frac{y_j - y_i}{t_j} x_i + (\phi_j - \phi_i) \frac{t_j x_i}{6} - \phi_i \frac{t_j^2}{6}$$

Substituting these values into equation (2.22) and rearranging:

$$\begin{aligned}
s(x) = & \frac{x_j - x}{t_j} y_i + \frac{x - x_i}{t_j} y_j + \frac{(x_j - x)}{6 t_j} [(x_j - x)^2 - t_j^2] \phi_i \\
& + \frac{(x - x_i)}{6 t_j} [(x - x_i)^2 - t_j^2] \phi_j
\end{aligned} \tag{2.24}$$

This equation completely defines the cubic spline function $s(x)$ in the interval $x_i \leq x \leq x_j$ in terms of the nodal values y_i , y_j , ϕ_i and ϕ_j . In matrix form, the equation is written as:

$$s(x) = F \{P\}, \tag{2.25}$$

in which

$$\begin{aligned}
F = & \left[\begin{array}{c|c|c} \frac{x_j - x}{t_j} & \frac{x - x_i}{t_j} & \frac{(x_j - x)^3}{6 t_j} - \frac{t_j}{6} (x_j - x) \\ \hline \frac{(x - x_i)^3}{6 t_j} - \frac{t_j}{6} (x - x_i) & & \end{array} \right],
\end{aligned} \tag{2.25.1}$$

$$\text{and } \{P\} = \{y_i \quad y_j \quad \phi_i \quad \phi_j\} \tag{2.25.2}$$

An examination of equation (2.25) shows that the second derivatives ϕ_i and ϕ_j at the nodes i and j are the only unknowns in the evaluation of $s(x)$ between these two nodes. These can be readily determined as follows. The slope $s'(x)$ is continuous over the nodes. This means that the slope of the spline at the node i in the interval $(h \text{ to } i)$ must be equal to that in the interval $(i \text{ to } j)$. Differentiating equation (2.25),

$$s'(x) = \left[-\frac{1}{t_j} \left| \frac{1}{t_j} \left| \frac{t_j}{6} - \frac{(x_j - x)^2}{2t_j} \right| \frac{(x - x_i)^2}{2t_j} - \frac{t_j}{6} \right] \begin{bmatrix} y_i \\ y_j \\ \phi_i \\ \phi_j \end{bmatrix} \quad 2.26$$

This is the slope of the curve between the nodes i and j . A suitable substitution of subscripts in equation (2.26) gives the slope between the nodes h and i . Evaluating this slope at the point $(x = x_i)$ and equating it to the value of $s'(x)$ at $(x = x_i)$, given by equation (2.26), the following relationship is obtained.

$$\begin{bmatrix} -\frac{1}{t_i} & \frac{1}{t_i} & \frac{t_i}{6} & \frac{t_i}{3} \end{bmatrix} \begin{bmatrix} y_h \\ y_i \\ \phi_h \\ \phi_i \end{bmatrix} = \begin{bmatrix} -\frac{1}{t_j} & \frac{1}{t_j} & \frac{-t_j}{3} & \frac{-t_j}{6} \end{bmatrix} \begin{bmatrix} y_i \\ y_j \\ \phi_i \\ \phi_j \end{bmatrix} \quad 2.27$$

Carrying out the matrix multiplication in this equation and rearranging the terms, we obtain:

$$t_i \phi_h + 2(t_i + t_j) \phi_i + t_j \phi_j = 6 \left(\frac{y_j - y_i}{t_j} - \frac{y_i - y_h}{t_i} \right) \quad 2.28$$

It was stated earlier that outside the range, $\phi_1 = \phi_n = 0$. By applying these conditions to the recursive relation of equation (2.28), the following system of simultaneous equations, for the nodal values of ϕ , is obtained.

$$T \{ \phi \} = \{ Y \}, \quad 2.29$$

in which

$$\underline{\mathbb{I}} = \begin{bmatrix} 2(t_2 + t_3) & t_3 & 0 & 0 & \dots & 0 \\ t_3 & 2(t_3 + t_4) & t_4 & 0 & \dots & 0 \\ 0 & t_4 & 2(t_4 + t_5) & t_5 & 0 & \dots & 0 \\ \vdots & \vdots & \vdots & \vdots & \vdots & \ddots & \vdots \\ 0 & \dots & 0 & t_{n-2} & 2(t_{n-2} + t_{n-1}) & t_{n-1} \\ 0 & \dots & 0 & t_{n-1} & 2(t_{n-1} + t_n) \end{bmatrix} \quad 2.30$$

$$\{\underline{\Phi}\} = \{\phi_2 \quad \phi_3 \quad \phi_4 \quad \dots \quad \phi_{n-2} \quad \phi_{n-1}\} \quad 2.31$$

$$\text{and } \{\underline{Y}\} = \begin{bmatrix} \frac{y_3 - y_2}{t_3} - \frac{y_2 - y_1}{t_2} \\ \frac{y_4 - y_3}{t_4} - \frac{y_3 - y_2}{t_3} \\ \frac{y_5 - y_4}{t_5} - \frac{y_4 - y_3}{t_4} \\ \vdots \\ \frac{y_{n-1} - y_{n-2}}{t_{n-1}} - \frac{y_{n-2} - y_{n-3}}{t_{n-2}} \\ \frac{y_n - y_{n-1}}{t_n} - \frac{y_{n-1} - y_{n-2}}{t_{n-1}} \end{bmatrix} \quad 2.32$$

Equation (2.29) is a tridiagonal set of linear simultaneous equations in ϕ , which has dominant diagonal terms. A solution of this set yields the values of the nodal second derivatives ϕ_i , with $i = 2, 3, 4, \dots, n-1$, for the cubic spline. The substitution of these values in equation (2.25), together with the values of ϕ_1 and ϕ_n equal to zero, defines the spline completely in the interval x_i to x_j . In addition, the tangent slope $s'(x)$ of $s(x)$ is also obtainable from equation (2.26), by substituting the values of ϕ_i and ϕ_j in this equation.

In the above derivation of the cubic spline function it is made sure that the spline gives the exact values of y_i at each node, with $i = 1, 2, \dots, n$. It also gives a continuous first derivative at all the nodes. Thus the first two of the three properties stated in section (2.5) are readily satisfied. The third property of minimizing the integral

$$I = \int_a^b [s^k(x)]^2 dx$$

is demonstrated below.

In the case of a cubic spline, k is equal to 2 and the above integral is written as

$$I = \int_a^b [s''(x)]^2 dx \quad 2.33$$

To prove that the cubic spline $s(x)$ gives a minimum value of the integral in equation (2.33), let $g(x)$ be an arbitrary function other than the spline. Further, let $g(x)$ and its derivatives, upto order n , be continuous and pass through all the points (x_i, y_i) , with $i = 1, 2, \dots, n$. Thus

$$g(x_i) = s(x_i) = y_i \quad \text{for } i = 1, 2, \dots, n$$

However, the arbitrary function $g(x)$ does not possess any other quality of the cubic spline $s(x)$.

The integral I given by equation (2.33) must be a minimum if

$$\int_a^b [g''(x)]^2 dx \geq \int_a^b [s''(x)]^2 dx$$

Utilizing the rules of definite integrals, the following equation is written:

$$\begin{aligned} I' &= \int_a^b [g''(x)]^2 dx = \int_a^b [s''(x)]^2 dx + \int_a^b [g''(x) - s''(x)]^2 dx \\ &\quad - 2 \int_a^b s''(x) [g''(x) - s''(x)] dx = I + J - 2K \end{aligned} \quad 2.34$$

The second derivative of the cubic spline vanishes outside the range x_1 to x_n . Thus $s''(x_1) = s''(x_n) = 0$. On the other hand, $s'''(x)$ is a constant. Taking the limits of the integration from $a = x_1$ to $b = x_n$ the term K in equation (2.34) can be integrated by parts to give

$$\begin{aligned} \int_{x_1}^{x_n} s''(x) [g''(x) - s''(x)] dx &= [s''(x)g'(x)]_{x=x_1}^{x=x_n} \\ &\quad - \sum_{\substack{i=1, n-1 \\ j=2, n}} \int_{x_i}^{x_j} g'(x) s'''(x) dx \\ &= [s''(x)s'(x)]_{x=x_1}^{x=x_n} + \sum_{\substack{i=1, n-1 \\ j=2, n}} \int_{x_i}^{x_j} s'(x) s'''(x) dx \end{aligned}$$

This can be reduced to:

$$\int_{x_1}^{x_n} s''(x) [g''(x) - s''(x)] dx$$

$$= \sum_{\substack{i=1, n-1 \\ j=2, n}} s'''(x) [s(x) - g(x)]_{\substack{x=x_j \\ x=x_i}}$$

Now at all the nodes $[s(x) - g(x)]$ is zero, which means that, in equation (2.34), $K = 0$. On the other hand, J is a complete square and thus non-negative. Hence $I' = I + J$ and $I' > I$. This proves that I is a minimum for the cubic spline $s(x)$.

2.7 APPLICATION OF THE CUBIC SPLINE FUNCTION TO DESCRIBE

$\tau_{oct} - \gamma_{oct}$ CURVES OF SAND

The versatility and the flexibility of the cubic spline function, derived in the previous section, make it readily applicable to describe the $\tau_{oct} - \gamma_{oct}$ curves of figure (2.2). The curves in this figure describe the stress-strain properties of the sand used during the experiments reported in this thesis. Each curve is for a particular initial value σ_{octi} and each set of data requires a different spline formulation. Some form of interpolation is necessary to predict the $\tau_{oct} - \gamma_{oct}$ behaviour for an intermediate value of σ_{octi} . Desai (1971), for instance, suggested the establishment of a number of secondary splines between the tangent slopes and σ_{octi} for various values of stress or strain. It is also possible to formulate a bicubic spline in a three dimensional space of τ_{oct} , γ_{oct} and σ_{octi} , Desai (1972). Trial solutions revealed that the variation of the tangent slope at a particular strain level between two consecutive values of σ_{octi} was not far from linear. It was

decided, therefore, to use a linear interpolation at any strain level to find the shear modulus for an intermediate value of σ_{octi} .

The cubic spline function $s(\gamma_{oct})$ describing any particular curve in figure (2.2) is defined completely by substituting γ_{oct} for x and τ_{oct} for y in equations (2.25), (2.26) and (2.29). The solution of the simultaneous equations (2.29) can be performed by any standard solution technique. The finite element program developed and described in chapter 6 included a computer routine for this purpose. But the special nature and purpose of this routine made it undesirable to be applied to solve such a simple problem. For this reason a separate program was written to formulate a cubic spline function for any number of curves. The program reads the nodal values of τ_{oct} and γ_{oct} for each curve and sets up the system of equations (2.29). The equations are then solved by a simple elimination technique to obtain the values of ϕ_i , with $i = 2, 3, 4, \dots, n-1$. The nodal values of τ_{oct} , γ_{oct} and ϕ for each value of σ_{octi} were written into a permanent disc file, ready to be read by any program that required these. This procedure also reduced the execution time of the main program. A listing of the cubic spline formulation program is given in Appendix I.

Figure (2.2) shows the nodal points and some intermediate computed points of the spline functions representing the set of experimental $\tau_{oct} - \gamma_{oct}$ curves. Experience showed that a successful spline interpolation was obtained if a smooth curve was first passed through the experimental points. The nodes were then selected on this curve rather than using the raw experimental points.

2.8 COMPARISON OF THE SPLINE AND THE HYPERBOLIC REPRESENTATIONS

For comparison purposes a hyperbolic formulation of the $\tau_{oct} - \gamma_{oct}$ curves of figure (2.2) was also obtained and used. Equation (2.16) may be rewritten as

$$\frac{\gamma_{oct}}{\tau_{oct}} = a + b \gamma_{oct}$$

This is a straight line with slope b and intercept a . For a number of values of τ_{oct} and γ_{oct} on each curve of figure (2.2), a linear regression analysis between γ_{oct}/τ_{oct} and γ_{oct} was performed. This yielded a pair of values for a and b . Substitution of these values in equation (2.16) completely defined the hyperbolas representing the curves in figure (2.2). One of these hyperbolas is shown in dashed lines in figure (2.2). The extent of inaccuracy of the hyperbolic representation is obvious. The spline formulation can certainly claim a greater closeness of fit than the corresponding single hyperbolic function.

It may appear, from figure (2.2), that the hyperbolic approximation of the $\tau_{oct} - \gamma_{oct}$ curve is acceptable. The apparently little difference between the two curves, however, influences the load-deflection curve of the structure resting on soil in a much marked way. Load-deflection diagrams obtained by Cunnell (1974) shows that these hyperbolas do not give results that agree with those obtained experimentally. Such curves obtained using spline functions will be compared with experiments in chapter 8.

2.9 SOME ANALOGIES OF THE SPLINE INTERPOLATION

The cubic spline function is a mathematical representation of

a continuous elastic beam with simple supports at the nodes. In this beam, the bending moment varies linearly between the supports with a change of slope of the moment diagram at the nodes. The resulting shape of the axis of the beam is thus a smooth curve. The equation of bending, applied to this beam, is $d^2y/dx^2 = M/EI$, where M is the moment and E and I are the beam's constants. The second derivative ϕ of the cubic spline function is also a straight line between any two nodes x_i and x_j . This is sometimes called the moment of the mathematical spline. The nodes through which the spline is made to pass are analogous to the simple supports of the beam and the value of the function at these points is $s(x_i) = y_i$, for all $i = 1, 2, \dots, n$. The third derivative of the cubic spline is constant between the nodes x_i and x_j , but has a discontinuity at the nodes. This is analogous to the discontinuity of the rate of change of curvature of the beam at the support points.

The spline interpolation between a given set of data points or nodes is also analogous to the finite element method of discretization of a continuum. The individual pieces of the curve are analogous to the finite elements, the nodes in both cases having a similar meaning. The spline functions, representing the piece of the curve, are analogous to the displacement functions in the finite elements approach. The conditions of continuity of the derivatives of the spline are similar to the compatibility requirements at the finite element boundaries.

CHAPTER 3

THE NON-LINEAR ANALYSIS OF SOIL

3.1 INTRODUCTION

The interaction analysis of a structure resting on soil can be carried out by the finite element approach. In that case the soil is represented using three dimensional solid elements. The element should be so chosen that it can conveniently and economically be included in a finite element program for solving large problems. A hexahedral solid element is described and developed for this purpose in this chapter.

The properties of the soil are non-linear and, therefore, the analysis using the three dimensional solid elements for soil must take account of this. A method of analysis, which follows the complete load-deflection history of the structure as well as the non-linear stress-strain paths of the three dimensional soil elements, is also described in this chapter.

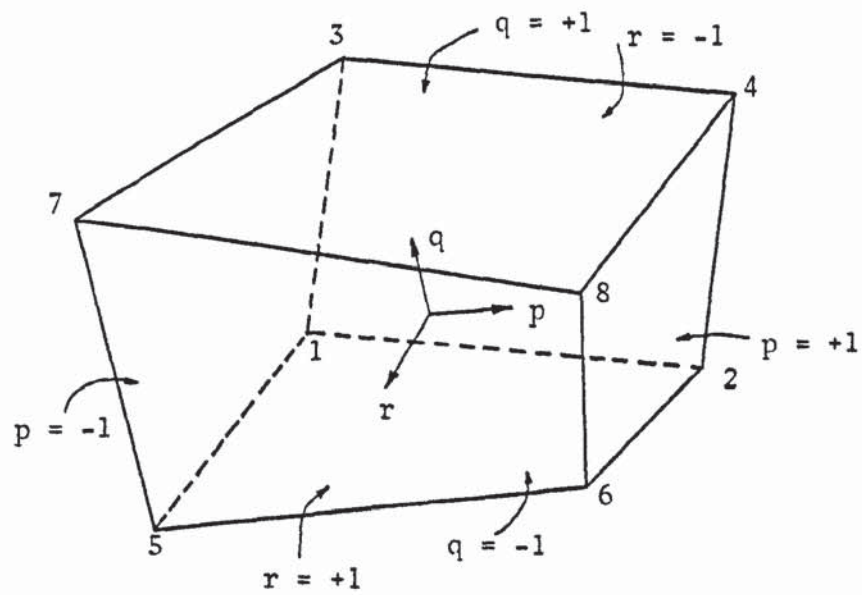
3.2 A SOLID ELEMENT

3.2.1 Selection of the solid element

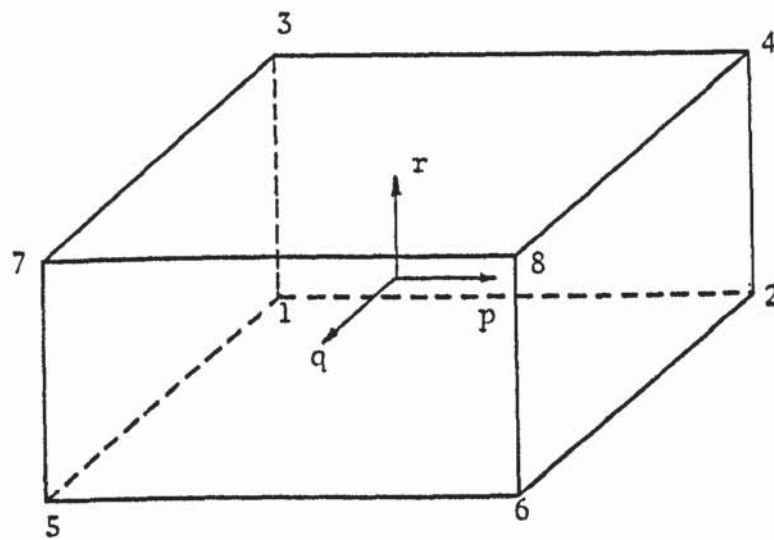
The isoparametric concept of finite element formulation offers a virtually unlimited choice of shape and order of elements. All of these stem from the same two basic element families. The essence of the concept is that the same interpolation functions used to determine the field displacements from their nodal values are used to determine the co-ordinates of any point in the element from the nodal co-ordinates. These functions are called "shape" functions, as they completely define the element shape. A suitable choice of these functions can define any element with an arbitrary shape.

The eight noded isoparametric hexahedral element shown in figure (3.1a) was used by Majid and Cunnell (1976) and was available to the author. When used, it was discovered to be very expensive on the computer time. The weakness of such an element is that it has to be formulated, starting from the shape function and following the entire process of constructing the matrices \underline{B} and \underline{D} in the integral $\underline{k} = \int_{\text{volume}} \underline{B}^T \underline{D} \underline{B} dV$ in every step of the analysis. Furthermore, the integration has to be carried out numerically. The difficulty increases especially when there are a large number of different element sizes. The stiffness matrix for each element has to be constructed separately. The transformation of the local co-ordinates of each element to the global system is also an integral part of the analysis using isoparametric elements. This too adds to the computer time. For these reasons, in the non-linear analysis of large structures, in which the element properties are changing continuously, it was discovered that the use of isoparametric elements becomes very uneconomical.

The finite element approach can be useful only if it can deal with large structures using existing computers with their limited capacity. Even then the cost of the analysis must be low. These aims can be achieved without any loss of accuracy provided that the stiffness matrix of a solid element is prepared and programmed in explicit form. Elements used to represent soil need not be of an irregular shape. The fact that Majid and Cunnell (1976) used elements with irregular shapes was merely to reduce the size of the problem so that larger ones could be solved. Not only they failed to achieve this aim but in fact, reduced the accuracy of their results by using larger elements. The fictitious boundary planes of the elements can be selected in a flexible manner. This



a) Linear isoparametric hexahedral element



b) Isoparametric rectangular parallelepiped element

FIGURE 3.1 EIGHT NODED LINEAR HEXAHEDRAL ELEMENTS

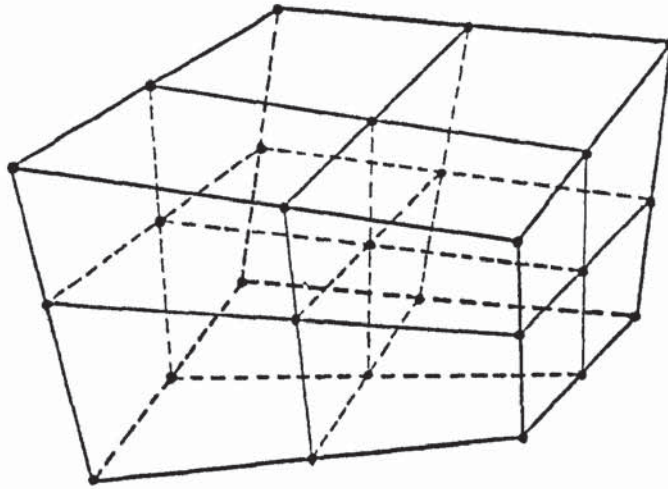
fact can be utilized to reduce the computer time considerably by developing a fixed shape rectangular parallelopiped element. The explicit derivation of the stiffness matrix of such an element is possible. Once this is done it becomes possible to solve real life problems quickly with the existing computers.

The rectangular parallelopiped element shown in figure (3.1b) is a special case of the arbitrarily shaped isoparametric element in figure (3.1a). The same set of shape functions N to describe the field variables ϕ with respect to the nodal variables ϕ^e can be used for both of them. So that

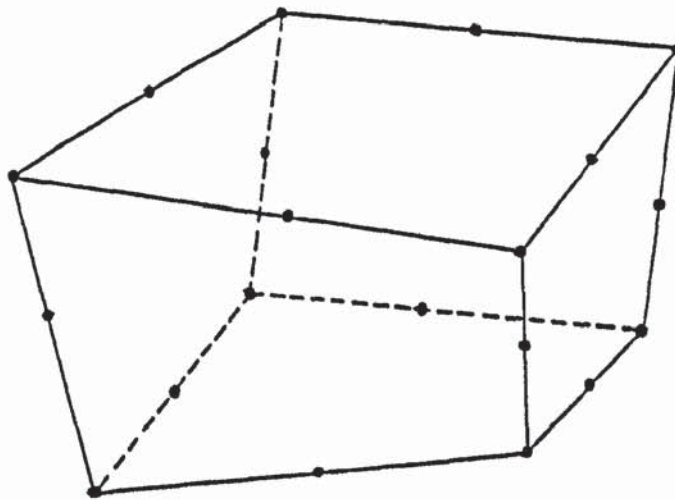
$$\phi = N\phi^e$$

The shape functions of the element shown in figures (3.1a and b) are linear, as only a linear variation of displacements can be defined along the edges. Higher order variations of displacements are, however, possible by having intermediate nodes inside the element and/or on the edges. An isoparametric hexahedral element of the Lagrangian family with a quadratic variation of the displacement is shown in figure (3.2a). The shape functions of this element are given by the products of the Lagrangian polynomials. The equivalent quadratic element of the Serendipity family with nodes on the element edges only is shown in figure (3.2b). However, in both the families the linear element is the same and is the one shown in figure (3.1a and b).

The two linear elements in figure (3.1) are defined by the same set of shape functions. They also satisfy the same conditions of continuity and convergence. Therefore, the same degree of accuracy is obtained by using either of them. However, the rectangular parallelopiped element of figure (3.1b) is superior,



a) Lagrangian family - 27 Nodes



b) Serendipity family - 20 Nodes

FIGURE 3.2 QUADRATIC ISOPARAMETRIC HEXAHEDRAL ELEMENTS

because its stiffness matrix can be prepared once and for all and programmed in terms of simple and explicit expressions. Before writing the computer program, the integrations involved are performed manually and, therefore, the stiffness matrix is obtained uniquely. In fact, the finite element mesh can be designed in such a way that the various solid elements can be grouped into a few elements of the same size. It is only necessary to construct the stiffness matrix of each group once. Later, as the material properties of these elements change, their stiffness matrices need not be constructed again but merely updated. Likewise, explicit expressions for strains and stresses within the element are obtained once and then used repeatedly during the entire process of the non-linear analysis. Thus a considerable reduction in computer time can be achieved by using the rectangular parallelepiped solid element to represent the soil under a structure. An important feature of this element is that its local axes can easily be made to coincide with the global axes and, therefore, no co-ordinate transformation is required. This too saves further computer time. It should be pointed out that the analysis of large structures requires both computer time and large storage. It will be shown later in this chapter how a great deal of computer storage is saved by the systematic use of the parallelepiped element. Later, in chapter 6, it will be shown that by constructing the overall stiffness matrix one joint at a time, the usage of the storage facility is improved to the extent that present day engineering structures can be solved with available computers.

3.2.2 Stiffness formulation of the rectangular parallelepiped element

While the displacement functions of the parallelepiped element

are given in the texts, e.g. Coates et al (1972), the explicit derivation of its stiffness matrix is not available. Because of its usefulness and for the sake of completeness, the stiffness matrix of this element is derived explicitly below in accordance with the procedure outlined in chapter 1.

Consider the rectangular parallelepiped element with the node numbering scheme as shown in figure (3.3). The origin of the local co-ordinates is chosen at node 1, while their directions are parallel to the element boundaries. The dimensions of the element are a , b and c along x , y and z directions respectively. Each node of the element is given three translational degrees of freedom, u , v and w in x , y and z directions respectively. The displacement functions of the element are written as:

$$u = \alpha_1 + \alpha_2 x + \alpha_3 y + \alpha_4 z + \alpha_5 xy + \alpha_6 yz + \alpha_7 xz + \alpha_8 xyz \quad 3.1a$$

$$v = \alpha_9 + \alpha_{10} x + \alpha_{11} y + \alpha_{12} z + \alpha_{13} xy + \alpha_{14} yz + \alpha_{15} yz + \alpha_{16} xyz \quad 3.1b$$

$$w = \alpha_{17} + \alpha_{18} x + \alpha_{19} y + \alpha_{20} z + \alpha_{21} xy + \alpha_{22} yz + \alpha_{23} xz + \alpha_{24} xyz \quad 3.1c$$

The displacement functions given by the above equations satisfy all the compatibility conditions of a conforming element given in chapter 1.

The values of the constants $\alpha_1, \alpha_2, \alpha_3, \dots, \alpha_{24}$ in equations (3.1) can be expressed in terms of the nodal displacements $u_1, v_1, w_1, u_2, v_2, w_2, \dots, u_8, v_8, w_8$. This is achieved by substituting the values of the co-ordinates of each node in turn in equations (3.1) and solving for $\alpha_1, \alpha_2, \dots, \alpha_{24}$. Thus, at node 1, $x = y = z = 0$ and $u = u_1$. Substituting these values in equation (3.1a),

$$\alpha_1 = u_1 \quad 3.2a$$

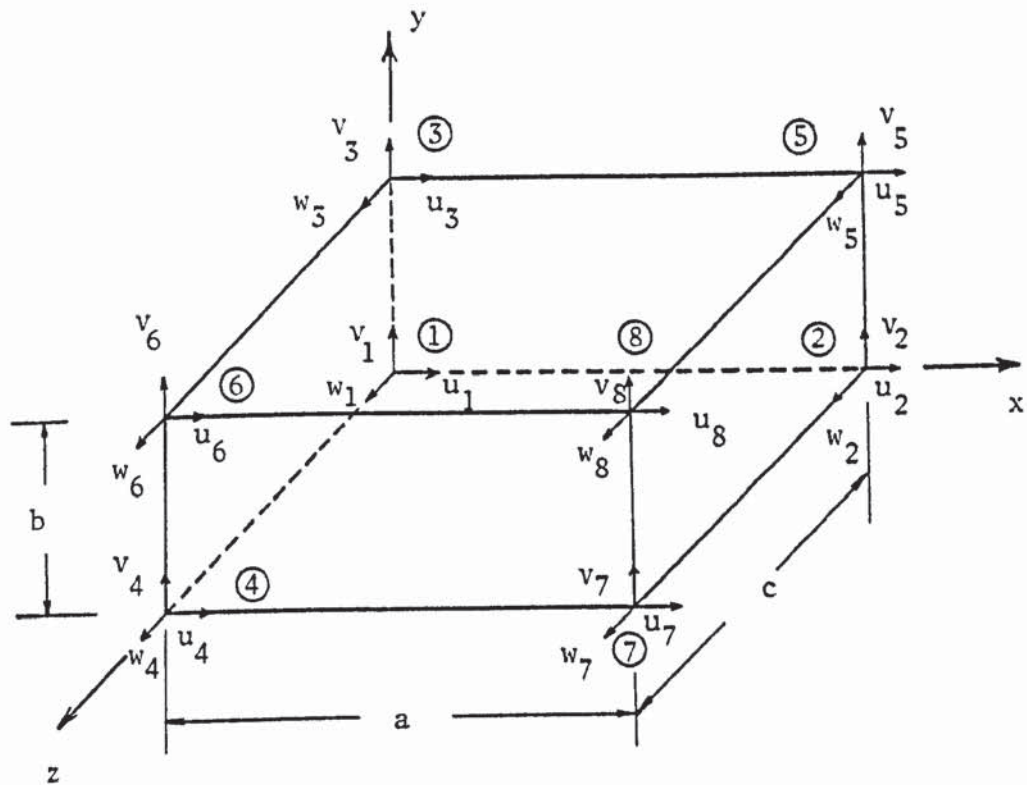


FIGURE 3.3 NOTATIONS FOR THE RECTANGULAR PARALLELOPIPED ELEMENT

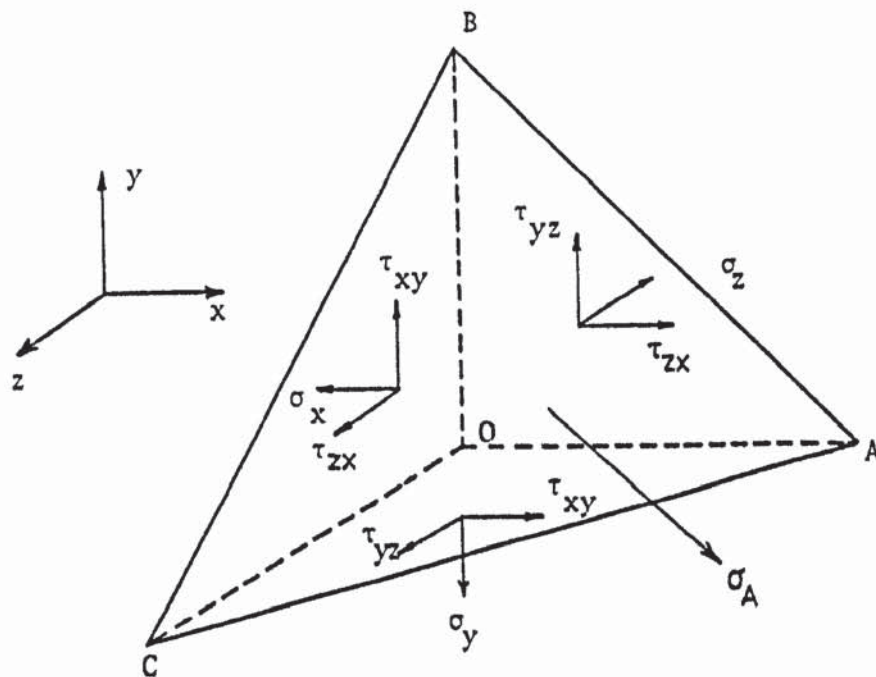


FIGURE 3.4 NOTATIONS FOR STRESSES

Similarly, at node 2, $x = a$, $y = z = 0$ and $u = u_2$, and, therefore,

$$u_2 = \alpha_1 + \alpha_2 a = u_1 + \alpha_2 a$$

$$\text{and} \quad \alpha_2 = \frac{1}{a} (u_2 - u_1) \quad 3.2b$$

Proceeding in the same manner and substituting the co-ordinates of nodes 3, 4, 8 in turn in equation (3.1a), the following values of α are obtained.

$$\alpha_3 = \frac{1}{b} (u_3 - u_1), \quad 3.2c$$

$$\alpha_4 = \frac{1}{c} (u_4 - u_1), \quad 3.2d$$

$$\alpha_5 = \frac{1}{ab} (u_1 - u_2 - u_3 + u_5), \quad 3.2e$$

$$\alpha_6 = \frac{1}{bc} (u_1 - u_3 - u_4 + u_6), \quad 3.2f$$

$$\alpha_7 = \frac{1}{ac} (u_1 - u_2 - u_4 + u_7), \quad 3.2g$$

$$\text{and} \quad \alpha_8 = \frac{1}{abc} (-u_1 + u_2 + u_3 + u_4 - u_5 - u_6 - u_7 + u_8) \quad 3.2h$$

Similar expressions for $\alpha_9, \alpha_{10} \dots, \alpha_{16}$ and $\alpha_{17}, \alpha_{18} \dots, \alpha_{24}$ can be obtained by substituting the nodal co-ordinates in equations (3.1b) and (3.1c) respectively. The solutions of $\alpha_9, \alpha_{10}, \alpha_{11} \dots, \alpha_{16}$ are given by replacing u_1, u_2, u_3 etc. by v_1, v_2, v_3 etc. in equations (3.2a, b,, h) respectively. Likewise, the solutions for $\alpha_{17}, \alpha_{18}, \alpha_{19} \dots, \alpha_{24}$ are given by replacing u_1, u_2, u_3 etc. by w_1, w_2, w_3 etc. in the same equations. Thus the following relationship is obtained.

$$\{\alpha\} = [C]^{-1} \{X\} \quad 3.3$$

where $\{\underline{\alpha}\} = \{\alpha_1 \ \alpha_2 \ \alpha_3 \ \dots \ \alpha_{24}\}$,

$$\{\underline{X}\} = \{u_1 \ v_1 \ w_1 \ u_2 \ v_2 \ w_2 \ \dots \ u_8 \ v_8 \ w_8\},$$

and \underline{C}^{-1} is a 24 x 24 matrix containing constant terms of the element dimensions a , b and c only.

The strain vector $\{\underline{\epsilon}\}$ is obtained by utilizing the strain-displacement relationships. By performing the appropriate partial differentiations of the displacement equations (3.1), the following relationship is obtained.

$$\{\underline{\epsilon}\} = \begin{bmatrix} \epsilon_x \\ \epsilon_y \\ \epsilon_z \\ \gamma_{xy} \\ \gamma_{yz} \\ \gamma_{xz} \end{bmatrix} = \begin{bmatrix} \partial u / \partial x \\ \partial v / \partial y \\ \partial w / \partial z \\ \partial u / \partial y + \partial v / \partial x \\ \partial v / \partial z + \partial w / \partial y \\ \partial w / \partial x + \partial u / \partial z \end{bmatrix} = \underline{A} \ \{\underline{\alpha}\} \quad 3.4$$

where \underline{A} is a 6 x 24 matrix containing terms of x , y and z only. Substituting for $\{\underline{\alpha}\}$ from equation (3.3) into equation (3.4),

$$\{\underline{\epsilon}\} = \underline{A} \ \underline{C}^{-1} \ \{\underline{X}\} = \underline{B} \ \{\underline{X}\} \quad 3.5$$

The 6 x 24 matrix \underline{B} is obtained by performing the matrix multiplication $\underline{A} \ \underline{C}^{-1}$. The elements of this matrix are given below explicitly:

$$b_{1, 1} = -b_{1, 4} = b_{4, 2} = -b_{4, 5} = b_{6, 3} = -b_{6, 6} = -\frac{1}{a} + \frac{y}{ab} + \frac{z}{ac} - \frac{yz}{abc}$$

$$b_{1, 7} = -b_{1, 13} = b_{4, 8} = -b_{4, 14} = b_{6, 9} = -b_{6, 15} = -\frac{y}{ab} + \frac{yz}{abc}$$

$$b_{1, 10} = -b_{1, 19} = b_{4, 11} = -b_{4, 20} = b_{6, 12} = -b_{6, 21} = -\frac{z}{ac} + \frac{yz}{abc}$$

$$b_{1, 16} = -b_{1, 22} = b_{4, 17} = -b_{4, 23} = b_{6, 18} = -b_{6, 24} = -\frac{yz}{abc}$$

$$b_{2, 2} = -b_{2, 8} = b_{4, 1} = -b_{4, 7} = -b_{5, 3} = b_{5, 9} = -\frac{1}{b} + \frac{x}{ab} \\ + \frac{z}{bc} - \frac{xz}{abc}$$

$$b_{2, 5} = -b_{2, 14} = b_{4, 4} = -b_{4, 13} = b_{5, 6} = -b_{5, 15} = -\frac{x}{ab} + \frac{xz}{abc}$$

$$b_{2, 11} = -b_{2, 17} = b_{4, 10} = -b_{4, 16} = b_{5, 12} = -b_{5, 18} = -\frac{z}{bc} + \frac{xz}{abc}$$

$$b_{2, 20} = -b_{2, 23} = b_{4, 19} = -b_{4, 22} = b_{5, 21} = -b_{5, 24} = -\frac{xz}{abc}$$

$$b_{3, 3} = -b_{3, 12} = b_{5, 2} = -b_{5, 11} = b_{6, 1} = -b_{6, 10} = -\frac{1}{c} + \frac{y}{bc} + \frac{x}{ac} - \frac{xy}{abc}$$

$$b_{3, 6} = -b_{3, 21} = b_{5, 5} = -b_{5, 20} = b_{6, 4} = -b_{6, 19} = -\frac{x}{ac} + \frac{xy}{abc}$$

$$b_{3, 9} = -b_{3, 18} = b_{5, 8} = -b_{5, 17} = b_{6, 7} = -b_{6, 16} = -\frac{y}{bc} + \frac{xy}{abc}$$

$$b_{3, 15} = -b_{3, 24} = b_{5, 14} = -b_{5, 23} = b_{6, 13} = -b_{6, 22} = -\frac{xy}{abc}$$

All the other elements of B are zero.

The stress-strain relationship is given by:

$$\{\sigma\} = D \{\epsilon\} \quad 3.6$$

The elastic properties matrix D , in three dimensional stress analysis, is given by:

$$\underline{D} = \frac{2G}{1-2\nu} \begin{bmatrix} 1-\nu & \nu & \nu & 0 & 0 & 0 \\ \nu & 1-\nu & \nu & 0 & 0 & 0 \\ \nu & \nu & 1-\nu & 0 & 0 & 0 \\ 0 & 0 & 0 & \frac{1-2\nu}{2} & 0 & 0 \\ 0 & 0 & 0 & 0 & \frac{1-2\nu}{2} & 0 \\ 0 & 0 & 0 & 0 & 0 & \frac{1-2\nu}{2} \end{bmatrix} \quad 3.6.1$$

in which G is the shear modulus and ν is the Poisson's ratio.

Finally, the stiffness matrix of the element is obtained from

$$\underline{k} = \int_0^c \int_0^b \int_0^a \underline{B}^T \underline{D} \underline{B} \, dx \, dy \, dz \quad 3.7$$

Performing the matrix multiplication indicated in equation (3.7) and carrying out the integration over the volume of the element for each term of the product, the stiffness matrix is explicitly obtained. It is noticed that the factor $2G/(1-2\nu)$ in the expression for \underline{D} in equation (3.6.1) is constant throughout the volume of the element and can be kept out of the integrations. Thus the stiffness matrix is expressed as a matrix of constant terms, with the Poisson's ratio being assumed to be a constant, multiplied by the variable shear modulus G . This facilitates the computation as only the shear modulus changes in the non-linear analysis procedure. In any step of the analysis, therefore, the current stiffness matrix of an element is obtained simply by multiplying the previously computed terms of this matrix by the instantaneous value of the shear modulus. The stiffness matrix of the rectangular parallelepiped element, expressed in this form, is explicitly given below:

$$k = G \begin{bmatrix} k_{11} & & & & & & & \\ & k_{21} & k_{22} & & & & & \\ & & & & & & & \\ & k_{31} & k_{32} & k_{33} & & & & \\ & & & & & & & \\ & k_{41} & k_{42} & k_{43} & k_{44} & & & \\ & k_{51} & k_{52} & k_{53} & k_{54} & k_{55} & & \\ & k_{61} & k_{62} & k_{63} & k_{64} & k_{65} & k_{66} & \\ & k_{71} & k_{72} & k_{73} & k_{74} & k_{75} & k_{76} & k_{77} \\ & k_{81} & k_{82} & k_{83} & k_{84} & k_{85} & k_{86} & k_{87} & k_{88} \end{bmatrix} \quad 3.8$$

symmetrical

in which each k_{ij} is a 3×3 submatrix. The submatrices are written explicitly below. In each case a , b and c are the element dimensions and the other symbols are as follows:

$$f = \frac{2}{1-2\nu}, \quad g = \frac{2(1-\nu)}{1-2\nu}, \quad h = \frac{2(1-4\nu)}{1-2\nu}$$

$$r = \frac{ab}{9c}, \quad s = \frac{bc}{9a}, \quad t = \frac{ac}{9b}$$

$$k_{11} = k_{88} = \begin{bmatrix} gs + t + r & & \text{symm.} \\ \frac{fc}{24} & gt + r + s & \\ \frac{fb}{24} & \frac{fa}{24} & gr + s + t \end{bmatrix}$$

$$k_{22} = k_{66} = \begin{bmatrix} gs + t + r & & \text{symm.} \\ -\frac{fc}{24} & gt + r + s & \\ -\frac{fb}{24} & \frac{fa}{24} & gr + s + t \end{bmatrix}$$

$$k_{33} = k_{77} = \begin{bmatrix} gs + t + r & & \text{symmetrical} \\ -\frac{fc}{24} & gt + r + s & \\ \frac{fb}{24} & -\frac{fa}{24} & gr + s + t \end{bmatrix}$$

$$k_{44} = k_{55} = \begin{bmatrix} gs + t + r & & \text{symmetrical} \\ \frac{fc}{24} & gt + r + s & \\ -\frac{fb}{24} & -\frac{fa}{24} & gr + s + t \end{bmatrix}$$

$$k_{21} = k_{86}^T = \begin{bmatrix} -gs + \frac{t}{2} + \frac{r}{2} & \frac{hc}{24} & \frac{hb}{24} \\ -\frac{hc}{24} & \frac{gt}{2} + \frac{r}{2} - s & \frac{fa}{48} \\ -\frac{hb}{24} & \frac{fa}{48} & \frac{gr}{2} + \frac{t}{2} - s \end{bmatrix}$$

$$k_{31} = k_{87}^T = \begin{bmatrix} \frac{gs}{2} + \frac{r}{2} - t & -\frac{hc}{24} & \frac{fb}{48} \\ \frac{hc}{24} & -gt + \frac{r}{2} + \frac{s}{2} & \frac{ha}{24} \\ \frac{fb}{48} & -\frac{ha}{24} & \frac{gr}{2} + \frac{s}{2} - t \end{bmatrix}$$

$$k_{32} = k_{76} = \begin{bmatrix} -\frac{gs}{2} - \frac{t}{2} + \frac{r}{4} & \frac{fc}{24} & -\frac{hb}{48} \\ \frac{fc}{24} & -\frac{gt}{2} - \frac{s}{2} + \frac{r}{4} & \frac{ha}{48} \\ \frac{hb}{48} & -\frac{ha}{48} & \frac{gr}{4} - \frac{t}{2} - \frac{s}{2} \end{bmatrix}$$

$$\underline{k}_{41} = \underline{k}_{85}^T = \begin{bmatrix} \frac{gs}{2} + \frac{t}{2} - r & \frac{fc}{48} & -\frac{hb}{24} \\ \frac{fc}{48} & \frac{gt}{2} + \frac{s}{2} - r & -\frac{ha}{24} \\ \frac{hb}{24} & \frac{ha}{24} & -gr + \frac{s}{2} + \frac{t}{2} \end{bmatrix}$$

$$\underline{k}_{42} = \underline{k}_{65}^T = \begin{bmatrix} -\frac{gs}{2} + \frac{t}{4} - \frac{r}{2} & -\frac{hc}{48} & \frac{fb}{24} \\ \frac{hc}{48} & \frac{gt}{4} - \frac{r}{2} - \frac{s}{2} & -\frac{ha}{48} \\ \frac{fb}{24} & \frac{ha}{48} & -\frac{gr}{2} - \frac{s}{2} + \frac{t}{4} \end{bmatrix}$$

$$\underline{k}_{43} = \underline{k}_{75}^T = \begin{bmatrix} \frac{gs}{4} - \frac{t}{2} - \frac{r}{2} & \frac{hc}{48} & -\frac{hb}{48} \\ -\frac{hc}{48} & -\frac{gt}{2} + \frac{s}{4} - \frac{r}{2} & \frac{fa}{24} \\ \frac{hb}{48} & \frac{fa}{24} & -\frac{gr}{2} + \frac{s}{4} - \frac{t}{2} \end{bmatrix}$$

$$\underline{k}_{51} = \underline{k}_{84}^T = \begin{bmatrix} -\frac{gs}{2} - \frac{t}{2} + \frac{r}{4} & -\frac{fc}{24} & \frac{hb}{48} \\ -\frac{fc}{24} & -\frac{gt}{2} + \frac{r}{4} - \frac{s}{2} & \frac{ha}{48} \\ -\frac{hb}{48} & -\frac{ha}{48} & \frac{gr}{4} - \frac{s}{2} - \frac{t}{2} \end{bmatrix}$$

$$\underline{k}_{52} = \underline{k}_{64}^T = \begin{bmatrix} \frac{gs}{2} - t + \frac{r}{2} & \frac{hc}{24} & -\frac{fb}{48} \\ -\frac{hc}{24} & -gt + \frac{r}{2} + \frac{s}{2} & \frac{ha}{24} \\ -\frac{fb}{48} & -\frac{ha}{24} & \frac{gr}{2} + \frac{s}{2} - t \end{bmatrix}$$

$$k_{53} = k_{74}^T = \begin{bmatrix} -gs + \frac{t}{2} + \frac{r}{2} & -\frac{hc}{24} & \frac{hb}{24} \\ \frac{hc}{24} & \frac{gt}{2} + \frac{r}{2} - s & -\frac{fa}{48} \\ -\frac{hb}{24} & -\frac{fa}{48} & \frac{gr}{2} + \frac{t}{2} - s \end{bmatrix}$$

$$k_{54} = \begin{bmatrix} -\frac{gs}{4} - \frac{t}{4} - \frac{r}{4} & -\frac{fc}{48} & \frac{fb}{48} \\ -\frac{fc}{48} & -\frac{gt}{4} - \frac{r}{4} - \frac{s}{4} & \frac{fa}{48} \\ \frac{fb}{48} & \frac{fa}{48} & -\frac{gr}{4} - \frac{s}{4} - \frac{t}{4} \end{bmatrix}$$

$$k_{61} = k_{82}^T = \begin{bmatrix} \frac{gs}{4} - \frac{t}{2} - \frac{r}{2} & -\frac{hc}{48} & -\frac{hb}{48} \\ \frac{hc}{48} & -\frac{gt}{2} - \frac{r}{2} + \frac{s}{4} & -\frac{fa}{24} \\ \frac{hb}{48} & -\frac{fa}{24} & -\frac{gr}{2} + \frac{s}{4} - \frac{t}{2} \end{bmatrix}$$

$$k_{62} = \begin{bmatrix} -\frac{gs}{4} - \frac{t}{4} - \frac{r}{4} & \frac{fc}{48} & \frac{fb}{48} \\ \frac{fc}{48} & -\frac{gt}{4} - \frac{r}{4} - \frac{s}{4} & -\frac{fa}{48} \\ \frac{fb}{48} & -\frac{fa}{48} & -\frac{gr}{4} - \frac{s}{4} - \frac{t}{4} \end{bmatrix}$$

$$k_{63} = k_{72}^T = \begin{bmatrix} \frac{gs}{2} + \frac{t}{2} - r & -\frac{fc}{48} & -\frac{hb}{24} \\ -\frac{fc}{48} & \frac{gt}{2} - r + \frac{s}{2} & \frac{ha}{24} \\ \frac{hb}{24} & -\frac{ha}{24} & -gr + \frac{s}{2} + \frac{t}{2} \end{bmatrix}$$

$$k_{71} = k_{83}^T = \begin{bmatrix} -\frac{gs}{2} + \frac{t}{4} - \frac{r}{2} & \frac{hc}{48} & -\frac{fb}{24} \\ -\frac{hc}{48} & \frac{gt}{4} - \frac{r}{2} - \frac{s}{2} & -\frac{ha}{48} \\ -\frac{fb}{24} & \frac{ha}{48} & -\frac{gr}{2} - \frac{s}{2} + \frac{t}{4} \end{bmatrix}$$

$$k_{73} = \begin{bmatrix} -\frac{gs}{4} - \frac{t}{4} - \frac{r}{4} & \frac{fc}{48} & -\frac{fb}{48} \\ \frac{fc}{48} & -\frac{gt}{4} - \frac{r}{4} - \frac{s}{4} & \frac{fa}{48} \\ -\frac{fb}{48} & \frac{fa}{48} & -\frac{gr}{4} - \frac{s}{4} - \frac{t}{4} \end{bmatrix}$$

$$k_{81} = \begin{bmatrix} -\frac{gs}{4} - \frac{t}{4} - \frac{r}{4} & -\frac{fc}{48} & -\frac{fb}{48} \\ -\frac{fc}{48} & -\frac{gt}{4} - \frac{r}{4} - \frac{s}{4} & -\frac{fa}{48} \\ -\frac{fb}{48} & -\frac{fa}{48} & -\frac{gr}{4} - \frac{s}{4} - \frac{t}{4} \end{bmatrix}$$

The stiffness matrix k is symmetrical. This implies that the submatrices have the relationship

$$k_{ij} = k_{ji}^T \quad \text{for } i = 1, 2, \dots, 8 \text{ and } j = 1, 2, \dots, 8.$$

The stiffness matrix given above is derived with respect to the local co-ordinates shown in figure (3.3). Since these axes are chosen parallel to the element boundaries, the same set of local co-ordinates can be used for all the solid elements. These, in turn, can be chosen to be parallel to the global axes of the complete system. As mentioned earlier, a co-ordinate transformation is thus unnecessary. Therefore, the stiffness matrix given above can be used in the form presented.

The stiffness matrix of the solid element is a full 24 x 24 matrix. However, it is also symmetric. Therefore, only 300 elements in the lower triangle need to be constructed once and for all and stored. In the program this lower triangle, for each type of element, was stored in a one dimensional row by row sequence. A unique relationship exists between the location of an element in the stiffness matrix and the address of that element in the one dimensional storage array. This is:

$$l = \frac{i(i-1)}{2} + j \quad 3.9$$

with $i \geq j$,

where i is the row number and j is the column number of an element in the stiffness matrix, and l is the address of the same element in the one dimensional array.

3.2.3 Calculation of the strains and the stresses in the solid element

Once the vector of the nodal displacements $\{X\}$ is obtained from an analysis, the strains at any point in the element can be calculated from equation (3.5). This is achieved by substituting the co-ordinates of the point in the B matrix derived in the previous sub-section. The stresses at the same point are calculated from equation (3.6) by premultiplying the strain vector by the D matrix evaluated for that element from equation (3.6.1).

It is usual to compute the stresses and the strains at the centroid of the element. Substituting the centroidal co-ordinates, $(\frac{a}{2}, \frac{b}{2}, \frac{c}{2})$, in the expression for B , the matrix can be evaluated at this point. The B matrix for the centroid is given in table

[illegible]

Table 3.1 **B** matrix for the centroid of the rectangular paralleloiped element

(3.1). The storage of this matrix for all the elements with different values of a, b and c, for use in equation (3.5) to calculate the strains in each step of the non-linear analysis, needs $3 \times 24 \times \text{NTE}$ elements. Here, NTE is the number of types of elements with different sets of a, b and c. On the other hand, repeated evaluation of this matrix for all the elements at each stage of loading is expensive on the computer time. It was, therefore, decided to perform the matrix multiplication of equation (3.5) by hand and write down explicit expressions for the strain components. These are,

$$\epsilon_x = \frac{1}{4a} (-u_1 + u_2 - u_3 - u_4 + u_5 - u_6 + u_7 + u_8) \quad 3.10a$$

$$\epsilon_y = \frac{1}{4b} (-v_1 - v_2 + v_3 - v_4 + v_5 + v_6 - v_7 + v_8) \quad 3.10b$$

$$\epsilon_z = \frac{1}{4c} (-w_1 - w_2 - w_3 + w_4 - w_5 + w_6 + w_7 + w_8) \quad 3.10c$$

$$\gamma_{xy} = \frac{1}{4a} (-v_1 + v_2 - v_3 - v_4 + v_5 - v_6 + v_7 + v_8) + \frac{1}{4b} (-u_1 - u_2 + u_3 - u_4 + u_5 + u_6 - u_7 + u_8) \quad 3.10d$$

$$\gamma_{yz} = \frac{1}{4b} (-w_1 - w_2 + w_3 - w_4 + w_5 + w_6 - w_7 + w_8) + \frac{1}{4c} (-v_1 - v_2 - v_3 + v_4 - v_5 + v_6 + v_7 + v_8) \quad 3.10e$$

$$\gamma_{zx} = \frac{1}{4a} (-w_1 + w_2 - w_3 - w_4 + w_5 - w_6 + w_7 + w_8) + \frac{1}{4c} (-u_1 - u_2 - u_3 + u_4 - u_5 + u_6 + u_7 + u_8) \quad 3.10f$$

These expressions were used in the computer program to calculate the strains at the centroid of an element from its nodal displacements. Similarly, direct expressions for stresses in terms of the strains were written by expanding equation (3.6). These expressions were used in the program to calculate the stresses at

the centroid of an element. This scheme of calculation of the strains and the stresses resulted in a considerable saving in both computer time and storage.

3.2.4 Calculation of the principal stresses

In figure (3.4) the Cartesian components of stress at a point in space are σ_x , σ_y , σ_z , τ_{xy} , τ_{yz} and τ_{zx} . Let σ_A be a principal stress acting on the principal plane ABC. Also let the normal to this plane have direction cosines l , m and n with respect to the x , y , z axes.

The equilibrium of the tetrahedron OABC can be expressed as:

$$\left\{ \begin{bmatrix} \sigma_x & \tau_{xy} & \tau_{zx} \\ \tau_{xy} & \sigma_y & \tau_{yz} \\ \tau_{zx} & \tau_{yz} & \sigma_z \end{bmatrix} - \sigma_A \begin{bmatrix} 1 & 0 & 0 \\ 0 & 1 & 0 \\ 0 & 0 & 1 \end{bmatrix} \right\} \begin{bmatrix} l \\ m \\ n \end{bmatrix} = \{0\} \quad 3.11$$

This equation can also be written in the form:

$$[\underline{M} - \lambda \underline{I}] \{q\} = \{0\}$$

which has a non-trivial solution only if the determinant

$$|\underline{M} - \lambda \underline{I}| = 0 \quad 3.12$$

The eigenvalues of equation (3.11) are the principal stresses and the eigenvector for each gives the corresponding values of l , m and n . It is possible to compute the principal stresses and their direction cosines by using a self-programmed or a package eigenvalue routine (e.g. NAG library routine F02ABA/F). But for a 3×3 matrix it was found that the repeated use of such a routine was uneconomical. A closed form solution proved to be more economical.

Expanding the determinant in equation (3.12), the following cubic equation is obtained.

$$\sigma_A^3 - J_1 \sigma_A^2 + J_2 \sigma_A - J_3 = 0 \quad 3.13$$

in which $J_1 = \sigma_x + \sigma_y + \sigma_z$,

$$J_2 = \sigma_x \sigma_y + \sigma_y \sigma_z + \sigma_z \sigma_x - \tau_{yz}^2 - \tau_{xz}^2 - \tau_{xy}^2,$$

and $J_3 = \sigma_x \sigma_y \sigma_z - \sigma_x \tau_{yz}^2 - \sigma_y \tau_{xz}^2 - \sigma_z \tau_{xy}^2 + 2\tau_{xy} \tau_{yz} \tau_{xz}$

are the first, the second and the third stress invariants respectively. A closed form solution for the three roots of a cubic equation has been given by Spiegel (1968). The solution of equation (3.13) is given explicitly below:

$$\begin{aligned} \text{Let } Q &= \frac{3J_2 - J_1^2}{9} \\ \text{and } R &= \frac{-9J_1 J_2 + 27J_3 + 2J_1^3}{54} \end{aligned}$$

When equation (3.13) has three real and unequal roots, the discriminant,

$$d = Q^3 + R^2,$$

is negative. The principal stresses, in this case, are given by:

$$\sigma_{A1} = 2\sqrt{-Q} \cos\left(\frac{\theta}{3}\right) + \frac{J_1}{3} \quad 3.14a$$

$$\sigma_{A2} = 2\sqrt{-Q} \cos\left(\frac{\theta}{3} + 120^\circ\right) + \frac{J_1}{3} \quad 3.14b$$

$$\sigma_{A3} = 2\sqrt{-Q} \cos\left(\frac{\theta}{3} + 240^\circ\right) + \frac{J_1}{3} \quad 3.14c$$

$$\text{where } \cos \theta = R/\sqrt{-Q^3}$$

If d is equal to zero, at least two of the principal stresses are equal. The principal stresses, in this case, are given by:

$$\sigma_{A1} = 2R^{1/3} + \frac{J_1}{3} \quad 3.15a$$

$$\sigma_{A2} = \sigma_{A3} = -R^{1/3} + \frac{J_1}{3} \quad 3.15b$$

Having obtained the values of the principal stresses from equations (3.14) or (3.15), it is necessary to calculate the direction cosines of each of these. Substituting the value of a principal stress, σ_A , in equation (3.11), a set of simultaneous equations is obtained; thus:

$$(\sigma_x - \sigma_A) \ell + \tau_{xy} m + \tau_{zx} n = 0 \quad 3.16a$$

$$\tau_{xy} \ell + (\sigma_y - \sigma_A) m + \tau_{yz} n = 0 \quad 3.16b$$

$$\tau_{zx} \ell + \tau_{yz} m + (\sigma_z - \sigma_A) n = 0 \quad 3.16c$$

Solving these by elimination, and remembering that $\ell^2 + m^2 + n^2 = 1$, explicit expressions for the values of ℓ , m and n for this principal stress are obtained. These are:

$$\ell = b_2 n \quad 3.17a$$

$$m = b_1 n \quad 3.17b$$

$$\text{and } n = \frac{1}{\sqrt{(1 + b_1^2 + b_2^2)}} \quad 3.17c$$

$$\text{where } b_1 = \frac{\tau_{zx}^2 - (\sigma_x - \sigma_A)(\sigma_z - \sigma_A)}{\tau_{yz}(\sigma_x - \sigma_A) - \tau_{xy}\tau_{zx}}$$

$$\text{and } b_2 = -\frac{\tau_{xy}b_1 + \tau_{zx}}{\sigma_x - \sigma_A}$$

A subroutine, PRINC, was written and included in the main finite element program to calculate the principal stresses and their

direction cosines from equations (3.14), (3.15) and (3.17) directly.

3.3 NON-LINEAR ANALYSIS TECHNIQUE

3.3.1 Introduction

The rectangular parallelepiped element developed earlier in this chapter is used extensively in this thesis to represent the soil under a structure. Most soils exhibit a non-linear stress-strain behaviour. This causes non-linearity in the load-deflection and the load-bending moment diagrams of the structure resting on the soil. The non-linearity of the soil properties must, therefore, be taken into account in the finite element analysis of the structure and its supporting soil. A functional representation of the highly non-linear $\tau_{\text{oct}} - \gamma_{\text{oct}}$ curves of soil was developed in chapter 2. A technique of analysis, in which the properties of the solid elements are represented by these curves, is described in the following sections.

3.3.2 Non-linear finite element analysis

In the general finite element formulation, the following two basic assumptions are made.

- (1) The strain-displacement relationship is linear and is given by

$$\{\underline{\epsilon}\} = \nabla \{\underline{U}\}$$

where $\{\underline{\epsilon}\}$ is the strain at a point in the element and $\{\underline{U}\}$ is the displacement vector at that point. ∇ is a suitable linear operator well known in the theory of elasticity, cf. Timoshenko and Goodier(1970).

- (2) The stress-strain relationship is linear and is given by

$$\{\sigma\} = \underline{D} \{\epsilon\}$$

where $\underline{\sigma}$ is the stress vector and \underline{D} is the elastic properties matrix.

The violation of the first of these two assumptions means that the fundamental variational formulation of the finite element method need to be altered. However, for small displacements, the linear strain-displacement relationship is considered to be sufficiently accurate. Geometrical non-linearity due to large displacements is excluded from this thesis. Non-linearity of the material properties, on the other hand, can be catered for without changing the fundamental finite elements concept. This is achieved by invoking the non-linear elasticity principle described in chapter 2. Thus the stress-strain relationship can be modified to:

$$\{\sigma\} = [\underline{D}(\sigma, \epsilon)] \{\epsilon\} \quad 3.18$$

Here the material properties matrix $\underline{D}(\sigma, \epsilon)$ is a function of the stress and the strain level and is no longer a constant. Similarly, the load-displacement relationship of the system can be written as:

$$\{\underline{L}\} = [\underline{K}(L, X)] \{\underline{X}\} \quad 3.19$$

where $\{\underline{L}\}$ is the known vector of applied loads and $\{\underline{X}\}$ is the vector of unknown displacements. The stiffness matrix $\underline{K}(L, X)$ is a function of the applied loads and the displacements.

The methods of non-linear analysis, utilizing the relationships (3.18) and (3.19), are either of an iterative or of an incremental form, Zienkiewicz (1977). Both of these methods require a repeated solution of the set of equations (3.19).

A typical load-deflection diagram of a structure supported on soil is represented in figure (3.5), where L is the applied load and X is the resulting deflection. In this figure point A represents the actual state in the structure when the total load acting is L^* and the resulting displacement is X^* .

Several schemes of iteration can be adopted to obtain the point A by the analysis. In the direct iteration method, shown in figure (3.5), the first solution is obtained by constructing the stiffness matrix, \underline{K}_0 , with the initial tangent moduli of the non-linear elements. This stiffness matrix is successively modified to \underline{K}_1 , \underline{K}_2 etc. by utilizing the secant moduli of the elements at the current levels of strains. Each time the structure is subjected to the full load, L^* .

The convergence of iteration is improved by the Newton-Raphson method, figure (3.6a). The analysis is started as before with the initial tangent moduli. However, the solution is successively improved by reanalysing the system for the "unbalanced" loads, ΔL_0 , ΔL_1 etc., as shown in figure (3.6a). In each analysis, the stiffness matrices, \underline{K}_1 , \underline{K}_2 etc., are constructed with the tangent moduli at the current level of strain in the elements. The unbalanced loads are calculated by transforming the difference, σ_0 , between the computed and the actual stresses for the current value of strain. Thus:

$$\{\Delta L\} = \int_{\text{volume}} B^T \{\sigma_0\} dV$$

In both the above schemes of iteration, the stiffness matrix has to be constructed and equation (3.19) has to be solved explicitly in each cycle. A modification of the Newton-Raphson method, in which the same initial stiffness matrix, \underline{K}_0 , is used repeatedly,

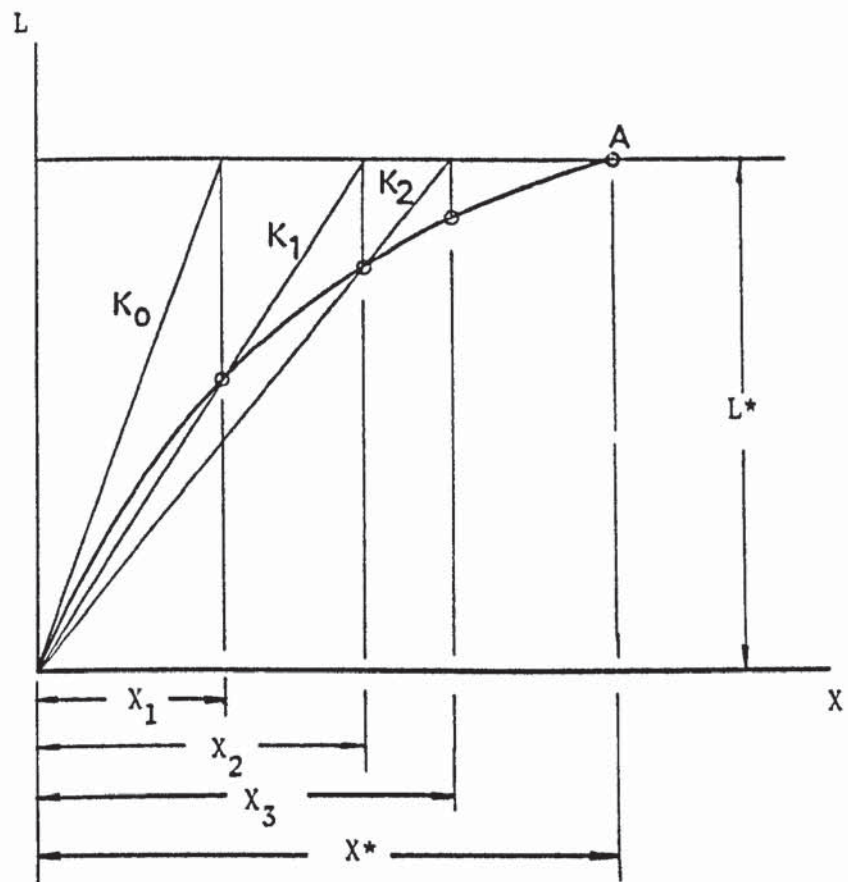
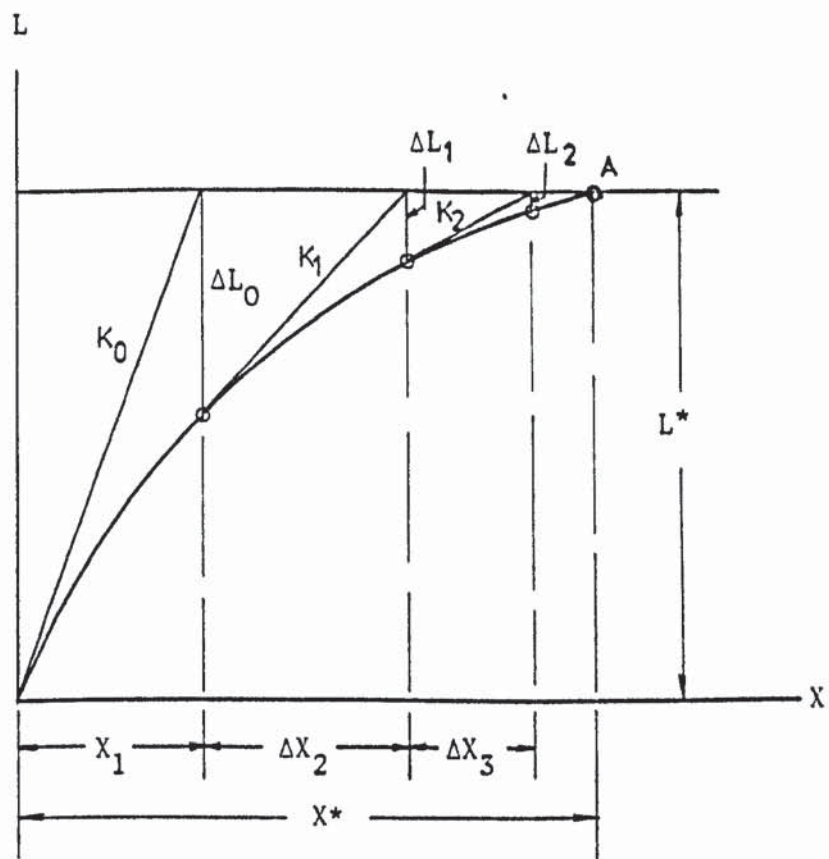
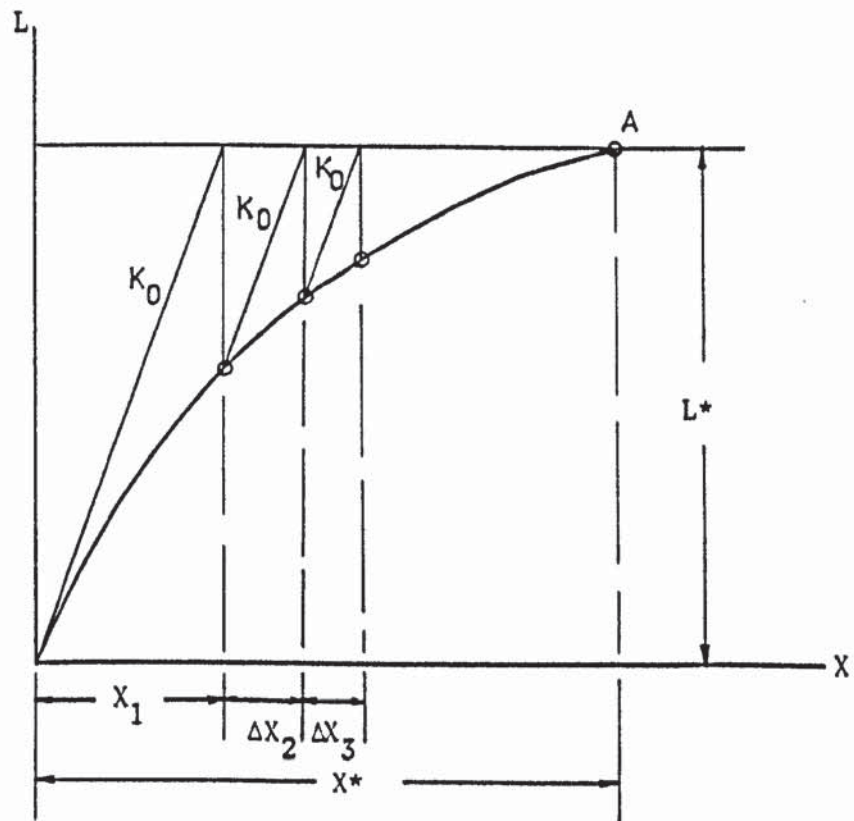


FIGURE 3.5 DIRECT ITERATION METHOD OF NON-LINEAR ANALYSIS



a) Newton-Raphson method



b) Modified Newton-Raphson method

FIGURE 3.6 NEWTON-RAPHSON ITERATION METHODS OF NON-LINEAR ANALYSIS

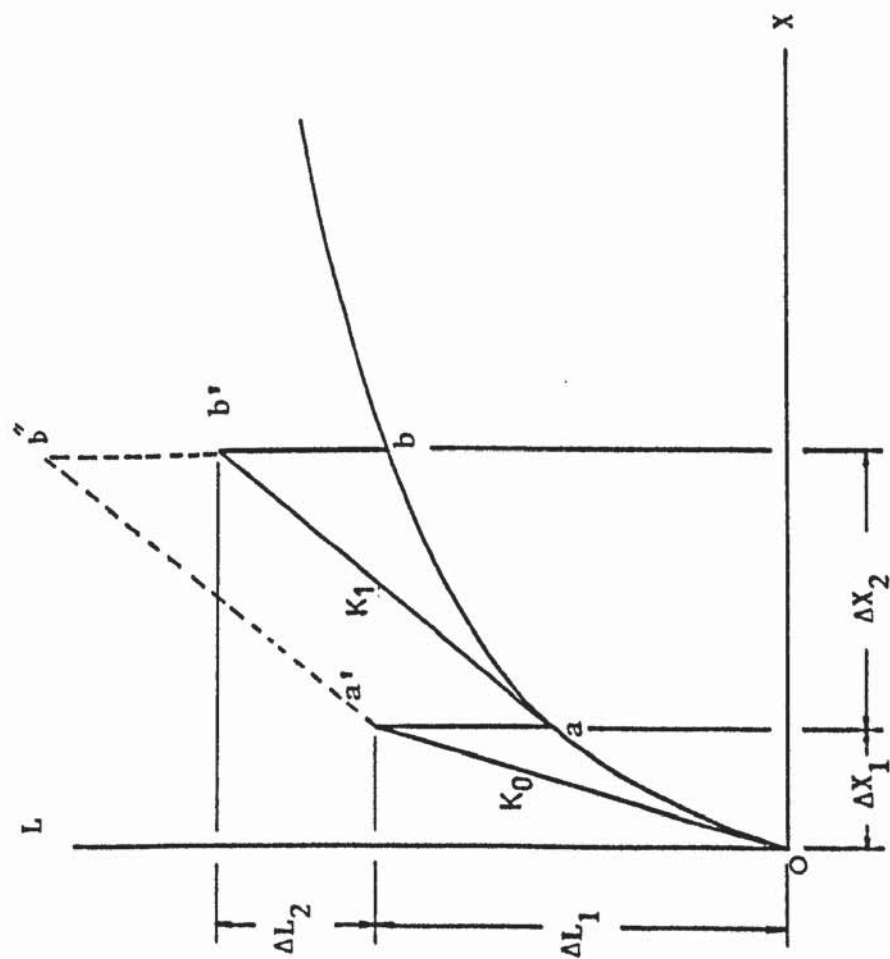
is shown in figure (3.6b). However, the convergence in this method is relatively slow. The Newton-Raphson iteration schemes are also called the "stress transfer" methods, as the residual stresses are converted to forces and transferred to the element nodes.

In all the above schemes, convergence is not always guaranteed, while the speed of the convergence is often unpredictable. Furthermore, the analysis produces only the final point on the load-deflection diagram and no knowledge of the intermediate states can be gained. In the non-linear "incremental" analysis, on the other hand, not only convergence is guaranteed but the load-deflection history can be traced upto the final applied load. Such a method has been extensively used in the past to analyse structure and/or soil problems, Majid and Craig (1972), Desai (1971) and Majid and Cunnell (1976). An incremental analysis technique is also used in this thesis. It is described here in the context of the three dimensional finite element analysis of a structure and its supporting soil.

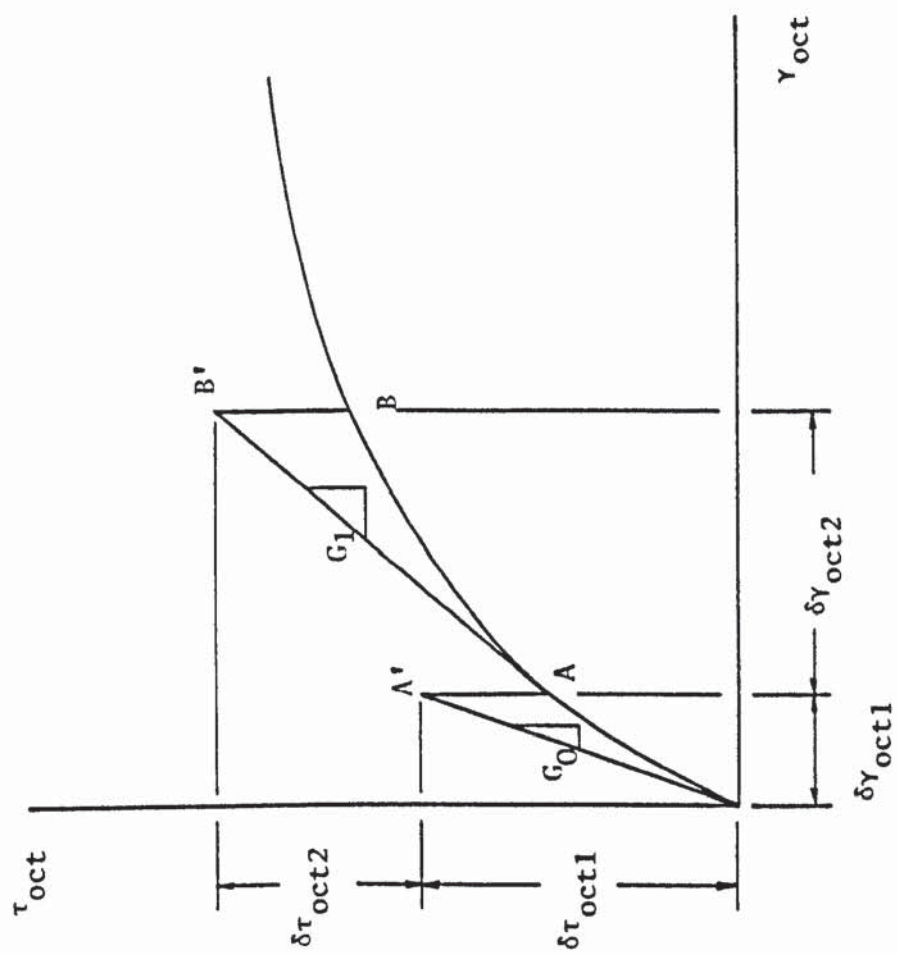
3.3.3 The incremental method

The non-linear three dimensional soil properties are expressed in terms of curves of octahedral shear stress and octahedral shear strain. Solid elements representing the soil under a structure have different values of initial octahedral normal stress. This influences their stress-strain behaviour under subsequent loading. Let the $\tau_{oct} - \gamma_{oct}$ curve shown in figure (3.7b) represent the stress-strain properties of a particular solid element in the mesh.

In the incremental method of analysis, the total load on the



a) Load-deflection diagram



b) Stress-strain diagram of an element

FIGURE 3.7 INCREMENTAL ANALYSIS SCHEME

structure is divided into a number of small increments. The system of equations (3.19) is solved repeatedly with each of these incremental loads. The stiffness matrix is obtained each time by substituting the values of the shear modulus, G , that correspond to the current level of the octahedral shear strain in each element.

At the unloaded state, the solid elements do not have any stress or strain. The initial tangent shear modulus, G_0 , for each element is calculated from a spline function representation of the $\tau_{oct} - \gamma_{oct}$ curve shown in figure (3.7b). This is used to construct the initial stiffness matrix, K_0 , figure (3.7a). A small increment of load ΔL_1 is applied and the resulting displacements ΔX_1 are obtained by solving the equation:

$$\{\Delta L\}_1 = K_0 \{\Delta X\}_1 \quad 3.20$$

The increments of strain due to this increment of load are calculated from:

$$\{\Delta \epsilon\}_1 = B \{\Delta X\}_1 \quad 3.21$$

The incremental stresses are calculated from the incremental strains as:

$$\{\Delta \sigma\}_1 = D_0 \{\Delta \epsilon\}_1 \quad 3.22$$

The elastic properties matrix D_0 in equation (3.22) is obtained by using the initial shear moduli, G_0 , of each element. For the solid element whose $\tau_{oct} - \gamma_{oct}$ curve is represented by figure (3.7b), the increments of the octahedral shear stress and the octahedral shear strain due to the load ΔL_1 is $\delta\tau_{oct1}$ and $\delta\gamma_{oct1}$ respectively. These represent the point A' on the figure. The point on the load-

deflection diagram of figure (3.7a) obtained after the application of the first incremental load, ΔL_1 , is a' . Point A corresponds to the strain $\delta\gamma_{oct1}$ on the actual $\tau_{oct} - \gamma_{oct}$ curve in figure (3.7b). The amount AA' is thus the error in the theoretical τ_{oct} of this element. The corresponding error in the load-deflection diagram is the amount aa' in figure (3.7a).

The tangent slope of the $\tau_{oct} - \gamma_{oct}$ curve at point A is evaluated by the spline functions. The value G_1 , thus obtained, gives the tangent shear modulus of the element at the current level of γ_{oct} . These new values of the shear modulus for each element are substituted into the stiffness matrix to obtain a new matrix. A further increment of load ΔL_2 is now applied and the structure and the soil are reanalysed with this new stiffness matrix. Such an analysis gives a new set of displacements ΔX_2 for the increment of load ΔL_2 alone. Equations (3.21) and (3.22), applied to this increment, give the increments of strains and stresses respectively. The corresponding increments in τ_{oct} and γ_{oct} in the single element are $\delta\tau_{oct2}$ and $\delta\gamma_{oct2}$ respectively. The total octahedral shear strain is obtained as the sum of $\delta\tau_{oct1}$ and $\delta\tau_{oct2}$ and the total octahedral shear strain as the sum of $\delta\gamma_{oct1}$ and $\delta\gamma_{oct2}$. The tangent shear modulus at point B on the $\tau_{oct} - \gamma_{oct}$ curve corresponding to the current total γ_{oct} is obtained. This defines the stiffness matrix for the next increment of the load. The procedure is repeated for successive increments of load until all the loads have been applied or failure has been reached.

In general, the incremental analysis number j is performed with the incremental load $\{\Delta L\}_j$ and with the tangent stiffness matrix $[K]_{j-1}$ corresponding to the shear moduli values at the end of the

last increment. The displacements, the strain and the stresses are successively accumulated to give the current state of these values.

It is evident that this method traces the load-deflection diagram of the structure and the soil system as well as the structural member forces and the stress-strain diagram of each soil element. However, in each increment there is a discrepancy between the computed points A' and a' , and the actual points on the curves, A and a . For most structures and soils these curves are convex downwards, as shown in figure (3.7). In such cases the theoretical curves always under estimate the displacements and the strains. Nevertheless, this discrepancy can be kept to a minimum by choosing a sufficiently small increment of load in each step. An improved solution can also be obtained by performing a Newton-Raphson type of iteration for each increment. However, this is only achieved by performing additional repetitive solutions of equation (3.19). The results obtained by using the procedure just described indicate very good agreement with those obtained experimentally. It is, therefore, considered that improving the method by making use of the Newton-Raphson method, while possible, is costly and unnecessary.

The incremental analysis technique has the merit of producing a convergent solution in all the cases. The accuracy of the results up to any desired degree can be achieved by choosing suitable increment sizes. Sharp changes in the curvature of the load-deflection diagrams can also be traced by applying small increments of loads in these regions. The method is readily applicable to problems of non-linearity due to crack propagation. This problem is described in chapter 4. The incremental analysis scheme is extensively used in this thesis.

CHAPTER 4

TENSION SEPARATION AND CRACK PROPAGATION

4.1 INTRODUCTION

Brittle materials undergo physical separation in the form of cracks and fissures due to the development of tensile stresses. Such separations cause a stress redistribution in the system and account for its non-linear behaviour. A degree of strain softening can be detected in such a cracked system. The stress concentrations around the cracks may lead to a drastic increase in the extent and the size of these cracks, which in turn cause further tensile stresses at the cracks.

In a complete system of a structure, its foundation and the supporting soil, non-linearity due to cracks and/or separations is possible. Separation may occur in any zone where the tensile stresses exceed the tensile strength of the material. This may be either within the soil mass or at the interface between the soil and the foundation. Experiments described in chapter 7 confirm this. Such a behaviour may also be experienced in many other types of structures and foundations.

As the soil is weak in tension, stress redistribution also occurs due to unsightly separations in the soil mass. However, such a separation within the mass of such materials as dry sand, is expected to be filled up by the neighbouring body of sand. This causes a complete redistribution of stresses as well as the actual material.

In some circumstances, the changed geometry of the system, due to cracks, may on subsequent loading, result in relaxation of the stresses in the cracked zone. This may cause the crack to close again.

On the other hand, new cracks can develop elsewhere in the system. Some of these may widen, bifurcate, extend in length or change direction. All these indicate a continuous change within the system until either equilibrium has been restored or failure is reached.

The purpose of this chapter is to develop and incorporate into the finite element analysis program, a method that takes the irregular behaviour described above into consideration. The method proposed is able to predict and allow the separation of the soil mass and/or the interface in a complete three dimensional system. The method is also able to follow the propagation of cracks and to arrest those that may show evidence of closure.

4.2 ANALYTICAL REPRESENTATION OF CRACKS

Appreciation of tensile weaknesses in the foundation materials has been shown by many research workers in the past. Leonards and Harr (1959) analysed an axisymmetrically loaded circular plate which was partially separated from the soil due to warping caused by temperature and shrinkage stresses. The foundation was assumed to be a Winkler model and the separation was only allowed to take place away from the central zone of the circle.

Tsai and Westmann (1967) extended Hetenyi's (1946) solution for a beam on an elastic Winkler type foundation to account for the poor tensile strength of the foundation. They introduced a modified relationship of load and displacement of a Winkler foundation with no tensile strength.

More recently finite element techniques have been applied to take account of cracking in physical systems. Ngo and Scordelis (1967) used triangular two dimensional finite elements to analyse reinforced

concrete beams with a predefined crack. The crack was included in the geometry of the finite element mesh as a gap of zero width between adjacent elements. Both the propagation and the arrest of cracks were beyond the scope of their approach.

Nilson (1968) used a similar technique in conjunction with a non-linear incremental analysis to predict the occurrence of a crack. A separation was manually inserted and the mesh reanalysed. Such a manual approach to the problem of crack propagation is possible. The effort, however, seems to be too high even for the simplest of problems.

Zienkiewicz, Valliappan and King (1968) utilized a stress transfer method for redistributing the tensile stresses by some restraining forces applied to the system. This was then reanalysed linear elastically with a reduced modulus in the direction of the tensile stress.

Phillips and Zienkiewicz (1967) used the above method of adjusting the stress level and the material property in the cracked zone to analyse concrete structures. Plane and axisymmetric finite elements were used in a non-linear incremental analysis.

Trikha and Edwards (1972) used a similar technique to predict cracks in prestressed concrete beams which had material nonlinearity. Only a two dimensional finite element approach was considered.

Riddington (1975) and Stafford Smith and Riddington (1977) used stiff linkage elements at the boundary between a masonry wall and its supporting beam to predict the separation between the two. When separation occurred at any point on the interface, the stiffness of the linkage element at that point was reduced to a low value to simulate a tensile failure.

The stress concentrations and the stress field singularities near a sharp crack have been investigated by workers in fracture mechanics. Alsharqi (1977) used an axisymmetric triangular finite element representation to analyse a solid of revolution with a sharp crack. The stress intensity at the tip of the crack was catered for by a special core type element which incorporated analytical solutions of stresses and displacements at the tip.

Most of the approaches described above are either inaccurate or inadequate because they consider cracking as a zone of material weakness. Majid and Al-Hashimi (1976) pointed out that a crack does not change the material properties. It only introduces a physical separation of the two parts of the material on either side. The separation was carried out by first introducing initially inactive joints to be associated with every active joint. These were then activated each time a crack occurred. This was done by separating the elements on one side of the crack from the parent joint and rejoining them to the new joint. For this purpose plane strain "triangular" and "isoparametric" quadrilateral finite elements were employed. Soil-cement samples with a constant elastic modulus in compression were considered. An incremental technique was used to follow the crack propagation upto and including failure. Cunnell (1974) also used the same technique with two dimensional isoparametric quadrilateral elements to analyse similar problems.

Majid and Al-Hashimi's (1976) method was used for two dimensional problems. It is considered that this method can be extended to cover the three dimensional cases studied here. This approach offers the possibility of initiation, extension, bifurcation, widening and closure of any pattern of cracks in the finite element mesh. It also

means that the crack width can be calculated at any stage of the loading. The logic of the method is easily programmable and an automatic crack propagation scheme is easily adaptable. This method constructs and solves the stiffness equations repeatedly as the loading progresses. The number of equations to be solved increases as new joints are activated. In this manner, as the cracks develop, the system becomes more flexible.

Based on the above approach, the development of a tension separation scheme applicable to non-linear three dimensional interaction problems is feasible. Such a scheme will be developed in the following sections. As the method would be included in a non-linear finite element program for complete structures and foundations, it is made entirely automatic.

4.3 DEVELOPMENT OF A TENSION SEPARATION METHOD

The method of automatic tension separation in a three dimensional finite element structural analysis proposed here is of a general nature. It can be applied to a wide variety of crack problems. Various forms of separation within the soil mass as well as at the interface between the structure and the soil can be experienced. Some typical patterns are shown in figure (4.1). Separations can occur between a wall or a slab of the structure and the surrounding soil. These are labelled AB, CD and EF in the figure. Separation may also occur between the soil and a boundary or a plane of symmetry as shown by GH. Cracks such as JK and LM within the soil mass both in the horizontal and the vertical directions are also likely.

4.3.1 Method of introducing a separation

The essence of the method is to assign two numbers to each joint in the finite element mesh that is likely to suffer a tension separation.

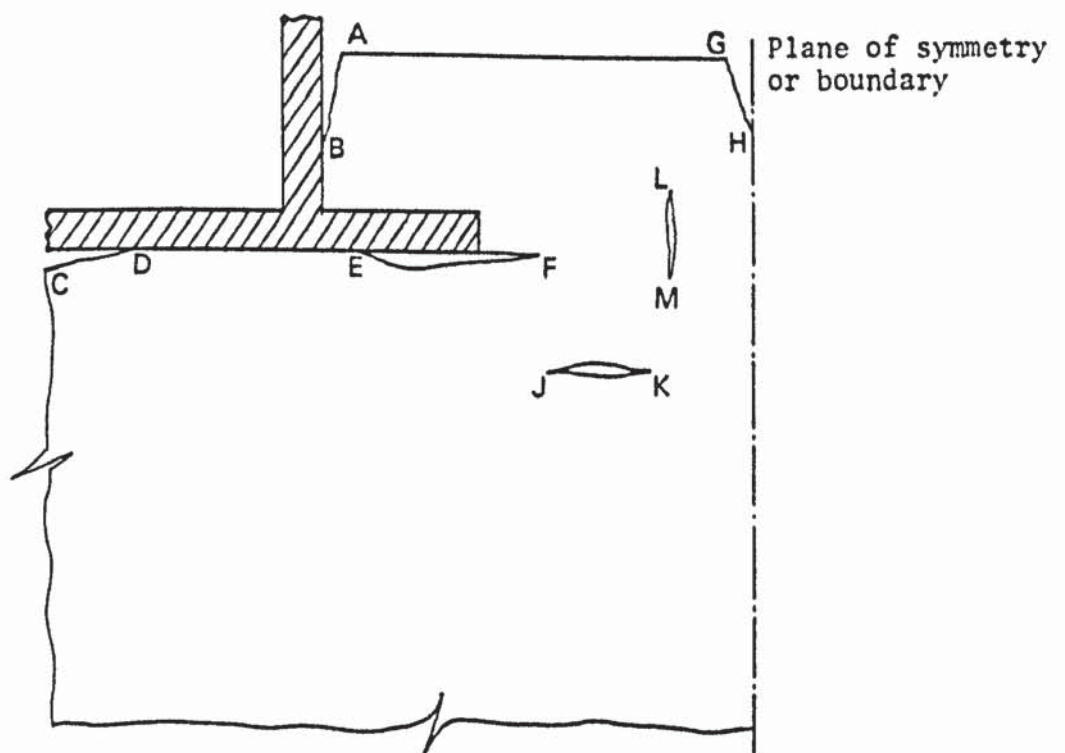
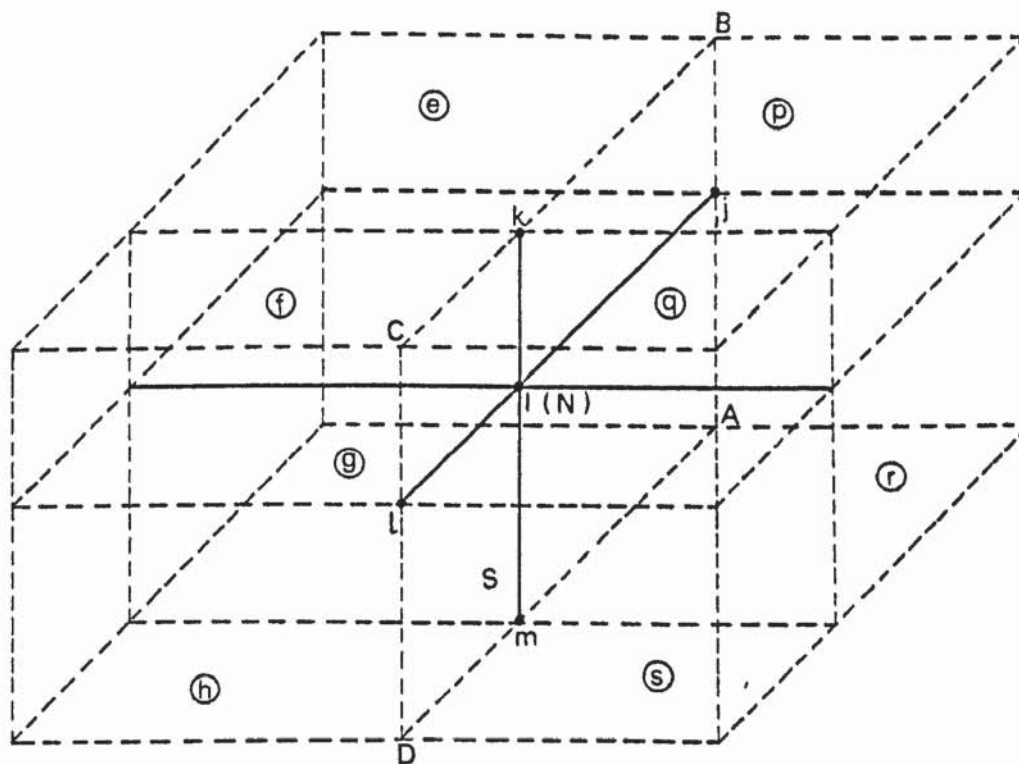


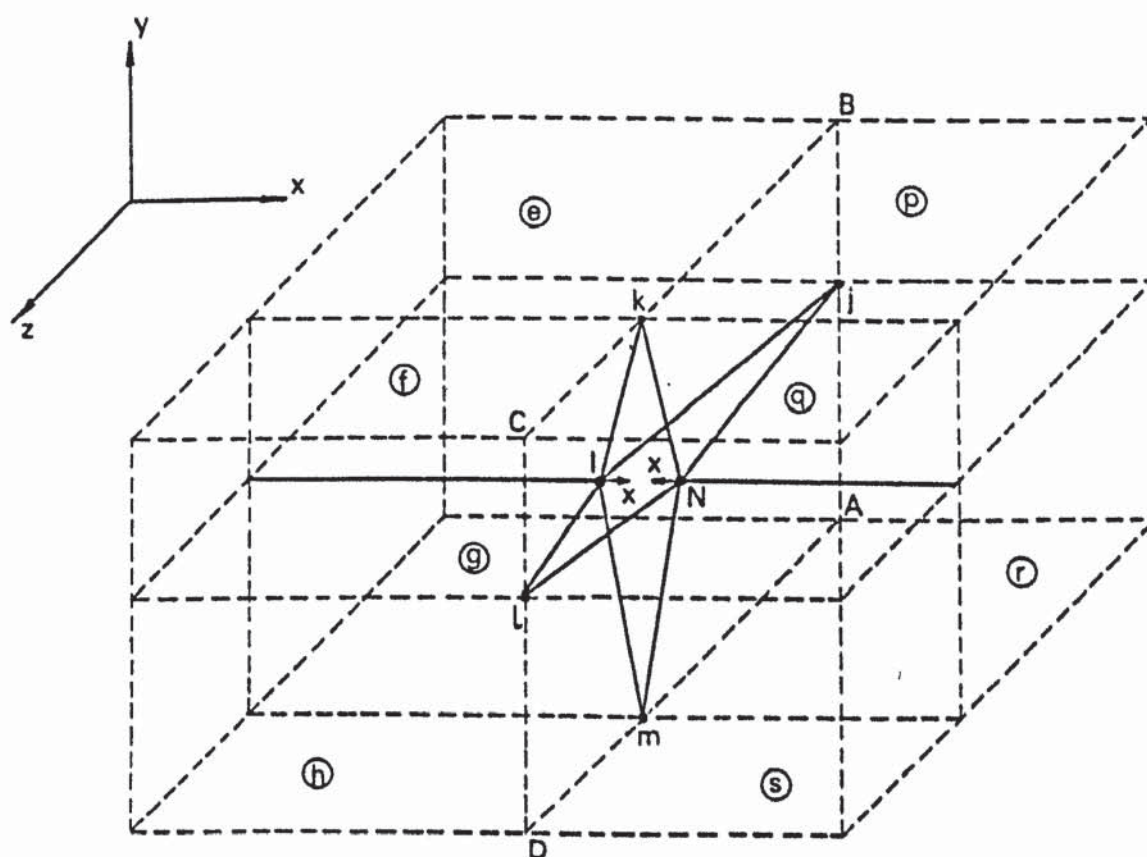
FIGURE 4.1 TYPICAL CRACKS IN A STRUCTURE-SOIL SYSTEM

ration. The joints are disconnected when such a separation is indicated. This takes place either within the soil mass or between a wall or a slab and the surrounding soil. This disconnection physically introduces a gap between adjacent elements meeting at that joint.

In figure (4.2a), (I) is a general joint in a three dimensional finite element mesh, which is considered to be likely to suffer a tensile stress. The joint is surrounded on all sides by eight rectangular parallelopiped solid elements. A joint (N) is associated with joint (I) and has the same co-ordinates in space as those of (I). Joint (N), however, has initially no degree of freedom and is simply a dummy joint associated with the active joint (I). To begin with, therefore, joint (N) will not take part in the finite element analysis and will not influence the calculation in any way. After the application of a number of increments of the loads, consider that tensile stress develops in a direction perpendicular to the plane ABCD, see figure (4.2). If the loading is continued, consider that at (I) the tensile stress is likely to exceed the tensile strength of the material. To cater for this, a separation at (I) is necessary to be introduced in the x-direction normal to the plane ABCD. This is achieved by altering the compatibility conditions between the elements on either side of the plane ABCD. The elements can no longer have a common node at (I). The elements p, q, r and s to the right of the plane ABCD must be disconnected from this joint. These are now connected to (N), which is activated by giving it its appropriate degrees of freedom. During the subsequent loading of the system, joint (N) is thus brought into action in the finite element analysis. The new "cracked" mesh, thus developed, is shown in figure (4.2b). The straight lines jl and km in the uncracked



(a) Uncracked state



(b) Cracked configuration

FIGURE 4.2 A GENERAL TENSION SEPARATION

mesh are now split into lines $j1l$, jNl , kIm and kNm with joint I to the left of N. These joints can now act independently and displace relative to each other in all directions.

In the uncracked state, all the eight elements e, f, g, h, p, q, r and s, contributed stiffness terms to joint (I). After the separation new rows and new columns are introduced to the stiffness matrix to correspond to the degrees of freedom of joint (N). Elements e, f, g and h will continue to contribute stiffness terms to (I). On the other hand, elements p, q, r and s will now contribute to rows and columns of joint (N). The dimension of the stiffness matrix thus increases by the extra number of rows and columns corresponding to the degrees of freedom of (N). As further cracks develop, the stiffness matrix continues to increase in size and the system becomes less stiff. It should be pointed out that, in the actual program, only the lower triangle of the stiffness matrix is stored and operated upon. Thus the increase in the stiffness matrix due to the columns of joint (N) is disregarded.

In the foregoing description a separation was permitted only in a direction normal to the boundaries of an element. In reality a separation occurs normal to the major principal tensile plane. The non-coincidence of element boundaries with this plane may lead to some error in the pattern of cracks. However, this is not a problem at the interface of a foundation and the soil, since the actual separation does, in fact, take place normal to such an interface. In a three dimensional stress system, the directions of the principal stresses are generally inclined in an arbitrary manner to the global axes. They are also changing continuously. This is due to the fact that as the applied loads increase and cracks propagate, the stresses

throughout the system change both in magnitude and in direction. However, it is not practicable to design the finite element mesh with element boundaries parallel to the principal planes at all the points. Neither is it viable to redesign the mesh with every change in the direction of the principal stress. An approximation is thus unavoidable. In the present method, a separation at a general joint was permitted only in the direction of the maximum tensile stress. It was considered that this would be a good approximation to the actual direction of the major principal tensile stress. During the theoretical analysis of the structures discussed in this thesis, the Cartesian axes were considered as the co-ordinate axes. Since the loads applied were always vertical it was considered that it is reasonable to assume that the principal axes were also parallel to the Cartesian axes. Furthermore, in the mass of the soil under a structure, a knowledge of the existence of a crack is considered to be significant even if its exact direction is not predicted. This is because the flexibility of the system in the cracked zone is increased by the inclusion of the separation whatever its direction is.

4.3.2 Criterion for the development of a crack

The structure - soil interaction problem is analysed by dividing the structure and the soil into suitable finite elements. Initially the finite element mesh is uncracked. The non-linear analysis is performed by an incremental technique. The total load is applied in small increments δP and the mesh is analysed repeatedly for these incremental loads. After each analysis the stress and the displacements are accumulated and the material properties are altered to conform with the current level of stress. A full description of the incremental approach has been given in chapter 3.

Figure (4.3a) represents the variation of the stress at a point with the external load. Consider that the system has already been analysed j times with j increments of load, each having a magnitude δP . Point 'A' in figure (4.3a) indicates the level of the applied load on the system and the corresponding state of a normal stress at a joint 'n' at this stage of the loading. As the loads are increased, let the letters i , j and k indicate three successive increment numbers. P_i and P_j are the total loads at the ends of increment numbers i and j respectively. The corresponding stresses at n are σ_i and σ_j . A linear extrapolation predicts the load P_k^* at which the stress at n reaches the tensile strength σ_t . Thus, from figure (4.3a),

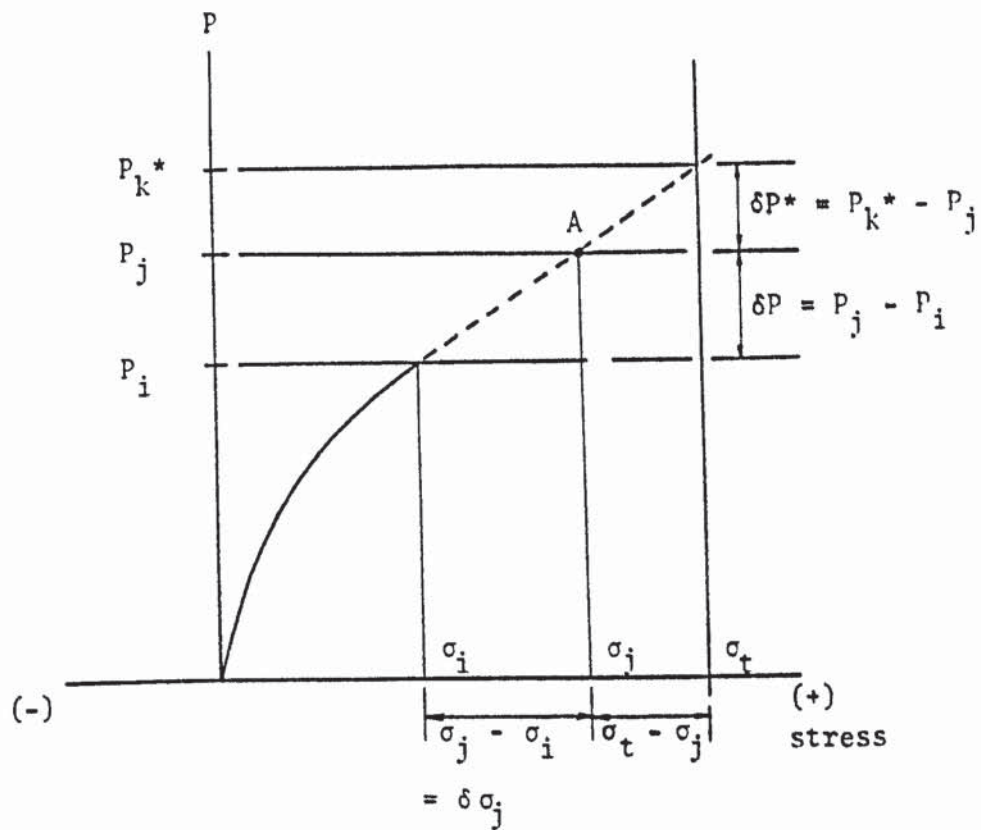
$$\frac{P_k^* - P_j}{P_j - P_i} = \frac{\sigma_t - \sigma_j}{\sigma_j - \sigma_i} \quad 4.1$$

Now $\delta P = P_j - P_i$ and if $\delta P^* = P_k^* - P_j$ and $\delta \sigma_j = \sigma_j - \sigma_i$, equation (4.1) becomes:

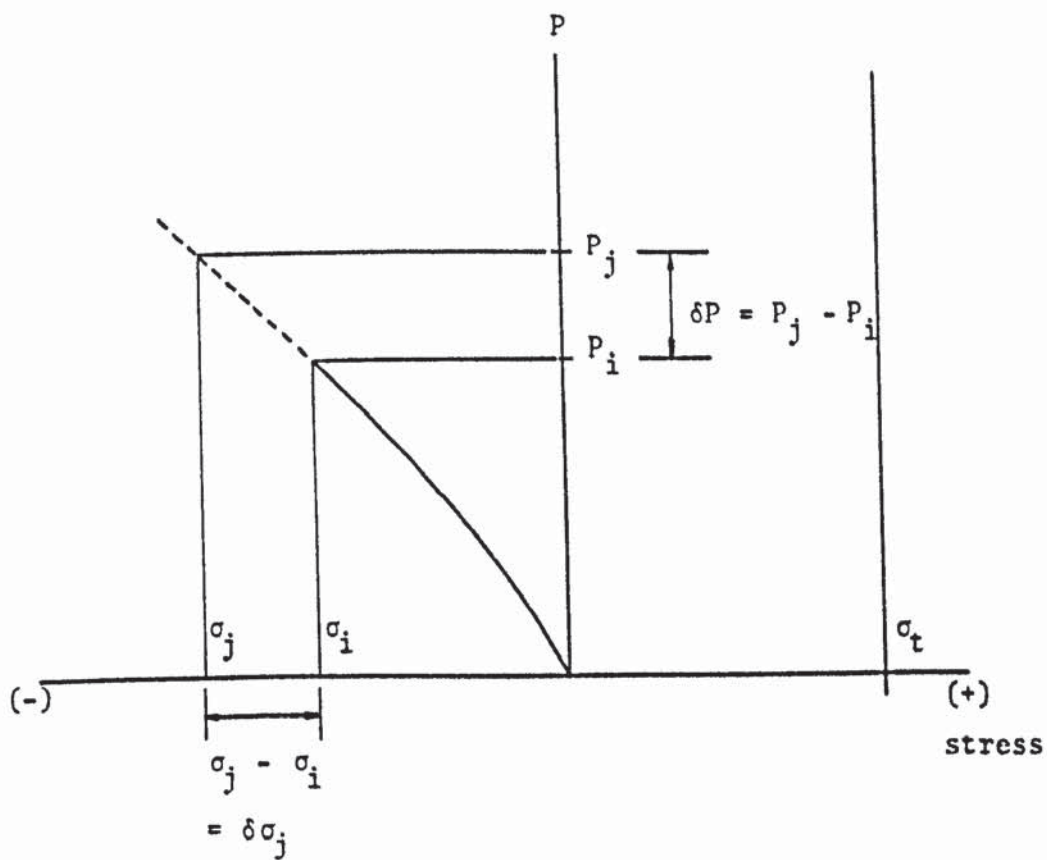
$$\frac{\delta P^*}{\delta P} = \frac{\sigma_t - \sigma_j}{\delta \sigma_j} \quad 4.2$$

If equal increments of load are used, then the total stress at n will reach the tensile strength σ_t when $(\delta P^*/\delta P)$ reaches a value of unity. A crack is then introduced at joint n for the next increment of the load.

In the above approach it can be seen that a value of $(\delta P^*/\delta P)$ slightly greater than unity would exclude a crack. On the other hand, a negative value of this fraction would initiate a crack in the next increment. It can be observed from figure (4.3a) and equation (4.2)

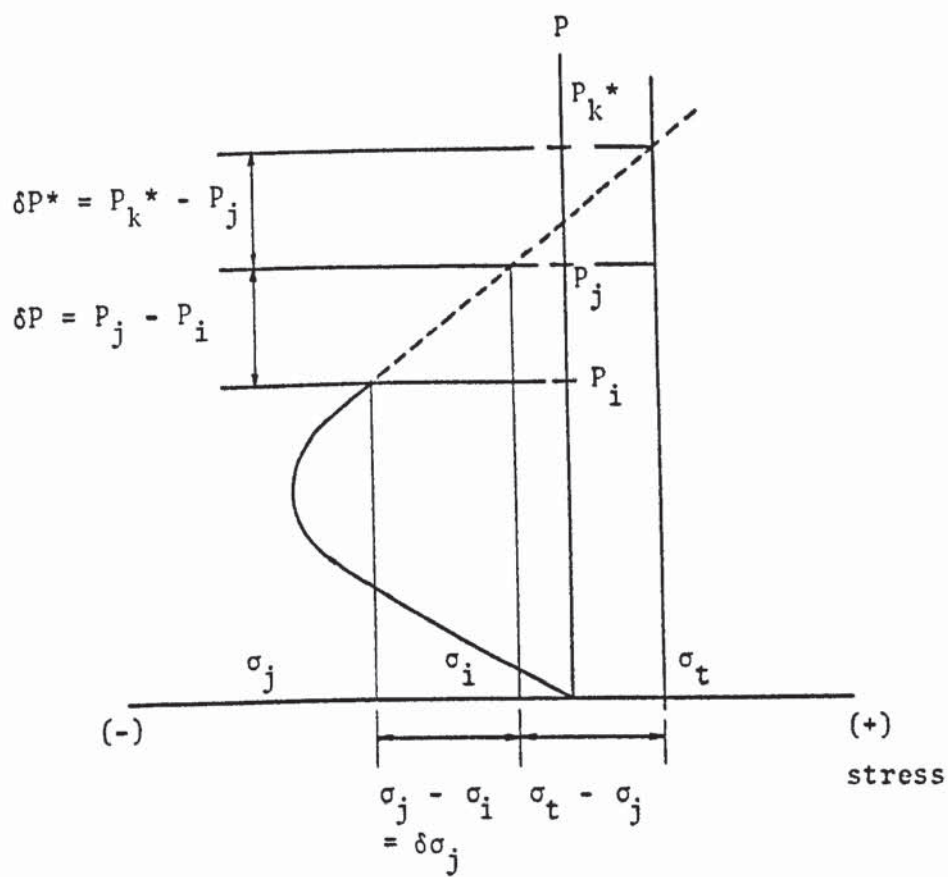


(a)

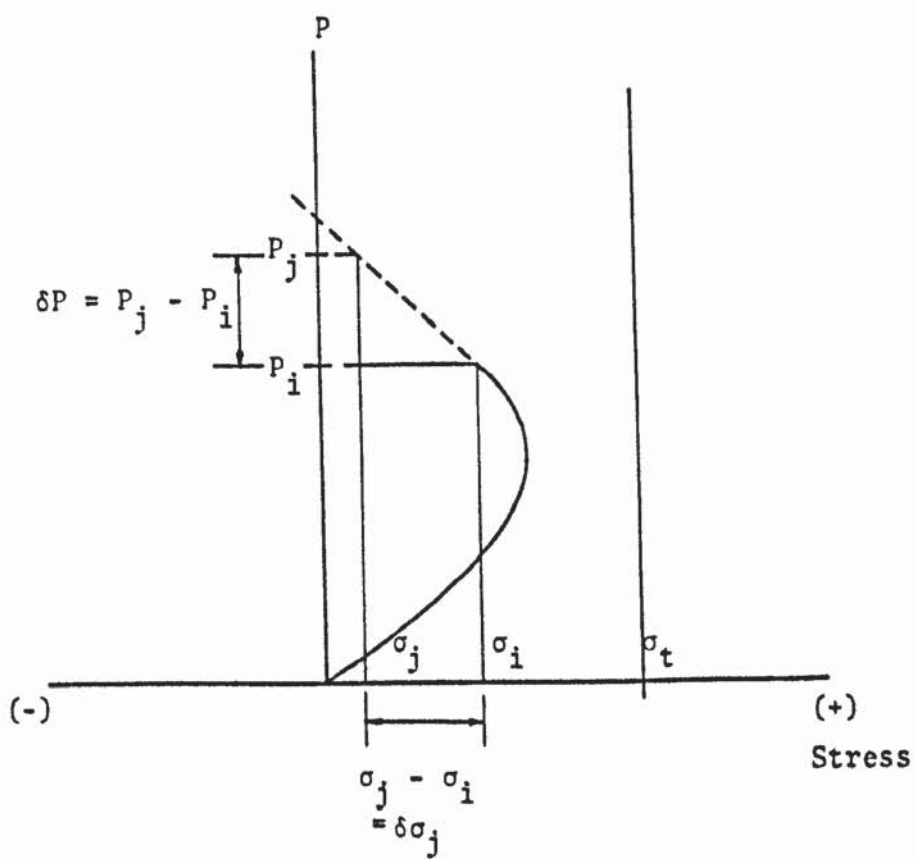


(b)

FIGURE 4.3 TYPICAL CASES OF LOAD-STRESS RELATIONSHIP
(continued to next page)



(c)



(d)

FIGURE 4.3 continued

that a negative value of $(\delta P^*/\delta P)$ means that the tensile strength σ_t has already been exceeded by the current stress σ_j . Thus limiting the value of $(\delta P^*/\delta P)$ to unity tends to under estimate the propagation of the cracks. As a measure of weighting against the chance of this happening, it was decided to limit the value of $(\delta P^*/\delta P)$ to 1.5 instead of unity. The criterion for the development of any new crack was thus selected to be,

$$\frac{\delta P^*}{\delta P} = \frac{\sigma_t - \sigma_j}{\sigma_j - \sigma_i} \leq 1.5 \quad 4.3$$

In this manner cracks that are likely to occur at any load between $P_j - \frac{\delta P}{2}$ and $P_j + \frac{\delta P}{2}$ are included in the j th incremental analysis.

So far it has been assumed that cracks can only take place in a zone which is initially in tension and continue to remain so. Experience showed that, during the loading process, the variation of stress in a zone can have different forms. Three such cases are shown in figures (4.3b), (c) and (d). Figure (4.3b) shows a case where the stresses are initially compressive and remain so throughout the loading history. A separation can never occur in this case. Nevertheless, this case should be detected and isolated to save the unnecessary computations. Figure (4.3c) shows a case where the initial stresses are compressive up to a stage and then tend to become tensile at later stages of loading. This case is characterized from that shown in figure (4.3b) by the fact that the increment of stress due to the j th increment of load, $\delta\sigma_j (= \sigma_j - \sigma_1)$, is positive. A check for the possibility of a crack is, therefore, necessary here. Figure (4.3d) shows the case of a tensile stress reversing to a

compressive one. In this case also $\delta\sigma_j$ is negative. Separation is not possible at this stage and need not be detected. On the other hand, this case is likely to indicate the closure of an existing crack, which should be catered for.

It is noticed that in both the cases of figures (4.3b) and (4.3d) a crack does not really take place. This is in spite of the fact that the criterion given by equation (4.3) is satisfied. This is merely because while $(\sigma_t - \sigma_j)$ is positive, $\delta\sigma_j$ is negative and hence the fraction is less than 1.5. A modification of equation (4.3) is thus warranted.

Rearranging the criterion in equation (4.3),

$$\frac{\sigma_t - \sigma_j}{\delta\sigma_j} - 1.5 < 0$$

or
$$\frac{\sigma_t - \sigma_j - 1.5 \delta\sigma_j}{\delta\sigma_j} < 0 \quad 4.4$$

The fraction in equation (4.4) is negative if

$$(a) \quad \sigma_t - \sigma_j - 1.5 \delta\sigma_j < 0 \quad 4.5$$

$$\text{while } \delta\sigma_j > 0 \quad 4.6$$

$$\text{and (b) } \sigma_t - \sigma_j - 1.5 \delta\sigma_j > 0$$

$$\text{while } \delta\sigma_j < 0$$

Obviously, satisfaction of the criterion (b) above does not really mean the initiation of a crack, as this represents the cases in figures (4.3b) and (4.3d). Criterion (a) in equations (4.5) and (4.6) is therefore selected for the initiation of any crack.

4.3.3 Classification of crack types

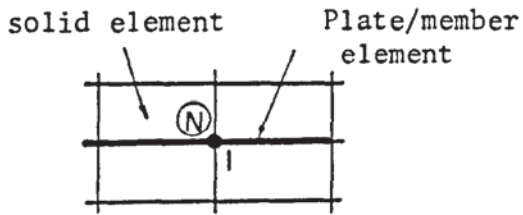
In the previous sections the method of tension separation was

developed for a general joint. The joint was surrounded on all sides by eight rectangular parallelopiped solid elements. The same techniques can be extended to joints at the interface between a plate or a member and solid elements. But the details of the action taken by the program, after each crack, would be different. Also the technique for the detection of the closure of a crack would be different. Furthermore, joints on a plane of symmetry or a boundary do not need a dummy joint associated with them.

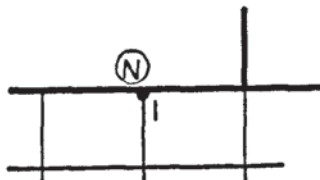
To tackle all the different cases of separation a systematic approach is necessary. To facilitate this, the various types of separations expected are classified into five different groups. Each joint that is likely to suffer a separation is given an index number indicating the type of separation expected. The various types of cracks are shown in figure (4.4) and described below.

Crack type 1: Joints having a crack of this type are given the index number 1. These joints are connected to plates and/or space frame members with rectangular parallelopiped solid elements on both sides of the plate or member, as shown in figure (4.4a). They are allowed to separate in the vertical direction only. The resulting cavity is thus horizontal. If the plates tend to move up from the solid elements below them, then the solid elements below the joint are separated from the parent joint (I). These are then attached to the corresponding dummy joint (N), as shown in the cracked configuration (i) of figure (4.4a). The plates and the solid elements above the joint remain attached to the parent joint. If, on the other hand, the plates exert downward pressure on the solid elements below them the opposite of the above is performed, as shown in configuration (ii) of figure (4.4a). The two configurations are determined by

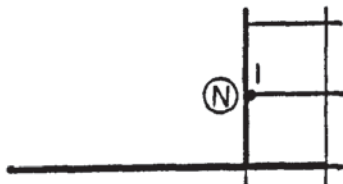
UNCRAKED STATE



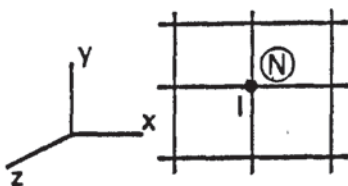
a) Crack type 1



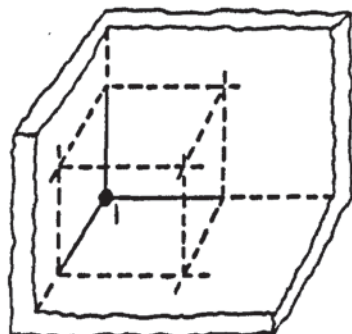
b) Crack type 2



c) Crack type 3

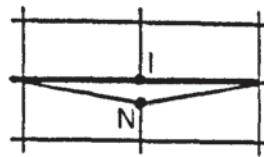


d) Crack type 4

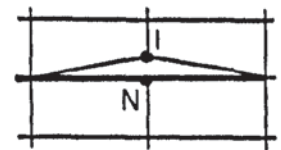


e) Crack type 5

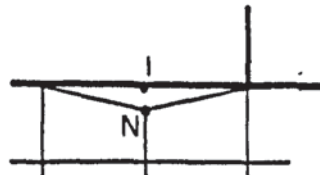
CRACKED CONFIGURATION



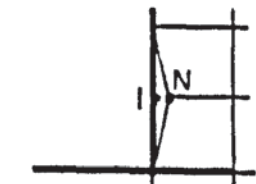
(i)



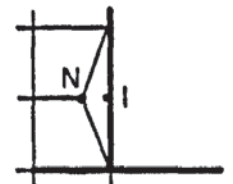
(ii)



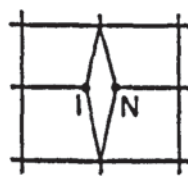
(i)



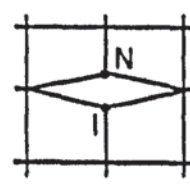
(i)



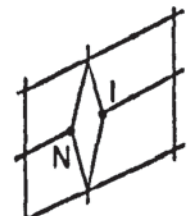
(ii)



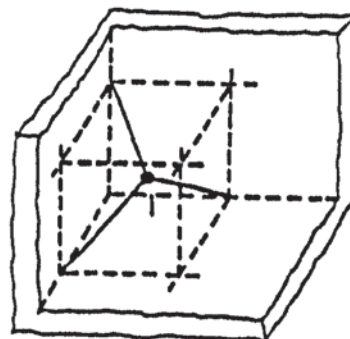
(i)



(ii)



(iii)



I = Parent joint, N = Dummy joint

FIGURE 4.4 TYPES OF CRACKS

testing the sense of the vertical displacement of the joint when a type 1 crack is indicated there. An example of this case is the separation of a horizontal footing or raft buried in the ground.

Crack type 2 (Figure 4.4b): This case is similar to type 1 except that the solid elements are present only on one side of a plate or member. The separation is in the vertical direction and it is performed by disconnecting the solid elements from the parent joint (I) and attaching them to the dummy joint (N). An example of this case is the vertical separation of a footing or raft resting on the ground surface.

Crack type 3 (Figure 4.4c): This is the case when the separation takes place in the horizontal direction. The plates and the members are vertical, as the side walls of a culvert, the abutments of a bridge or the walls of a basement floor. After a crack has taken place, the solid elements are attached to the dummy joint (N). The plate and member elements continue to remain connected to the parent joint (I).

Crack type 4 (Figure 4.4d): This is the case considered in section (4.3.1). The joint is surrounded by solid elements only. The separation is free to occur in any direction, depending on the relative magnitudes of the normal tensile stresses. It is necessary to calculate the normal stresses in all three co-ordinate directions. If more than one stress satisfy the criterion of equations (4.5) and (4.6), then a separation is initiated only in the direction of the stress which gives the lowest value of $(\delta P^*/\delta P)$.

Crack type 5 (Figure 4.4e): This is for a joint on the boundary of the soil in contact with a rigid plane such as rock. This is also

the case for a joint on the plane of symmetry, on one side of which only the body is analysed. The joints in this category need a different treatment from the others. No dummy joint need be associated with such joints. These joints would normally have freedom of in-plane movements only, the out of plane degree of freedom being restrained. When a tensile separation, out of the plane, takes place, the restriction on the out of plane degree of freedom is lifted. The separation can take place in two directions at the intersection of two boundary planes and in all three directions at a corner, as shown in figure (4.4e).

4.4 CLOSURE OF CRACKS

It was indicated earlier that some of the cracks may show signs of closure at a later stage of loading. The method presented here takes account of this fact and closes such cracks as the loading progresses. This is achieved by calculating the width of the crack at each stage of loading and checking its sign. If a negative width is detected indicating an overlapping of the two planes on either side of the crack, the crack is closed. This is done by simply rejoining the elements to their parent joint. The degree of freedom of the dummy joint is reset to zero. For the closure of a boundary separation it is necessary to remove the out of plane degree of freedom of the joint.

4.5 PROCEDURE FOR A CRACK PROPAGATION ANALYSIS

To utilize the above method of determination, initiation, propagation and closure of cracks satisfactorily, an initial knowledge of the zones where cracks may develop is necessary. The problem may first be analysed without any crack and the directions and positions

of the tensile stresses determined. The finite element mesh may then be redesigned if necessary. The joints and the mesh are renumbered. This finite element mesh is then analysed by the non-linear incremental procedure with facilities of crack propagation.

Initially the mesh is uncracked and the analysis starts in the normal way. Once a crack is detected at a point, the elements on either side of the crack are separated by activating the dummy joint. At this stage the crack width is zero and both the parent and the dummy joint have the same values of co-ordinates and displacements. Further loading will cause these joints to displace relative to each other. The crack width is given by the relative displacement of the joints. If the joints displace towards each other and overlap, the crack is closed. As the loading progresses new cracks develop elsewhere in the mesh in both the horizontal and the vertical directions. A crack may also increase in length by the separation of more joints along the crack. Thus the system becomes less and less stiff and the stresses alter continuously.

4.6 AN EXAMPLE ON CRACK PROPAGATION

To ascertain the credibility of the procedure given above, an example analysis problem was undertaken. A non-linear three dimensional problem with analytical or experimental results is not available in the literature. It was, therefore, decided to analyse the three dimensional equivalent of one of Majid and Al-Hashimi's (1976) two dimensional examples.

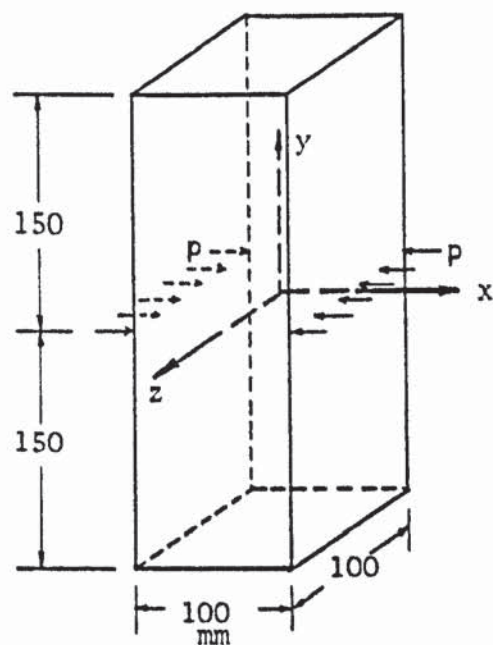
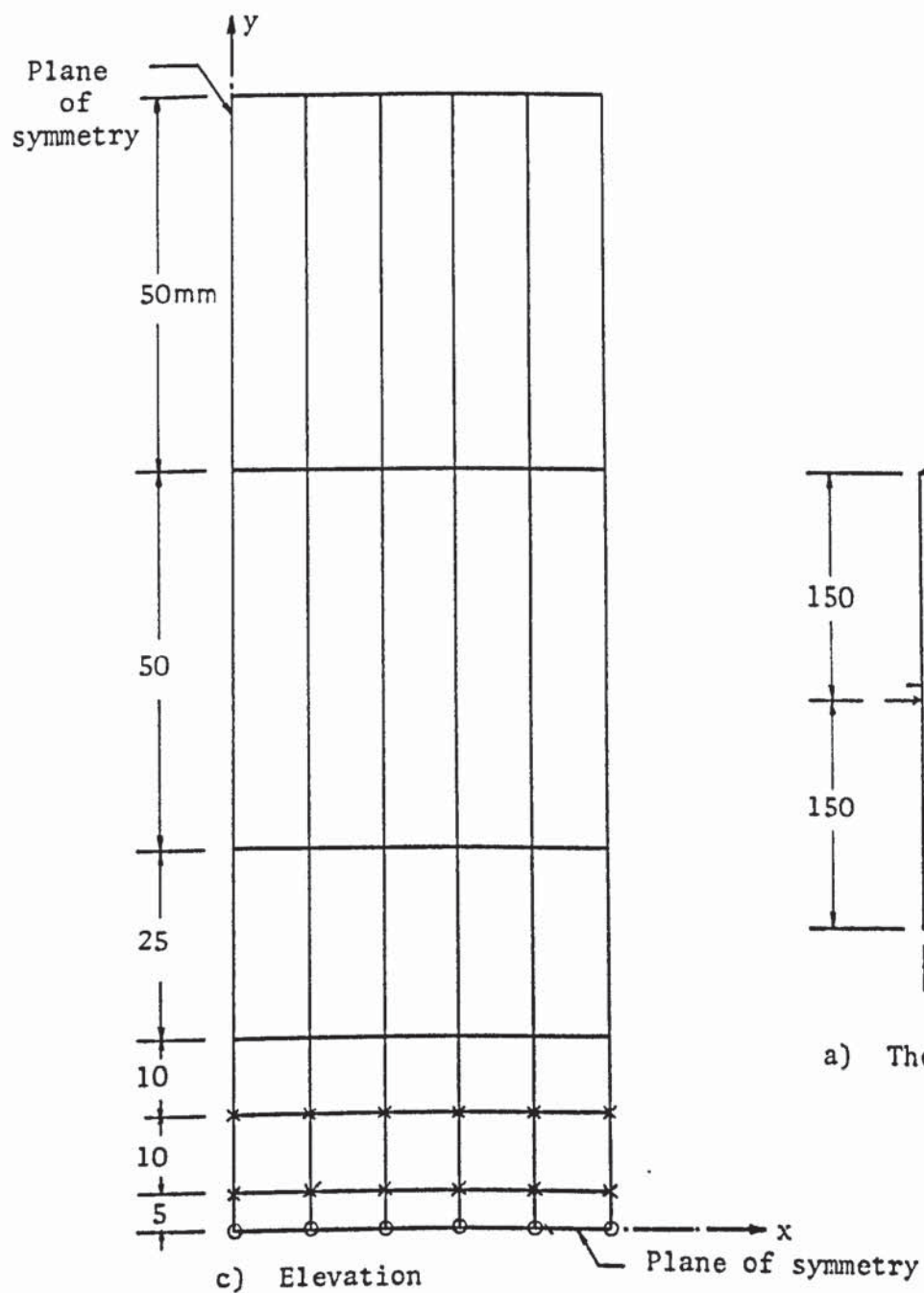
This was a 9:1 soil-cement specimen. The soil consisted of 90 per cent sand and 10 per cent clay. The modulus of elasticity of the material was 3.34 kN/mm^2 , the tensile strength was 830 kN/m^2 and the Poisson's ratio was 0.065. The experimental specimen was a square prism

100 x 100 x 300 mm with line loads applied as shown in figure (4.5a).

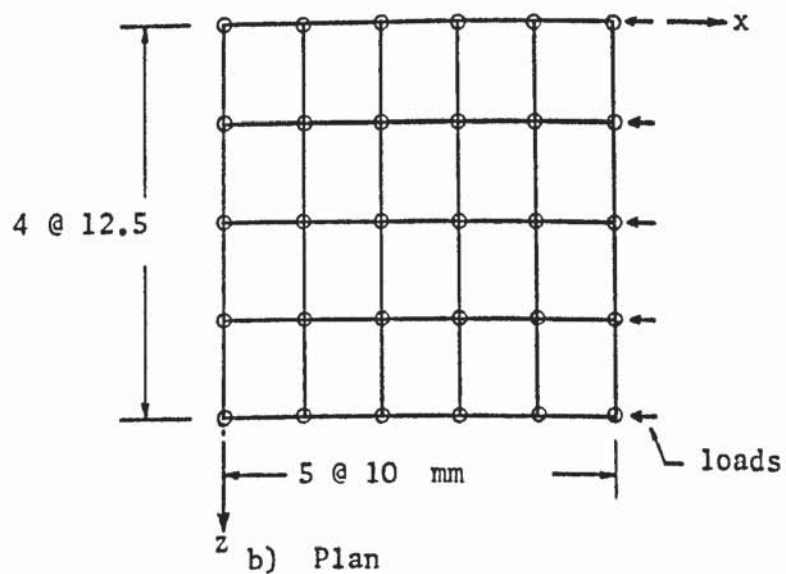
The finite element mesh used to analyse the specimen is shown in figure (4.5b) and (c). Only a quarter of the prism was analysed by taking advantage of the symmetry. Joints shown by crosses had dummies. These joints were type 4 and were free to crack in the direction in which the ratio $(\delta P^*/\delta P)$ of equation (4.3) was the least. Joints on the horizontal plane of symmetry were type 5. These were free to separate in all three directions. No other joint was expected to crack.

An equal increment of load of 7.25 N/mm was used. All the cracks detected by the analysis were in the y-direction. Generally, at lower loads, the cracks occurred all at once in a row of joints parallel to the z-axis. At higher values of loads, they tended to start at the joints on the boundary parallel to and away from the xy co-ordinate plane. This was immediately followed by separations of all the other joints in that row parallel to the z-axis. The progress of the cracks for the centroidal xy plane is shown in figure (4.6). The numbers indicate the order of formation of each crack. The variation of crack widths with load at the points A and B in figure (4.6e) is shown in figure (4.7).

As the finite element program was not written to perform a failure analysis, a precise evaluation of the failure load was not possible. But, as can be seen in figure (4.6) at a load of 145 N/mm the sample cracked severely. A further increment of load in the analysis resulted in substantial increases in the widths of the cracks. The value of $p = 145$ N/mm may, therefore, be taken as the failure load. This is about 3.58 per cent higher than the experimental value obtained by Majid and Al-Hashimi (1976). The theoretical failure load obtained by Majid and Al-Hashimi was 145.1 N/mm.



a) The specimen



- x Joints with a dummy
- ⊙ Boundary joints with index = 5

FIGURE 4.5 FINITE ELEMENT MESH OF EXAMPLE PROBLEM

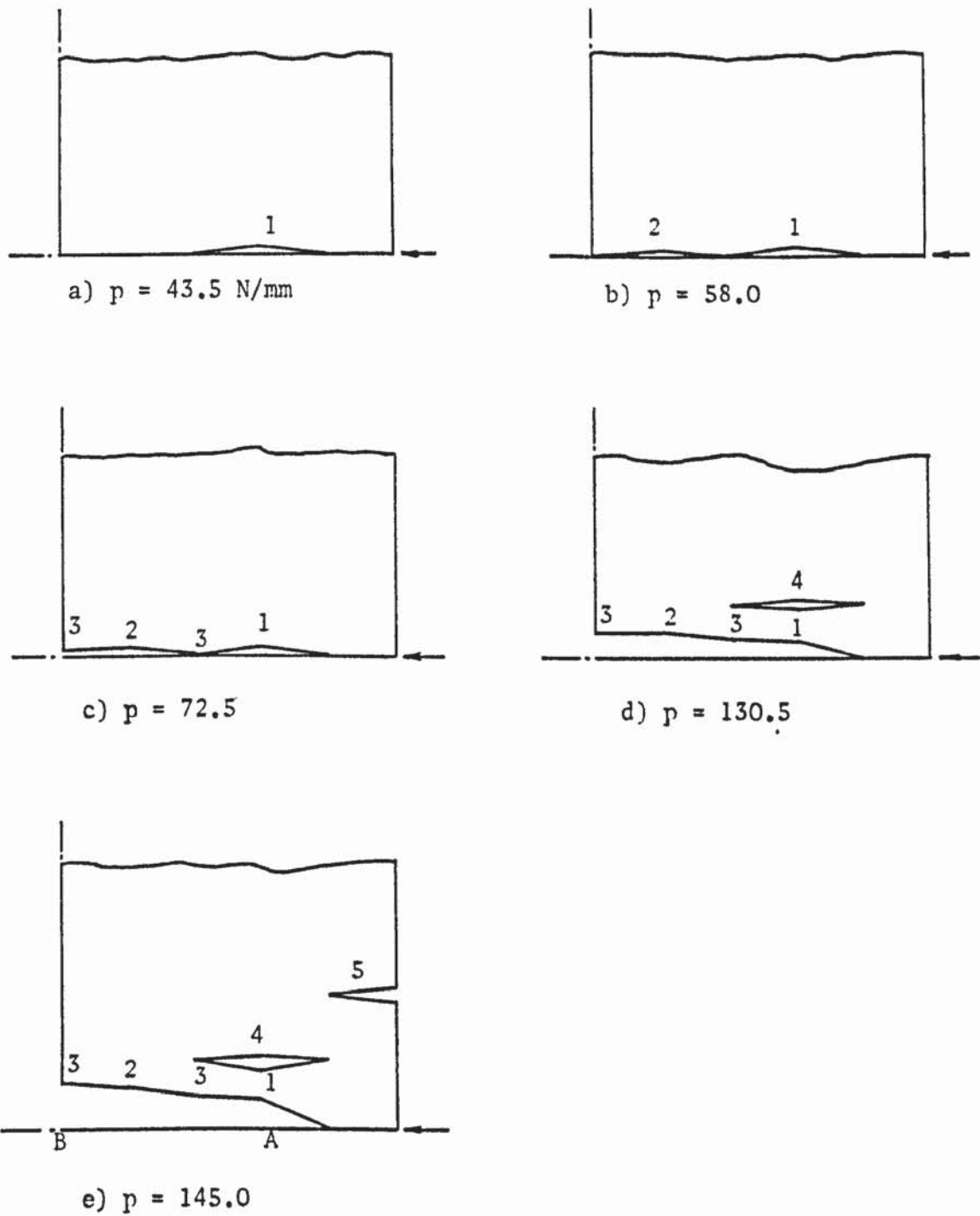


FIGURE 4.6 PORGRESS OF CRACKS IN CENTROIDAL xy PLANE OF EXAMPLE PROBLEM

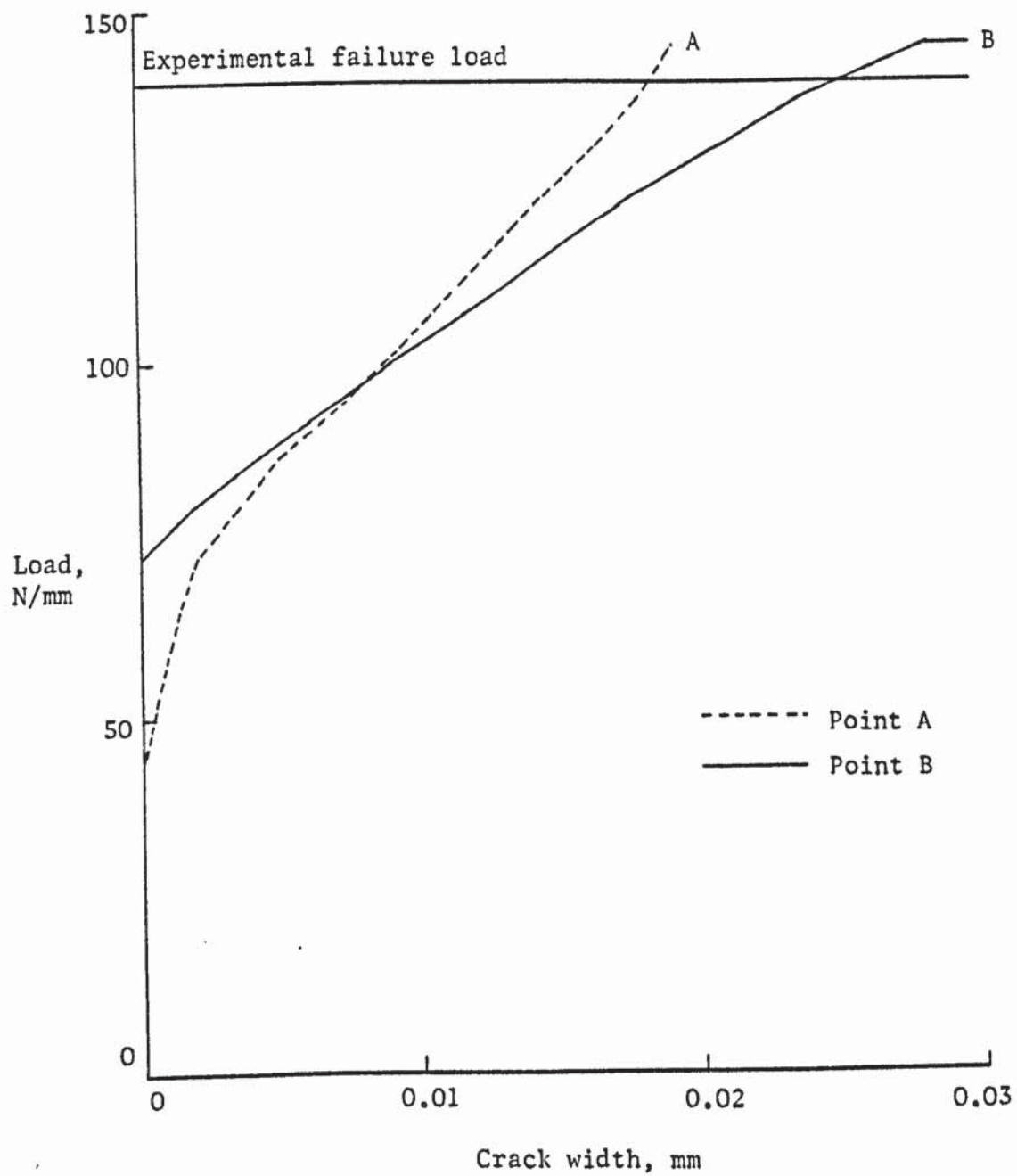


FIGURE 4.7 VARIATION OF CRACK WIDTH WITH LOAD.

CHAPTER 5

ANALYSIS OF STRUCTURES RESTING ON CLAY

5.1 INTRODUCTION

In clay soils a distinction is often made between the short term or immediate settlement and the long term consolidation settlement. The total settlement is expressed as the sum of these two components. It is possible to obtain $\tau_{oct} - \gamma_{oct}$ curves to give the total settlement of a clay soil by performing drained triaxial tests on the clay sample. However, settlements of such soils are frequently calculated from the results of oedometer tests by assuming a one dimensional strain condition. Under true one dimensional conditions, however, the immediate settlement is zero. The total settlement is therefore assumed to be equal to that obtained from the results of the oedometer test. However, under most structures the strain conditions are not one dimensional and the effect of lateral strains may be quite significant. Nevertheless, the utilization of the consolidation test data in a three dimensional analysis is possible. A method of analysis of a complete structure resting on clay is developed in this chapter. The method makes use of the consolidation test data for computing the ultimate long term displacements of clay under three dimensional conditions.

5.2 SETTLEMENT CALCULATION IN CLAY

Terzaghi's (1943) theory of one dimensional consolidation assumes that during any one increment of load the ratio, m_v , of the change of the volumetric strain to the change of the vertical effective stress remains constant with time. The constant m_v is

commonly known as the coefficient of volume compressibility. In an oedometer test the strain takes place in the vertical direction only. Therefore the volumetric strain is equal to the vertical strain. Thus, Terzaghi's proposition leads to a piecewise linear relationship of the vertical strain and the vertical effective stress. The slope of each linear segment is the value of m_v corresponding to a particular range of effective stresses.

In the conventional soil mechanics method, the settlement of a layer of clay is calculated by employing the above theory of one dimensional consolidation. The layer is usually divided into a finite number of sub-layers each of thickness δy . The increase, ΔS , in the total long term settlement of the layer, due to an increase, $\Delta \sigma_y$, in the vertical effective stress is given by:

$$\Delta S = \sum m_v \Delta \sigma_y \delta y \quad 5.1$$

The principal drawback of equation (5.1) is that it neglects Poisson's ratio. This means that it assumes that the lateral stresses do not have any influence on the vertical settlement of the layer. This assumption may lead to a significant error in the predicted settlement for cases where Poisson's ratio ν is not zero. Davis and Poulos (1968) have calculated the settlements of a uniformly distributed circular loading area resting on the surface of an elastic, isotropic and homogeneous clay layer. Even for this axisymmetric case the settlement calculated by equation (5.1) underestimates the true settlement for values of ν greater than 0.25. The error is likely to be more pronounced in an arbitrary three dimensional case of a non-linear and non-homogeneous clay.

In the conventional approach, simplification is also made in the calculation of the stresses to be used in equation (5.1). The soil is usually idealized as an elastic, isotropic and homogeneous semi-infinite continuum. A uniform or linearly distributed surface load is applied on the continuum and the vertical stresses at various depths are calculated. All the analytical solutions of such a problem originate from the classical Boussinesq solution for a point load on the surface of an elastic semi-infinite continuum. The applicability of this solution to soils, which may be non-linear, non-homogeneous, anisotropic and of a finite extent, is questionable. Burland, Broms and deMello (1977) have quoted results for several such cases. The Boussinesq stresses for most of these cases differ significantly from the actual stresses. The inadequacy of the Boussinesq solution in a finite layer even with the assumptions of linear elasticity and homogeneity has also been confirmed by Girija Vallabhan and Reese (1968). They have shown that the finite element results of the settlements of an elastic layer supporting a uniform circular load coincide with the Steinbrenner solution (Terzaghi, 1943) of an elastic layer. But the Boussinesq solution assuming a semi-infinite continuum grossly overestimated their results.

Therefore, the use of equation (5.1) and Boussinesq stresses oversimplifies the problem. The finite element method overcomes many limitations of the conventional approach. Non-homogeneity and non-linearity of the soil are easily accounted for.

5.3 REPRESENTATION OF THE NON-LINEAR PROPERTIES OF CLAY

In an oedometer test sample the coefficient of volume compressibility is given by:

$$m_v = \frac{\Delta \epsilon_y}{\Delta \sigma_y} \quad 5.2$$

where $\Delta \epsilon_y$ is the increase in the vertical strain due to an increase $\Delta \sigma_y$ in the vertical stress. But due to the presence of the lateral stresses, $\Delta \sigma_x$, the true vertical strain is:

$$\Delta \epsilon_y = \frac{\Delta \sigma_y}{E} - \frac{2\nu \Delta \sigma_x}{E} \quad 5.3$$

The lateral strain is given by:

$$\Delta \epsilon_x = \frac{\Delta \sigma_x}{E} (1-\nu) - \frac{\nu \Delta \sigma_y}{E} = 0 \quad 5.4$$

Combining equations (5.2), (5.3) and (5.4) and eliminating the stress and the strain terms, the following relationship is obtained.

$$E = \frac{1}{m_v} \left(\frac{1 - \nu - 2\nu^2}{1 - \nu} \right) \quad 5.5$$

As each value of m_v corresponds to a particular range of pressure, a non-linear relationship between E and the stress is obtained by using equation (5.5). A method of analysis of a structure resting on clay that follows this relationship is described below.

5.4 FINITE ELEMENT INTERACTION ANALYSIS OF THE STRUCTURE AND THE CLAY

The structure, the foundation and the soil are represented by suitable finite elements and are analysed as an integral body.

The non-linear soil properties are supplied as a table of the values of m_v and the corresponding stress range. An iterative scheme of analysis is employed to follow the non-linear properties given by this table.

The analysis starts with the determination of the vertical base reactions of the structure assuming a fully fixed foundation. These reactions are then applied on the surface of the soil as uniformly distributed foundation pressures. The vertical stresses at the centroids of each soil element are calculated by assuming the soil to be an elastic and isotropic semi-infinite continuum. This is conveniently achieved by making use of the direct expressions for stresses due to a rectangular area loaded on a Boussinesq* medium given by Love (1929). A value of m_v corresponding to the vertical stress in each soil element is chosen from the supplied table. The corresponding values of E are calculated from equation (5.5) for each soil element.

The structure, the foundation and the soil are then analysed as an integral body by the finite element method. This gives a new set of stresses throughout the soil mass. The value of E for each soil element are modified to correspond to these new stresses by using the values of m_v at different stresses. The finite element analysis is then repeated with these new values of E . The convergence is tested after each analysis by calculating the differences in the displacements at all the joints given by two successive analyses. The analysis is stopped when these differences become less than a specified percentage of the current displacements. The iteration scheme is summarized below:

* It should be stated that throughout this thesis the term Boussinesq refers to the conventional approach of stress calculation in soil neglecting the structure.

- 1 Analyse the structure assuming fixed supports and obtain the reactions.
- 2 Neglecting the structure, apply these reactive loads on the surface of the soil and calculate the stresses at the centroid of each soil element by Boussinesq's equations.
- 3 Obtain values of m_v corresponding to the Boussinesq stresses in each element and calculate E from equation (5.5).
- 4 Analyse the structure, the foundations and the soil as an integral system by the finite element method.
- 5 Obtain the stresses at the centroid of each soil element from the finite element analysis and modify the values of E to correspond to these new stresses.
- 6 Repeat steps 4 and 5 until convergence is achieved. This is given by the condition that the differences in the displacements of all the joints obtained by two successive analyses are less than a specified tolerance.

The method developed above is very comprehensive and can be used to analyse various configurations of structure and soil. It starts with the conventional soil mechanics approach and gradually corrects the results. Thus, a check of the discrepancy of the two can readily be made. The scheme of iteration proposed here has a very high convergence rate. For the problems analysed in this thesis between 3 and 6 iterations were required to achieve a tolerance of 1% for the deflections of all the joints.

5.5 TENSION SEPARATION IN CLAY

The method of tension separation presented in chapter 4 was developed in the context of an incremental technique of analysis. A crack was included in the finite element mesh if an extrapolation

of the stresses indicated a tensile failure in the next increment of the load. In the iterative method of the analysis of clay, described in the previous section, the full value of the load is applied in each cycle. A modification of the method of initiation of a crack is therefore necessary. In this case a crack is initiated if the stress at a point given by the previous cycle of iteration has already exceeded the tensile strength of the material. The rest of the method remains unaltered.

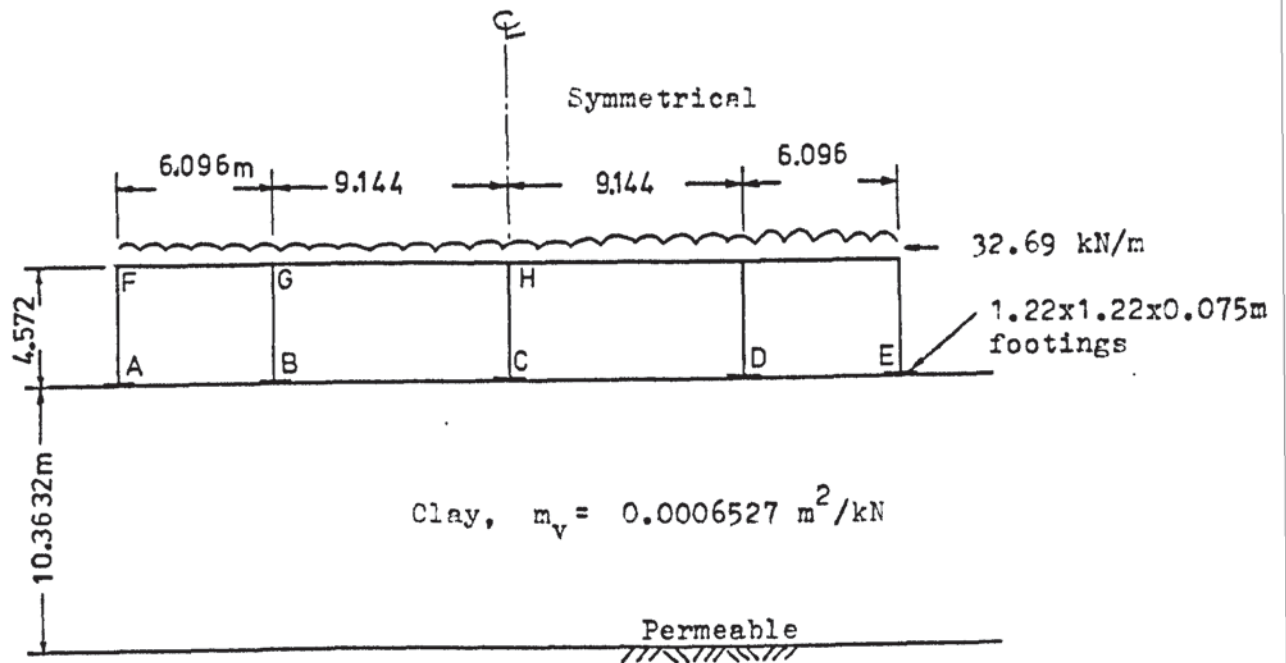
5.6 EXAMPLES OF THE ANALYSIS OF STRUCTURES

RESTING ON CLAY

5.6.1 Four-bay plane frame

The plane frame, shown in figure (5.1), was analysed by Larnach (1970) by using an interactive analysis method proposed originally by Chamecki (1956). Only the vertical settlements of the column bases were considered by Larnach and the conventional method of the calculation of stresses by Boussinesq's equations was used. The settlements were calculated by equation (5.1) which neglects the effect of Poisson's ratio of the soil. The settlements were then successively modified by taking the flexural rigidity of the frame into account.

The same frame is analysed here by the method developed in the previous sections. The frame rests on a layer of clay supported by a rigid permeable stratum. The property of the clay is assumed to be represented by a single value of m_v of $0.6527 \times 10^{-3} \text{ m}^2/\text{kN}$ for all values of the stress. The structural members are made out of steel with the values of E , I and ν as shown in figure (5.1) and the uniform load is 32.69 kN/m. Each column is



PROPERTIES OF THE MEMBERS

$$E = 208.5 \times 10^6 \text{ kN/m}^2$$

$$\nu = 0.3$$

$$I_{AF} = 8.9867 \times 10^{-5} \text{ m}^4$$

$$I_{BG} = 13.4801 \times 10^{-5} \text{ m}^4$$

$$I_{CH} = 17.9735 \times 10^{-5} \text{ m}^4$$

$$I_{FG} = 19.9705 \times 10^{-5} \text{ m}^4$$

$$I_{GH} = 47.9292 \times 10^{-5} \text{ m}^4$$

FIGURE 5.1 PLANE FRAME EXAMPLE

supported by a 1.22 m square steel pad of 75 mm thickness.

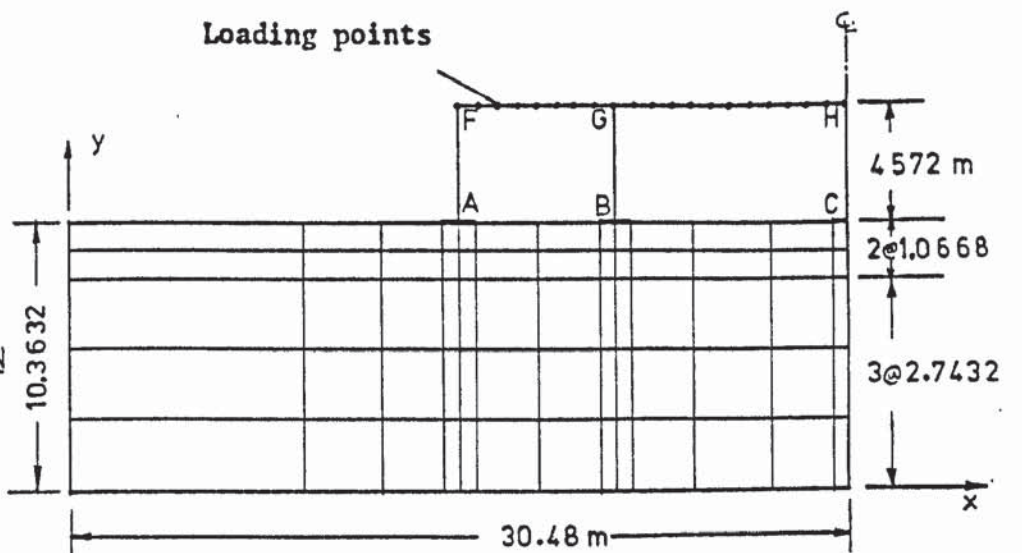
Although the frame is two dimensional, the stresses in the ground disperse in three dimensions. A three dimensional finite element representation of the soil is therefore necessary. Because the frame is symmetrical about column CH and also about the longitudinal centroidal axis of the beams, it is only necessary to analyse a quarter of the frame. A zone of the soil around the frame is influenced by and interact with the frame. An extent of 15.24 m, which is equal to half the total length of the frame, was considered on either side of the frame along its length. In the lateral horizontal direction an extent of 9.144 m, which is equal to the largest bay span, was also considered on either side. Experience showed that, as the stresses in the soil diminished rapidly away from the footings, the zone considered was quite adequate. The boundary of this zone was considered to be rough and completely rigid.

Two mesh sizes were considered. The coarser one is shown in figure (5.2a). This consists of 441 joints, 260 solid elements, 5 plate and 23 prismatic member elements. The finer mesh is shown in figure (5.2b) and has 1309 joints with 924 solid, 5 plate and 23 member elements. The analyses showed that tensile stresses developed near the surface of the clay mid-way between footings B and C. The fine mesh in figure (5.2b) was therefore modified to allow tensile separations. 63 dummy joints were included in this zone as shown by the crosses in figure (5.2b). Thus a total of three different finite element meshes were used for this problem. These are:

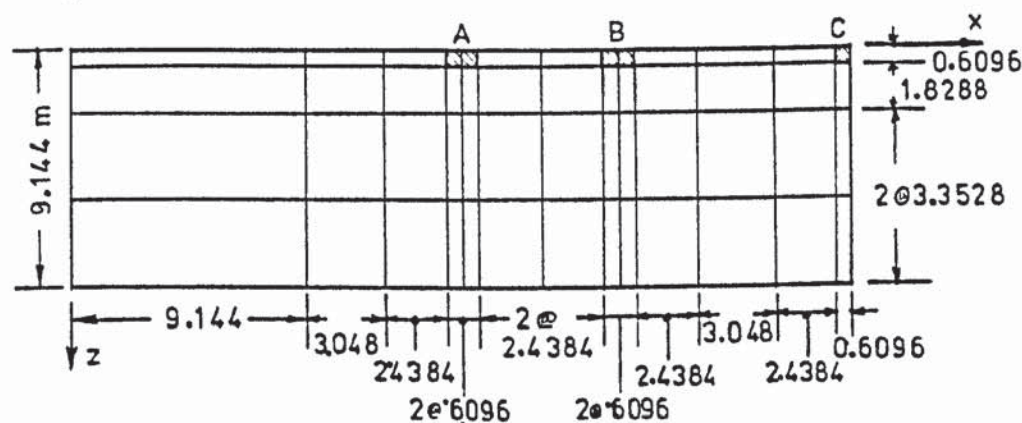
FEl: A coarse mesh with 441 joints.

No of joints = 441
 No of solids = 260
 No of plates = 5
 No of members = 23

ELEVATION



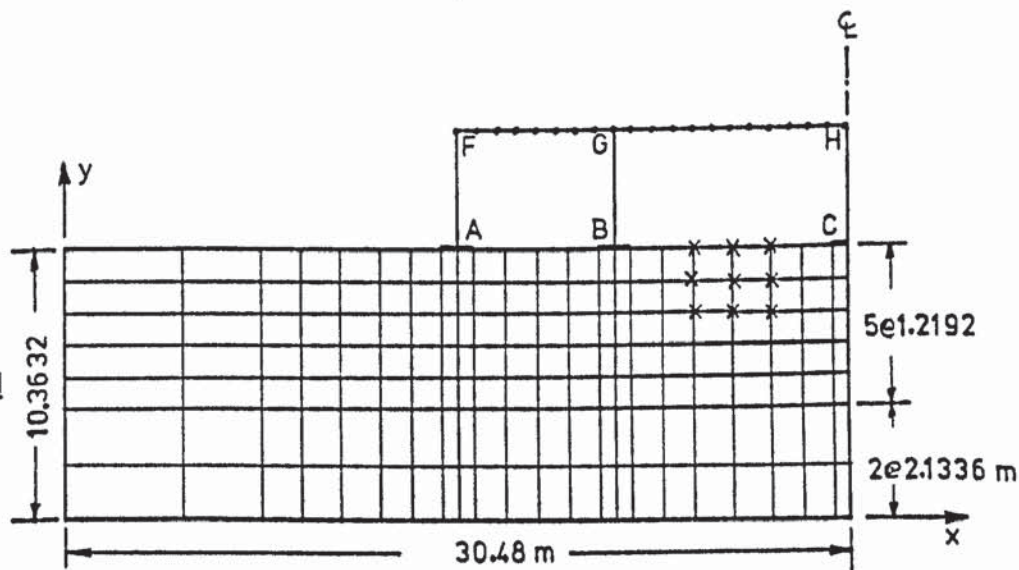
PLAN



(a) Coarse mesh FE1

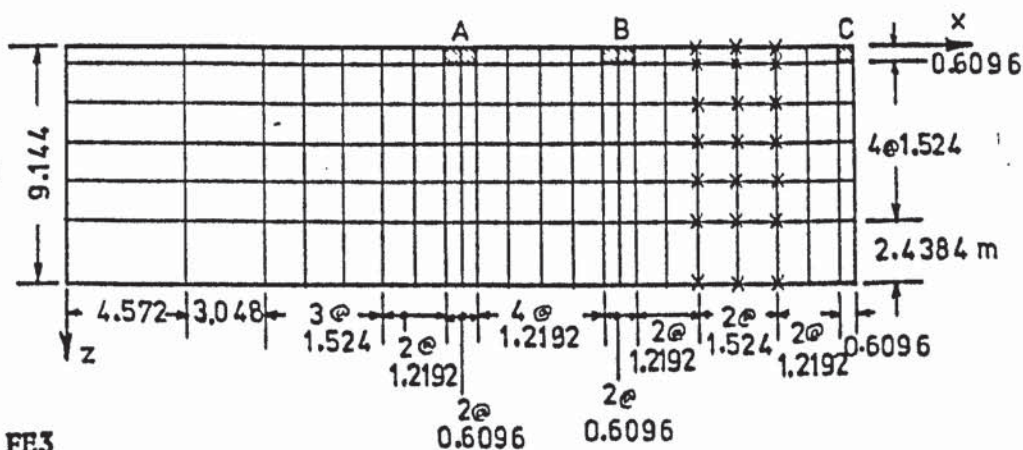
No of joints = 1309
 No of solids = 924
 No of plates = 5
 No of members = 23

ELEVATION



x = Dummy joints

PLAN



(b) Fine mesh FE2 and FE3

FIGURE 5.2 FINITE ELEMENT MESH FOR PLANE FRAME

FE2: A fine mesh with 1309 joints but no cracks were allowed.

FE3: The fine mesh with 1309 active joints and 63 dummies to allow for crack developments.

In the design of the finite element meshes consideration was given to the high stresses developed directly under the footings. A finer division was therefore used in these zones, transforming gradually into a coarser division away from the footings, as shown in figure (5.2a and b). In all the cases a large number of joints were placed on the top beam to represent the uniformly distributed applied load closely. These loading points are shown in figure (5.2) by small dark dots.

5.6.2 Results of the plane frame example

5.6.2.1 The influence of Poisson's ratio

Several analyses were carried out with different values of ν for each of the cases described above. Some of the results obtained for the case FE1 are shown in figure (5.3). Curve 1 shows the influence of ν on the differential settlement between columns A and B while curve 2 shows this influence on the differential settlement of columns B and C. The value of m_v was kept constant. It is noticed from these curves that the differential settlements are significantly influenced by Poisson's ratio. Notice in figure (5.3), that there is not much change in the differential settlements up to a value of ν of about 0.25. This is what Davis and Poulos (1968) also observed; but as ν exceeds this value, there is an alarming increase in the differential settlements. These change rapidly and the curves become asymptotic to the line $\nu = 0.5$. As computational difficulties arise with a value of $\nu = 0.5$, the maximum value of ν used here was 0.49. It is

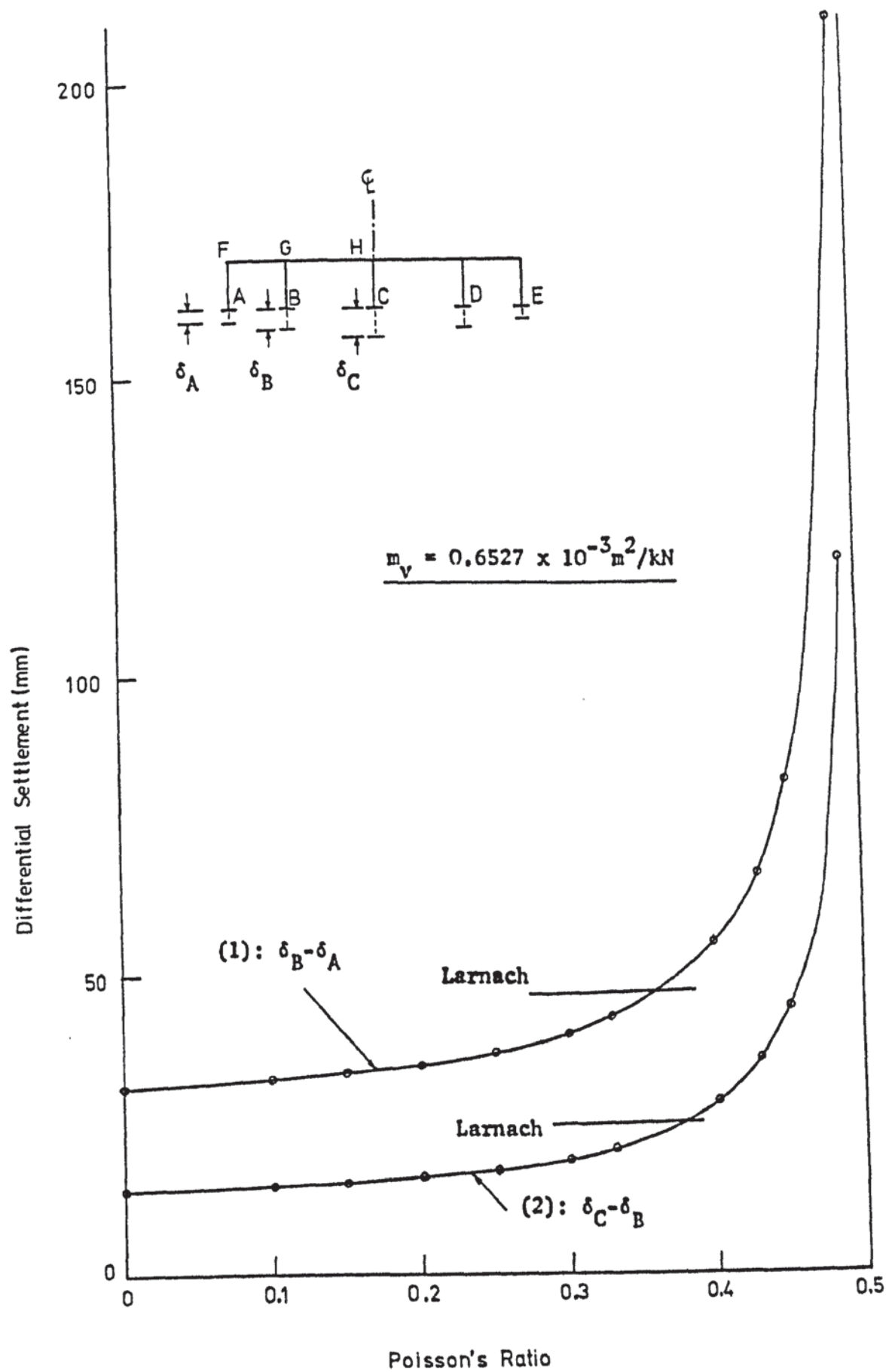
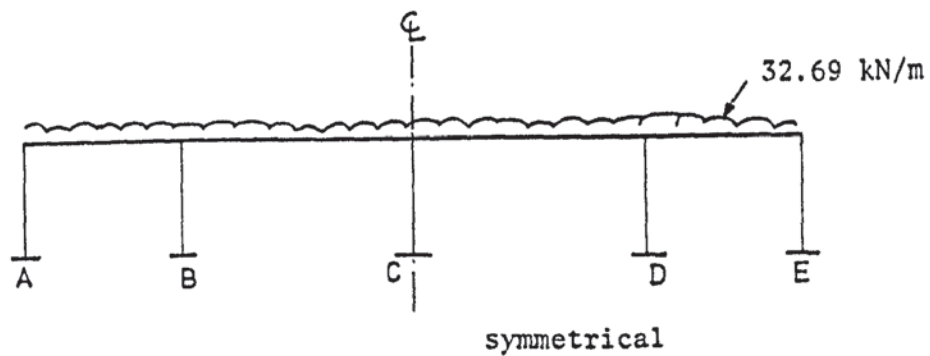


FIGURE 5.3 VARIATION OF DIFFERENTIAL SETTLEMENTS WITH POISSON'S RATIO

noticed that the settlement can be of very severe magnitude in clays with a high value of ν . Consequently, the simple calculation suggested by equation (5.1) assuming a zero Poisson's ratio will lead to a gross underestimation of the settlements of such soils. A detailed analysis of the kind suggested in this thesis may therefore become necessary.

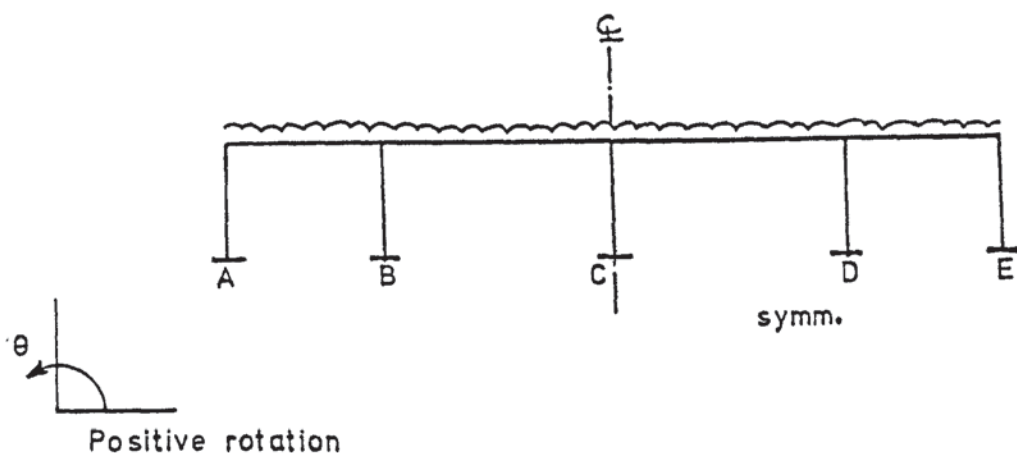
5.6.2.2 Comparison of the results

A summary of the results of the base reactions of the plane frame, obtained from the various analyses, is given in table (5.1). Corresponding results of the settlements and the rotations at the base are given in table (5.2). The reactions in row 1 of table (5.1) are those of a fixed base frame. These are then used to calculate the settlements by a conventional method, using equation (5.1). These settlements are given in row 1 of table (5.2). The second row in both the tables gives the results obtained by Larnach after modifications made to the settlements due to the stiffness of the structure. The rest of the tables gives the results obtained by the analysis of the complete system by the finite element method. It is noticed that when the interaction of the structure with the soil is considered, a complete redistribution of the reactions takes place. Generally, this redistribution alters the base reactions of the external columns A and B considerably. But the change at the central column C is less significant. This indicates that the support reactions are affected by the rotation of the column bases. Bases A and B both settle and rotate while base C only settles but does not rotate. The rotations of the column bases A and B obtained by the finite element analyses are



Row No	Analysis method		Base reactions, kN		
			A	B	C
1	Fixed bases		79.3	262.0	313.8
2	Larnach (1970)		113.4	234.2	301.3
3	FE1	$v = 0$	97.3	244.6	312.6
4		$v = 0.2$	98.7	243.6	311.8
5		$v = 0.33$	100.8	241.8	311.2
6		$v = 0.49$	120.0	233.8	288.8
7	FE2	$v = 0$	99.2	243.7	310.6
8		$v = 0.33$	102.9	240.7	309.2
9	FE3	$v = 0$	99.0	243.2	312.0
10		$v = 0.33$	103.8	239.2	310.4

TABLE 5.1 RESULTS OF THE BASE REACTION OF PLANE FRAME



Row No	Analysis method		Settlements, mm			Differential settlements, mm		Rotations, $\times 10^{-3}$ radians	
			δ_A	δ_B	δ_C	$\delta_B - \delta_A$	$\delta_C - \delta_B$	θ_A	θ_B
1	Conventional method		40.4	126.8	151.3	86.4	24.5	-	-
2	Larnach (1970)		45.7	92.4	116.8	46.7	24.4	-	-
3	FE1	$v = 0$	24.4	55.6	69.8	31.2	14.2	2.10	1.05
4		$v = 0.20$	27.1	61.9	78.2	34.8	16.3	1.61	0.68
5		$v = 0.33$	33.2	75.8	96.4	42.6	20.6	0.95	0.07
6		$v = 0.49$	219	429	547	210	118	-27.5	-19.2
7	FE2	$v = 0$	29	64.7	81.7	35.7	17	2.35	0.98
8		$v = 0.33$	40.7	90.3	115	49.6	24.7	1.10	-0.10
9	FE3	$v = 0$	29.1	65.3	82.9	36.2	17.6	2.23	0.52
10		$v = 0.33$	40.7	90.5	116	49.8	25.5	0.89	-0.38
11	FE4a	$v = 0$	29.5	64.9	82.1	35.4	17.2	-	-
12		$v = 0.33$	31	65.8	83.6	34.8	17.8	-	-
13	FE4b	$v = 0$	29.5	64.9	82.1	35.4	17.2	-	-
14		$v = 0.33$	46.5	98.6	125.3	52.1	26.7	-	-

TABLE 5.2 SETTLEMENTS AND ROTATIONS OF COLUMN BASES OF THE PLANE FRAME

given in table (5.2). The rotation of A is generally more than that of B. As a result, the reaction at A changes more than that at B for all the finite element analyses. Both of these reactions change more than that at C. Table (5.2) shows that as the value of ν increases the base rotations change rapidly and then reverse sign and become excessive for $\nu = 0.49$. The reactions also change markedly, with an increasing ν , from those obtained by a fixed base analysis.

The conventional method calculates the stresses at various depths in the soil by applying the fixed base reactions on the soil surface and using Boussinesq's equations. The values of the settlements obtained by this method may be expected to coincide with those of the finite element analysis for $\nu = 0$. However, comparing the results given in row 1 of table (5.2) with those in rows 3, 7 and 9, it is noticed that this is not so. In the finite element interaction analysis the structure plays its part in reducing the differential settlements. As one base begins to settle excessively, the rest of the structure comes to its aid. In this process the stiffness of the beam plays an important part in redistributing the loads among the columns. By comparing the settlement values in rows 1 and 3 of table (5.2), it is seen that the settlements of all the columns have reduced due to the interaction. However, the settlement at A has reduced by only 40% compared to the reductions of 56% and 54% at B and C respectively. This indicates that column A now carries a bigger share of the load; which is also obvious from table (5.1). As a result the differential settlements are also reduced.

Larnach's analysis included the stiffness of the structure but used the conventional method of settlement calculation from

Boussinesq stress and equation (5.1). The settlement values obtained in this manner are given in row 2 of table (5.2). These do not coincide with the finite element results even when ν is taken to be zero. In fact, Larnach's results, with $\nu = 0$ correspond to those obtained by the finite element analysis but with ν nearer 0.33, see figure (5.3). This discrepancy is due to the disagreement between the Boussinesq stresses for a semi-infinite continuum and the true stresses in the finite clay layer.

The vertical stresses, σ_y , in the soil under the frame are shown in figures (5.4), (5.5) and (5.6). In these figures the full lines represent the vertical stresses obtained by the finite element analysis FE2 while the dashed lines show the stresses calculated from Boussinesq's equations. Figure (5.4) shows the variation of σ_y in the horizontal x direction at various depths below the surface. The variation of σ_y along the depth directly under the footings is shown in figure (5.5). Finally, figure (5.6) shows this variation in the lateral z direction at various depths below the surface. It can be seen in all these figures that, directly under the foundations, the Boussinesq stresses are considerably higher than the finite element stresses. However, deeper in the soil and also away from the footings the difference between the two stresses becomes less marked. Larnach's settlements are calculated on the basis of the Boussinesq stresses directly under the footings. Therefore, these settlements are considerably higher than those obtained by the finite element analysis for a zero Poisson's ratio. As mentioned earlier, results obtained by Girija Vallabhan and Reese (1968) for the settlements of a shallow elastic layer also demonstrate that Boussinesq overestimates the stresses.

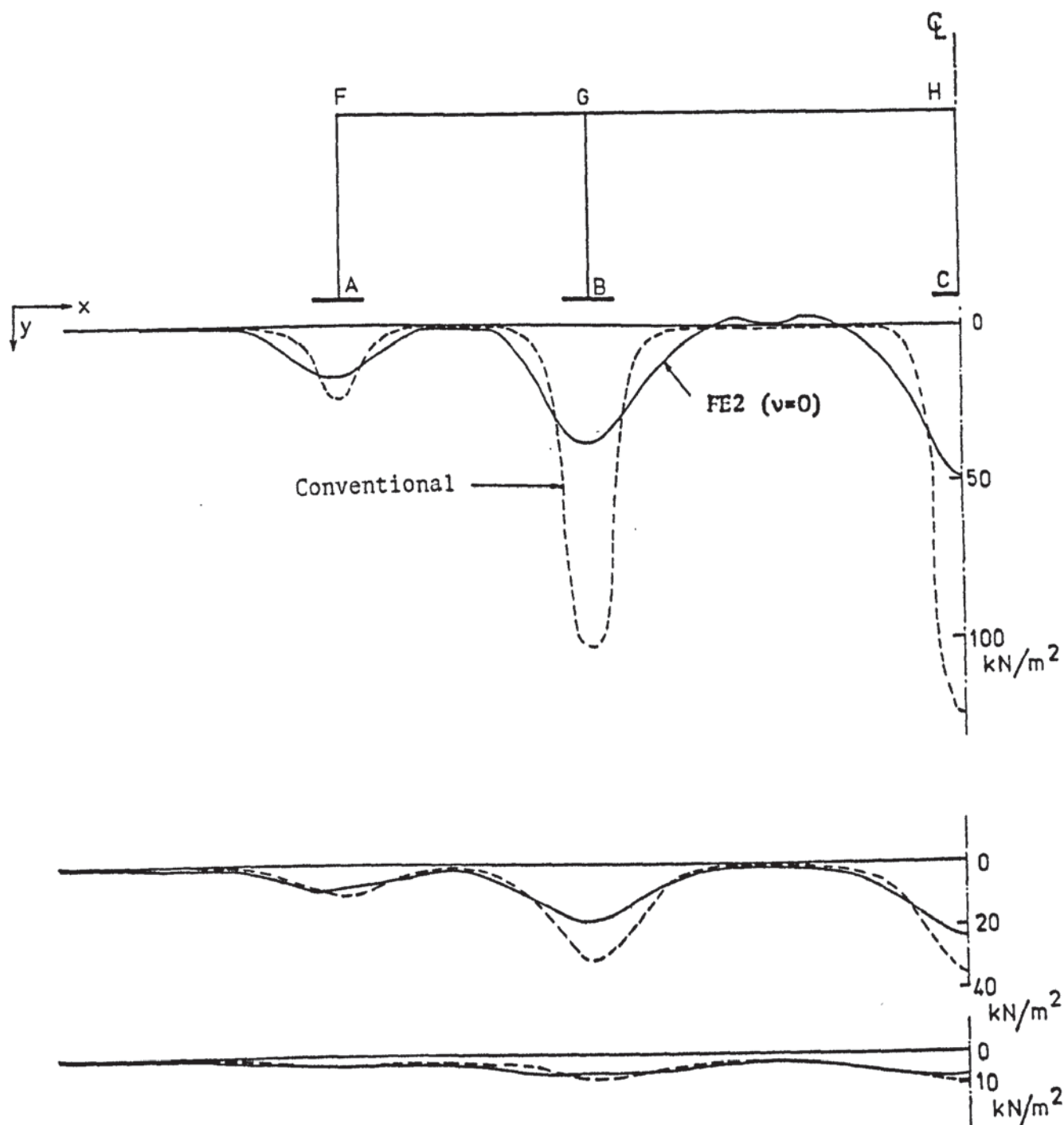


FIGURE 5.4 VARIATION OF σ_y IN THE x DIRECTION AT
VARIOUS DEPTHS BELOW THE SURFACE

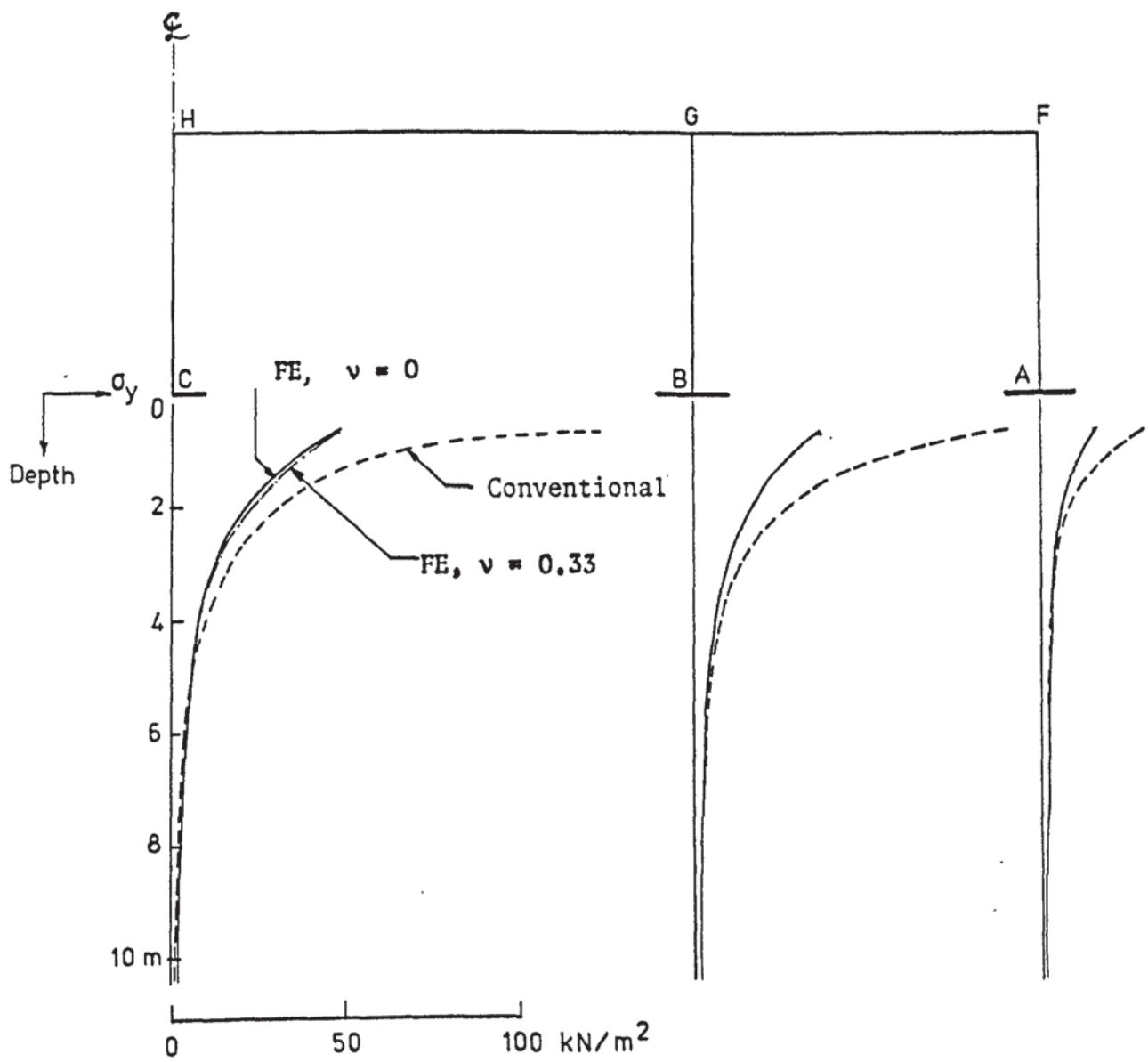


FIGURE 5.5 VARIATION OF σ_y WITH DEPTH DIRECTLY
UNDER THE FOOTINGS

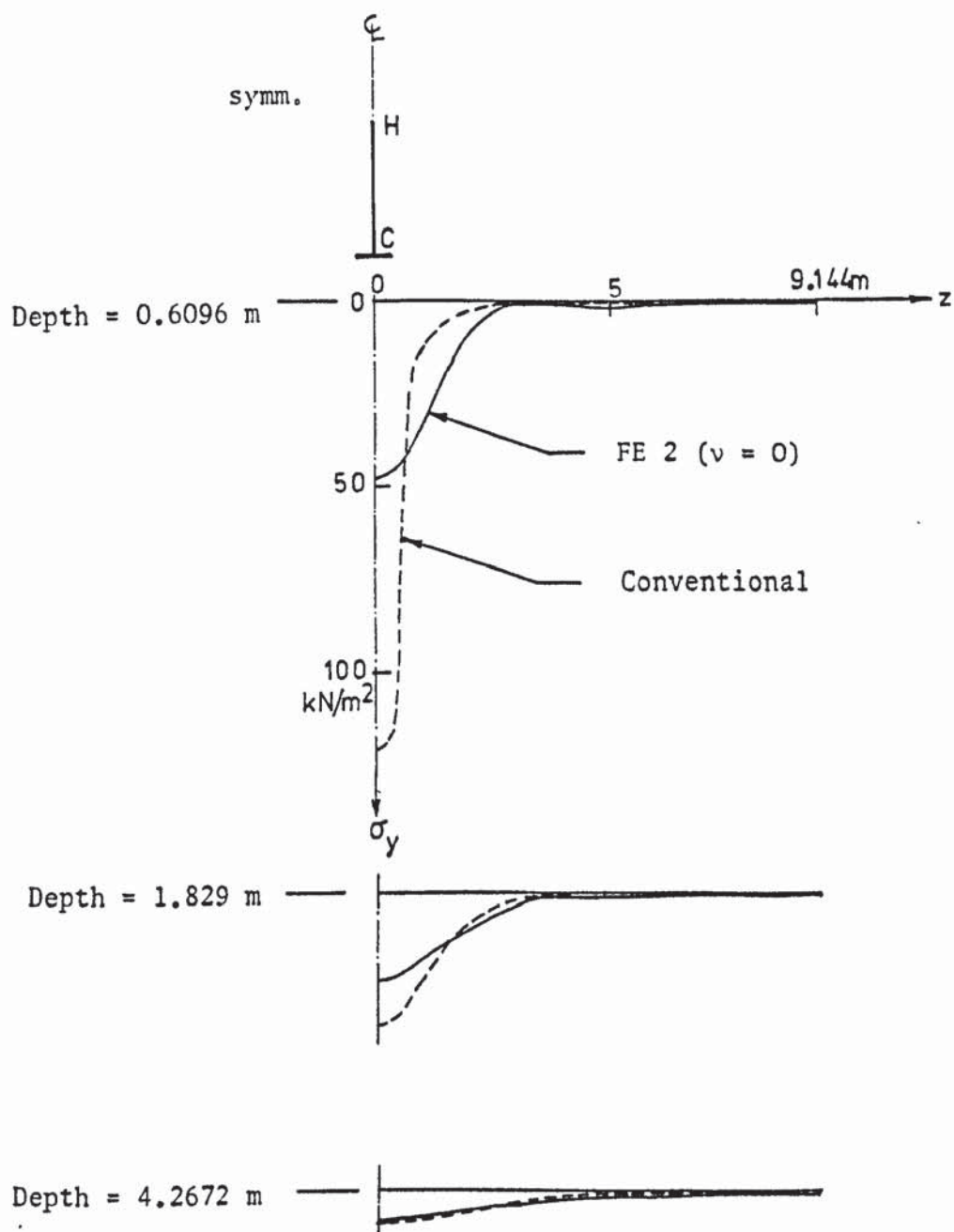


FIGURE 5.6 VARIATION OF σ_y IN z DIRECTION AT VARIOUS DEPTHS BELOW THE SURFACE

It is clear that using Boussinesq stresses compensates for the lack of consideration for Poisson's ratio. This fact also partially accounts for the high, and therefore 'safe', values of the settlements obtained by the conventional method in row 1 of table (5.2).

In this table, the analysis FE4a was performed by calculating the settlements from equation (5.1), but with the stresses obtained from a finite element interaction analysis. The stresses are not much different for different values of ν , as shown under the central footing C in figure (5.5). Thus the differential settlements for $\nu = 0$ and $\nu = 0.33$ given in rows 11 and 12 respectively of table (5.2) are nearly equal. This is because equation (5.1) does not consider the effect of Poisson's ratio. These values in turn are close to the results for $\nu = 0$ obtained by the finite element analyses FE1, FE2 and FE3. This points out the limited adequacy of equation (5.1) which can only be applied to cases where $\nu = 0$. Even in this case, the value of the stress to be used in equation (5.1) should be calculated by a refined analysis.

The analysis FE4b was performed in the same way as FE4a except that the effect of the Poisson's ratio was included in the expression for the settlement, as given below:

$$\Delta S = \Sigma m_v \cdot \Delta \sigma_y \cdot \delta y \cdot \left(\frac{1 - \nu}{1 - \nu - 2\nu^2} \right) \quad 5.6$$

For a zero Poisson's ratio equations (5.1) and (5.6) are identical. Thus the settlements in rows 11 and 13 are the same. But those for $\nu = 0.33$ obtained from the two equations are markedly different. These are shown in rows 12 and 14 of the table. The values of the differential settlements obtained from equation (5.6) are not far from those obtained by the finite element interaction analysis,

see rows 8, 10 and 14. This suggests that a modification of the one dimensional settlement equation to the expression in equation (5.6) is in order. But for predicting the settlements under structures with any accuracy, the stresses to be used in equation (5.6) must be obtained by a refined interaction analysis.

The values of the settlements obtained for the fine mesh FE2 are somewhat higher than those for the coarse mesh FE1. This is because a model with a finer finite element mesh has more degrees of freedom and is therefore less stiff. The maximum variation of the differential settlements between the two meshes FE1 and FE2 is 16.6%. This indicates that a fairly coarse finite element mesh may be adequate to obtain an acceptable interaction analysis.

The inclusion of tensile separations in the soil in the analysis with mesh FE3 did not alter the values of the differential settlements to a significant extent for this particular frame. These are shown in rows 9 and 10 of table (5.2). The maximum difference between these results and those obtained with the same mesh FE2 but without dummy joints is 3.4 per cent. This is because the magnitude and the extent of the tensile stresses developed were very small, see figure (5.4). However, in many cases such separations will govern the interactive behaviour of the structure and the soil as will be shown in chapter 8. Consideration must therefore be given to tensile separations to avoid an underestimation of the settlements.

The bending moment diagrams for the columns and the beams of the frame are shown in figures (5.7) and (5.8). In these figures, curve 1 represents the bending moments obtained by a finite element interaction analysis with $\nu = 0.33$. Curve 2, on the other

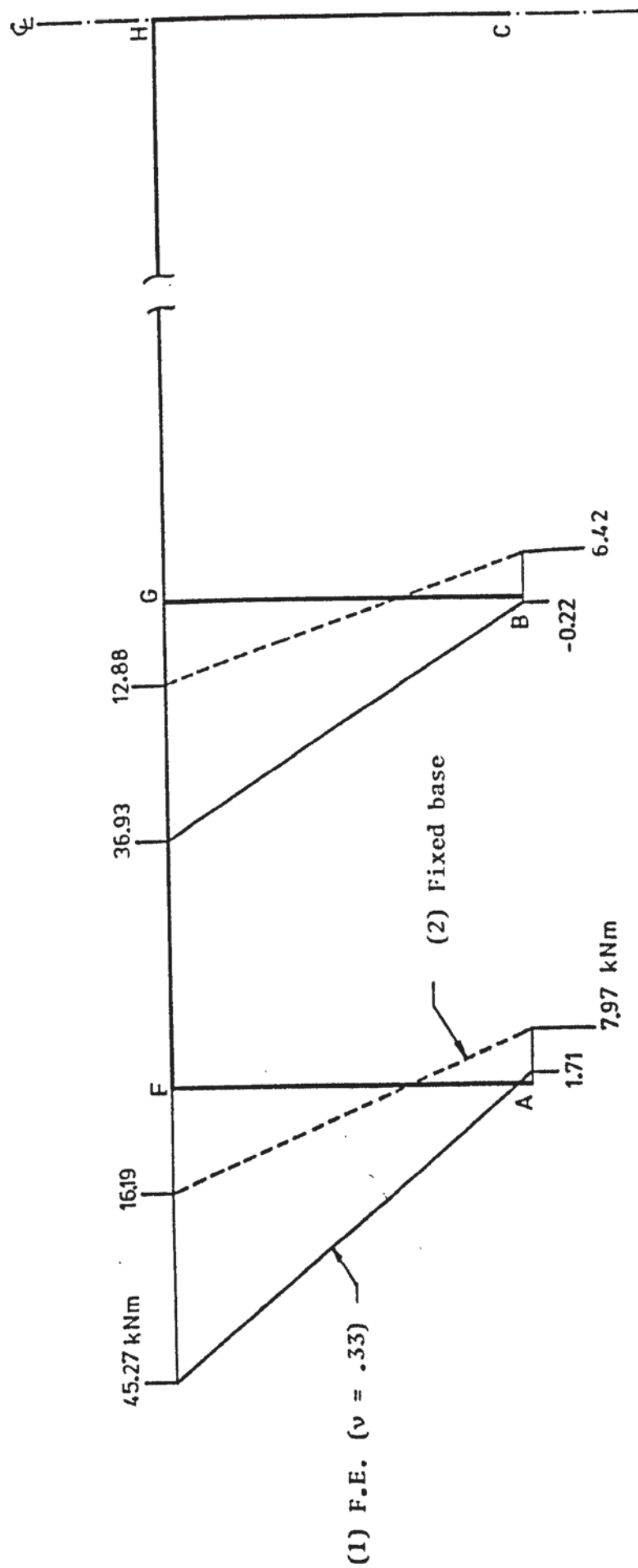


FIGURE 5.7 BENDING MOMENTS IN THE COLUMNS OF THE PLANE FRAME

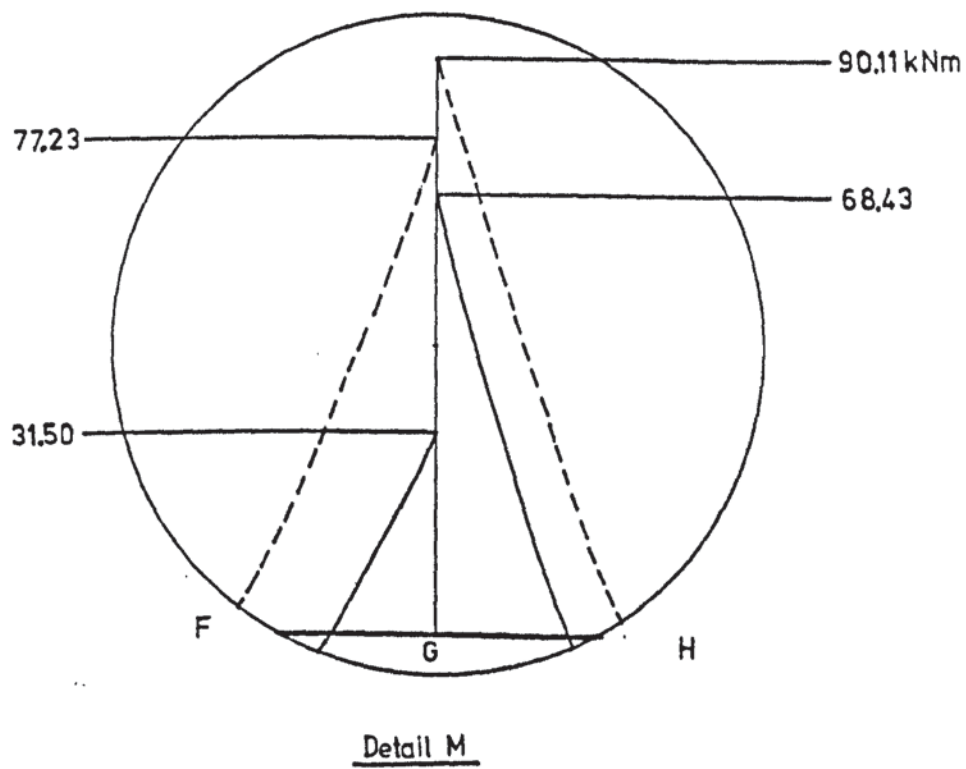
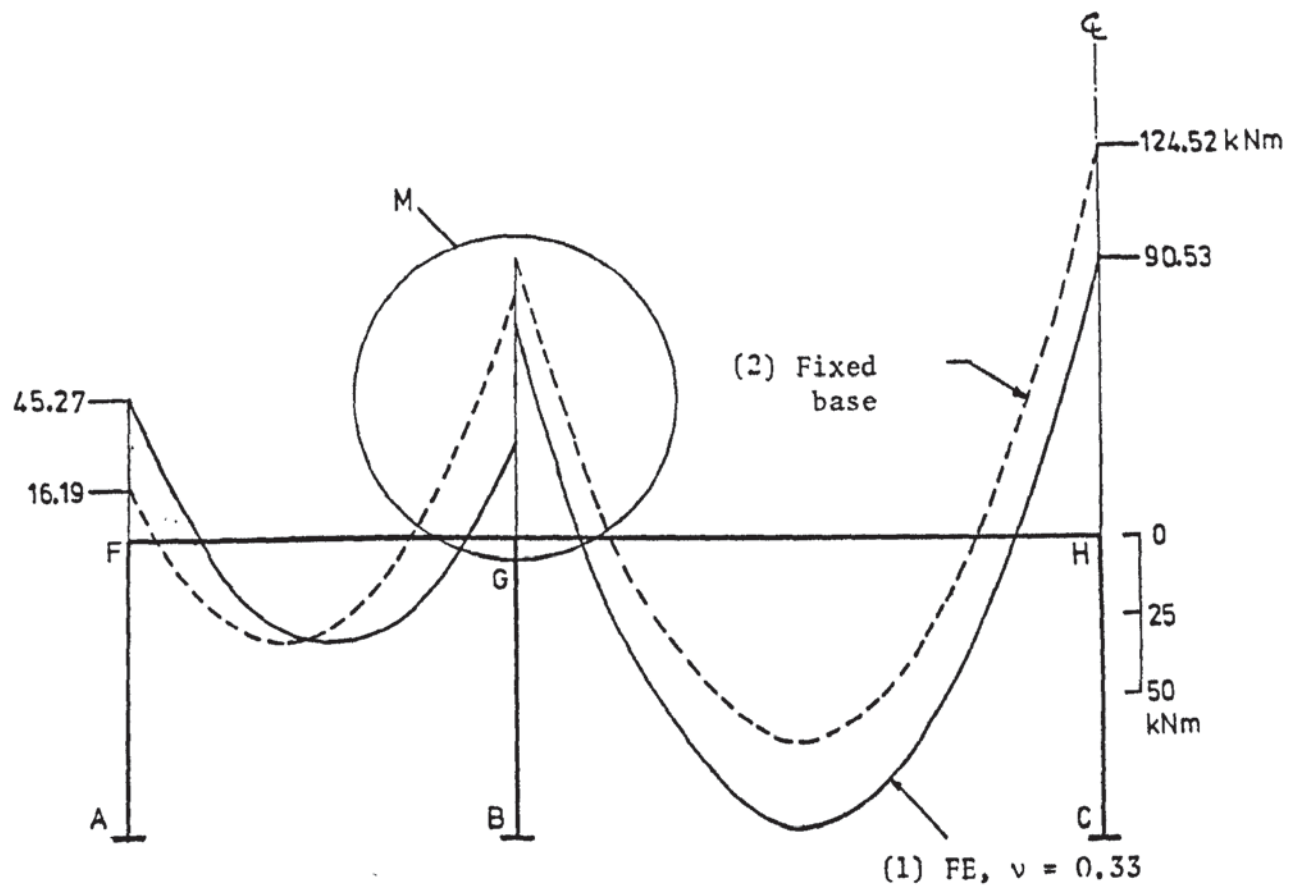


FIGURE 5.8 BENDING MOMENTS IN THE BEAMS OF THE PLANE FRAME

hand, indicates those obtained by assuming the column bases to be completely fixed. The bending moments obtained for the other values of ν were similar to those for $\nu = 0.33$. The maximum difference between these for $\nu = 0$ and $\nu = 0.33$, for example, was about 22%. The redistribution of the bending moments due to the interaction is significant in both the beams and the columns of the frame. The maximum difference between these obtained by the interaction and the fixed base analyses is as high as 187%. The interaction analysis shows very low and even reverse bending moments at the column bases, see figure (5.7). This is caused by the rotation and the consequent relaxation of the moments at these points. This reduction in the base moments increases the column top bending moments by as much as 187% at the point G in the column BG. Neglecting the base rotations increases the bending moments at the bases and reduces them at the top due to the "carry over" effect. Instead of a carry over factor of 0.5, it is noticed that only between -0.006 and 0.038 of the bending moments developed at the top of the columns are in fact carried over to the bases. Even in the beams, the difference between the bending moment diagrams obtained by the two methods is significant. The maximum difference is some 59% at the end G of the beam FG, see figure (5.8). However, this difference is mainly due to the differential settlements and not so much as a result of the base rotations. It is noticed that the fixed base analysis generally underestimates the span moments and overestimates the end moments in the beams. This is inaccurate and can produce a faulty design specially of a reinforced concrete frame. It is concluded that an accurate analysis requires the consideration of base rotations as well as the differential

settlements of these bases. A fixed base analysis or the consideration of the differential settlements only leads to gross inaccuracies.

5.6.3 Analysis of the plane frame resting on a non-linear clay

In the last sub-section, m_v was assumed to be constant. In reality m_v is variable and dependent on the stress level. The plane frame was therefore reanalysed by varying the value of m_v with the stress level but keeping the thickness of the clay layer the same as before. The properties of the clay were taken from an oedometer test data given in the text by Peck, Hanson and Thornburn (1974). The values of m_v for this clay and the corresponding stress range are shown in table (5.3).

The problem was analysed first with the coarse mesh FE1 and then with the fine mesh FE3 with facilities for crack propagation. The results are presented in table (5.4), where it is noticed that the differential settlements are lower than those given in table (5.2) for a fixed m_v . This is because, at moderate and high stresses, the clay is stiffer as indicated in table (5.3). The same trend of results as with the linear clay is also observed here. Both the redistribution of the reactions and the increase in the differential settlements become exaggerated for values of ν closer to 0.5. The difference in the results of the coarse mesh analysis and the fine mesh crack propagation analysis is again not very pronounced. The maximum difference of differential settlement between the two analyses is 9.1 per cent for a value of $\nu = 0.33$.

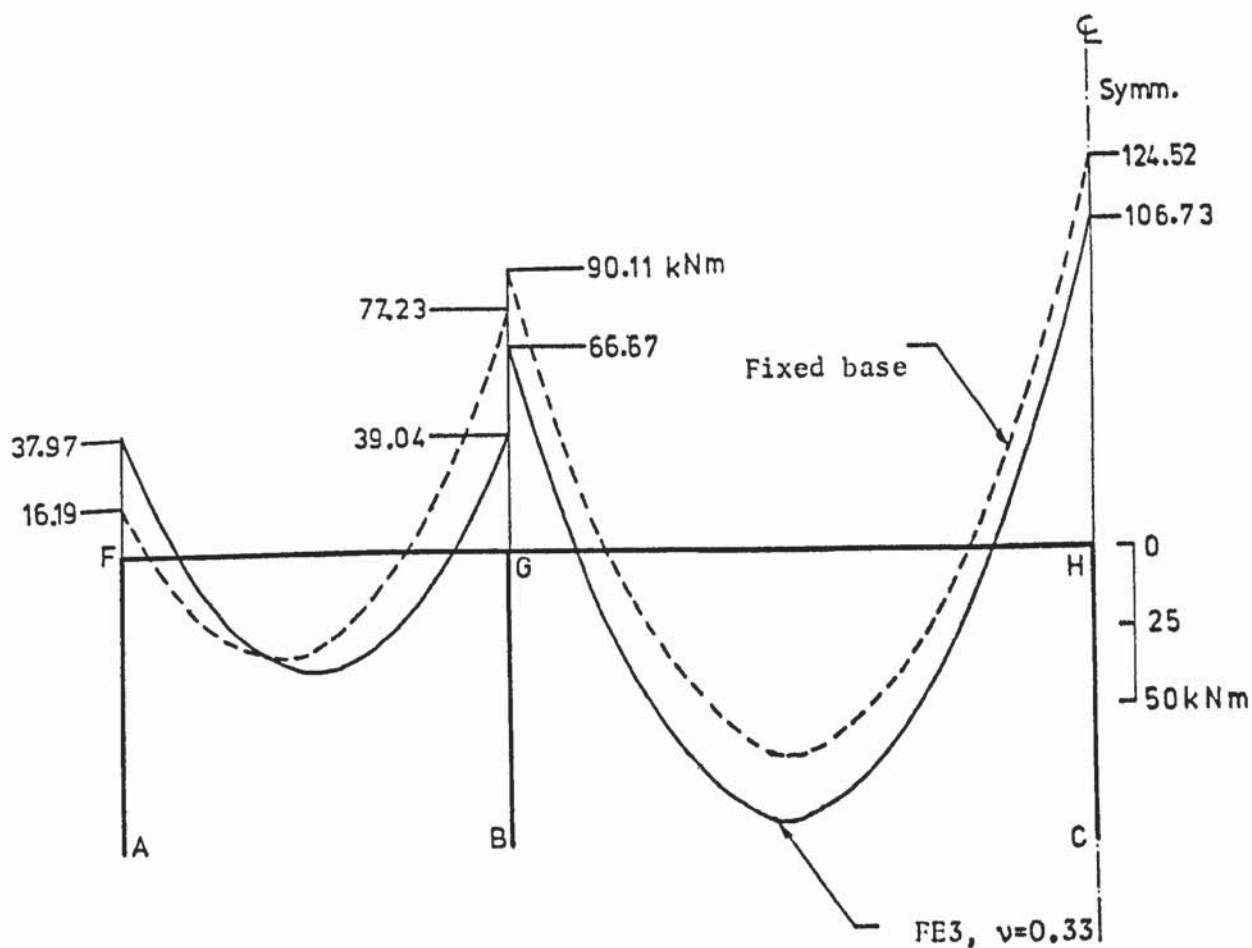
The bending moment diagrams are shown in figure (5.9). The full lines indicate the bending moments obtained by the finite

Vertical stress (kN/m ²)	Void ratio	m_v ($\times 10^{-3}$ m ² /kN)
0	0.959	0.7214
6.3681	0.950	0.4026
12.7363	0.945	0.5652
25.4725	0.931	0.4464
50.9930	0.909	0.4734
101.8902	0.863	0.4101
203.9719	0.785	0.2362
407.9438	0.699	0.1198
815.8877	0.616	
Larnach's m_v used in section 5.6.2		0.6527

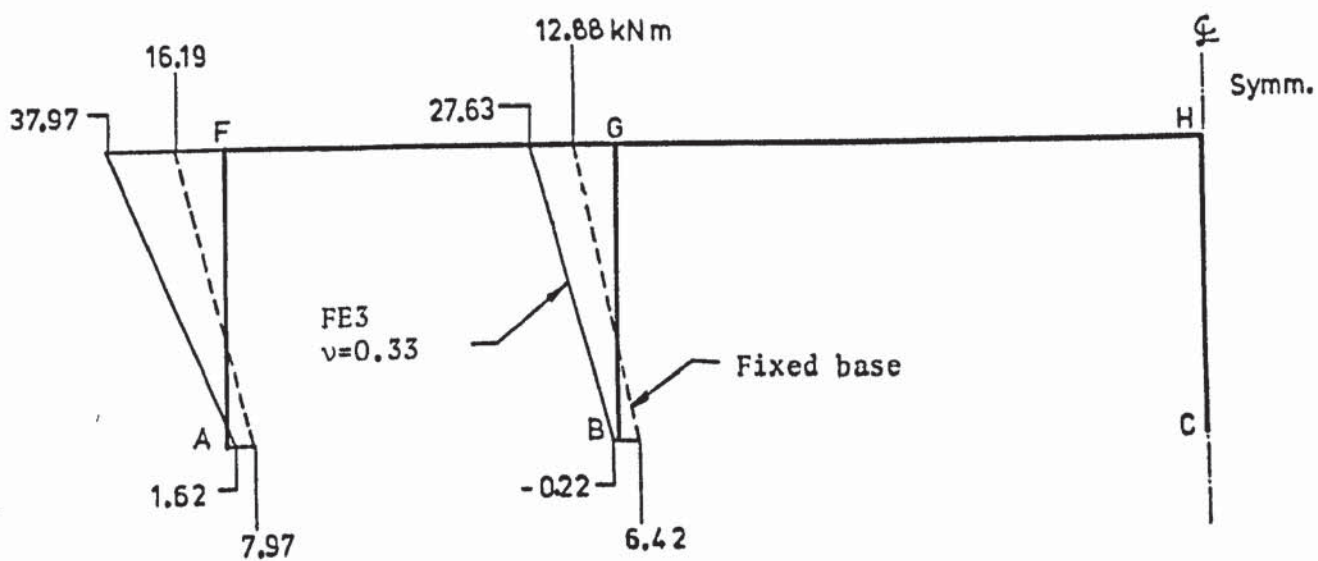
TABLE 5.3 PROPERTIES OF THE NON-LINEAR CLAY

Analysis method		Base reactions (kN)			Diff. settlements (mm)	
		A	B	C	($\delta_B - \delta_A$)	($\delta_C - \delta_D$)
Conventional method		79.3	262.0	313.8	62.0	11.8
FE1	$v = 0$	96.3	245.1	313.6	28.6	12.6
	$v = 0.2$	96.7	244.8	313.4	31.7	14.2
	$v = 0.33$	99.3	242.9	312.0	38.6	17.9
	$v = 0.49$	124.6	226.8	293.6	194.0	108.0
FE3	$v = 0.33$	99.3	242.5	312.8	39.3	16.4

TABLE 5.4 RESULTS OF THE PLANE FRAME ON NON-LINEAR CLAY



Bending moments in beams



Bending moments in columns

FIGURE 5.9 BENDING MOMENT DIAGRAMS OF THE PLANE FRAME RESTING ON NON-LINEAR CLAY

element analysis FE3 with $\nu = 0.33$ and the dashed lines indicate those obtained by assuming the supports to be fixed. The redistribution of the column bending moments due to the rotations of the bases is again significant. The maximum difference of the column bending moments obtained by these two analyses is as high as 135% occurring at F. In the beam this difference is as high as 49%.

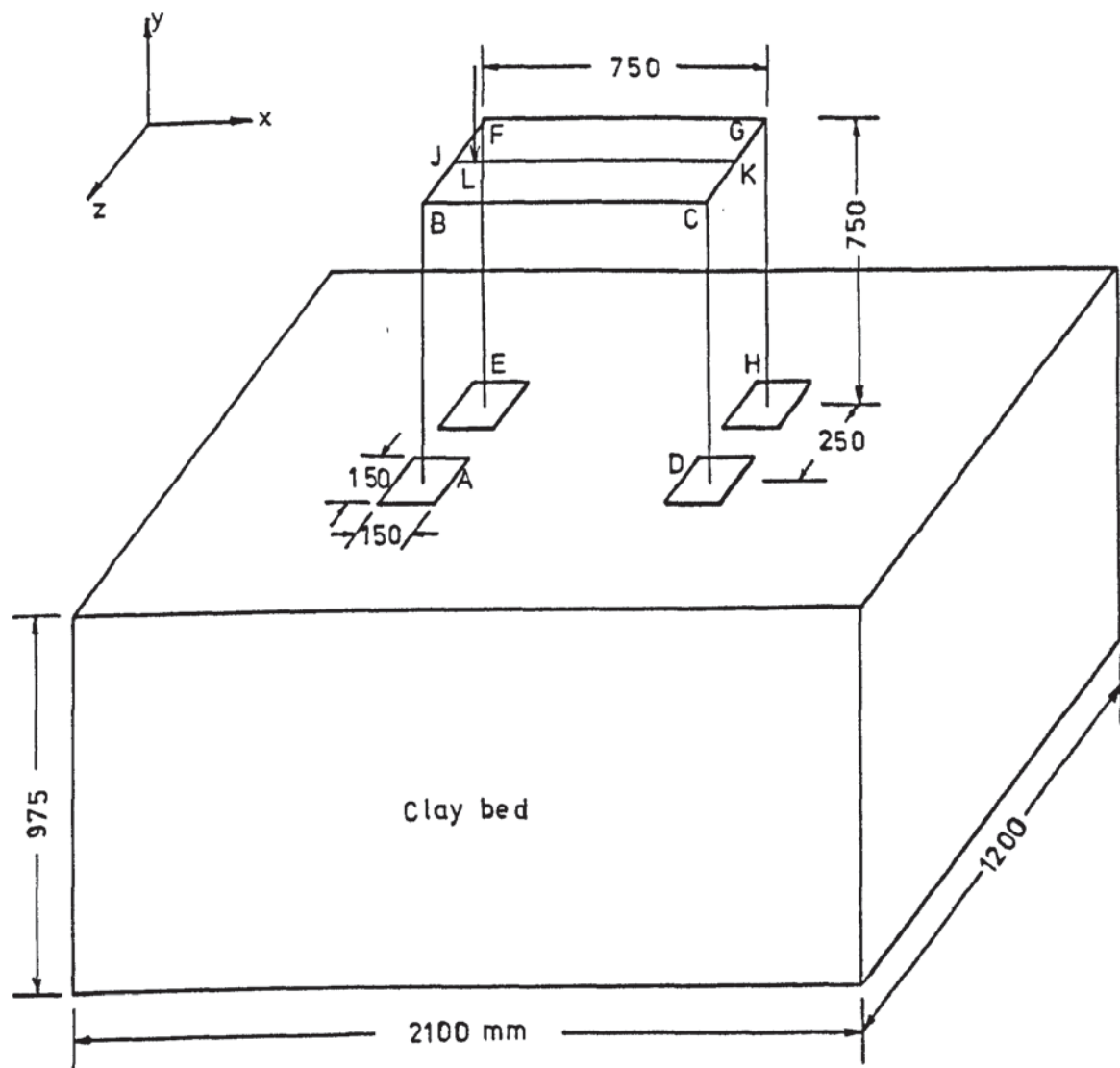
5.6.4 Analysis of a single-bay space frame

As a second example, the single-bay space frame shown in figure (5.10) resting on a confined mass of clay was analysed. This was a model structure made out of 25 mm square mild steel bars. The footings were 150 x 150 x 25 mm thick mild steel plates. The material properties of the members and the footings are also given in figure (5.10). The non-linear properties of the clay are assumed to be those given in table (5.3).

A single vertical load of 3.5 kN was applied eccentrically on the central beam. The structure was symmetrical about the vertical plane passing through this beam and therefore only half of the structure was considered. The finite element mesh for the complete structure and the soil is shown in figure (5.11). The divisions on the top beam were necessary to facilitate the grouping of the joints to be described in chapter 6. Three separate analyses were carried out.

These are:

- 1 The complete structure and the soil as an integral unit, see figure (5.11).
- 2 The structure was then removed. The pads and the soil were analysed, subject to the vertical loads obtained from a fixed base analysis of the frame. This model is shown in Figure (5.12).



Properties of the members

$$E = 206.9 \times 10^3 \text{ N/mm}^2$$

$$\nu = 0.3$$

Properties of the footings

$$E = 170.6 \times 10^3 \text{ N/mm}^2$$

$$\nu = 0.28$$

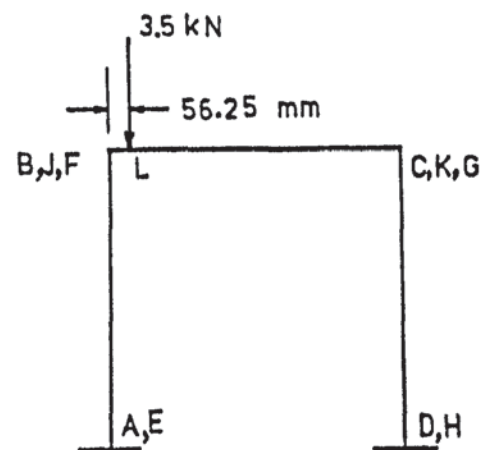
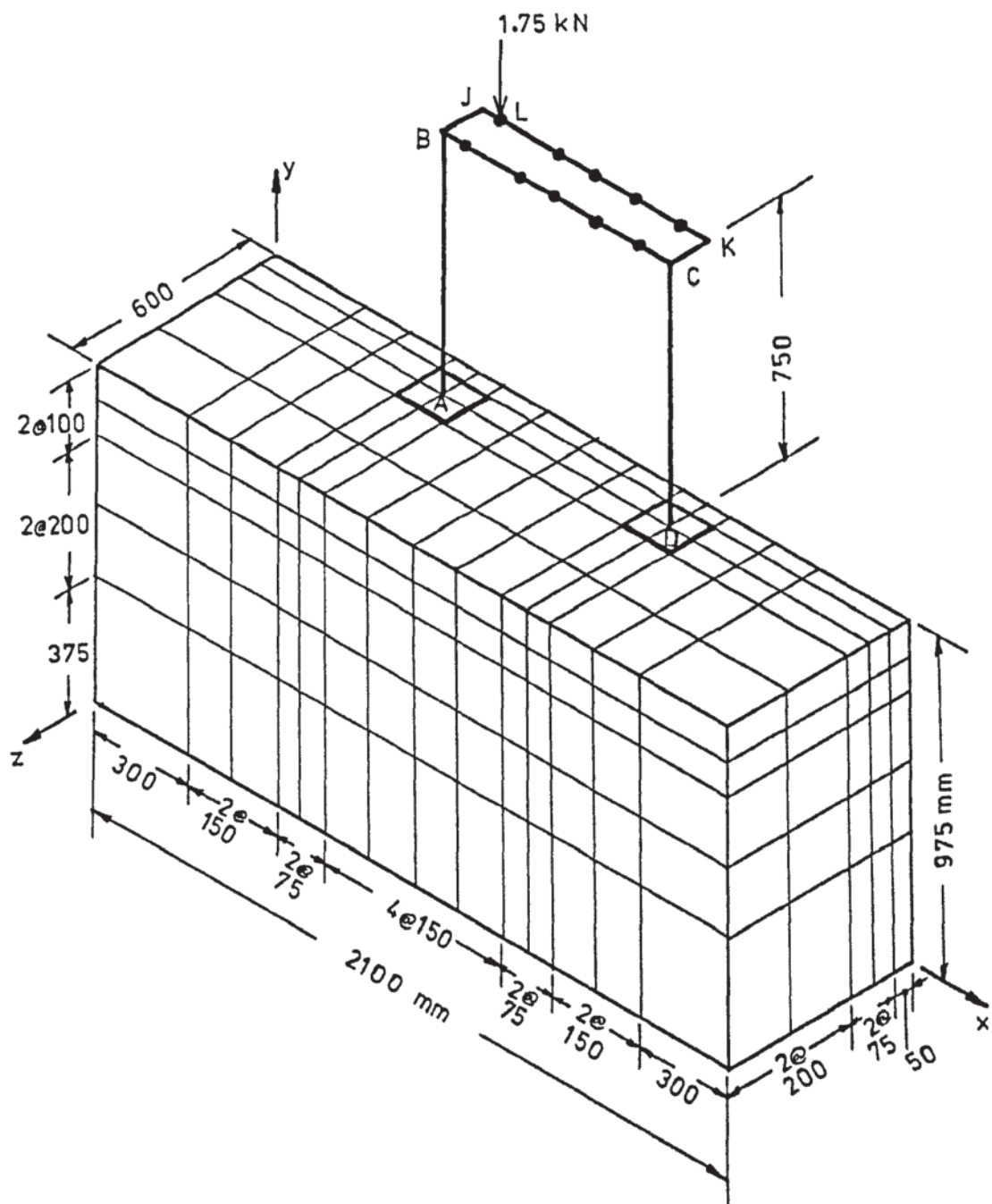


FIGURE 5.10 SPACE FRAME EXAMPLE



No of joints = 554
 No of solids = 350
 No of plates = 8
 No of members = 16

FIGURE 5.11 FINITE ELEMENT MESH FOR SPACE FRAME EXAMPLE

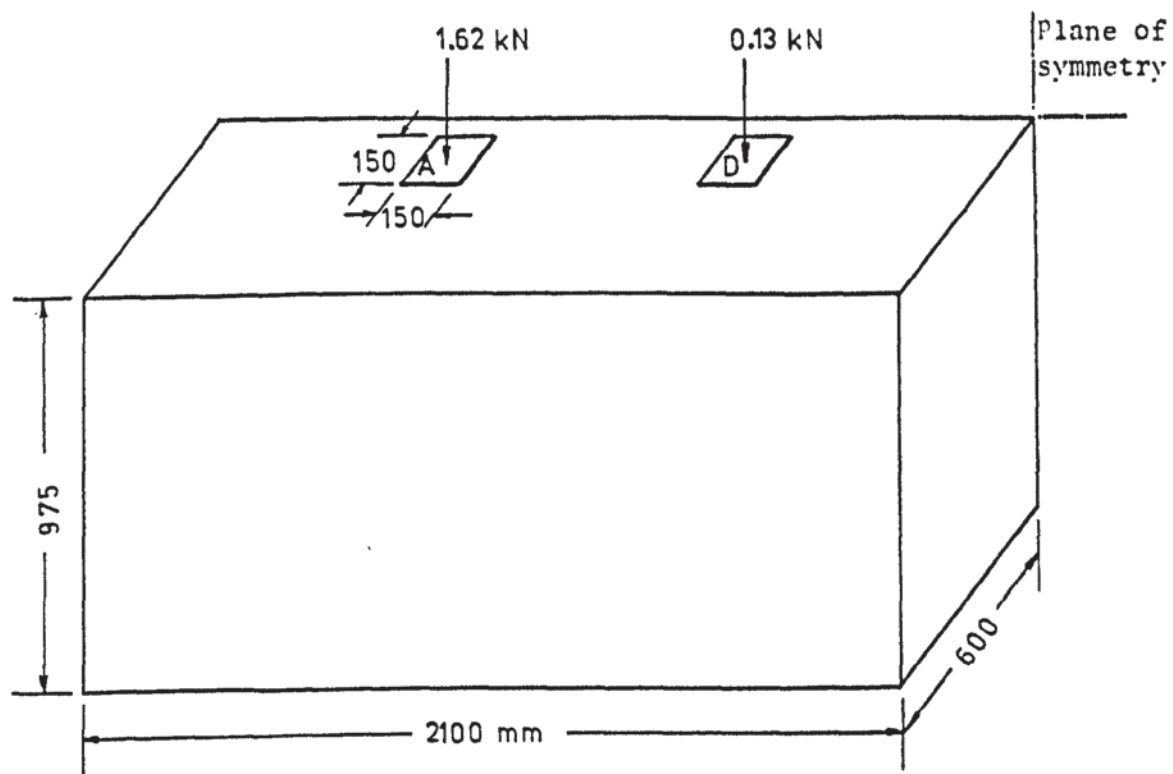


FIGURE 5.12 MODEL FOR ANALYSIS 2

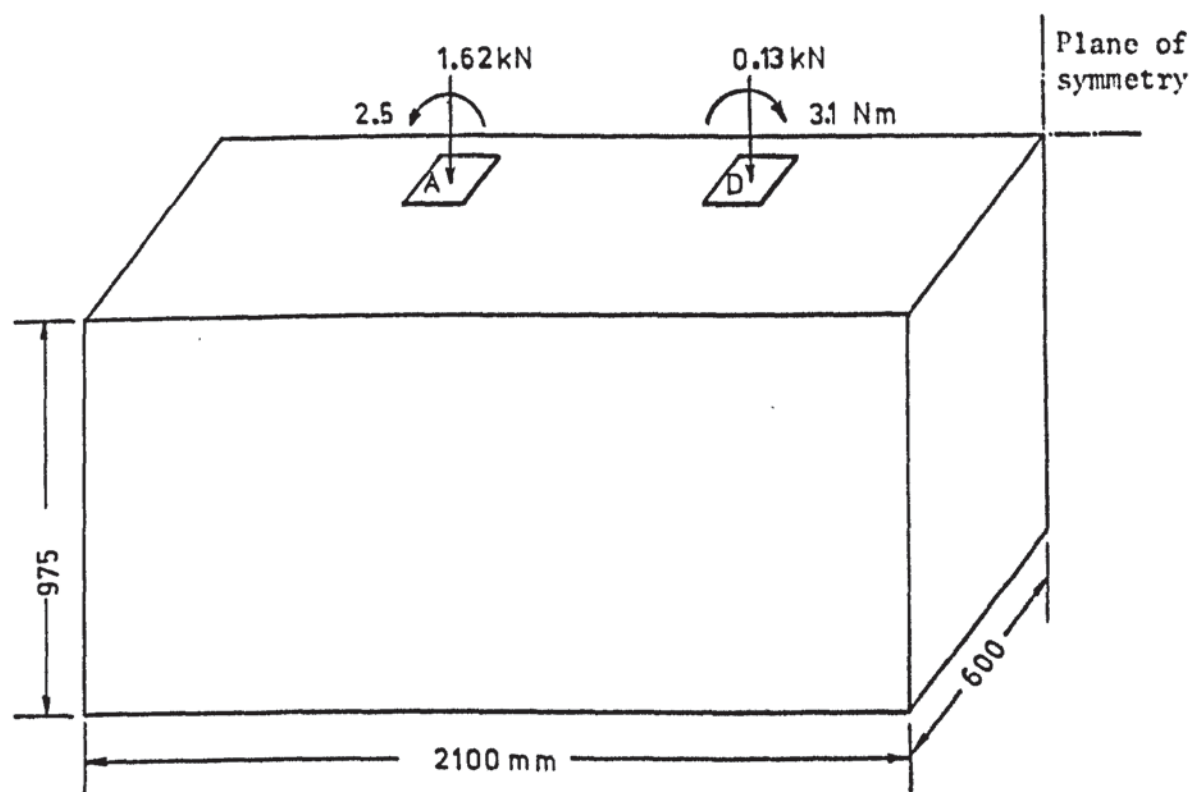


FIGURE 5.13 MODEL FOR ANALYSIS 3

3 Analysis (2) was repeated but this time with vertical loads and moments acting on the pads, as shown in figure (5.13). The base moments were also obtained from a fixed base analysis.

The differential settlements between the left (A, E) and the right (D, F) footings as obtained by the various analyses are given in table (5.5). The same trend of results as that of the plane frame example is also experienced here. The conventional method of settlement calculation using Boussinesq stresses and equation (5.1) again gives a higher value than that obtained by the finite element analysis with $\nu = 0$. This is so even when the structure is removed. The increase of the differential settlement with ν is once again demonstrated. The effect of the interaction of the structure with the soil in reducing the differential settlements is also demonstrated. Analysis (1) gives the lowest values while analysis (3) gives the highest differential settlements. The discrepancy between these results is as high as 12%. This figure is likely to be higher for more complex frames with greater stiffnesses.

The bending moments about the z-axis, for the part ABCD of the frame, are shown in figure (5.14). Lines 1, 2 and 3 represent the bending moments obtained by the finite element interaction analysis (1) with values of ν equal to 0, 0.33 and 0.45 respectively. The bending moments obtained by assuming fixed supports are shown by lines 4. The redistribution of the bending moments in both the beams and the columns are evident in the figure. As ν increases the bending moments become more and more different from those obtained by a fixed base analysis. However, even with $\nu = 0$, an interaction analysis redistributes the bending moments significantly.

Method of analysis			Differential settlement (mm)
Conventional method			4.3
Analysis 1	Finite element interaction analysis of complete structure and soil	$\nu = 0$	3.3
		$\nu = 0.33$	4.8
		$\nu = 0.45$	9.8
Analysis 2	Finite element analysis of the footings and the soil with vertical fixed base reactions applied as external loads on the footings.	$\nu = 0$	3.5
		$\nu = 0.33$	5.1
		$\nu = 0.45$	10.6
Analysis 3	Finite element analysis of the footings and the soil with fixed base vertical reactions and moments applied as external loads on the footings.	$\nu = 0$	3.7
		$\nu = 0.33$	5.3
		$\nu = 0.45$	10.9

TABLE 5.5 RESULTS OF THE ANALYSIS OF THE SPACE FRAME

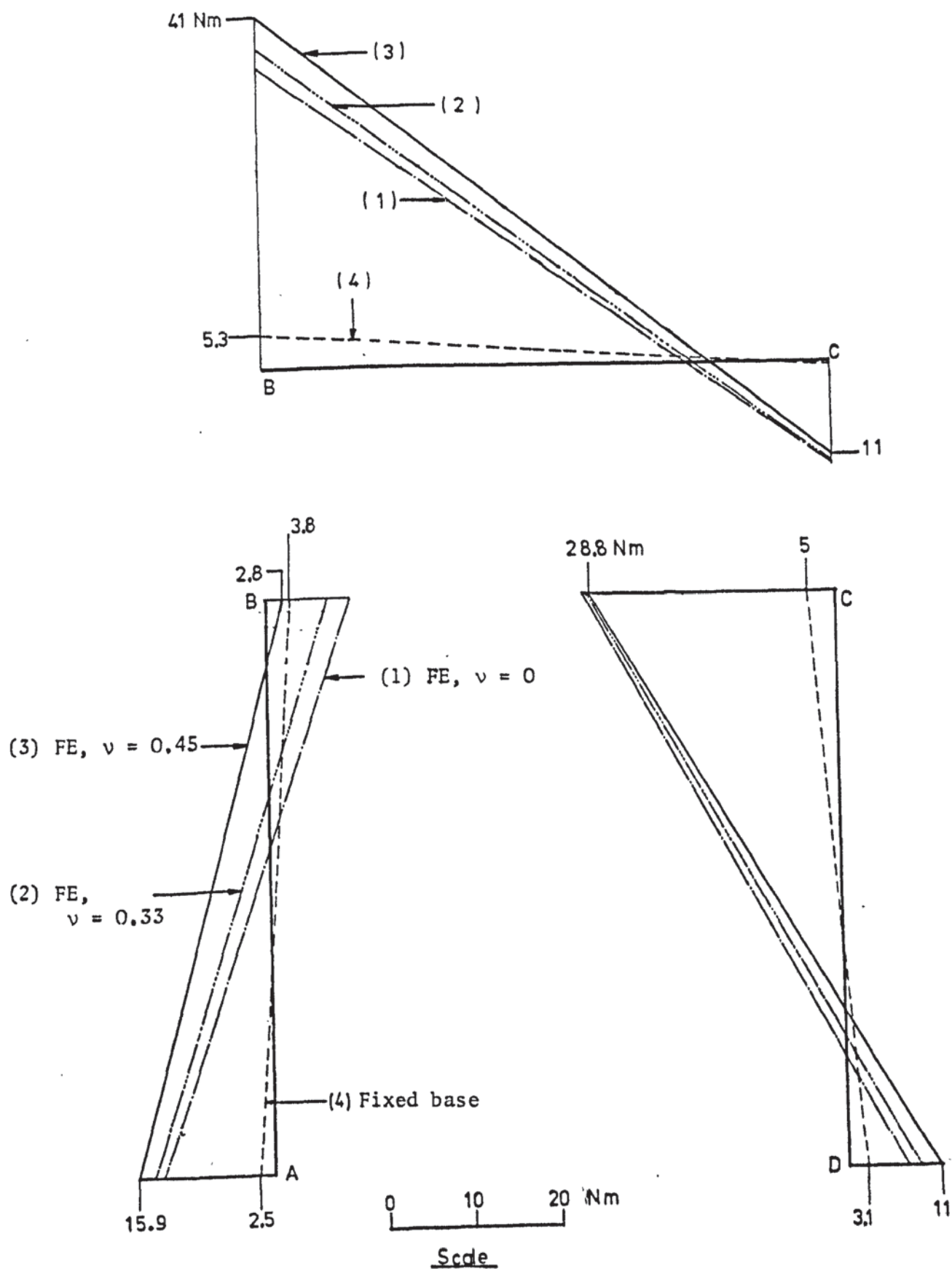


FIGURE 5.14 BENDING MOMENTS IN THE SPACE FRAME

CHAPTER 6

THE FINITE ELEMENT COMPUTER PROGRAMS

6.1 INTRODUCTION

The essential features of an interaction problem have been listed in chapter 1. In the subsequent chapters, methods of considering non-linearity and crack propagation have been described. The purpose of this chapter is to utilize these methods and develop finite element programs for the analysis of a complete structure together with its foundations and the soil. The nature of the programs is general and they can be used to analyse large practical structures. The largest example given in this thesis is a 50-storey space frame resting on clay with 1632 joints and about 4500 degrees of freedom. The programs are written in such a way as to reduce the use of the computer core storage and the execution time. The input data is largely automated so that only a small amount of manual effort is necessary to run the programs. All the programs described here are written in FORTRAN to be run on the CDC 7600 computer at the University of Manchester Regional Computer Centre.

6.2 THE FINITE ELEMENTS USED

Majid and Williamson (1967) used a combination of space frame members and rectangular plates to perform a linear analysis of complete three dimensional structures. Most structures can be discretized by a number of elements of these two basic types. The soil, however, is a three dimensional continuum, requiring the use of a three dimensional solid element. Therefore a total of three different finite elements were included in the programs. These are listed below:

(1) Space frame member elements

These elements were developed by Majid (1972). In addition to representing the centre line of the frame members they can take account of the irregularities at the ends of the members. The element can also be used to represent plane frame members by restricting the out of plane movements of its end joints. The element is described in Appendix II.

(2) Rectangular plate elements

These elements have both in-plane and out of plane forces and displacements. They can either be used as plate bending elements or as shear wall elements by a suitable selection of the degrees of freedom and the stiffness terms. These elements were taken from a package developed by Bray (1973). The element is also described in Appendix II.

(3) Rectangular parallelopiped solid elements

This is a regular prismoidal element with eight nodes and a linear variation of displacements between the nodes. Each node of the element can have three translation degrees of freedom. The element has been fully described in chapter 3.

For all the above elements the stiffness matrix was formed explicitly and no numerical integration was required. In this manner considerable computer time was saved. A suitable combination of these elements enables the analysis of a large variety of problems. However, for structures which do not lend themselves to a discretization to these elements alone, it is only necessary to add a few more elements to the program library. The overall method of analysis remains unaltered.

6.3 THE COMPUTER PROGRAMS

The non-linear analysis is performed by two distinct methods. When the mechanical properties of the soil are given by an explicit set of $\tau_{\text{oct}} - \gamma_{\text{oct}}$ curves, the incremental method described in chapter 3 is used. On the other hand, an iterative technique is used with soils whose properties are given by a set of m_v and their corresponding stresses. A suite of programs was written to perform each of these two types of analysis. The programs are identical except for the processes of updating the non-linear material properties and controlling various stages of the analysis.

6.4 STORAGE OF THE STIFFNESS MATRIX

Two classical computer problems associated with the displacement method of analysis of large structural problems are the storage of the stiffness matrix and the mill time required for the solution of the simultaneous equations. The analysis of a complete structure, its foundation and the soil gives rise to a large, sparse, symmetric and positive definite stiffness matrix. The number of equations to be solved is also very high. Therefore, the scheme of storage of the stiffness matrix was carefully selected to reduce the use of the core space without an undue increase in the execution time.

The stiffness matrix of a structural system is symmetrical containing a large number of zeros. The non-zero elements are concentrated near the leading diagonal, as shown in figure (6.1). Advantage is frequently taken of these features by storing the lower triangle of the matrix. As a further improvement Jennings (1966, 1977) proposed a variable band width storage scheme in which only the elements between the first non-zero and the leading diagonal element in each row are stored. This is achieved by storing the



1	1	symmetrical						
2	2	3						
3		4	5					
4		6	7	8				
5			9	10	11			
6		12	13	14	15	16		
7						17	18	
8			19	20	21	22	23	24
	1	2	3	4	5	6	7	8

FIGURE 6.2 COMPACT STORAGE SCHEME

elements in a continuous row-by-row sequence. Thus only the area of the stiffness matrix bounded by the full stepped lines in figure (6.1) is stored. This compact storage scheme is also adopted here. The saving in storage of this scheme over a fixed band width scheme is evident in the figure.

The compact storage scheme is illustrated in figure (6.2), in which each blank square indicates a zero element which is disregarded. The numbers in this figure indicate the address locations in the one dimensional sequence where the elements are stored. For example, the element in row 6 and column 4 is stored at address 14. To locate an element of the stiffness matrix in the storage array, it is necessary to know the address of the diagonal element in each row. A one dimensional diagonal address sequence array, DAS, was declared to hold these addresses. A list of the variables and the arrays in the programs is given in Appendix III. The array DAS for the matrix in figure (6.2) is:

DAS = [1 3 5 8 11 16 18 24]

The length of this array is equal to the number of rows in the stiffness matrix. Thus the location, ℓ , of the element in row i and column j of the matrix is given by:

$$\ell = \text{DAS}(i) - i + j$$

6.5 CONSTRUCTION OF THE STIFFNESS MATRIX

The compact storage scheme of Jennings is very efficient in saving computer storage. Nevertheless, the storage requirements of a large structure can still be high. For some of the large problems analysed in this thesis as many as one million storage locations were needed. Such a huge number of elements necessitated

the use of the backing store facilities so that only a part of the stiffness matrix is held in the core. Care is needed to reduce the time to transfer these elements to and from the backing store. The backing store facilities are best utilized by constructing the stiffness matrix \underline{K} in a sequential order. When a part of this matrix is fully constructed it is written into the backing store. The same area of the core space can then be used to construct the next part of the stiffness matrix. To reduce the number of transfers, matrix \underline{K} should be subdivided in such a way as to make its parts independent of each other.

The stiffness matrix is constructed by superimposing the stiffness contributions of the individual elements. The element stiffness matrices, whose stress-strain relationships are linear, remain unaltered throughout the analysis. These are therefore constructed only once. On the other hand, the properties of the soil elements are altered after each cycle of the analysis. The overall stiffness matrix is therefore constructed in two phases. In the first phase, the matrix is constructed with the contributions from the elastic elements only. This incomplete stiffness matrix remains unaltered in the successive analyses. In the second phase of construction, the contributions from the non-linear elements are superimposed on this matrix. In each increment of the load or in each iteration, only the second phase of the construction is repeated.

However, when new rows and columns are introduced to the stiffness matrix due to the development of a crack, the overall stiffness matrix changes. In this case the first phase of the construction has to be repeated. Two different methods of the

construction of the overall stiffness matrix by keeping only a part of it in the core at any one time have been developed. These are described in the following sub-sections.

6.5.1 The method of joint groups

6.5.1.1 Development of the method

In this method the fundamental consideration is that the construction of the stiffness matrix should proceed element by element. Thus each element is taken in turn and its contributions are superimposed on the rows and the columns of the stiffness matrix. All the elements contributing to this particular portion of the stiffness matrix are considered and the construction proceeds to the element contributing to the next part of \underline{K} . To achieve this sequence of construction, the joints in the finite element mesh are divided into a number of groups. The joints in group number i are only connected to the joints in groups h and j . Here $h = i-1$ and $j = i+1$. Thus an element that contributes to the rows and the columns of group i can also contribute to groups h and j . In the computer program, care was taken to ensure that only groups i and j are kept in the core simultaneously. The parts of \underline{K} corresponding to the groups j and $j+1$ are constructed after transferring group i to the backing store. Thus the construction of the stiffness matrix proceeds using only a limited core storage corresponding to two consecutive joint groups.

6.5.1.2 Computer implementation of the method

The division of the joints into groups is carried out automatically. The only data necessary is the highest joint number of the first joint group, $NJ1$. To each joint in the finite element mesh, the program associates a joint, which is the lowest

numbered joint directly connected to it. This is called the least joint number of a particular joint. With the last joint number NJ1 of group number 1 known, the program automatically assigns the last joint number of each subsequent group. Thus each joint group contains a number of consecutive joints.

The subroutine JGROUP divides the joints into groups. The procedure is demonstrated by the example finite element mesh shown in figure (6.3). A convenient value of NJ1 for this problem is 4. The program scans through successive joints to check if the least joint number of a joint is less than or equal to the last joint number of the preceding group. The highest joint number satisfying this requirement is the last joint number of the current group. All the intermediate joints also belong to this group. The highest joint number with the least joint less than 4 is 9 in figure (6.3). Although a lower numbered joint, 7, does not have its least joint number in group 1, all the joints from 5 to 9 are included in group 2. This ensures that no element contributes to more than two consecutive groups. The last joint numbers of groups 3 and 4 in the figure are 14 and 19 respectively. The subroutine also calculates the solid, plate and member element numbers belonging to each group. An element is said to belong to a joint group if its lowest numbered node is in this group. Thus the elements that belong to each joint group in the figure are as follows:

Joint Group	Solid Element No.	Plate No.	Member No.
1	1		
2	2		1,2
3	3	1	3,4
4			5

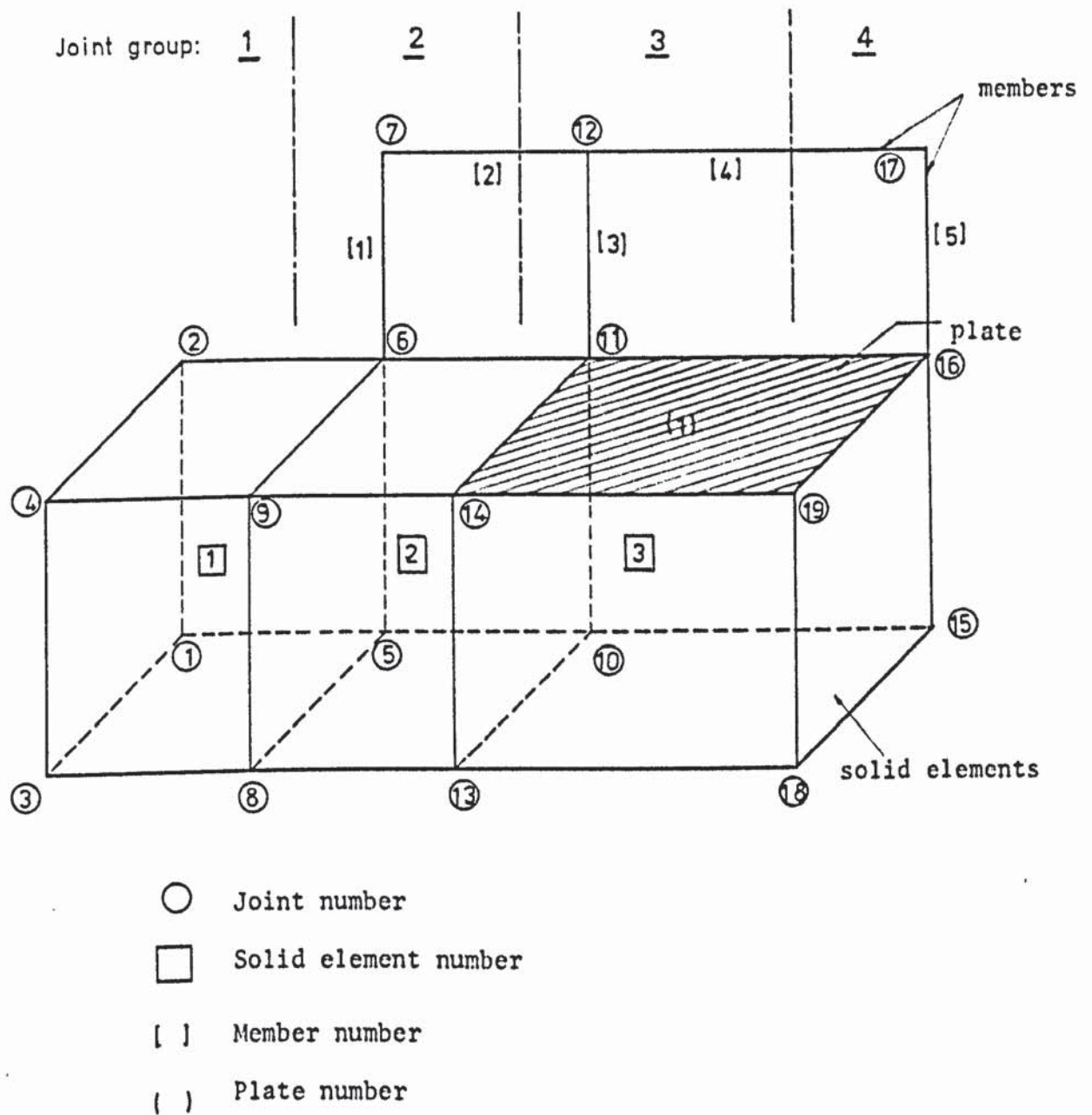


FIGURE 6.3 A FINITE ELEMENT MESH TO DEMONSTRATE JOINT GROUPING

However, these elements may also contribute to the next joint group. The flowchart of subroutine JGROUP is shown in figure (6.4). The symbols are:

NJG = Total number of joint groups,
 NOJ = Total number of joints in the mesh,
 JGRP(J) = Last joint number of group J,
 NEJG(J) = Number of solid elements in group J,
 LGRP(J,I) = Solid element number I in group J,
 NPJG(J) = Number of plate elements in group J,
 LPGRP(J,I) = Plate number I in group J,
 NMJG(J) = Number of member elements in group J,
 LMGRP(J,I) = Member number I in group J.

Another basic information necessary is the last element number in the one dimensional stiffness array, see section (6.4), that correspond to each joint group. This is calculated in subroutine FORMDAS where the diagonal address sequence of the stiffness array is formed. These basic joint group informations are stored in the core in a COMMON block to be accessed during the construction of \underline{K} .

As mentioned earlier the global stiffness matrix is constructed in two phases, with the first phase being performed only once. In this phase, each pair of consecutive joint groups is considered in turn. The stiffness contributions of the plate and member elements that belong to the first group of this pair are superimposed on the global \underline{K} . If this group does not have any element of these two types the construction proceeds to the next pair. Otherwise, the part of \underline{K} corresponding to the first group of the pair is written into the direct access backing store unit DA6. The part corresponding to

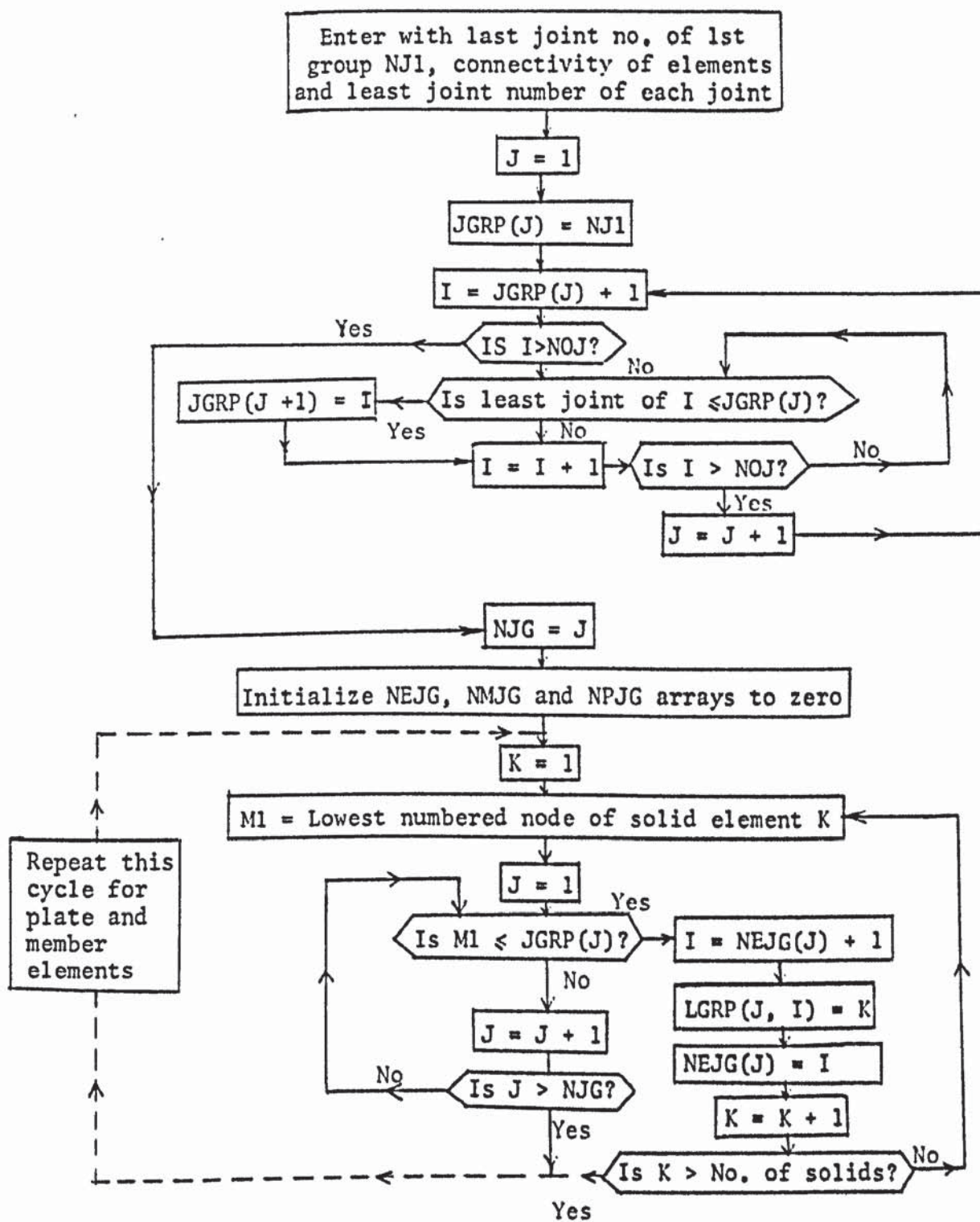
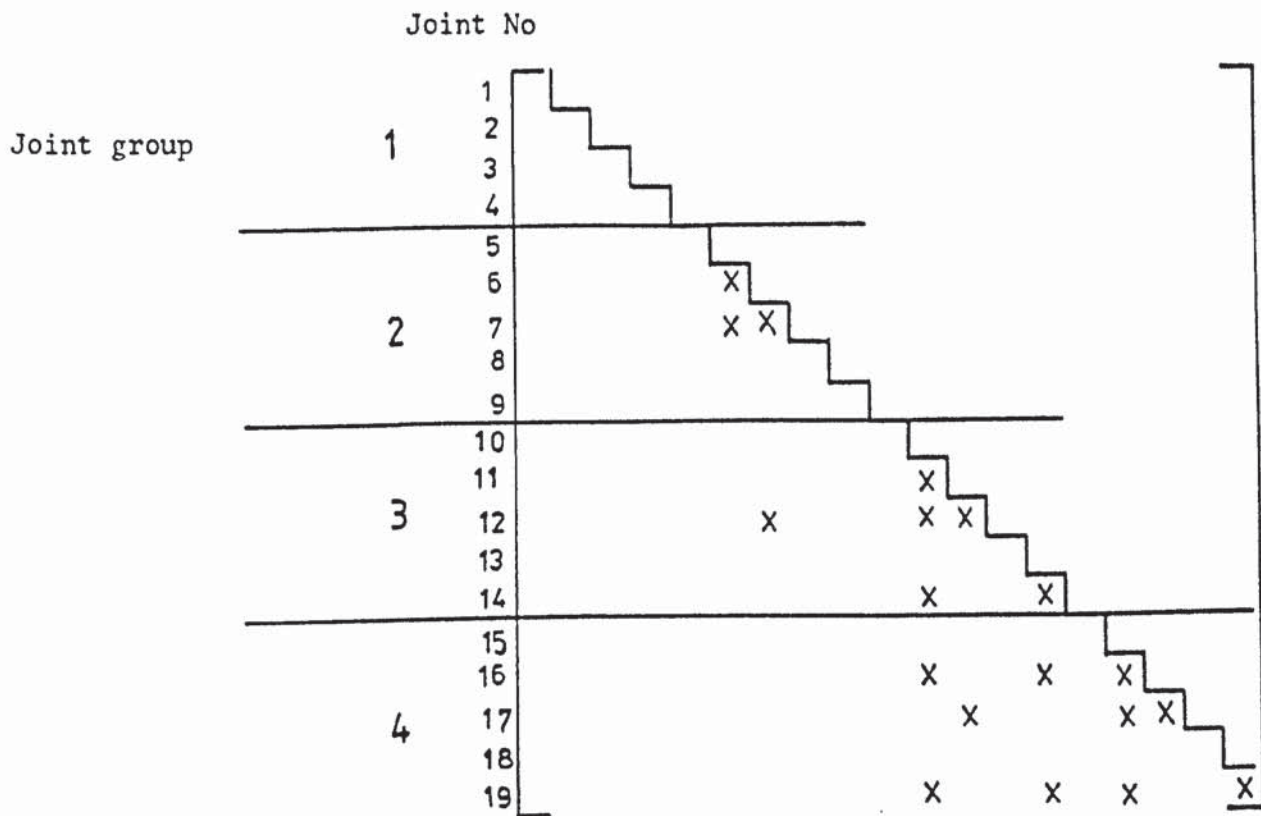


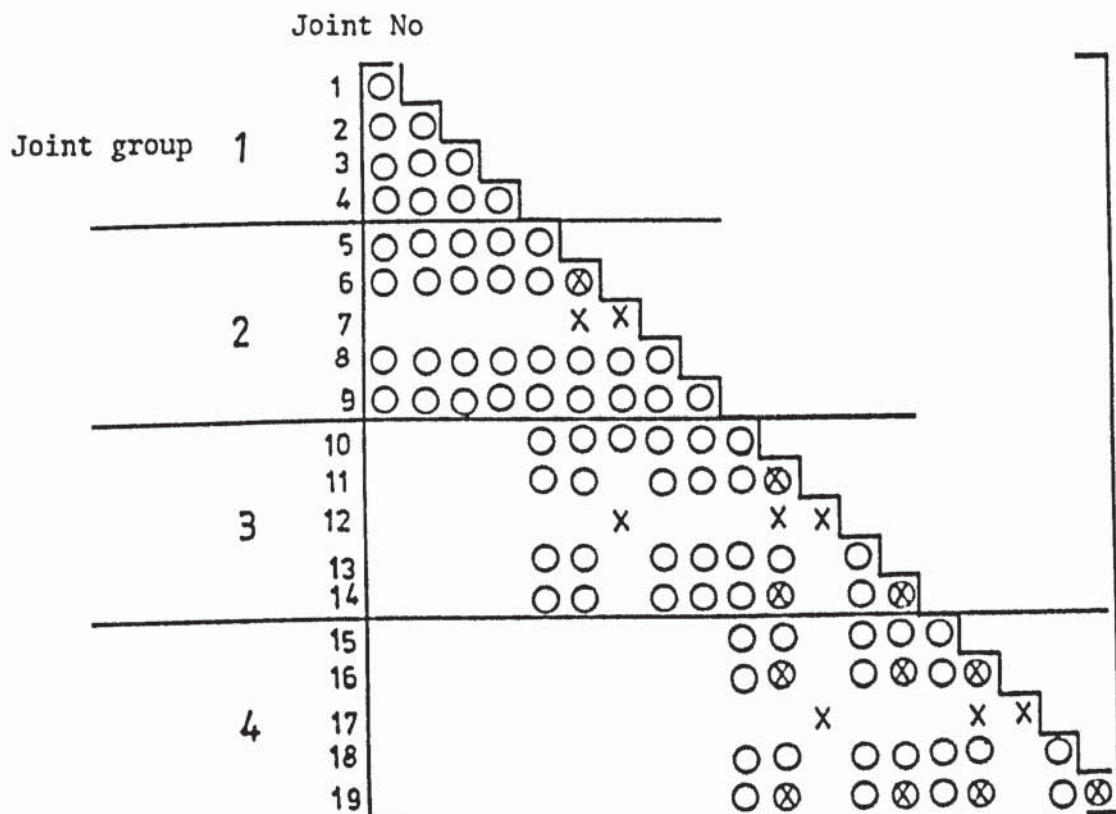
FIGURE 6.4 FLOWCHART OF SUBROUTINE JGROUP

the second group is moved forward in the core and the same area is used for the next pair of joint groups. If at any stage during the construction it is indicated that the second group in a pair does not have any plate or member element, then both the groups are written into DA6 at the same time. By following this procedure the stiffness contributions of the plate and member elements are placed in their appropriate locations in the one dimensional stiffness array at the same time as they are evaluated. At the end of this procedure the entire stiffness array is in the backing store unit DA6. However, this array is still incomplete and is yet to receive contributions from the solid elements. The incomplete stiffness matrix after the first phase for the mesh in figure (6.3) is shown in figure (6.5a). The flowchart for this phase of the construction is shown in figure (6.6).

The contributions to the stiffness matrix from the solid elements are calculated in the second phase. The scheme of construction is shown diagrammatically in figure (6.7). Each pair of joint groups is again considered in turn. At a particular stage, the first group i of this pair has already received contributions from the solid elements belonging to the preceding group h . If joint group i also receives contributions from a plate or a prismatic member, the part of \underline{K} corresponding to this group is copied from DA6 into the space in core reserved for the second group, j , of the pair. This part is then superimposed on the part of the stiffness matrix in core which correspond to group i . The stiffness contributions of the solid elements belonging to group i are then evaluated and superimposed on \underline{K} . Some of these elements also contribute to the part corresponding to group j . When all such solid elements have been considered,



(a) First phase (for members and plates)



(b) Second phase (complete \underline{K})

X Contribution of members/plates ○ Contribution of solid elements
 ⊗ Contribution of both

FIGURE 6.5 STIFFNESS MATRIX FOR PROBLEM IN FIGURE 6.3

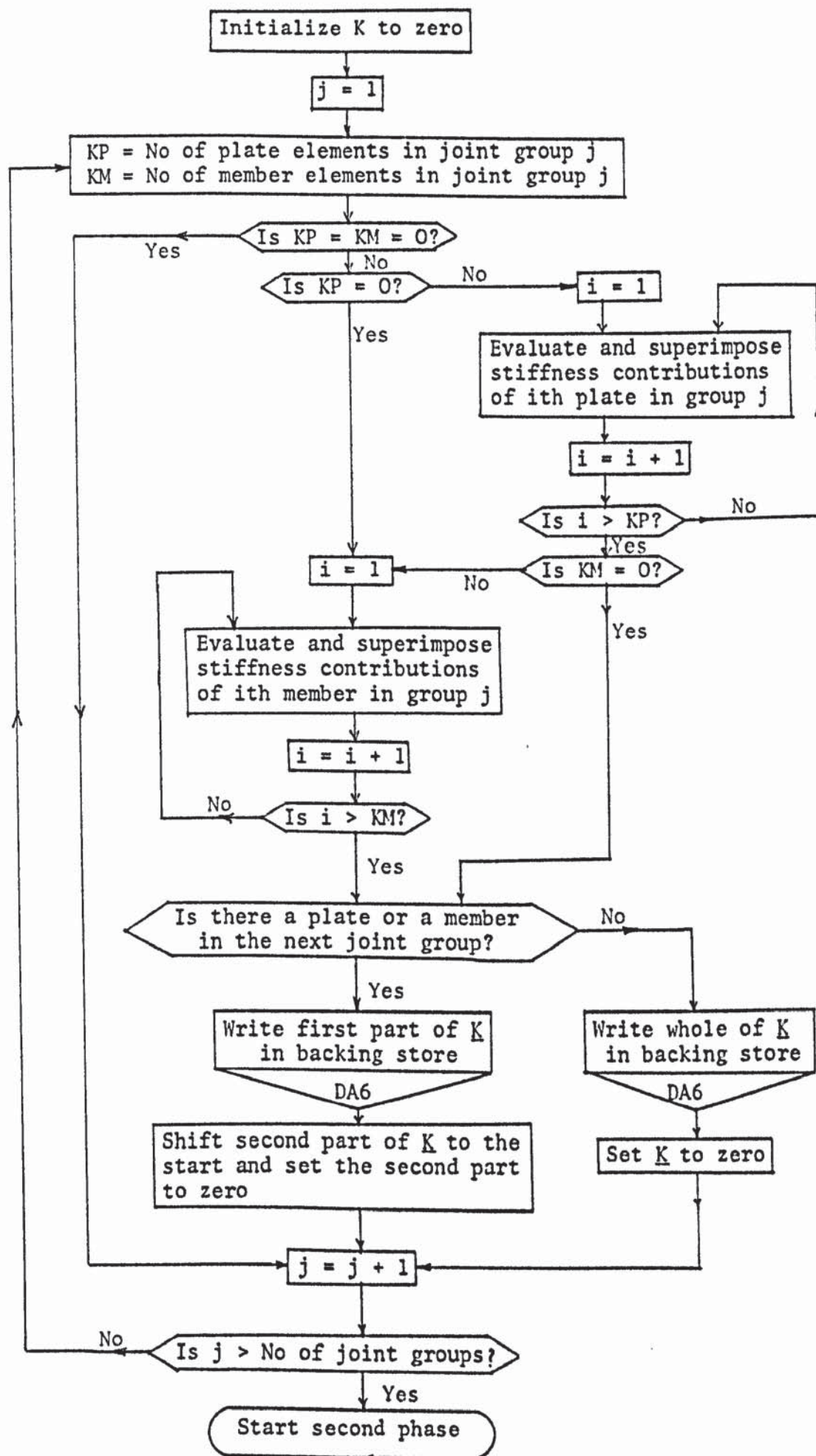


FIGURE 6.6 FLOWCHART FOR THE FIRST PHASE OF CONSTRUCTION OF \underline{K}

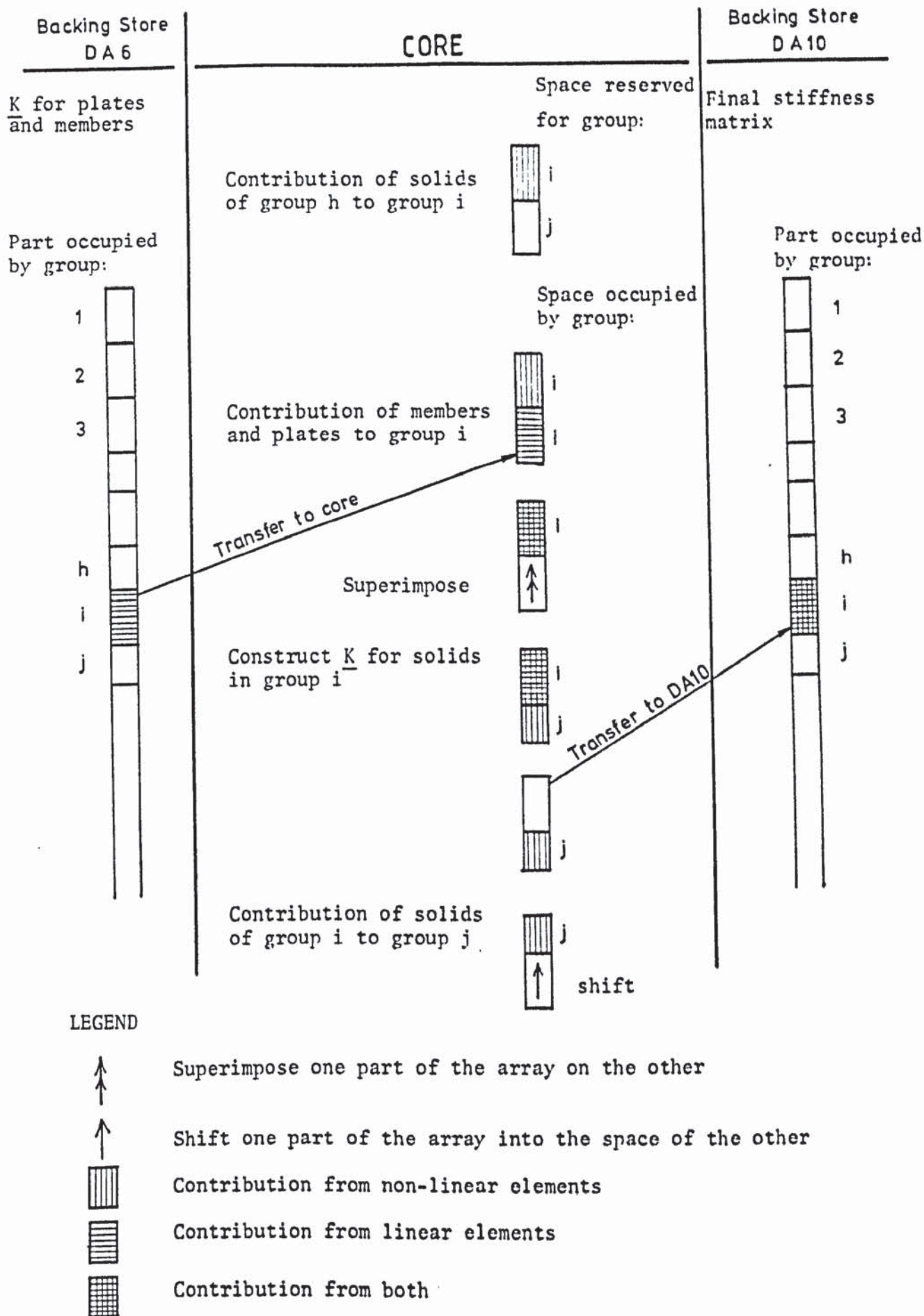


FIGURE 6.7 SCHEME OF THE SECOND PHASE OF CONSTRUCTION OF THE STIFFNESS MATRIX

the part of the stiffness matrix corresponding to group i is complete. It is then written into the backing store unit DA10 ready to be read during the solution process. The part of the stiffness matrix corresponding to the second group j is shifted forward to the start of the stiffness array in the core. The construction of \underline{K} then proceeds to the next pair of joint groups j and $j + 1$. At the end of the second phase of construction the stiffness matrix of the system is complete and is held in the backing store DA10. The completed stiffness matrix of the problem in figure (6.3) is shown in figure (6.5b). This matrix is used in the current increment or iteration of the analysis. The procedure is repeated and a new stiffness matrix is written into DA10 in each increment or iteration. On the other hand, the incomplete stiffness matrix residing in DA6, is kept unaltered and used over and over again.

The validity of the joint grouping method was established by comparing the results of an analysis using this method with one storing the full matrix in the core. There was no discrepancy between the two. The method was used extensively to analyse a structure, its foundation and the soil. But for very large problems, in the order of 1000 joints, the method was found to be inadequate. This is because it needs a core space sufficient to store twice the size of the part of the stiffness matrix that correspond to the largest joint group. The maximum core space available for this purpose when using the CDC 7600 computer was found to be between 35000 and 40000 elements. Although the size of the joint groups can be kept fairly uniform by a careful numbering of the joints, it can not be reduced sufficiently to fit into this space for the very large problems. A second method of constructing \underline{K} was therefore necessary. This is

described in the next section and its superiority is emphasized by the fact that it does not use any core storage space exclusively for the stiffness matrix.

6.5.2 Construction of \underline{K} by joints

In this method the stiffness matrix is again constructed in two phases by making use of the backing store units DA6 and DA10. In each phase the construction proceeds one joint at a time. In the first phase, all the elastic elements having one of their nodes connected to a particular common joint are considered in turn. Their stiffness contributions to this joint are evaluated and superimposed on the stiffness matrix. The part of \underline{K} corresponding to this joint is then written into the backing store unit DA6. The same space in core is then used for the construction of the next joint. In the second phase of the construction, each joint is again considered in turn. If there is a plate or member element connected to this joint, the part of \underline{K} corresponding to this joint is copied into the core from the backing store DA6. The solid elements connected to this joint are then considered in turn. Their stiffness contributions to this joint are evaluated and superimposed on the part of the stiffness matrix in the core. This part is then written into the backing store unit DA10 ready to be read by the solution routine. The same area of the core is then used for the next joint.

It is noticed here that this method considers an element more than once during the construction of the stiffness matrix. However, the stiffness terms of the elements are evaluated from explicit expressions once and for all. Therefore, the method does not involve any extra computation. As the solid element stiffness matrices are kept in the backing store the number of transfers is somewhat

increased. This method is superior to the last one because it does not need any storage for the joint group information or any computation to evaluate these. The only core space necessary is to hold the stiffness array for one joint, which does not exceed six rows. In the actual program this array is in fact kept in a temporary store which is subsequently used for other purposes. Thus, the storage requirement for this method is nil. For the moderately sized problem of a space frame on a sand bed, with 1197 degrees of freedom, the joint by joint method needed about 10 per cent more time for 15 increments of the load than the joint grouping method.

6.6 SOLUTION OF THE SIMULTANEOUS EQUATIONS

6.6.1 Preparation

For large problems Jennings and Tuff (1970) have proposed the segmentation of the stiffness matrix into a number of blocks containing some contiguous rows of the matrix. Choleski's triangular factorization was used to reduce successively each of these blocks. However, Choleski's factorization sometimes gives problems with negative arguments under the square root, Croxton (1974). Indeed the method was tried by the author and similar problems were encountered when the stiffness matrix did not have particularly dominant diagonal terms. In the method of solution described below the segmentation technique of Jennings and Tuff is used with a Gaussian elimination method instead of Choleski's factorization.

The stiffness matrix is divided into a number of segments in such a way that each segment contains a number of complete rows. The direct access backing store unit DA10 is also divided into fixed length blocks in which each complete segment wholly or partially

fills the block. For an efficient transfer between the core and the backing store the length of the blocks is kept equal to a multiple of the buffer size. The buffer size on the CDC 7600 computer is 1000 octal (512 decimal) words capable of holding 512 real elements. Therefore, a block size of 512 elements is used for most of the problems analysed in this thesis. For very large problems, it was found that sometimes a single row of the stiffness matrix contained more than 512 elements. In such cases a block length equal to two buffers (1024 elements) was used. A facility is included in the program to print out a message when any row contains more elements than the specified block size. The block size can then be increased to suit the problem.

The methods of the construction of \underline{K} described in the previous sections consider a single joint or a group of joints at a time. The number of elements in the part of \underline{K} corresponding to a joint or a group of joints is not necessarily equal to the block size used. A fixed length block of the stiffness matrix can contain more than one joint or joint groups. The stiffness matrix is divided into the solution blocks in a subroutine CSDIV. The subroutine stores the last row number of each block in an array IC. For an efficient transfer between the core and the backing store, it is necessary to manipulate the stiffness array in blocks of the same size. In the second phase of the construction, the final stiffness matrix is written into DA10 ready to be solved. A subroutine WRITW was written to transfer the completed part of \underline{K} corresponding to a joint or a group into DA10 in units of a fixed length block. A temporary working array A is used to copy the elements forming a block in the current part of \underline{K} . This array is then written in full

into the backing store DA10. Thus if a joint or group does not contain a round number of blocks, the array A is used to store the fractional block until the rest of the block have been constructed. The flowchart of the subroutine, for a block size IZ, is shown in figure (6.8). The symbols in the flowchart are:

I = block number being written

LEFT = number of elements left over from the previous joint
or joint group

MC = location of the start of this block in DA10

and LML = location in the overall stiffness array of the last
element of the previous joint or group.

6.6.2 The solution routine

The method of solution presented here uses the Gaussian elimination technique modified to suit the compact storage scheme and the backing store facility. In the elimination method the co-efficient matrix is reduced to an upper triangle by successive row elimination. During this process, for any row PQ in figure (6.9), only the elements in the triangular area RPQ are involved. During the reduction of any block, only those blocks with the last row number greater than or equal to the first non-zero column number of this block are involved. The block being reduced is the active block and resides in the core. The blocks whose elements are necessary for the reduction are copied into the core successively and are passive. Thus, in figure (6.9), the following are the passive blocks of each active block;

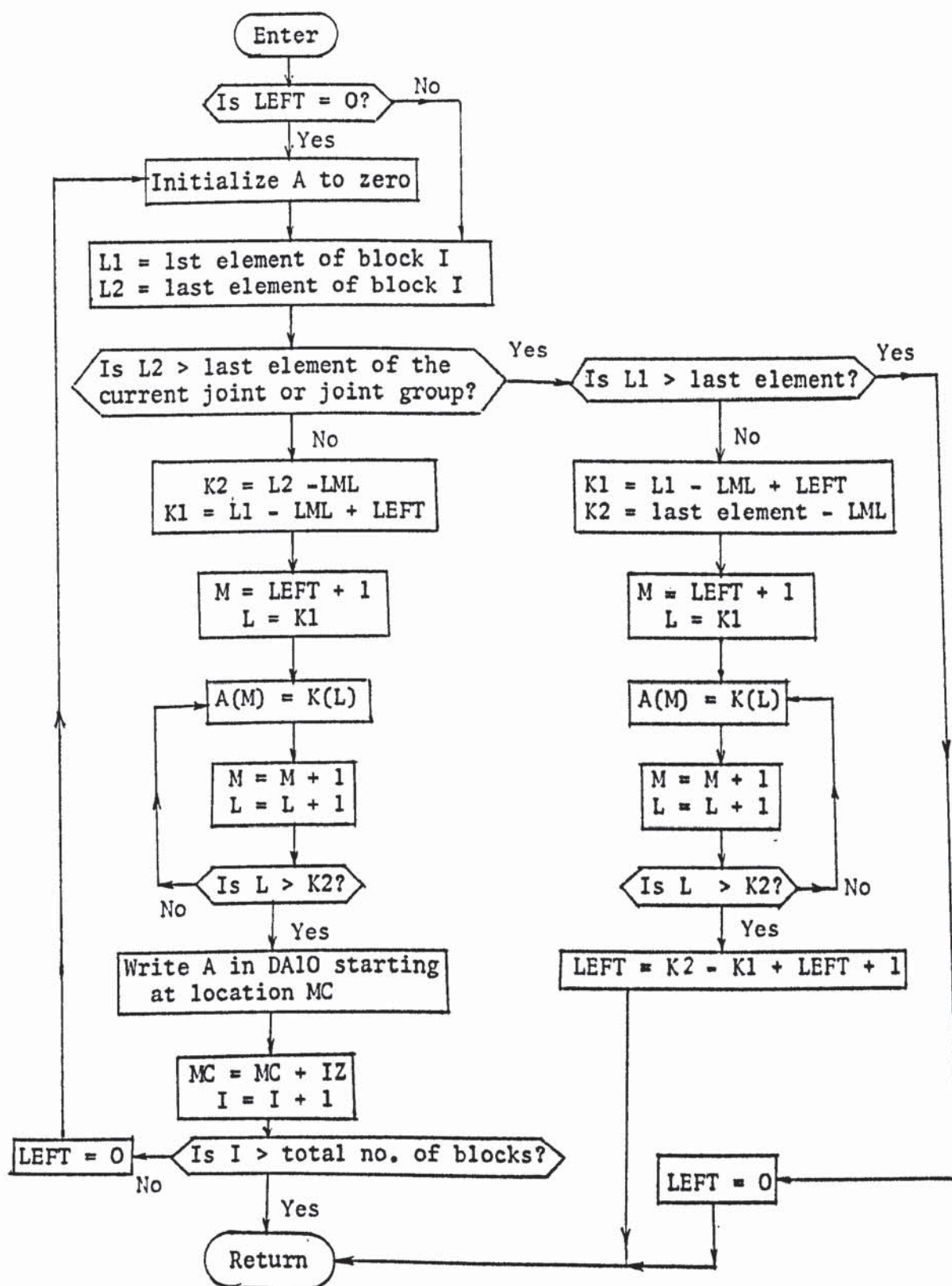


FIGURE 6.8 FLOWCHART OF SUBROUTINE WRITW

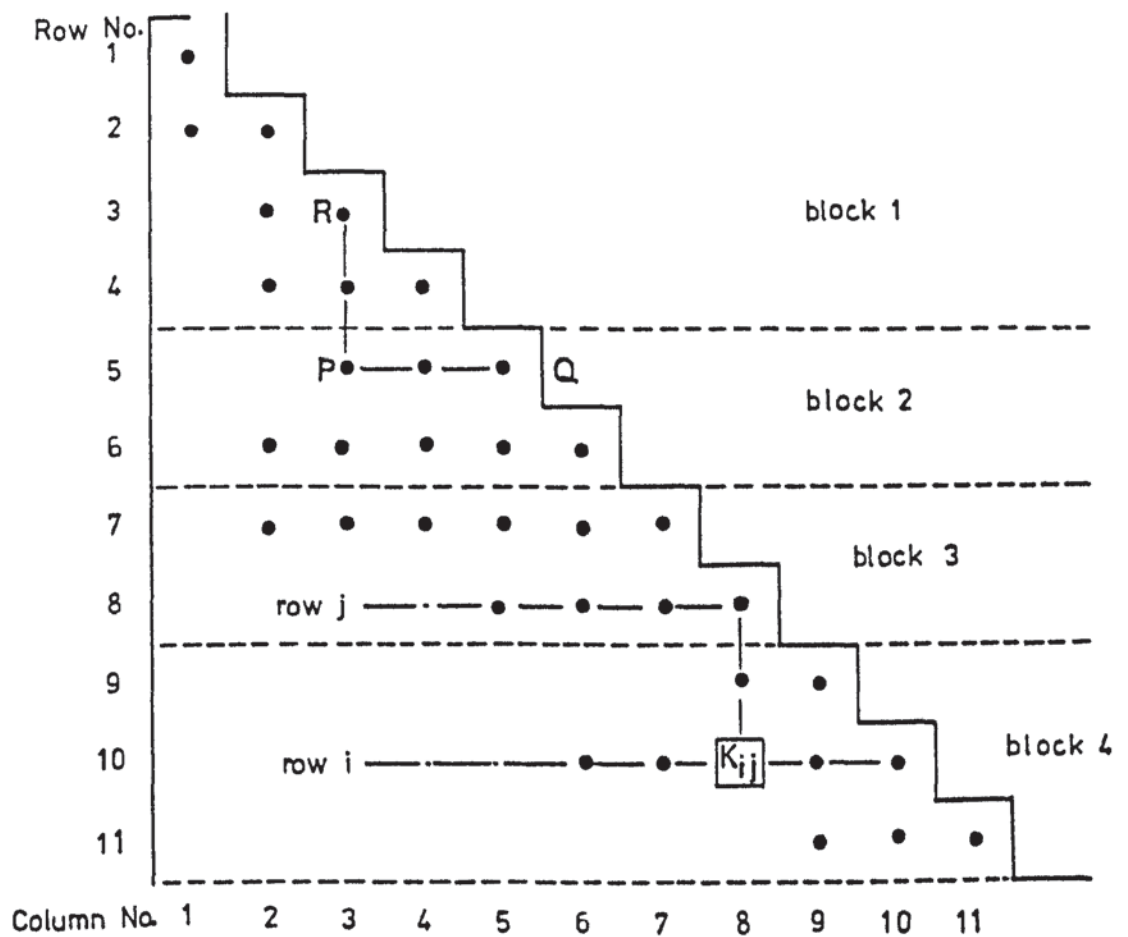


FIGURE 6.9 REDUCTION PROCESS OF THE SOLUTION ROUTINE

Active block	Passive blocks
1	1
2	1, 2
3	1, 2, 3
4	2, 3, 4

An array, IB, is constructed in the subroutine CSDIV to contain the first passive block number required by each active block. The reduction continues from block to block with each block being brought successively into the core from the backing store. After the reduction, each block contains the reduced elements of the upper triangle in a transposed form. The reduced blocks are written back into DA10 at the same locations as they previously occupied. The reduction process requires some temporary reduction factors C_{ij} for each element K_{ij} . An array, C, was declared in the routine to have the same number of elements as the active block. The elements of this array has a one to one correspondence with the elements of the active block. These are also stored in a one dimensional sequence. The reduction factor C_{ij} for an element K_{ij} is:

$$C_{ij} = K_{ij} - \sum_{m=r}^{j-1} C_{im} K_{jm} \quad 6.1$$

Here r is the greater of r_i and r_j , with r_i being the column number of the first non-zero element of row i and r_j that for row j . The elements K_{ij} are then replaced by $C_{ij} K_{jj}$ and the diagonal elements K_{ii} by the reciprocal of C_{ii} . In figure (6.9) it is assumed that the elements $K_{10,8}$ in block 4 is about to be reduced and that block 3 is currently in the core as the passive block. By equation (6.1), the reduced element $K_{10,8}$ becomes:

$$K_{10,8} = K_{8,8} (K_{10,8} - C_{10,6} K_{8,6} - C_{10,7} K_{8,7})$$

Here $i = 10$, $j = 8$, $j-1 = 7$, $r_i = 6$, $r_j = 5$ and $r = 6$.

The reduction of the right hand side vector, b , proceeds in parallel with the stiffness matrix. For any row i the quantity b_i in the right hand side is replaced by:

$$b_i = \frac{1}{C_{ii}} (b_i - \sum_{m=r_i}^{i-1} C_{im} b_m) \quad 6.2$$

At the end of the reduction process, the backing store unit DA10 contains the transposed upper triangle of the reduced stiffness matrix. The reduced last block of this matrix and the reduced right hand side vector are in the core. The back substitution process requires the subtraction of the product $K_{im} b_i$ from each element b_m of the right hand side. Here i is the successive row number from the last to the first for each value of m from r_i to $i-1$. The back substitutions on all the elements b_m of the right hand side, involving a particular row i of the reduced stiffness matrix, are performed in one operation. This reduces the block transfers from the backing store. When all the rows of the last block, n , of the stiffness matrix have been considered, the next block $n-1$ is copied into the core. The back substitution of the right hand side continues for the rows in this block. The process is repeated until the first block has been copied into the core and operated upon. At the end of the back substitution the right hand side vector is transformed into the solution vector of the system of equations.

The flowchart of the sequence of operations during the reduction process is shown in figure (6.10). The detailed flowchart of the

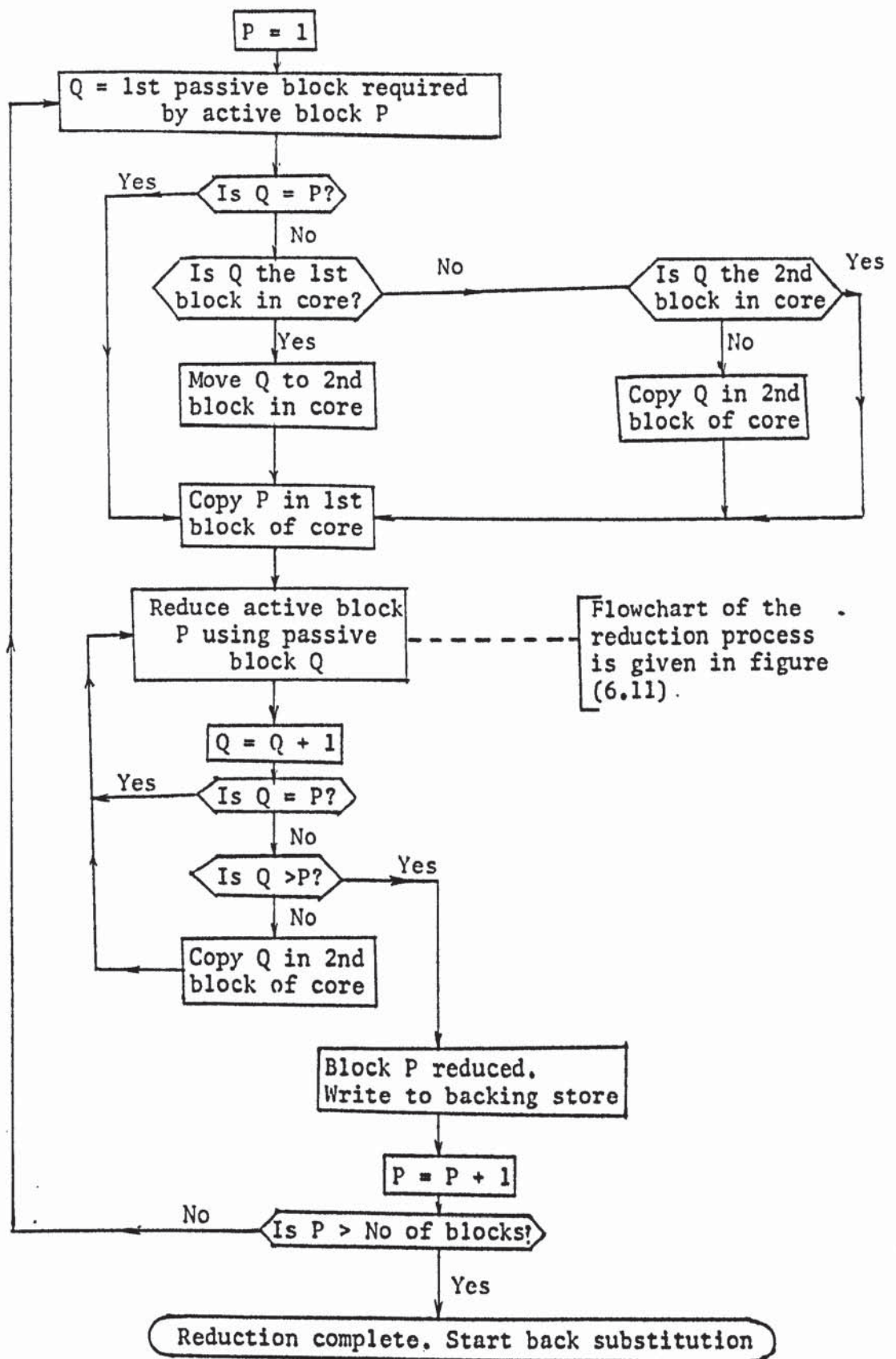


FIGURE 6.10 FLOWCHART OF THE REDUCTION SEQUENCE

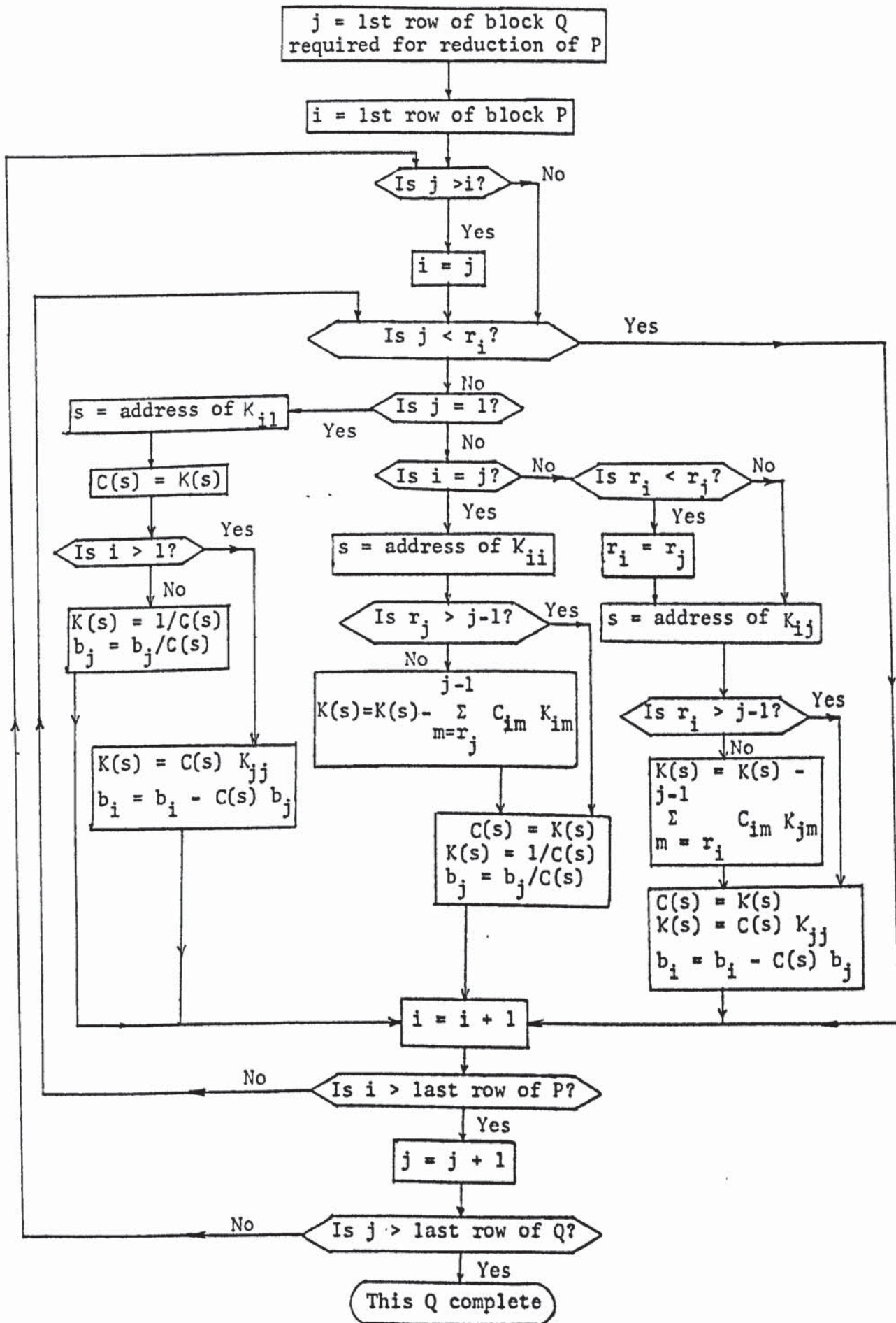


FIGURE 6.11 FLOWCHART FOR REDUCTION OF BLOCK P WITH PASSIVE BLOCK Q

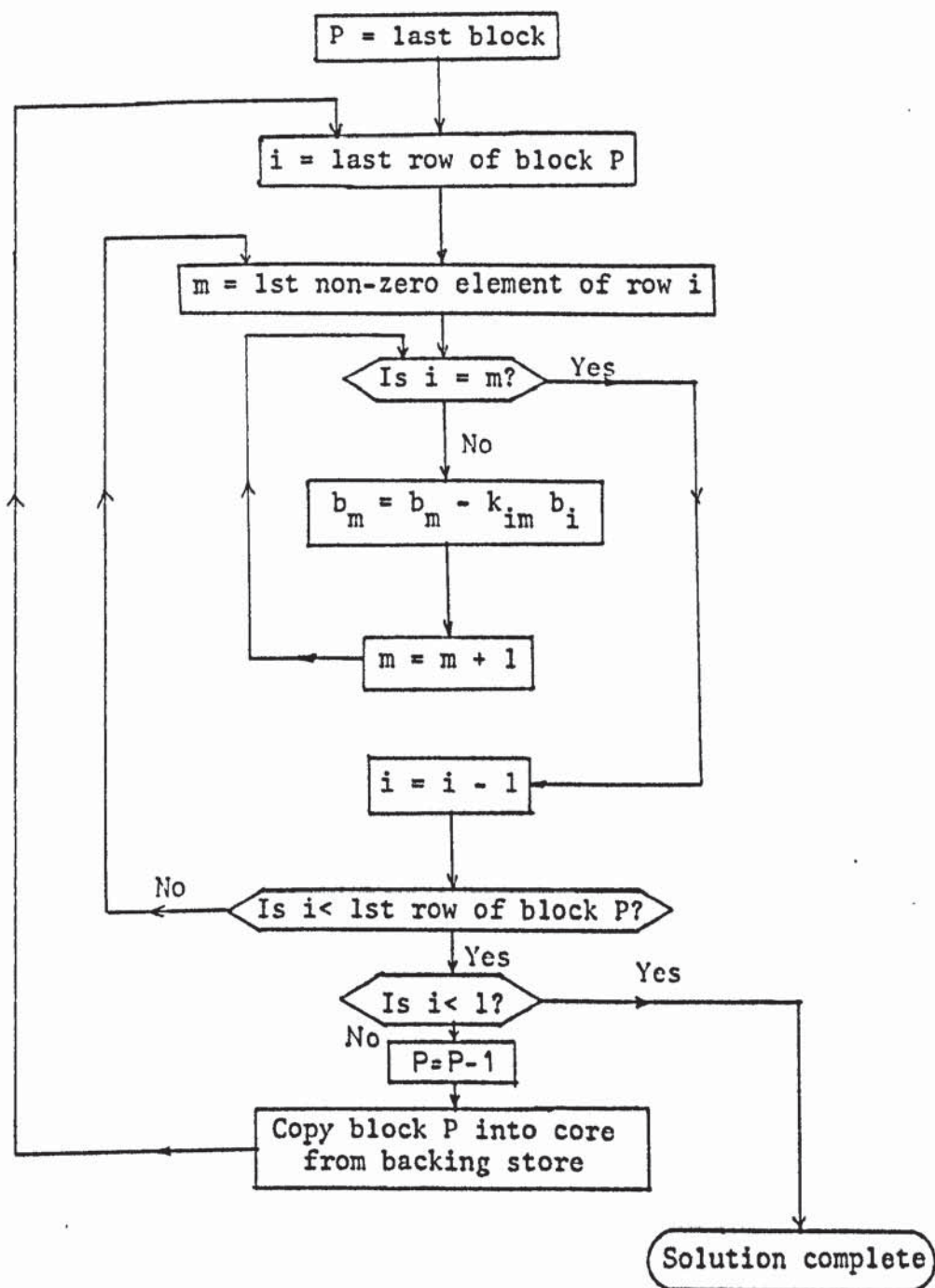


FIGURE 6.12 FLOWCHART OF THE BACK SUBSTITUTION PROCESS

reduction of a typical active block P with a passive block Q is shown in figure (6.11). The back substitution process is illustrated in the flowchart in figure (6.12).

6.7 THE USE OF SPLINE FUNCTIONS

In the incremental analysis, the non-linear $\tau_{oct} - \gamma_{oct}$ curves of the soil are represented by spline functions. As stated in chapter 2, a separate computer program was written to formulate the spline functions for a set of $\tau_{oct} - \gamma_{oct}$ curves. For any particular set of curves obtained for a given soil, this program is run only once and the output is used repeatedly for all the analyses with this soil. The output of the program consists of the nodal values of τ_{oct} , γ_{oct} and the second derivatives ϕ of each curve. This output is recorded in a permanent disc file.

The main finite element incremental program reads the data written in the disc file by the spline formulation program. A subroutine GVALUE is included in the main program to calculate the values of τ_{oct} and G for any value of γ_{oct} . The routine is entered before each increment of the load to obtain the instantaneous shear modulus of each solid element.

The flowchart of the spline subroutine GVALUE is shown in figure (6.13). For a particular solid element the routine first establishes the two $\tau_{oct} - \gamma_{oct}$ curves in the immediate neighbourhood of the σ_{octi} value of the element. For each of these curves the two nodes i and j to the left and to the right of the given γ_{oct} value in the element are determined. By using the input values of ϕ_i and ϕ_j together with the values of τ_{oct} at the nodes i and j, the value of the shear modulus is calculated as the first derivative

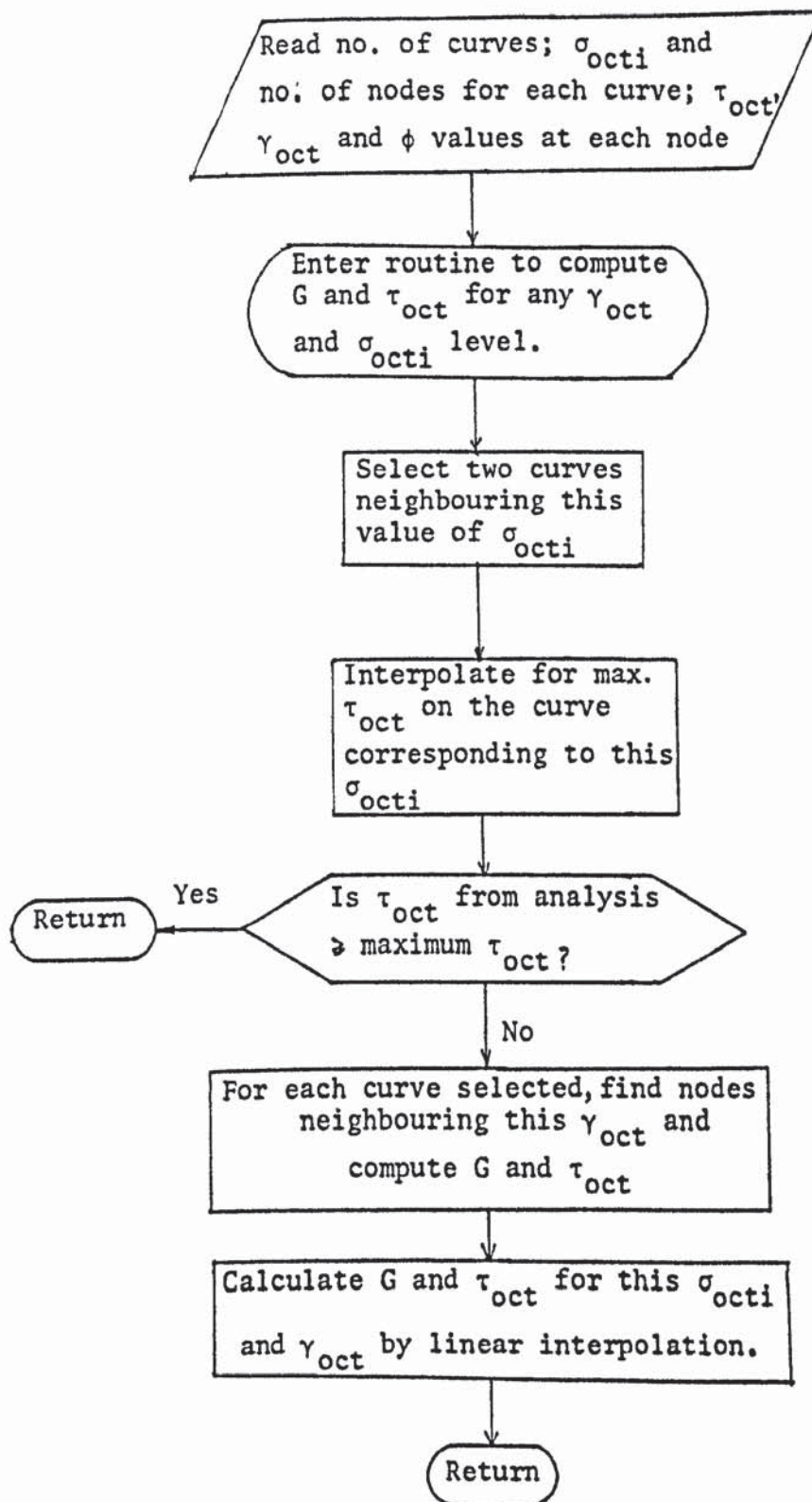


FIGURE 6.13 FLOWCHART OF SUBROUTINE GVALUE

of the spline function for the given value of γ_{oct} . A linear interpolation of the values of G obtained for the two curves gives the shear modulus for the required value of σ_{octi} .

6.8 COMPUTER IMPLEMENTATION OF THE CRACK PROPAGATION METHOD

A method of following the crack propagation and tension separation in a structure-soil system has been developed in chapter 4. To implement the method, a subroutine SEPRTN was written and is included in the general finite element program. A call is made to this subroutine, after each increment of load or after each cycle of iteration, to detect any new separation or the closure of any existing crack.

The input data to the program, for this purpose, consists of the tensile strengths of the soil at the joints where a crack check is to be performed. These are held in an array TS(3,ITS), where ITS is the total number of such joints. The tensile strengths of clay and other cohesive soils can be determined experimentally. Loose and cohesionless material, such as the dry sand used in the experiments described in chapter 7, is incapable of sustaining any tension. The tensile strengths of such materials can be taken as the compressive stresses developed due to the body forces. A crack can only occur when these compressive stresses have been counteracted by the tensile stresses developed due to the applied load.

Another array IX(4,NOJ), where NOJ is the total number of joints in the mesh including the dummy joints, is used to hold the various informations about each joint. The first row of the array contains the degrees of freedom of the joint in an index form. The index of the degrees of freedom is a six digit integer. Each digit can have a value of 1 or 0 to indicate the presence or the absence of a degree of

freedom. The first digit refers to a translation in x direction δ_x , the second to that in y direction and so on, as follows:

$$\delta_x \quad \delta_y \quad \delta_z \quad \theta_x \quad \theta_y \quad \theta_z$$

Degree of freedom 1 1 1 1 0 1

In the example above the degree of freedom 111101 of a joint means the joint is free to have translations δ_x , δ_y and δ_z in x, y and z directions respectively. It is also free to rotate about x and z axes, but the rotation θ_y about the y-axis is suppressed. All the dummy joints are initially given a zero degree of freedom in all directions.

The second row of the array IX holds the least numbered joint directly connected through an element to each joint. For a dummy joint this is initially generated as the same joint to be changed later to the appropriate number when the joint becomes active. In figure (6.14), the joint indicated by a dark dot at the centre of the mesh is given two numbers 14 and 15. The least joint number of joint 14 is 1. At the uncracked state this number for joint 15 is also 15, as this is a dummy joint. When it becomes active due to the development of the crack shown in the figure, its least joint number is altered to 4. Thus the second row of IX changes continuously as each dummy joint becomes active or an active joint returns to the dummy state due to the closure of a crack.

The third row of this array contains the crack index numbers denoting the type of separation each joint is expected to suffer. An index value of zero is given to all joints that are not likely to suffer any separation or is itself a dummy joint.

The fourth row of IX is used as a working space. An integer quantity is held in this row for each joint. This is denoted by ICS

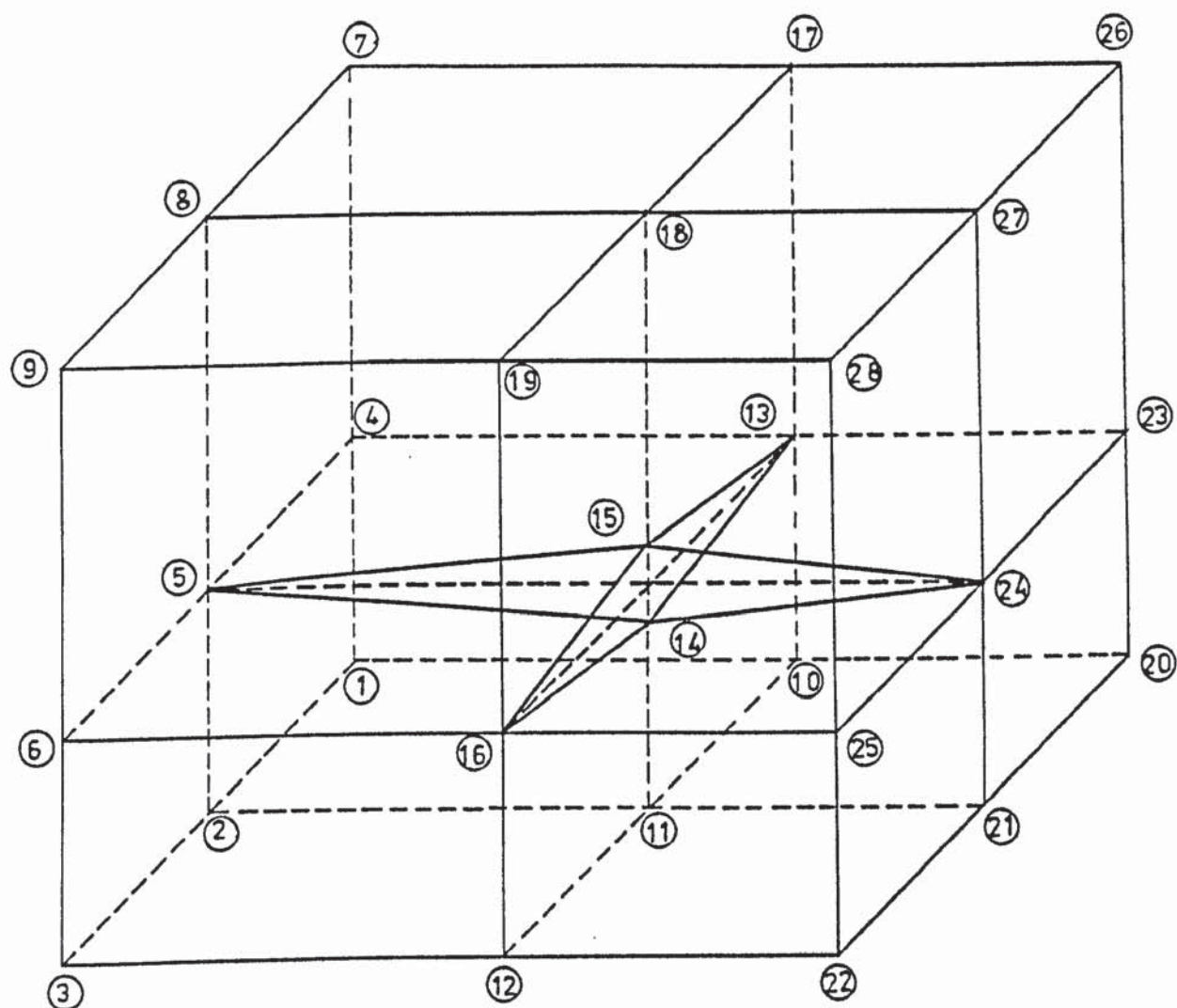


FIGURE 6.14 LEAST JOINT NUMBER OF A JOINT

and is called the crack state indicator. ICS is a four digit integer of the form 'k ℓ mn'. The first digit k facilitates the detection of the closure of a crack. It can have a value of 1, 2 or 5. A value of k = 1 is given to the joint at a separation, for which the displacement of the parent joint minus that of the dummy joint would have a positive value to indicate a closure. This relative displacement would have to be negative to show a closure when k = 2. The value of k = 5 indicates a boundary separation where no dummy joint is used. The other three digits of ICS, ℓ , m and n, have a value of 1 or 0, indicating the presence or the absence of a separation in x, y and z directions. The initial value of ICS is zero for all the joints and remains so for those that do not suffer any separation. As each separation occurs, the value of ICS for the joint involved is changed to indicate the presence of a separation and the type of such a separation.

Each joint that is likely to suffer a separation is given two numbers, one being the dummy and having a zero degree of freedom. Joints on the boundary, separating normal to the boundary, do not need an associated dummy. The parent joint and its dummy are numbered consecutively. This eliminates the necessity of storing the information about the dummy joint number of each joint. Furthermore, this approach would result in a narrow band width of the stiffness matrix after separation.

6.8.1 Description of subroutine SEPRTN

The formal parameters of subroutine SEPRTN consists of informations about the current increment number, the number of joints and solid elements in the system and two integer indicators, INDDOF and INDCRK. On entry, INDDOF and INDCRK both have zero values. As each crack is

initiated or closed, they are increased by 1. INDCRK is increased only when a new joint becomes active or a joint returns to the dummy state. INDDOF is increased for the above reason as well as when any change in the degree of freedom of a joint is made. Various operations in the general finite element program are dependent on these two variables. A non-zero INDCRK would mean a total change in geometry and connectivity of the mesh while a non-zero INDDOF on its own would mean a change in the structure of the stiffness matrix. All the other data are kept in COMMON blocks and accessed by the subroutine.

The flowchart of subroutine SEPRTN is shown in figure (6.15). The stresses are calculated by the finite element program at the centroid of each solid element. The nodal stresses, which are of importance here, are calculated in this subroutine by averaging the centroidal stresses of the solid elements connected to each joint. A check is then made to ascertain whether the current increment number is the first one, as in this case the closure of cracks has no meaning and need not be checked. Otherwise, each joint with a non-zero ICS is checked for a negative crack width and if this is indicated, the crack is removed in the manner described in section (4.4). The flowchart of the part of the subroutine for this operation is shown in figure (6.16). Next the crack prediction loop is entered to implement the procedure developed in section (4.3) and its sub-sections. The flowchart for this program loop is shown in figure (6.17).

6.9 AUTOMATIC DATA GENERATION

To reduce the manual data preparation, a facility is included in the programs to generate automatically most of the finite element

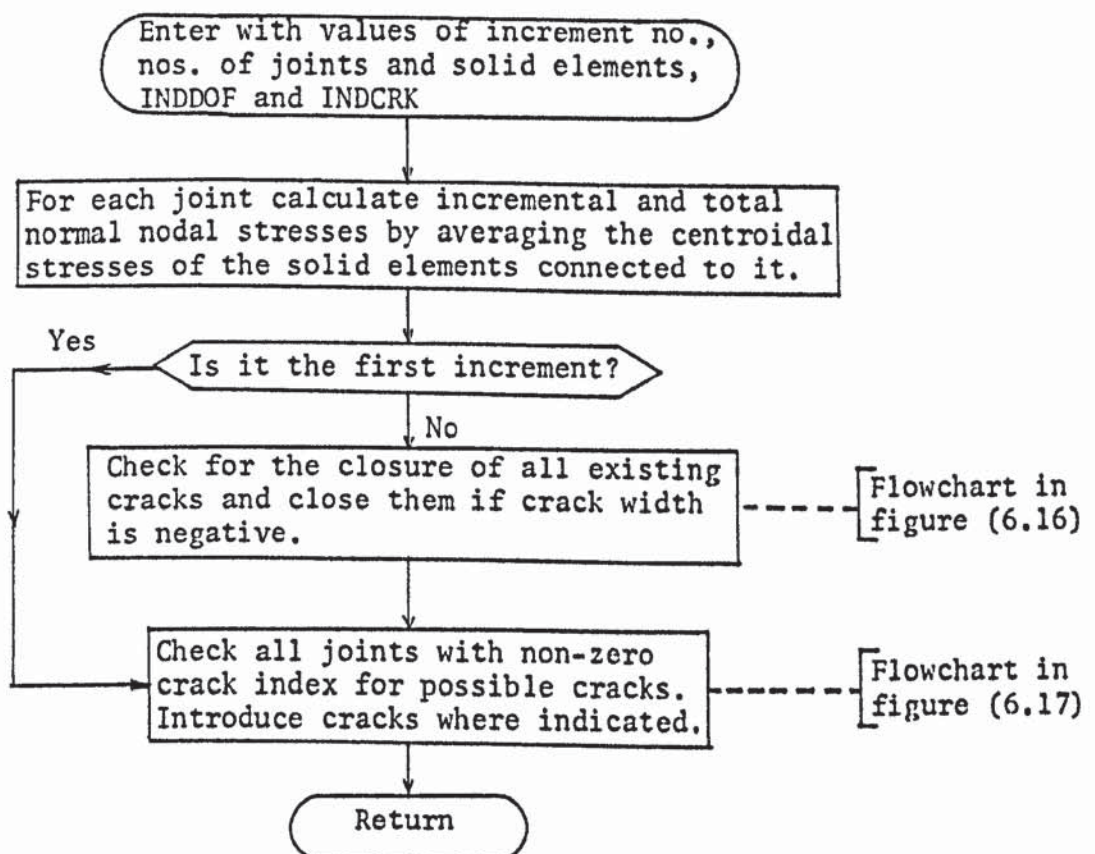


FIGURE 6.15 SIMPLIFIED FLOWCHART OF SUBROUTINE SEPRTN

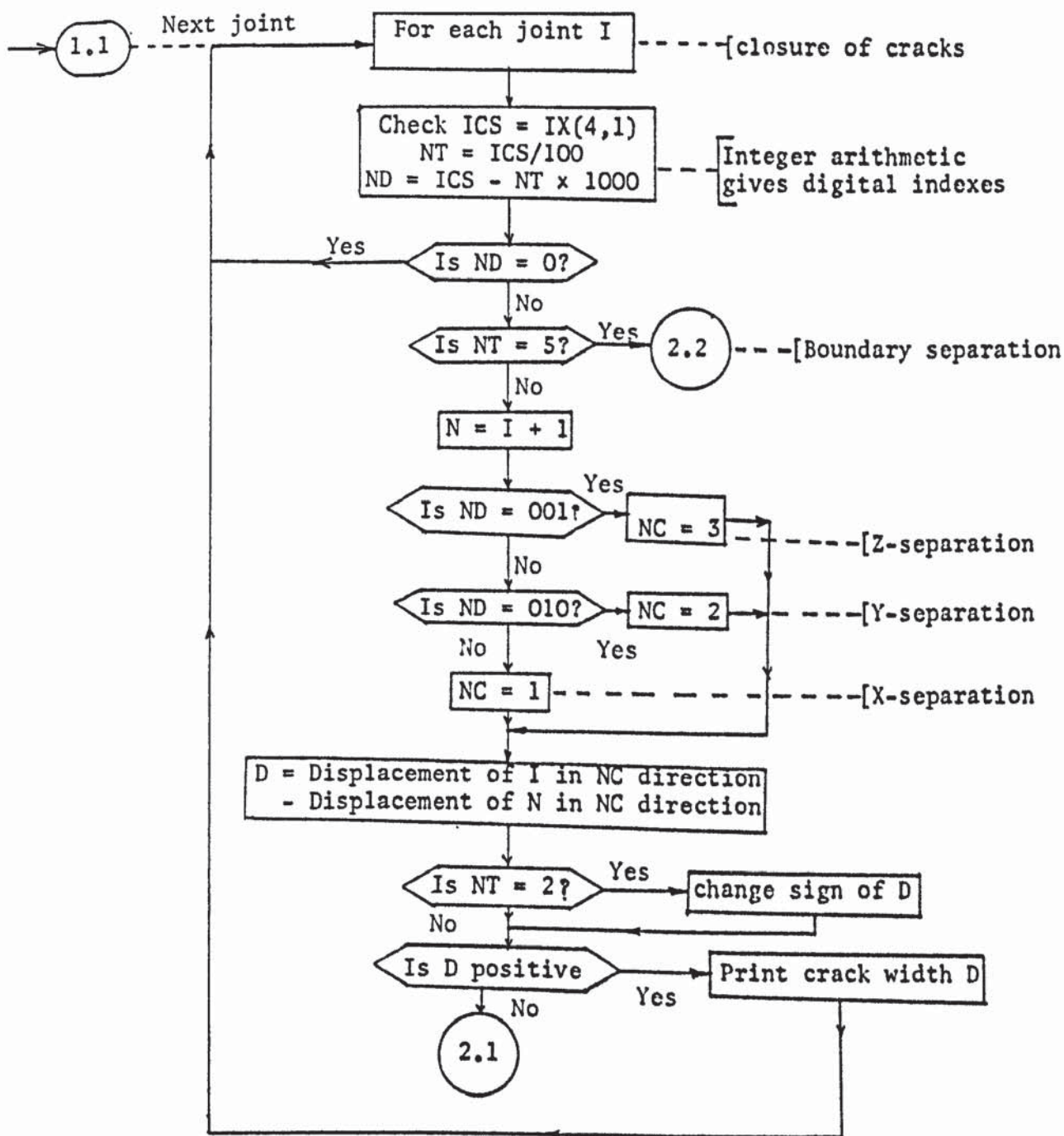


FIGURE 6.16 FLOWCHART OF CRACK CLOSURE LOOP IN SUBROUTINE SEPRTN

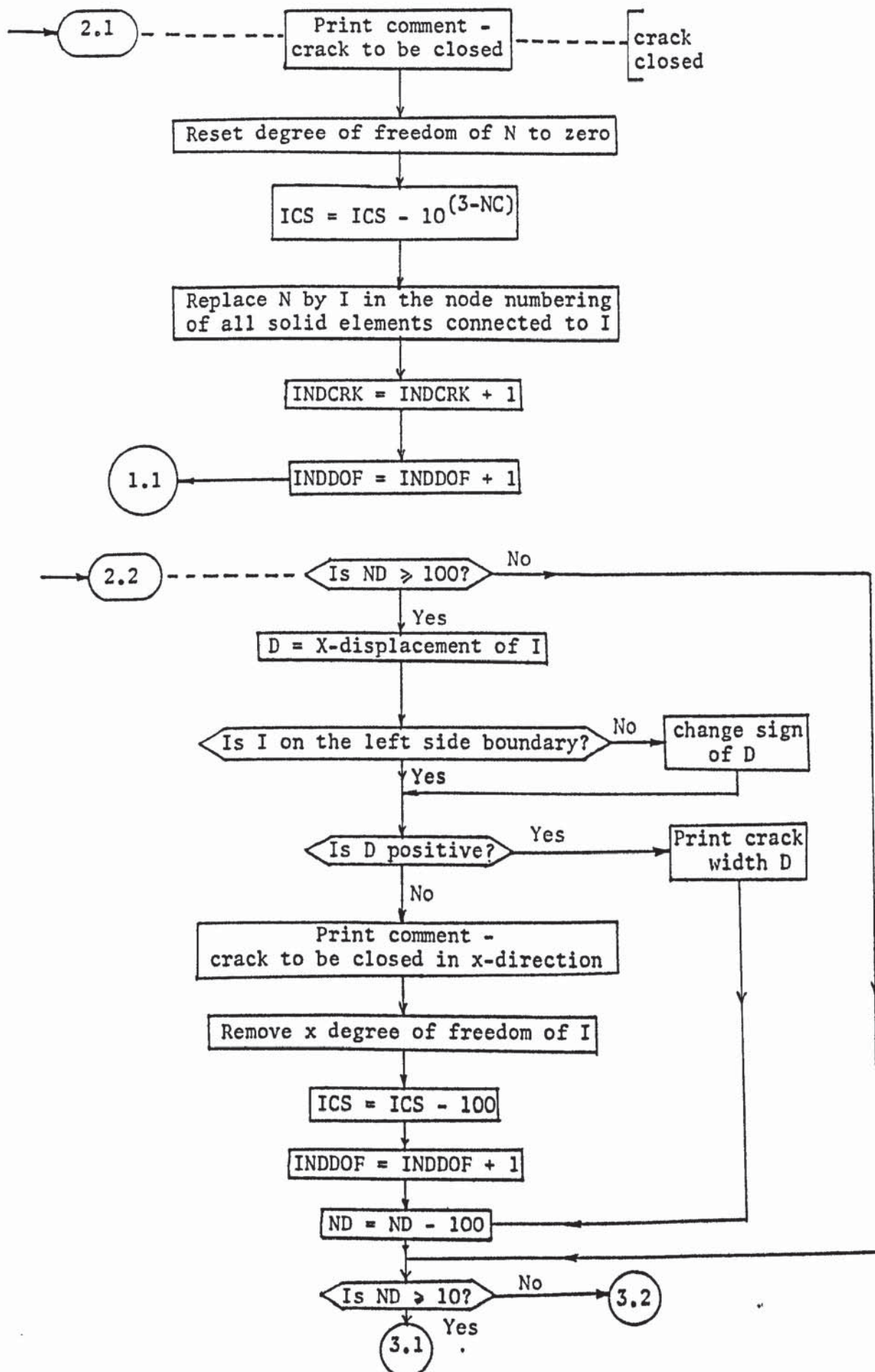


FIGURE 6.16

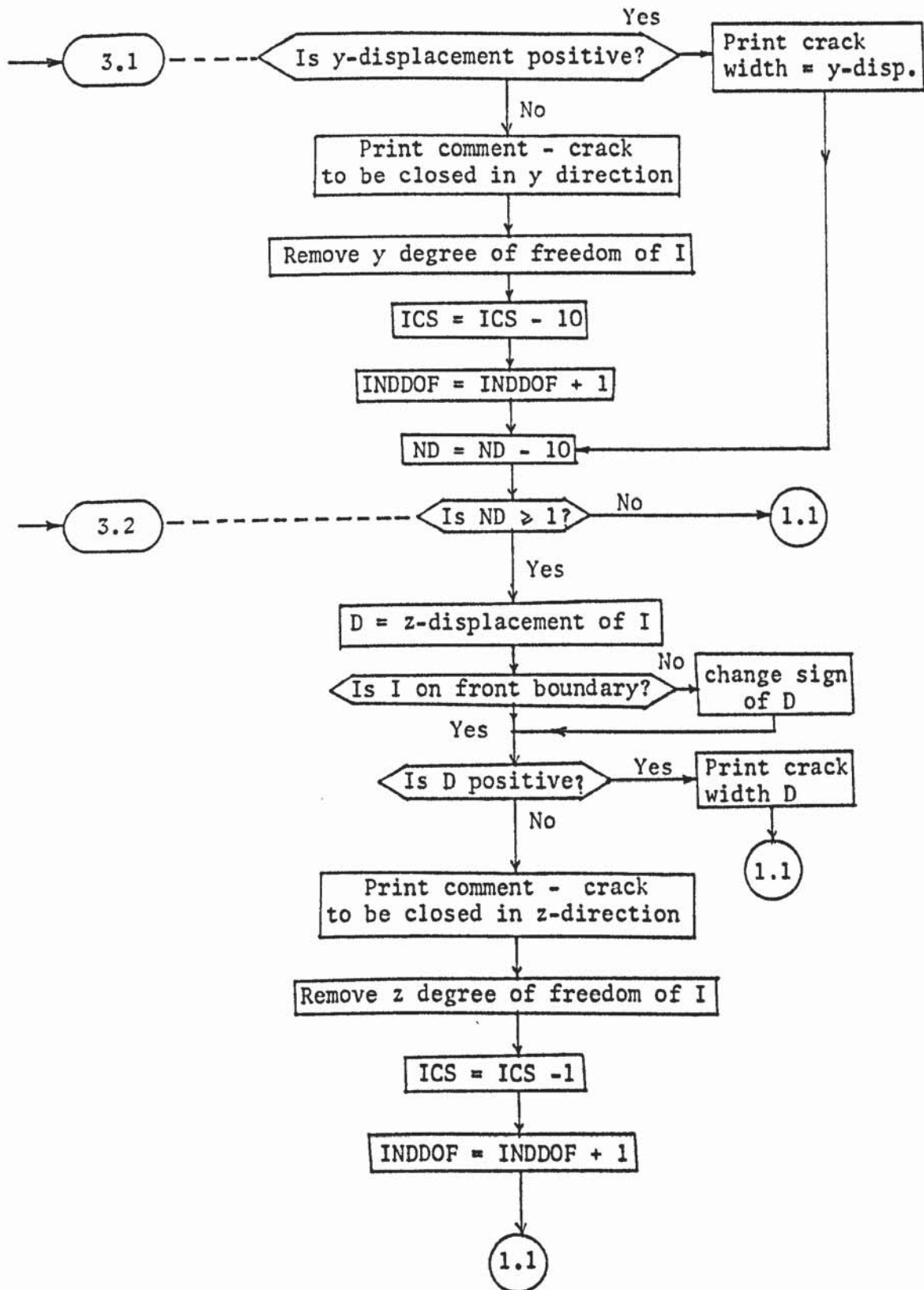


FIGURE 6.16

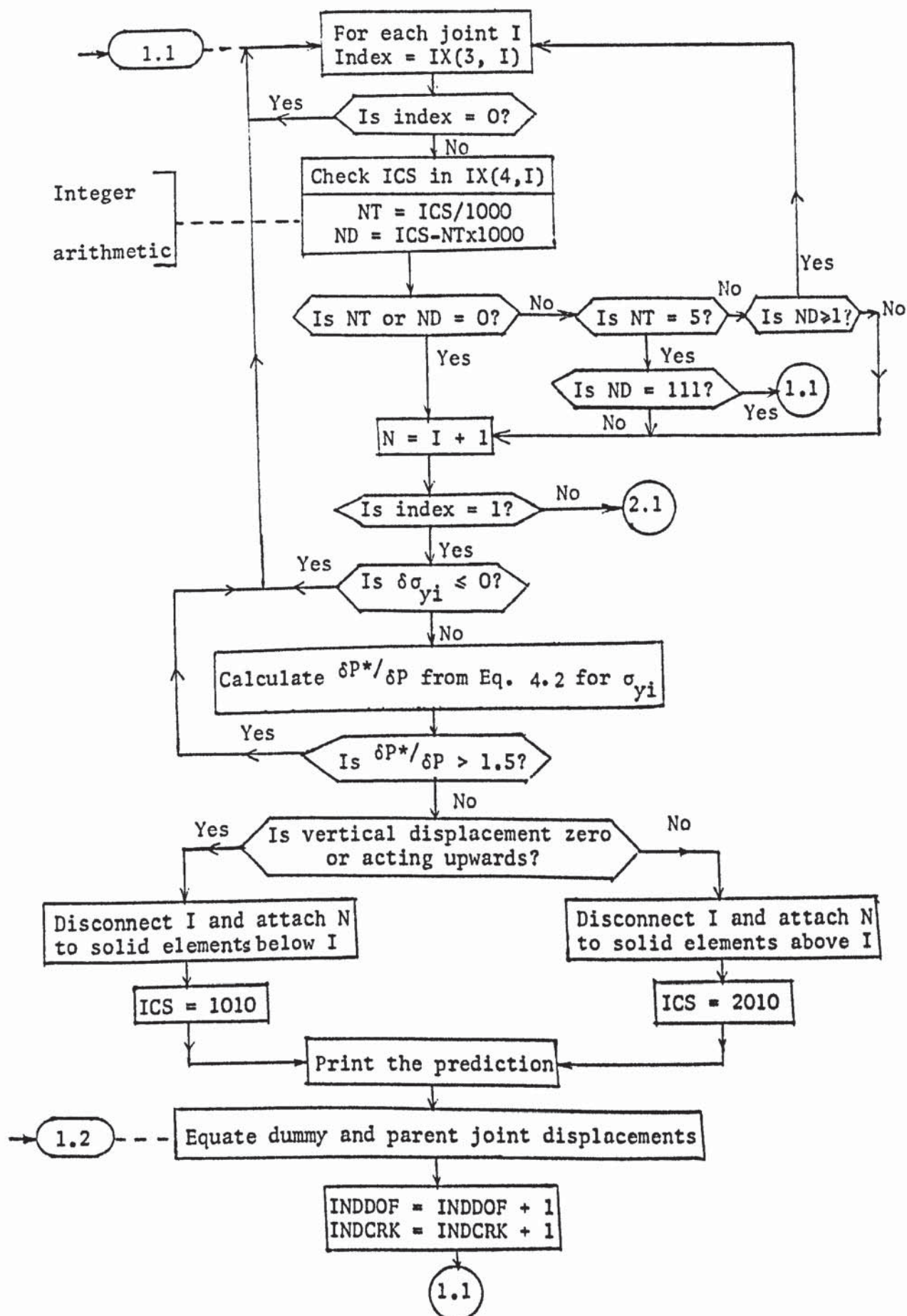


FIGURE 6.17 FLOWCHART OF CRACK INITIATION LOOP IN SUPROUTINE SEPRTN

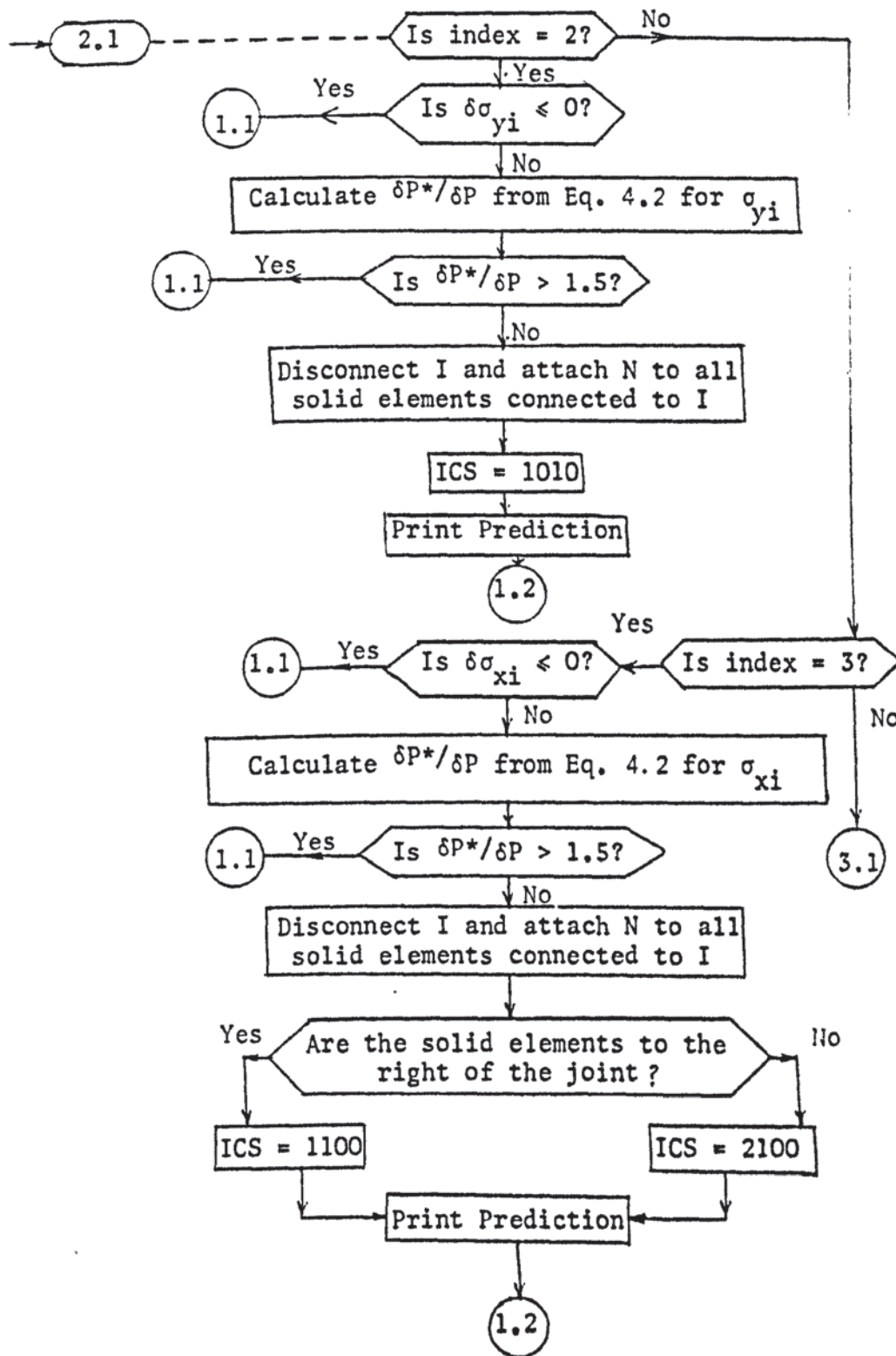


FIGURE 6.17

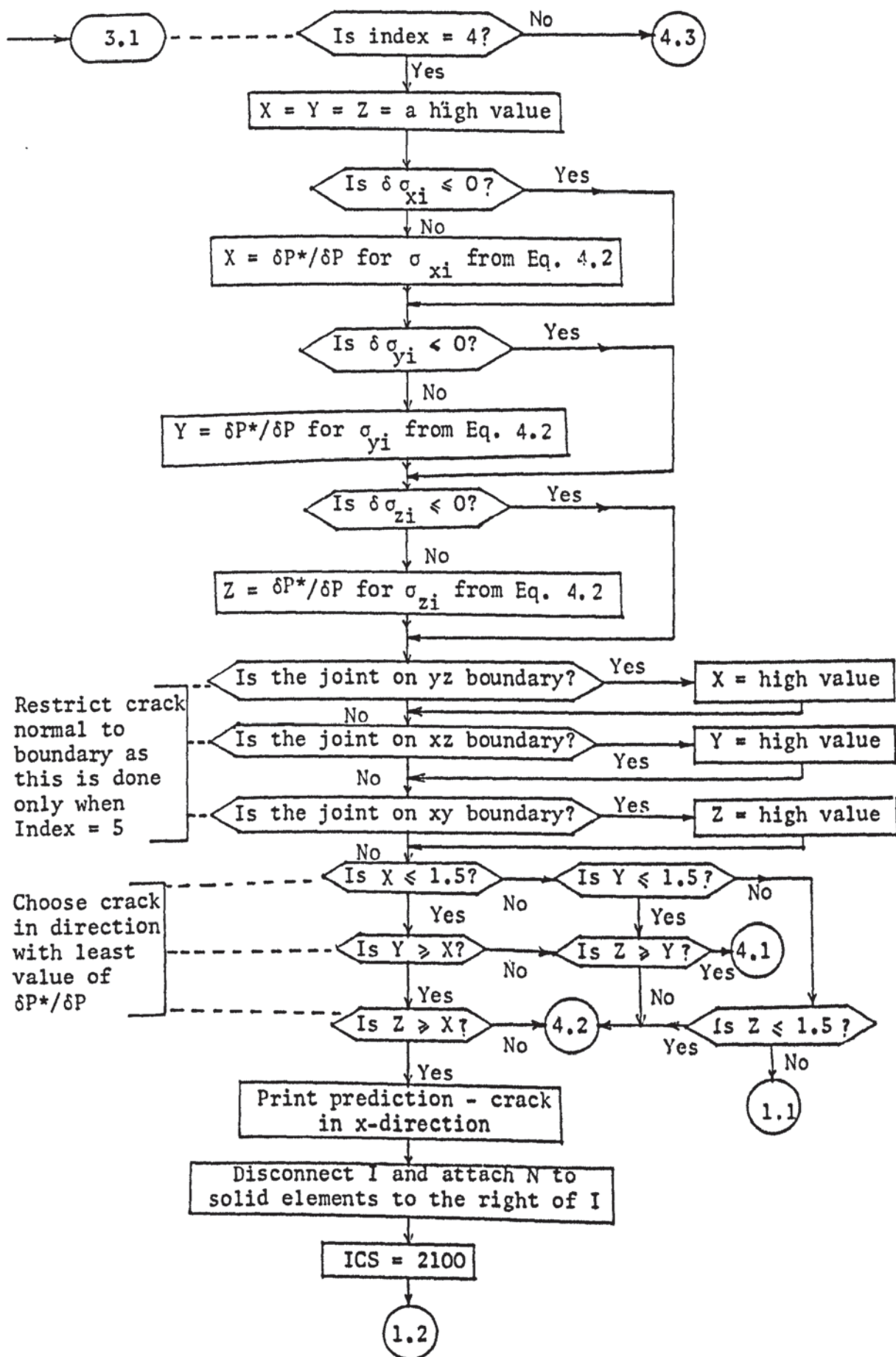


FIGURE 6.17

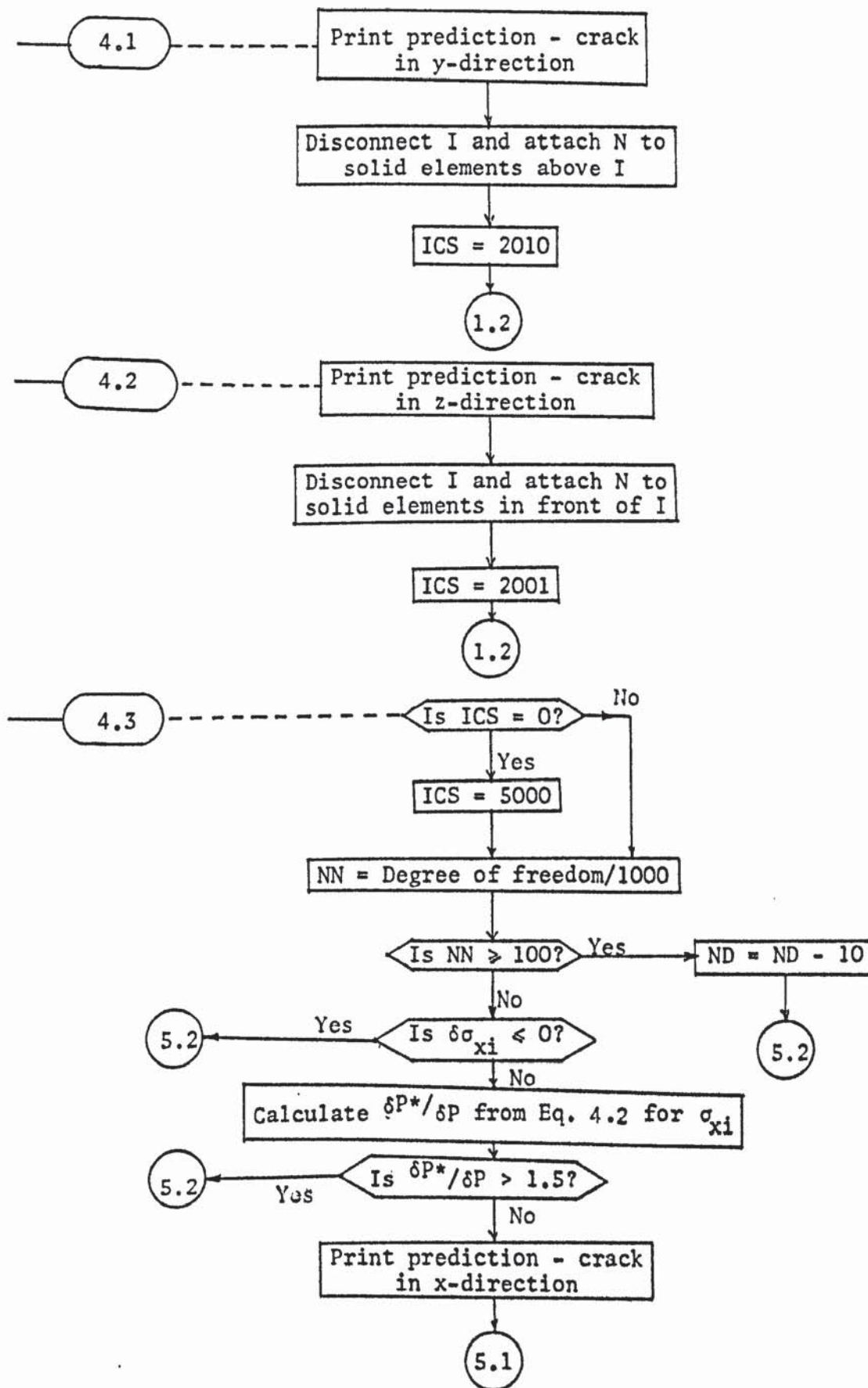


FIGURE 6.17

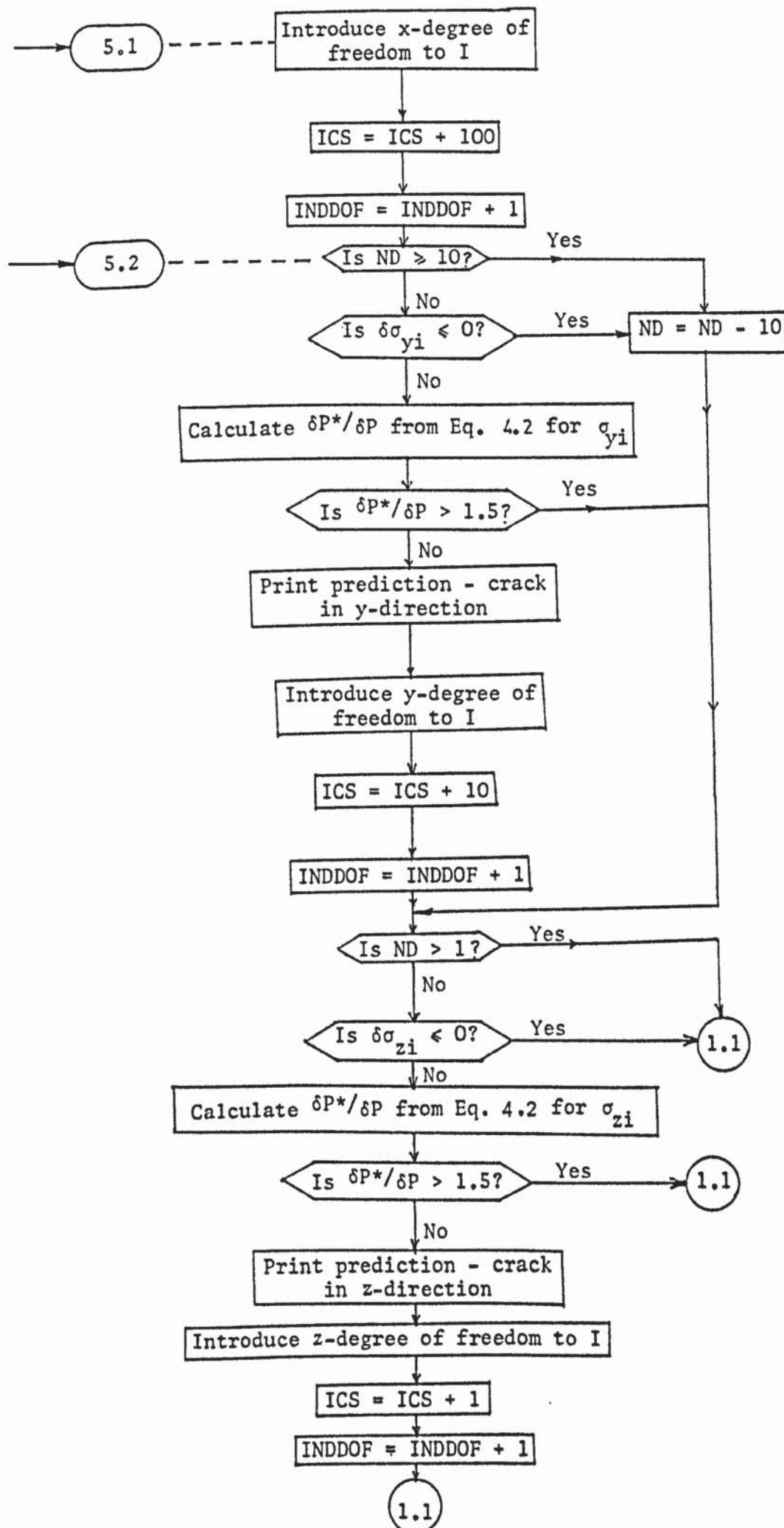
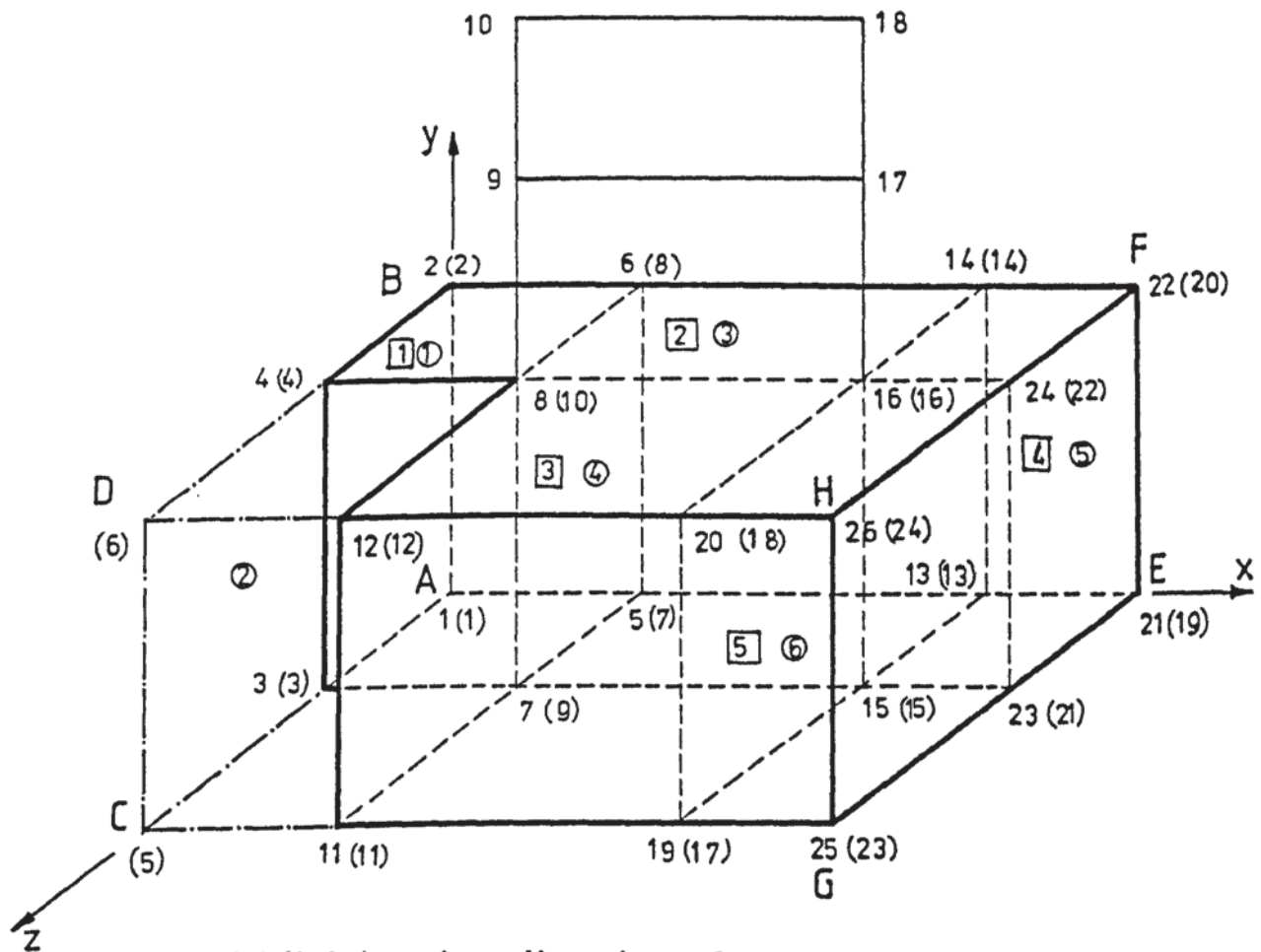


FIGURE 6.17

data. The programs automatically perform the finite element division of the soil into rectangular parallelepiped solid elements and assign the joint numbers at their nodes. They also generate the x, y and z co-ordinates of these joints as well as their degrees of freedom and least joint numbers. As the finite element mesh for a structure resting on soil can often be irregular, the automatic data generation process is made very flexible. Thus any arbitrary grid of finite elements can be generated.

An example grid is shown in figure (6.18). This consists of a frame resting on an irregular body of soil. The actual joint numbers are shown outside the parentheses beside each joint. Three figures on the data specify the directions in which the number of subdivision of the soil is the least, the next and the most. In the example of figure (6.18), these are y, z and x directions respectively. The program reads the x co-ordinates of the yz dividing planes, y co-ordinates of the xz planes and z co-ordinates of the xy planes. The body of the soil is then divided by these orthogonal planes. In this manner, the basic grid of solid elements enclosed within the block ABCDEFGH in the figure is obtained. Joint number (1) is assigned to the joint nearest to the origin of co-ordinates and the other joints are numbered in an uninterrupted sequence. The numbers vary most rapidly in the direction with the least number of divisions and least rapidly in the direction with the most number of divisions. In the figure, these basic joint numbers are shown within the parentheses next to each joint. The solid elements are also numbered in the same sequential order as the joints. The basic solid element numbers are shown encircled in figure (6.18).



Subdivisions in y direction = 1

Subdivisions in z direction = 2

Subdivisions in x direction = 3

() indicates joint number in basic grid

○ indicates solid number in basic grid

□ indicates actual solid element number

An Actual joint number is shown by a number not enclosed in any symbol

FIGURE 6.18 EXAMPLE OF AUTOMATIC DATA GENERATION

As can be seen in the figure, the actual grid is irregular and does not coincide with the basic grid generated so far. The solid element number 2 generated by the program does not exist. Furthermore the joints on the frame resting on the soil have not been included in the basic joint numbering sequence. The basic grid is therefore gradually modified by the program to transform it to the actual mesh. In figure (6.18), the joint numbers (1) to (4) of the basic grid are correct. But joints (5) and (6) are missing. Therefore, two joints of the basic grid have to be missed out at joint number (7). The program reads the number to be added to each basic grid joint number at such irregularities to obtain the actual joint number. For joint (7) of the basic grid this value is -2. Thus 2 is subtracted from the joint numbers (7) onwards, until another irregularity is encountered. This occurs at joint number (11), since two joints 9 and 10 of the structure have now to be added. Thus at this stage a value of +2 appears in the data which is added to the basic joint numbers. This and the previous number of -2 are accumulated and the sum is added to the basic joint numbers until the next irregularity of numbering is encountered. This occurs at basic joint number (17) where a further value of 2 has to be added. At the end of this process the numbers of the joints in the soil part of the mesh are the actual numbers.

The solid element numbers are also modified in the same way. In the example, a value of -1 is to be added to the solid element number (3) and onwards of the basic grid. The program then assigns the actual joint numbers at the various nodes of each solid element in such a way that the local axes of the elements are the same as the global axes.

The x, y and z co-ordinates of each joint are then calculated from the co-ordinates of the various dividing planes that intersect at a joint. The degrees of freedom of the joints are calculated by checking their positions in the grid. All the internal joints that do not lie on a boundary are given three translational degrees of freedom, 111000. The degree of freedom normal to the boundary is restrained for a joint that lies on the boundary. Thus for a joint on the xz boundary the degree of freedom is 101000, and for a joint at the intersection of the xz and the yz boundaries this is 001000. The rotational degrees of freedom of joints such as 8 and 16, where a member element meets the solid elements, remain undefined. For these joints the generated degree of freedom is modified by adding a quantity to it. For joints 8 and 16 this quantity is 111, so that their final degree of freedom is

$$111000 + 111 = 111111$$

This facility can also be utilized to remove a degree of freedom from the generated one. If, for example, the same data for the problem in figure (6.18) is used to perform a fixed base analysis of the structure alone then a quantity -111000 is supplied to the program for joints 8 and 16. This reduces their degree of freedom to zero.

The dummy joints for a crack propagation analysis pose no problem in the automatic data generation. These are dealt with by considering an irregularity in the basic mesh joint numbering at the joints immediately following them. The co-ordinates of a dummy joint are automatically equated to those of its parent joint and the degree of freedom is set to zero.

At the end of the data generation process the solid elements and

the joints connected to them are completely defined. But the data for the joints, such as 9, 10, 17 and 18 in the example, which are not connected to a solid element in any way have to be input manually. The connectivity and the properties of the plate and the member elements have also to be supplied manually. However, the least joint number for each joint is automatically calculated by the program by checking through the connectivity of the various elements.

The programs also contain the option of supplying all the data manually, if the special geometry of the finite element mesh warrants this. For some of the larger problems analysed in this thesis the method of data generation described above was slightly modified to suit the special need of the problem. For example, for a multi-storey framed building the space member data were also automatically generated. However, these modifications are entirely problem dependent and not general. Therefore, they are not described in detail here.

6.10 THE STRUCTURE OF THE COMPUTER PROGRAMS

Each computer program was developed by a logical combination of a number of subroutines. The only differences between the programs are in the control of the analytical procedure. The various subroutines used can be classified into four groups according to their functions. These are described below.

(a) Control routines:-

Main Segment: This segment of the program is used to read and generate the data of the problem. The joint numbering and the solid elements connectivity data are automatically generated from a few input parameters. It also generates the initial values of the non-linear elastic parameters. It carries out the first phase of the

construction of the global stiffness matrix and controls the overall method of the analysis.

Subroutine ASMBLRP: This routine performs the second stage of the construction of the global stiffness matrix. It reads the incomplete stiffness matrix from the backing store DA6 and superimposes on it the stiffness terms of the non-linear solid elements before each stage of the analysis. It then transfers the complete stiffness matrix to the backing store DA10.

Subroutine CONTROL: After each increment of the loads or each cycle of iteration, this subroutine alters the material properties of the non-linear elements to conform with the current level of stresses. It accumulates the joint displacements and the element stresses and strains in an incremental method of analysis. In the iterative program, it tests for the convergence of the joint displacements.

(b) Ancillary subroutines:-

The subroutines in this category are listed in Table (6.1) with a note on each of their functions.

(c) Element subroutines:-

These subroutines are used to formulate each type of element used in the program. Two functions of these routines are to evaluate the element stiffness matrices and to calculate the stresses, the strains, the forces and the moments. The subroutines in this group are listed in Table (6.2).

(d) Speciality subroutines:-

Subroutine SEPRTN: This routine controls the crack propagation and the tension separation in the analysis. It has been described

Name	Functions
LJNO	Generation of the least joint number of each joint
JGROUP	Division of the joints into groups
GVALUE	To calculate the instantaneous values of G from the spline functions of $\tau_{oct} - \gamma_{oct}$ curves for the incremental programs only
BOUSSTR	To calculate the Boussinesq stresses at the centroids of the solid elements due to the applied point or distributed loads on the surface
LOADS	To reconstruct the right hand side vector after each increment of load or each cycle of iteration
CSDIV	Division of \underline{K} into fixed length solution blocks
WRITW	To copy parts of \underline{K} into backing store DA10 in fixed length blocks
DISVEC	Formation of the joint displacements matrix from the solution vector
OPENWF	To declare workfiles for use as backing stores
CLOSWF	To close the workfiles at the end of the analysis
WRITWF	To write strings of elements into a backing store in fixed length records to minimize indexing of the element locations
READWF	To read strings of elements from a backing store in fixed length records
MOVARR	To shift the positions of elements in an array

TABLE 6.1 ANCILLARY SUBROUTINES

Name	Functions
SKRPPD	To construct stiffness matrices of the rectangular parallelopiped solid elements and to write them in backing store
RPPDST	To calculate the stresses and strains in solid elements from nodal displacements
PRINC	To calculate principal stresses at the centroids of the solid elements
STIFMEM	To control construction of stiffness matrices of the space frame member elements
FORMDC	To calculate the direction cosines of members
ASELTER	To form stiffness terms of the members
CONSMKA	To construct k_A matrices of members for the calculation of forces and moments
MEMFCOM	To calculate forces and moments of members
WRITE11	To superimpose the on-diagonal stiffness sub-matrix of end 1 of member on global K
WRITE21	To superimpose the off-diagonal stiffness sub-matrix of member on the global K
WRITE22	To superimpose the on-diagonal stiffness sub-matrix of end 2 of member on global K
RECTPLT	To control construction of stiffness matrix of rectangular plate elements
RFDC	To calculate direction cosines of plate axes
RECWRIT	To superimpose stiffness terms of plates on the global K
RPSTRES RPDBA	To calculate stresses and moments in the rectangular plates

TABLE 6.2 ELEMENT SUBROUTINES

fully in section (6.8.1).

Subroutine SOLVE: This subroutine solves the system of equations $\underline{L} = \underline{KX}$ by using the compact storage scheme and the backing store facilities by the method of Gaussian elimination. The subroutine has been fully described in section (6.6.2).

6.11 USE OF THE CORE STORE

In the computer programs a significant part of the available core space is required for storing the program instructions and the local variables. The rest is used by the arrays declared to hold the various matrices and vectors. Some of these arrays are however temporary and can either be destroyed or copied into the backing store when they are no longer needed. The operations in the programs are logically ordered in such a way that the same area is used repeatedly for storing the various arrays. In a FORTRAN program this is accomplished by using the COMMON blocks and the EQUIVALENCE declarations. The more frequently used permanent arrays are however always kept in the core as a large number of core-backing store transfer increases the running time.

The use of the core store for the temporary arrays in the incremental program which constructs the stiffness matrix by joints is shown in table (6.3). The available core space is divided into three units each of which stores different arrays at different times. The arrays AA, BB, CC, JMISS and LMISS are required during the automatic data generation and are stored in unit 1. When this is completed, the unit stores the stiffness array that corresponds to a particular joint during the construction and the solution processes. Core unit 2 is occupied by the load vector $\Delta \underline{L}$ and subsequently by the

Step No	Operations	Core area unit No		
		1	2	3
1	Arrays required for automatic data generation	AA, BB, CC, JMISS, LMISS		
2	Construct 1st phase of K	K		
3	Construct 2nd phase of K	K		
4	Construct load vector		ΔL	
5	Solve simultaneous equations	K	ΔX	
6	Incremental joint displacements	DOSP		
7	Incremental element stresses		DSQ	
8	Total element stresses			TQ
9	Copy TQ to backing store, calculate total joint displacements			TOSP
10	Incremental joint stresses	SNQ		
11	Form total displacement vector, calculate plate and member forces		X	
12	Copy TOSP to backing store and bring TQ in core, calculate new element properties			TQ
13	Total joint stresses TNQ to share Unit 1 with SNQ	SNQ, TNQ		
14	Copy TOSP into core, perform crack propagation analysis			TOSP
15	Repeat steps 2 to 14 if mesh geometry altered due to crack; otherwise repeat steps 3 to 14.			

TABLE 6.3 USE OF CORE SPACE IN INCREMENTAL PROGRAM

displacement vector $\Delta \underline{X}$. The latter is used to calculate the joint displacement matrix DOSP which occupies unit 1. $\Delta \underline{X}$ is then overwritten by the incremental element stress matrix DSQ. Core unit 3 is occupied alternately by the total element stress matrix TQ and the total joint displacement matrix TOSP, one being sent to the backing store when the other is in use. The incremental joint stress matrix SNQ is constructed from the element stresses DSQ, the latter being overwritten by the total displacement vector \underline{X} . The total joint stress matrix TNQ shares unit 1 with SNQ during the crack propagation analysis. The procedure is repeated for each increment of the loads.

6.12 TESTS ON THE COMPUTER PROGRAMS

6.12.1 Tests of accuracy

The accuracy of the various finite elements was established by analysing simple problems under tension, compression and bending loads. The results were checked against hand calculations and a very good agreement was found. For larger problems the accuracy of the programs have been determined by model tests. The tests are described in chapter 7 and the experimental results are compared with the theoretical computed results in chapter 8. Again a good agreement is obtained.

6.12.2 Computer time

Further tests were carried out on the programs to ascertain the cost of running large jobs. The problems analysed had various configurations of the finite element mesh and various total numbers of degrees of freedom. Non-linear problems, with upto 4500 unknown degrees of freedom, have been analysed by these programs. However,

the dimensions of the arrays in the programs are so adjusted that still larger problems can be analysed. Generally the execution times of the programs increase with the increase in the number of degrees of freedom. This is because the stiffness matrix becomes larger and there are more numbers of equations to be solved. The mill time of the computer for one cycle of iteration or one increment of the load is plotted in figure (6.19) against the total number of degrees of freedom for a number of problems. A mean curve is drawn through some of the points as a rough guide. While this curve indicates a parabolic relationship, some of the points show a wide scatter. This indicates that the cost of a problem does not depend on the number of degrees of freedom alone. Besides, in a problem where crack propagation is included, the number of degrees of freedom changes continuously. In figure (6.19) the computer time is plotted against the initial number of degrees of freedom for such problems. In a fixed band width storage scheme a parabolic relationship is known to exist between the band width of the stiffness matrix and the computer time. In the present method a variable band width storage scheme is adopted and a different number of elements are stored and operated upon for each row of the stiffness matrix. The computer mill time is plotted in figure (6.20) against the total number of elements of the stiffness matrix stored. A parabolic relationship is also indicated here. However, the points are less scattered about the mean curve in figure (6.20) than in figure (6.19). This shows that the estimate of the cost of analysing a problem can be obtained more accurately by assessing the size of its stiffness matrix stored in the compact scheme than from its number of degrees of freedom.

The total number of elements stored depends on the number of

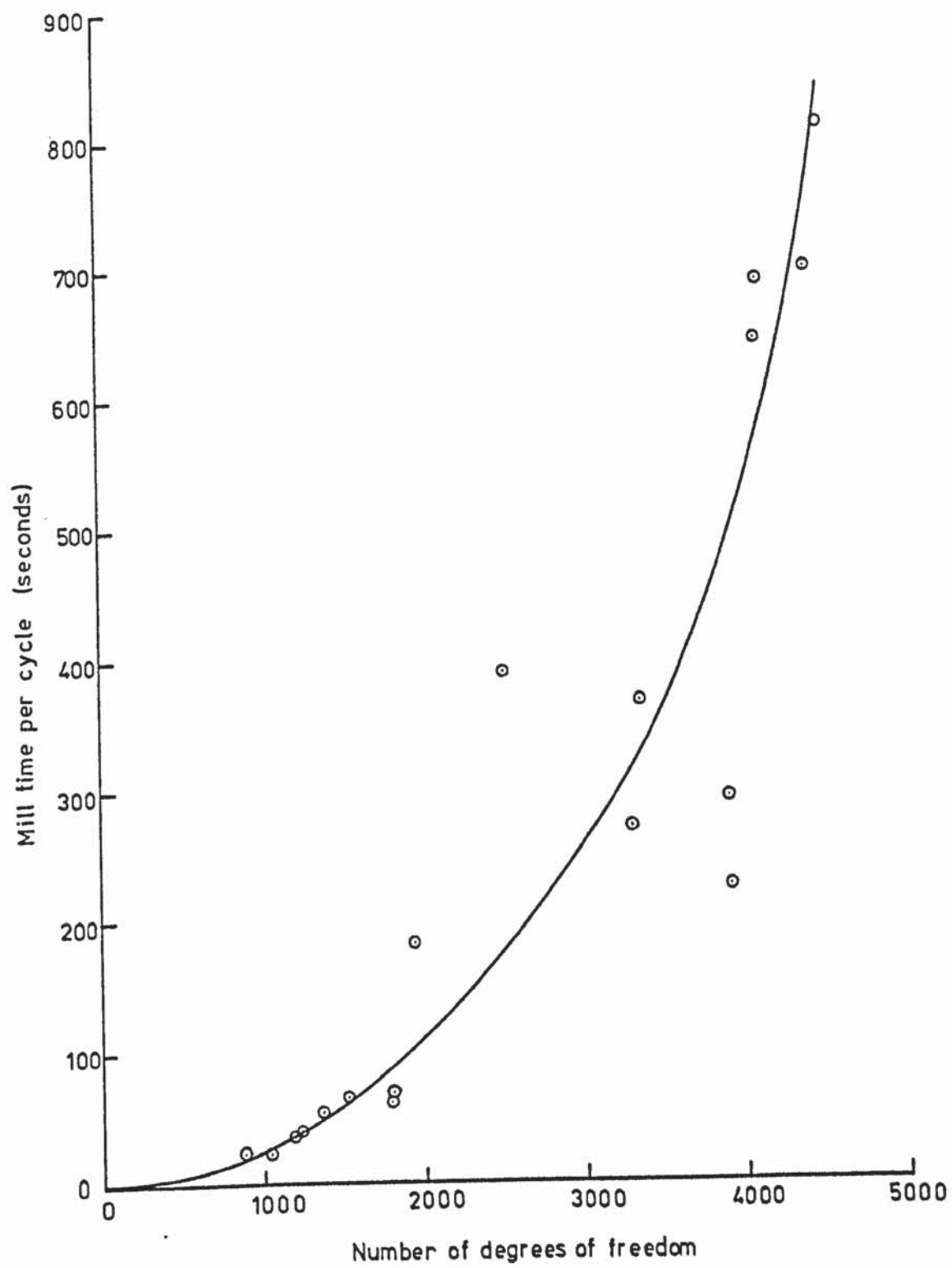


FIGURE 6.19 COMPUTER MILL TIME FOR VARIOUS DEGREES OF FREEDOM

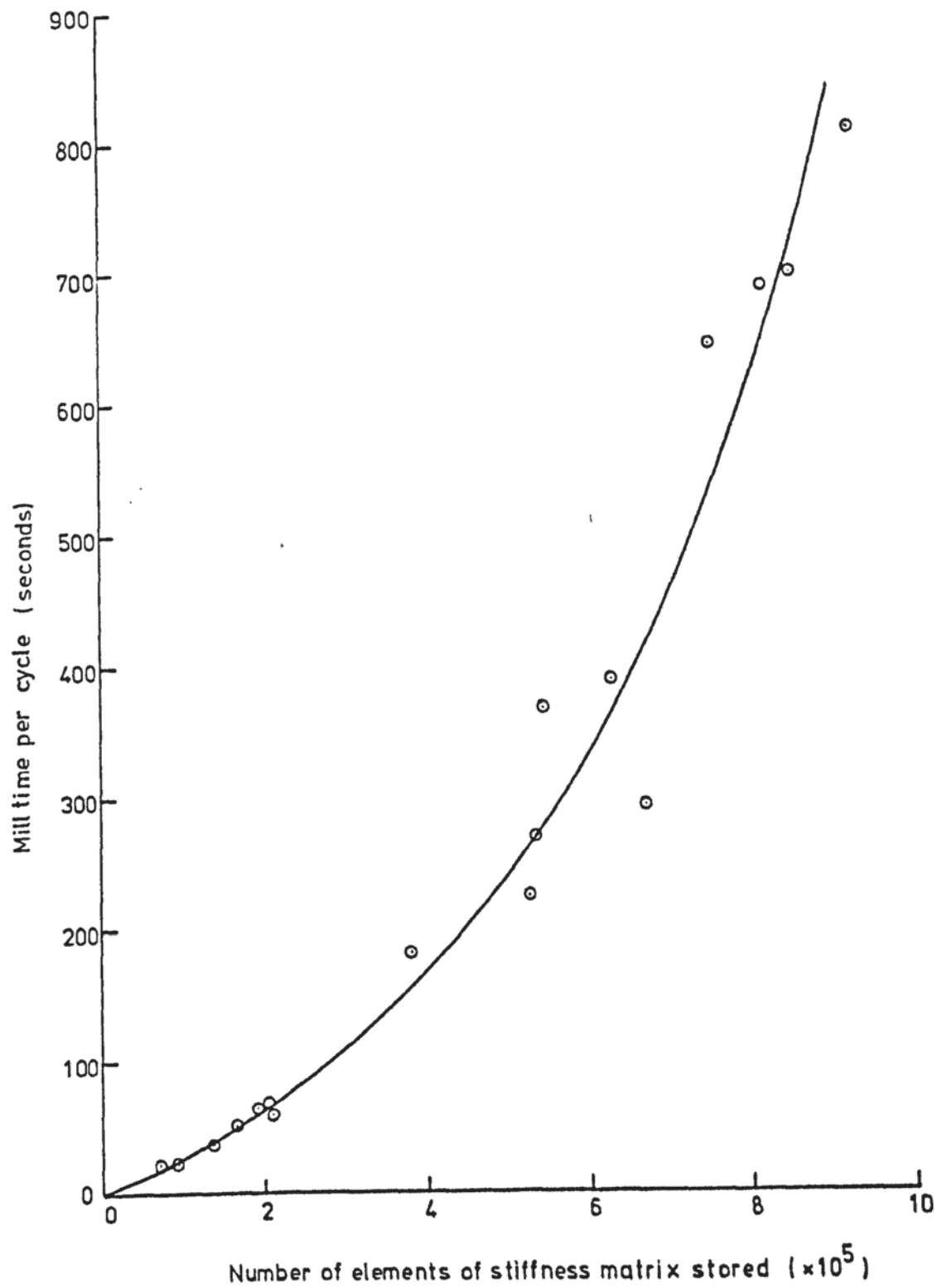


FIGURE 6.20 COMPUTER MILL TIME FOR VARIOUS SIZES OF STIFFNESS MATRIX

elements between the first non-zero element and the leading diagonal of each row of the stiffness matrix. The length of this row is decided by the difference between the number of a joint and its least joint number. This difference can be kept to a minimum by a careful joint numbering so that the difference between the joint numbers at the various nodes of an element is small. The cost of a problem thus depends largely on the design and numbering of the finite element mesh apart from the size of the problem. A bad joint numbering can introduce a large number of zero elements to be stored between the first non-zero element and the leading diagonal of a row. In the automatic data generation method described in section (6.9), the joints are numbered in such a way that the numbers vary most rapidly in the direction with the minimum number of joints and least rapidly in the direction with the maximum number of joints. This generally results in a low difference between the joint numbers at the various nodes of a solid element.

6.12.3 Commerical cost

The commercial cost of running a job varies from one computer to another. Furthermore, the efficiency and speed of the machine, the priority or urgency of the job, the facilities for data preparation all affect the cost of a job.

The problems analysed in this thesis were all run on the CDC7600 computer at the University of Manchester Regional Computer Centre. As the centre did not operate a computer bureau service, a quotation on the commerical price of running a job was not available. However, based on other centres which operate such a service, a rough estimate of £3000 per 3600 seconds of mill time of the CDC7600 computer is obtained. This means that the cost of a job in pounds sterling can

be estimated roughly from figure (6.19) and (6.20) by multiplying the appropriate mill time by 0.833. For the largest problem analysed in this thesis the computer time was about 800 seconds per cycle. This is a fifty storey three dimensional framed structure resting on a bed of clay and is described in chapter 9. Five cycles of iteration were necessary for the convergence of the displacements. The cost of running this job is estimated to be about £3300, which is considered to be quite reasonable for the size of the problem. Another large problem described in chapter 9 is that of a complex of four silos resting on a bed of chalk. The total cost of analysing this problem is estimated to be about £1000. This is also a reasonable figure for the magnitude of the problem.

6.13 CONCLUSION

The finite element computer programs described in this chapter are of a versatile nature and can be used to solve a wide variety of structure-soil interaction problems. They can also be used to analyse isolated systems of structures or three dimensional and irregular solids. The various finite elements included in the programs can be applied in any arbitrary combination to represent many physical problems. The automatic data generation scheme reduces the manual data input and results in an economical use of the programs.

The cost of analysing a structure interacting with its supporting foundation and soil is not exorbitant, as is commonly believed it would be. The programs thus offer a promising possibility of obtaining exhaustive analytical results for structure-soil interaction problems.

CHAPTER 7

MODEL EXPERIMENTS

7.1 INTRODUCTION

The experiments were performed on model structures resting on a prepared bed of sand. The model tests were designed to obtain a three dimensional condition in the test system. Testing of a two dimensional system or of an isolated pad or strip footing resting on soil, as has normally been done in the past, cannot unveil the complex interaction of a complete structure with the soil. Therefore, it was decided to test models of complete structures of different shapes and supports as a continuation to tests carried out by Cunnell (1974).

The measurement and the study of the stresses and the strains in the soil are useful but difficult. However, they are only important in as much as they affect the behaviour of the structure which produces them. It was considered that if the analytical behaviour of the structure agrees satisfactorily with the experimental ones, then it is safe to assume that the analytical soil behaviour can also be taken as sufficiently accurate. Equally important is the fact that the measurement of stresses in the soil under a structure is usually associated with expensive gadgets and thus increases the cost of the experiments. For the above reasons, it was decided to measure the displacements and the bending moments at various points on the structure alone. No attempt was made to determine experimentally the contact pressure and the stresses within the soil underlying the model structure.

7.2 VARIOUS TESTS PERFORMED

There were two basic elements in the experiments. These are the model structure and the soil. The soil was represented by a controlled uniform bed of loose dry sand contained in a concrete tank. While it is possible to represent soils other than sand in the theoretical analysis, dry sand was used in the tests because it is easy to manouver and control its properties. The same conditions of uniformity and density of the sand bed was reproduced for each and every experiment that was performed. This enabled the same set of stress-strain curves of the sand to be used to analyse all the model tests. This was achieved by emptying the sand tank after each test and refilling it under controlled conditions and with a standard procedure before each new test.

The other element of the system, the structure, can be altered. Various structures exhibit various modes and degrees of interaction with the soil. These depend on the shape of each structure, the manner it is supported as well as the overall stiffness of the structure and the relative stiffness of its components. There are an unlimited choice of structures each of which would exhibit a different behaviour from the other. In the present investigation, four representative models were chosen for test purposes. These are described below.

7.2.1 Test series A - Single-bay space frame model

This was a single-storey single-bay three dimensional frame resting on four separate footings as shown in figure (7.1). The footings rested on the surface of the sand bed contained in the test tank. This structure was tested under similar conditions by Cunnell

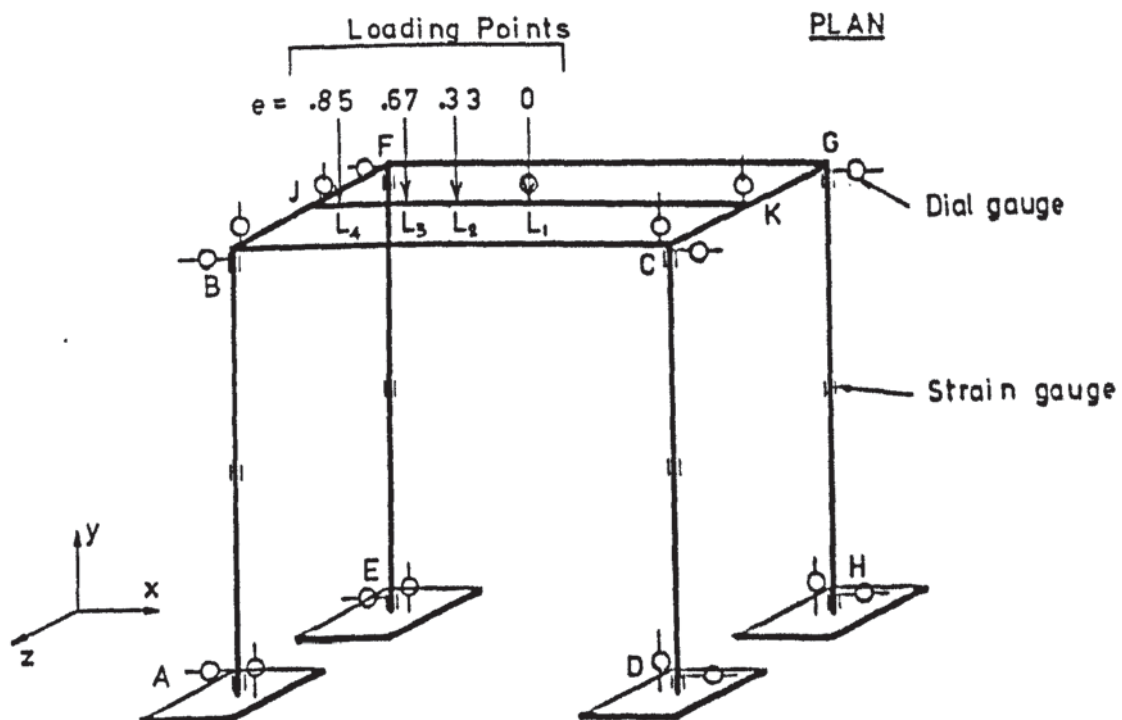
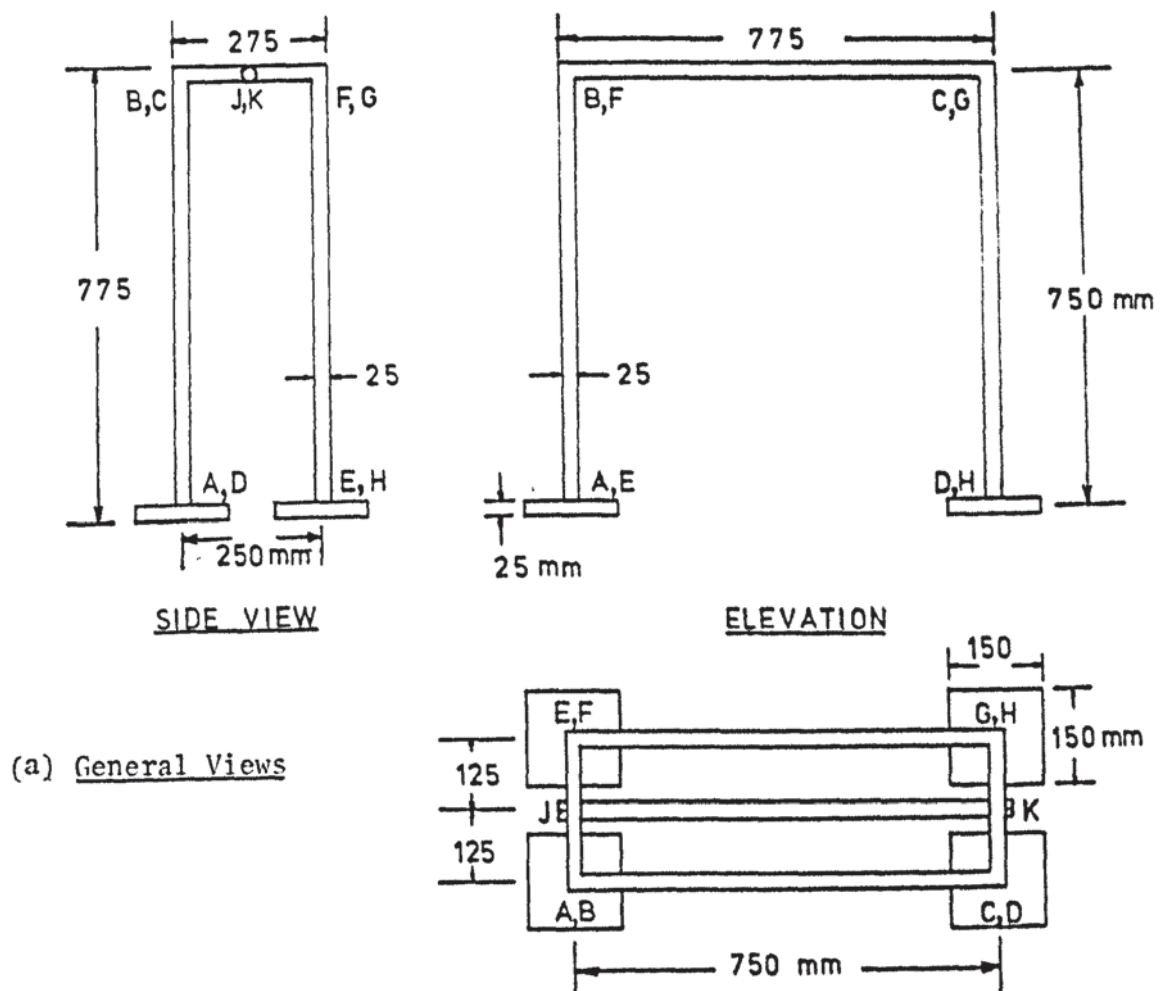


FIGURE 7.1 MODEL STRUCTURE FOR TEST SERIES A

(1974), but without the measurement of the stresses in the structure. The tests were repeated by the author with measurements of the strains by electrical resistance strain gauges to obtain the experimental bending moments data.

The beams and the columns of the model were all made of 25 x 25 mm square solid section black mild steel bars and the footings of 25 mm thick mild steel plates. The joints were 100% arc welded except the ones at the ends of the central beam which were securely bolted.

For each test the model was loaded, by slowly applied increments of dead weights, at single points on the central beam JK (see figure 7.1b). The position of the load was varied along this beam to test the structure under loads of various eccentricities. Four tests were performed on this model with values of eccentricity, $e = 0, 0.33, 0.67$ and 0.85 , with the load at L_1, L_2, L_3 and L_4 respectively. Here e is the ratio of the distance of the load from the centre of beam JK to the half-length of the beam.

Displacement readings were taken by dial gauges of 0.01 mm and 0.001 inch gauge divisions at various points on the structure to read values of the differential settlement and the sway. These were placed at A, E, H and D to record the vertical settlements of the footings and the horizontal displacements of the column bases. They were also placed at B, F, G and C to read the displacements at the top of the columns. Gauges at J, L_1 and K recorded the deflections of the beam JK. Strain gauges with gauge length 5 mm were located at the base, the mid-height and the top of each column as shown in figure (7.1b). A pair of gauges were used at each point on the opposite faces of the column to measure the bending moments about the z-axis. For this and each of the other

structures, the surfaces in contact with soil were covered by sand paper to prevent any slip between the two.

7.2.2 Test series B - Box culvert model

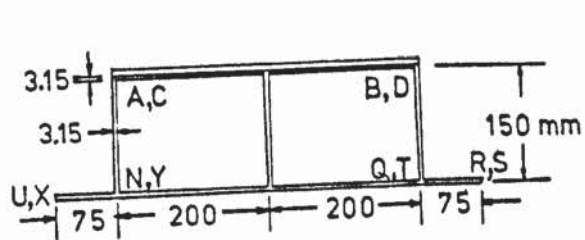
Box culverts are normally buried almost completely in the soil and they exhibit a considerable degree of interaction with it. To the author's knowledge these have never been tested. This series of tests was performed on the model of a twin box culvert as shown in figure (7.2). The model was made of 3.15 mm thick mild steel plates welded together in a jig to form a twin-chambered section. Two 3.15 x 6 mm strips of the same plate were welded to the top deck of the culvert to represent the parapets. For each test the culvert was buried in the sand up to the top level on the two sides, while the twin box and its fronts were kept empty. The arrangement of the culvert in the sand bed is shown in figure (7.3) where the trapeziodal spaces such as LMANBQVW are empty. This situation simulated the clear drainage way and an approaching and a leaving roadway connected by the top deck ABCD of the culvert.

Six tests were performed on this model for various load cases. The loads were vertical and applied on the top deck at points H, G, F, E, J and K in figure (7.2) by means of a hydraulic jack. The loading scheme for the box culvert tests is given in table (7.1).

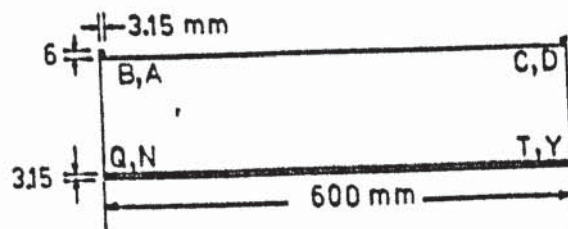
Load case	e_x	e_z	Point
B1	0	0	H
B2	0.33	0	G
B3	0.67	0	F
B4	1.0	0	E
B5	1.0	0.36	J
B6	1.0	0.72	K

Note: e_x and e_z are defined in figure (7.2)

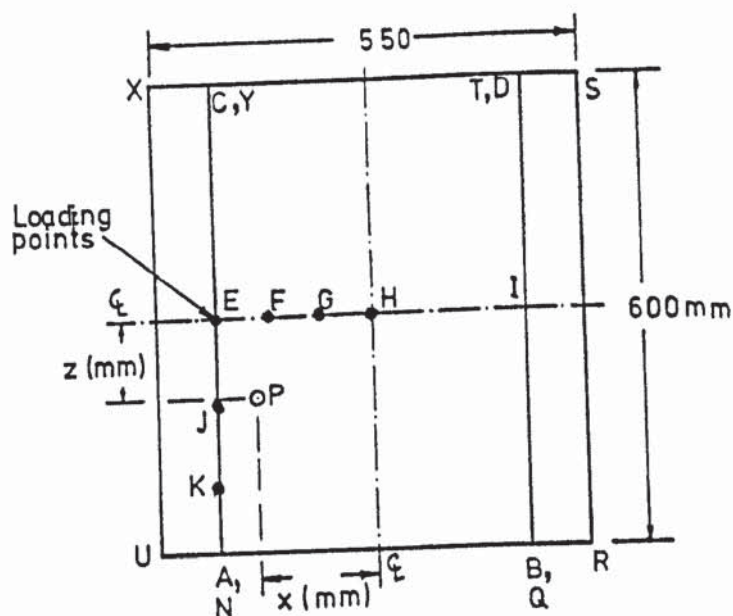
TABLE 7.1 LOADING SCHEME FOR BOX CULVERT TESTS



ELEVATION



SIDE VIEW



PLAN

Definition of eccentricities of point P:-

$$e_x = \frac{x}{200} ; e_z = \frac{z}{300}$$

FIGURE 7.2 BOX CULVERT MODEL OF TEST SERIES B

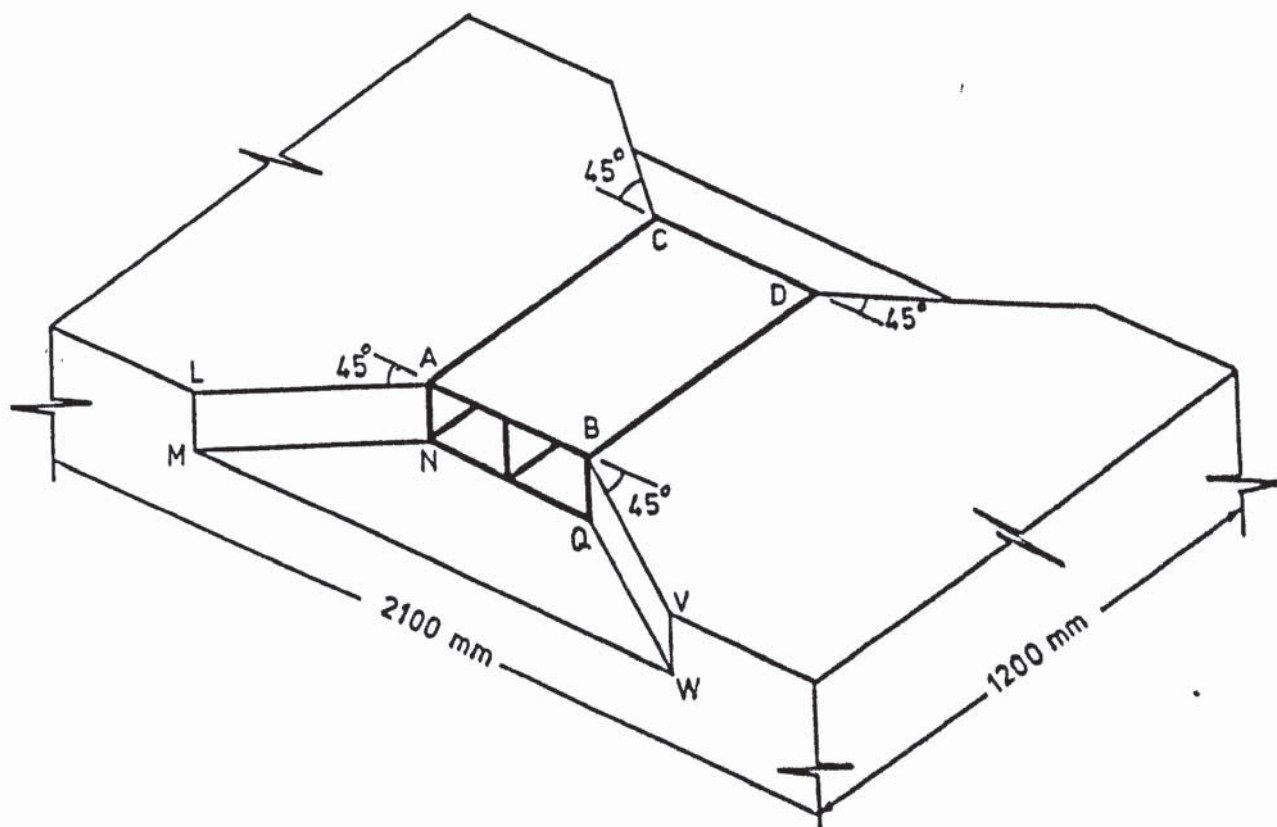


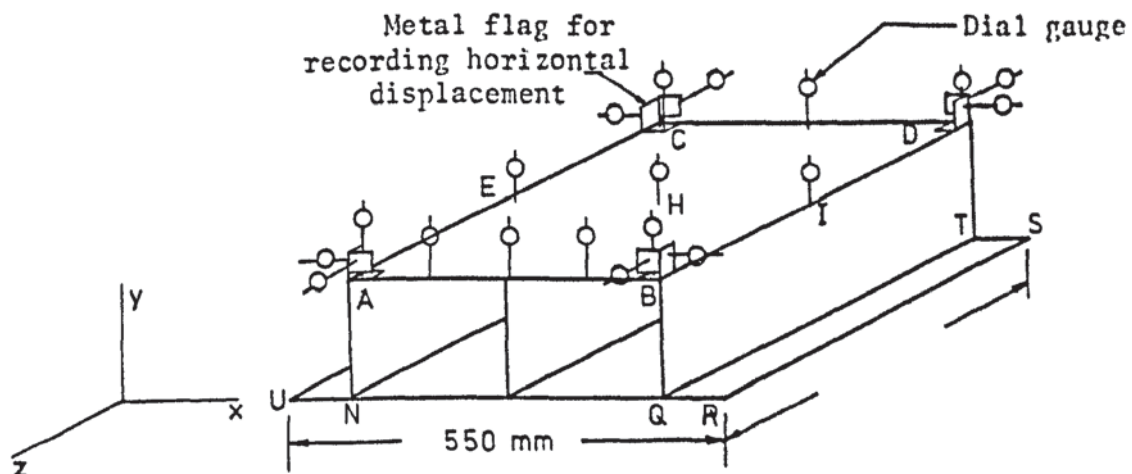
FIGURE 7.3 ARRANGEMENT OF CULVERT IN SAND BED

Vertical displacements were recorded by dial gauges on the top deck of the culvert along the edges AB and CD and also along the centre at E, H and I, see figure (7.4a). 50 mm high metal flags, glued to the corners of the culvert at A, B, C and D, were used to measure the horizontal displacements in x and z directions, as shown in the figure. Strain gauges were fixed around the culvert at a cross section 150 mm from the front edge. The locations of the strain gauges are shown by the numbers 1 to 14 in figure (7.4b). A pair of strain gauges, each of 5 mm gauge length, were used at each location on both sides of the plate.

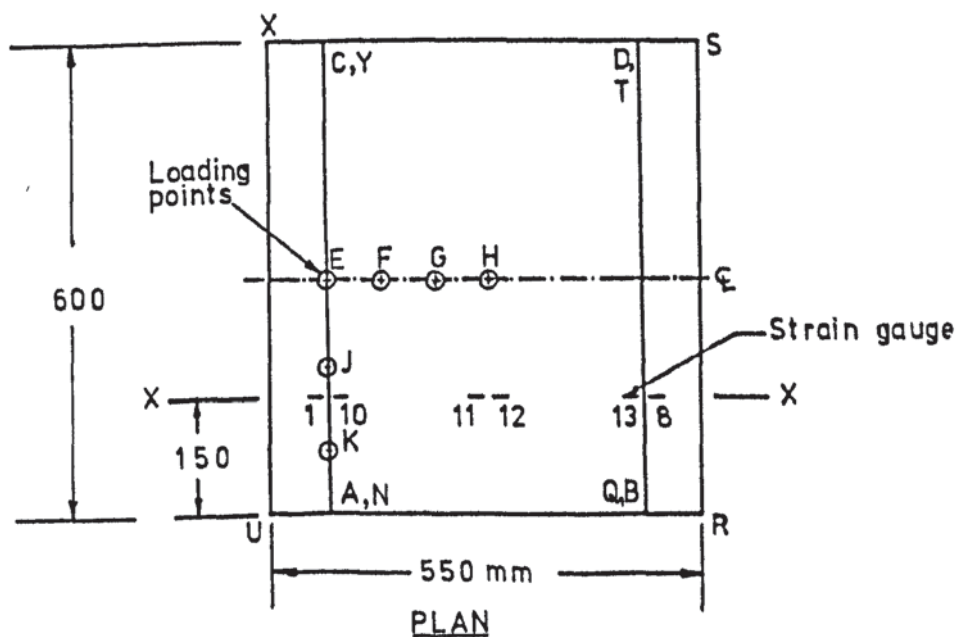
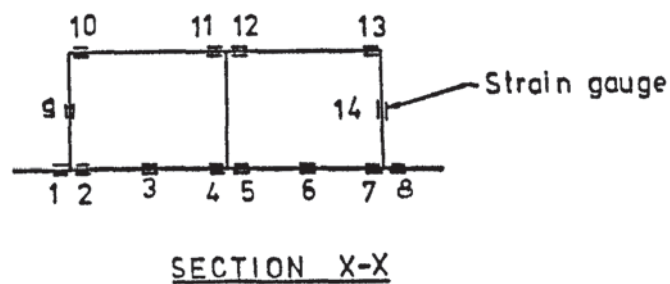
7.2.3. Test series C - A tall structure

This consisted of four slender columns with a latticed foundation structure as shown in figure (7.5). It resembles a gravity type offshore oil production platform. Although such an oil platform is subjected to the forces of waves, the precise treatment of these is beyond the scope of the present work. The interaction of a structure, with a high ratio of height to base area, and its supporting soil was the item of interest in this series of tests. The configuration and the depth of the base structure were altered to investigate the effect of changing structural rigidity on the interaction between the soil and the structure. In one of the tests, column AB was removed and a three-legged model was tested to show the effect of the failure of a column on the interactive behaviour of the structure and to investigate the effect of irregularities.

The four main columns, AB, CD, EF and GH, of the model were 19 mm diameter bright mild steel bars threaded at the top and the bottom. The bottom of the columns were machined to a pointed end

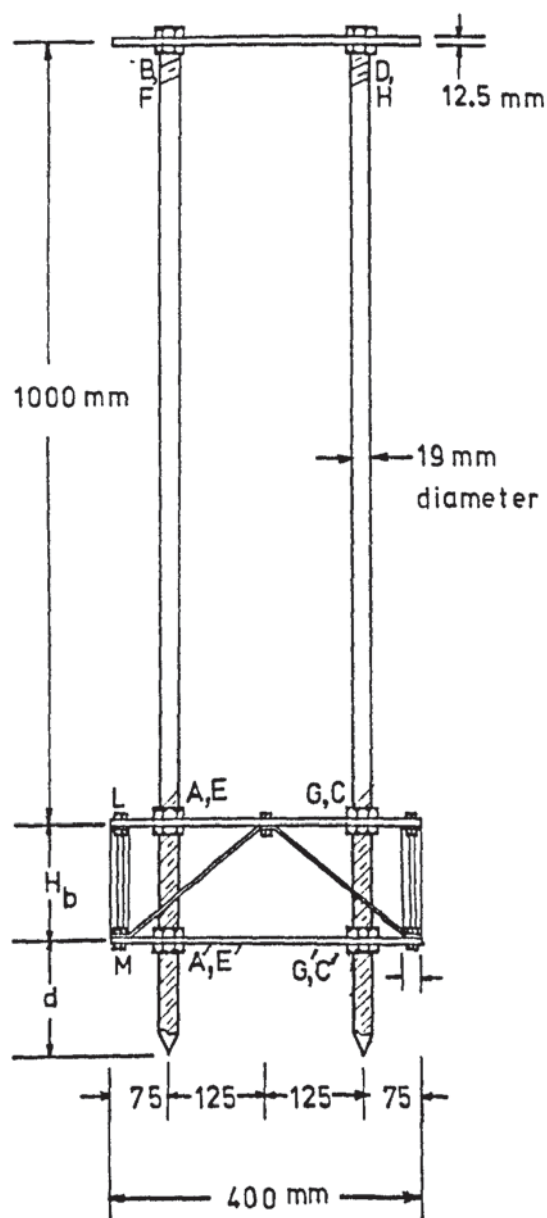


(a) Dial gauge locations

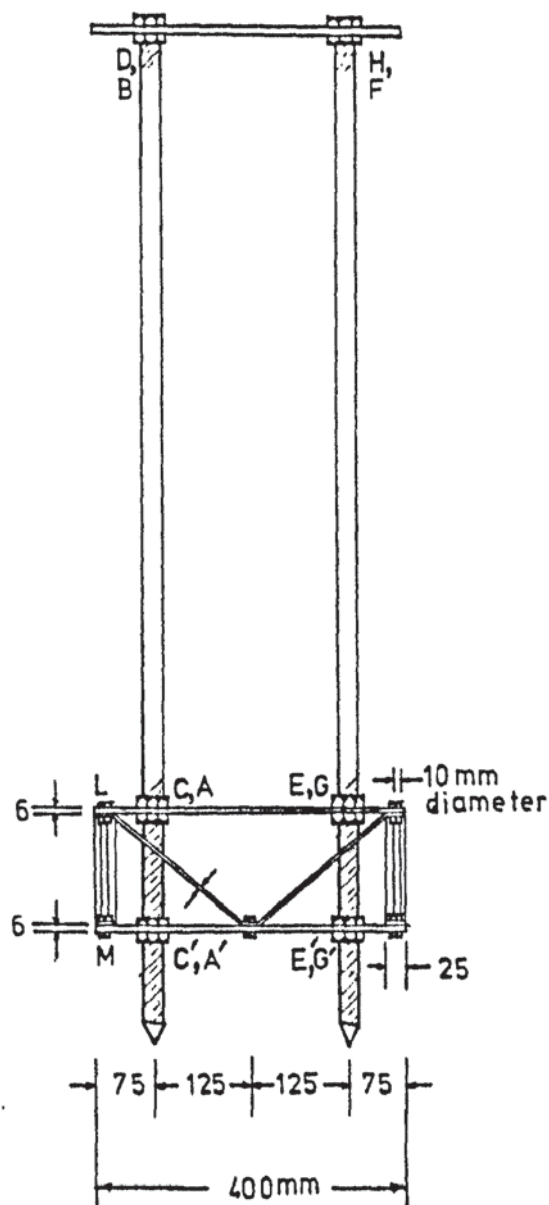


(b) Loading points and strain gauge locations

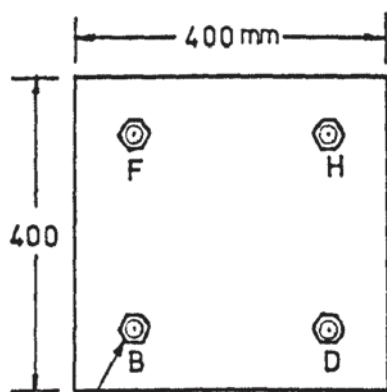
FIGURE 7.4 GAUGE LOCATIONS AND LOADING POINTS ON CULVERT



FRONT VIEW



SIDE VIEW



Column AB

TOP VIEW

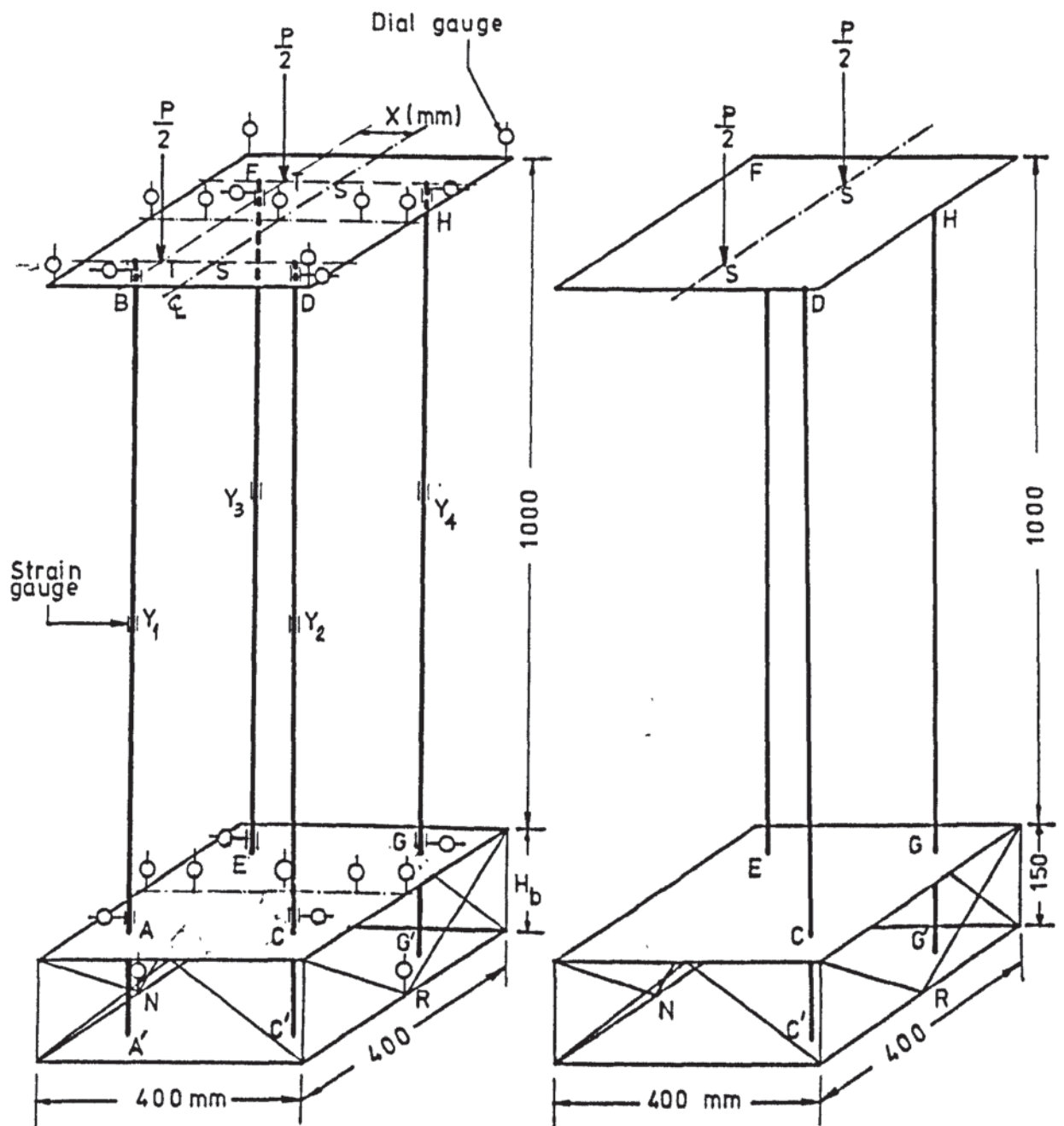
Model No	Dimensions (mm)	
	H_b	d
C1	150	150
C2	75	225
C3	0	300
C4	150	150 (Column AB removed)
C5	0	0

FIGURE 7.5 DETAILS OF THE TALL STRUCTURE MODEL

to facilitate the positioning of the structure in the sand. The top platform BDFH was 12 mm thick mild steel plate and the two base plates ACEG and A'C'E'G' were 6 mm thick mild steel. The four vertical members such as LM at the corners of the base were 10 mm diameter bright mild steel bars. The diagonal members in the base were bent strips of 3 mm x 25 mm mild steel plate.

The various elements of the model were joined together by nuts and bolts and no welding was used. The basic model C1 had a height H_b between the base plates of 150 mm. Two other models were derived from this by altering H_b , each time keeping the height of the columns AB, CD, EF and GH constant at 1 m. The base height was reduced to 75 mm for model C2 by using a new set of vertical and diagonal elements in the base and shifting the lower plate A'C'E'G' upwards. Model C3 was made by removing the base members altogether and reducing the distance H_b to zero. Finally, model C4 was made identical to C1 ($H_b = 150$ mm) except that column AB was removed as shown in figure (7.6b).

The loads on the model were applied by a lever arm arrangement at two points S,S or T,T on the top plate as shown in figure (7.6a). Separate tests were performed with the loads at S ($e = 0$) and at T ($e = 0.4$). Strain gauges were fixed at three points on each column, just above the base at A, C, E and G, at mid-height points Y_1 , Y_2 , Y_3 and Y_4 and at the top at B, D, F and H. Dial gauges were located to record horizontal displacements at the base and the top of each column as shown in figure (7.6a). They were also used to read vertical deflections at N and R at the base, along the centre lines of the upper base plate and the top plate and at the corners of the top plate. A total of 24 strain gauges



(a) FOUR COLUMN MODEL

(b) THREE-COLUMN MODEL

[Gauge locations same as in (a)]

$$\text{Eccentricity of the applied load} = \frac{X}{200}$$

FIGURE 7.6 TALL STRUCTURE MODEL SHOWING LOAD AND GAUGE LOCATIONS

and 24 dial gauges were used for most of the tests in this series.

A further test was performed on model C3 with the portion of the legs below the base plate cut off, leaving no protruding pile in the soil. This test was done with $e = 0.4$ and will be called test C5. A summary of the tests in this series is given in table (7.2).

Model	Test No.	Base height, H_b (mm)	Column extension in sand, d (mm)	No. of columns	Eccentricity of load, e
C1	C1 a	150	150	4	0.0
C1	C1 b	150	150	4	0.4
C2	C2 a	75	225	4	0.0
C2	C2 b	75	225	4	0.4
C3	C3 a	0	300	4	0.0
C3	C3 b	0	300	4	0.4
C4	C4	150	150	3	0.0
C5	C5	0	0	4	0.4

TABLE 7.2 SUMMARY OF THE TESTS IN SERIES C

7.2.4 Test series D - Three-bay space frame

The last series of experiments was performed on a single-storey three-bay steel frame shown in figure (7.7). All the members were made of 19 mm square black mild steel bars and welded together. Two different foundation structures were used to study the effect of the foundation stiffness. Tests D1 were performed with the frame supported by individual square pad footings under each column. The pads A, C, E, G, J, L, N and Q were 19 mm thick mild steel plates and are shown by firm lines under the columns in

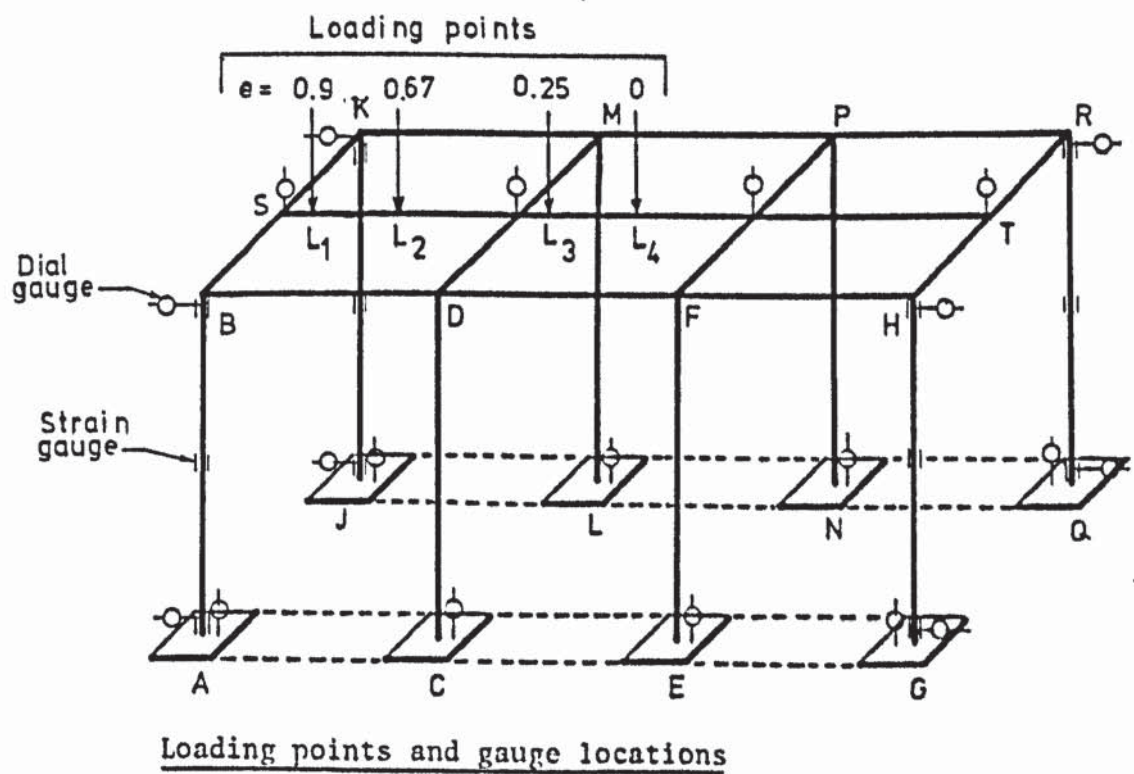
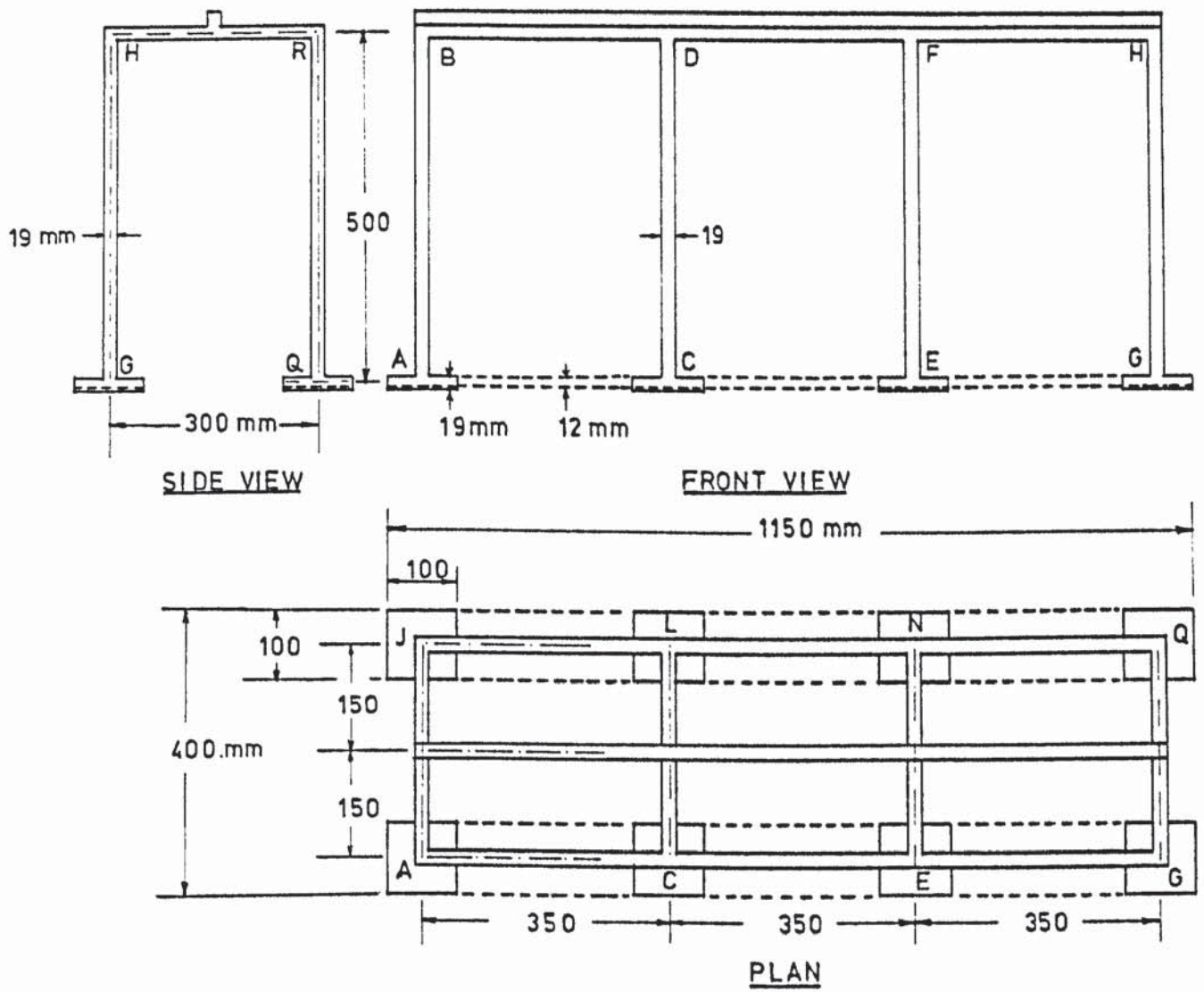


FIGURE 7.7 THREE-BAY SPACE FRAME MODELS OF SERIES D

figure (7.7). These footings were later replaced by two strip foundations under the four columns on each side of the frame for the tests D2. The strips were 12 mm thick mild steel plates and are shown by the dashed lines in the figure.

The load was applied at a single point such as L_1 , L_2 , L_3 and L_4 on the central beam ST of the frame by a dead weight mechanism. Four tests were performed on each of the models D1 and D2 with the load at different eccentricities. The loading points are shown in figure (7.7), where the eccentricity e is the ratio of the distance of the load from the centre of the beam ST to half the total length of this beam.

Strain gauges were fixed at the base, the mid-height and the top of the outer columns AB, JK, GH and QR. Dial gauges were located to read the horizontal and the vertical displacements of the footings A, J, G and Q and the vertical displacements of footings C, E, L and N. They were also used to record the horizontal displacement of the column tops at B, K, H and R and the vertical displacements along the central beam ST as shown in figure (7.7).

7.3 MECHANICAL PROPERTIES OF THE STRUCTURE MATERIAL

The materials used in the model structures of all the tests were mild steel. The tests were designed so that the models were stressed within the elastic limits of their materials. The modulus of elasticity, E , and the Poisson's ratio, ν , are the only parameters necessary to describe their mechanical behaviour. Samples were collected from the material used to construct the various components of each model. They were then tested in tension

according to BS 18. A summary of the results obtained from these tests is shown in table (7.3).

7.4 PROPERTIES OF THE DRY SAND

The same sand was used in the test bed for all the tests. This was a washed Leighton Buzzard brown sand of a fairly uniform grading. The particle size distribution of the sand is shown in figure (7.8). The sand had a black material mixed with it mainly between the sizes of 0.15 mm and 0.3 mm. The specific gravity of the sand was determined to BS 1377 as 2.655.

7.4.1 Determination of the stress-strain properties of the sand

Soils in general, and the dry sand used in the test bed in particular, exhibit an essentially non-linear stress-strain relationship. In order to represent closely the properties of this sand in the non-linear finite element analysis, it is essential to determine these properties under the conditions pertinent to the test bed.

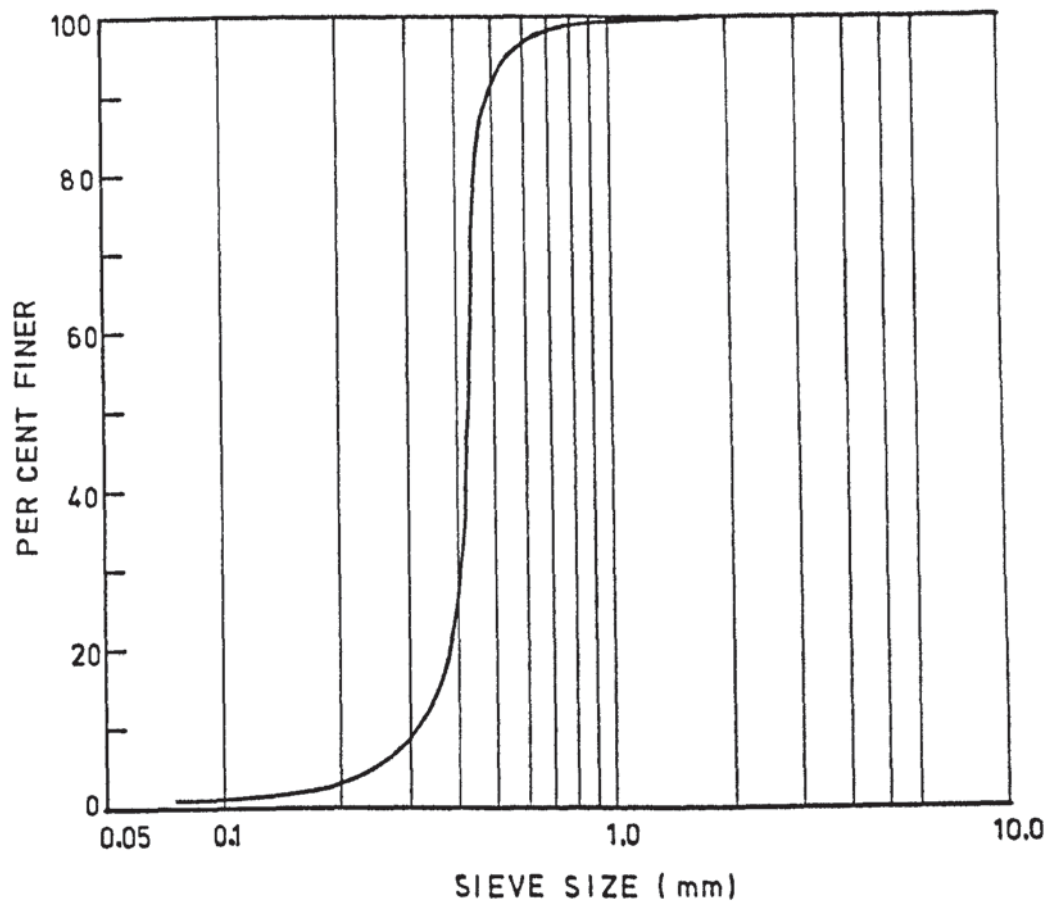
It is most likely that a generalized state of three dimensional stress exists in the experimental bed. Ideally, therefore, the test used to determine the soil properties should be able to control the three principal stresses independently. Such tests are too expensive and too involved to justify their application to anything but special research in soil mechanics. Therefore, a choice has to be made from the more standard methods of laboratory testing of dry sand.

As the soil particles are unlikely to crush in compression under the applied stresses and also as a general tensile failure is unlikely, the predominant strength characteristic is likely to be that in shear. The shear box test, however, seems to be inappropriate because it simulates a plane strain behaviour. The axi-symmetric

POISSON'S RATIO $\nu = 0.3$

Test	Component of model	Material	Ultimate strength (N/mm ²)	Yield strength (N/mm ²)	Modulus of elasticity (kN/mm ²)
Series A single-bay space frame	Beams and columns	Mild steel bars	-	-	206.9
	Footings	Mild steel plates	-	-	170.6
Series B Box culvert	Body and kerb	Mild steel plates	348.1	258.5	223.4
Series C Oil platform type tall structure	Main columns	Bright drawn mild steel bars	519.0	364.6	205.4
	Vertical members in base	Bright drawn mild steel bars	601.6	473.3	204.3
	Diagonal strips in base	Mild steel plates	345.7	259.9	213.9
	Top platform	Mild steel plates	476.9	300.2	193.5
	Base plates	Mild steel	365.5	251.8	218.1
Series D Three-bay space frame	Beams and columns	Mild steel bars	443.7	281.4	200.0
	Single and strip footings	Mild steel plates	432.1	272.5	204.4

TABLE 7.3 MECHANICAL PROPERTIES OF MODEL STRUCTURE MATERIALS



Effective grain sizes $D_{10} = 0.32 \text{ mm}$

$D_{30} = 0.4 \text{ mm}$

$D_{60} = 0.44 \text{ mm}$

Uniformity coefficient $C_u = \frac{D_{60}}{D_{10}} = 1.38$

Coefficient of curvature $C_z = \frac{D_{30}^2}{D_{10} D_{60}} = 1.14$

FIGURE 7.8 PARTICLE SIZE DISTRIBUTION OF THE SAND

cylindrical compression test seems to be the obvious alternative because of its relative proximity to three-dimensional state. Such tests are more generally known as the triaxial tests and were used to determine the mechanical properties of the dry sand.

The test conditions were dictated solely by the conditions in the model test bed. Some of these were that the initial confining pressures in the sand bed were very small, the sand was dry and the air in the voids was likely to escape under pressure to allow the volume changes to take place.

7.4.2 The Triaxial Apparatus

The apparatus was assembled in a manner recommended by Bishop and Henkel (1957) and Cunnell (1974). It was designed to perform the following functions:

- (a) to apply a low all-round pressure,
- (b) to apply and measure the deviatoric stress ensuring that the major principal stresses are vertical throughout the length of the sample,
- (c) to allow and measure volume changes of the sample under stress by draining air out of or into it, and
- (d) to check for the extent of anisotropy in the sand by measuring volumetric and axial strains under hydrostatic stress conditions.

The assembled apparatus is shown diagrammatically in figure (7.9). The triaxial cell was a standard one used for 100 mm diameter samples, slightly modified to accommodate a dial gauge inside the cell. The justification for placing the dial gauge inside the cell was that the axial deformations of the sample were to be

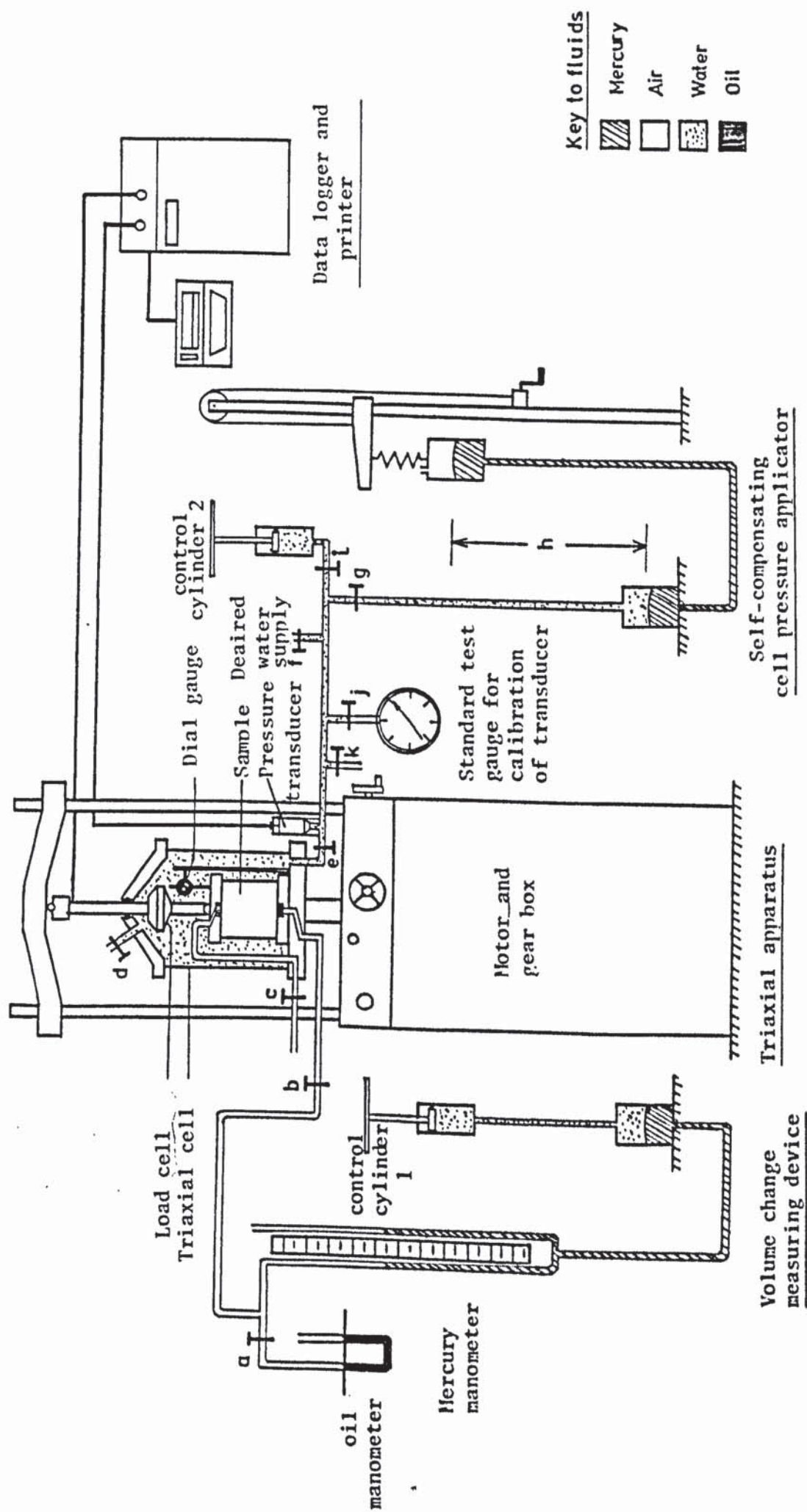


FIGURE 7.9 SCHEMATIC LAYOUT OF THE TRIAXIAL TEST ASSEMBLY

recorded together with the volume change readings under hydrostatic conditions to satisfy the requirements of function (d) stipulated above. The conventional method of attaching the dial gauge to the loading ram above the cell proved to be unsuitable because of the considerable weight of the ram that acted on the sample disrupting the hydrostatic state. The gauge used was a Baty, 0.01 mm per division, with a full range extension of 25 mm.

The triaxial loading frame was a conventional device manufactured by Wykeham Farrance and had a capacity of 10 imperial tons. It was fitted with a motor and gear box assembly, capable of applying a constant rate of strain to the sample by raising the cell base against the top frame of the apparatus. The load was transferred to the top beam of the frame through a Wykeham Farrance cone face electronic load cell which had a capacity of 450 kg. The load cell was located inside the cell eliminating the necessity of taking account of the friction between the loading ram and the bush in the cell cap. Readings of voltage changes in the load cell were obtained on a Modulog data logger made by Intercole Systems Limited. The machine incorporated a digital display voltmeter and a paper tape punch and tele-writer unit for automatic recording of data. The voltmeter had a sensitivity of between 0.15 mV and 1 mV per digit.

The cell pressure range used for the tests was extremely low and, so, extreme care was taken in their application and measurement. The pressure was applied by the head difference in a self-compensating mercury pot arrangement. It consisted of two Hg pots, one resting on the ground and topped up with water, and the other connected to it by a flexible tubing. The second mercury pot was

attached by a spring to a trolley travelling along a vertical rail by operating a hand winch. The stiffness of the spring was so adjusted that any change in the levels of the mercury in the two pots, due to a change in the volume of the sample or a slow leakage, was compensated by an appropriate change in the length of the spring, thereby keeping the head difference, h in figure (7.9), constant. The cell pressure was measured by an electronic pressure transducer made by Consolidated Electrodynamics. Readings from the pressure transducer were also obtained on the Modulog data logger.

The volume change measuring device consisted of a mercury manometer connected to a mercury pot resting on the ground. The pot was topped up with water and connected to a control cylinder which could be operated to induce a change of pressure in the pot. A very sensitive light oil manometer was connected in parallel to the mercury manometer. The specific gravity of the oil used being very low compared to that of mercury, a slight difference of level in the mercury manometer limbs was reflected in the oil manometer to a magnified scale. The device was connected by a flexible tube to the sample through a porous stone located in the base platten. Any volume change of the sample was accompanied by a corresponding change in pressure in the air in the sample. This was readily reflected in the sensitive oil manometer. By operating the control cylinder 1, the oil in the manometer limbs was brought back to equal heights, indicating the return of the air pressure in the sample to atmospheric. The level of the mercury in the other manometer changed due to this process, but still remained at equal heights in the two limbs. Since, a change of pressure in a fluid is inversely proportional to that of its volume, the change in volume of air in the

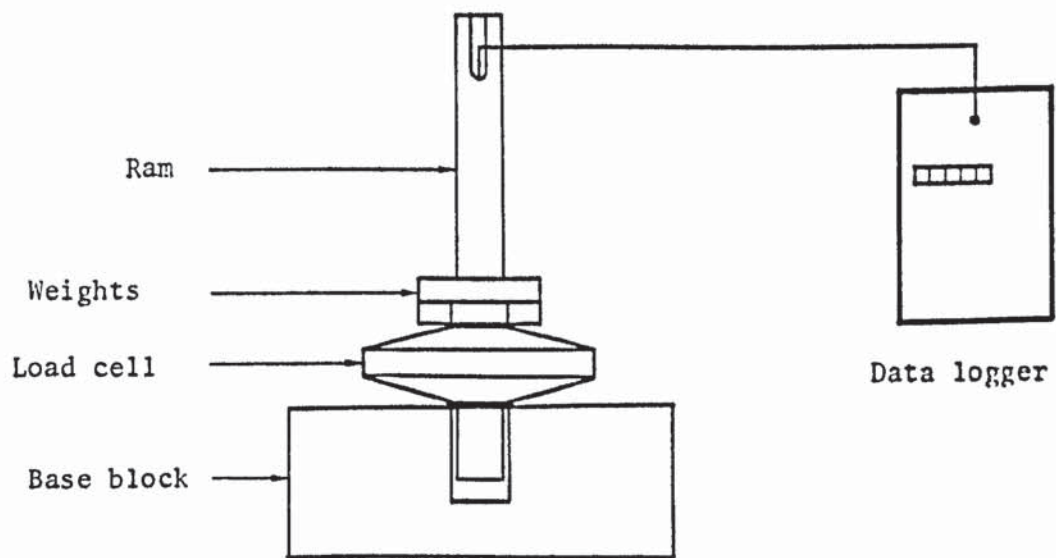
sample was related to the alteration of the height of mercury, which was read off a scale attached to the manometer.

7.4.3 Calibrations

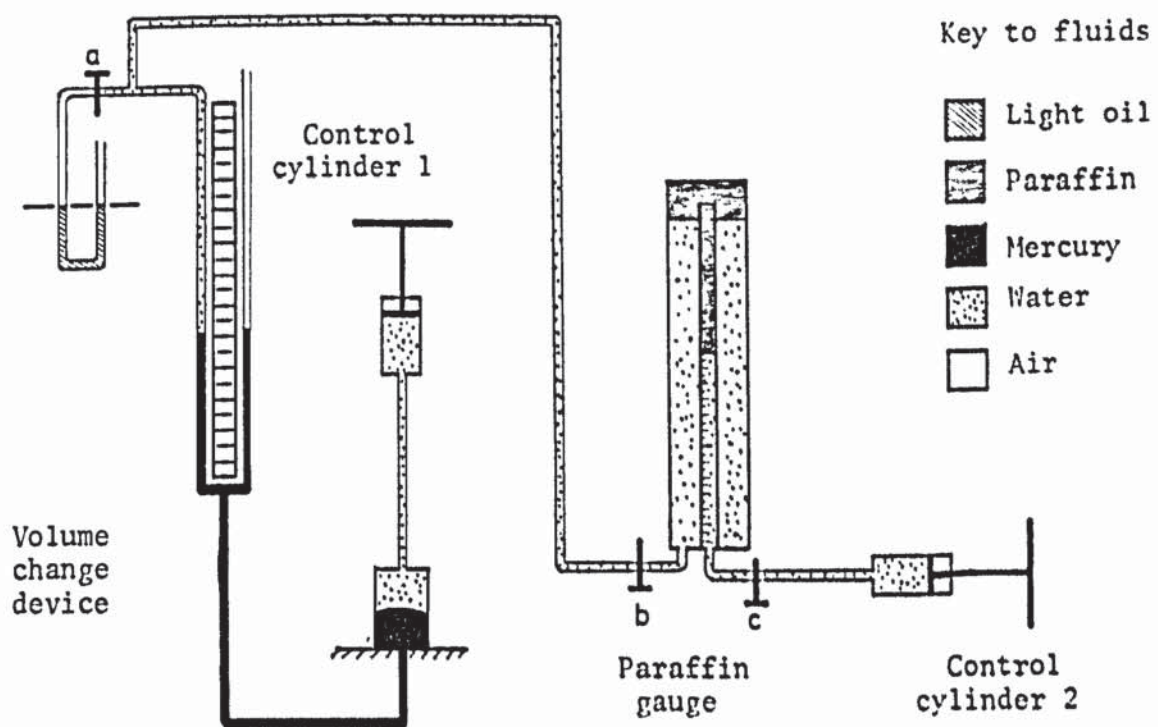
It was necessary to calibrate the load cell, the cell pressure transducer and the volume change device to correlate the readings obtained from them with the quantities they were used to measure.

(a) The load cell: The load cell was seated on a wooden block with a hole to accommodate the lower part of the ram, figure (7.10a). The terminal was connected to the data logger and the voltage reading for zero load was obtained. Weights with radial slots were then slid on the ram in increments of about 4.5 kg. Readings for each increment were obtained on the data logger. Similar readings were obtained for the unloading sequence. A linear regression analysis of the readings gave a correlation coefficient of 0.99998 and a calibration factor of 0.6353 N/digit on a X50 scale on the data logger with a constant supply voltage of 10V.

(b) Cell pressure transducer: The transducer was calibrated by comparison with a standard test gauge made by Budenberg Gauge Company. The test gauge was connected to the apparatus assembly as shown in figure (7.9). Valves e, f and g were shut and valves i and j were opened. The transducer was wired to the data logger. Valve k was opened and the transducer reading was obtained at atmospheric pressure. It was then shut and control cylinder 2 operated to record a pressure on the test gauge. Corresponding pressure transducer reading was obtained on the data logger. The process was repeated in increments for a complete cycle of loading and unloading. A linear regression analysis of the readings gave



(a) Calibration of load cell



(b) Calibration of volume change device

FIGURE 7.10 CALIBRATIONS OF TRIAXIAL SET UP COMPONENTS

a correlation coefficient of 0.99991 and a calibration factor of 0.0475 kN/m^2 per digit on a X50 scale on the data logger with a constant supply voltage of 10v.

(c) Volume change device: The sample end of the volume change device was filled with water and connected to a sensitive paraffin volume-change gauge. The paraffin gauge consisted of a calibrated tube enclosed in a larger diameter jacket, figure (7.10b). The tube was calibrated in tenth of a ml. The jacket and the tube were partly filled with a coloured paraffin at the top and water in the rest. The inner tube was connected to a control cylinder. Valve a was kept shut and valves b and c were opened. A small pressure was introduced in the inner tube of the paraffin gauge by operating the control cylinder 2 of figure (7.10b). This caused a movement of fluids in the system and was observed as a change in the level of paraffin in the inner tube of the paraffin gauge. The volume of the displaced fluid was read off the calibration on this tube. This displacement of fluid and the corresponding change in pressure were reflected in the mercury manometer of the volume change device. Valve b was then shut and the mercury in the two limbs of the manometer were brought back to level by operating the control cylinder 1. The new level of mercury was recorded and the difference between this and the initial reading gave the reading on the volume change device that corresponded to the displaced volume of fluid indicated in the paraffin gauge. The process was repeated for various values of the volume change. A linear regression analysis of the data gave a correlation coefficient of 0.99895 and a calibration factor of 0.2588 ml per cm reading on the volume change device. The linear regression analyses of all the calibration results were performed

by a program on a Texas SR56 programmable pocket calculator.

7.4.4 Preparation of the sample

A sample size of 100 mm diameter and 100 mm height was used and was formed in a purpose made assembly, shown in figure (7.11). The sample former assembly consisted of a two-piece split former, a pair of aluminium plattens for the top and the bottom of the sample, and a rubber membrane to fit inside the split former. Both the top and the bottom plattens had polished surfaces and porous stones were inset into them. The stones were connected to the channels in the cell base, in order to establish drainage of fluid to and from the sample. The plattens were made larger than the sample area and had a diameter of 118 mm. The top platten had a ball seat where the loading ram could rest. The split former was built in such a way that the top and the bottom plattens could fit loosely and rest in the lips at its ends. The lip at the top had a slot in it to allow the displaced air to escape when the sample was formed. The inside diameter and the height of the split former were both 100 mm.

The various channels and tubes were cleared using compressed air. Four 90 mm diameter latex rubber discs with central holes of 20 mm diameter and a few radial slits were prepared. Silicon grease was applied lightly on the two plattens taking care not to block the central porous stones. One latex disc was applied on each platten and smoothened with further grease applied on it. A second disc was then applied over it. This arrangement was adopted to reduce the horizontal constraints at the ends of the sample.

Five O-rings were slid on the split former to hold it firmly. A rubber membrane was fitted squarely on the bottom end of the former. Two of the O-rings were rolled down over the membrane to hold it

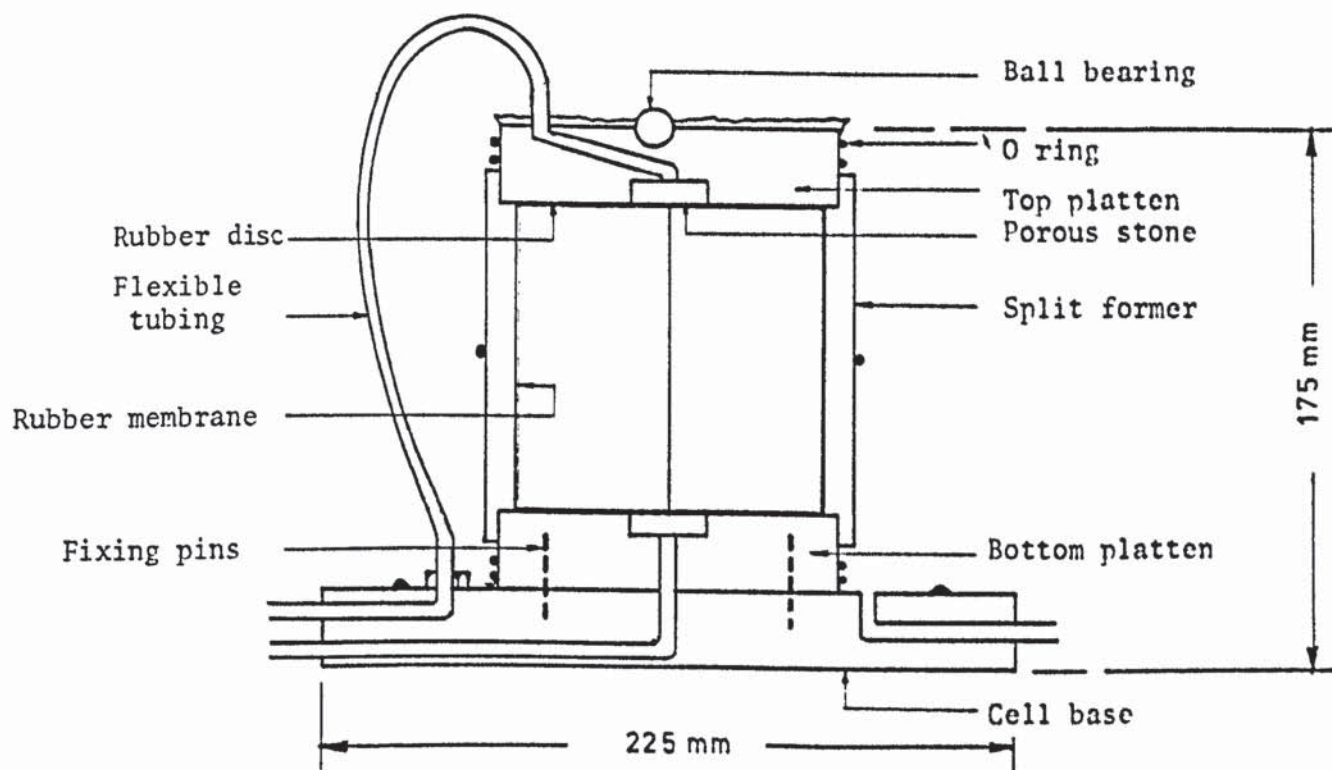


FIGURE 7.11 SAMPLE FORMER ASSEMBLY

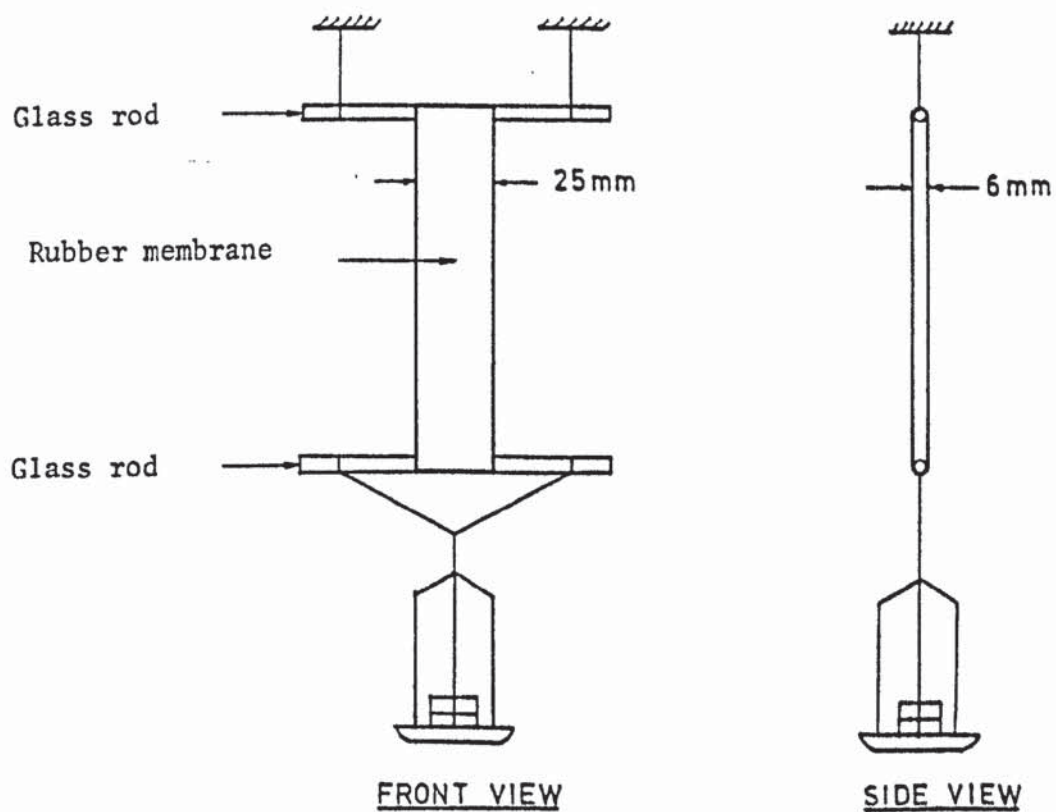


FIGURE 7.12 APPARATUS FOR MEASURING RUBBER MEMBRANE MODULUS

tightly against the former. The end of the membrane inside the former was stretched gently and fitted over the top end of the former. Any air trapped between the membrane and the former could be removed by stretching the membrane over the gap in the top lip of the former. Two O-rings were rolled up and the membrane was held against the former. The completed former was then placed on the bottom platten and the lower two O-rings were rolled up to allow the lower part of the membrane to be rolled down against the side of the platten. Compressed air was then blown through the porous stones to remove any possible blockage by grease.

The assembly, complete with the cell base, was then carried down to the model test rig for pouring the sand into the former under test conditions. A polythene jacket was put over the assembly to cover all parts except the top opening and was held in place by an O-ring. The former was placed at the centre of the test bed and filled by a pass of the hopper. The test rig and the hopper is described in section 7.5. The assembly was then recovered from the bed and excess sand removed from the top leaving the sample about 3 mm taller than the former for an easy removal of the former. The polythene jacket was taken off and the assembly carried back to the triaxial testing laboratory. It was then cleaned thoroughly on the outside using compressed air.

7.4.5 Experimental procedure

The cell base, complete with the sample in the former, was placed on the triaxial testing machine. The top platten was placed on the sample and pressed gently into contact, letting the air escape through the gap in the former lip. The O-rings holding

the top of the membrane were rolled down and the membrane rolled up against the platten. Two O-rings were rolled up to fix the membrane to the top platten. All the taps were connected and the valves shut. Valves b and c, figure (7.9), were opened and air was gently sucked by mouth, out of valve c, to introduce a small suction, which was recorded as about 2 cm of Hg on the volume change manometer. Valve c was shut and the sample left under suction until the suction maintained itself for about 10 minutes, otherwise it was readjusted and the process repeated. Failure to maintain the suction after a few adjustments would mean a leak somewhere in the system rendering it unusable. While the sample was still under suction the O-ring holding the split former together was gently rolled down on the bottom platten and the former carefully removed without disturbing the sample. The diameter of the sample was measured with a micrometer fitted with broad brass feet to avoid indenting the sample. The height of the sample was measured using a Vernier scale.

The back cover of the dial gauge was taken off and the inside was sprayed with a water-proofing silicon compound. It was fitted to its stand which was then screwed into a hole in the cell base.

The ball bearing was mounted on the top platten and the cell, complete with the load transducer, was placed over the sample and secured to the cell base. Valves d, e and f were opened and de-aired water was introduced into the cell. When water flowed out of valve d, valves e and f were shut and then valve d was also shut. This sequence was adopted as closing valve d before the others would subject the specimen to the full head of water in the supply mains.

The load cell and the cell pressure transducer were connected to the data logger which was set to display the two readings alternately and continuously at 2 second intervals. Valve g was opened and the height h was adjusted to give the desired reading of the cell pressure transducer. The self-compensating device was then isolated by shutting g. Valve i was opened and control cylinder 2 was operated to produce the same cell pressure reading as that with the mercury pot. This eliminated the necessity of a large readjustment by the self-compensating device which was then brought into action by opening valve g.

Valve c was opened and then shut again to bring the voids in the sample back to atmospheric pressure. Valve a was opened to bring the oil manometer of the volume change device into operation. Initial readings on the volume change scale and the dial gauge were recorded. The sample was then subjected to the cell pressure set up by the self-compensating mercury pots by opening valve e. The sample was left to 'consolidate' under ambient pressure, while control cylinder 1 was continuously operated to maintain level in the oil manometer of the volume change device indicating atmospheric pressure inside the sample. Volume change and dial gauge readings were taken at intervals during this state of hydrostatic pressure to furnish data for checking the extent of anisotropy.

When no further movement could be detected the load cell was brought down to rest on the ball bearing on the top platten. The cell was moved up until the top end of the loading ram touched the ball bearing underneath the reaction beam. The readings of the dial gauge and the load cell were noted at this stage. The gearbox was set for a constant displacement of 0.04 mm per minute.

This corresponded to an axial strain of about 2.4 per cent per hour on the sample. The motor was switched on and the sample subjected to the deviatoric stress. Control cylinder 1 was operated continuously to maintain atmospheric pressure inside the sample while it kept on undergoing volume changes. The self-compensating mercury pot device eliminated the necessity of readjusting the cell pressure with the volume changes. But for very small cell pressures, in the order of 3.36 kN/m^2 , it was found that, the head difference h being very small, the device did not perform well and control cylinder 2 had to be used from time to time to maintain a constant reading on the cell pressure transducer.

Readings of volume change, load and axial deformation were taken at convenient intervals of strain, care being taken to appreciate the changes in curvature of the stress-strain curve. When the load readings had dropped off or remained constant for a long time the loading was discontinued by switching the motor off and lowering the cell base. The cell was drained and dismantled. The sand was collected and weighed to calculate the initial porosity of the sample.

7.4.6 Calculations

Several corrections to the experimental readings had to be made to calculate the true stresses and strains in the sample. The cell pressure was measured at the cell base which was acted upon by the full head of water inside the cell. At mid-height of the sample the pressure was less than that recorded, by an amount H_c , where H_c is the height between the centre of the sample and the cell base. The true cell pressure at the centre of the sample was therefore

$\sigma_c' = \sigma_c - \gamma_w H_c$, where σ_c is the indicated cell pressure and γ_w the unit weight of water.

The rubber membrane offered some resistance to axial deformations when it was stretched and acted upon by the cell pressure. Poisson's ratio of rubber being close to 0.5 the hoop tension was negligible and no correction was made to the cell pressure for this effect. The correction to axial pressure was made in accordance with BS 1377 and was based on the assumptions that the membrane was capable of taking compression under cell pressure conditions and that the sample deformed as a right cylinder. At axial strain ϵ_1 the unit resisting stress due to the membrane is given by

$\frac{\pi D_o M \epsilon_1}{a}$, where M is the compression modulus of the membrane per unit width, D_o is the initial diameter of the sample and a is the corrected area of the sample at strain ϵ_1 .

The compression modulus of rubber membrane could not be measured directly, but it is reasonable to assume that it is equal to the extension modulus. The extension modulus was determined in accordance with BS 1377, by hanging a 25 mm wide circumferential strip of membrane between two glass rods and applying loads in a pan attached to the lower rod, figure (7.12). A value of M of 0.37 N/mm was obtained.

One other correction that had to be made to the load readings, was that due to the weights of the top platten, the ball bearing and the load cell. If W is the combined weight of these, the correction is W/a . No correction was made for the self weight of the sample, as it was judged to have negligible effect on the principal stresses.

The major principal stress σ_1 was obtained from the expression,

$$\sigma_1 = \frac{1}{a} (L + W - \pi D_o M \epsilon_1) + \sigma_c' \left(1 - \frac{a_p}{a}\right) \quad 7.1$$

where L is the load recorded by the transducer, and a_p is the area of the loading piston. The axial strain ϵ_1 and volumetric strain ϵ_v were calculated respectively from

$$\epsilon_1 = \frac{\Delta}{H_o} \text{ and } \epsilon_v = \frac{\delta V}{V_o} \quad 7.2$$

where Δ is the axial deformation recorded on the dial gauge, δV the measured volumetric deformation and H_o and V_o are the initial height and the initial volume of the sample respectively. The corrected area of the sample at axial strain ϵ_1 and volumetric strain ϵ_v was calculated from:

$$a = \frac{V_o}{H_o} \left(\frac{1 - \epsilon_v}{1 - \epsilon_1} \right) \quad 7.3$$

assuming that the sample remained a right cylinder after deformation.

The intermediate and minor principal strain ϵ_3 was calculated as:

$$\epsilon_3 = (\epsilon_v - \epsilon_1)/2 \quad 7.4$$

All the above calculations were programmed on the Texas SR56 pocket calculator.

7.4.7 Results of the triaxial tests

The results of the triaxial tests performed under various cell pressures are shown in table (7.4). The table shows the major principal

Test No.	σ_{octi} (kN/m ²)	σ_{1f}	$R = \frac{\sigma_{1f}}{\sigma_{octi}}$	Porosity $\eta, (\%)$	$A = \frac{\epsilon_{vh}}{3\epsilon_{1h}}$
1	14.03	48.61	3.46	42.60	1.10
2	9.58	37.75	3.94	41.89	1.13
3	5.19	25.05	4.83	42.35	1.10
4	3.36	15.90	4.73	42.90	1.15

TABLE 7.4 TRIAXIAL TEST RESULTS

stress at failure σ_{1f} , stress ratio R at failure and the initial porosity η . The anisotropy ratio A in the table is given by:

$$A = \frac{\epsilon_{vh}}{3\epsilon_{1h}} \quad 7.5$$

where ϵ_{vh} and ϵ_{1h} are the volumetric and the axial strains respectively under hydrostatic conditions. For an isotropic material under true hydrostatic conditions the volumetric strain is equal to three times the axial strain so that the value of A is unity. The observed values of A being greater than 1, indicate that the sand was layered having less strain in the axial than in the lateral direction.

The deviatoric stress ($\sigma_1 - \sigma_3$) and the volumetric strain ϵ_v are plotted against the major principal strain ϵ_1 in figure (7.13). The decrease in volume at low stresses is characteristic of a fairly loose sand. The effect of increasing cell pressure in reducing the volumetric strain is noticed in figure (7.13b). Mohr's circles for the principal stresses at failure and Coulomb's failure envelope are shown in figure (7.14). The values of the apparent angle of internal friction ϕ' and the apparent cohesion c'

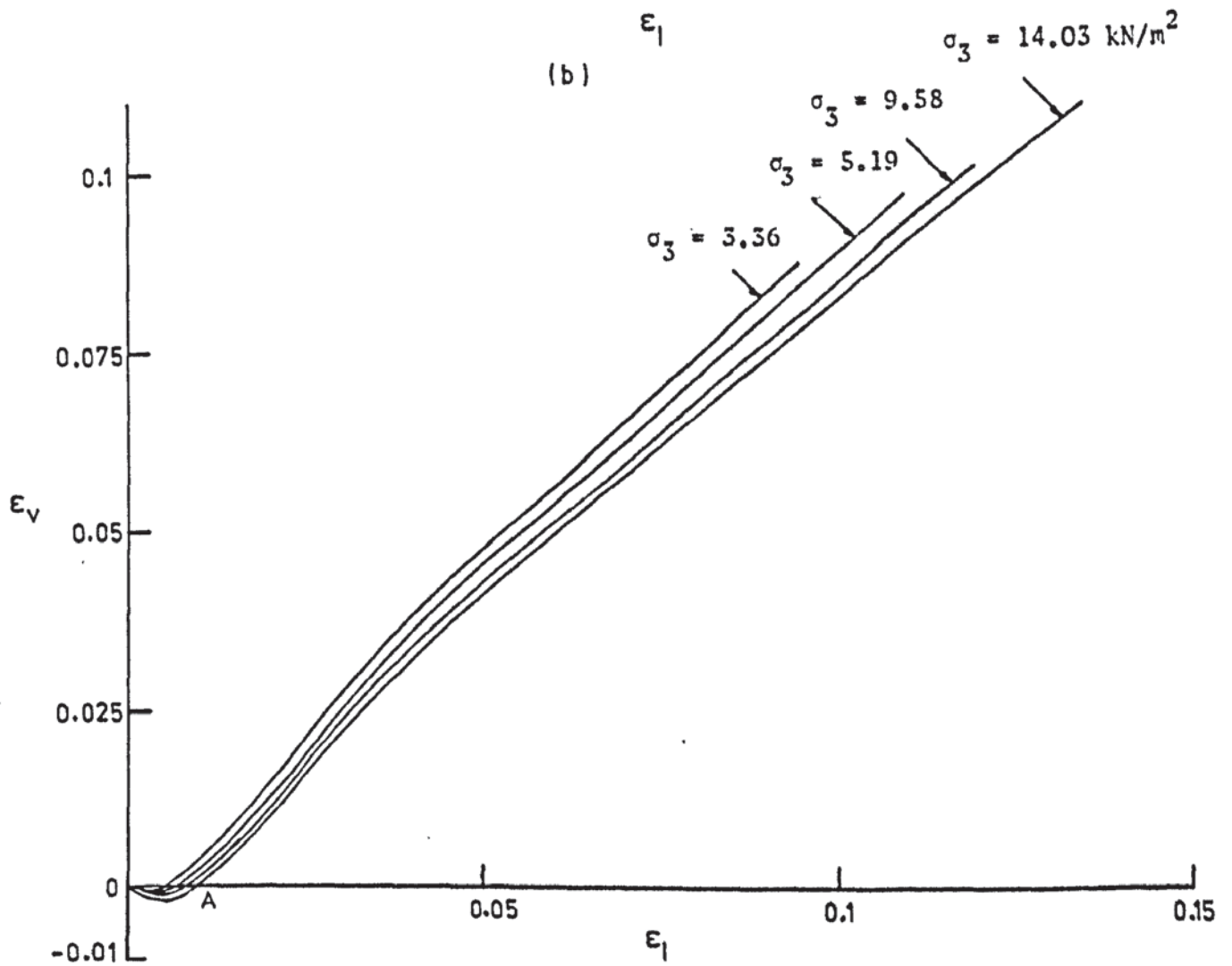
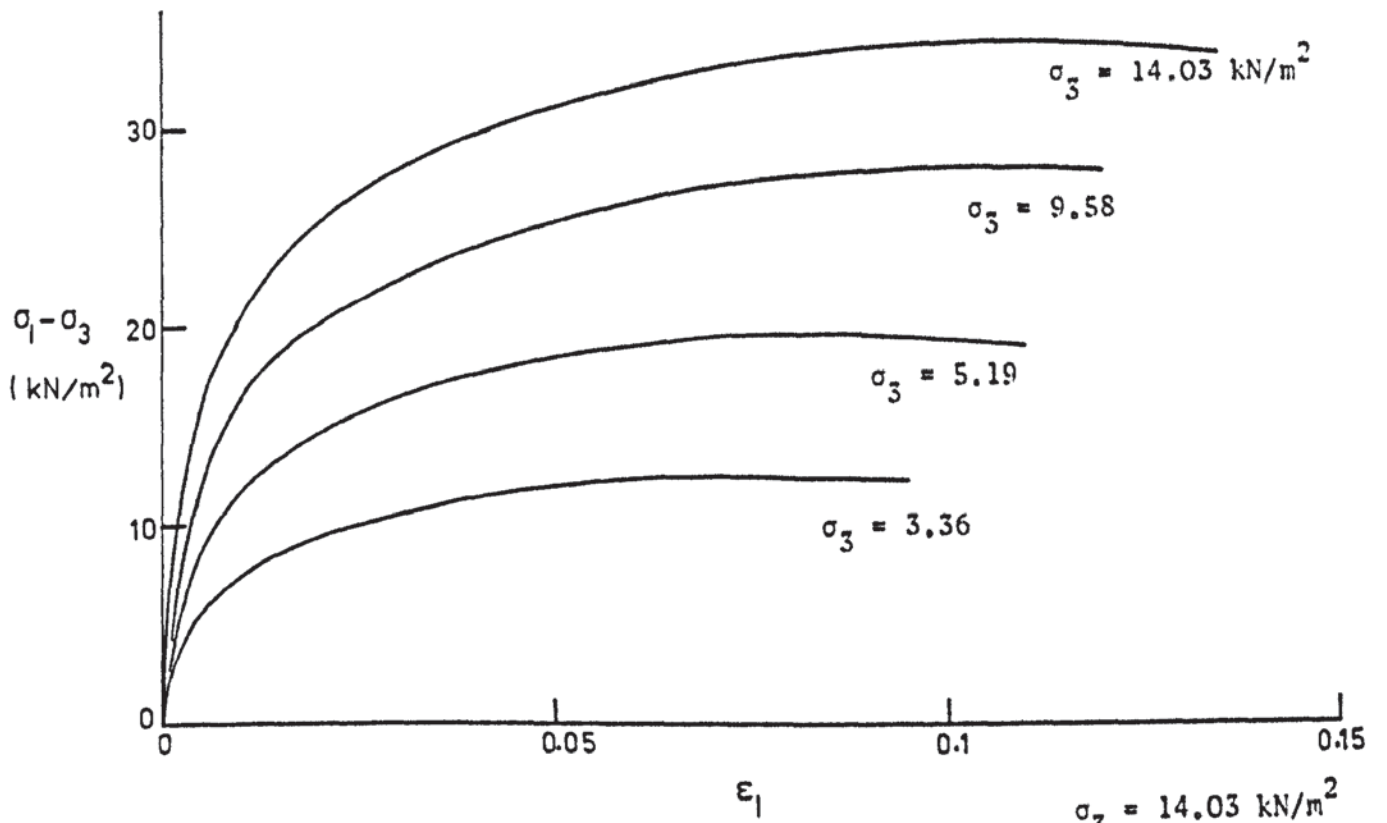


FIGURE 7.13 TRIAXIAL TEST RESULTS

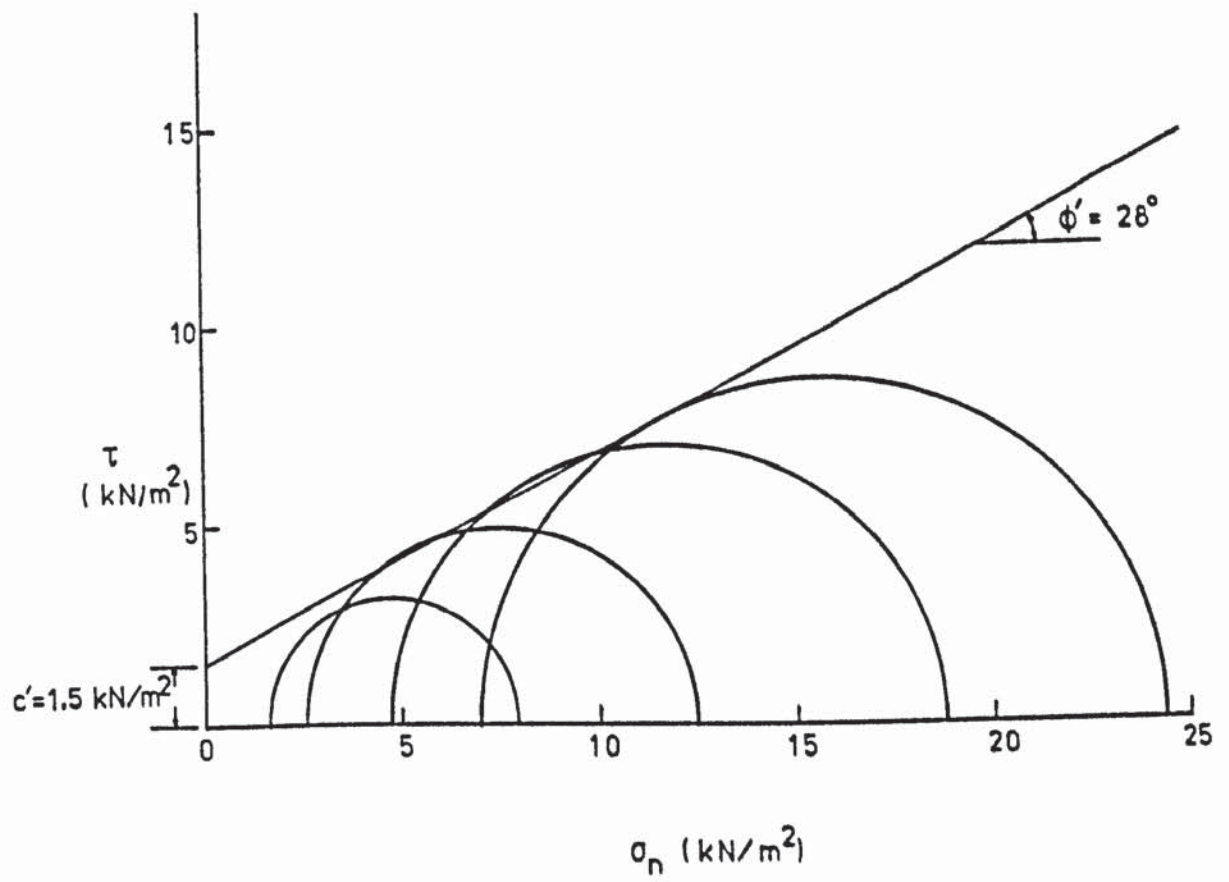


FIGURE 7.14 MOHR'S CIRCLES AND FAILURE ENVELOPE OF THE SAND

were obtained as 28° and 1.5 kN/m^2 respectively. The results of the tests agree well with those obtained by Ponce and Bell (1971).

7.4.8 Calculation of Poisson's ratio

The value of Poisson's ratio, ν , for sand can be calculated from the measurements of volumetric strains in the triaxial tests. Assuming isotropy and elasticity at a particular level of stress and taking the elastic modulus, E , as the tangent slope of the stress-strain curve at that point, the generalized Hooke's law can be applied to the triaxial test parameters. In terms of principal stresses, Hooke's law may be written as

$$\epsilon_1 = \frac{1}{E}(\sigma_1 - 2\nu\sigma_3) \quad 7.6$$

$$\epsilon_3 = \frac{1}{E}(\sigma_3 - \nu\sigma_1 - \nu\sigma_3) \quad 7.7$$

From equations (7.6) and (7.7), the volumetric strain is given by:

$$\epsilon_v = \epsilon_1 + 2\epsilon_3 = \frac{1}{E}(\sigma_1 - 2\nu\sigma_1 + 2\sigma_3 - 4\nu\sigma_3) \quad 7.8$$

Replacing Young's modulus E by $2G(1+\nu)$, where G is the shear modulus, and factorizing equation (7.8),

$$\epsilon_v = \frac{1-2\nu}{2(1+\nu)G}(\sigma_1 + 2\sigma_3)$$

$$\text{or } \frac{1-2\nu}{1+\nu} = \frac{2\epsilon_v G}{\sigma_1 + 2\sigma_3} \quad 7.9$$

Solving equation (7.9) for ν ,

$$\nu = \frac{\sigma_1 + 2\sigma_3 - 2\epsilon_v G}{2(\sigma_1 + 2\sigma_3 + G \epsilon_v)} \quad 7.10$$

It is clear from this derivation that ν is a function of the stress level. Taking the values of G from the spline function representation of the $\tau_{oct} - \gamma_{oct}$ curves, the values of ν for various γ_{oct} are obtained from equation (7.10). These values for the tests with various σ_{octi} are shown in table (7.5). As the sand undergoes volume contractions at low values of γ_{oct} , Poisson's

γ_{oct}	Values of ν			
	$\sigma_{octi} = 3.36 \text{ kN/m}^2$	$\sigma_{octi} = 5.19 \text{ kN/m}^2$	$\sigma_{octi} = 9.58 \text{ kN/m}^2$	$\sigma_{octi} = 14.03 \text{ kN/m}^2$
0	0.5	0.5	0.5	0.5
0.005	0.501	0.516	0.515	0.526
0.01	0.481	0.484	0.501	0.510
0.015	0.441	0.449	0.461	0.469
0.02	0.431	0.437	0.441	0.451

TABLE 7.5 VALUES OF POISSON'S RATIO

ratio becomes greater than 0.5. While it is possible to include a variable ν in the finite element analysis, there is evidence that this does not influence the final results of the analysis to a significant degree, Girija Vallabhan and Jain (1972). Besides, as the value of ν approaches 0.5 numerical difficulties are encountered. It was therefore decided to use a constant value of $\nu = 0.45$ for all the stresses.

7.5 THE TEST RIG

Two basic elements of the test rig were the sand bed and the loading frame. The rig was similar to that designed and used by

Cunnell (1974). However, several modifications were made to the design and the whole rig was reconstructed. The sand was contained in a rigid concrete tank instead of a perspex one as used by Cunnell. This was done to avoid any bulging out of the tank as it was filled with sand or when the structures were loaded. Such deformation of the tank was harmful as a rigid boundary of the soil was assumed in the analysis. Furthermore, Cunnell observed a settlement of the sand bed due to the disturbance caused by traffic and vibrating machinery. This was prevented in the present rig by constructing it in an underground laboratory away from such disturbances. The concrete tank and the reaction frame surrounding it are shown in figure (7.15). The components of the rig are described in the following sections.

7.5.1 Sand bed and deposition apparatus

The most important single factor for a satisfactory sand bed is the creation and the repeated reproduction of a known uniform porosity. It was therefore necessary to use a suitable apparatus and a standard procedure to form the bed.

The rectangular reinforced concrete tank used to contain the sand bed had dimensions 2.1 x 1.2 x 1.2 m as shown in figure (7.15). The 150 mm thick walls and the 100 mm thick base of the tank were precast in separate units and joined together by bolts. The tank was elevated 460 mm from the floor to facilitate emptying of the tank through a hole (A) in the base, as shown in figure (7.15). The 75 mm hole was situated at a corner and could be opened and shut by operating a lever attached to a sliding cover plate.

The sand was deposited in the test tank by a travelling hopper sand rain device. As the hopper was moved across the tank a rain

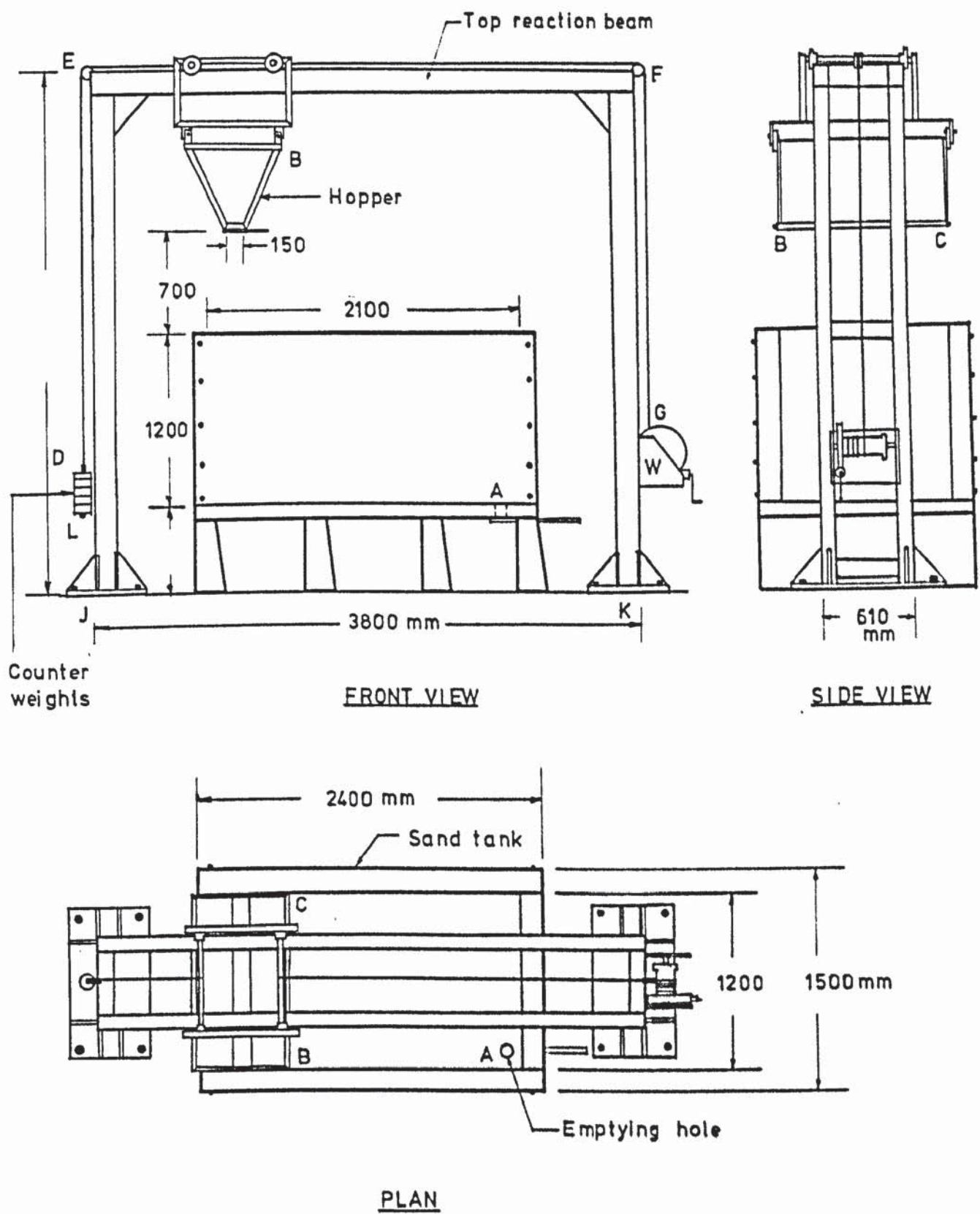


FIGURE 7.15 THE TEST RIG

of sand poured from it and gradually filled the tank. The wedge shaped hopper was attached to a steel framed trolley travelling on the top beams of the reaction frame. The length BC of the hopper was the same as the inside width of the tank and its capacity was 0.28 m^3 . It had two perforated plates at the base, one of which could be slid against the other by operating two levers at the ends of the hopper. This produced a variation in the size of the opening of the perforations which varied from 0 to 11 mm. The trolley had two axles and four wheels travelling on and guided by the top beam. A long piece of stranded steel wire DEFG was attached at the centre of each axle which ran along the top beam of the rig and passed over the pulleys at E and F attached at an angle at the ends of the beam. The end G of one rope was attached to and wound over the drum of the worm geared winder W. This had a very low worm gear ratio of 19:1 and needed only a moderate effort to move the hopper assembly. Manual winding was adopted as a suitable motor and gearbox could not be obtained. After some practice a constant speed of the trolley of about 30 mm per second at an angular speed of worm of 1.5 revolutions per second was achieved and maintained. A counterweight L was attached to the rope at the other end of the trolley. This reduced the jerks of the hopper as it moved over the top beam EF. The counterweight was sufficiently heavy to ensure a reverse travel of the empty hopper after a pure as the worm gear was unwound.

7.5.2 The reaction frame

The reaction frame JEFK, see figure (7.15) and plate (7.1), was constructed of 150 x 100 x 6.25 mm steel box sections, formed

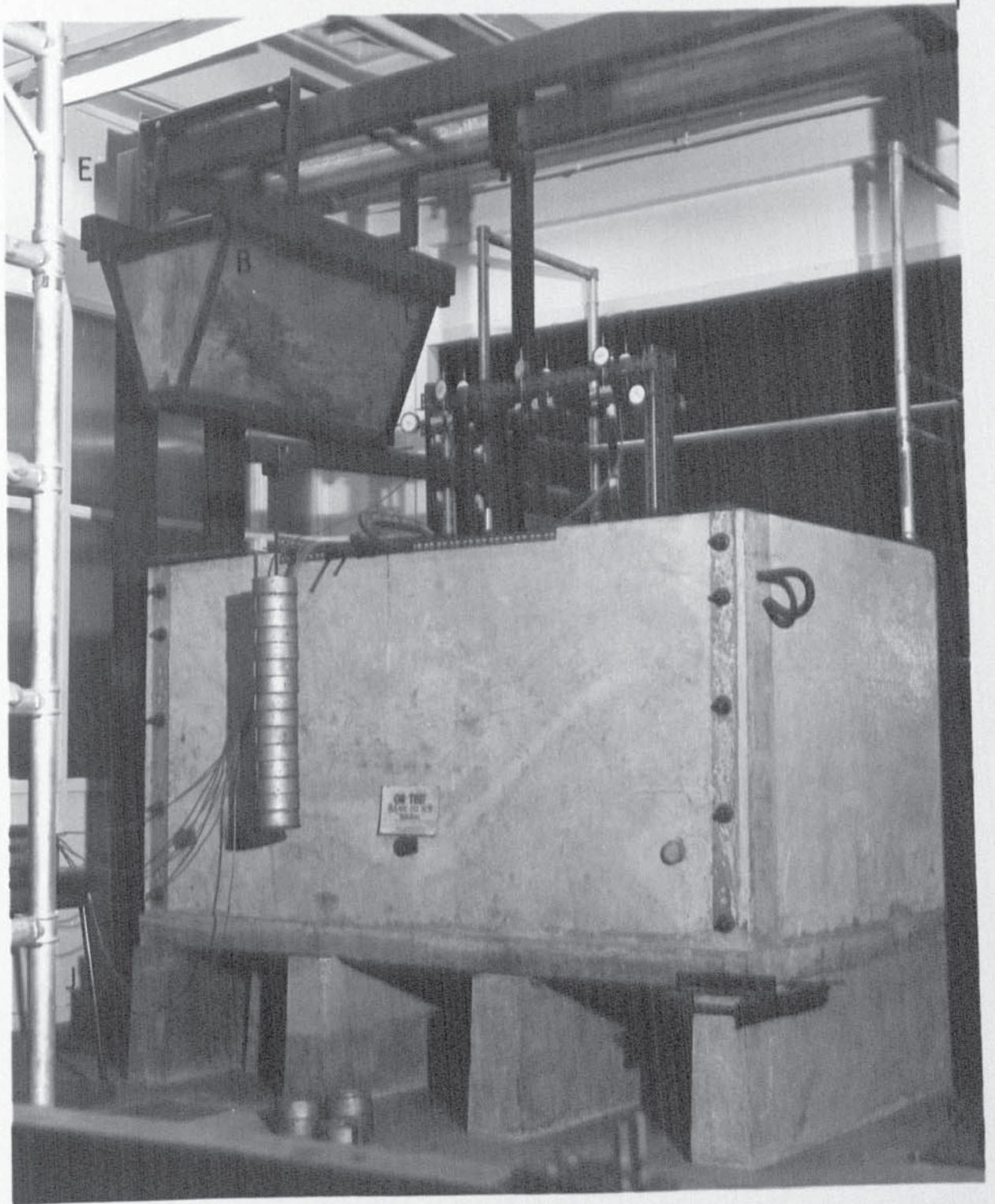


PLATE 7.1 THE RIG WITH A TEST OF SERIES A IN PROGRESS

into two parallel right-angled rigid frames, laterally interconnected by pieces of the same section. As mentioned earlier it also served as a support for the travelling hopper trolley. For this reason the frame had to surround the sand tank and be high enough to ensure that the decreasing height of fall of sand rain with the filling of the tank had little effect on the uniformity of porosity in the bed. The columns of the frame were welded and screwed by gussets to two 535 mm x 1070 mm x 25 mm thick steel plates which were in turn secured to the floor by four 16 mm Rawl bolts on each side. A general view of the rig with a test of series A in progress is shown in plate (7.1).

7.5.3 Standardization of the sand deposition method

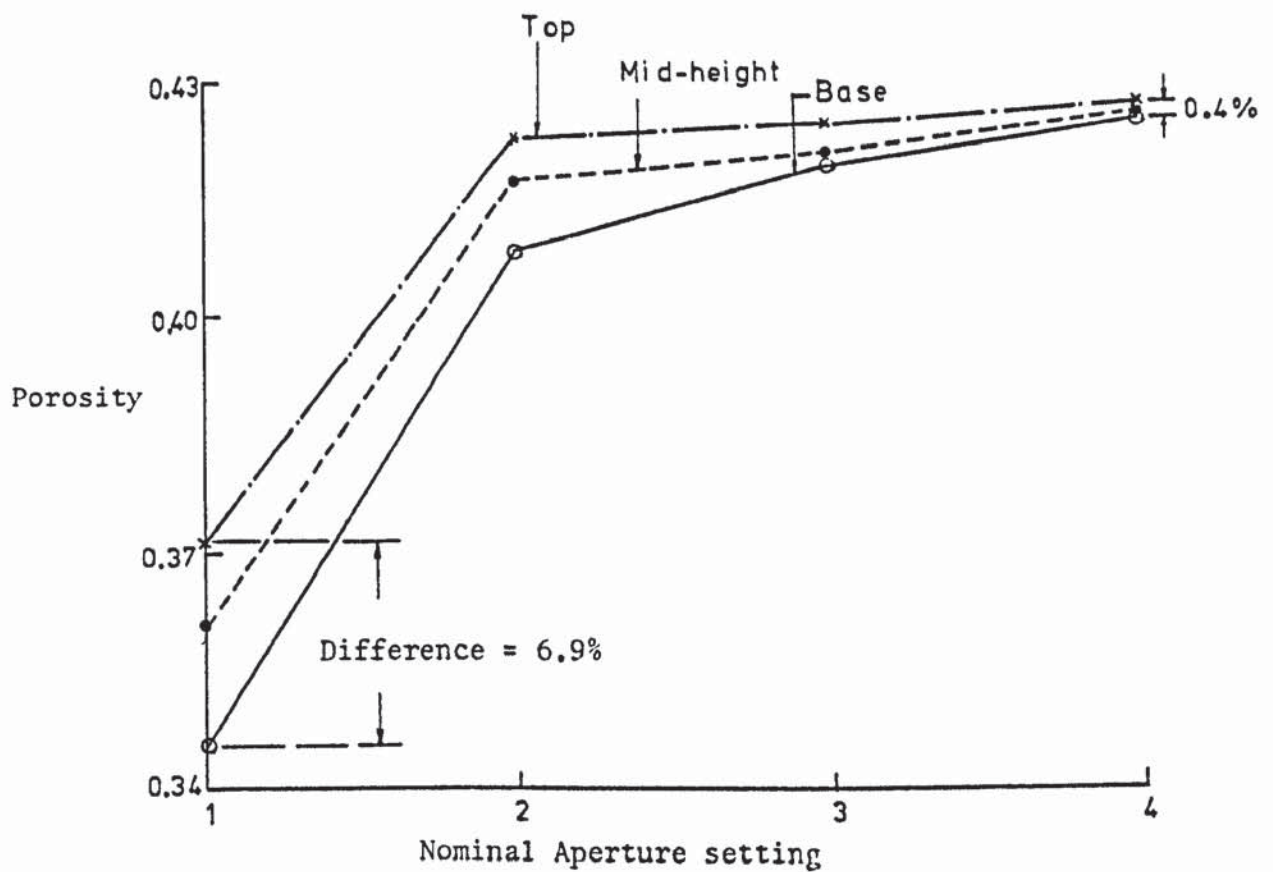
The sand deposition apparatus was calibrated by checking and controlling the porosity of the sand bed and a standard method of pouring was adopted. The apertures at the bottom of the pouring hopper could be varied in size by operating the lever which had four stops, 1 through to 4, giving an increasing size of opening. The height of fall varied, as the tank was filled, between 1.9m at the bottom and 0.7 m at the top of the tank. To calibrate the apparatus, trial runs of the hopper were made at various aperture settings. The porosity was measured by placing density tins of a known volume under the sand rain and weighing the sand collected in them. These tins were brass cylinders 50 mm in diameter and 38 mm high with a perforated base covered by a fine wire gauze to help the trapped air to displace. Seven tins were placed in a cluster at the centre of the bottom of the tank and a run of the hopper with each aperture setting was made. Each

time the speed of the hopper was kept fixed by revolving the hand winch at 1.5 revs per second. The sequence was repeated with the tins placed at mid-height and at the top level of the sand tank. The values of the porosities obtained are shown against the aperture settings for various heights of the tins in figure (7.16a). It is observed that the height of fall has some effect on the porosity, specially so at narrower aperture settings. But this was considered as acceptable because the variation reduced from 6.9% at aperture setting 1 to only 0.4% at aperture setting 4. The very low porosity at aperture setting 1 may be attributed to the fact that the tins could not be filled by one run of the hopper and a second layer of sand over the first was necessary. It was decided to use the aperture setting 4 and a constant speed of revolution of 1.5 r.p.s. for all the tests.

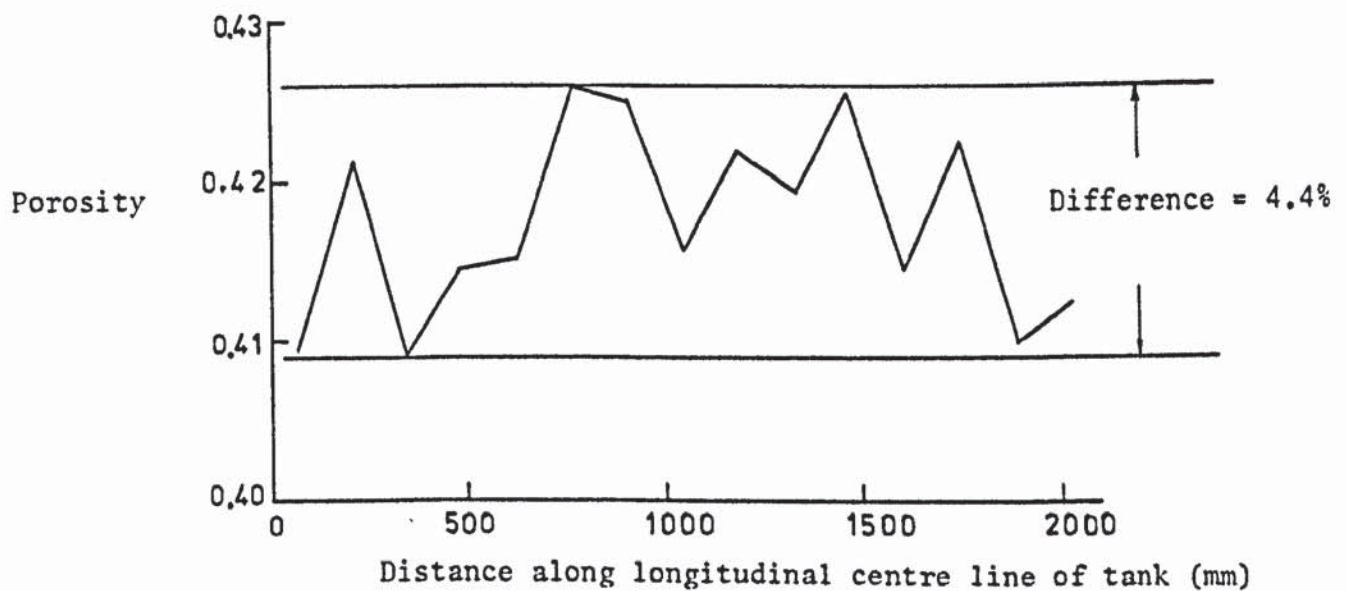
Next, the variation of porosity along the longitudinal direction of the tank due to a decreasing level of sand in the hopper was checked for aperture position 4. Fifteen density tins were placed equidistant from each other on the base of the tank along its longitudinal centreline. The resulting porosities are shown in figure (7.16b). It can be seen in this figure that no more than a random variation occurs and no distinct effect of decreasing level of sand in the hopper is detected. The maximum variation of porosity was 4.4%.

7.6 THE LOADING SYSTEMS

Because of the variable geometry of the different models tested a single loading system could not be used for all the tests. A lever arm and dead weight arrangement was used for the



(a) Variation of porosity with aperture size



(b) Variation of porosity along longitudinal direction at aperture setting 4.

FIGURE 7.16 CALIBRATION OF SAND DEPOSITION APPARATUS

tests in series A, C and D, while a hydraulic jack had to be resorted to for applying loads on the partly buried box culvert model of test series B.

7.6.1 Loading device for test series A, C and D

The dead weight system for the models of series A, C and D consisted basically of a horizontal lever beam AB and a vertical reaction shaft CD, as shown in figure (7.17). The reaction shaft was clamped to a top beam T of the rig by means of a heavy clamping block K. The shaft could be raised or lowered by drilling extra holes at appropriate locations to match the height of the structure being tested. Fine adjustments of the height could be achieved by operating the vertical bolts at G and H in the clamp. The shaft was made from 75 x 50 x 3 mm steel box sections, equipped at the lower end C by a steel piece machined to a knife edge.

The horizontal lever beam AB was also made from the same box section. A steel piece was pushed in at the end B of the beam and a 90° V-notch, R, was machined on it. This formed the seat for the knife edge of the shaft. The apex of the notch was made to lie on the longitudinal centroidal axis PQR of the beam. Two circular holes were drilled through the box section, at points P and Q in figure (7.17a and c). These were countersunk to a sharp edge and aligned in such a manner that the longitudinal centre line of the beam was tangential to the top of the hole at Q and to the bottom of that at P. This ensured that all the contact points lay on the centre line of the lever AB, as shown in figure (7.17c). The distance PQ was made three times the distance QR to obtain a lever ratio of 1:4. The load was applied by placing weights on a pan

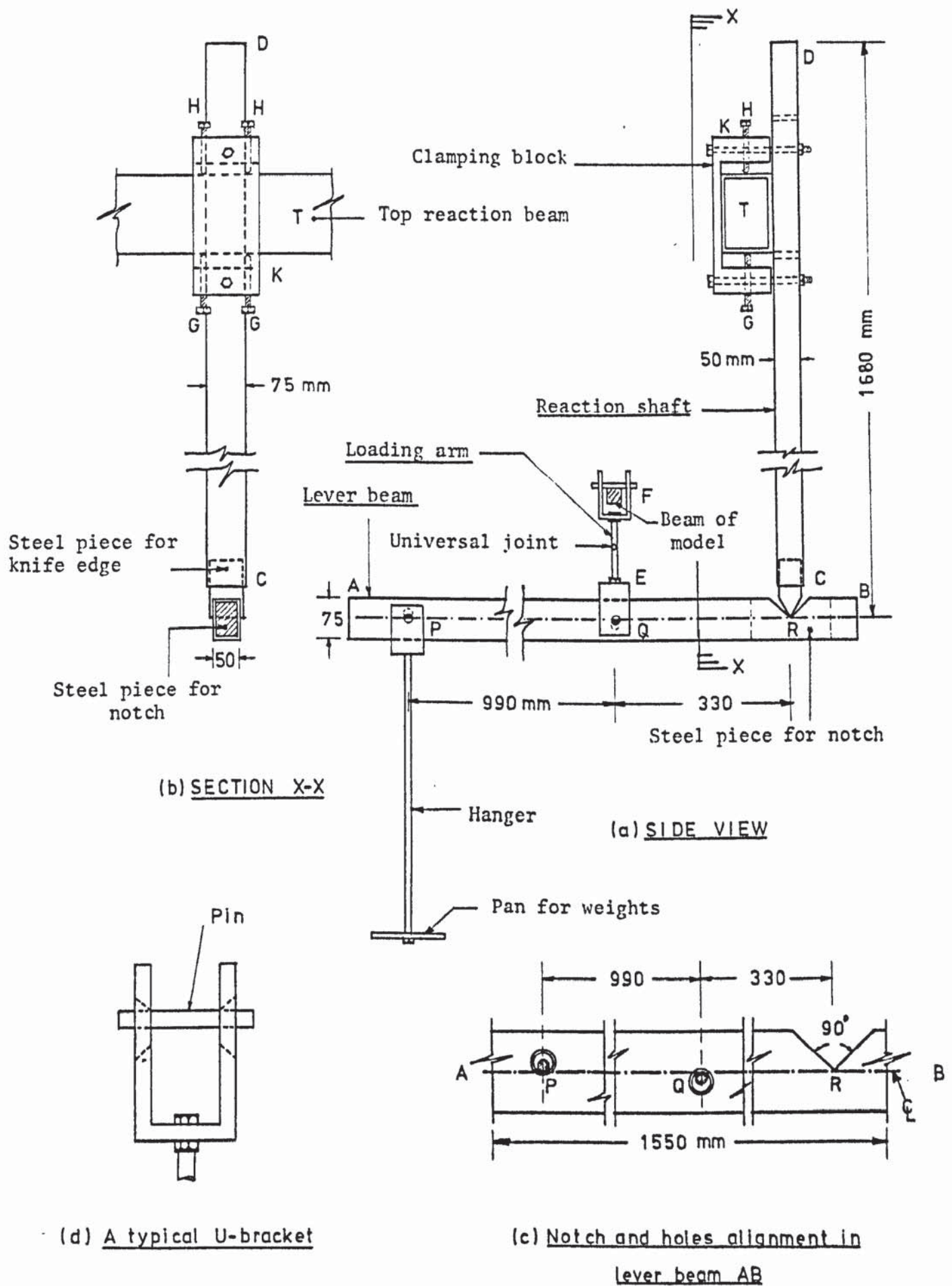


FIGURE 7.17 DEAD WEIGHT LOADING SYSTEM

attached to a hanger supported by a U-bracket and pin at P on the lever beam.

The load was transmitted to the model structure by means of a loading arm EF in figure (7.17a). For the models of series A and D, the loading arm consisted of two U-brackets, of the type shown in figure (7.17d), connected by a link with a universal joint. A pin was passed through the holes in the upper U-bracket and over the central beam of the models. The lower U-bracket was connected to the lever beam AB by a pin passing through the hole at Q. A different loading arm was used for the models in series C, as in this case the load was to be applied on a plate. The arrangement is shown in figure (7.18) and plate (7.2). It consisted of two 32 mm diameter steel rollers L and M connected by two steel plate slings. Each roller had two 25 mm grooves G and H shown in figure (7.18) cut at 450 mm on centres. The top roller M had two 50 mm collars J and K, in the same figure, fitted on it equidistant from the grooves G and H. The bottom roller L had a third groove N cut at the centre and a sharp edged ring was passed around it. The ring S, in figure (7.18), was connected by a link TY and a U-bracket to the lever beam AB at the point Q.

All the holes in various parts of the loading system were countersunk to a sharp edge and made at least 50% larger in diameter than the pins or rollers passing through them. This reduced the friction at the contact points.

7.6.2 Loading device for test series B

For the reason that the box culvert model of series B was buried in the sand bed, a dead loading arrangement, with a lever

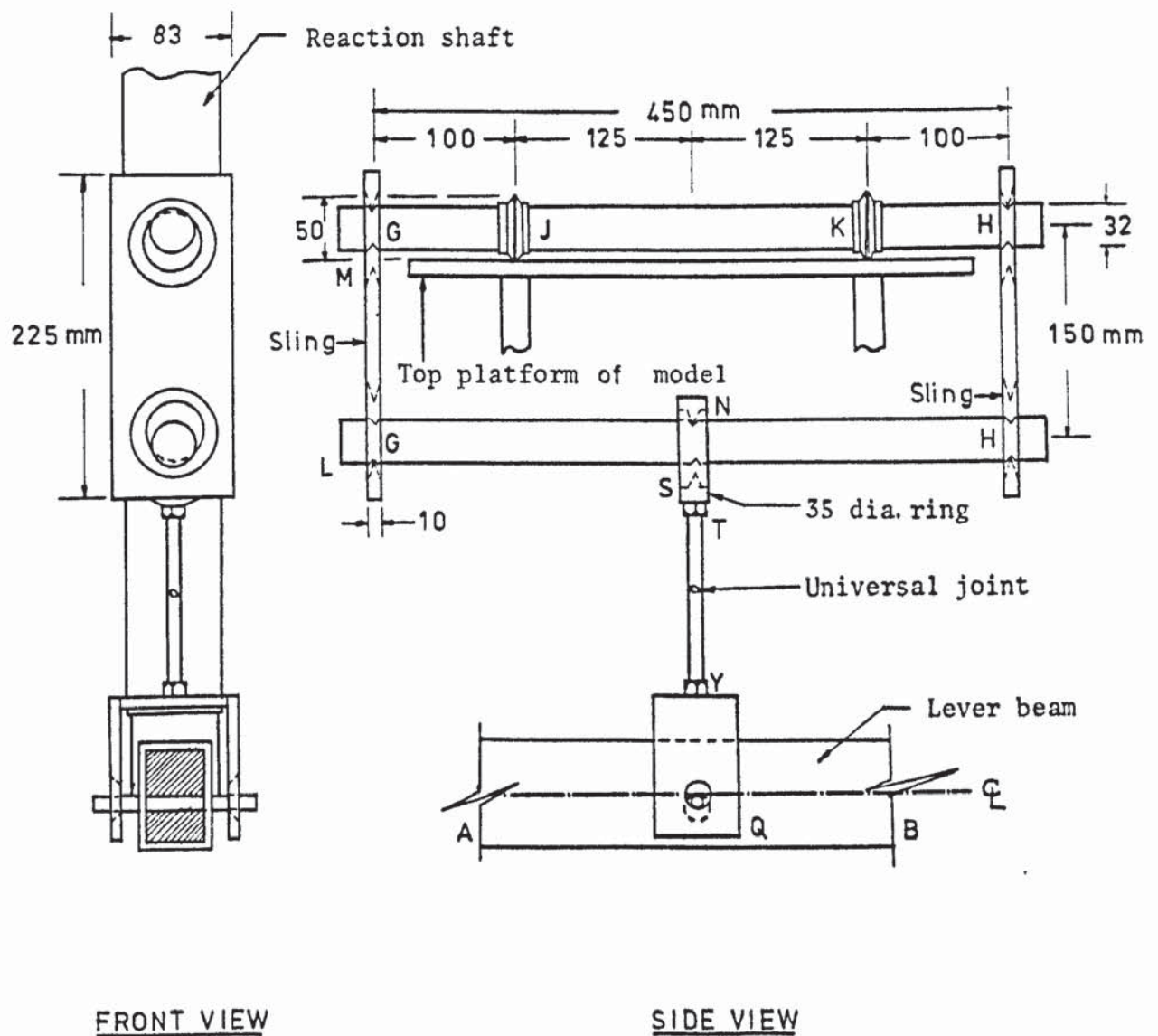


FIGURE 7.18 LOADING ARM FOR TEST SERIES C

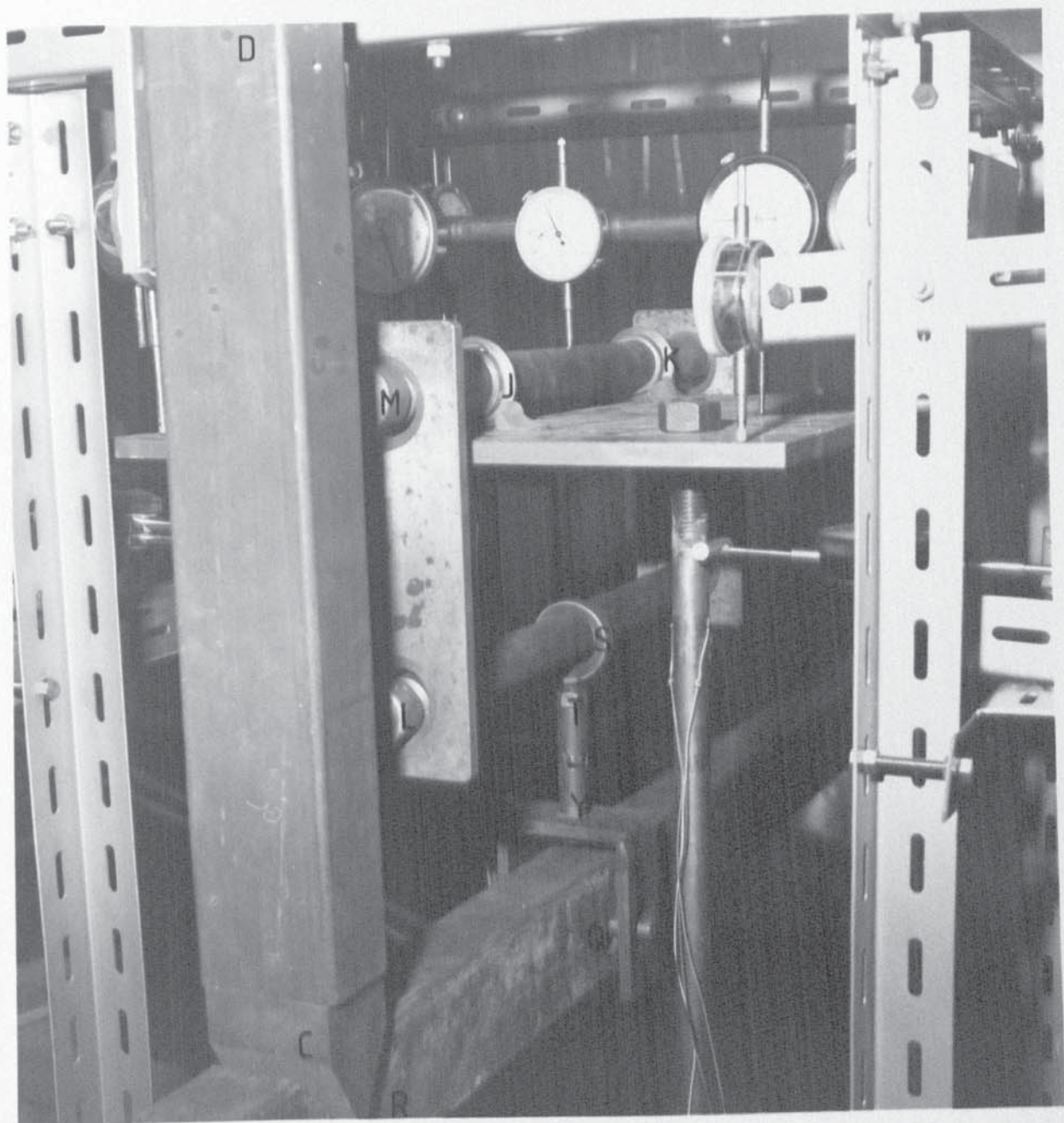


PLATE 7.2 LOADING DEVICE FOR TALL STRUCTURE MODEL

beam passing through the model, was not practicable. A hydraulic jack system was therefore adopted. The arrangement used is shown in figure (7.19). Each end of the reaction beam AB in the figure was connected by a sliding clamp C to the flange of a channel section D. The channel D was pressed firmly against the columns of the test rig by using a second channel E and tightening the bolt at F. Thus the reaction was transmitted to the rig by friction only. The system was designed so that the point of application of the load could be moved freely from one point to another. The hydraulic jack was fitted with a proving ring R of 1 tonne capacity. The jack was operated by a hand pump situated remote from the assembly. The load was transmitted to the top deck of the culvert by a 20 mm diameter hemispherical point Q. The proving ring R was calibrated using a universal testing machine and was found to have a sensitivity of 5.8 N per division. The hydraulic jack was found to have one drawback in that the load reading fell off slightly as the structure settled in the sand. To alleviate this, the hand pump was continuously operated and a constant reading on the proving ring dial was maintained.

7.7 EXPERIMENTAL PROCEDURE

The experimental procedure was similar for all the tests performed, except for some details. The procedure is described in general terms in the following sub-sections pointing out any special operation for a particular structure.

7.7.1 Preparation of the sand bed

Some sand was placed in the empty tank and banked at the ends to minimize a heap at the centre as the bed was filled.

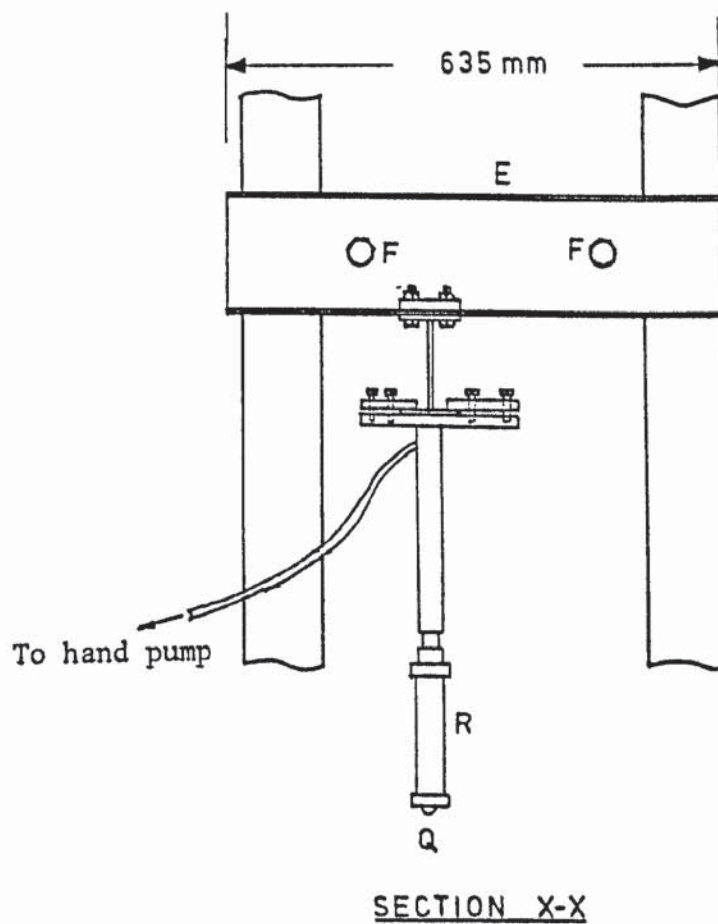
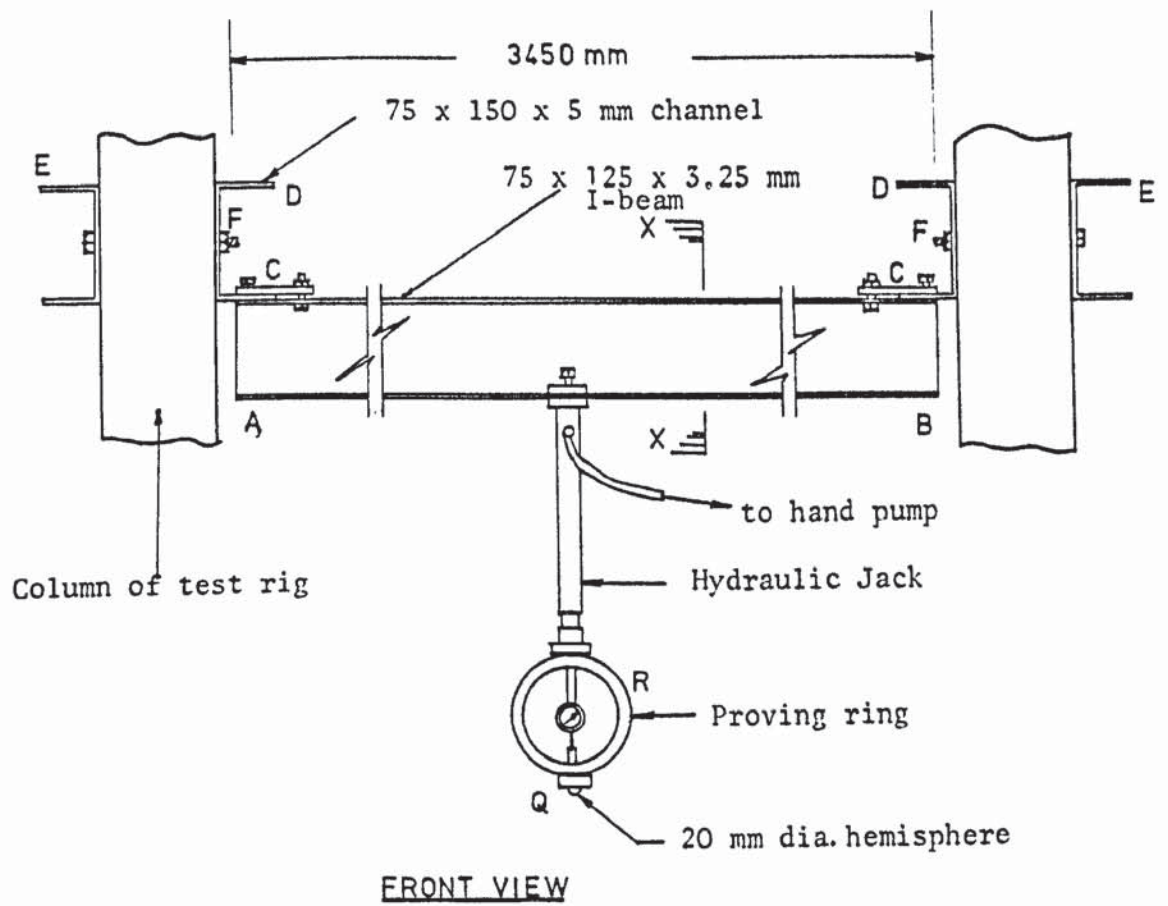


FIGURE 7.19 LOADING ARRANGEMENT FOR BOX CULVERT

Sand was collected in small tins from the storage containers and placed on the platform of a fork lift truck. The truck was driven to the rig, the platform raised and the tins emptied into the hopper at the top of the rig. The operation was repeated until the hopper was full. The hopper was then moved across the length of the bed by operating the hand winch at ground level. The aperture was set at position 4 and the speed was maintained at 1.5 revolutions per second. At this speed and aperture size the hopper was empty at the end of the run. The hand winch was then wound in the reverse direction and the hopper travelled back to the starting location.

The hopper was filled again and the operation of pouring was repeated until sand was deposited to the required level in the tank. For the tests in series A, C and D, where the model structure rested on the surface of the sand, the surface was screeded level and the model, complete with the strain gauges and wiring, was placed centrally on the sand bed with the help of a fork lift truck and aided by plumb bobs.

For the box culvert tests in series B, the pouring was continued until the required level of the base of the model was reached and the surface was screeded level. The model was then placed centrally on the sand surface with the strain gauge connection cables tucked neatly on it. A wooden trough was rested on the sand tank directly over the box culvert. Two sheets of polythene AB and CD were hung over its sides to form a curtain around the culvert, as shown in figure (7.20a). A barrier EFGH made of two pieces of hard board and latex rubber sheets, figure (7.20c), was placed at each corner of the box culvert to form

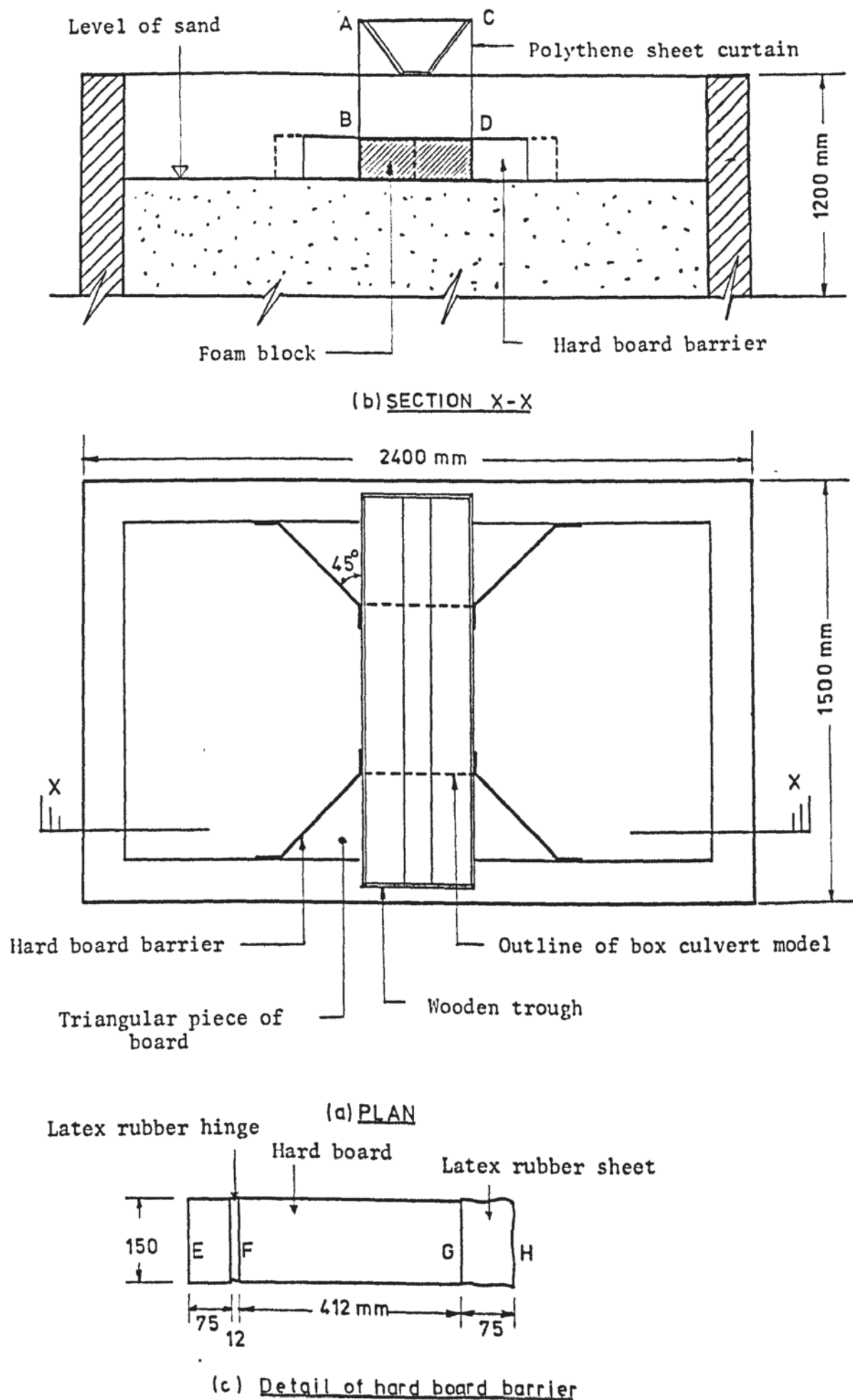


FIGURE 7.20 ARRANGEMENT FOR BURYING THE CULVERT IN SAND

the shape of wing walls. A light weight rectangular block of foam was placed on each open end of the culvert. A triangular piece of hard board was then placed in each of the triangular spaces between the foam block and the wing. This arrangement prevented sand from depositing above or in front of the culvert openings. A few more passes of the hopper were made in the usual way until the sand level had reached the top level of the culvert. The sand surface on both sides of the culvert was screeded level. The trough with the polythene curtains was then removed carefully. The sand deposited in the triangular spaces between the wings and foam blocks was then cleared by vacuum pump, taking care not to disturb the culvert and the main body of sand in any way. The foam blocks and the triangular pieces of board guarding the previous surface of sand were carefully removed. The culvert was now partially buried in sand in the manner shown in figure (7.3). The hard board barriers forming the wings had to be kept in place to prevent sand from falling off. The low stiffness of the latex rubber holding the barrier was not enough to resist any lateral deformation of the sand thus supported. For every filling of the tank several density tins were placed at different heights in the tank to check the porosity after the test had been completed.

7.7.2 The test procedure

After a model has been placed for test on a freshly filled bed of sand a frame of light angle sections was built around it to hold the dial gauges. The frame was supported by the walls of the sand tank and the top beams of the rig. The dial gauges were checked and fitted to the frame at the required positions.

The wires leading from the strain gauges were connected to the strain indicator extension box. A data logger was not available in the testing laboratory and manual strain readings had to be taken. The strain indicator used was a Peekel rechargeable battery operated model. Initial readings of the dial gauges and strain gauges were obtained and recorded in a tabular form.

The loading system was then placed over the model structure, the loading point being carefully located at the desired position. Plasticene was used to aid the location of the point. Extreme care was taken to ensure that the reaction shaft and the loading arm were both absolutely vertical, checking them with a spirit level. With the hydraulic jack loading system it was made sure that the reaction beam was level and the jack itself vertical. A set of dial and strain gauge readings were taken with the weight of the dead loading system only acting on the model.

With both systems of loading the basic approach to the test was to obtain displacement and strain readings at slowly applied increments of load until an appreciable amount of settlement had occurred. Care was taken to ensure that no part of the structure yielded or buckled rendering it useless for further tests. This was necessary also because the post-yield behaviour of the structural material was not included in the analysis. Approximately 18 to 20 increments of the load were applied for most of the tests. A time lapse of about 20-25 minutes was allowed between the application of a load and the recording of the readings to ensure that all movements due to this load had stopped. The interlocking and the reorganization of the sand grains in the test beds caused this delay in the displacements.

A test of series B and one of series C in progress are shown in plates (7.3) and (7.4) respectively.

At the conclusion of a test the structure was gradually unloaded and the loading system dismantled. The strain indicator was disconnected, the dial gauge frame removed and the model structure recovered from the sand bed. The tank was then emptied by opening the hole in the base and collecting the sand in small tins. It was necessary to shovel the sand in the tank towards the hole from time to time. Each complete sequence of filling, testing, dismantling and emptying took approximately six man-days of laboratory work.

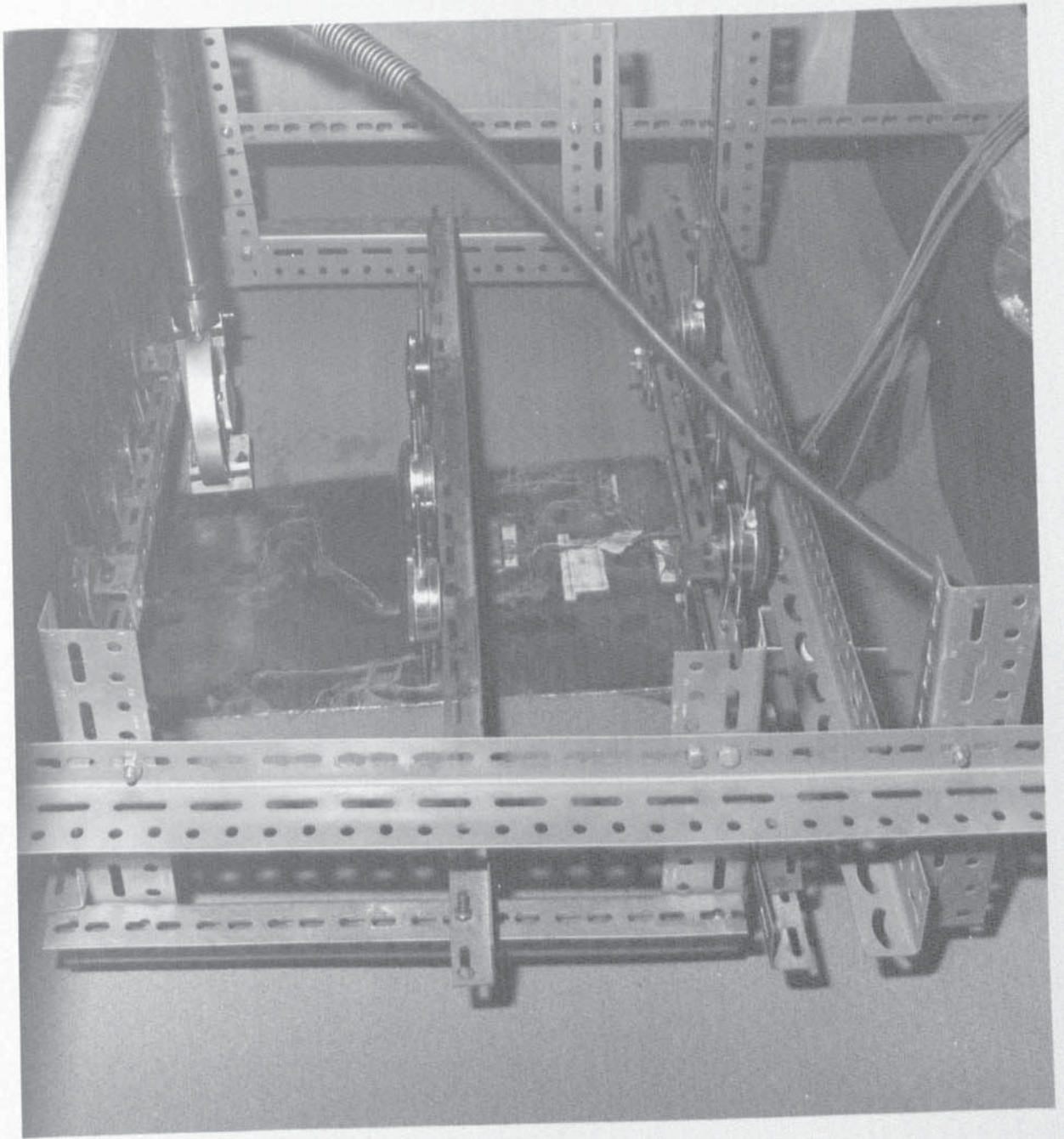


PLATE 7.3 A TEST ON THE BOX CULVERT MODEL OF SERIES B IN PROGRESS

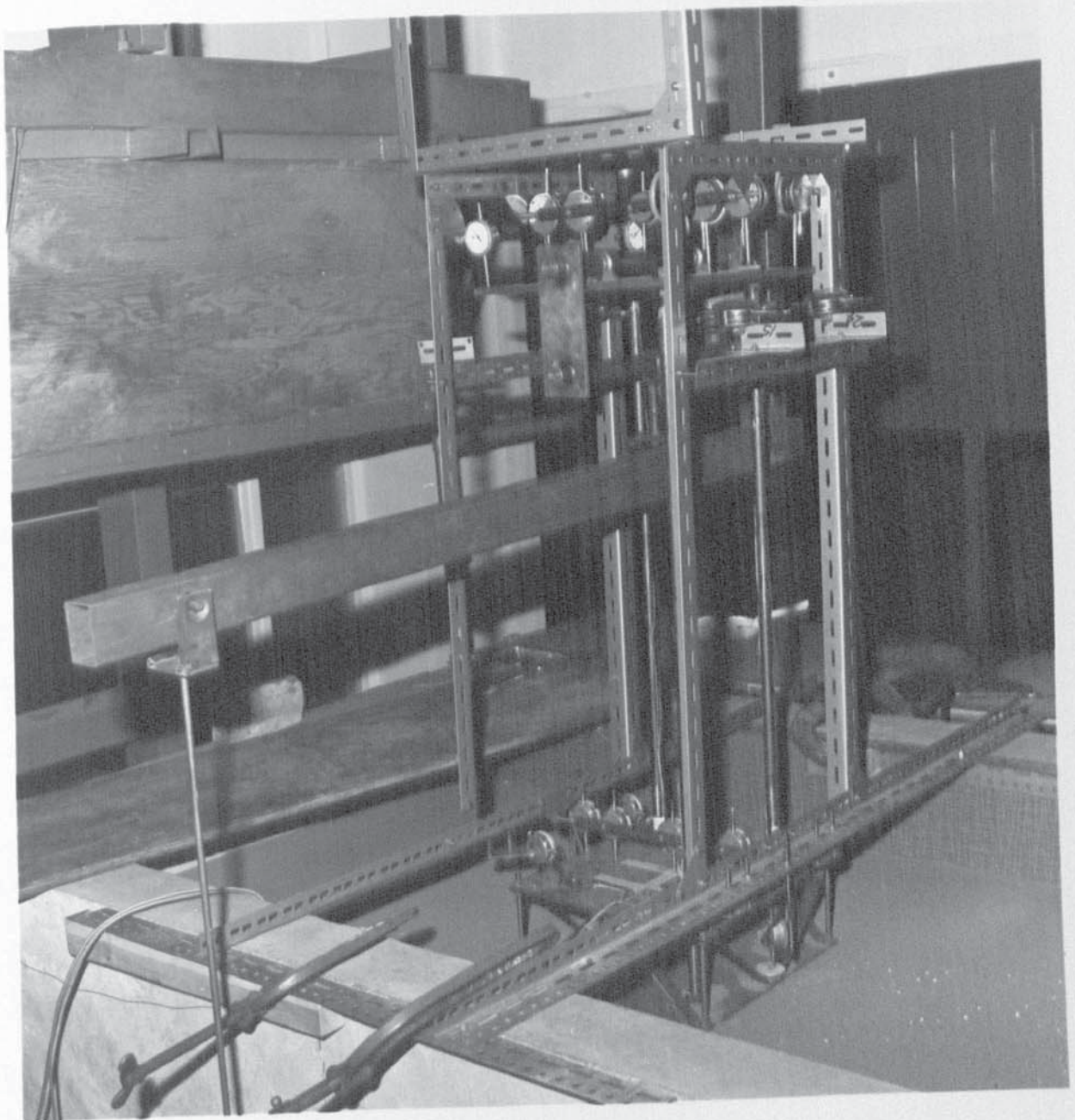


PLATE 7.4 A TEST ON THE TALL STRUCTURE MODEL OF SERIES C IN PROGRESS

CHAPTER 8

COMPARISON OF EXPERIMENTAL AND THEORETICAL RESULTS

8.1 INTRODUCTION

In this chapter the experimental results of the model structures described in chapter 7 are discussed and compared with the theoretical ones. This is done for the settlements of the foundations and the deflections and bending moments in the structure, for which experimental readings were obtained. The stresses in the soil obtained by analysing the complete system are also presented. The notations used to describe the models are the same as those of chapter 7.

8.2 FINITE ELEMENT ANALYSIS OF THE MODELS

The sand supporting the model structures was reproduced with the same density for each test. The properties of the sand were determined by triaxial tests and represented by the set of $\tau_{oct}-\gamma_{oct}$ curves shown in figure (2.2). The spline function representation of these curves given in chapter 2 were followed in the analysis by the incremental method described in chapter 3.

Each $\tau_{oct}-\gamma_{oct}$ curve of the set in figure (2.2) corresponds to a particular value of the initial octahedral normal stress σ_{octi} . These stresses are caused by the action of the body forces before the structure is loaded. The sand in the test tank was divided into a number of solid finite elements, each of which had a different value of σ_{octi} depending on its location. To determine these σ_{octi} for each finite element, the soil was analysed on its own, subject only to the body forces applied at the joints. The resulting value of σ_{octi} at the centroid of each element was stored in a disc

file to be read as data by the main analysis program. The normal stresses at the joints were also calculated and stored to give the tensile strengths required by the crack propagation analysis.

The finite element meshes used for the various model structures are described below. In each case the joints on the boundary of the tank were given freedom of displacement in the plane of the boundary but was restrained against any out of plane movement. This is because the interior of the tank was finished to a smooth surface giving a low frictional resistance to the sand grains. A joint connected only to the soil elements was given δ_x , δ_y and δ_z degrees of freedom, while for a joint on a plate element the in-plane rotation was suppressed. For each analysis between 12 and 15 increments of the load were used.

8.2.1 Model A: A space frame

This model is shown in figure (8.1a) and was also analysed by Cunnell (1974) using isoparametric elements for the soil. It is symmetrical about the central beam JK on which the load was applied at points L_1 , L_2 , L_3 and L_4 with the eccentricity e equal to 0, 0.33, 0.67 and 0.85 respectively. Only one half of the structure and the soil was analysed. The finite element mesh for this problem is shown in figure (8.1b). The soil was divided in such a way as to reduce the number of solid elements with different dimensions. The divisions on the beams JK and BC were used to reduce the size of the joint groups. Joint L_3 in figure (8.1b) was moved to the left to point L_4 in figure (8.1a) when the load was applied at $e = 0.85$. The same data was used for the various load cases each time altering the position of the load. The mesh consisted of 554 joints, 350 solid elements, 8 plates and 16 members.

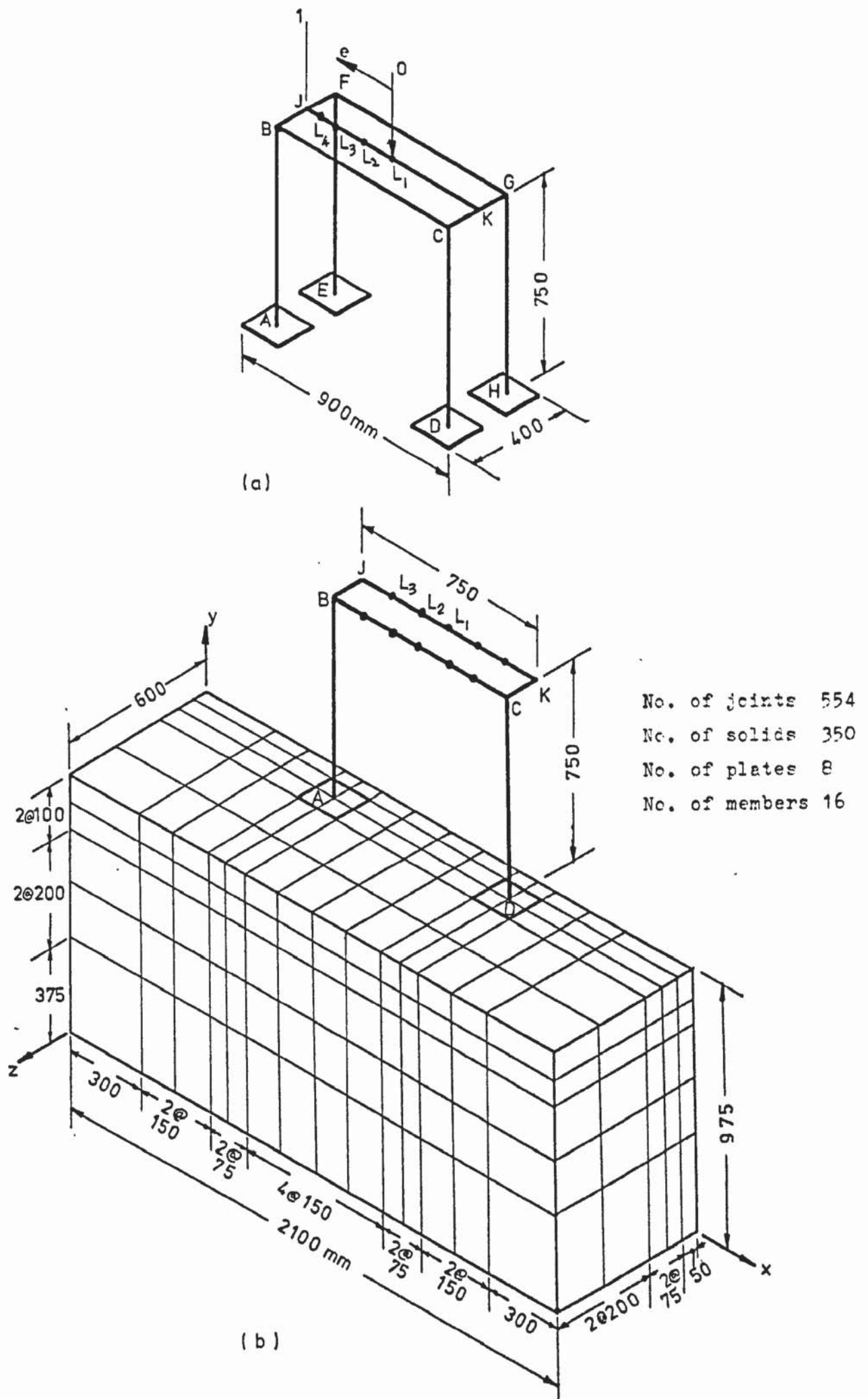


FIGURE 8.1 FINITE ELEMENT MESH FOR SPACE FRAME MODEL

8.2.2 Model B: A box culvert

The finite element mesh of the box culvert and the soil is shown in figure (8.2). This mesh with the full culvert was used for the cases when the load was applied at points J and K. The eccentricity e_x for these points is unity and the eccentricity e_z is 0.36 for J and 0.72 for K. In the actual experiments the sand in the trapezoidal area such as LMANBQVW at the front and the rear of the culvert was removed, see figure (7.3). This zone was approximated in the finite element mesh by removing the solid elements from the front and the rear of the culvert as shown in figure (8.2b). The soil model was represented by 816 solid elements. The parapets AB and CD in figure (8.2a) were each divided into four prismatic member elements and the culvert itself was represented by 108 plate elements.

It was observed during the test with the load at J and K that the edge TY of the base of culvert separated from the soil as shown in plate (8.1). The wall BDQT separated from the soil in the horizontal x direction, but the cavity created by this separation was subsequently filled up by the sand. A trial analysis revealed that tensile stresses developed in the soil in these regions and also to the right of the edge RS and to the left of the edge UX of the base, see figure (8.3). To cater for the separation due to these tensile stresses, 130 dummy joints were introduced at the joints shown by the circles in the figure. The final mesh consisted of 1192 joints in addition to the dummies.

When the load was applied on the centre line EI of the culvert, see figure (8.2a), only half of the culvert was analysed utilizing symmetry about this line. The finite element mesh for this case is

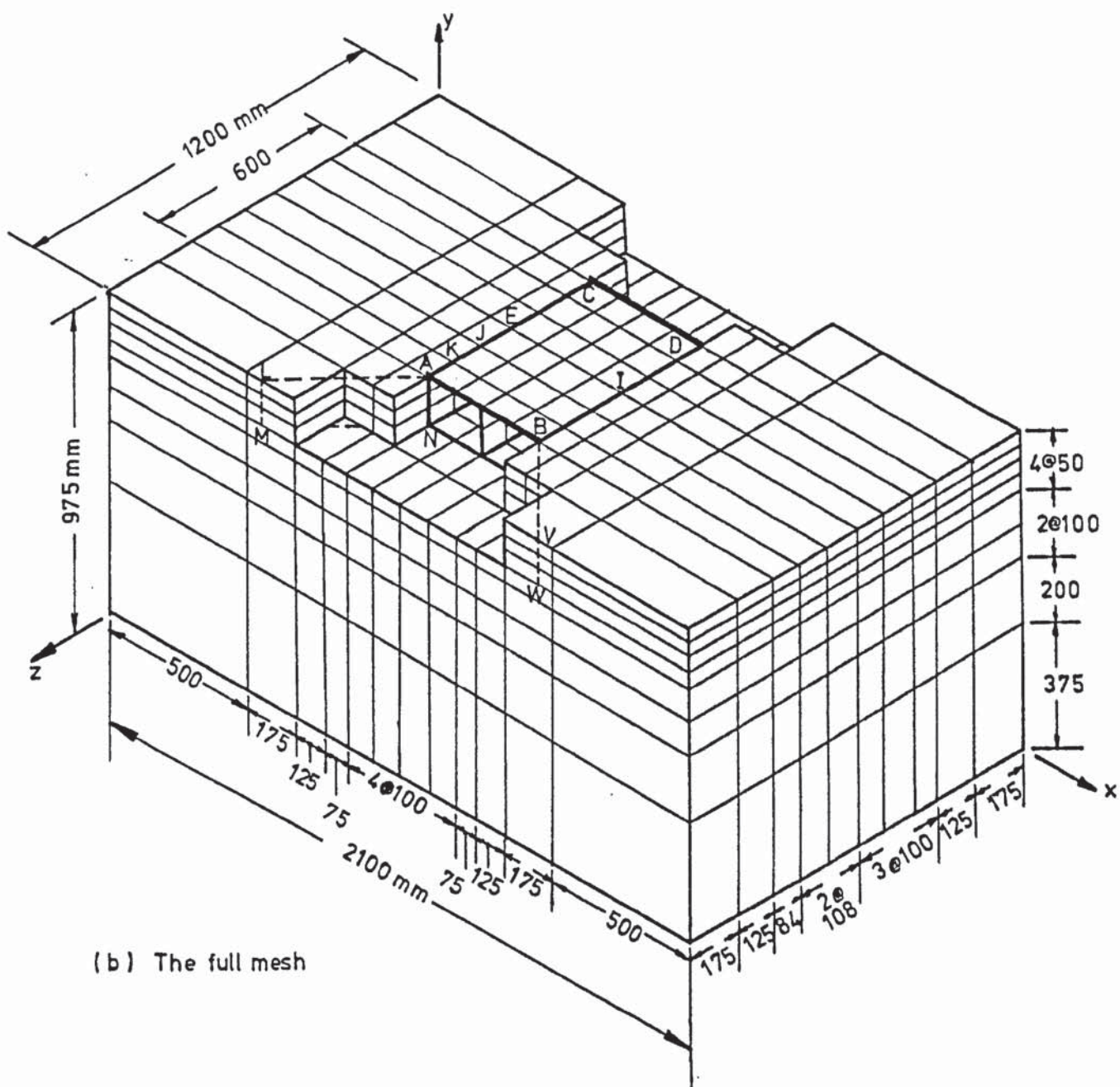
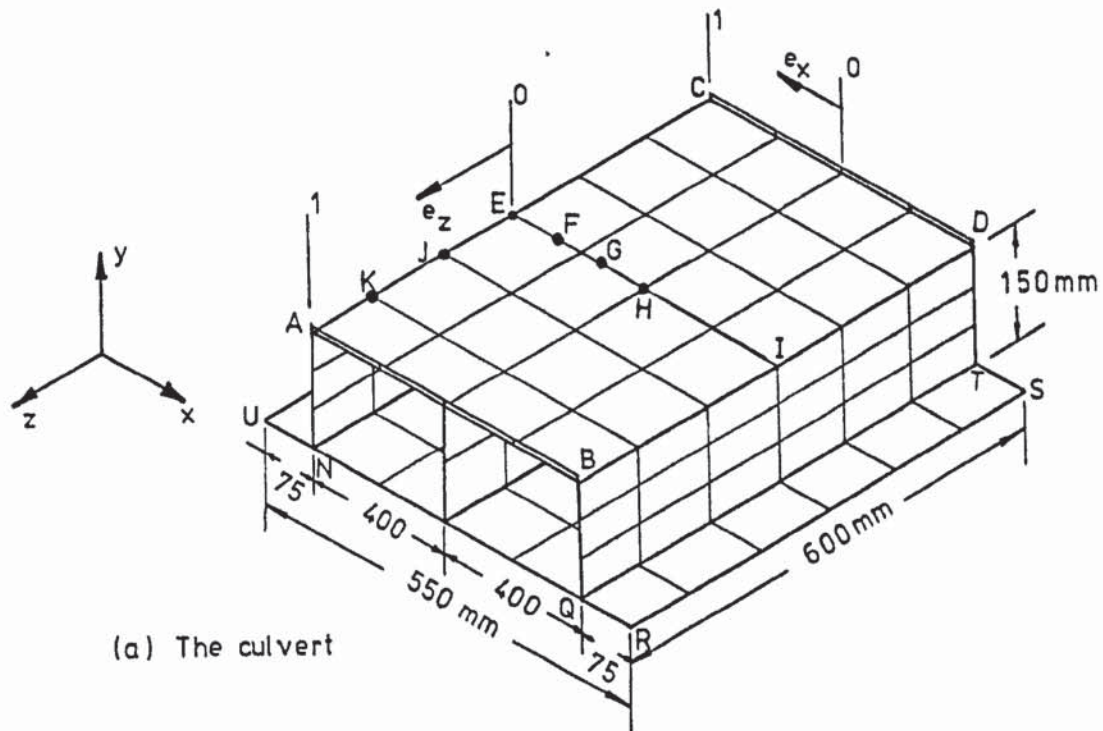


FIGURE 8.2 FINITE ELEMENT MESH OF FULL BOX CULVERT

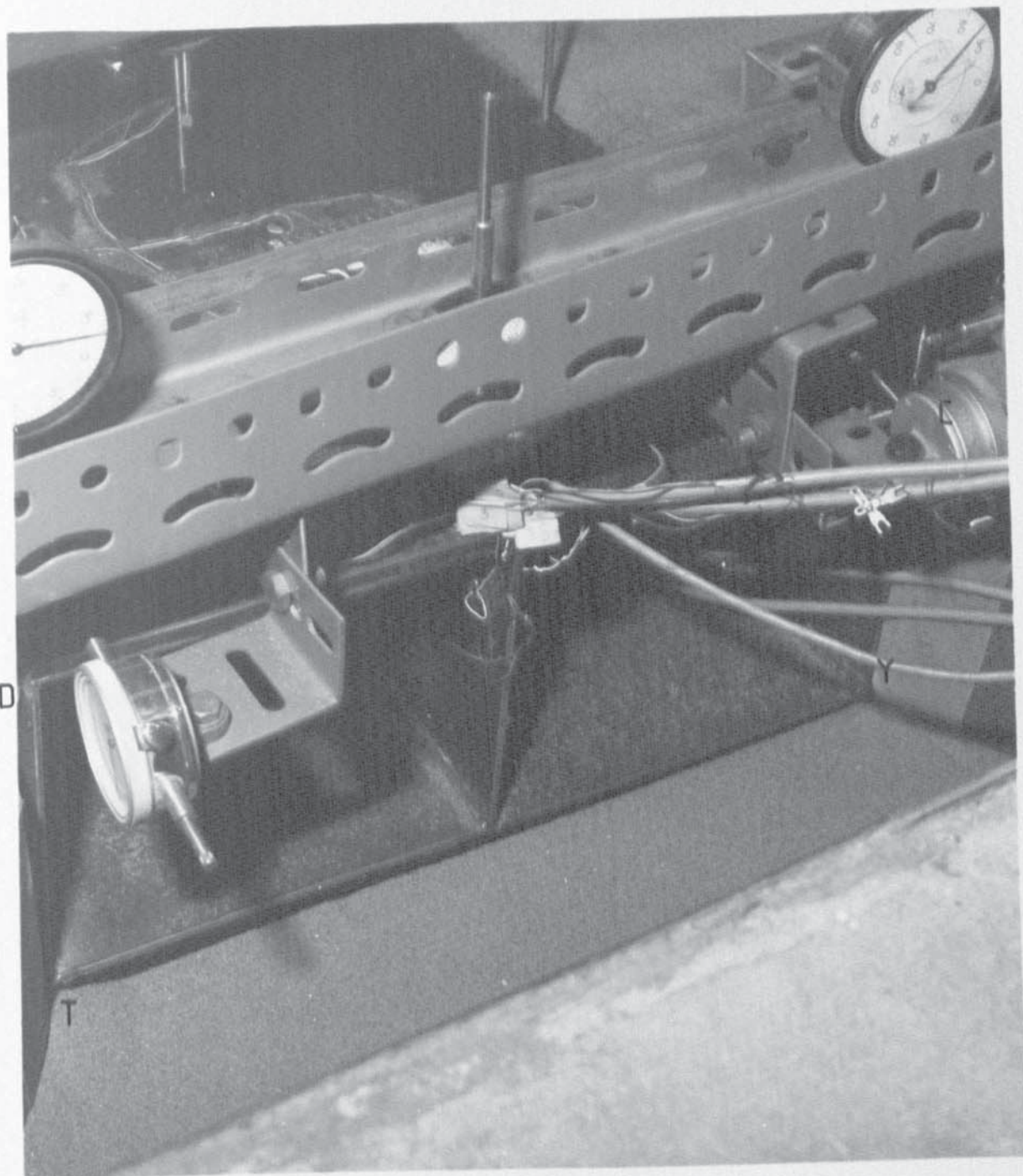
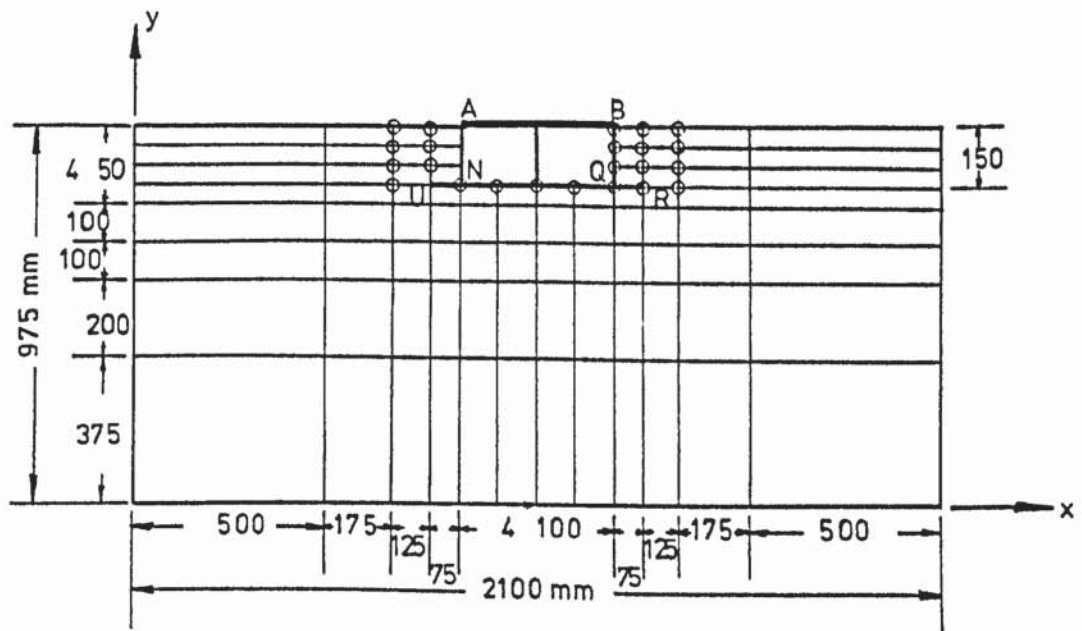
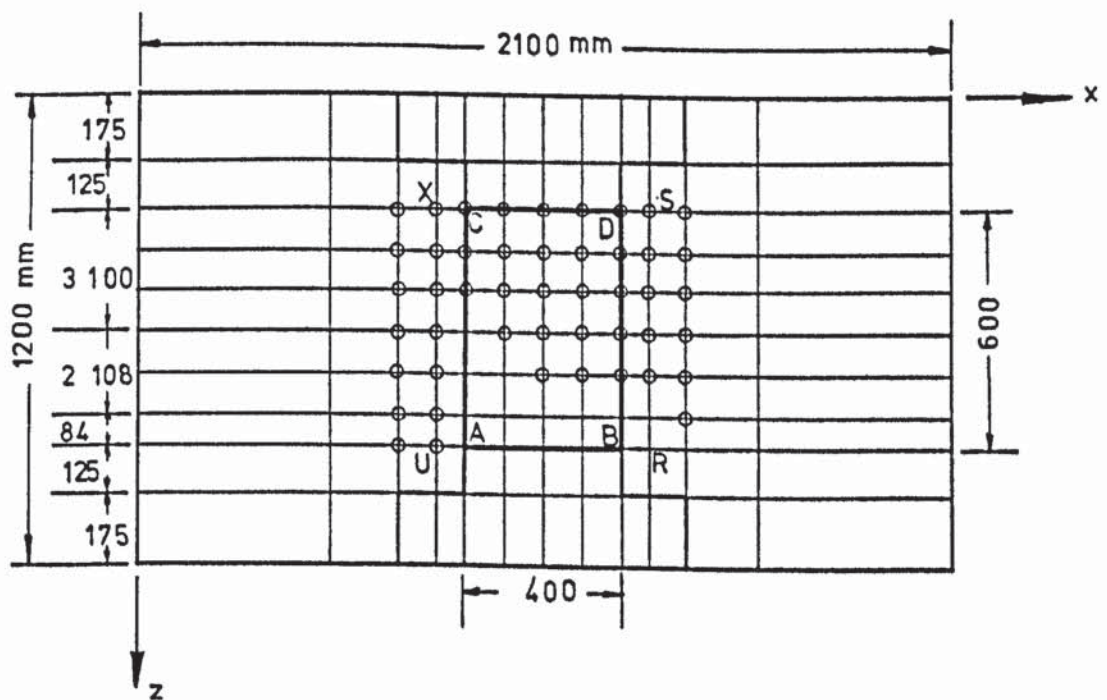


PLATE 8.1 A VIEW OF THE BOX CULVERT SHOWING SEPARATION OF THE BASE FROM SOIL



(b) ELEVATION



◆ Joint with a dummy

(a) PLAN

FIGURE 8.3 FINITE ELEMENT MESH OF BOX CULVERT SHOWING DUMMY JOINTS

shown in figure (8.4), where the loading points are shown by the letters H, G, F and E having $e_x = 0, 0.33, 0.67$ and 1 respectively. In the tests with these load cases no separation was observed and therefore no dummy joint was used in the analysis. The finite element model consisted of 656 joints, 408 solid elements, 57 plates and 5 member elements.

8.2.3 Model C: A tall structure

The finite element mesh for the tall structure model and the soil is shown in figure (8.5). The models in this series which had four main columns were symmetrical about the x centre line shown in the figure. For these cases only half of the finite element mesh in front of the centre line in figure (8.5) was analysed. The height H_b of the base was varied between 0 and 150 mm and the same data was used for analysing the cases C1, C2, C3 and C5; all of which had four columns. The main columns AB, CD etc. and their extensions in the soil were represented by prismatic members. The members inside the soil were connected to the soil at all the joints on them. In soil mechanics the friction piles are sometimes assumed to be attached to the soil at a single point at the centre or at the two-third point. As the column extensions were considered to behave as piles, the analysis of model C2 was repeated by connecting them to the soil at 2/3 point only. The loads were applied either at the points S to obtain an eccentricity e equal to 0.0 or T to obtain $e = 0.4$.

Column AB was removed in model C4 and thus symmetry was lost. For this case the full finite element model shown in figure (8.5) was analysed but column AB was removed. The model consisted of 991 joints, 672 solid elements, 52 plates, 24 member elements and 2678 unknown degrees of freedom.

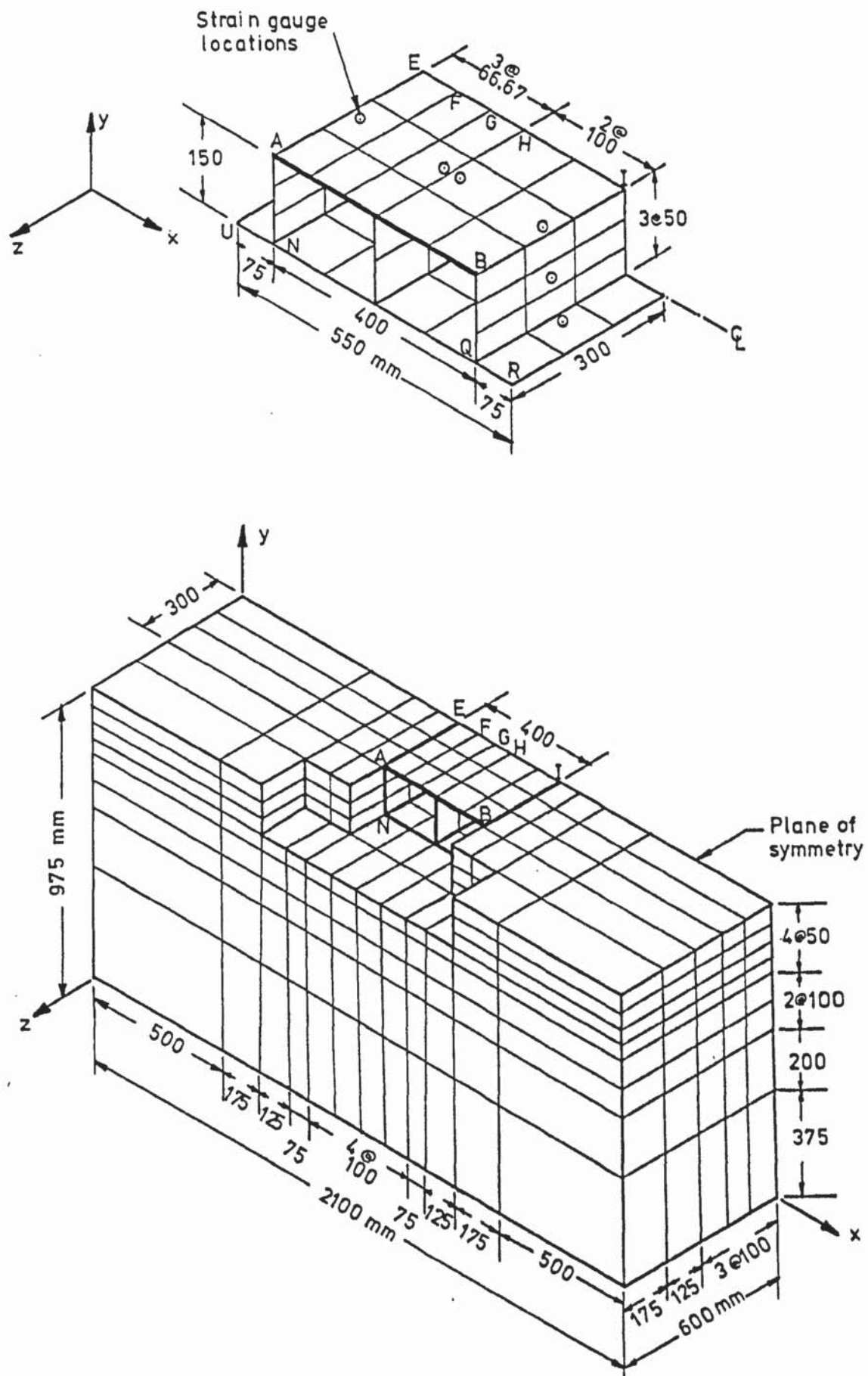


FIGURE 8.4 FINITE ELEMENT MESH OF HALF BOX CULVERT

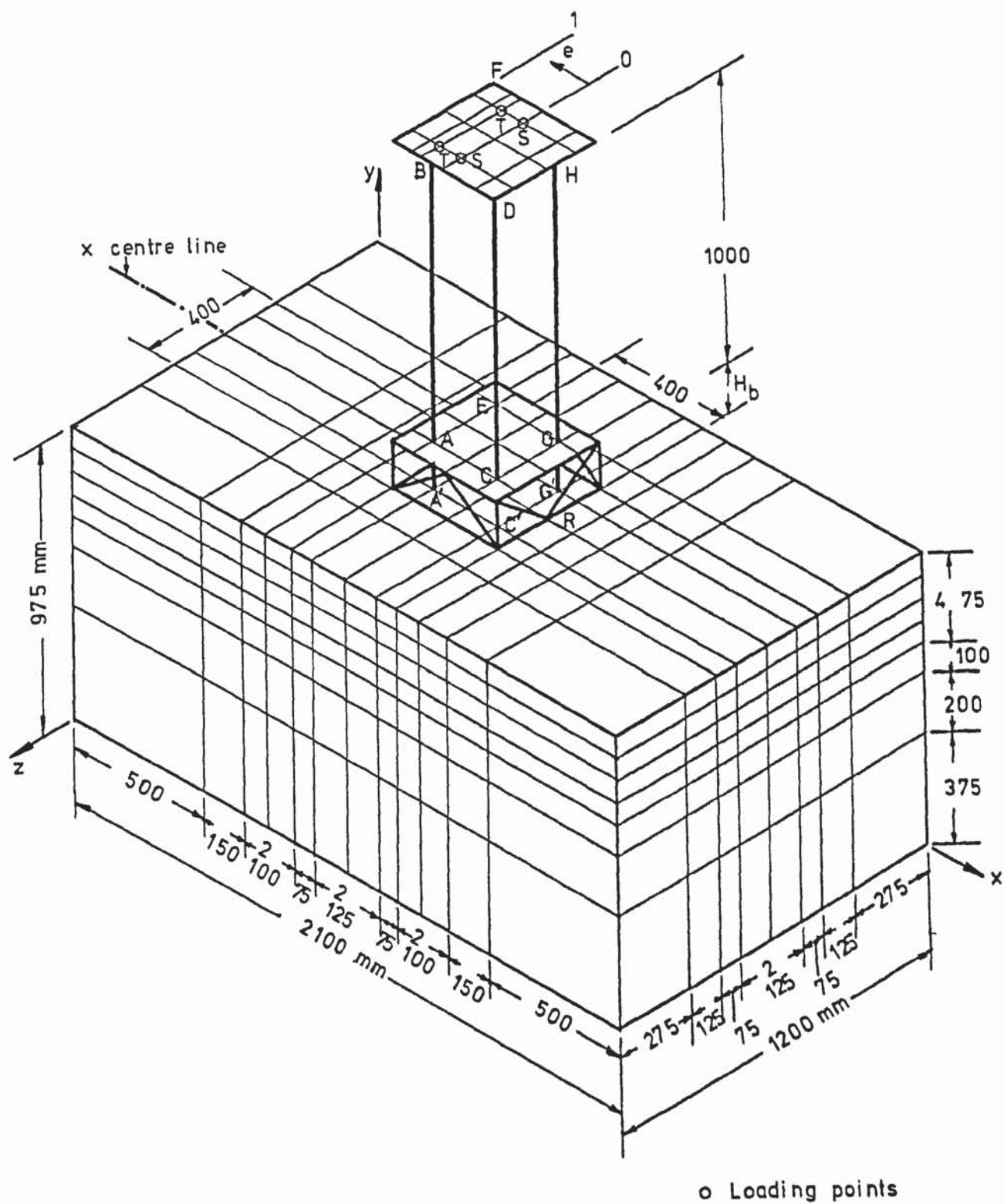


FIGURE 8.5 FINITE ELEMENT MESH FOR THE TALL STRUCTURE MODEL

8.2.4 Model D: A three-bay space frame

Two different foundations were used in the experiments with this model. The first consisted of eight individual pad footings under the columns and the second was a pair of strip footings. The finite element mesh for the frame with the pad footings is shown in figure (8.6). The structure was symmetrical about the central beam ST and therefore half of the frame and the soil was analysed. During the experiments with this model, footings E, N, G and Q separated from the soil when the load was applied at points L_1 and L_2 . To cater for these separations in the analysis, 18 dummy joints were introduced at footings E and G which are shown by the small circles in figure (8.6b). The finite element model consisted of 710 active joints, 18 dummy joints, 450 solid elements, 16 plates, 32 members and 1831 initial degrees of freedom.

When the strip footings were used the structure and the soil were represented by the finite element mesh shown in figure (8.7). In the experiments with this model, the parts of the footings to the right of columns CD and LM were observed to separate from the soil when the load was at L_1 and L_2 . To cater for these separations 30 dummy joints were introduced at the joints shown by the small circles in figure (8.7b). The finite element model consisted of 710 active joints, 30 dummies, 450 solid elements, 28 plates, 32 member elements and 1849 initial degrees of freedom.

8.3 RESULTS OF MODEL A - SINGLE-BAY SPACE FRAME

8.3.1 Experimental calculations

As stated in chapter 7, dial gauges were placed on the footings A, D, E and H of the frame to record the vertical settlements. However, these could not be located exactly at the centre of the footings

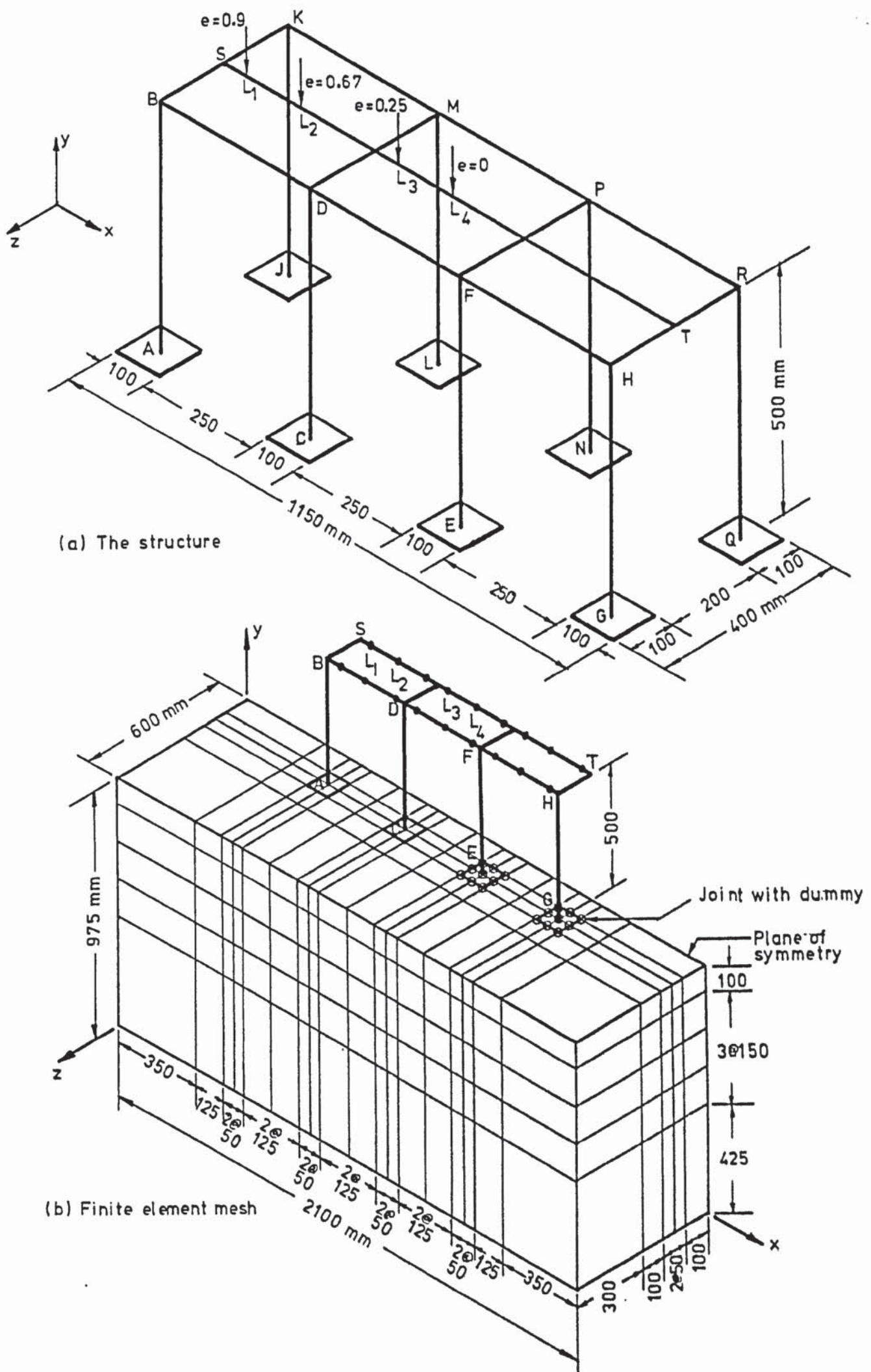


FIGURE 8.6 FINITE ELEMENT MESH FOR THREE-BAY FRAME WITH PAD FOOTINGS

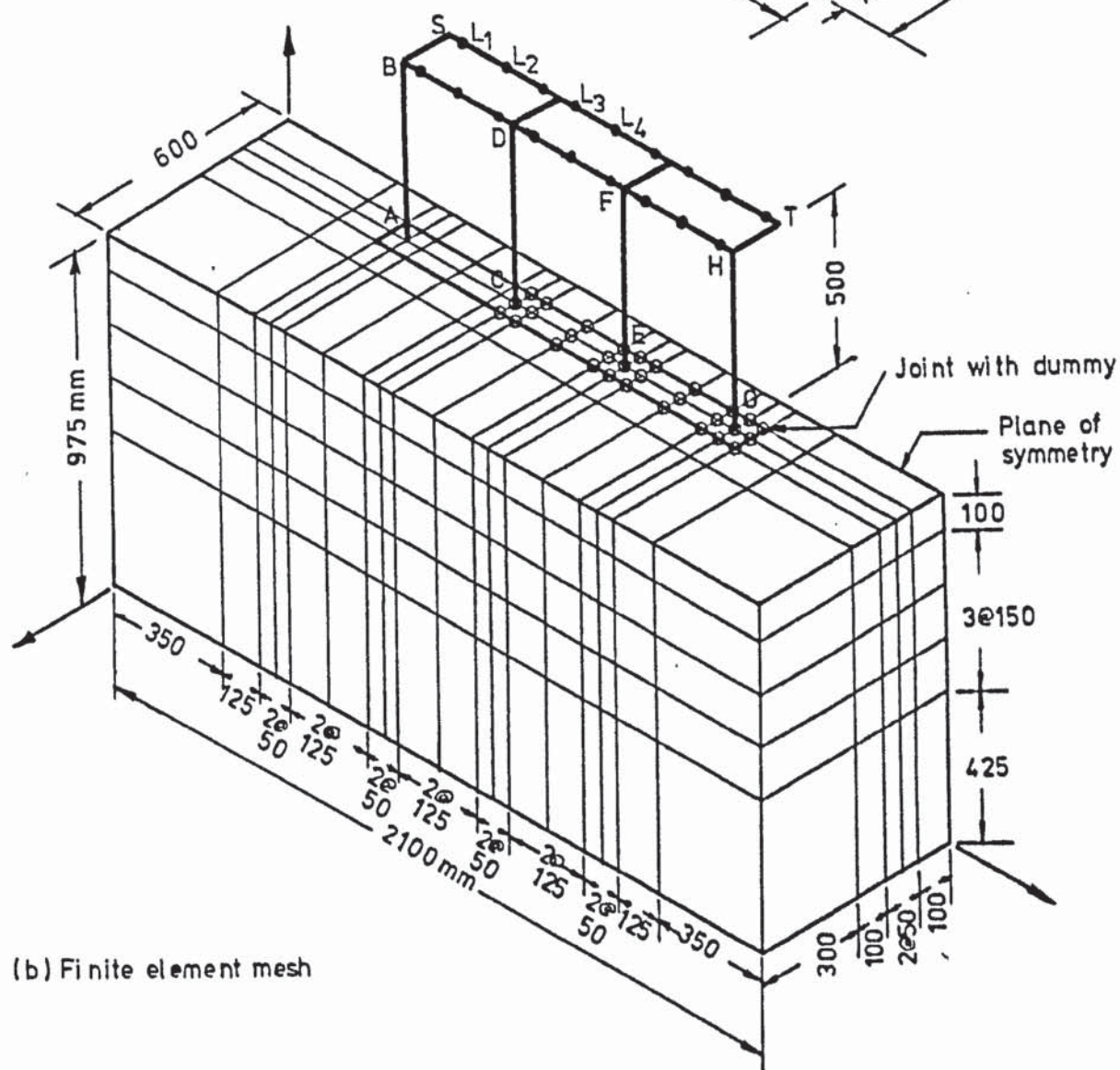
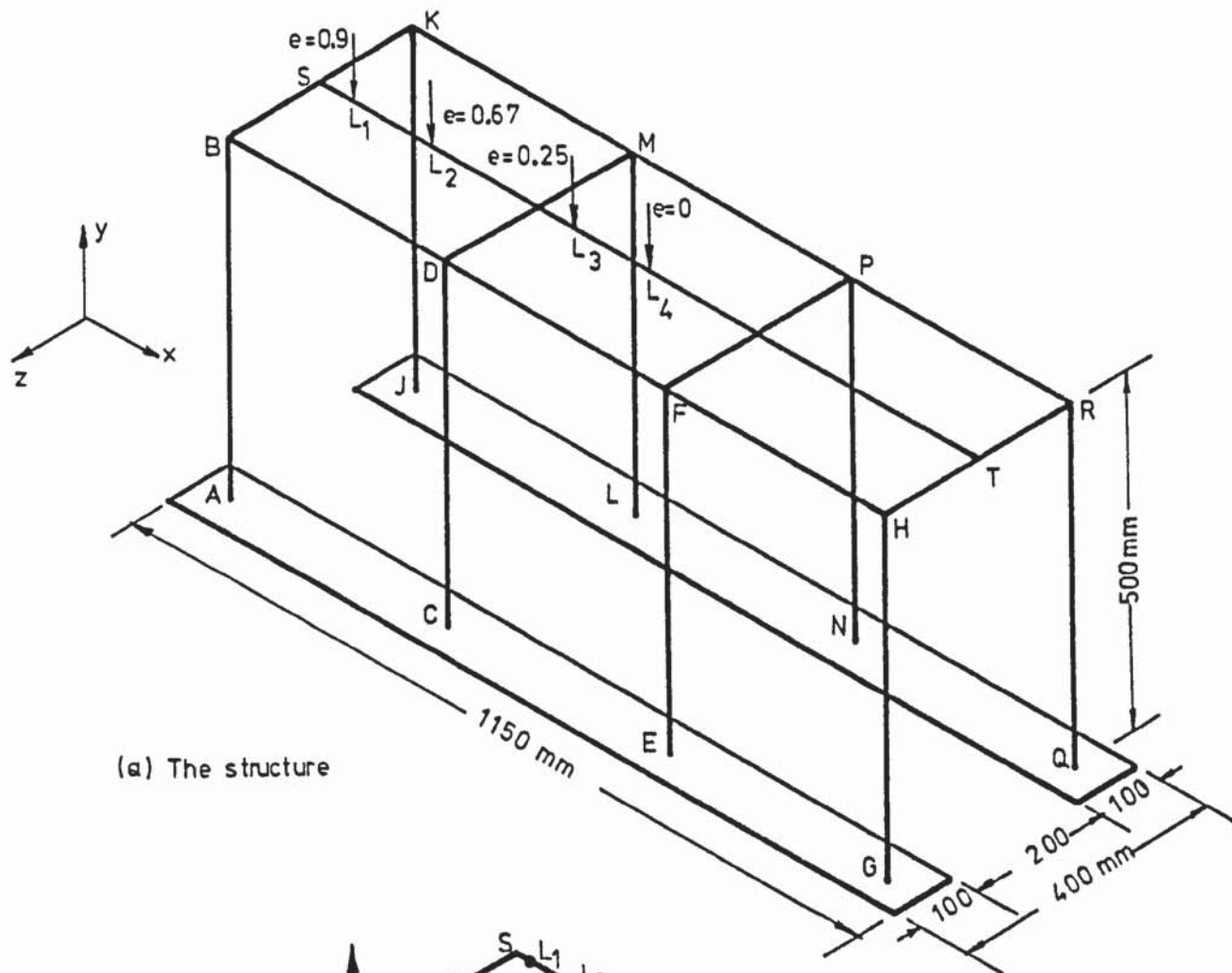


FIGURE 8.7 FINITE ELEMENT MESH OF THREE-BAY FRAME WITH STRIP FOOTINGS

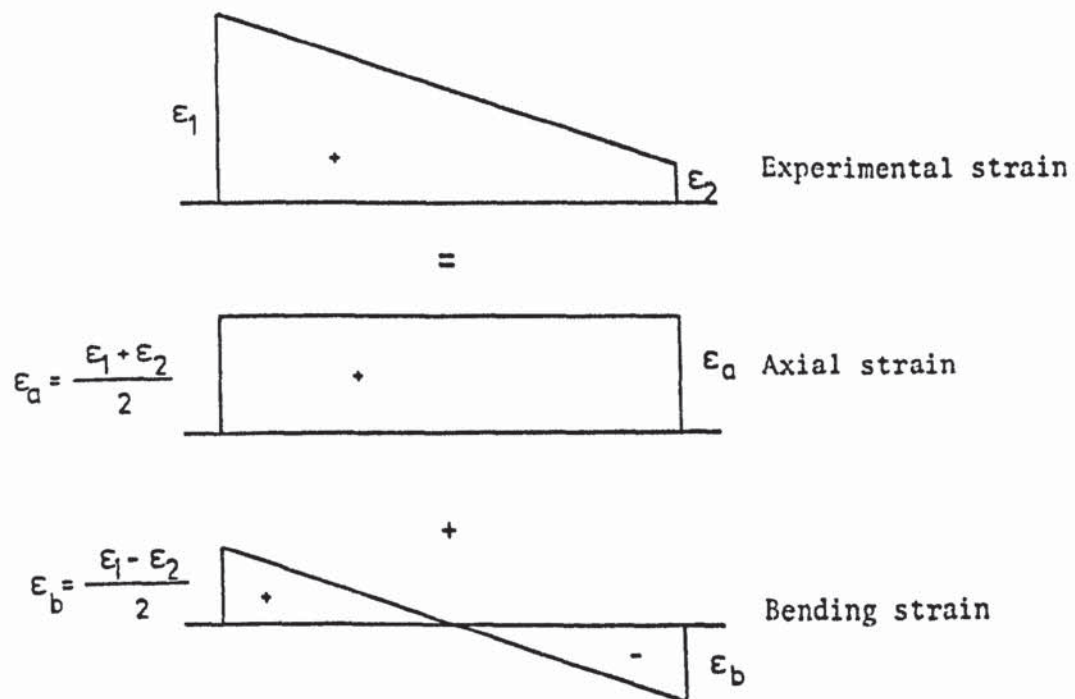
and were placed about 30 mm from the columns. A linear extrapolation of the gauge readings was performed in a manner suggested by Cunnell (1974) to obtain the settlements directly under the columns. The differential settlement was calculated as the difference between the average settlement for pads A and E and that for pads D and H, see figure (8.1). The sway was calculated as the difference of the average horizontal displacement of points B, C, F and G at the top of the columns and that of the column bases A, D, E and H.

A pair of strain gauges on opposite faces of a column were used at three points on each column. These recorded the surface strains ϵ_1 and ϵ_2 which contained both the axial component ϵ_a and the bending component ϵ_b , see figure (8.8a). They were separated as shown in the figure and the bending strain was multiplied by the section modulus and E to obtain the bending moment. The gauges could not be located exactly at the column base A or at the junction B of the beam and the column axes, see figure (8.8b). These were located at three points L, M and N on each column. A mean straight line was passed through the bending moment ordinates at these three points and extended. This gave the bending moment at any point along the column. As the space frame was symmetrical about the central beam JK, the moments at corresponding points in frames ABCD and EFGH, see figure (8.1), were averaged.

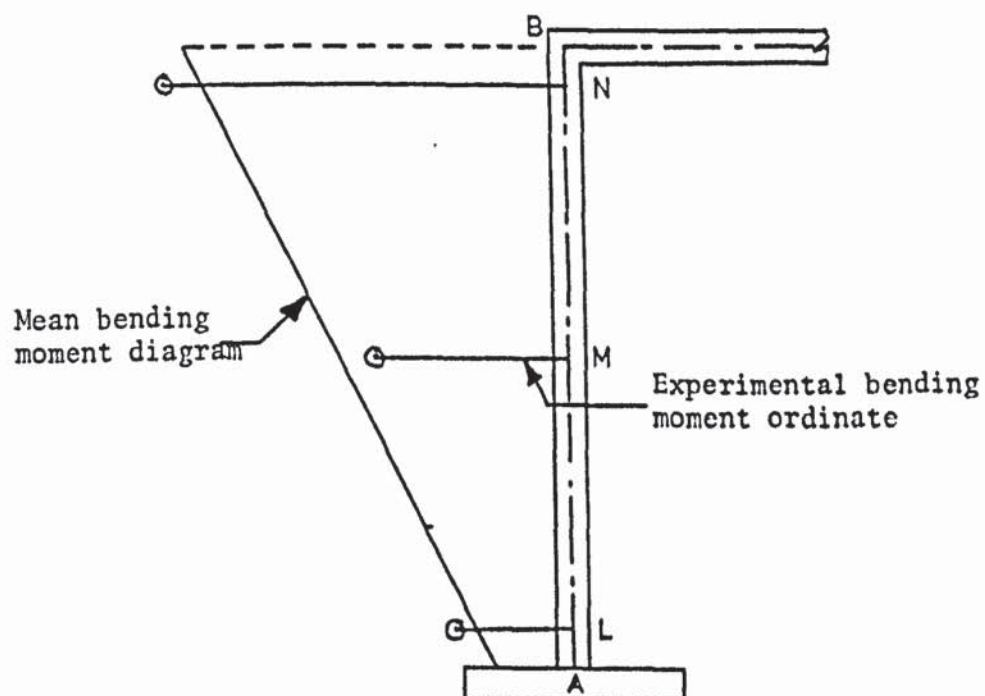
8.3.2 Deflections and settlements of the structure

The single-bay space frame was also tested by Cunnell (1974) for deflection measurements. These did not agree with the theoretical values as he used a hyperbolic representation of the soil properties.

Figure (8.9) shows the variation with the load of the average settlement of footings A, D, E and H when the load is applied at



(a) Separation of axial and bending strains



(b) Interpolation of bending moments

FIGURE 8.8 EXPERIMENTAL BENDING MOMENT CALCULATION

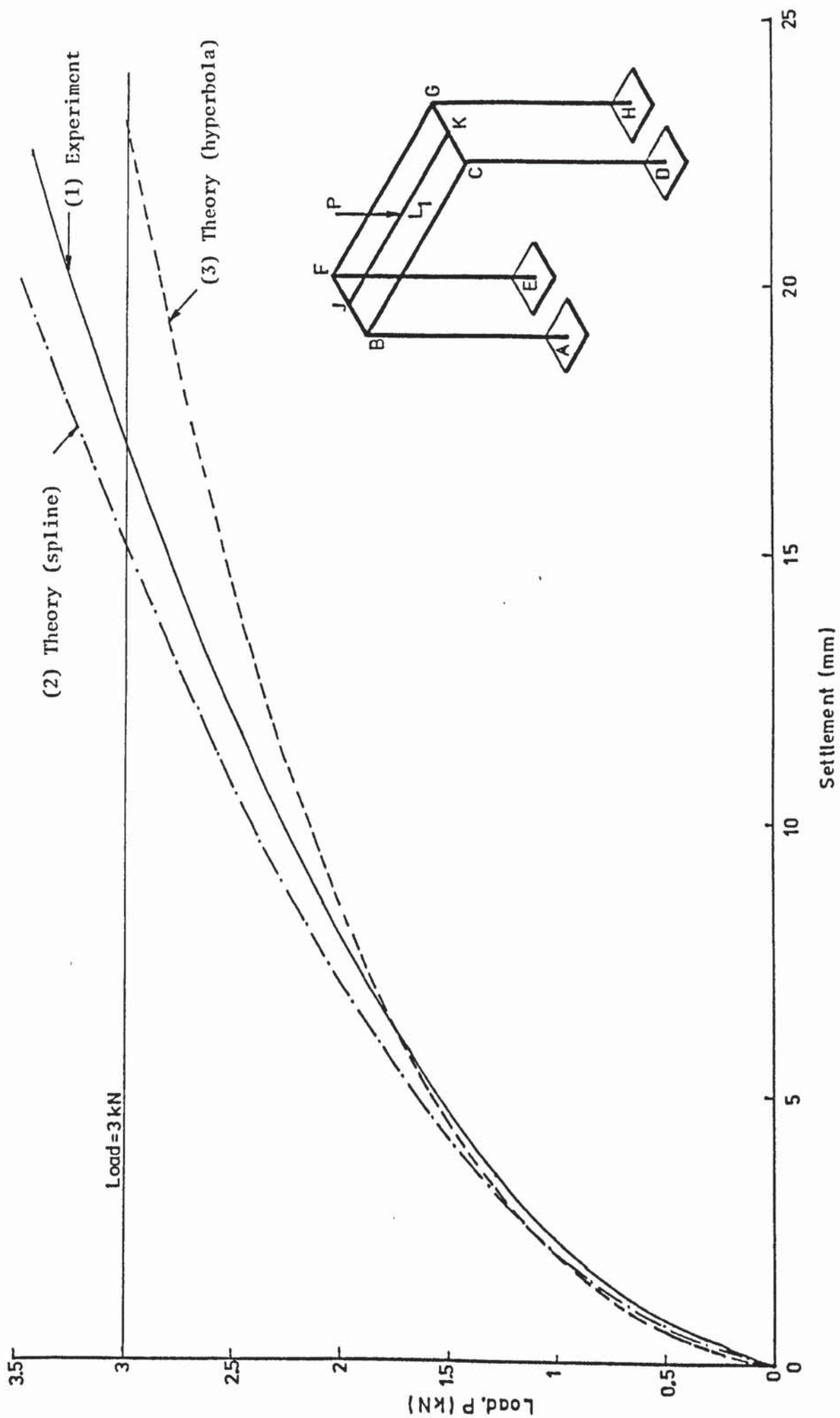


FIGURE 8.9 AVERAGE FOOTING SETTLEMENT OF SINGLE-BAY FRAME FOR $e = 0$

point L_1 with eccentricity $e = 0$. Curve (1) in the figure represents the experimental load-settlement relationship. Curve (2) represents the footing settlement obtained by the author using the finite element analysis of the frame and the soil. The spline function representation of the soil properties was used here. Curve (3) was obtained using the hyperbolic representation. As shown in chapter 2, the hyperbola underestimates the soil strains at low stresses and overestimates them at high stresses. This is also reflected in the load-settlement diagram. The settlement is underestimated initially but as the load increases these are overestimated.

The analysis using the spline functions, on the other hand, underestimates the settlement consistently. The difference is due to the inherent approximation involved in the incremental method. At a load of 3 kN curve (3) overestimates the settlement by 33% while curve (2) underestimates it by only 9%. This shows that the spline functions give a closer approximation of the load-settlement curve. These were therefore used to analyse all the model structures and the analytical results presented in the rest of this chapter were all obtained by using these functions.

The differential settlement between the left hand pads A and E and the right hand pads D and H are plotted against the load in figure (8.10). These are shown for eccentricity $e = 0.33, 0.67$ and 0.85 when the load was at L_2, L_3 and L_4 respectively. The sway of the frame is plotted against the applied load in figure (8.11). The variation of the differential settlement and the sway with the eccentricity of an applied load of 2 kN is shown in figure (8.12). The load-deflection curves in figures (8.9), (8.10) and (8.11) are non-linear, reflecting the non-linear material properties of the

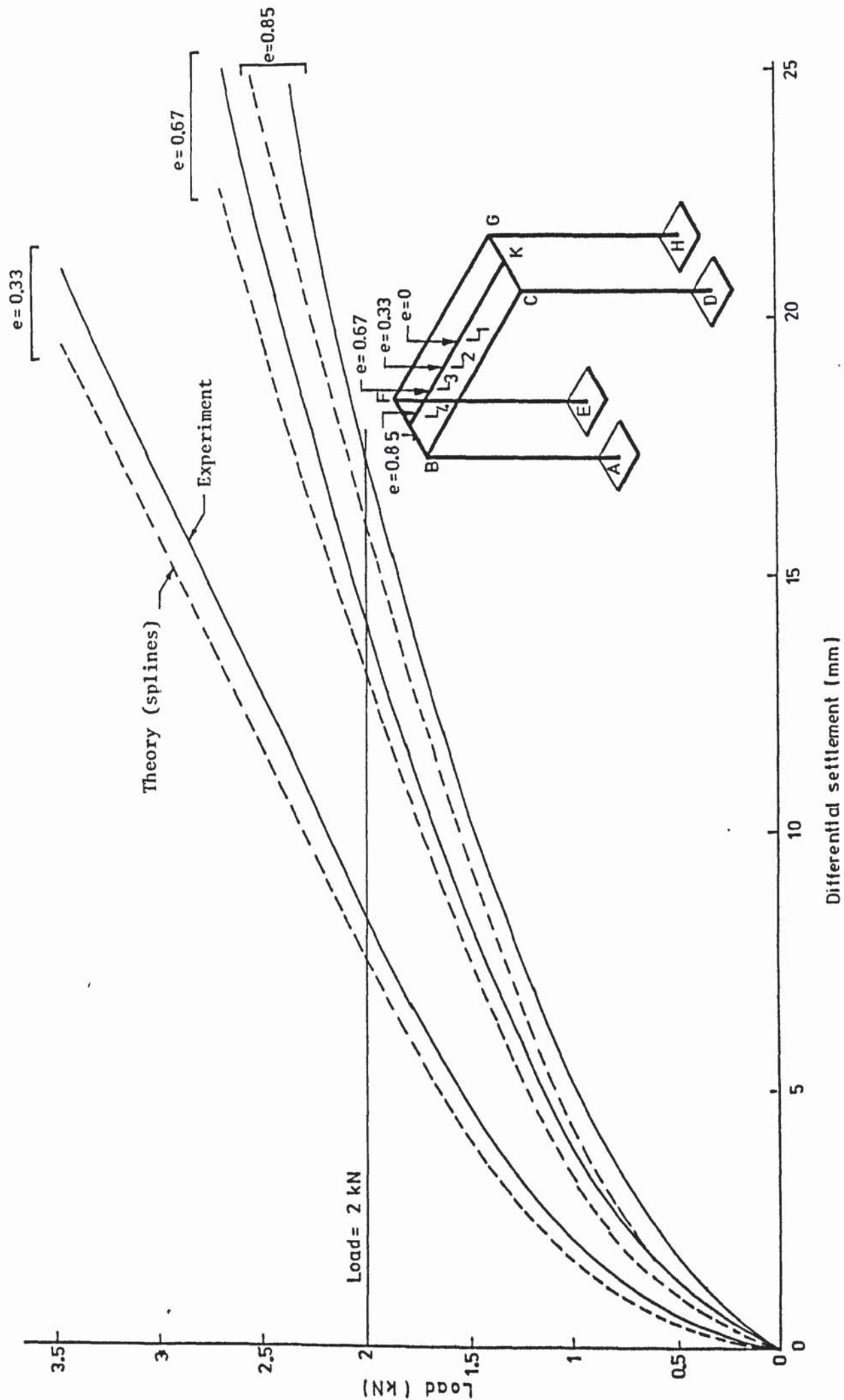


FIGURE 8.10 LOAD-DIFFERENTIAL SETTLEMENT DIAGRAMS OF THE SPACE FRAME

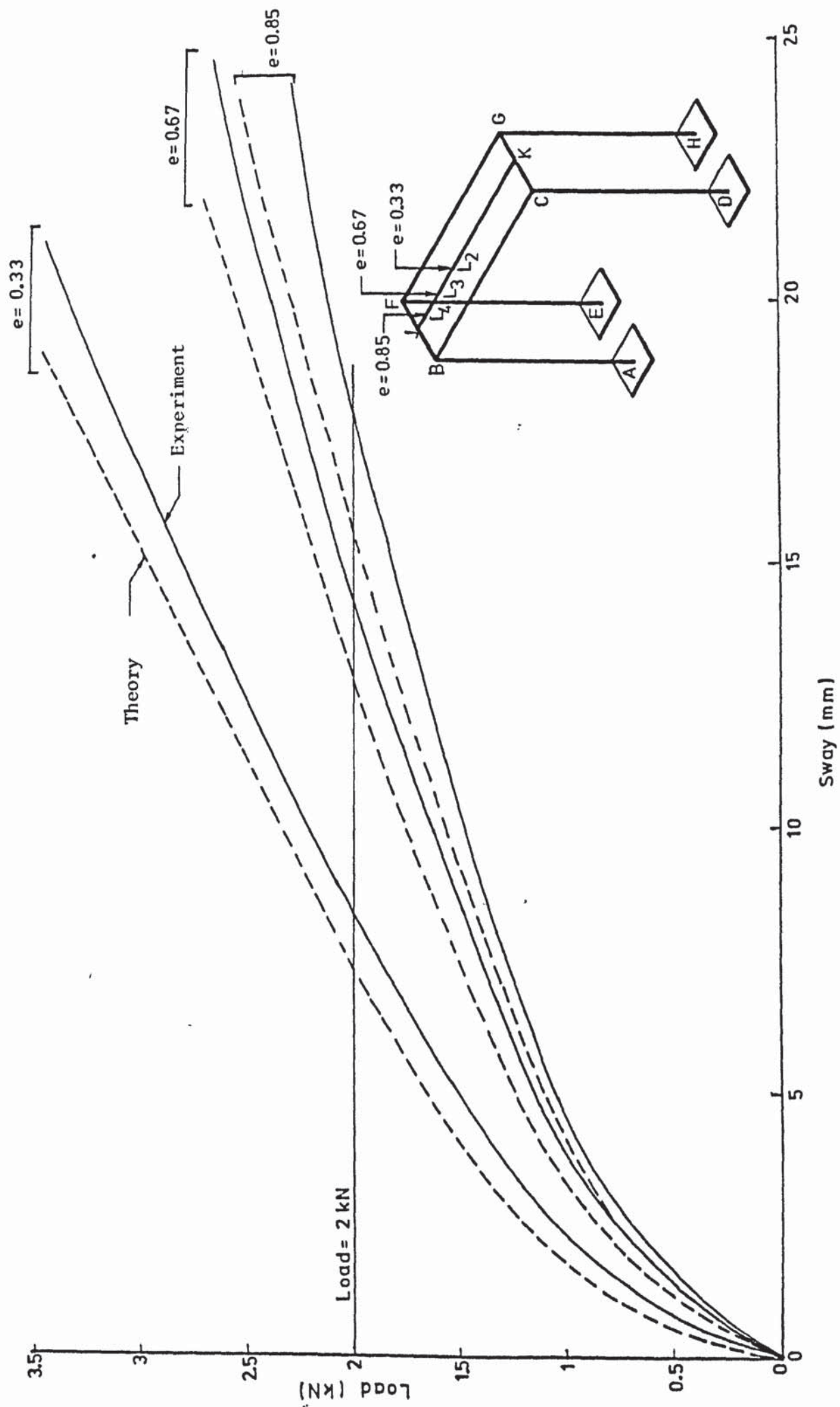
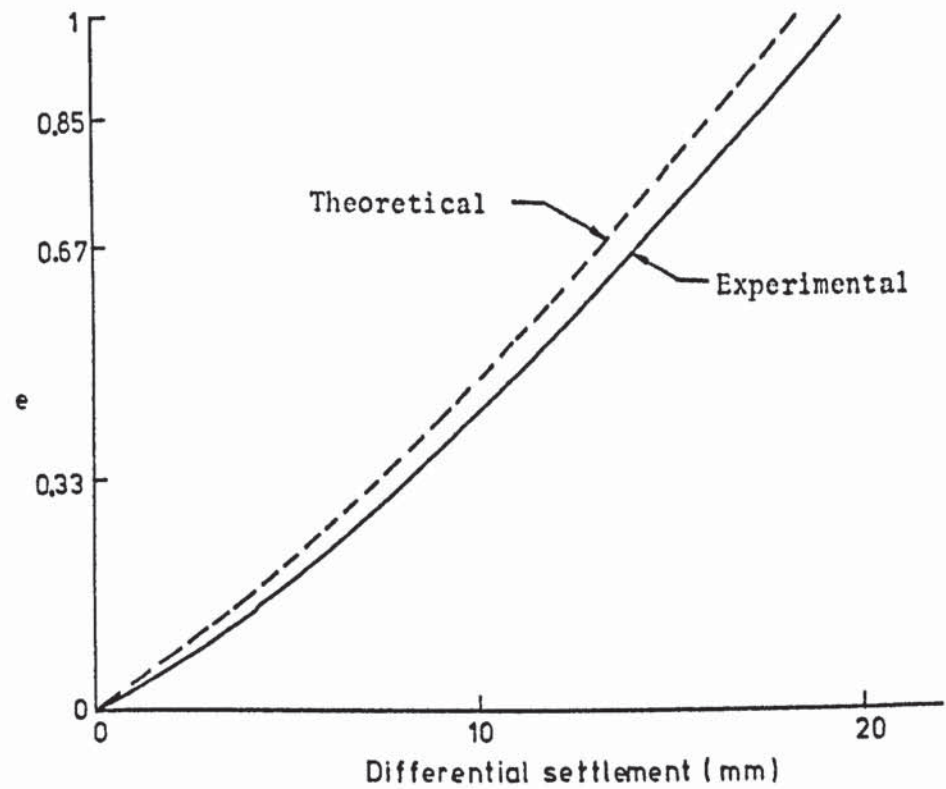
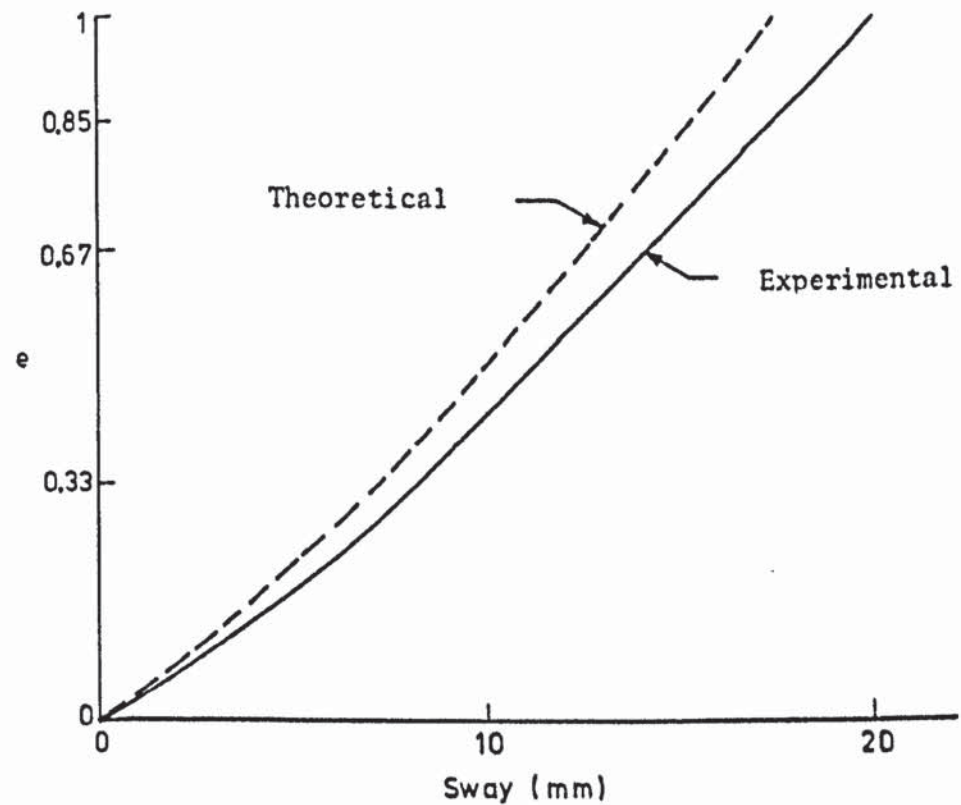


FIGURE 8.11 LOAD-SWAY DIAGRAMS OF THE SPACE FRAME



(a) Eccentricity vs. differential settlement graph



(b) Eccentricity vs. sway graph

APPLIED LOAD = 2 kN

FIGURE 8.12 VARIATION OF THE DEFLECTIONS WITH ECCENTRICITY

soil. The soil elements immediately under the footings are near the surface and therefore have a low value of σ_{octi} . These elements are weaker than the ones deeper in the soil. At early stages of the loading these elements are highly stressed and reach the peak of their stress-strain curves, see figure (2.2). This may be the reason for the initial non-linearity of the load-deflection curves.

As the loading progresses the highly stressed zone spreads away from the footings and more and more elements reach the peak of their stress-strain curves. Consequently, the load-deflection curves lean towards the horizontal and tend to straighten up. This shows that the failure of a structure-soil system is gradual and a rigid plastic type of failure does not occur.

In figure (8.9), (8.10) and (8.11), the theoretical curves underestimate the deflections. This is in spite of the fact that the spline functions represent the stress-strain curves very closely. The actual $\tau_{oct}-\gamma_{oct}$ curve for a point directly under column AB of the frame for load case $e = 0$ is shown by curve (1) in figure (8.13). The incremental method calculates the tangent slope of the $\tau_{oct}-\gamma_{oct}$ curve at a particular value of γ_{oct} and uses this to construct the stiffness matrix. As explained in chapter 3 and figure (3.7b), this method does not follow the true stress-strain curve exactly. The error accumulates as the loading progresses. The $\tau_{oct}-\gamma_{oct}$ curve actually followed in the analysis is shown by curve (2) in figure (8.13). The error in the analysis was however kept small by using small increments of the load. This did not exceed 15% of the actual τ_{oct} at any γ_{oct} level for the point under column AB. This error was much lower elsewhere in the soil.

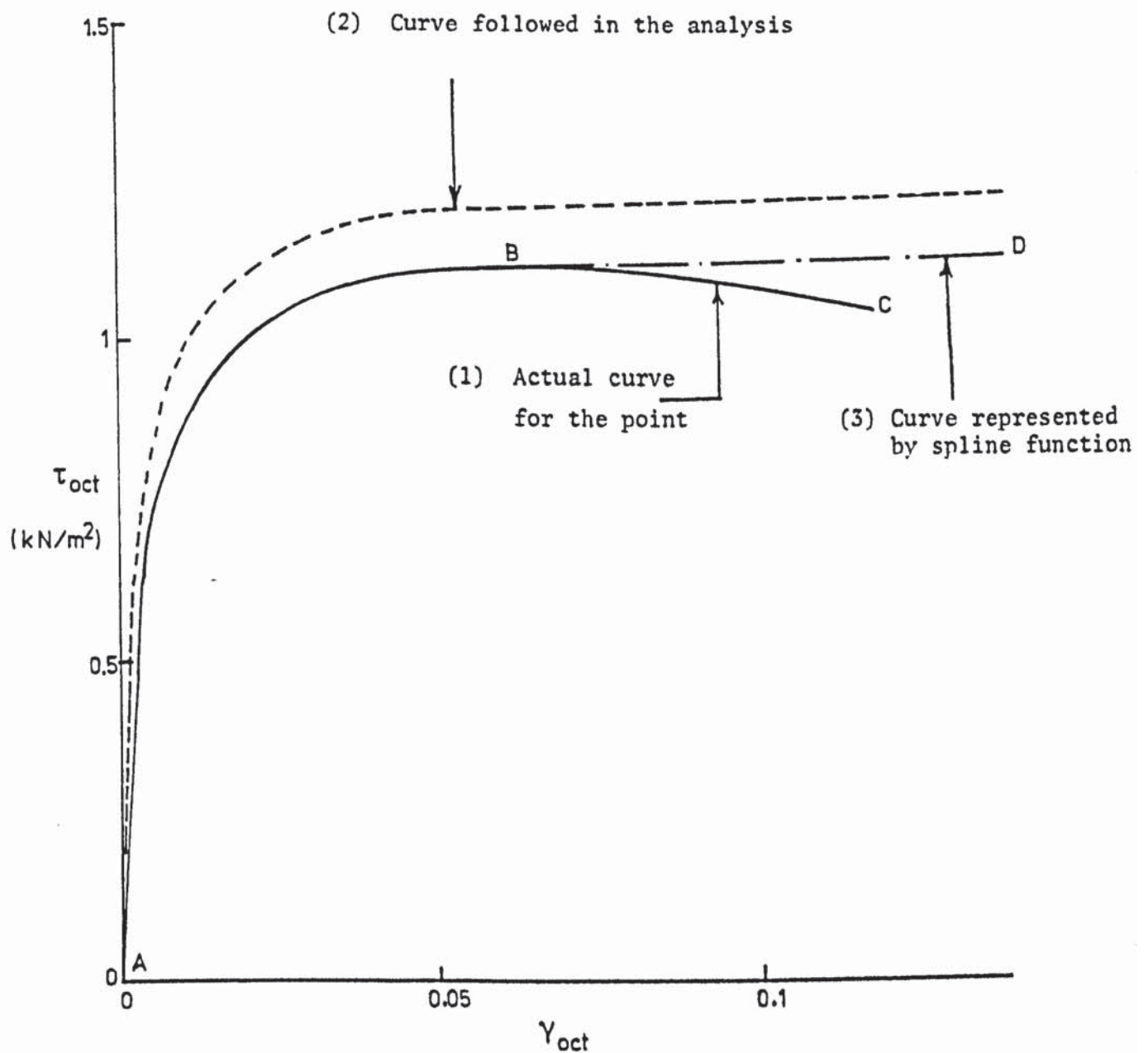


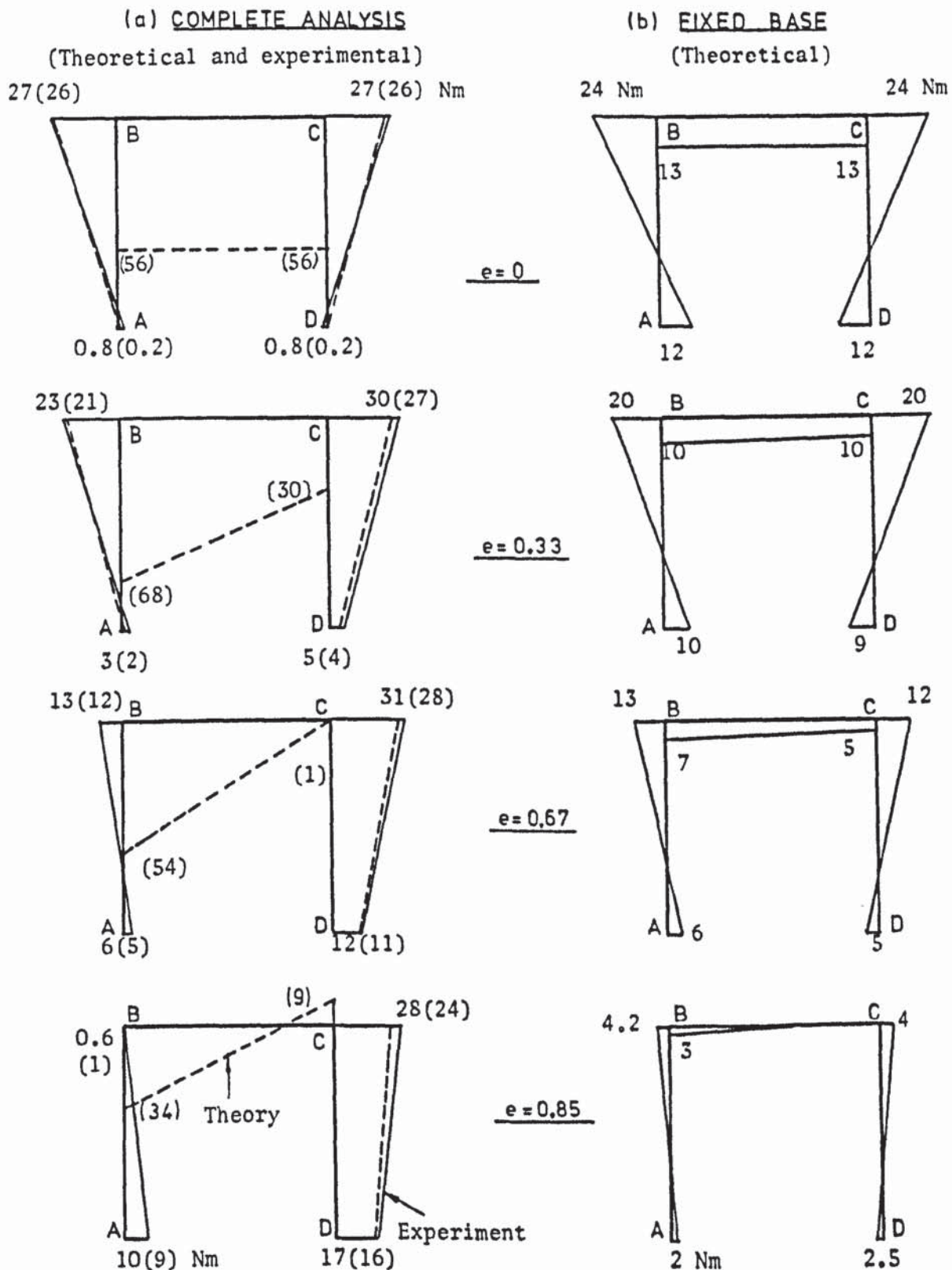
FIGURE 8.13 τ_{oct} - γ_{oct} CURVES AT A POINT DIRECTLY UNDER COLUMN AB

For the differential settlements at a load of 2 kN, shown in figure (8.12), the errors are 9.6% for $e = 0.33$ and 7% for $e = 0.67$ and $e = 0.85$. The corresponding errors in the sway are 12.2%, 10.7% and 12.6% for $e = 0.33$, 0.67 and 0.85 respectively. These are considered to be within acceptable engineering accuracy.

8.3.3 Bending moments

The bending moments about the z-axis in frame ABCD at an applied load of 2.8 kN are shown in figure (8.14). The dashed lines and the values in parentheses in figure (8.14a) indicate the bending moments obtained by analysing the space frame together with the soil using the spline function representation. The solid lines in the same figure indicate the experimental bending moments. The diagrams in figure (8.14b) were obtained by analysing the structure assuming its bases to be completely fixed. A very good agreement between the theoretical and the experimental bending moments is obtained in figure (8.14a) except where the values are very low. The maximum difference for the significant bending moments is about 11% which occurs at the top of column CD for $e = 0.85$. For $e = 0$ this difference is only 4%. An analysis of the structure and the soil for this load case using a hyperbolic representation of the soil properties gave a maximum difference of as much as 22%. The disagreement between the lower bending moment values obtained by using the spline functions and those obtained experimentally may have been caused by the inadequacy of the rather small, 5 mm, strain gauges in recording such low strains.

It is noticed in the figure that there is a considerable difference between the actual bending moments and those obtained for a fixed base condition. This is so even when $e = 0$ and the

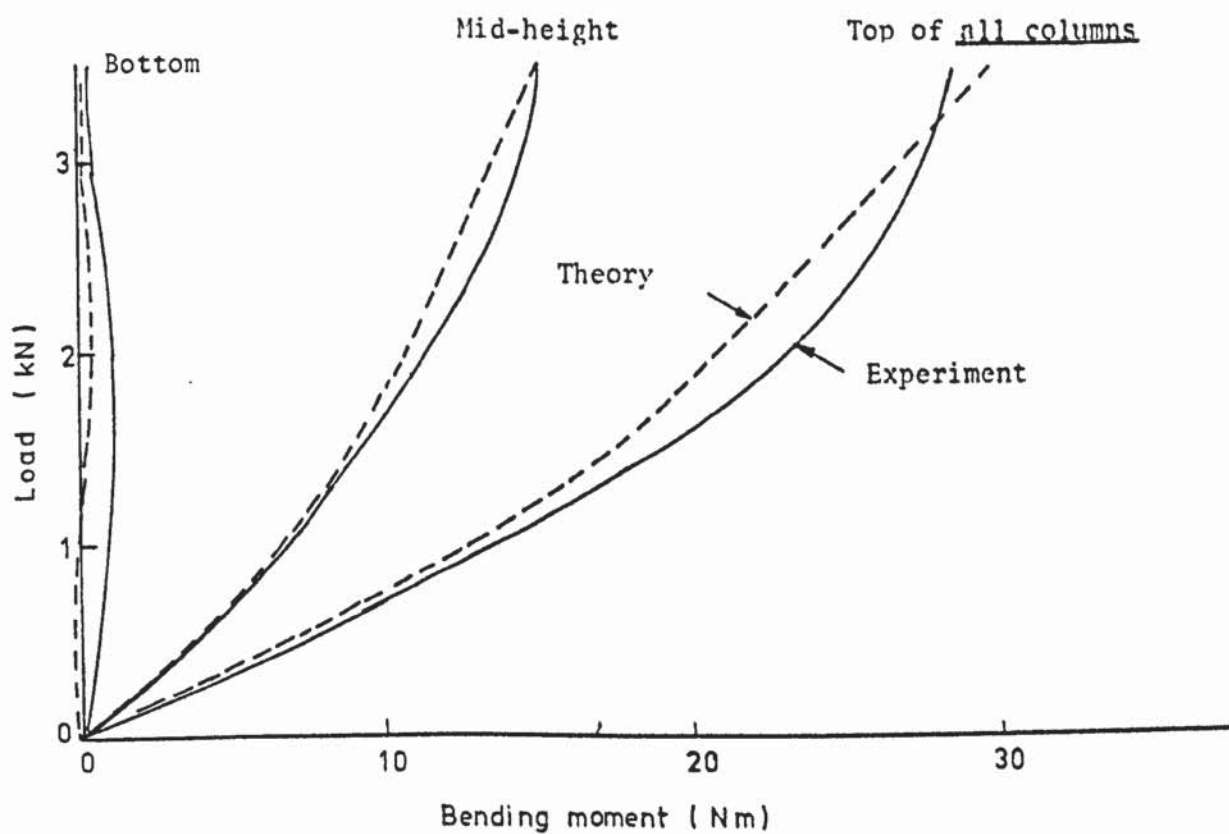


FIGURES IN PARENTHESES
INDICATE THEORETICAL
VALUES

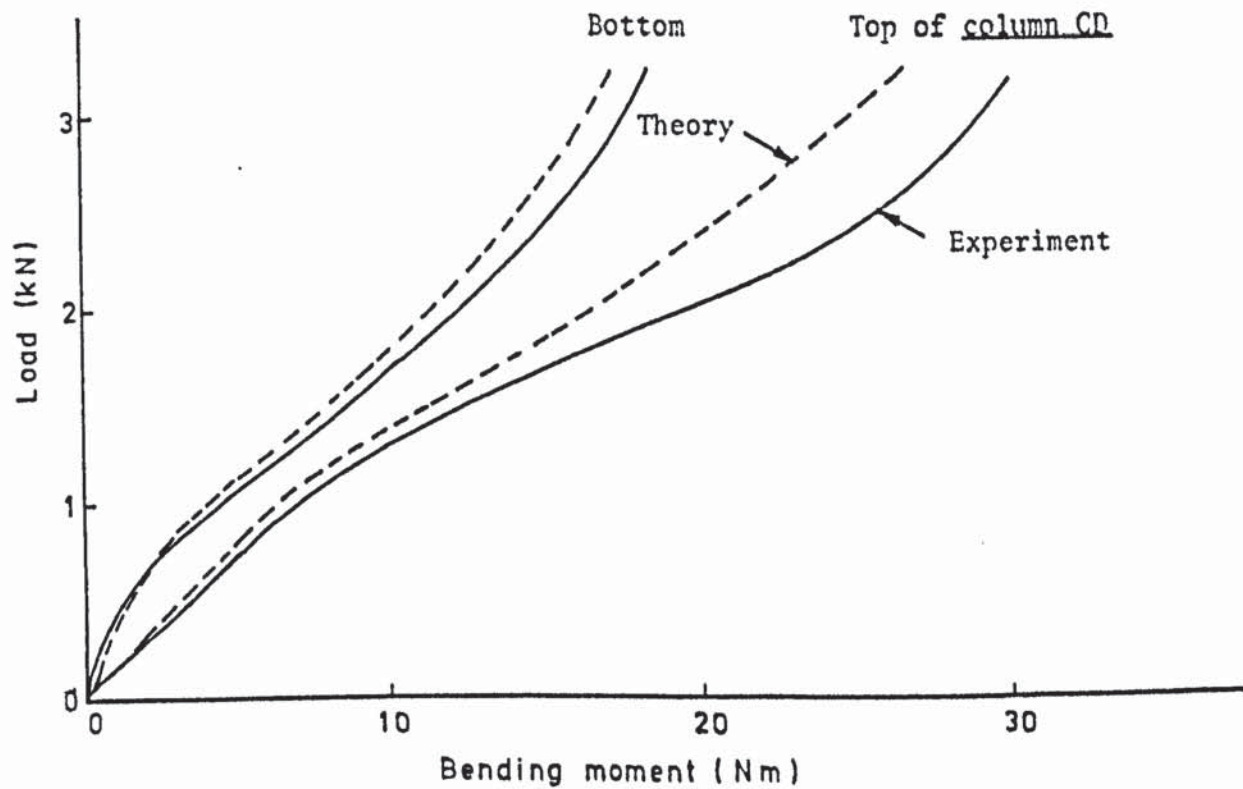
PLOTTED ON TENSION SIDE

FIGURE 8.14 BENDING MOMENT DIAGRAMS OF FRAME ABCD IN THE SPACE
FRAME AT A LOAD OF 2.8 kN

frame does not suffer any sway or differential settlement. However, the moments at the column bases cause a non-uniform pressure distribution under the footings thus rotating the bases. This rotation reduces the bending moments at the supports and alters their value elsewhere in the frame. This points out the importance of considering the base rotations in addition to the other displacements in an interactive analysis. As the eccentricity of the load increases, the redistribution of the bending moments becomes more pronounced due to the effects of sway and differential settlement. At $e = 0.85$ the bending moments at B and D are opposite in sign to those obtained by the fixed base analysis. As in this case the load is applied near column AB, the fixed base analysis gives low values of the moments throughout the frame. As this column settles the stiffness of the beams causes column CD to come to its aid. As a result CD also settles. In this process column CD takes a higher share of the load and its bending moments increase. The load-bending moment graphs for the columns of the frame with $e = 0$ are shown in figure (8.15a). Those for column CD with $e = 0.85$ are shown in figure (8.15b). The firm lines indicate the experimental moments and the dashed lines show the theoretical ones. While a good agreement of these two curves exists at the initial loads, they become separate after a load of about 2 kN tending to coincide again at higher loads. The maximum error at a load of 2 kN is 15.8%, which occurs at the top of column CD for $e = 0.85$. This discrepancy is considered to be caused by the development of a failure surface under the footings which was not exactly represented in the analysis.



(a) $e=0$



(b) $e=0.85$

FIGURE 8.15 LOAD-BENDING MOMENT GRAPHS OF SPACE FRAME

ABC in figure (8.13) represents the actual stress-strain curve of a point in the soil. As the load increases, more and more elements in the soil reach the post-peak zone BC of their stress-strain curves. As the negative value of G in this portion introduces difficulties in the solution of the simultaneous equations, the spline function followed the straight line BD with a slope equal to that of the curve at B. It is considered that since in reality the soil elements fail and follow the drooping curve BC, a body of the soil under the footings rotates in a slip surface causing the increased column moments. Following curve BD in the analysis could not reproduce this failure. This may be the cause for the difference between the theoretical and the experimental bending moments at higher loads.

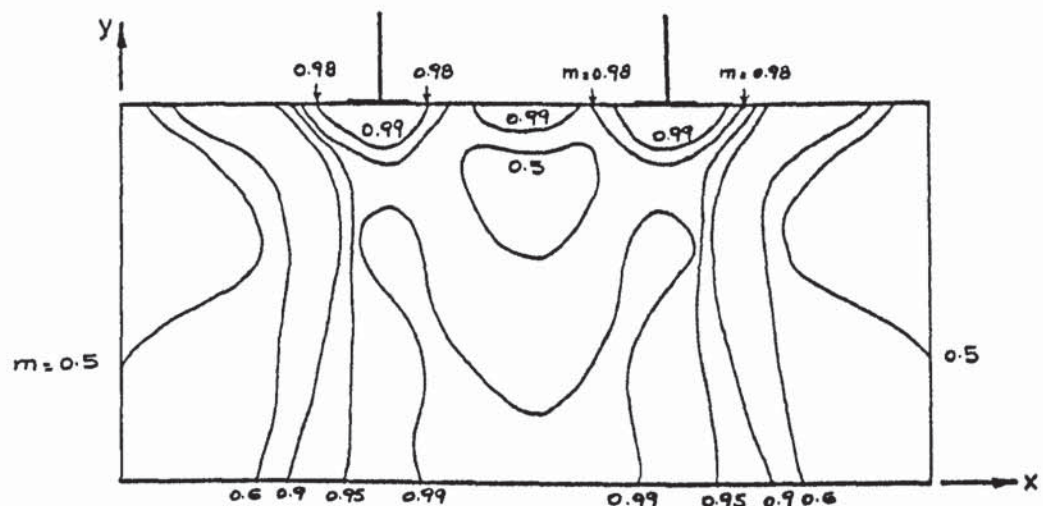
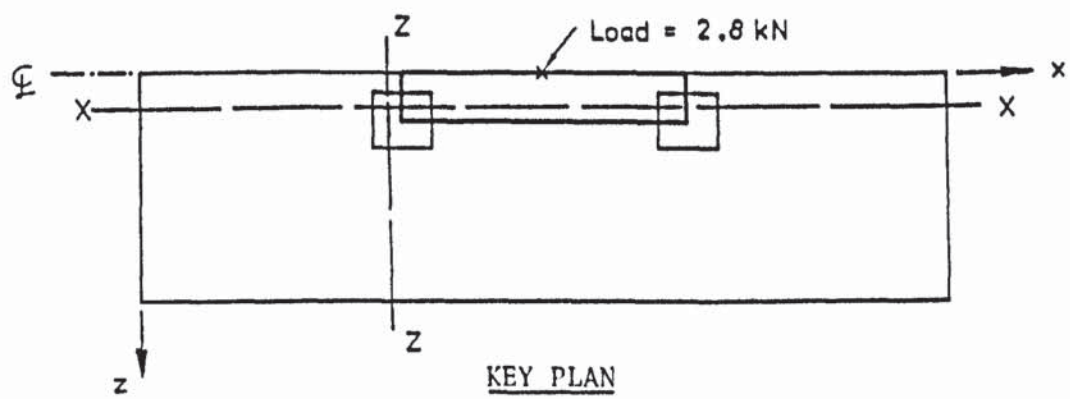
8.3.4 Stresses in the soil

The contours of the various stresses in the soil under this frame have been given by Majid and Cunnell (1976) and are not repeated here. A distinct column of high vertical stress directly under the footings was also observed by the author. The contours of $m = \cos\beta$, in the two vertical planes passing through the left footing, A, of the frame are shown in figure (8.16) for $e = 0$. Here β is the angle between the major principal stress and the vertical. The concentration of the lines of high m under the footings shows that the major principal stresses were nearly vertical under the footings.

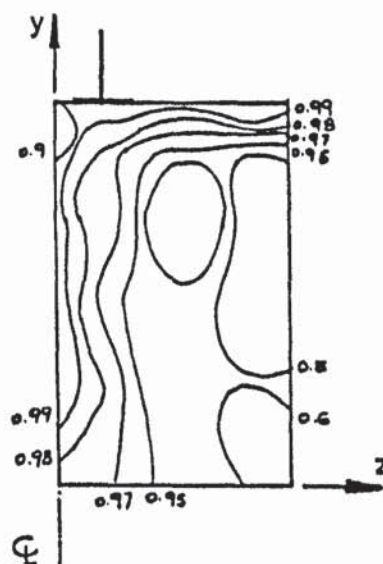
8.4 RESULTS OF MODEL B - THE BOX CULVERT

8.4.1 Deflections

As the box culvert was loaded along the centre line EI, at



(a) SECTION X-X



(b) SECTION Z-Z

FIGURE 8.16 CONTOURS OF DIRECTION COSINE m OF THE MAJOR PRINCIPAL STRESS FOR $e = 0$

points E, F, G and H, see figure (8.17), the settlements of points on the edges AC and BD were nearly uniform. When the load was applied along the edge AC at points J and K, edge AB settled more than CD. In fact CD moved upwards. The vertical displacements of point E are plotted against the applied load in figure (8.17) for various eccentricities. The theoretical curves, shown by the dashed lines, underestimate the experimental results and the errors accumulate as the load increases. The error at a load of 4 kN is 12% for case B1 falling down to 4% for B6. In general, however, there is good agreement between the theoretical and the experimental results.

The settlement of point E is plotted against the eccentricity e_x in figure (8.18a) for load cases B1, B2, B3 and B4 with $e_z = 0$ at a load of 4 kN. As the load moves from H to E, the deflection at E increases steadily. For $e_x = 1$, the settlement of the same point is plotted against the eccentricity e_z in figure (8.18b). As the load moves along EA, with e_z increasing, the settlement at E increases further. With $e_x = 1$, the settlement at E is 7.1% higher for $e_z = 0.72$ than for $e_z = 0$.

Both experimental and theoretical observations showed that, with $e_x = 1$, the side CD moved up away from the soil. This happened when e_z was 0.36 and 0.72. A view of the culvert tested with $e_z = 0.72$ is shown in plate (8.1) where it is noticed that a part of the culvert is separated from the soil. Confirmation of this separation theoretically is given later. Evidently, the separation of the culvert base from the soil reduces the contact area and aggravates the settlement of the part in contact.

In figure (8.19), the vertical displacement of point C is

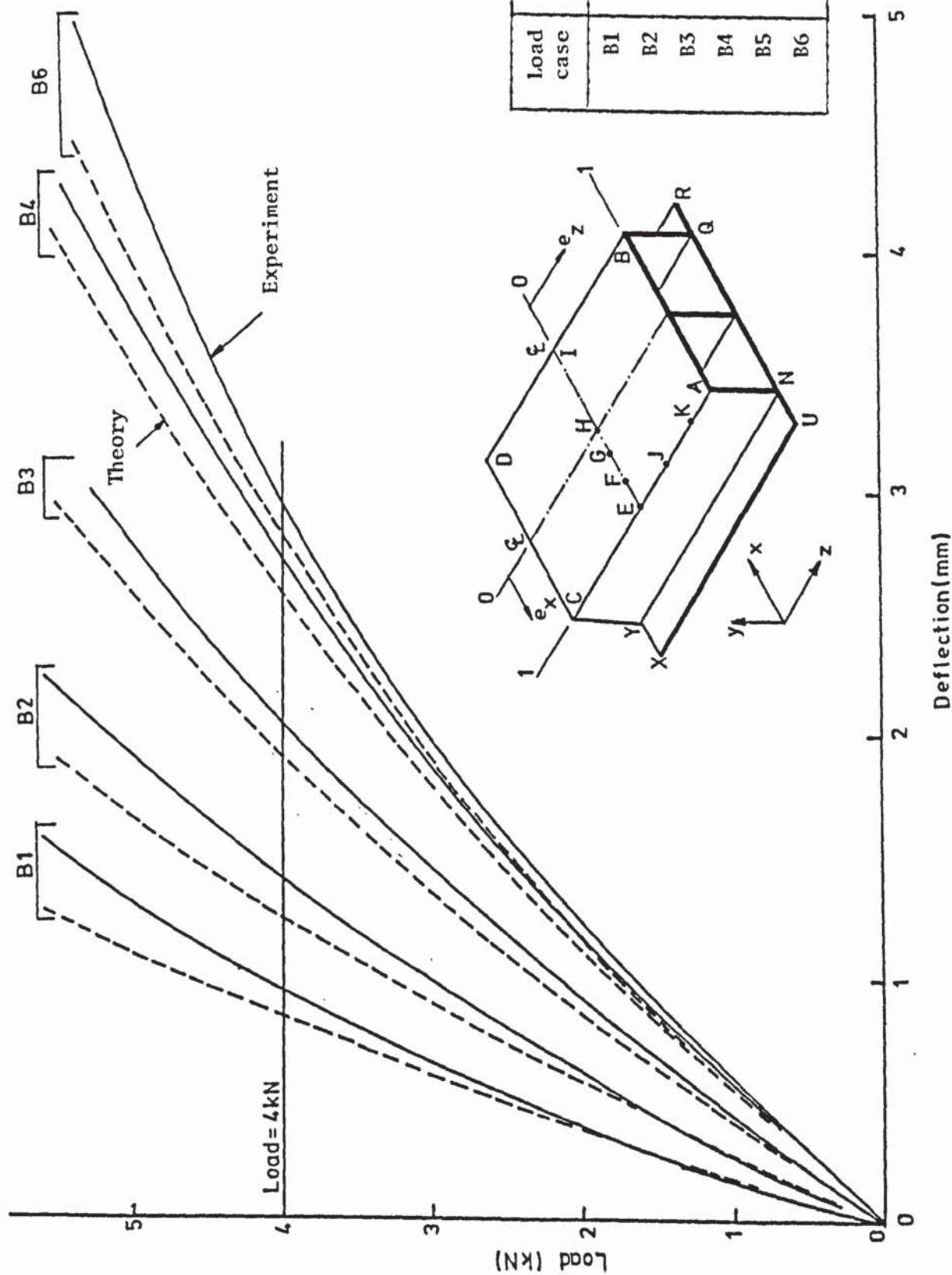


FIGURE 8.17 VERTICAL DEFLECTIONS OF POINT E ON THE BOX CULVERT

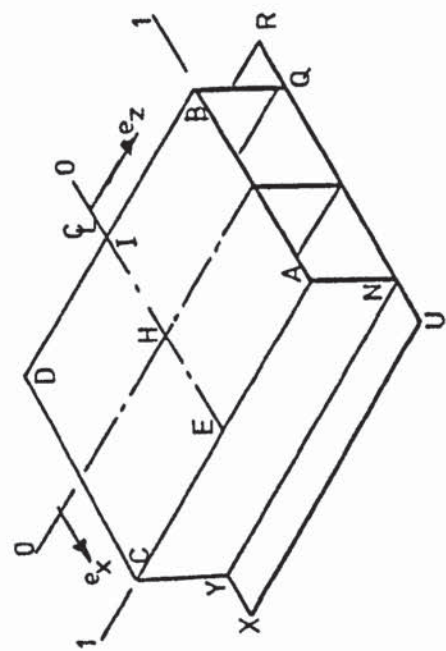
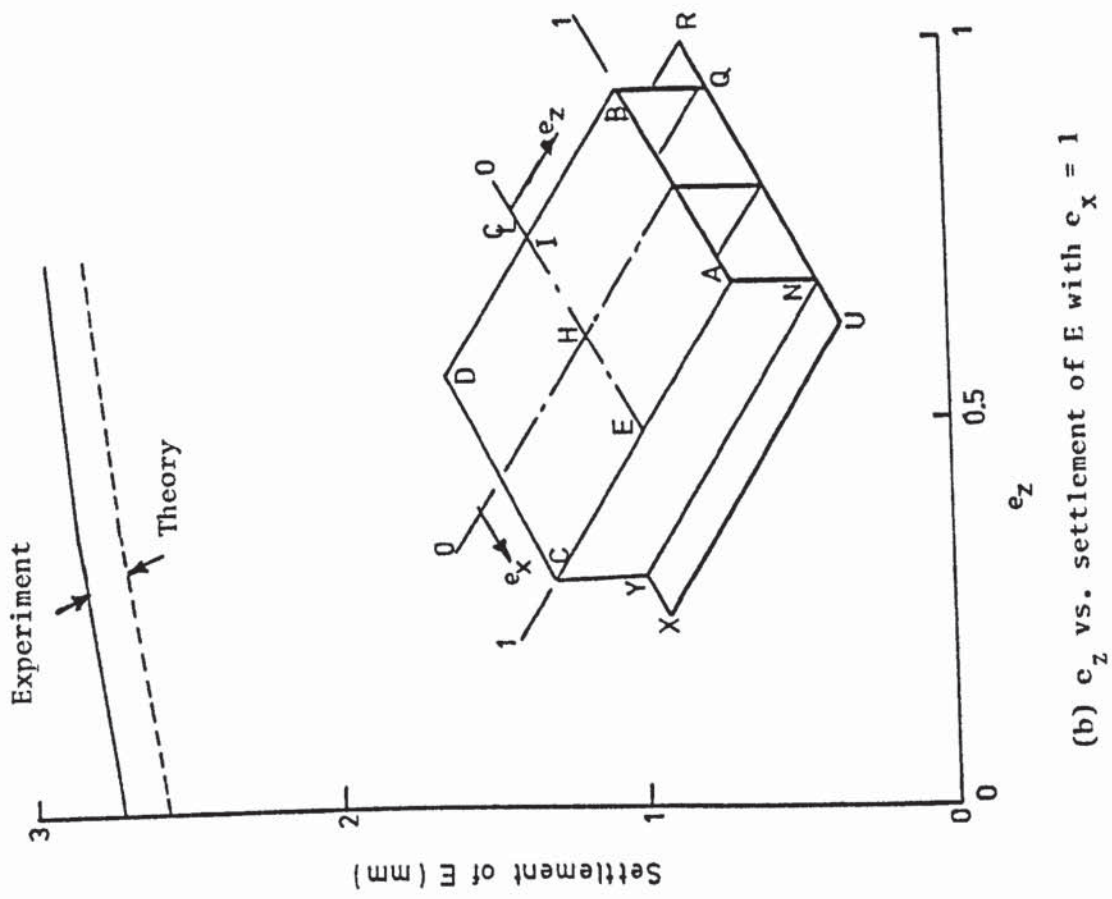
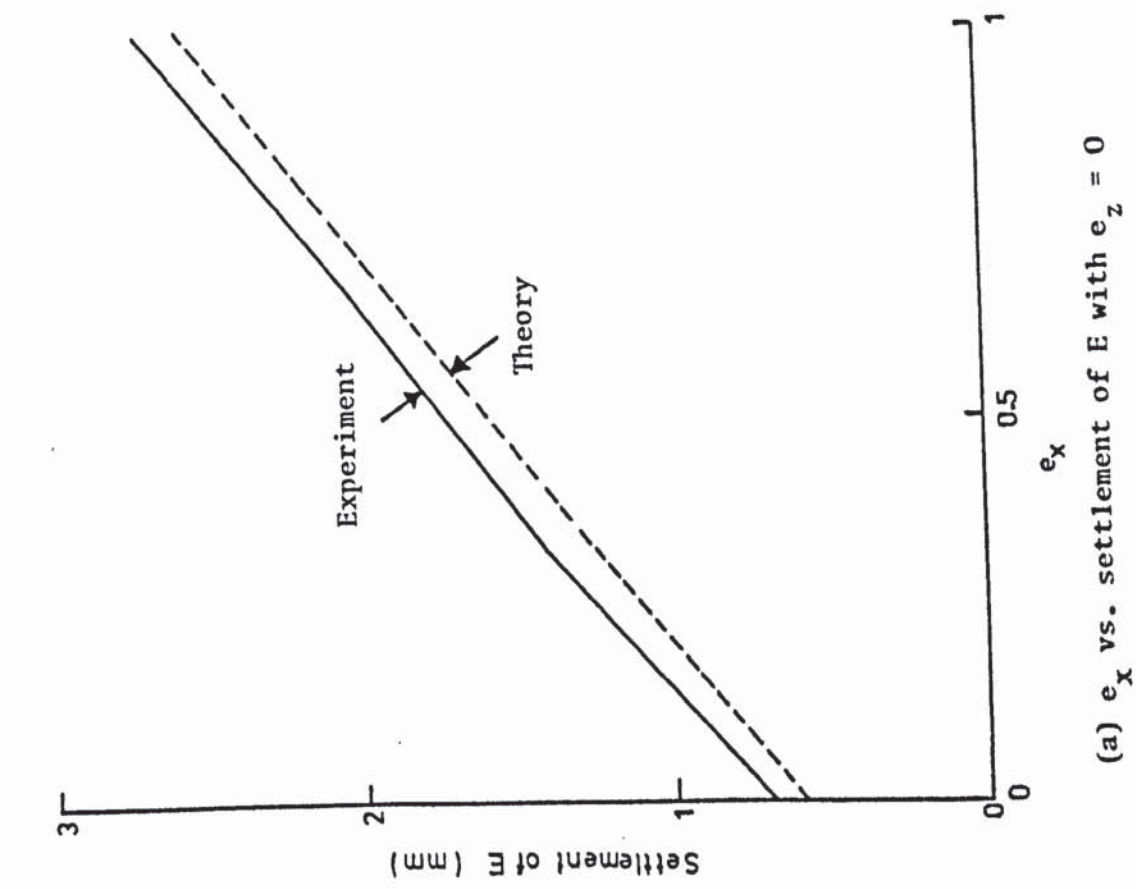


FIGURE 8.18 SETTLEMENTS OF POINT E OF BOX CULVERT AT A LOAD OF 4 kN

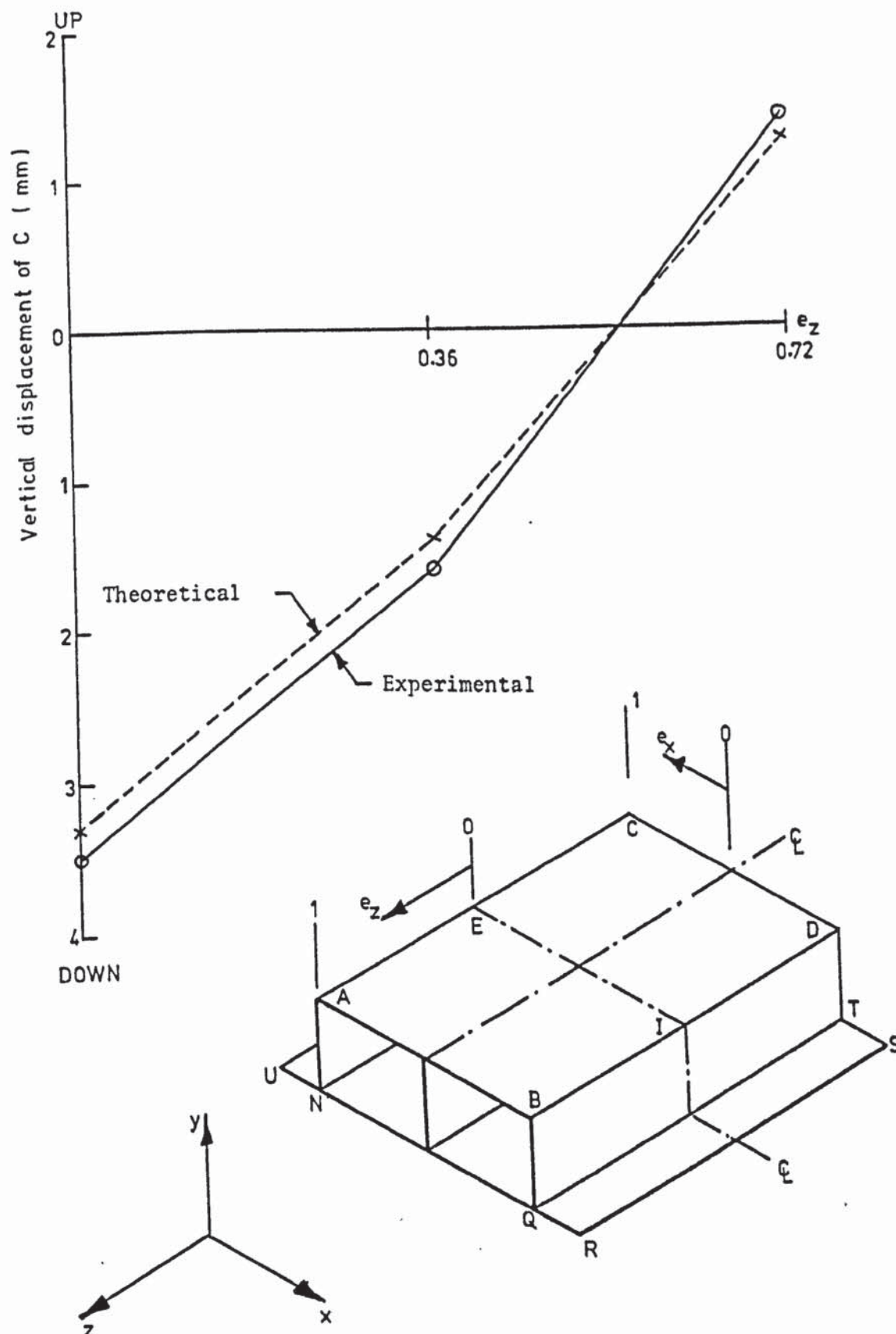


FIGURE 8.19 VERTICAL DISPLACEMENT OF POINT C WITH INCREASING e_z FOR $e_x = 1$ AND LOAD = 4.8 kN

plotted against the eccentricity e_z . This is when the applied load is 4.8 kN and $e_x = 1$. At $e_z = 0$, point C moves down by some 3.5 mm. As e_z increases, the downward settlement of C reduces and at $e_z = 0.72$, this point moves up by 1.4 mm.

The behaviour of the culvert is in direct contrast to that assumed in conventional analyses in which the load is assumed to be distributed on infinitely flexible area. In this manner, the stiffness of the structure is neglected and movements are considered to be downward throughout.

A comparison of the experimental and the theoretical load-displacement diagram of corner A is shown in figure (8.20) for load case B6 with $e_x = 1$ and $e_z = 0.72$. Curves (1) and (2) indicate the horizontal displacements δ_x and δ_z respectively and curve (3) shows the vertical displacement δ_y . Although the culvert sways in the horizontal directions, the predominant displacement is in the vertical direction as the applied load is vertical. The displacements recorded by curves (1) and (2) are small but significant as they point out that the culvert is being distorted in three directions even under a vertical load.

The theoretical and the experimental displacements agree well in all the cases. The difference between the theoretical and the experimental values, at a load of 4 kN, are 19.2%, 13.5% and 4.4% for δ_x , δ_z and δ_y respectively. The higher errors in the first two displacements are considered to be experimental as it was found to be very difficult to measure such small values.

For load case B6, the culvert distorted as shown by the exaggerated diagram in figure (8.21). The relative vertical displacements of corners B, C and D with respect to corner A are shown by curves (1), (2) and (3) in figure (8.22). This figure relates to load

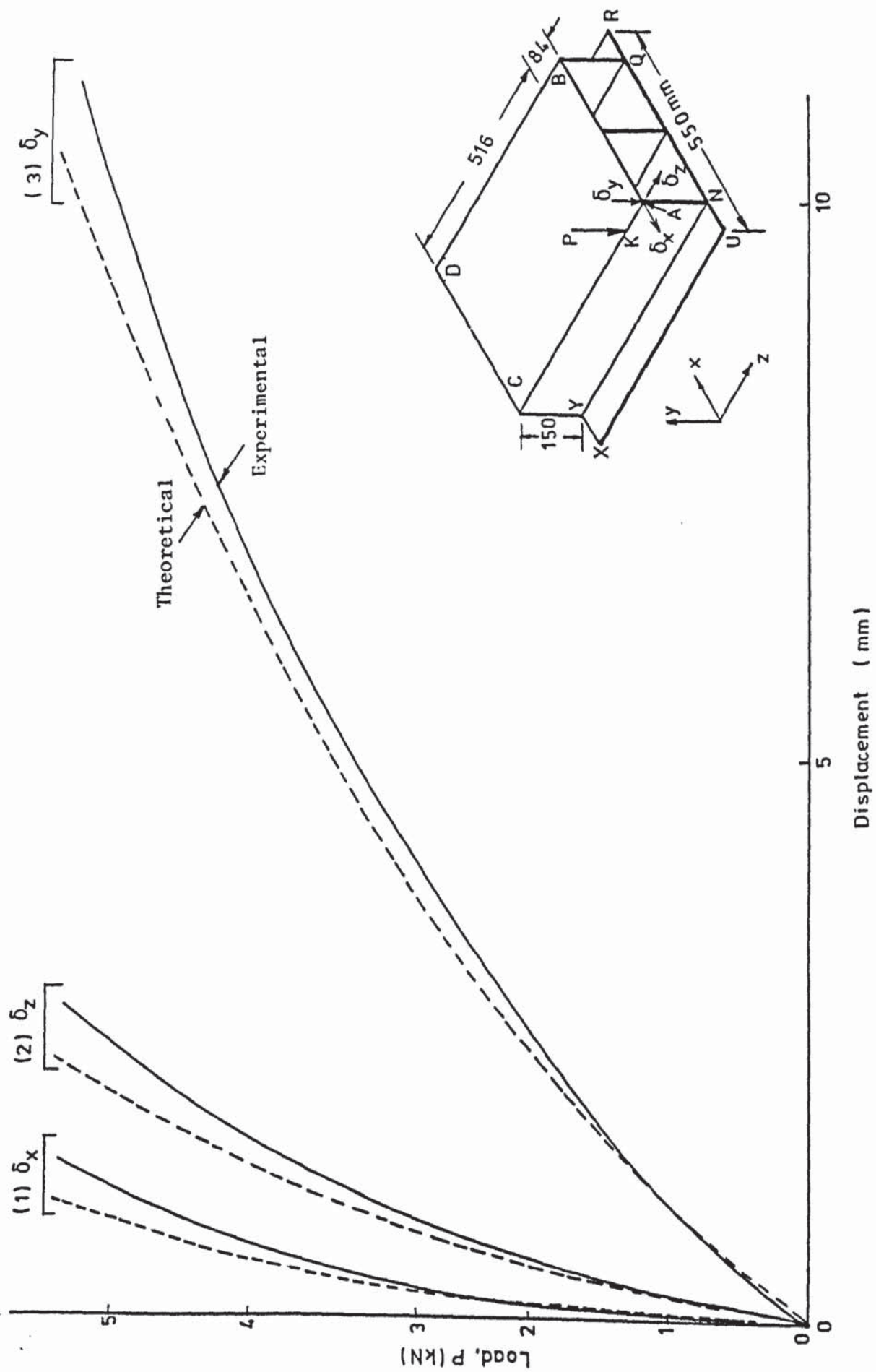


FIGURE 8.20 DISPLACEMENTS OF CORNER A OF BOX CULVERT; $e_x = 1$, $e_z = 0.72$

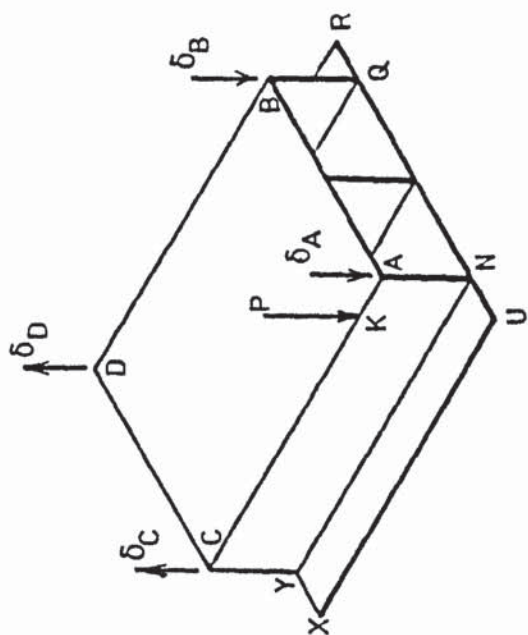
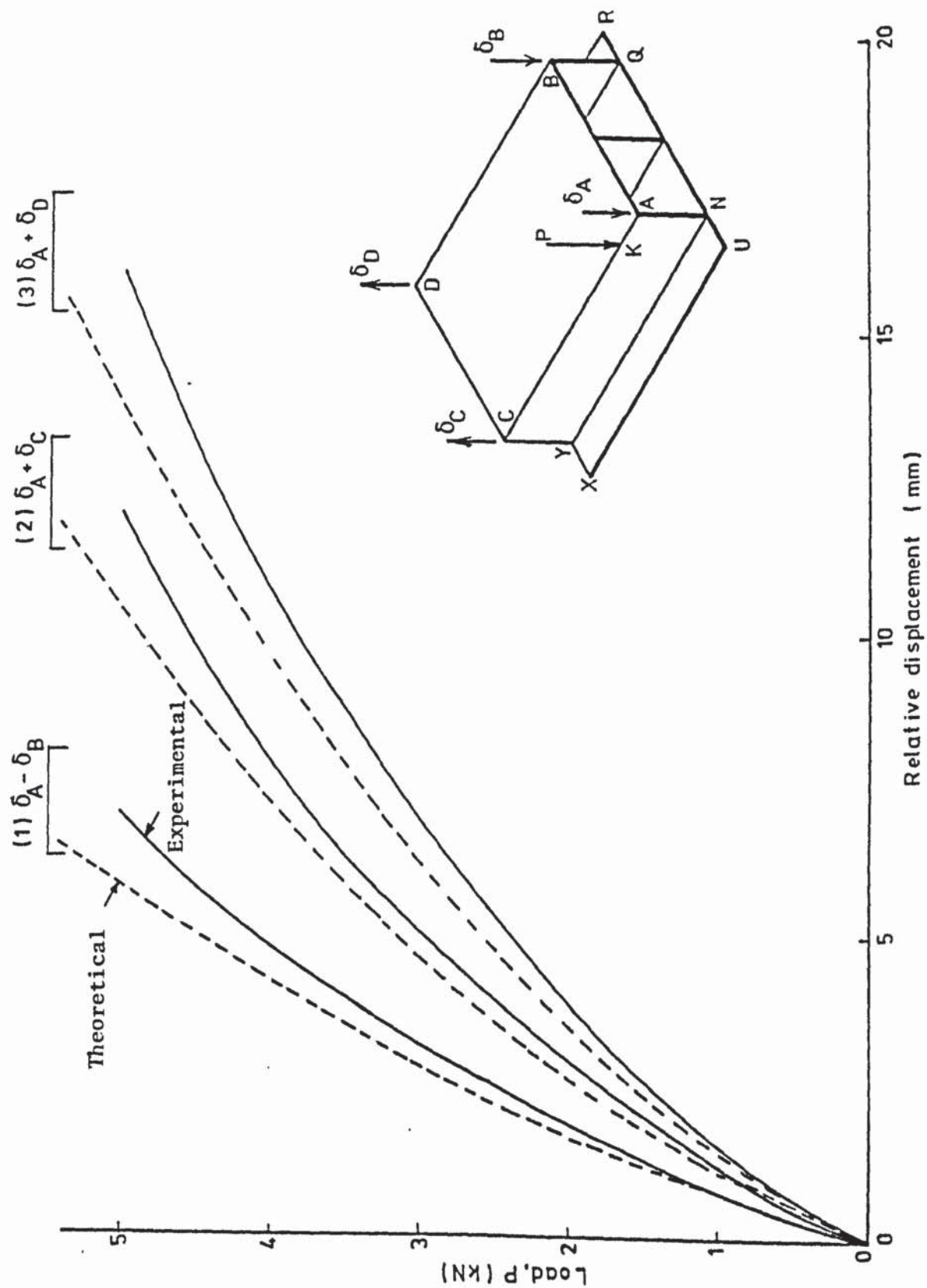


FIGURE 8.22 RELATIVE VERTICAL DISPLACEMENTS OF THE CORNERS OF BOX CULVERT
FOR LOAD CASE B6

case B6 with $e_x = 1$ and $e_z = 0.72$, see figure (8.17). Corner B, being nearer A than the others, suffers the least relative displacement and corner D, being the furthest, suffers the most. The higher relative displacements of C and D are also caused by the fact that they move upwards while A and B both move down. Figures (8.21) and (8.22) indicate that the culvert undergoes displacements, distortions and a rigid body rotation.

The theoretical curves in figure (8.22) underestimate the experimental values by 11.3%, 8.2% and 9.4% for corners B, C and D respectively at a load of 4 kN. Generally, however, there is good agreement between the theory and the experiment.

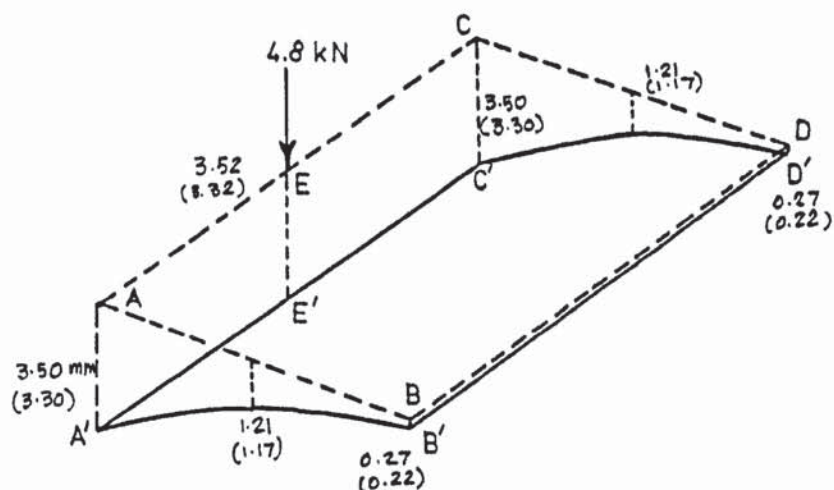
The deflected shape of the top plate ABCD of the culvert for load cases B4, B5 and B6 are shown in figures (8.23a, b and c) respectively. The diagrams are plotted for the vertical displacements only at a load of 4.8 kN. The theoretical values are shown in the parentheses beside the experimental ones. The percentage errors at corner A which suffers the largest displacement are shown beside each diagram and do not exceed 9.3%.

8.4.2 Tension separation

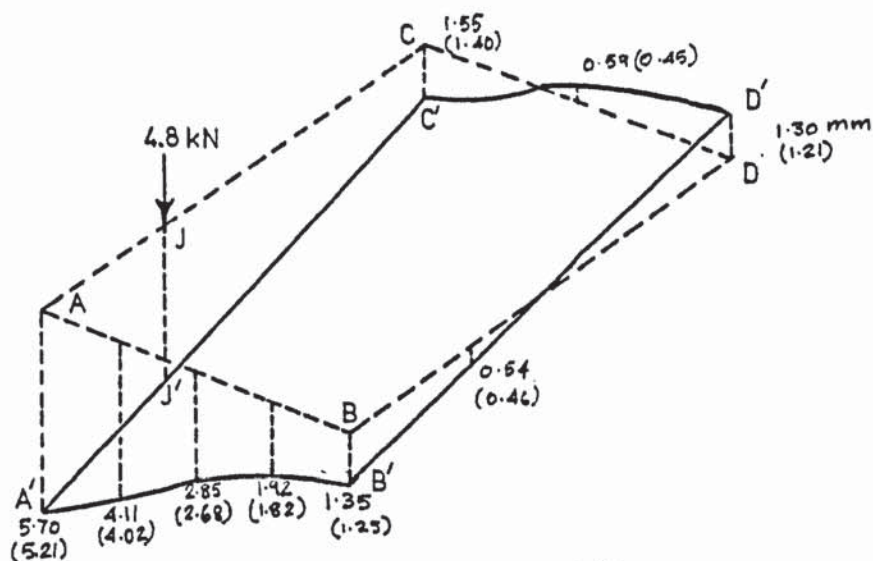
In cases B5 and B6, as the applied load was increased, part of the base and wall BDQT, see figure (8.2), separated from the soil. To cater for the separation in the analysis, dummy joints were introduced and cracks were allowed to take place. Tensile stresses developed at some of these joints and the analysis followed the cracks as the load was gradually increased.

Figure (8.24) shows the progress of the separation of base URXS of the culvert from the soil for case B5 and figure (8.25) shows it for case B6. The crosses on the diagrams indicate a

- Error at A = 5.7%
- (a) Load case B4
- $e_x = 1, e_z = 0$



- Error at A = 8.6%
- (b) Load case B5
- $e_x = 1, e_z = 0.36$



- Error at A = 9.3%
- (c) Load case B6
- $e_x = 1, e_z = 0.72$

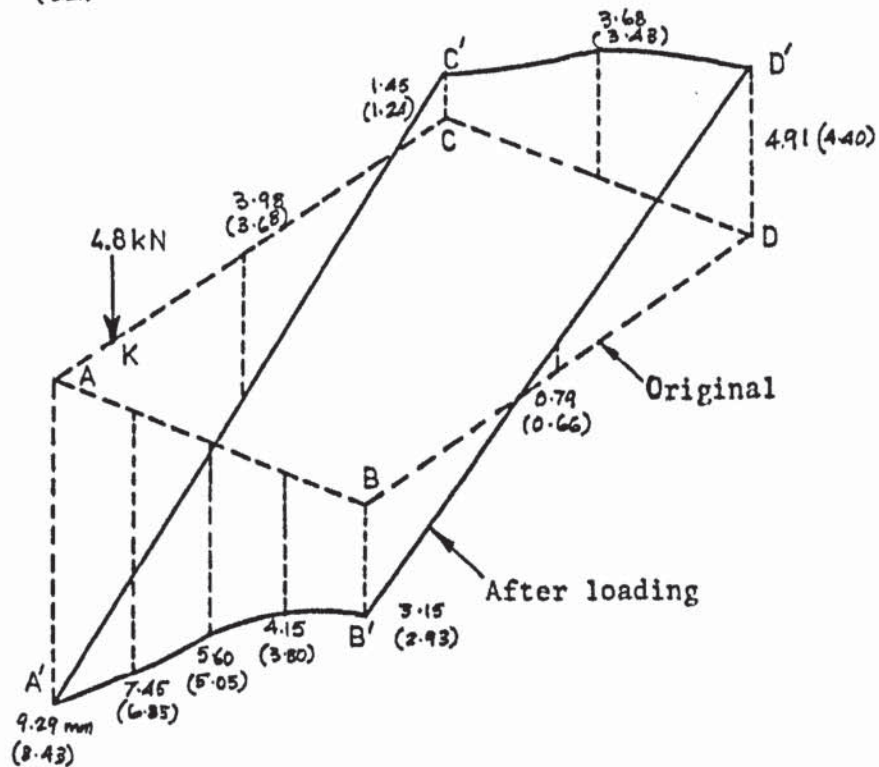
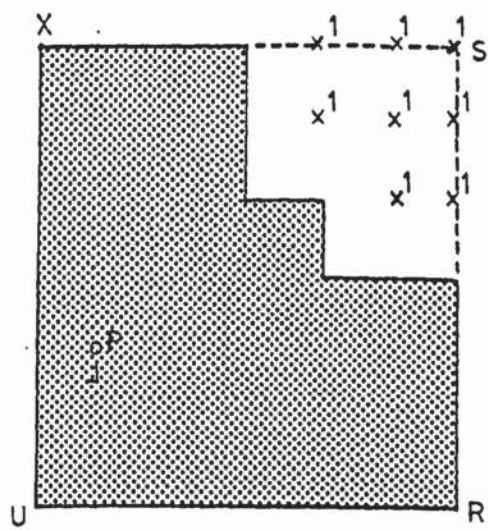
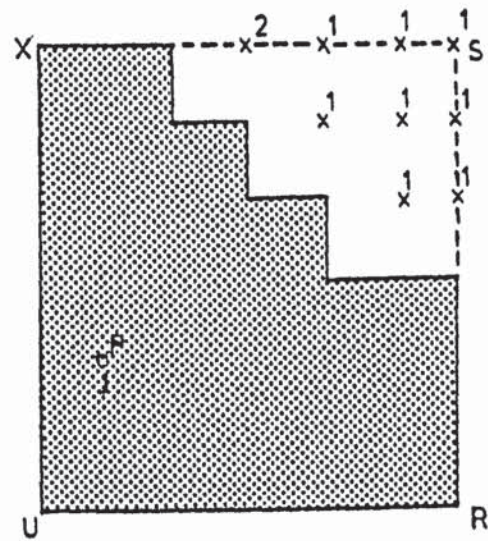


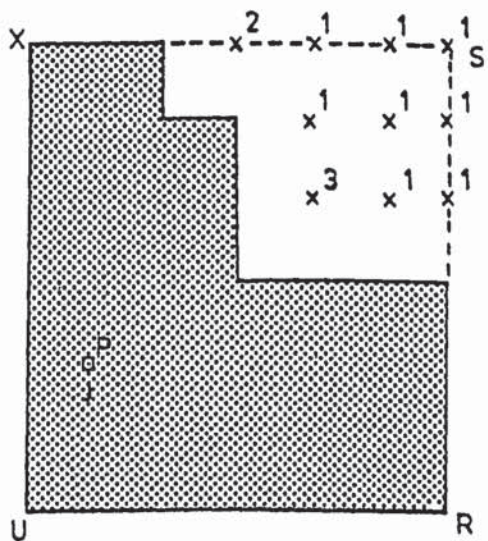
FIGURE 8.23 DEFLECTED SHAPE OF THE TOP PLATE OF CULVERT



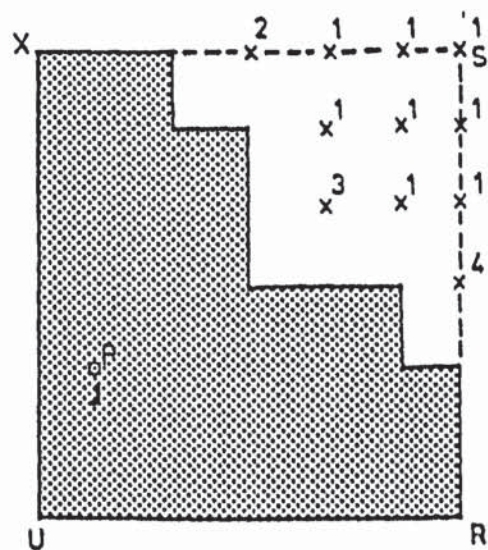
1. $P = 0.6 \text{ kN}$



2. $P = 1.2 \text{ kN}$



3. $P = 1.8 \text{ kN}$



4. $P = 2.4 \text{ kN}$

No change occurs
after this load


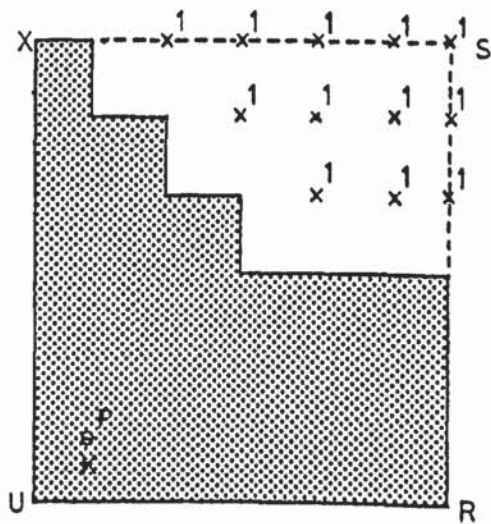
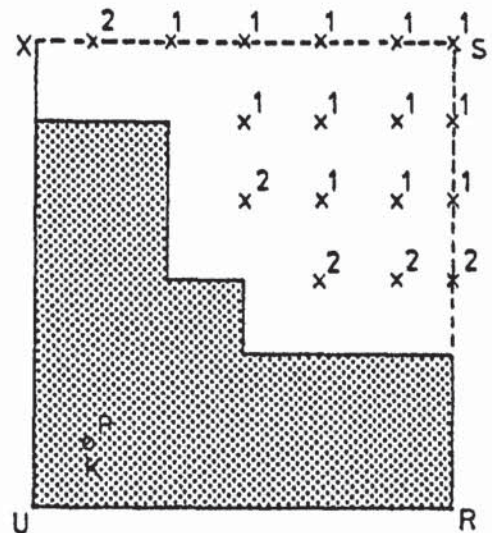
x Joints separated from ground
 Part of base fully in contact with ground

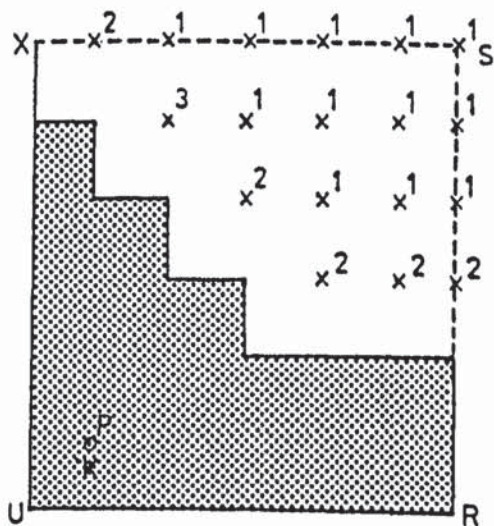
FIGURE 8.24 PROGRESS OF SEPARATION OF BASE OF CULVERT,
LOAD (CASE B5) ACTING AT J



1. $P=0.6 \text{ kN}$



2. $P=1.2 \text{ kN}$



3. $P=1.8 \text{ kN}$

No change occurs after
this load

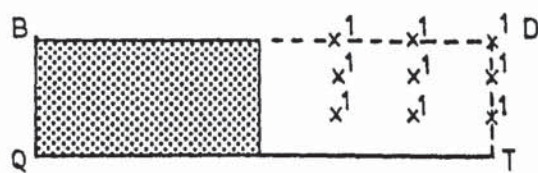
x Joint separated from
soil
Part of base fully in
contact with soil

FIGURE 8.25 PROGRESS OF SEPARATION OF BASE OF CULVERT,
LOAD (CASE B6) ACTING AT K

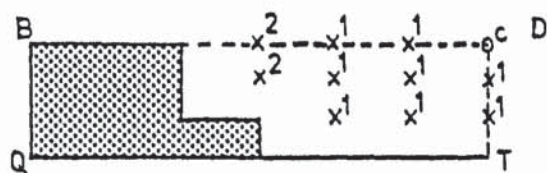
separated joint and the numbers on them indicate the order of formation of the cracks. The shaded part indicates the portion of the base still in contact with the soil. In figure (8.24) eight joints separated simultaneously at a load of 0.6 kN, acting at J. These joints are marked number (1). As the load was increased, the separated area increased. Each diagram in the figure represents the occasion when a new joint separated. At a load of 2.4 kN, (stage 4), a total of 11 joints separated and about 30% of the base lost contact with the soil. No further separation occurred after that.

As e_z was increased from 0.36 to 0.72 in case B6, with the load acting at K, the cracks became more widespread, see figure (8.25). Twelve joints separated at stage 1 at a load of 0.6 kN and 18 at stage 3 at a load of 1.8 kN. Although more joints separated in this case than in B5, a stable situation was reached earlier when cracks stopped spreading at a load of 1.8 kN. About 50% of the base lost contact with the soil.

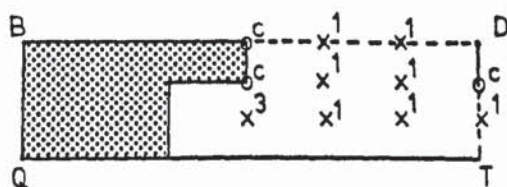
Figures (8.26) and (8.27) show the separation in the horizontal x direction of wall BDQT of the culvert obtained analytically for load cases B5 and B6 respectively. In addition to allowing a separation to take place, the computer program allows the closure of a crack when this takes place. The program can also reopen a crack if necessary at a later stage of the loading. In the figures a cross indicates a crack, the letter c indicates a crack that has just been removed and r indicates a joint where a separation takes place for a second or subsequent time. In both cases B5 and B6 the separation continued to alter its extent throughout the loading history.



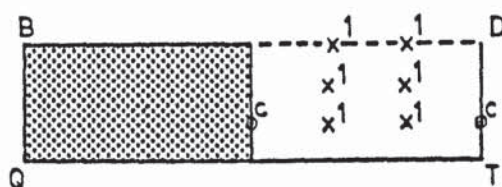
1. $P = 0.6 \text{ kN}$



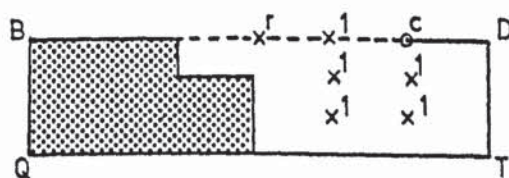
2. $P = 1.2 \text{ kN}$



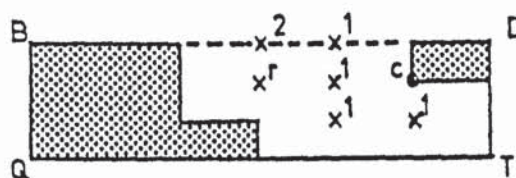
3. $P = 1.8 \text{ kN}$



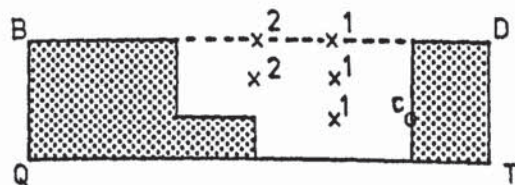
4. $P = 2.4 \text{ kN}$



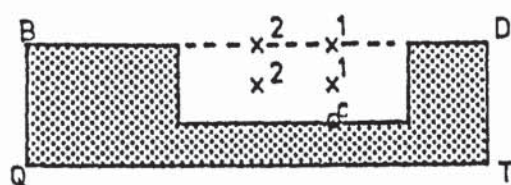
5. $P = 3.0 \text{ kN}$



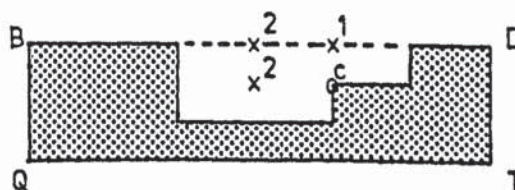
6. $P = 3.6 \text{ kN}$



7. $P = 4.2 \text{ kN}$



8. $P = 4.8 \text{ kN}$



9. $P = 5.4 \text{ kN}$

\times Joint separated from soil
 c Crack closed at this load
 x^r Crack reopened


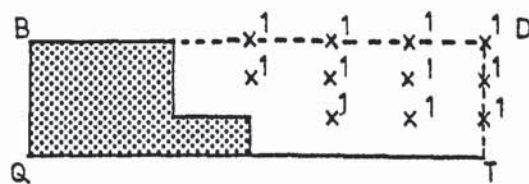
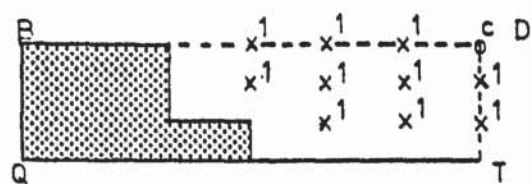
 Part of wall fully in contact with soil

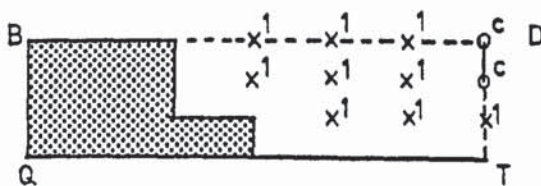
FIGURE 8.26 PROGRESS OF SEPARATION OF WALL BDQT, LOAD (CASE B5) AT J



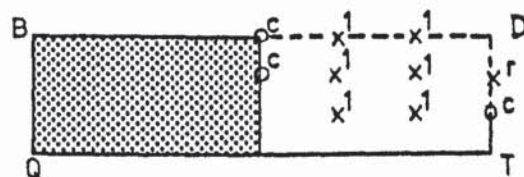
1. $P = 0.6 \text{ kN}$



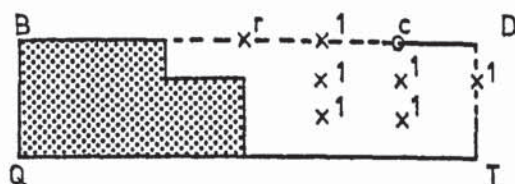
2. $P = 1.2 \text{ kN}$



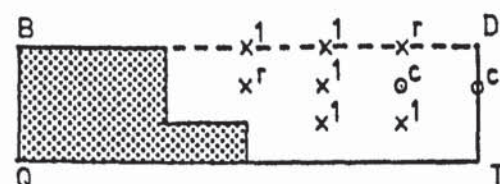
3. $P = 1.8 \text{ kN}$



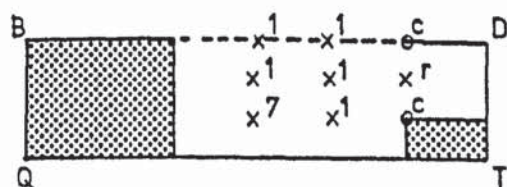
4. $P = 2.4 \text{ kN}$



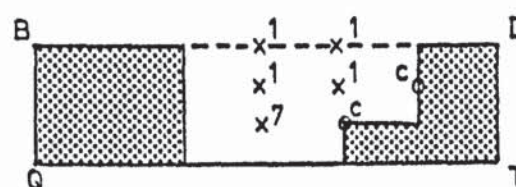
5. $P = 3.0 \text{ kN}$



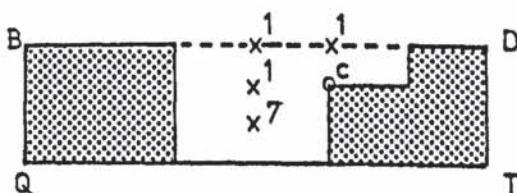
6. $P = 3.6 \text{ kN}$



7. $P = 4.2 \text{ kN}$



8. $P = 4.8 \text{ kN}$



9. $P = 5.4 \text{ kN}$

x Joint separated from soil

o^c Crack closed at this load

x^r Crack reopened


 Part of wall fully in contact with soil

FIGURE 8.27 PROGRESS OF SEPARATION OF WALL BDQT, LOAD (CASE B6) AT K

It is considered that as the load is increased, the part of the soil above the protruding base QTRS, see figure (8.2), is lifted up. This causes some of the cracks between this part of soil and wall BDQT to close. While 50% of the wall separated from the soil at a load of 0.6 kN, only 28% remained separated at the end of the analysis in load case B5. The sudden separation at a low load and the continuous change of the cracked configuration were also observed in case B6, as shown in figure (8.27). In this case 61% of the wall separated at a load of 0.6 kN and only 39% remained separated at the end of the analysis.

The width of a crack is initially zero and increases with the load. The variation of the width of separation with the load at points Z and T on the base of the culvert is shown in figure (8.28). It is noticed that the width of a crack increases when the eccentricity e_z increases from 0.36 to 0.72. The difference between the width of a crack for the two eccentricities is 78% at point Z and 77% at point T at a load of 4.8 kN. This example demonstrates the intricate behaviour of a structure-soil system. Such a behaviour is difficult to be traced experimentally or by an analysis of the structure or the soil on their own.

8.4.3 Bending moments

Strain gauges were fixed at several locations around the culvert, see chapter 7, to obtain the experimental values of the bending moments at these points. These bending moments are compared in this section with those obtained by analysing the complete culvert and the soil. They are also compared with the bending moments obtained by an analysis of the culvert ignoring the soil.

The finite element analysis of the culvert and the soil gave the bending moments at the centroids of the plate elements. The

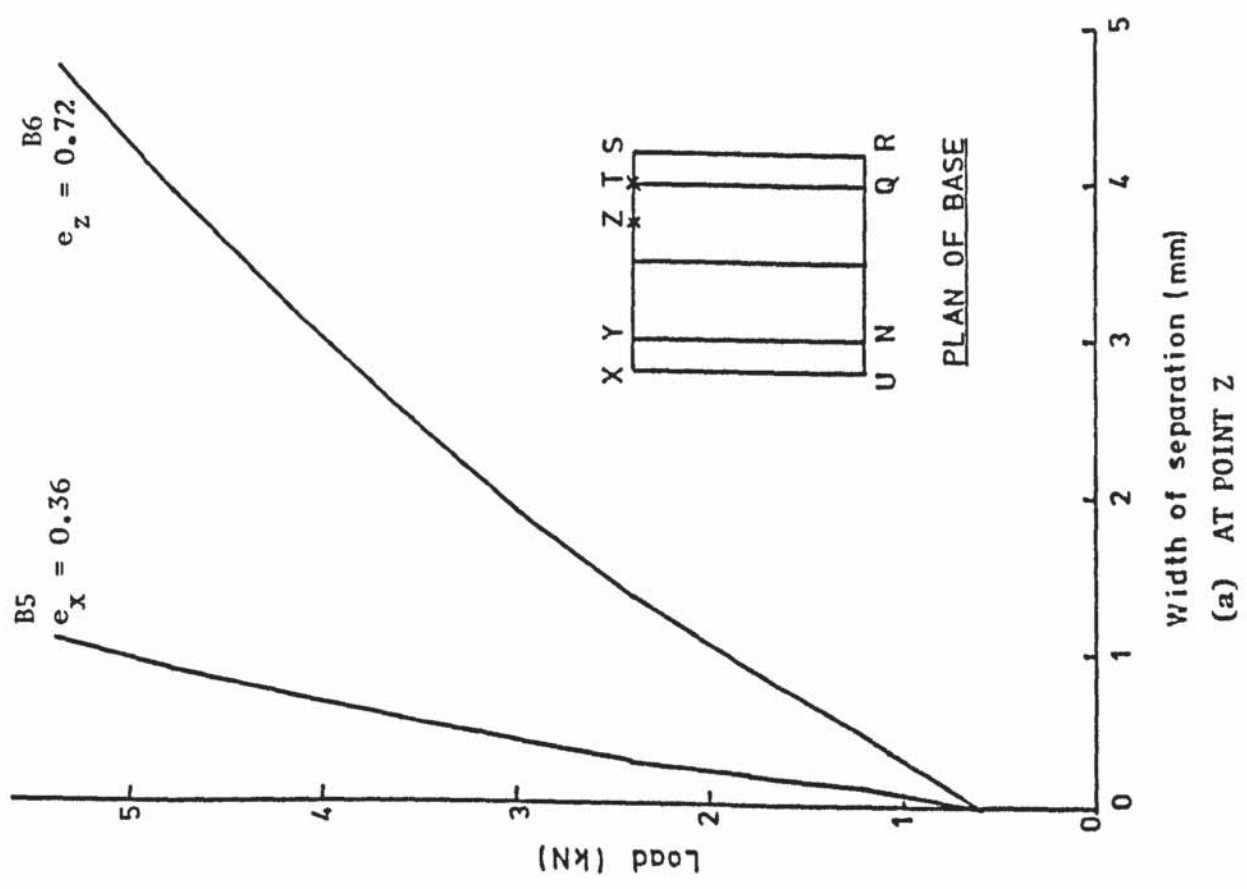
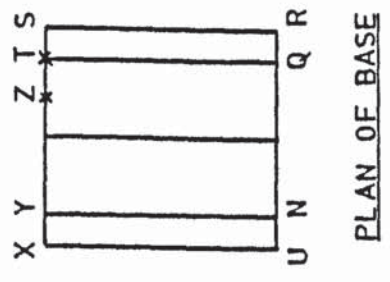
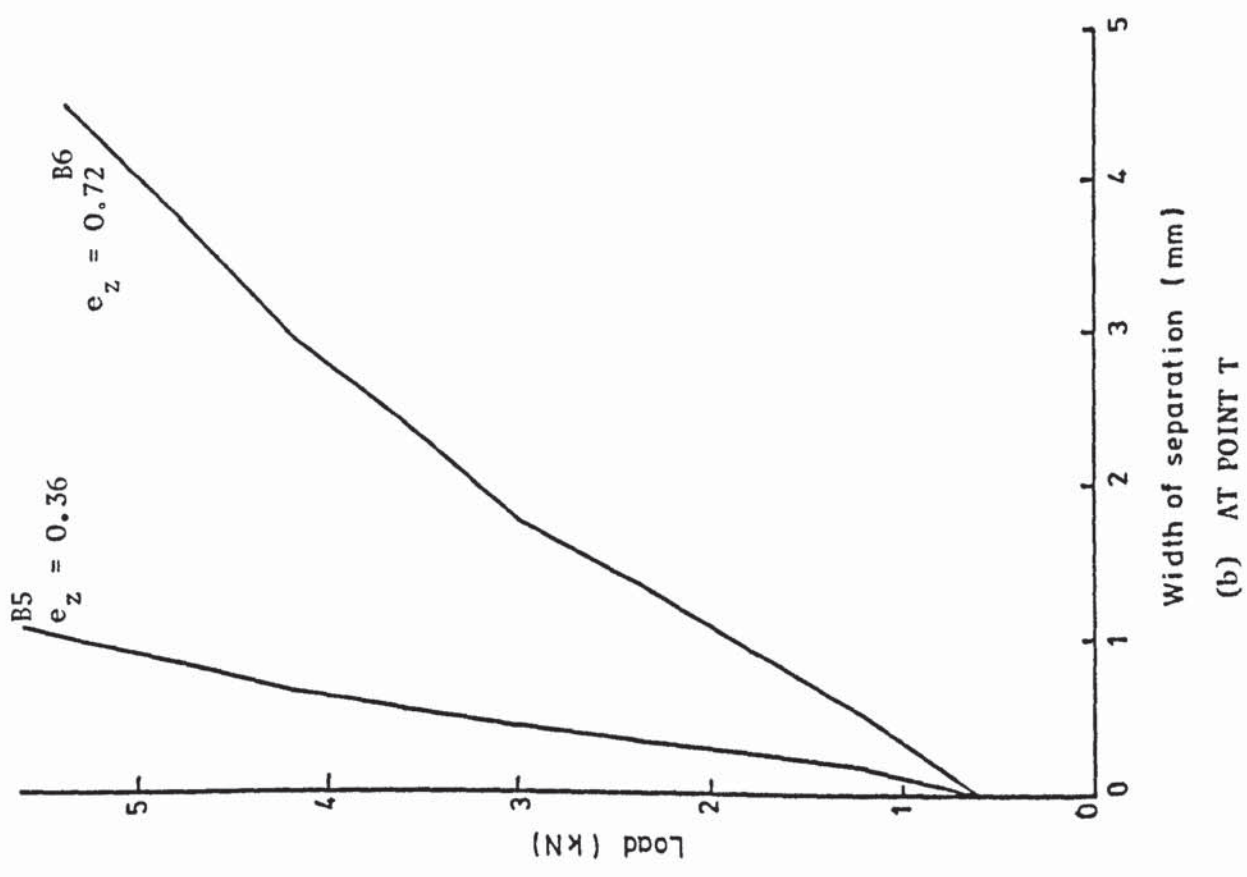


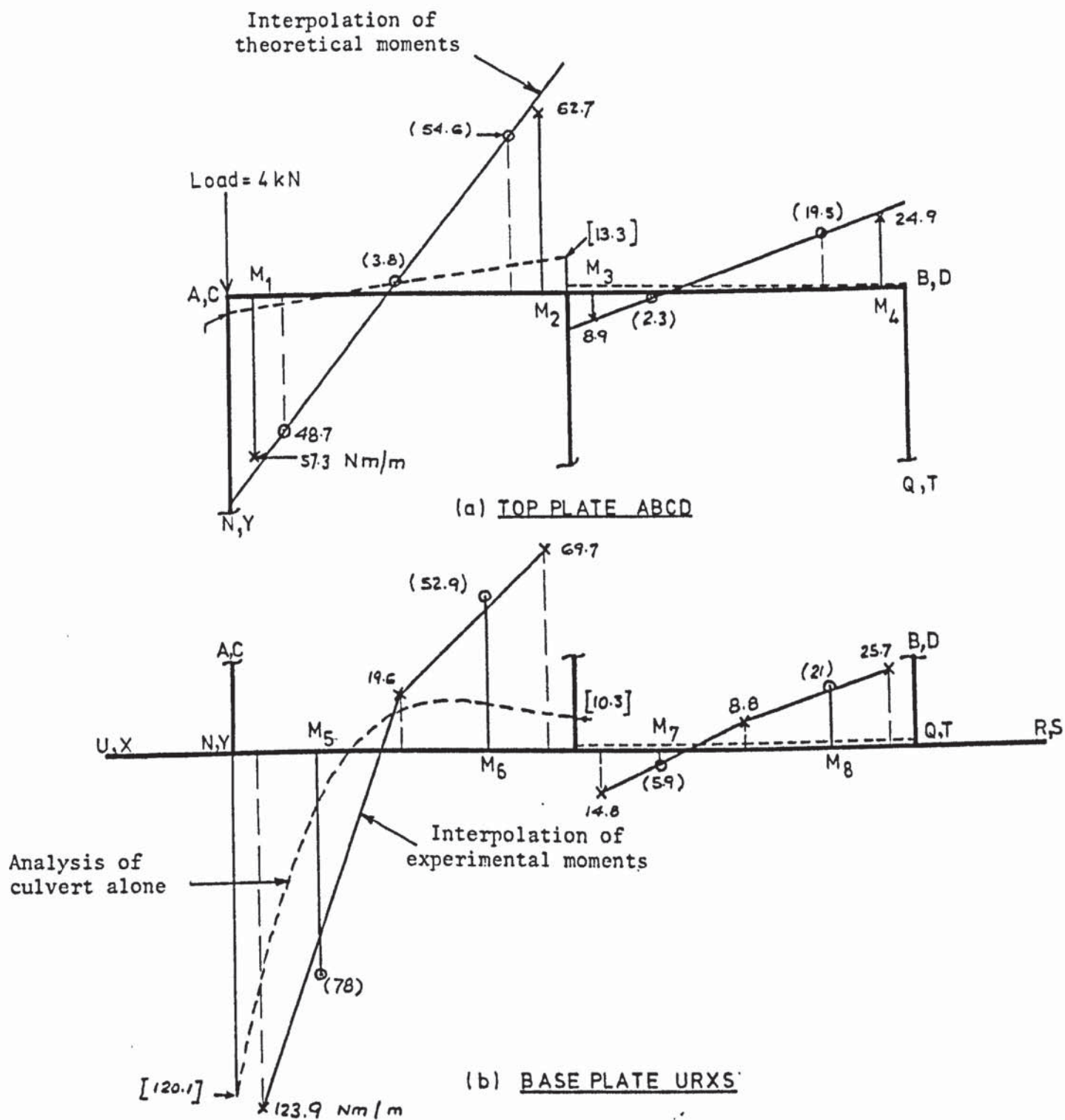
FIGURE 8.28 LOAD vs. WIDTH OF SEPARATION AT THE BASE OF CULVERT

strain gauge positions do not coincide with the centroids of these elements. To compare the theoretical and the experimental moments a linear interpolation of the values was performed. In figure (8.29a) the experimental bending moments are known at points M_1 , M_2 , M_3 and M_4 on the top plate ABCD and are shown by the values beside a cross. The theoretical bending moments are located by the circles and their values within the parentheses. In the top plate ABCD, the theoretical points are connected by straight lines and extended as shown in the figure. The theoretical bending moments at points M_1 , M_2 , M_3 and M_4 are then interpolated.

Figure (8.29b) shows the bending moments in the base plate URXS of the culvert. The theoretical bending moments are known at points M_5 , M_6 , M_7 and M_8 on this plate. In this case the experimental points shown by the crosses are connected and the interpolated experimental moments are obtained at M_5 , M_6 , M_7 and M_8 .

It is considered that, due to the non-uniform soil pressure, the bending moments in the base plate URXS do not vary linearly. Therefore, the experimental values obtained by a straight line interpolation at M_5 , M_6 , M_7 and M_8 are only approximate. In the top plate ABCD however the straight line interpolation was found to be reasonable. In one analysis of the culvert and the soil a fine division on this plate was used and 14 points with known theoretical moments were obtained. When plotted, these moments showed a straight line variation.

For comparison, a conventional analysis of the culvert alone, ignoring the soil, was also performed. For this analysis the contact pressure under base URXS was assumed to be uniform for the



○ (78) Analysis of culvert and soil

× 123.9 Experimental values

[120.1] Analysis of culvert alone

LOAD CASE B4; $e_x = 1$, $e_z = 0$

FIGURE 8.29 INTERPOLATION OF BENDING MOMENTS IN BOX CULVERT

central load case and linearly varying for the eccentric load cases, as shown in figure (8.30a and b). In both cases, a linearly varying horizontal pressure γy was assumed to act on the walls. Here, γ is the unit weight of the soil and y is the depth below the surface. A unit strip of the culvert was analysed using a plane frame analysis program. This was subjected to the above pressures and the external load. The applied load and the assumed contact pressure were under equilibrium and it was assumed that all the joints in the structure were free to displace. The bending moment diagrams obtained by this analysis are shown by the dashed lines in figure (8.29). It is noticed that there is a gross disagreement between these moments and those obtained experimentally and by analysing the culvert and the soil together.

A comparison of the bending moments at an applied load of 4 kN, at points M_1 to M_8 of the culvert, for various loading points, is shown in table (8.1). There is a good agreement between the experimental and the finite element analysis results for points M_1 , M_2 , M_3 and M_4 on the top plate ABCD for all cases. The analysis generally overestimates the moments but the maximum error is only 11.2% which occurs at M_3 for case B4. The analytical errors are larger at points M_5 , M_6 , M_7 and M_8 in the base plate URXS as the true experimental bending moments at these points are not known. Even so the maximum error is 20.4% which occurs at M_5 for load case B4.

The bending moments obtained by the non-interactive analysis of the culvert alone are significantly different from the experimental ones. While this analysis overestimates the moments by as much as 56.8% for case B1, it generally underestimates them for the eccentric load cases B2, B3 and B4. At point M_3 , for case B3, it

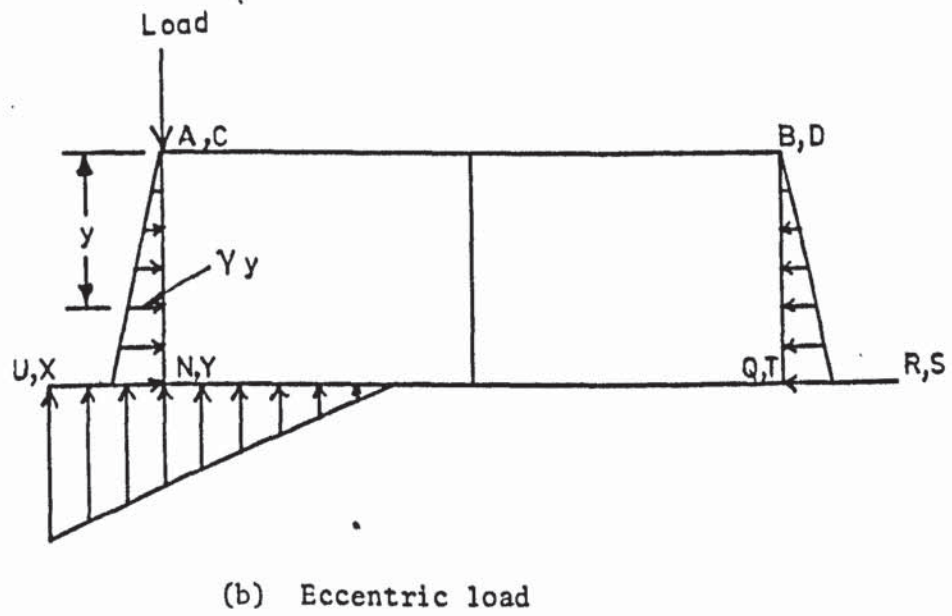
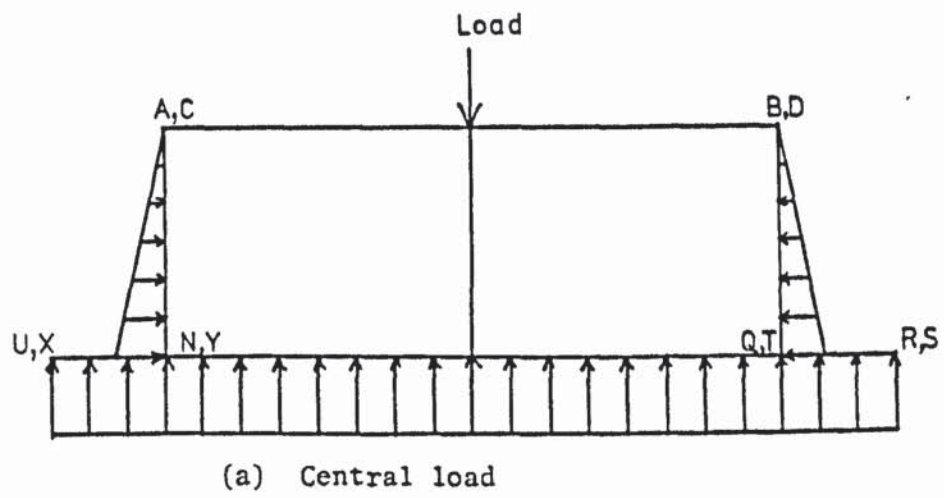


FIGURE 8.30 ASSUMED SOIL PRESSURE FOR CONVENTIONAL ANALYSIS

Load Case	Point	Experimental b. moment (Nm/m)	Finite ele- ment analysis (Nm/m)	% Error	Non-inter- active analysis (Nm/m)	% Error
B1 $e_x = 0$ $e_z = 0$	M ₁	-56.9	-62.5	9.8	-77.0	35.3
	M ₂	75.2	82.2	9.3	101.1	34.3
	M ₃	75.2	82.2	9.3	101.1	34.3
	M ₄	-56.9	-62.5	9.8	-77.0	35.3
	M ₅	-30.8	-34.8	13.0	-48.3	56.8
	M ₆	50.9	54.3	6.7	59.0	15.9
	M ₇	50.9	54.3	6.7	59.0	15.9
	M ₈	-30.8	-34.8	13.0	-48.3	56.8
B2 $e_x = 0.33$ $e_z = 0$	M ₁	-44.3	-43.4	-2.0	-99.8	125.3
	M ₂	27.7	30.4	9.7	6.5	-76.5
	M ₃	-49.9	-53.7	7.6	-37.0	-25.9
	M ₄					
	M ₅	-16.0	-14.3	-10.6	-44.2	176.3
	M ₆	22.8	20.7	-9.2	21.8	-4.4
	M ₇	54.9	56.4	2.7	51.1	-6.9
	M ₈	-32.5	-34.5	6.2	-31.4	-3.4
B3 $e_x = 0.67$ $e_z = 0$	M ₂	-42.8	-45.1	5.4	-77.5	81.1
	M ₃	3.5	3.4	-2.9	-35.0	1100.0
	M ₄	-34.9	-36.8	5.4	-1.6	-95.4
	M ₅	-23.7	-26.5	11.8	-19.8	-16.5
	M ₆	-17.5	-20.6	17.7	-19.7	12.6
	M ₇	29.8	33.2	11.4	22.5	-24.5
	M ₈	-24.5	-27.5	12.2	-8.0	-67.3
B4 $e_x = 1$ $e_z = 0$	M ₁	57.3	63.1	10.1	4.6	-92.0
	M ₂	-62.7	-68.6	9.4	-11.9	-81.0
	M ₃	8.9	9.9	11.2	-1.1	-112.4
	M ₄	-24.9	-27.1	8.8	-2.0	-92.0
	M ₅	64.8	78.0	20.4	20.3	-68.7
	M ₆	-49.1	-52.9	7.7	-15.1	169.2
	M ₇	5.1	5.9	15.7	-0.6	-111.8
	M ₈	-18.7	-21.0	12.3	-1.1	-94.1

TABLE 8.1 COMPARISON OF BENDING MOMENTS IN BOX CULVERT, LOAD = 4kN

shows a reverse sign of the moment and gives a magnitude 10 times higher than the actual.

It is noticed in figure (8.29) that as the load was applied on the left hand side wall ACNY, the non-interactive analysis shows negligible moments at points M_3 , M_4 , M_7 and M_8 on the right hand side of the culvert. In reality the right hand side suffers significant bending moments due to the non-uniform settlement of the structure. The culvert distorts due to the settlement and this causes increased moments throughout the structure.

8.4.4 Stresses in the soil

The distribution of the vertical stresses at various depths under the culvert is shown in figures (8.31), (8.32), (8.33) and (8.34) for load cases B1, B2, B3 and B4 respectively. The stresses are for the vertical section 4-4, shown on the top left hand side diagrams in the figures. This section was chosen because it was nearest to the centre of the culvert for which the theoretical stresses were calculated. In all the figures the applied load is 2.5 kN. The firm lines indicate the stresses obtained by the finite element analysis of the whole system. The dashed lines and the values in the parentheses are the stresses obtained by Boussinesq's solution using Newmark's charts. As the scale of these charts become very large at shallow depths, indicating the incompatibility of Boussinesq's solution at the surface, these latter stresses could not be obtained at a depth less than about 100 mm.

In figure (8.31), the contact pressure was assumed to be uniform when using the charts. This accounts for the relatively uniform pressure distribution obtained from these. On the other hand, as the point load was applied directly on the central wall, the finite

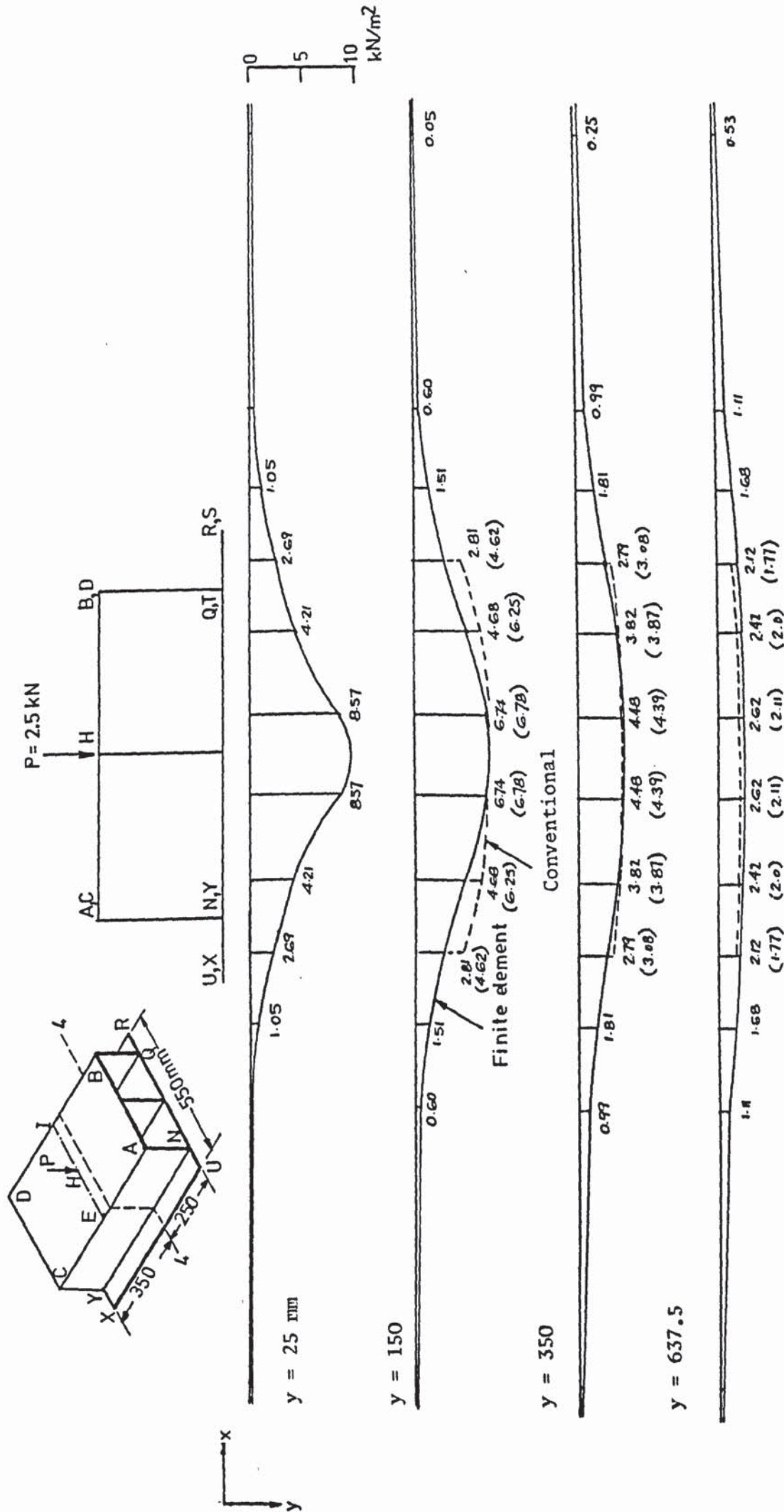


FIGURE 8.31 DISTRIBUTION OF VERTICAL STRESS AT VARIOUS DEPTHS UNDER BASE URXS OF THE CULVERT FOR LOAD CASE B1 AT SECTION 4-4

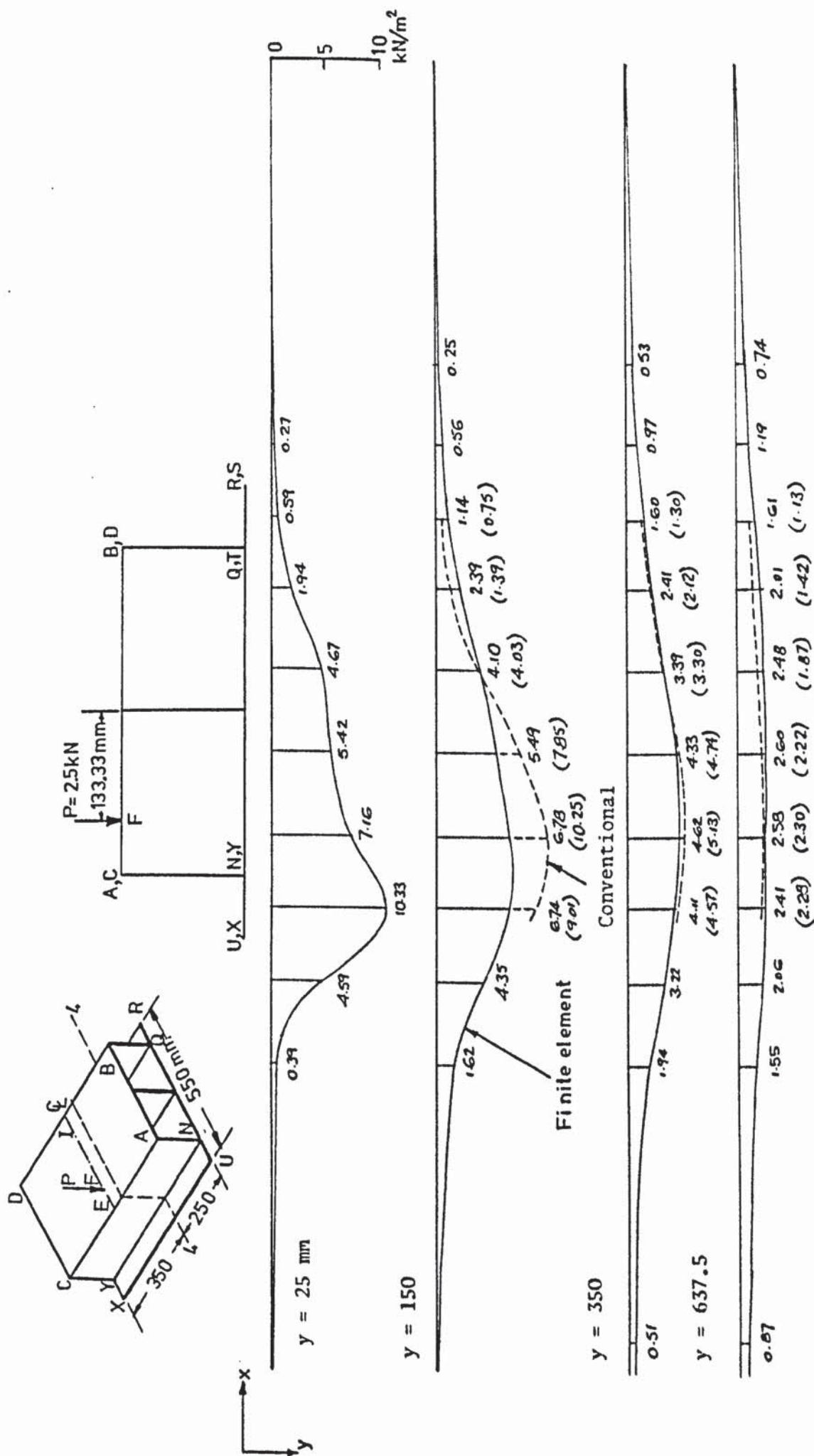


FIGURE 8.33 DISTRIBUTION OF VERTICAL STRESS AT VARIOUS DEPTHS UNDER BASE URXS OF THE CULVERT AT SECTION 4-4 FOR LOAD CASE B3

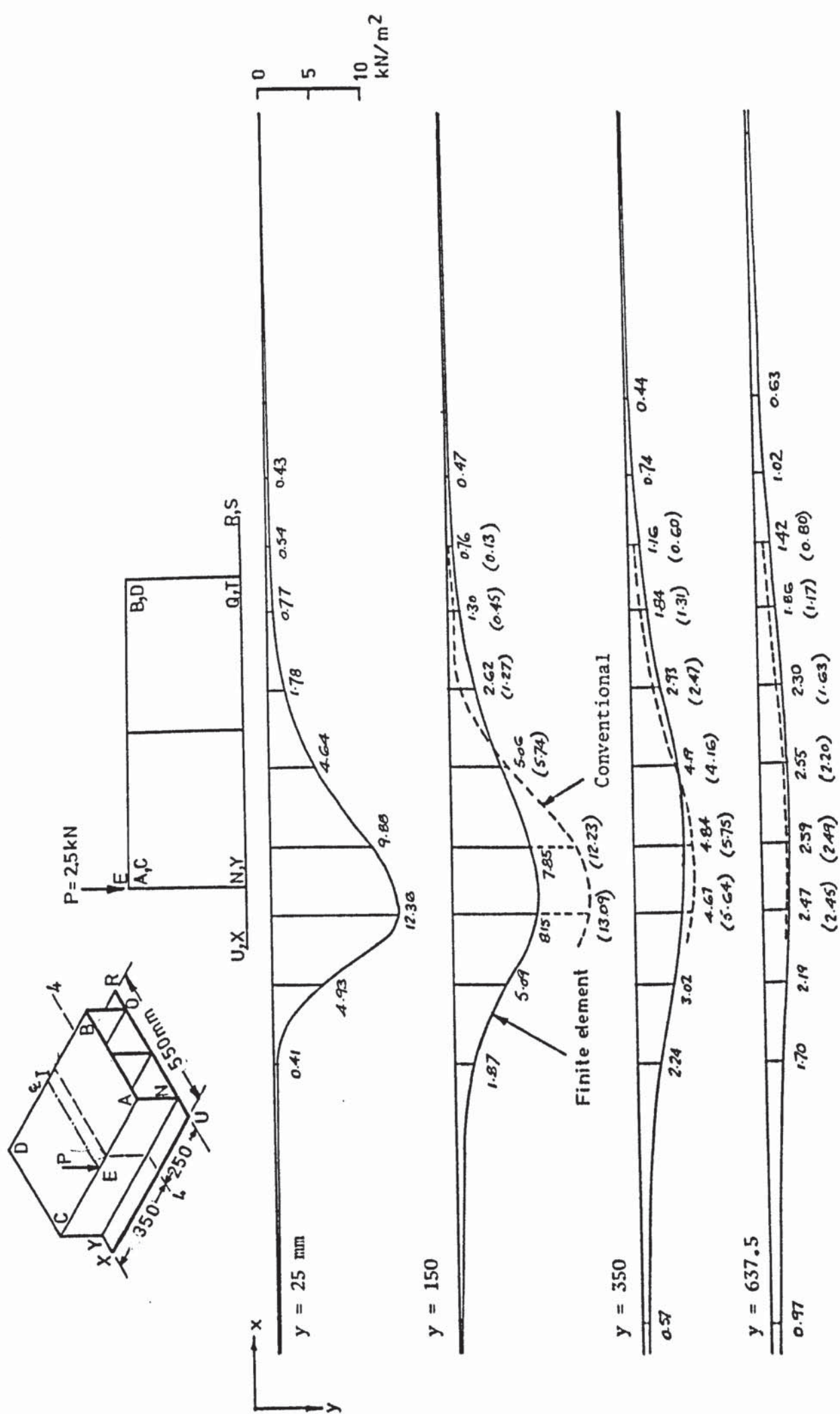


FIGURE 8.34 DISTRIBUTION OF VERTICAL STRESS AT VARIOUS DEPTHS UNDER BASE URXS OF THE CULVERT AT SECTION 4-4 FOR LOAD CASE B4

element analysis gives a high stress at the centre. The difference between these and Boussinesq stresses reduces with depth and the two curves almost coincide at a depth of 350 mm. The finite element stresses are slightly higher than the Boussinesq ones at 637.5 mm due to the proximity of the rigid base of the sand tank. The influence of this rigidity is neglected in Boussinesq's solution as the soil is assumed to be a semi-infinite continuum.

When the load is applied at points G and F in figure (8.32) and (8.33) respectively, a concentration of stress directly under the left hand side wall ACNY and the central wall is observed. As the load rests on wall ACNY in figure (8.34), the stresses are high directly under it and diminish rapidly away from it. The disagreement between the finite element and the Boussinesq stresses increases with the eccentricity of the load as the walls of the culvert interact with each other and share the load. The difference between the two stresses at the maximum ordinate is 0.6%, 9.8%, 51.2% and 60.6% for cases B1, B2, B3 and B4 respectively. In all the cases the difference reduces with depth and the finite element stresses are slightly higher near the base of the tank.

The vertical stresses under the culvert for various load cases are superimposed and a stress envelope is drawn in figure (8.35). At a point such as A', the curves intersecting the vertical line B'C' give the stress ordinates at this point as a point load travels along the centreline EI of the top deck ABCD. The stress envelope shows high stresses directly under the walls reducing between two walls and also away from the culvert. This is because the loads are transmitted to the base through the walls which interact with each other and share them. The realistic analysis

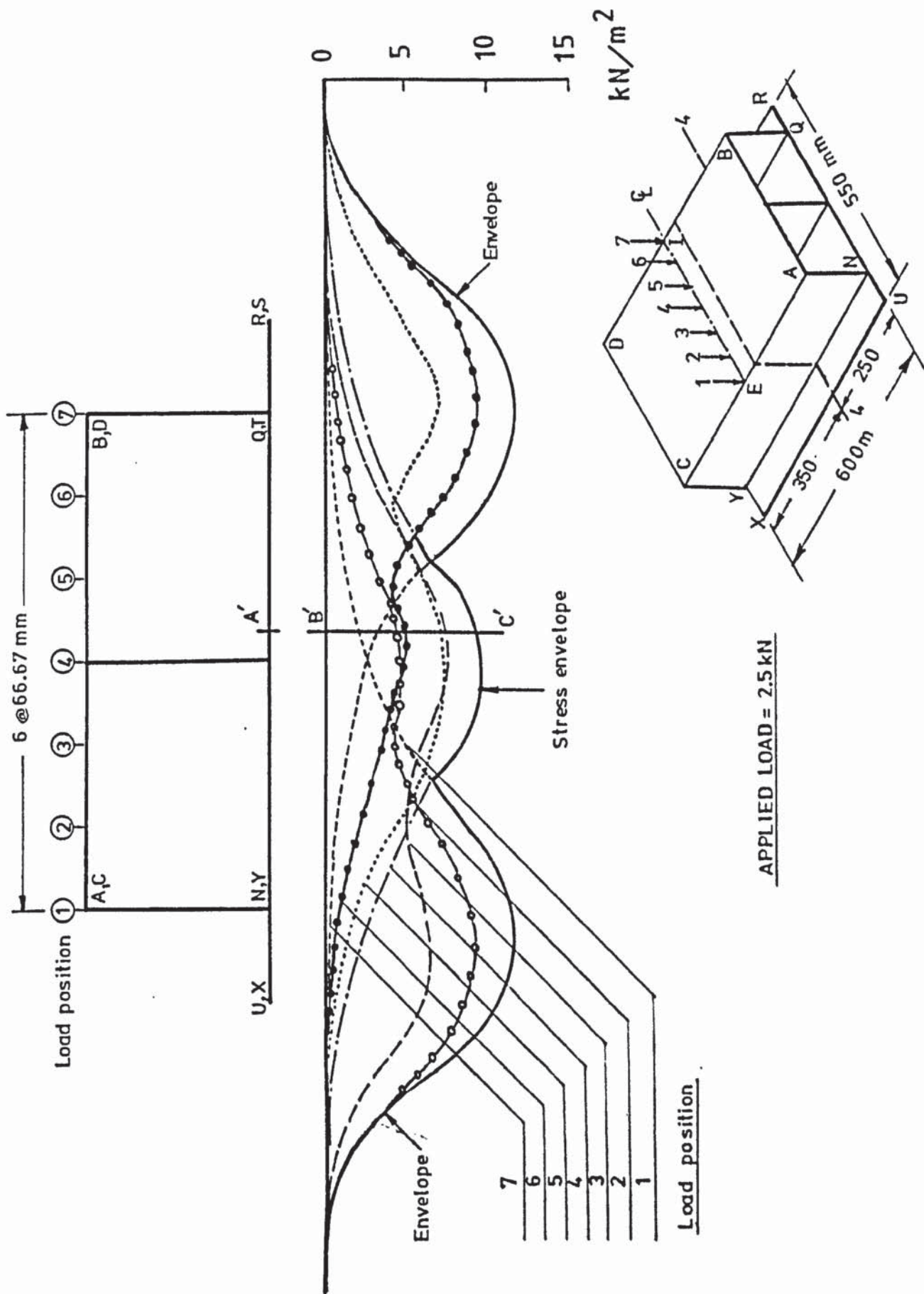


FIGURE 8.35 VERTICAL STRESSES UNDER THE CULVERT AT SECTION 4-4 AS A POINT LOAD TRAVELS ALONG THE CENTRE OF TOP DECK ABCD

of a box culvert must consider such a stress envelope created by the moving load instead of assuming a uniform or linearly varying contact pressure distribution.

The contour lines of the vertical stress in section 4-4 for load case B4 are shown in figure (8.36). A distinct column of high stresses is observed directly under the loaded wall ACNY with a concentration of the stress at the toe of the protruding base UNXY. Some tensile stresses developed and their loci are shown by the dashed lines. The extent and the magnitude of these stresses are very small and are not considered to develop significant separations in the soil.

The distribution of the vertical stress on a horizontal plane 25 mm below the base of the culvert is shown in figures (8.37), (8.38) and (8.39) for load cases B1, B4 and B6 respectively. Even for the central load case B1 in figure (8.37) the stress variation is highly non-uniform in both x and z directions. The non-uniformity is more pronounced in the x direction than in the z direction in both figures (8.37) and (8.38). The difference between the maximum and the minimum stresses in the x direction is in excess of 96% and that in the z direction is about 57% in both cases. As the load is applied at point K in figure (8.39) the non-uniformity of stress becomes excessive. While the maximum stress is 23.16 kN/m^2 near the load it reduces to zero away from it. Beyond this area the base separated from the ground.

The distribution of the horizontal stress σ_x on the sides of the culvert is shown in figures (8.40) and (8.41) for load cases B1 and B4 respectively. While the magnitudes of these stresses are small their distribution is again highly non-uniform and non-linear.

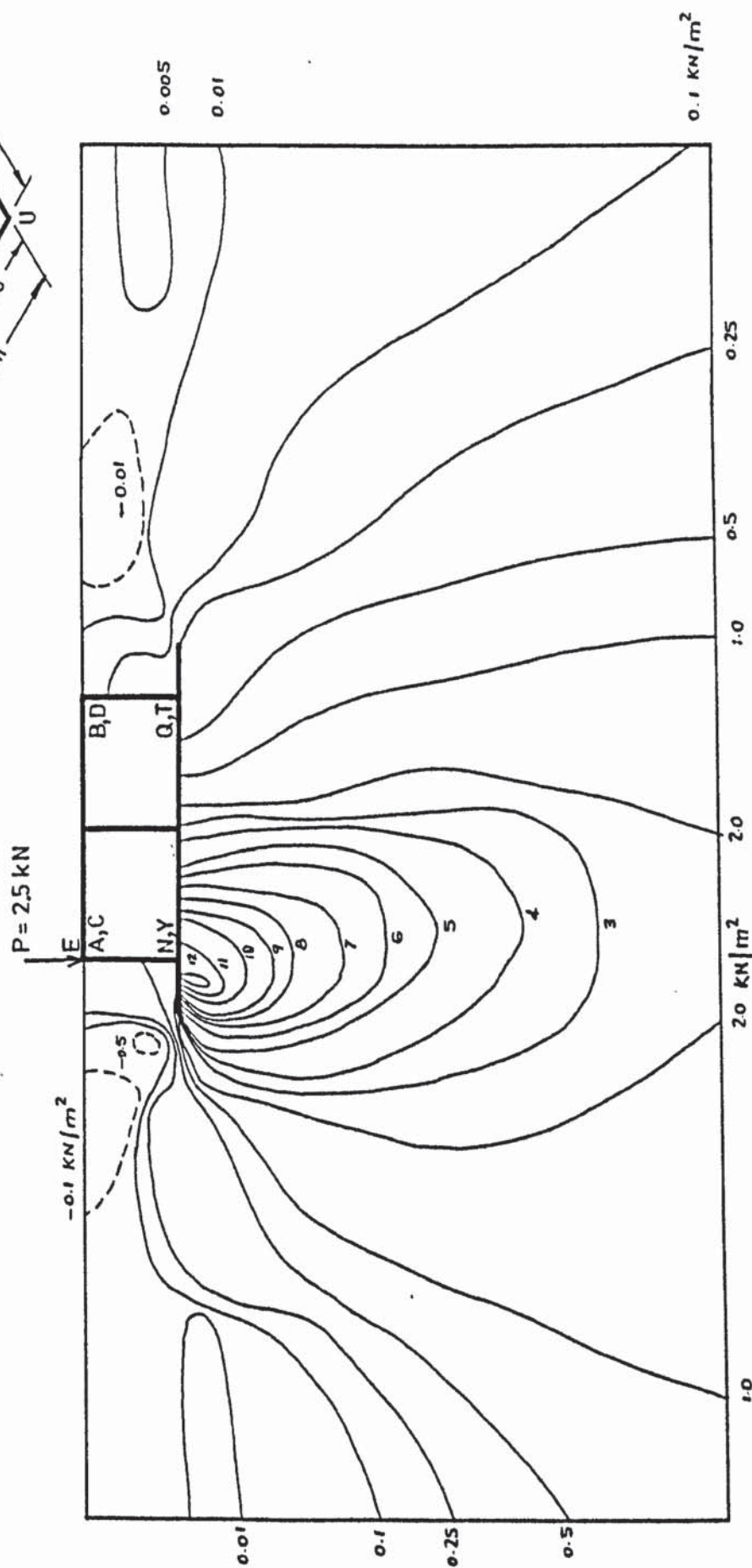
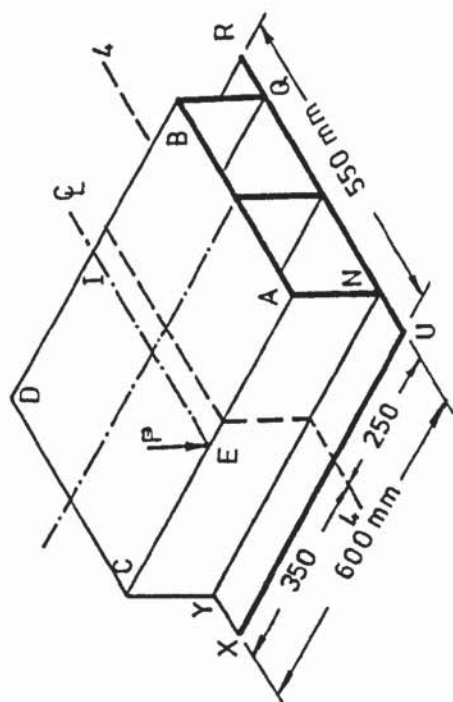


FIGURE 8.36 LOCI OF EQUAL VERTICAL STRESSES IN THE SOIL AROUND THE BOX CULVERT AT SECTION 4-4 FOR LOAD CASE B4

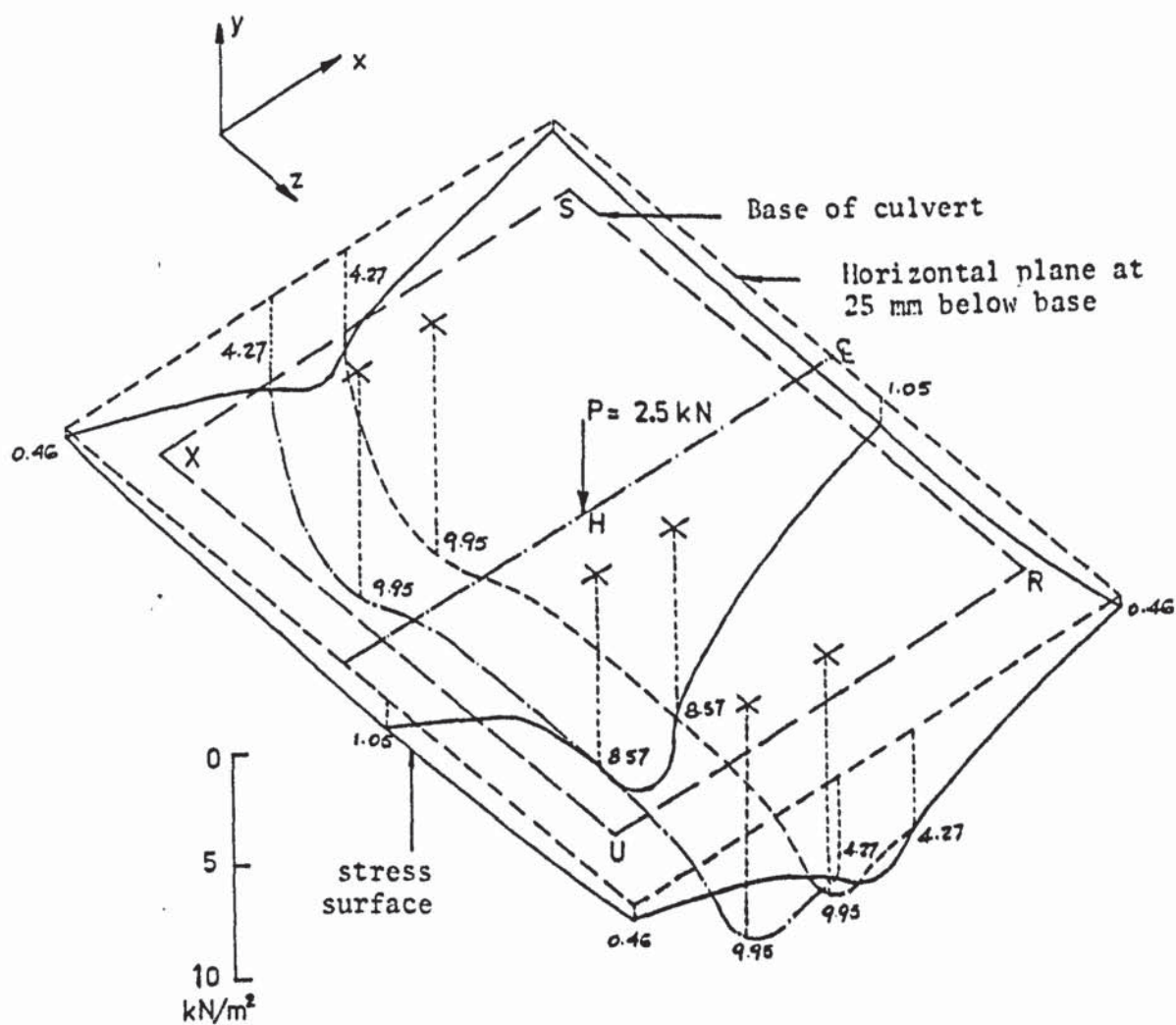


FIGURE 8.37 DISTRIBUTION OF VERTICAL STRESS ON A HORIZONTAL PLANE
25 mm BELOW BASE OF CULVERT FOR LOAD CASE B1

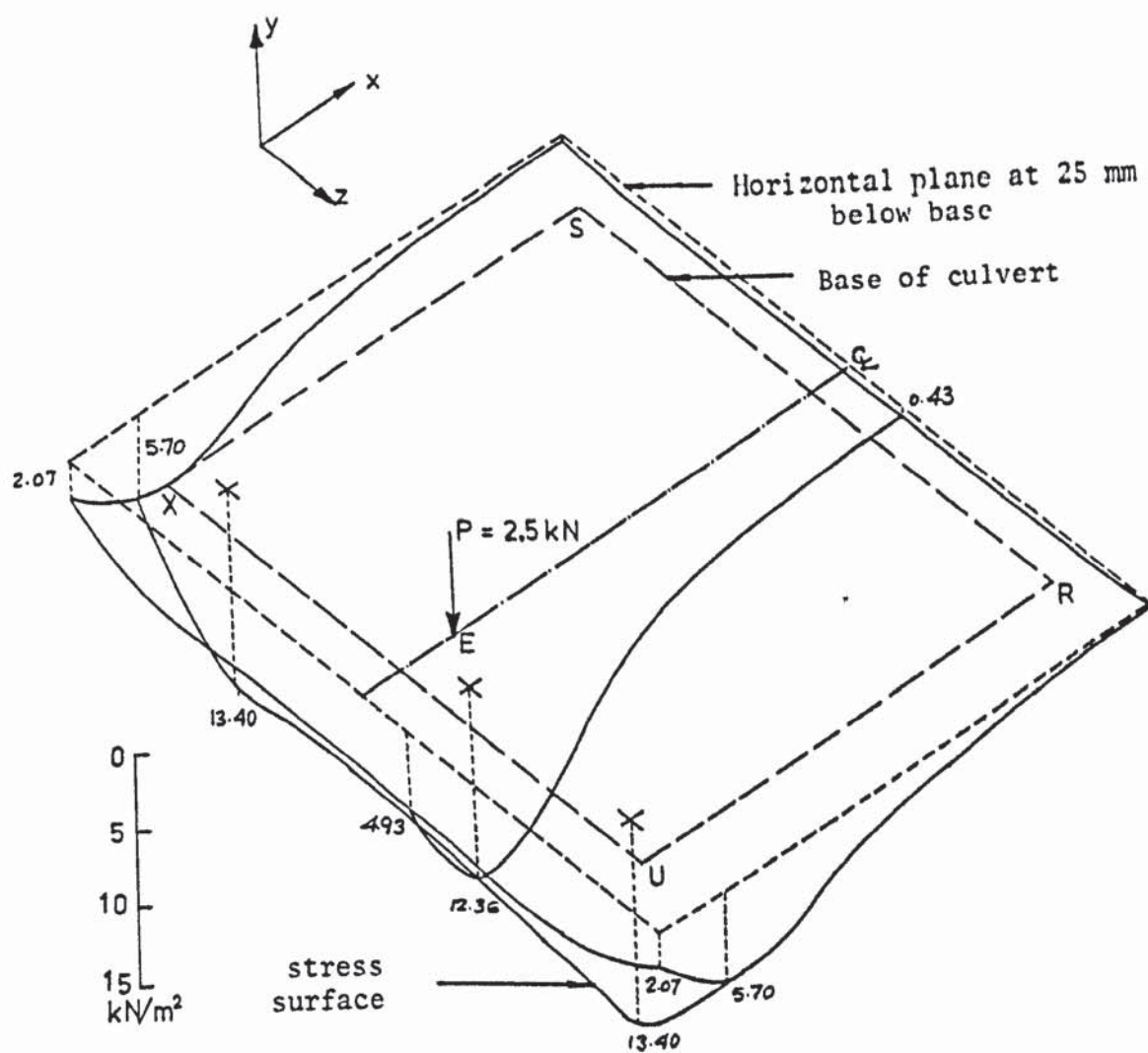


FIGURE 8.38 DISTRIBUTION OF VERTICAL STRESS ON A HORIZONTAL PLANE 25 mm BELOW BASE OF CULVERT FOR LOAD CASE B4

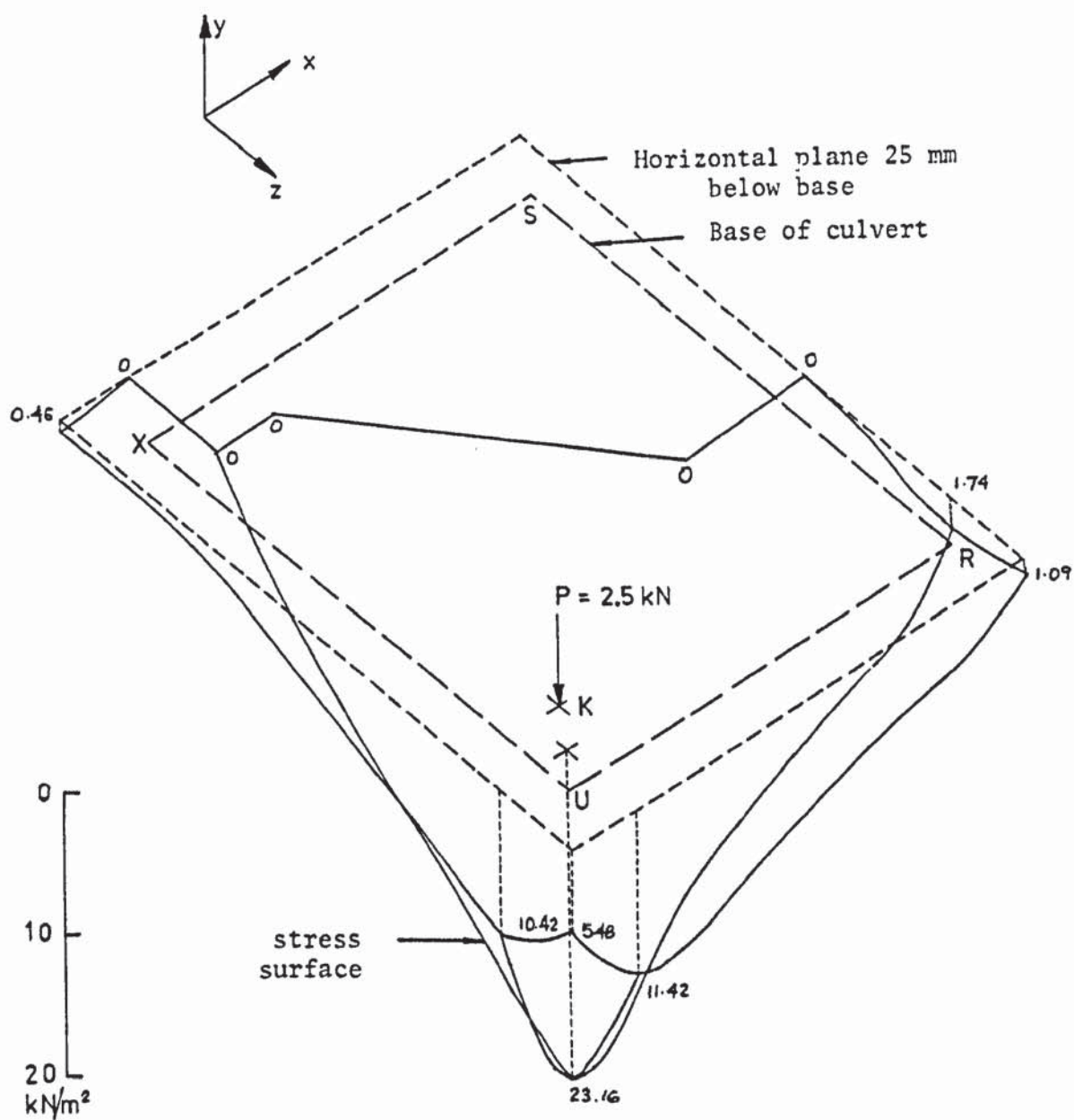
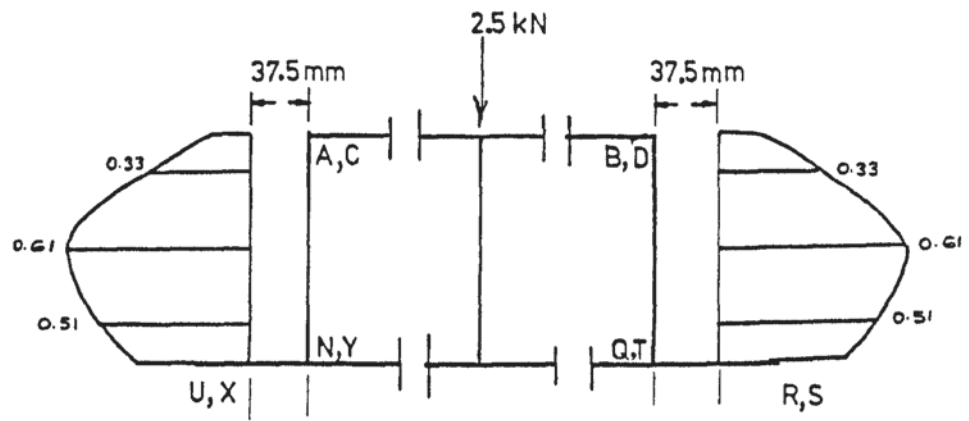
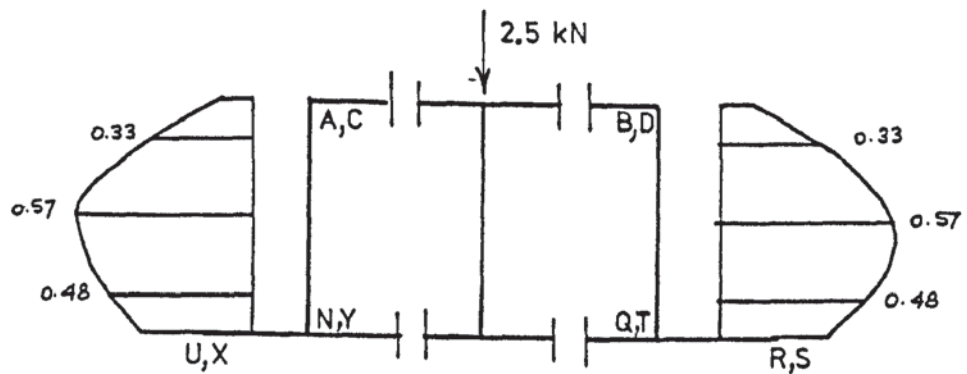


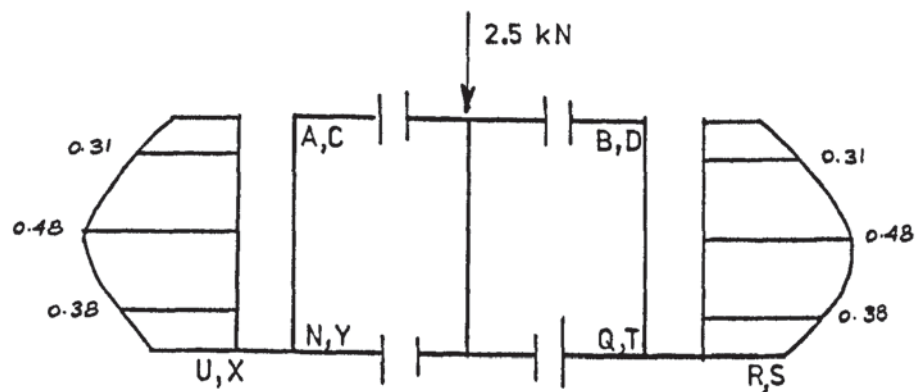
FIGURE 8.39 DISTRIBUTION OF VERTICAL STRESS ON A HORIZONTAL PLANE 25 mm BELOW BASE OF CULVERT FOR LOAD CASE B6



Section 3-3 and 4-4



Section 2-2 and 5-5



Section 1-1 and 6-6

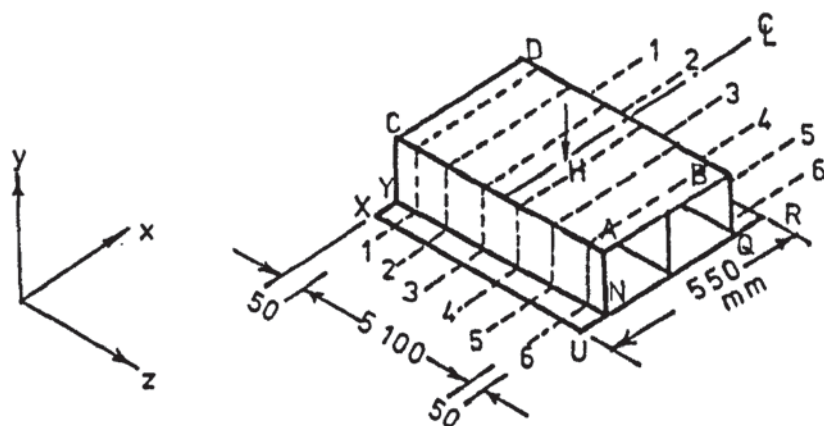


FIGURE 8.40 DISTRIBUTION OF HORIZONTAL STRESS σ_x ON THE WALLS OF THE CULVERT FOR LOAD CASE B1

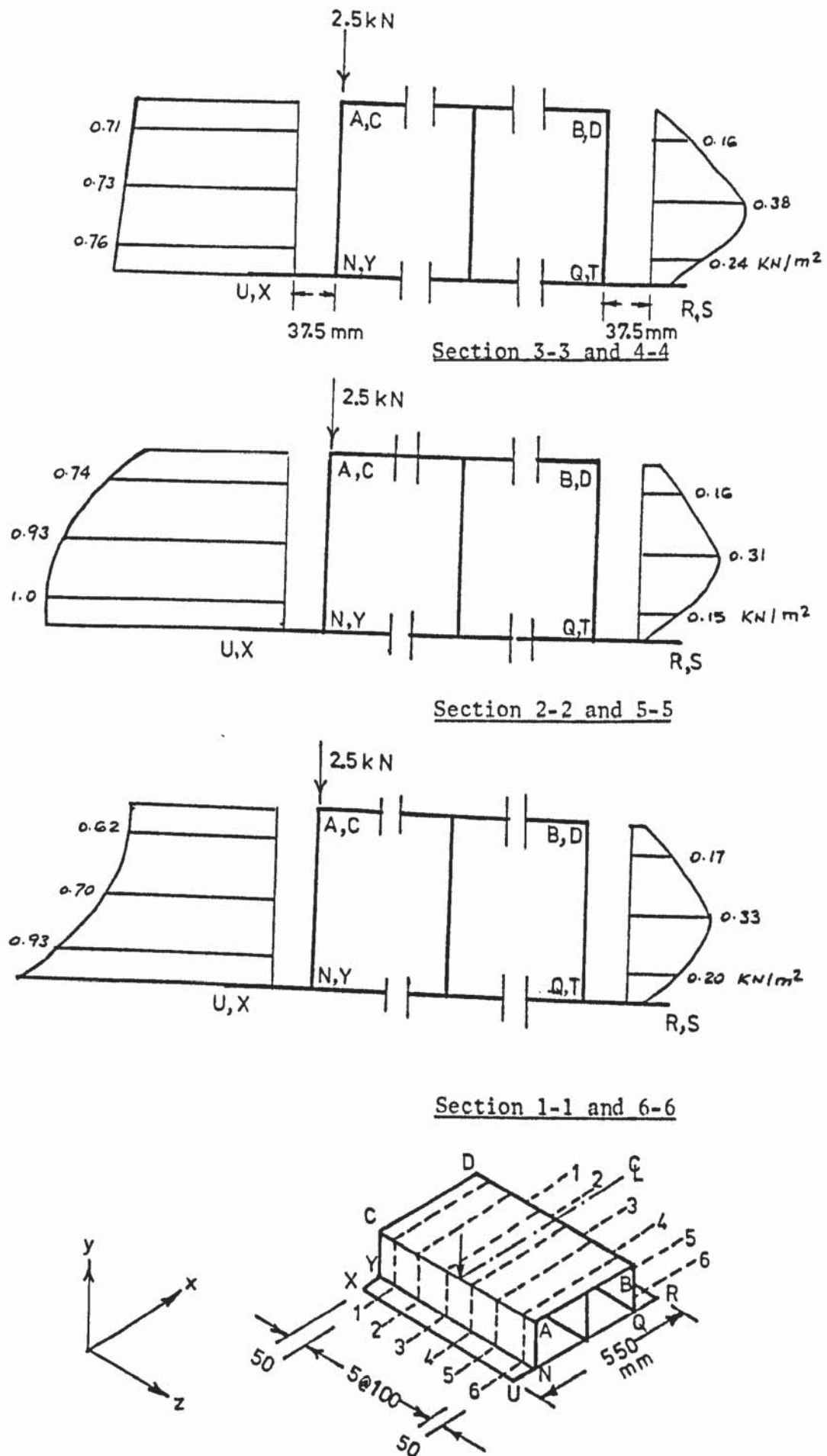


FIGURE 8.41 DISTRIBUTION OF HORIZONTAL STRESS σ_x ON THE WALLS OF THE CULVERT FOR LOAD CASE B4

This is in distinct contrast with the linear stress variation normally assumed in such cases. The non-uniform pressure distribution is caused by the pressure exerted by the wall as the culvert deforms. The variation of this stress for the other load cases was similar and is not presented.

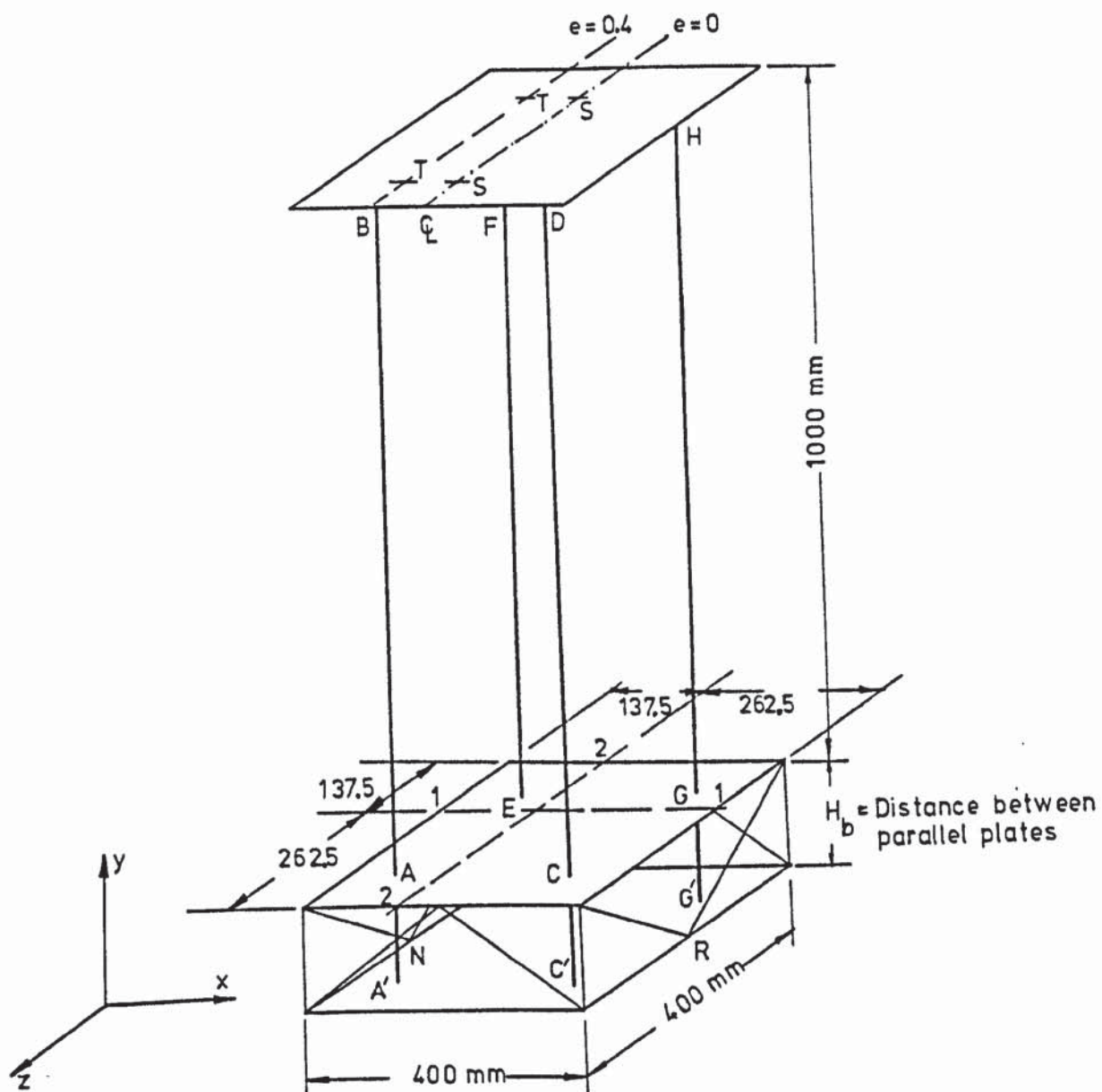
8.5 RESULTS OF MODEL C: TALL STRUCTURE

8.5.1 Deflections

The notations used to discuss the results of this model are shown in figure (8.42). The average settlements at points N and R for the four-column models with loads at the centre points S ($e = 0$) are shown in figure (8.43). The solid lines indicate the experimental load-deflection curves and the dashed lines indicate the theoretical ones. As the height of the base H_b increases the settlements also increase. These are plotted against H_b at a load of 5 kN in the figure. The increased settlement is considered to be caused by two factors: (i) As H_b increases the foundation becomes more flexible and its contribution in reducing the settlements decreases. (ii) The length of the columns in the soil below the base reduces as H_b is increased. As these columns act as piles, the reduction in their length increases the settlement.

The theoretical curves underestimate the experimental settlements and the difference increases at high loads due to the accumulation of the errors in the incremental method. At a load of 5 kN the errors are 16.3%, 7.9% and 7.7% for tests C3a, C2a and C1a respectively. The high error in the first case is considered to be due to the experimental errors in measuring small displacements.

The differential settlements between the points N and R, on



Model No.	Test case	H_b (mm)	No. of columns	Eccentricity of load, e	Loading points	Remarks
C1	C1a	150	4	0	S	
C1	C1b	150	4	0.4	T	
C2	C2a	75	4	0	S	
C2	C2b	75	4	0.4	T	
C3	C3a	0	4	0	S	
C3	C3b	0	4	0.4	T	
C4	C4	150	3	0	S	Column AB removed
C5	C5	0	4	0.4	T	Piles cut off

FIGURE 8.42 NOTATIONS FOR MODEL C - TALL STRUCTURE

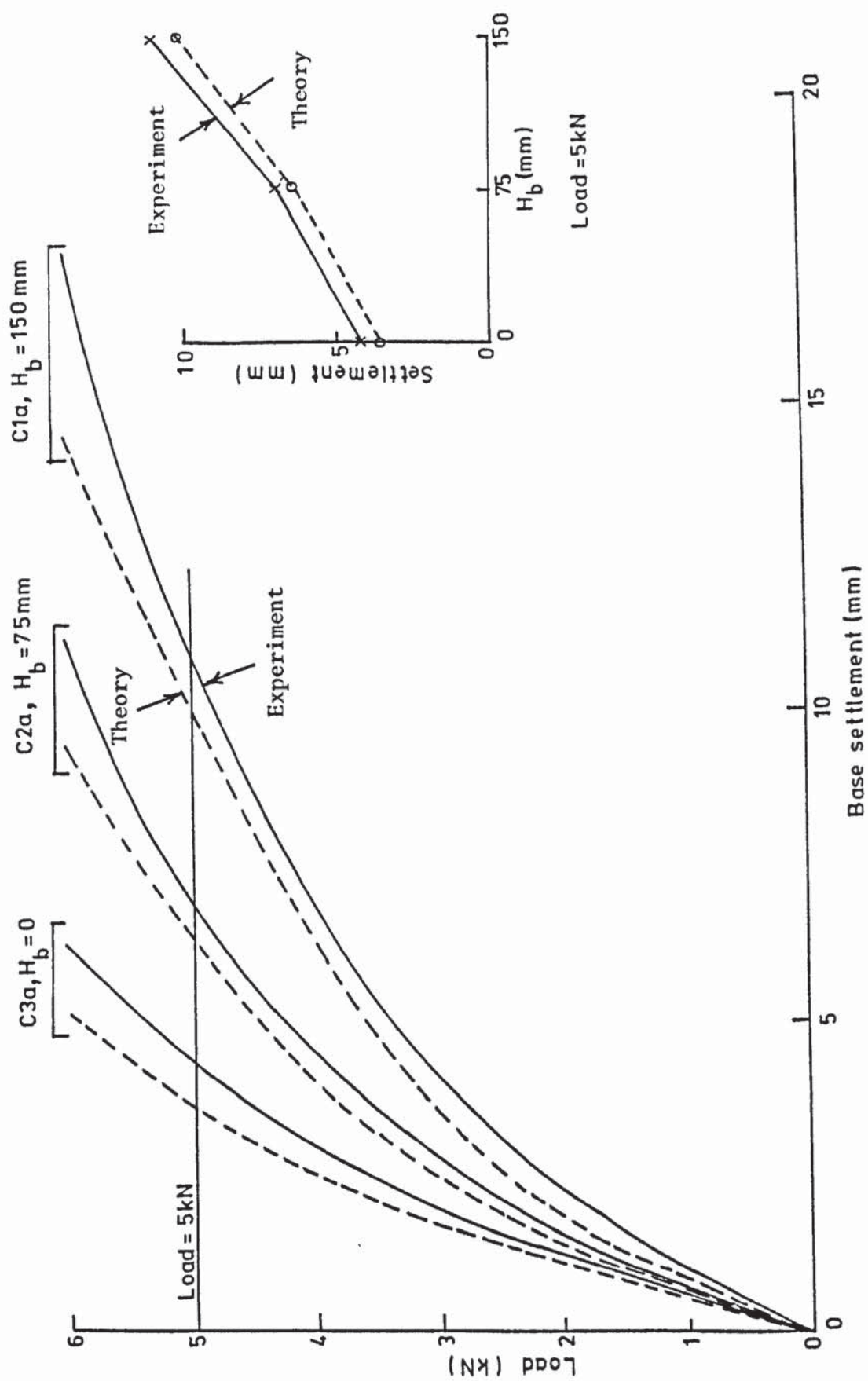


FIGURE 8.43 AVERAGE BASE SETTLEMENTS OF MODELS C FOR $e = 0$

the base plate, are plotted against the load in figure (8.44) for the eccentrically loaded four-column frames. These also increase with an increase in H_b as shown by the inset diagram. The solid lines in the figure indicate experimental values and the dashed lines show the theoretical ones. The curve with the dark dots indicate the values obtained by the finite element analysis by attaching the piles to the soil at two-third points only. While connecting these to the soil throughout their length results in an underestimation of the settlements in all the cases, attaching them at the $2/3$ length overestimates these. For case C2b, for which this analysis was done, the first method underestimates the differential settlement at 5 kN by 9.8% and the second method overestimates it by 25.4%. It is considered that, with the computer program available, connecting the piles to the soil throughout their lengths is more accurate for this type of problem. The theory underestimates the settlements by 14.9% and 9.2% for the cases with $H_b = 0$ and $H_b = 150$ mm respectively at a load of 5 kN.

The sway was calculated as the difference of the average horizontal x displacement of the points B, D, F and H, see figure (8.42), and that of points A, C, E and G. These are plotted against the applied load in figure (8.45) for the same cases as those in figure (8.44). Once again it is observed that connecting the piles to the soil at the $2/3$ point overestimates the deflection. This amounts to 22.3% at a load of 5 kN while the analysis with the piles connected to the soil elements throughout their lengths underestimates the sway by 10.8%. The underestimations for the cases of $H_b = 0$ and $H_b = 150$ mm amount to 12.8% and 10.5% respectively.

In both models C3b and C5, H_b was zero and the load was applied

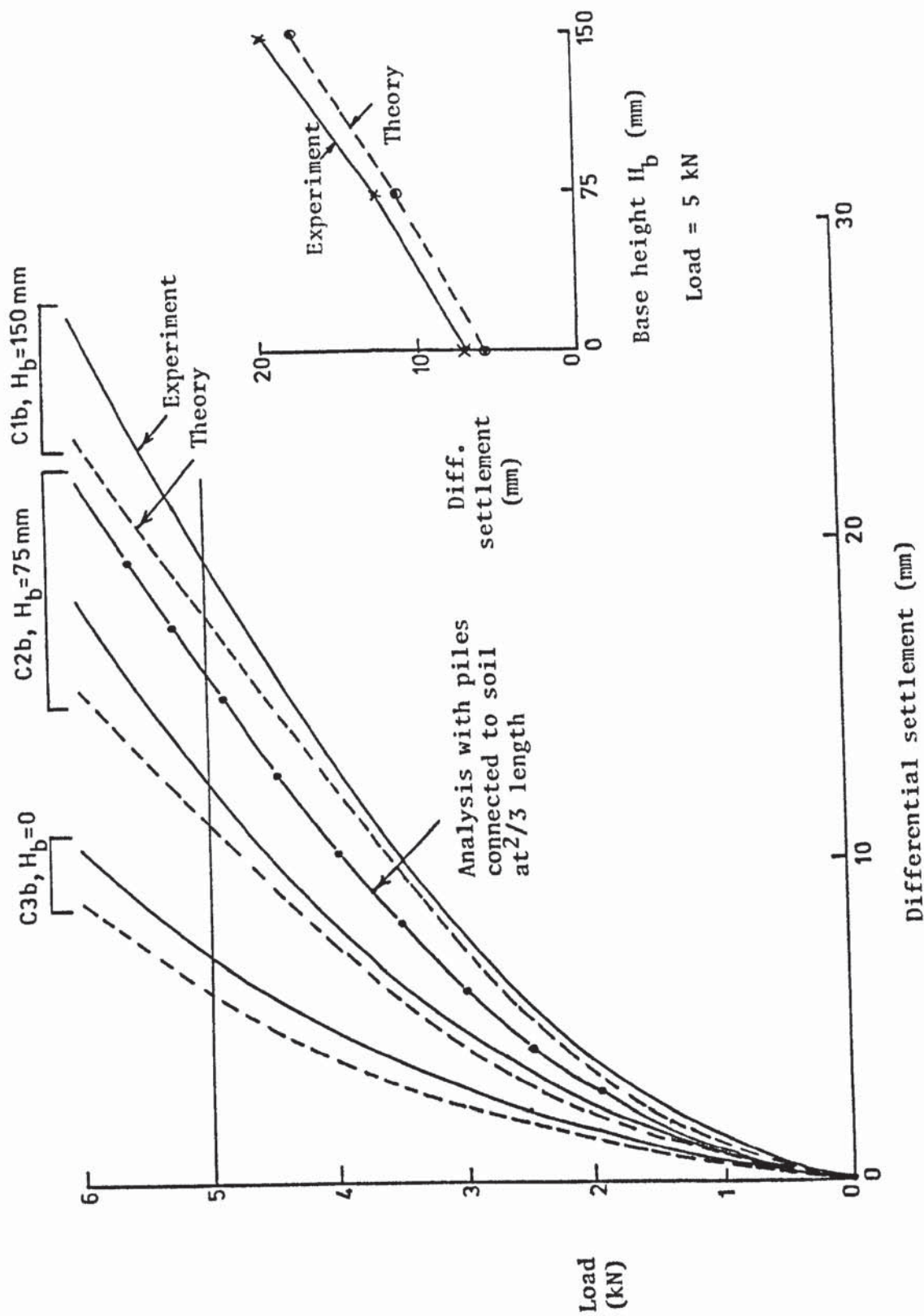


FIGURE 8.44 LOAD-DIFFERENTIAL SETTLEMENT DIAGRAMS OF MODELS C WITH $E = 0.4$

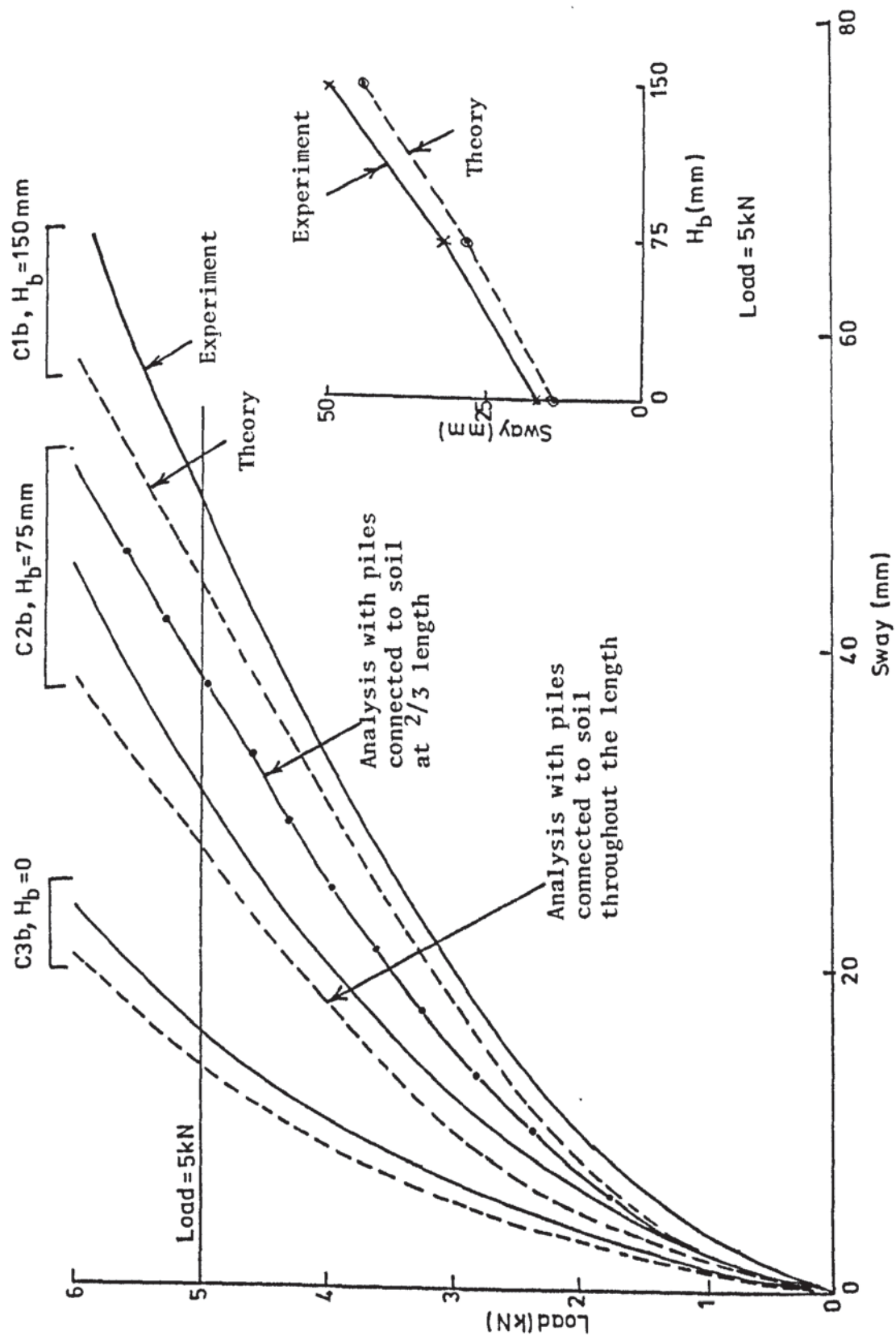


FIGURE 8.45 LOAD-SWAY DIAGRAMS OF MODELS C WITH $e = 0.4$

at $e = 0.4$, but the piles in C5 were cut off. The load-differential settlement and the load-sway diagrams of these two cases are compared in figures (8.46) and (8.47) respectively. As expected, removing the piles increases both the differential settlement and the sway. The former is increased by 25.5% and the latter by 19% at a load of 5 kN. It is observed in figures (8.46) and (8.47) that when the piles are not present there is a closer agreement between the theory and the experiment. At a load of 5 kN the theory underestimates the differential settlement of the model with piles by 14.9% and that of the one without piles by only 8.6%. The difference in the sway is 12.8% and 7% for the cases with and without the piles respectively. It is considered that connecting the piles to the soil throughout their lengths causes the increased discrepancy between the theory and the experiment. This indicates that a certain amount of slip occurs between the piles and the soil which is not represented in the analysis. As was shown earlier, connecting the piles to the two-third points overestimates the deflections. Therefore, the exact representation lies somewhere between these two cases.

To aggravate irregularity, one of the columns was removed. The vertical settlement of point R on the base plate is plotted against the load for the three-column model C4 in figure (8.48). The theory underestimates the settlements by 10.5% at a load of 5 kN. The values of the settlements are higher than the average base settlements of the four-column model C1a with the same H_b given in figure (8.43). At a load of 5 kN this difference is 18.5% for the experimental values. This is considered to be due to the fact that as column AB is removed, the other columns are more heavily loaded

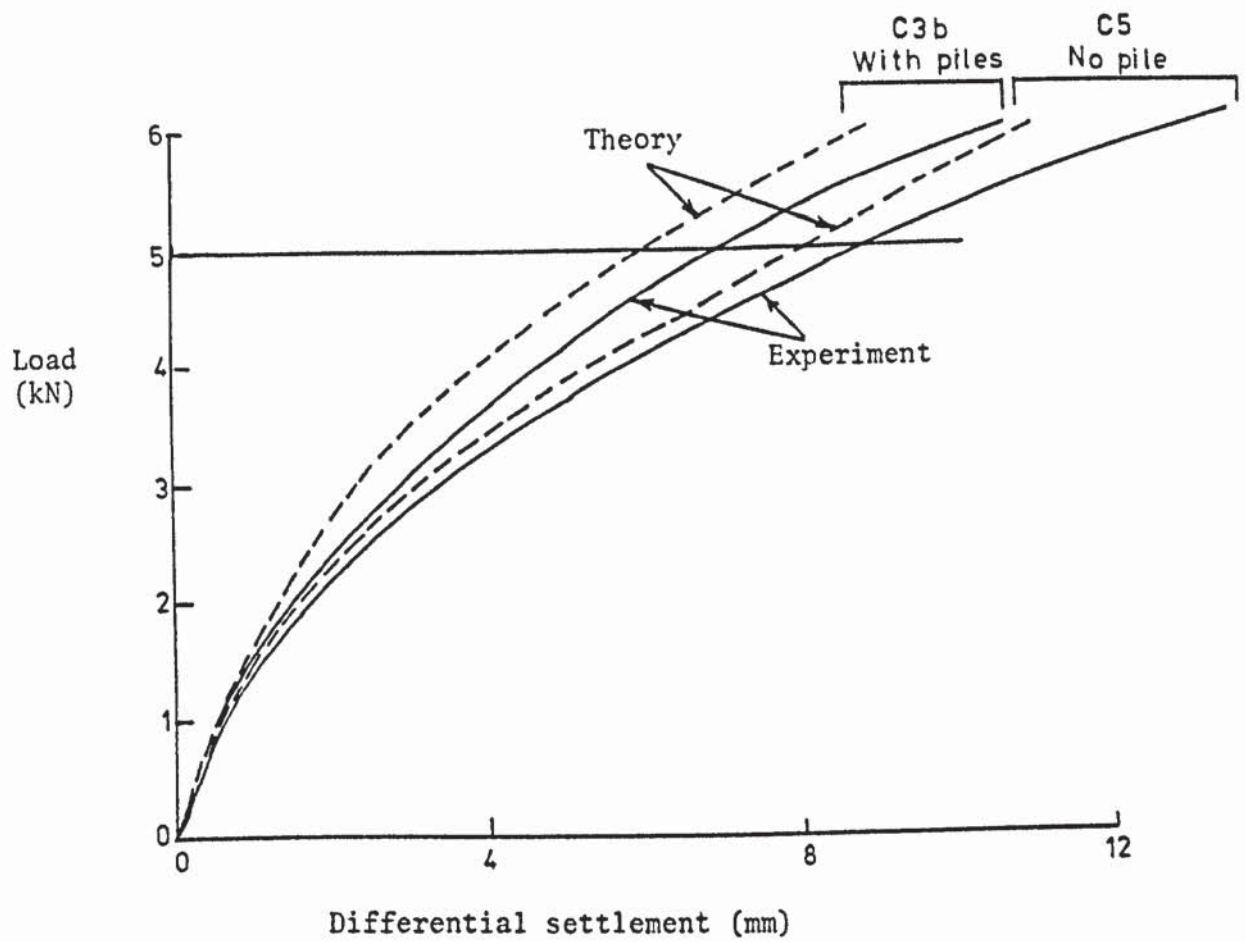


FIGURE 8.46 COMPARISON OF SETTLEMENTS WITH AND WITHOUT PILES, $e = 0.4$

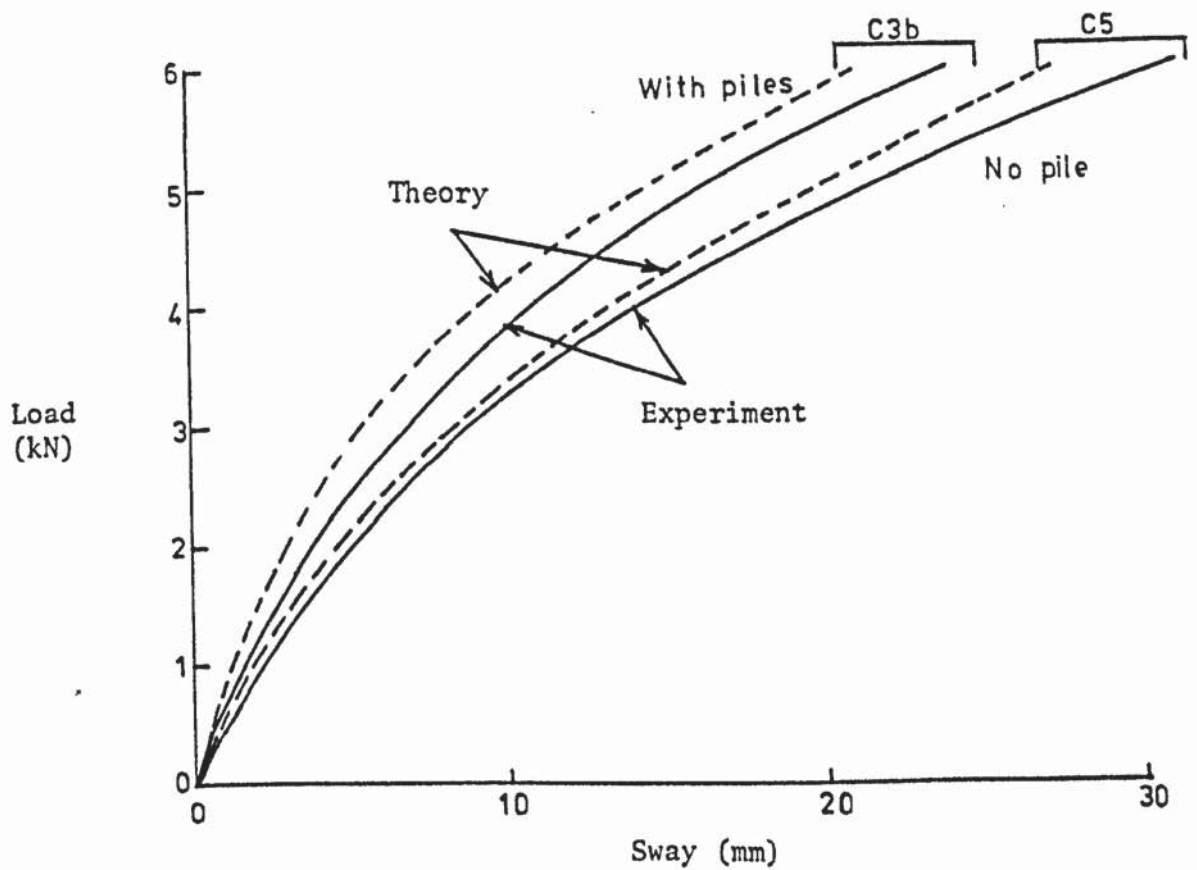


FIGURE 8.47 COMPARISON OF SWAY WITH AND WITHOUT PILES, $e = 0.4$

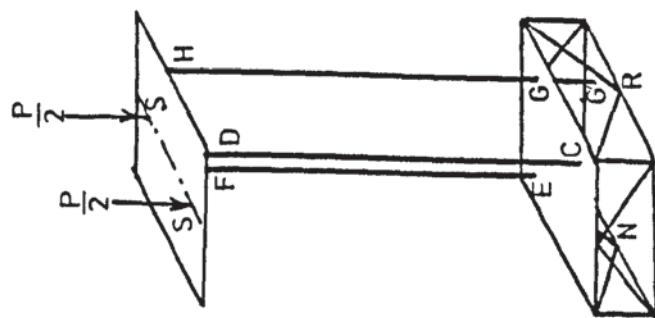
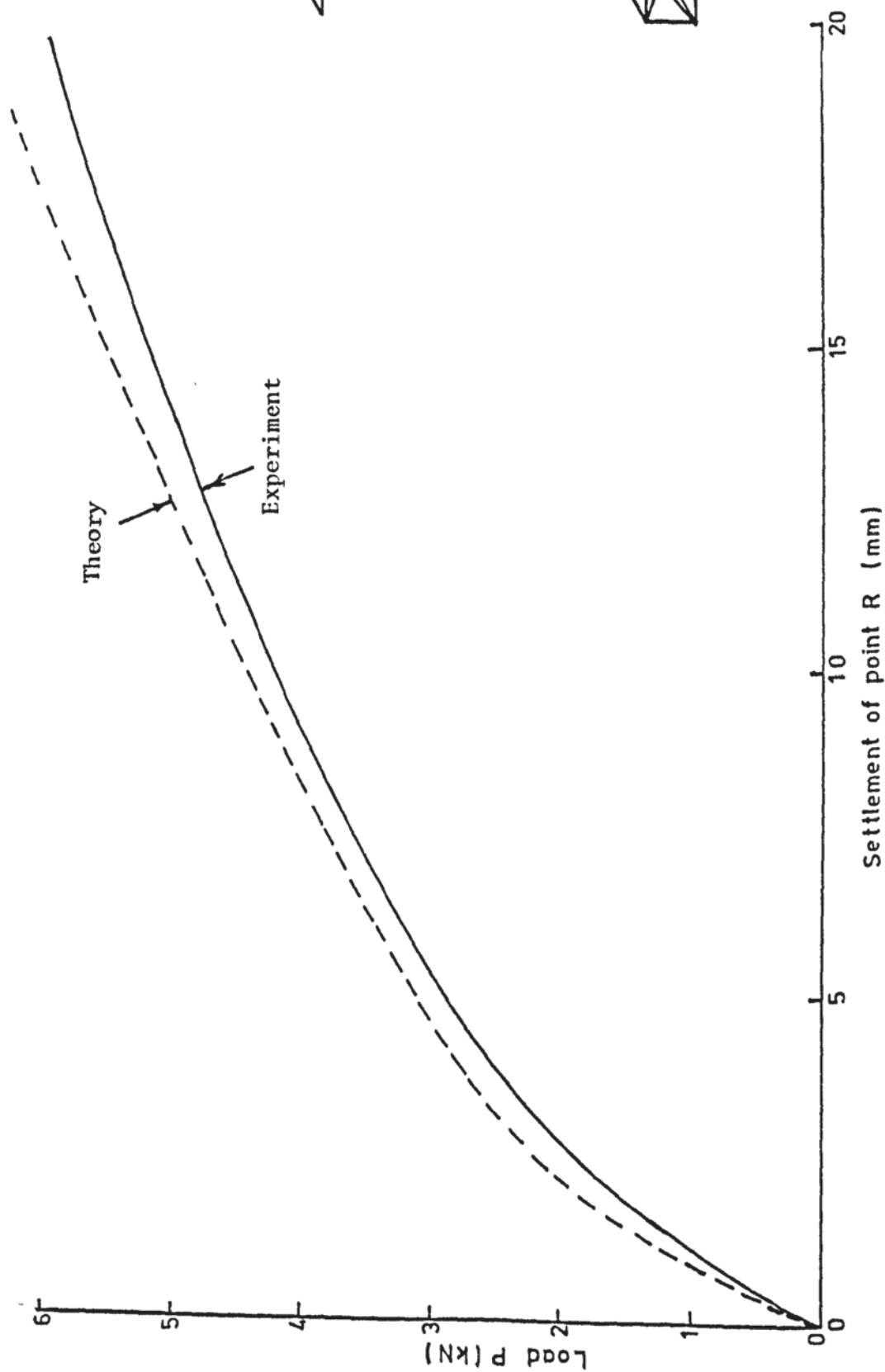


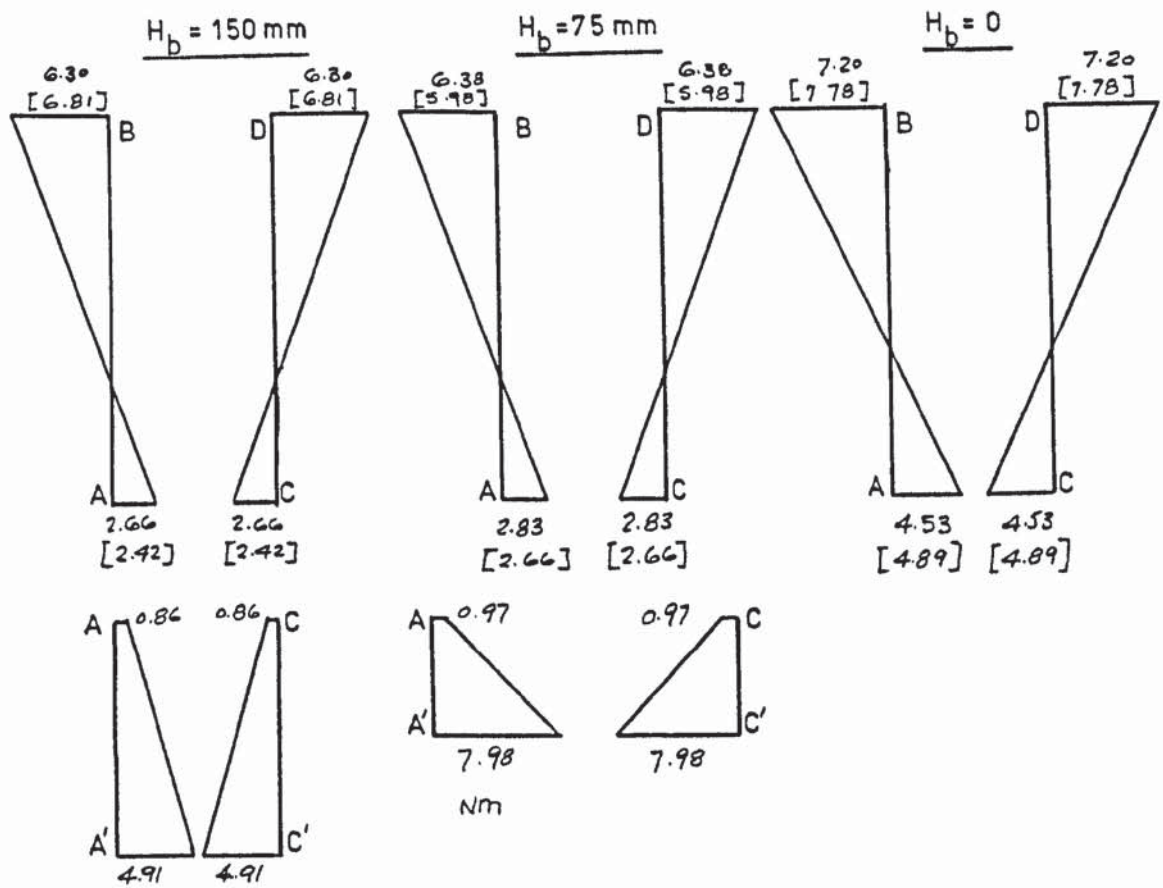
FIGURE 8.48 LOAD-SETTLEMENT DIAGRAM OF POINT R IN THE BASE PLATE
OF THREE-COLUMN MODEL C4

causing the structure to settle more on the right hand side.

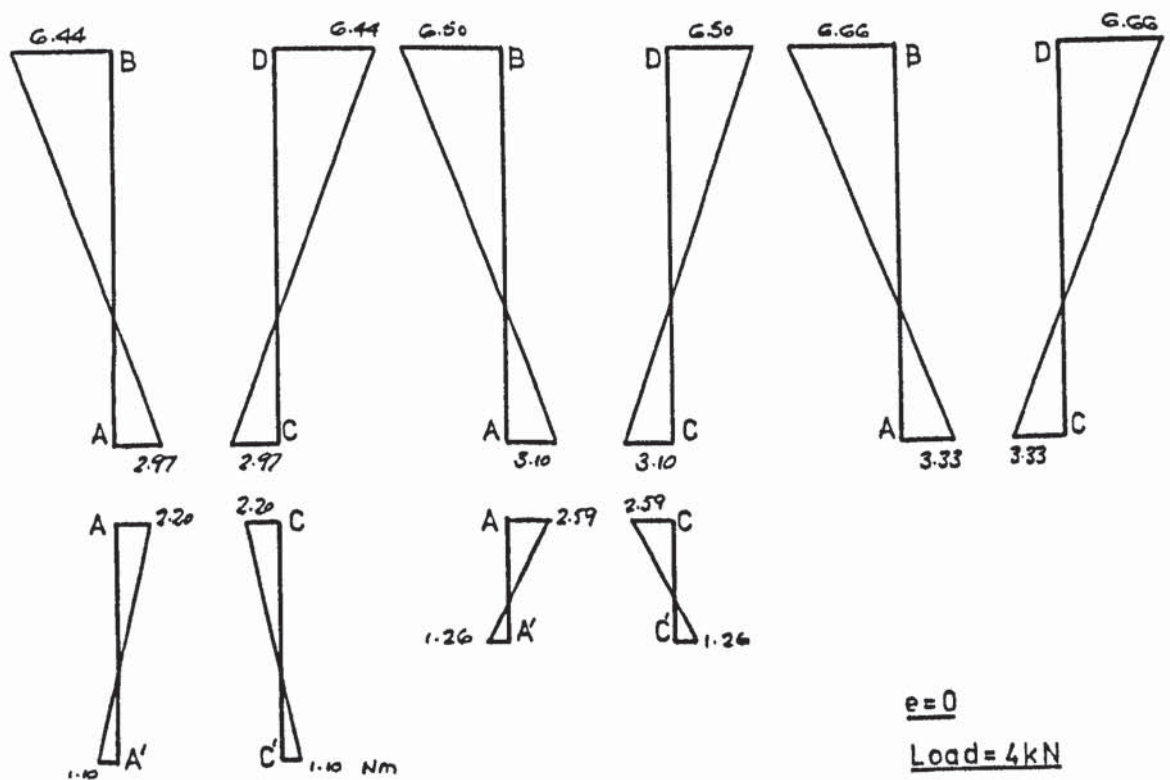
8.5.2 Bending moments

The bending moments about the z-axis in columns AB and CD for a load of 4 kN acting at the centre ($e = 0$) of the four-column models are shown in figure (8.49). The diagrams in figure (8.49a) are obtained by the analysis of the complete system and the values in the square brackets are experimental. The latter values were not recorded in the portions AA' and CC' of the columns inside the base and therefore only the theoretical values are given. There is a good agreement between the experimental and the theoretical bending moments, the maximum difference being only 9.9% which occurs at end A of column AB in the model with $H_b = 150$ mm.

The bending moments obtained by assuming the base of the model to be fully fixed are shown in figure (8.49b). It is noticed that these moments in portions AB and CD of the columns above the base are almost the same as those in figure (8.49a). However, the redistribution of the moments in portions AA' and CC' in the base for $H_b = 150$ and 75 mm and that at the column base for $H_b = 0$ are quite significant. While the maximum difference between the column moments of the fixed base and the flexible base analyses for the first two cases is only 11.7%, this difference at A and C for $H_b = 0$ is 26.5%. Inside the base for the cases of $H_b = 150$ and 75 mm there is a reversal of sign of the moments. The difference is as high as 167% at A and C for $H_b = 75$ mm. This indicates that in a tall structure the redistribution of the moments is more significant near the base of the structure than at points at the top. This is also observed in a 50-storey space frame and will be shown in chapter 9.



(a) Flexible base analysis



(b) Fixed base analysis

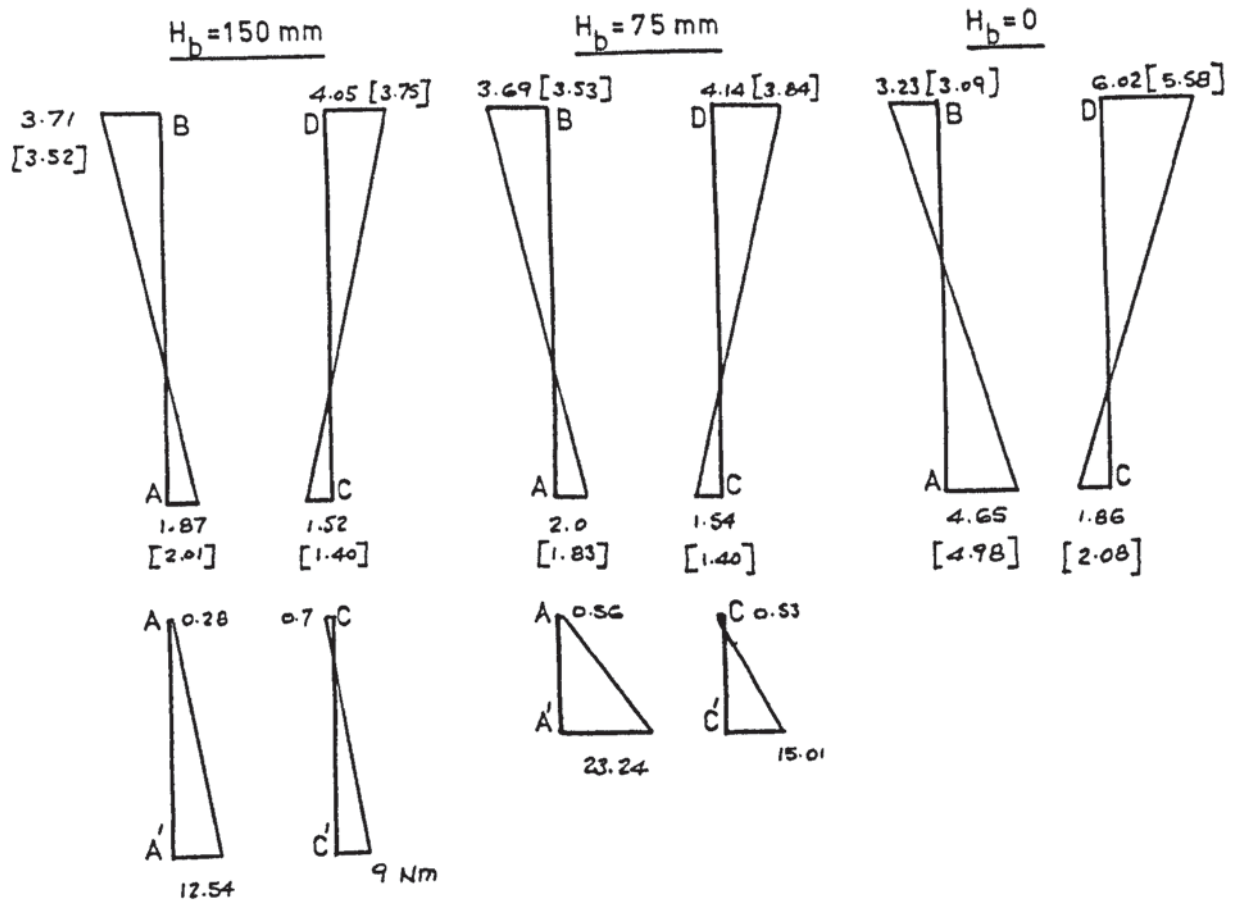
[FIGURES IN BRACKETS ARE EXPERIMENTAL VALUES]

FIGURE 8.49 BENDING MOMENTS IN Nm ABOUT z-AXIS IN FOUR-COLUMN MODEL C

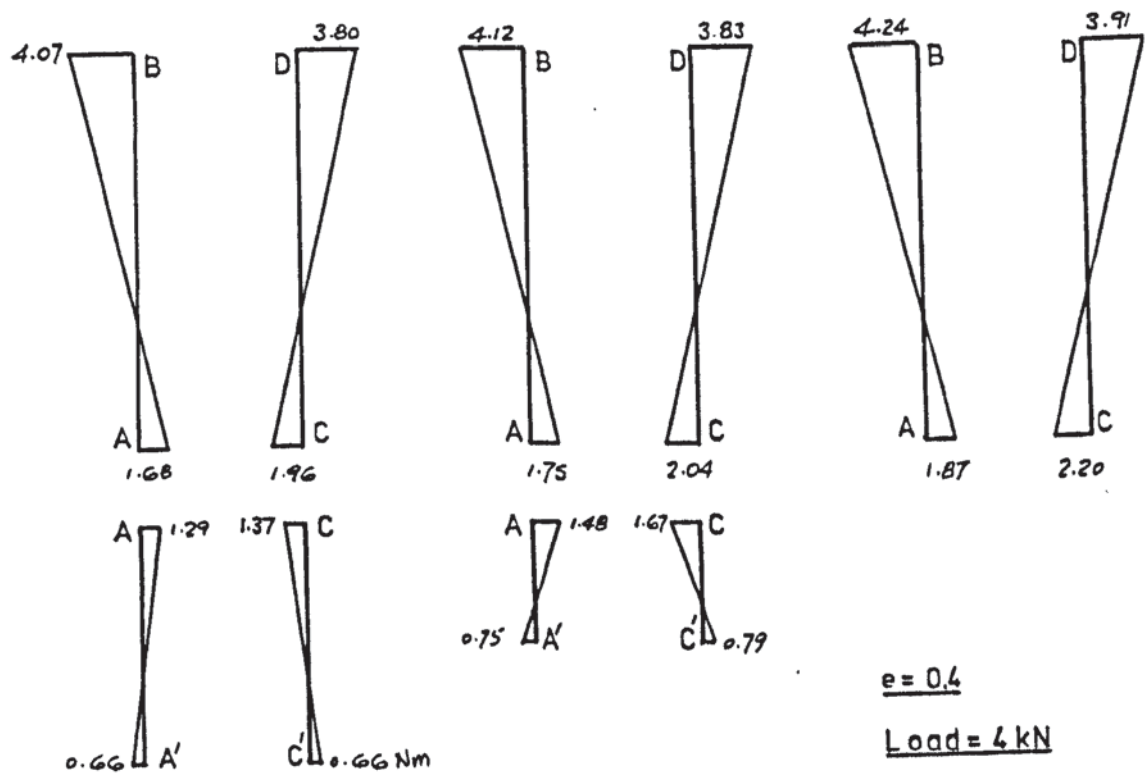
The bending moment diagrams of the same models for the eccentric load case $e = 0.4$ are shown in figure (8.50). The maximum difference between the theoretical and the experimental values in figure (8.50a) is 10.6% which occurs at C for $H_b = 0$. The difference between the bending moments obtained by the flexible base analysis and that by the fixed base analysis is again more prominent near the base than at the top. The maximum difference at the top is 35% occurring at D for $H_b = 0$ and that at point A in the same case is 59.8%. Inside the base in columns AA' and CC' this difference is as high as 361% which occurs at A for $H_b = 150$ mm. The high redistribution of the moments in the base is considered to be caused by its stiffness playing a part in reducing the base rotations. These moments are not carried over to the top as the columns are rather slender.

The bending moments in the columns of the three-column model C4 about the z-axis and the x-axis are shown in figures (8.51a) and (8.51b) respectively at a central load of 4 kN. The firm lines indicate the bending moments obtained by the interactive analysis and the dashed lines indicate those obtained by assuming a fully fixed base. The experimental values are shown within the square brackets. The maximum difference between the experimental and the theoretical values is recorded as 11.8% which occurs at end G of column GH.

The axial forces in all the columns of the four-column model C1, with a central load, were equal. However, when column AB was removed in model C4, the two diagonally opposite columns CD and EF carried most of the axial load. At a centrally applied load of 4 kN, CD and EF carried 2.02 kN and 1.96 kN respectively while



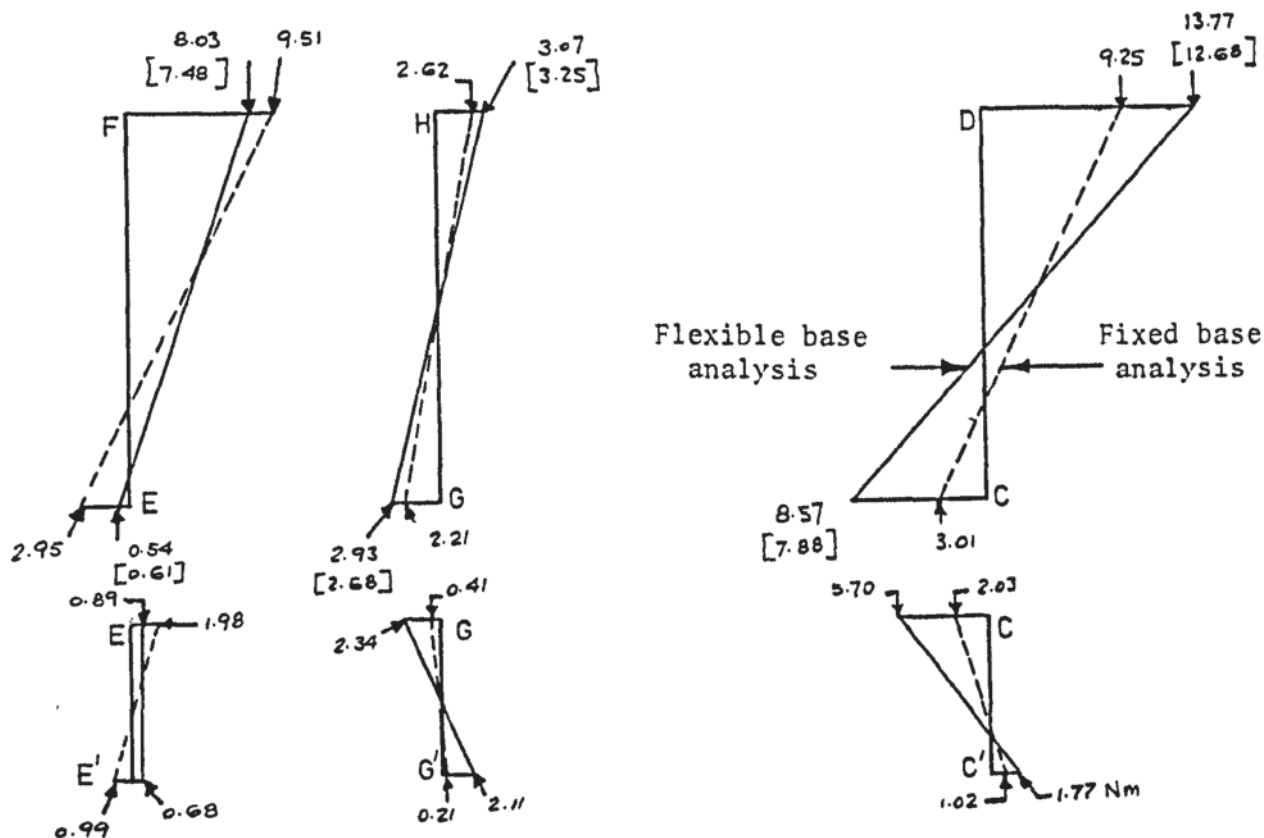
(a) Flexible base analysis



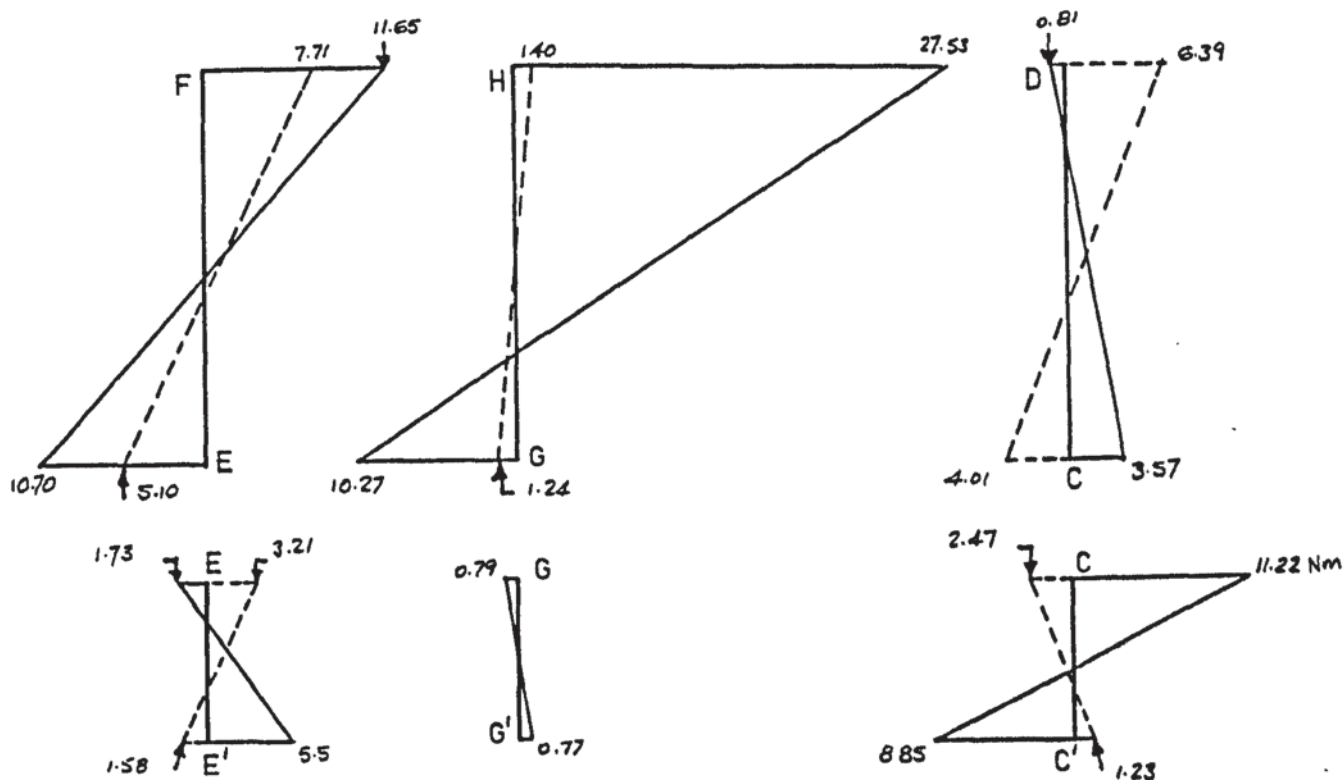
(b) Fixed base analysis

[FIGURES IN BRACKETS ARE EXPERIMENTAL VALUES]

FIGURE 8.50 BENDING MOMENTS IN Nm ABOUT z AXIS IN FOUR-COLUMN MODEL C



(a) Moments about z-axis



LOAD = 4 kN

(b) Moments about x-axis

[FIGURES IN BRACKETS ARE EXPERIMENTAL VALUES]

FIGURE 8.51 BENDING MOMENTS IN THREE-COLUMN MODEL C 4

column GH carried only 0.02 kN. While this is the case, it is noticed in figure (8.51) that column GH suffers quite significant bending moments. These moments are very much in excess of those predicted by a fixed base analysis, being as much as 20 times for M_z at the top of column GH. While a fixed base analysis predicts both low axial force and low bending moment in this column, it actually suffers a low axial force and a high bending moment. This situation can be critical if the column is made of concrete.

8.5.3 Stresses in the soil

The vertical stresses at various depths in section 1-1, see figure (8.42), are shown, for case Cla, in figure (8.52). These stresses in the vertical section 2-2 are shown in figure (8.53). In both these figures it can be seen that there is a column of high vertical stresses directly under the base, which diminishes rapidly away from it. The stresses are higher at a depth of 137.5 mm, which is near the end of the piles, than at the shallower depth. The difference is as much as 48.3% at the centre. At a shallower depth of 37.5 mm the stresses are higher near the piles at P and Q and lower between the piles at R, see figure (8.52). It is considered that high stresses develop near the piles and these are the maximum at their tips.

The vertical stresses in section 1-1 under the same structure with the load at $e = 0.4$ are shown at various depths in figure (8.54). While the stresses are higher near the tip of the piles ($y = 137.5$ mm) than at the shallow depth of 37.5 mm, they are also more non-uniform. This is because the left hand side columns AB and EF are more heavily loaded than the right hand side ones. The stresses in section 2-2 passing through the maximum stress ordinate in figure

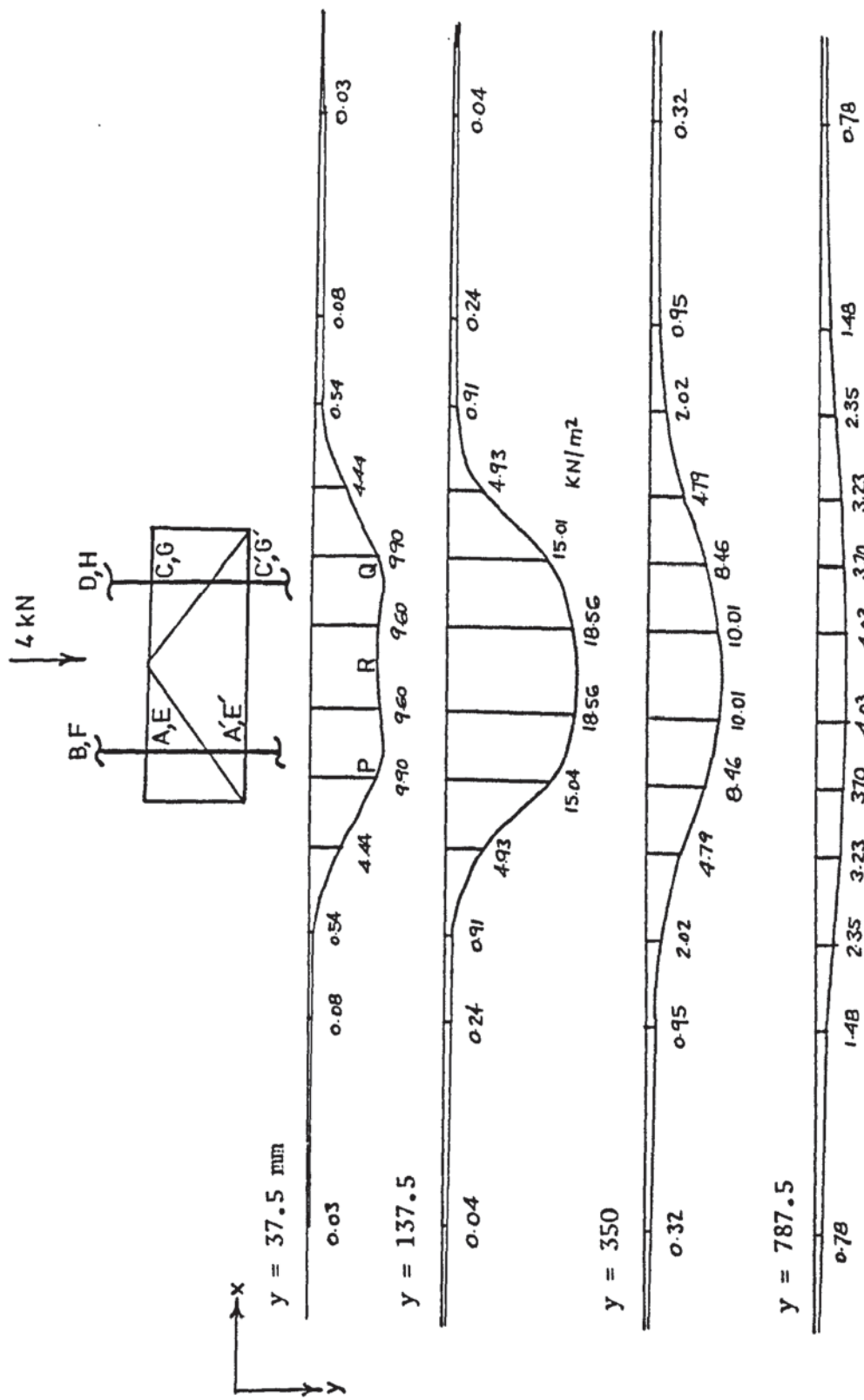


FIGURE 8.52 VERTICAL STRESSES IN SECTION 1-1 AT VARIOUS DEPTHS UNDER THE TALL STRUCTURE
MODEL C1a WITH $e = 0$

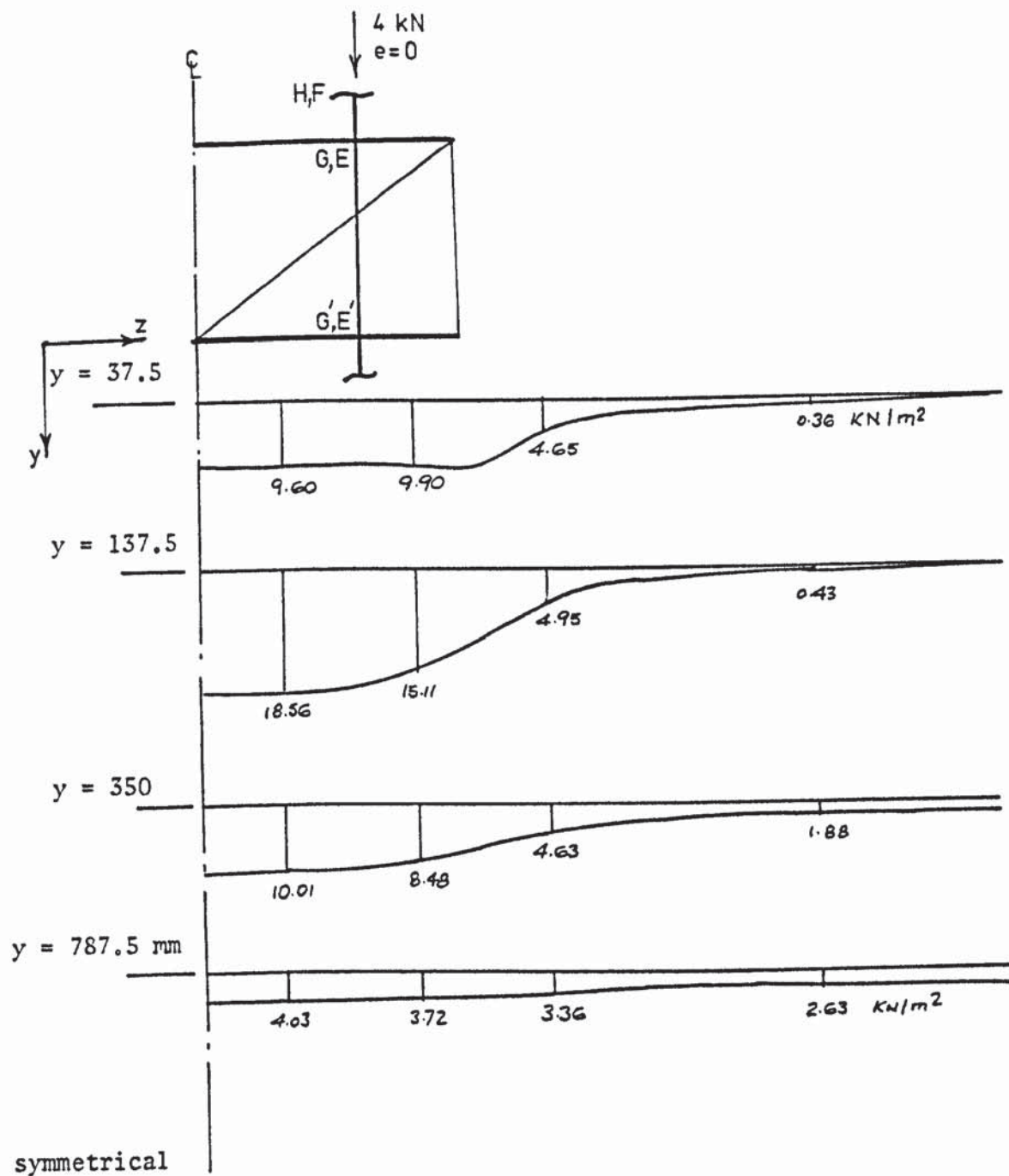


FIGURE 8.53 VERTICAL STRESSES IN SECTION 2-2 AT VARIOUS DEPTHS UNDER TALL STRUCTURE MODEL C1a WITH $e = 0$

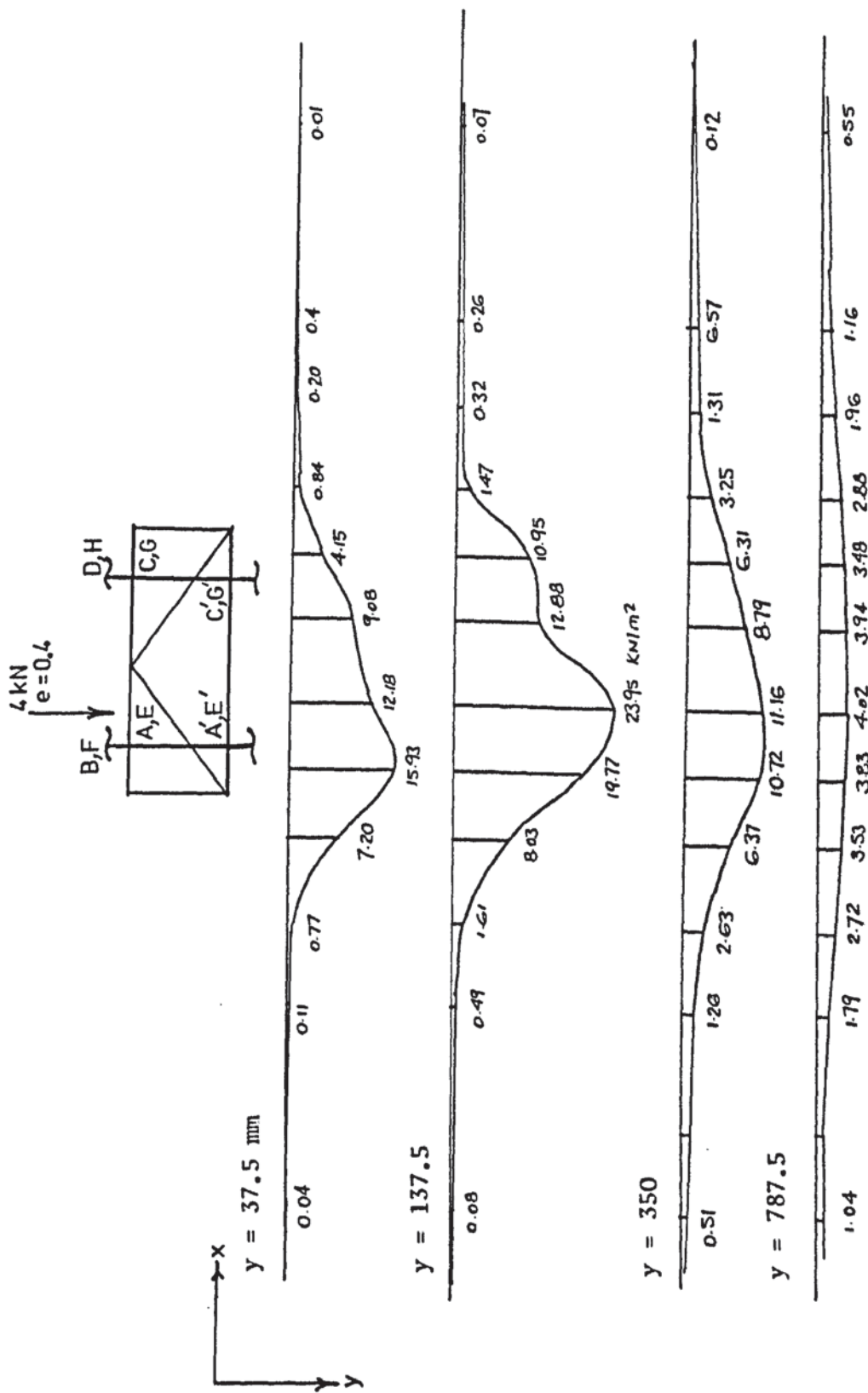


FIGURE 8.54 VERTICAL STRESSES IN SECTION 1-1 AT VARIOUS DEPTHS UNDER TALL STRUCTURE MODEL C1b WITH $e = 0.4$

(8.54) are shown in figure (8.55). Again a zone of high stress under the base is noticed which reduces rapidly away from the base.

The stresses under the three-column model C4, in sections 1-1 and 2-2, are shown in figures (8.56) and (8.57) respectively. The same observations as the centrally loaded four-column model are made here. At a depth of 787.5 mm the maximum stress ordinate reduces to about 21% of its value at a depth of 137.5 mm. In the lateral direction the reduction of stress is more rapid at shallow depths than at deeper levels. This is because the stresses tend to become uniform at great depths. At a depth of 37.5 mm, the stress in section 1-1 reduces to about 3% of the maximum ordinate at a distance of only 150 mm beyond the base. In section 2-2, at the same depth, this distance is about 300 mm.

8.6 RESULTS OF MODEL D: THREE-BAY FRAME

8.6.1 Deflections and settlements

Since the structure is symmetrical about the central beam ST, the results of the two frames ABHG and JKRQ, see figure (8.6), are identical and only frame ABHG is discussed. The settlements of the points A, C, E and G at the column bases are shown in figures (8.58) and (8.59) for the pad and the strip footings respectively. As the eccentricity e of the load increases, there is an increase in the settlements of both types of foundation. This is because when the load is applied in the outer bay ABCD, column bases E and G separate from the ground and move upwards. This reduces the bearing area of the foundation and increases the contact pressure.

The points shown by small circles in the figures indicate the

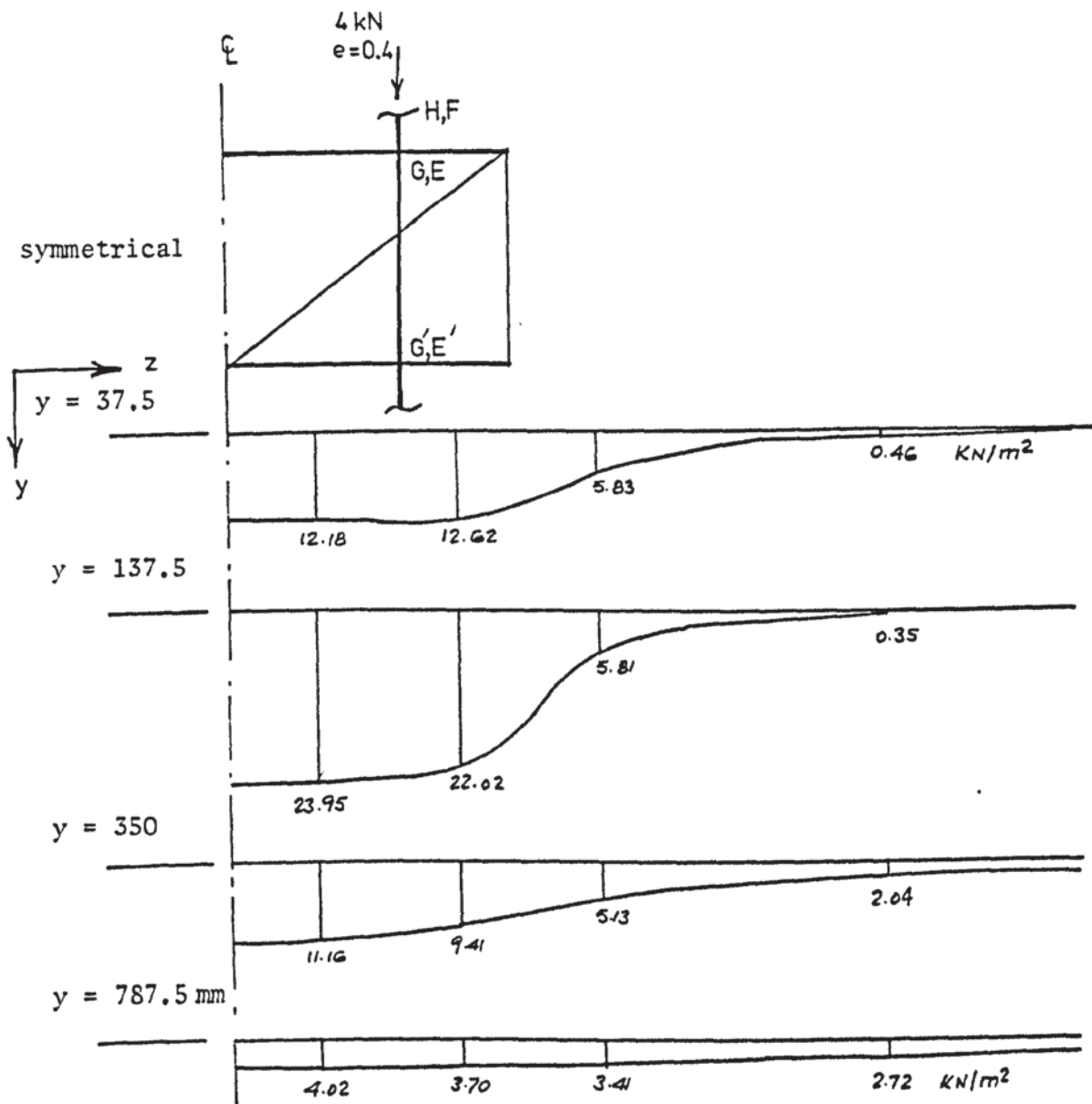


FIGURE 8.55 VERTICAL STRESSES IN SECTION 2-2 AT VARIOUS DEPTHS UNDER TALL STRUCTURE MODEL C1b WITH $e = 0.4$

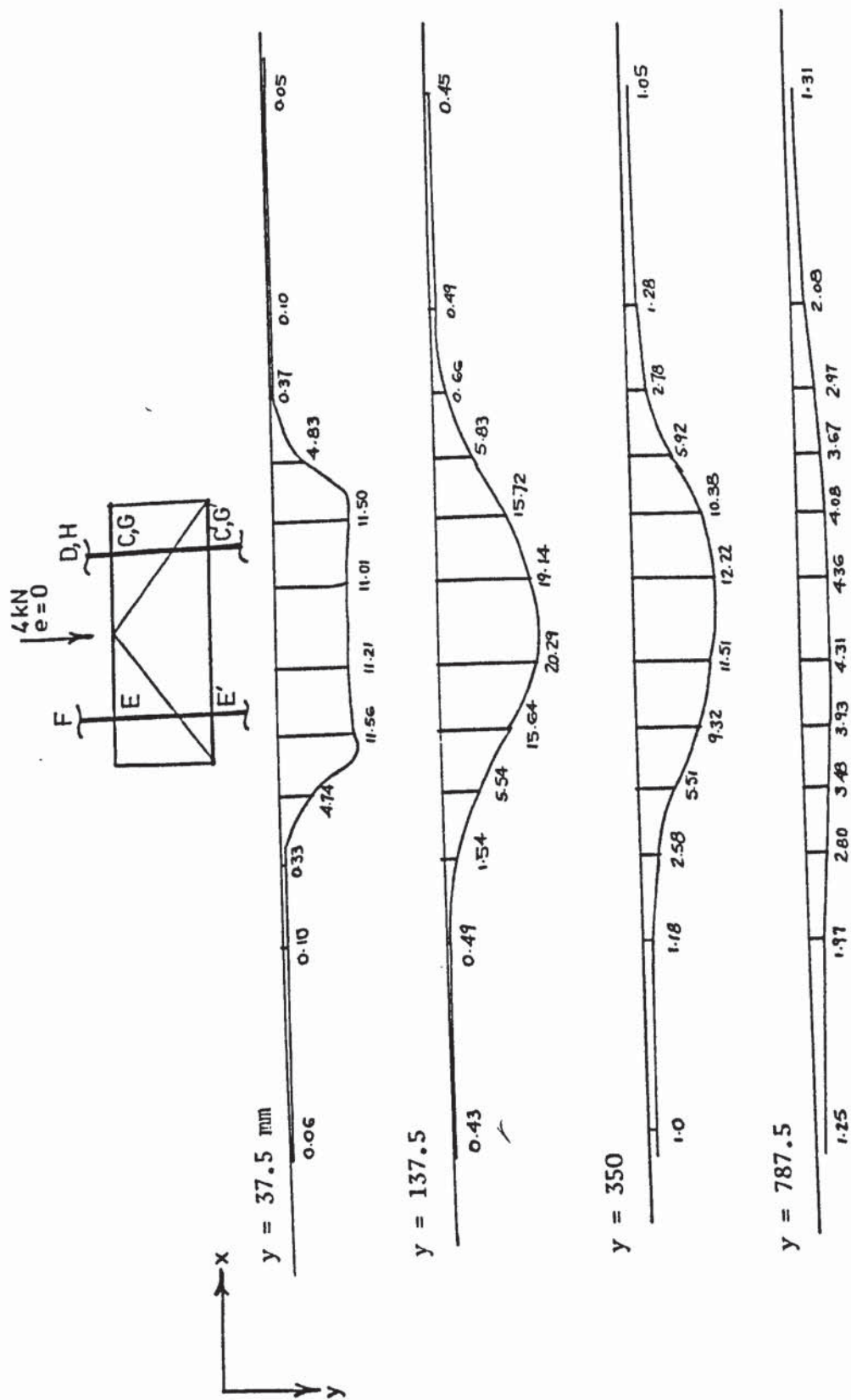


FIGURE 8.56 VERTICAL STRESSES IN SECTION 1-1 AT VARIOUS DEPTHS UNDER THREE-LEGGED TALL STRUCTURE MODEL C4

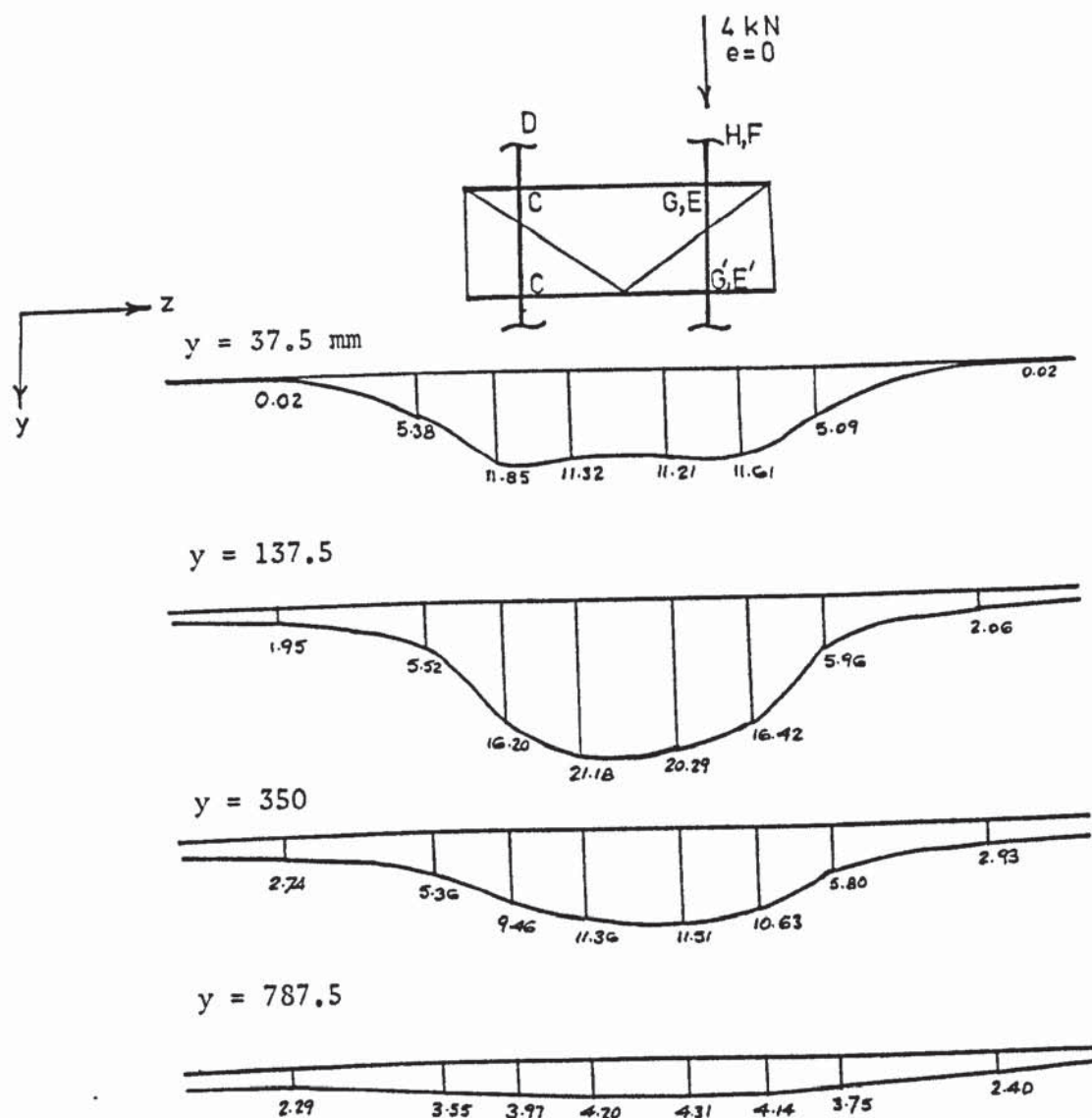


FIGURE 8.57 VERTICAL STRESSES IN SECTION 2-2 AT VARIOUS DEPTHS UNDER THREE-LEGGED TALL STRUCTURE MODEL C4

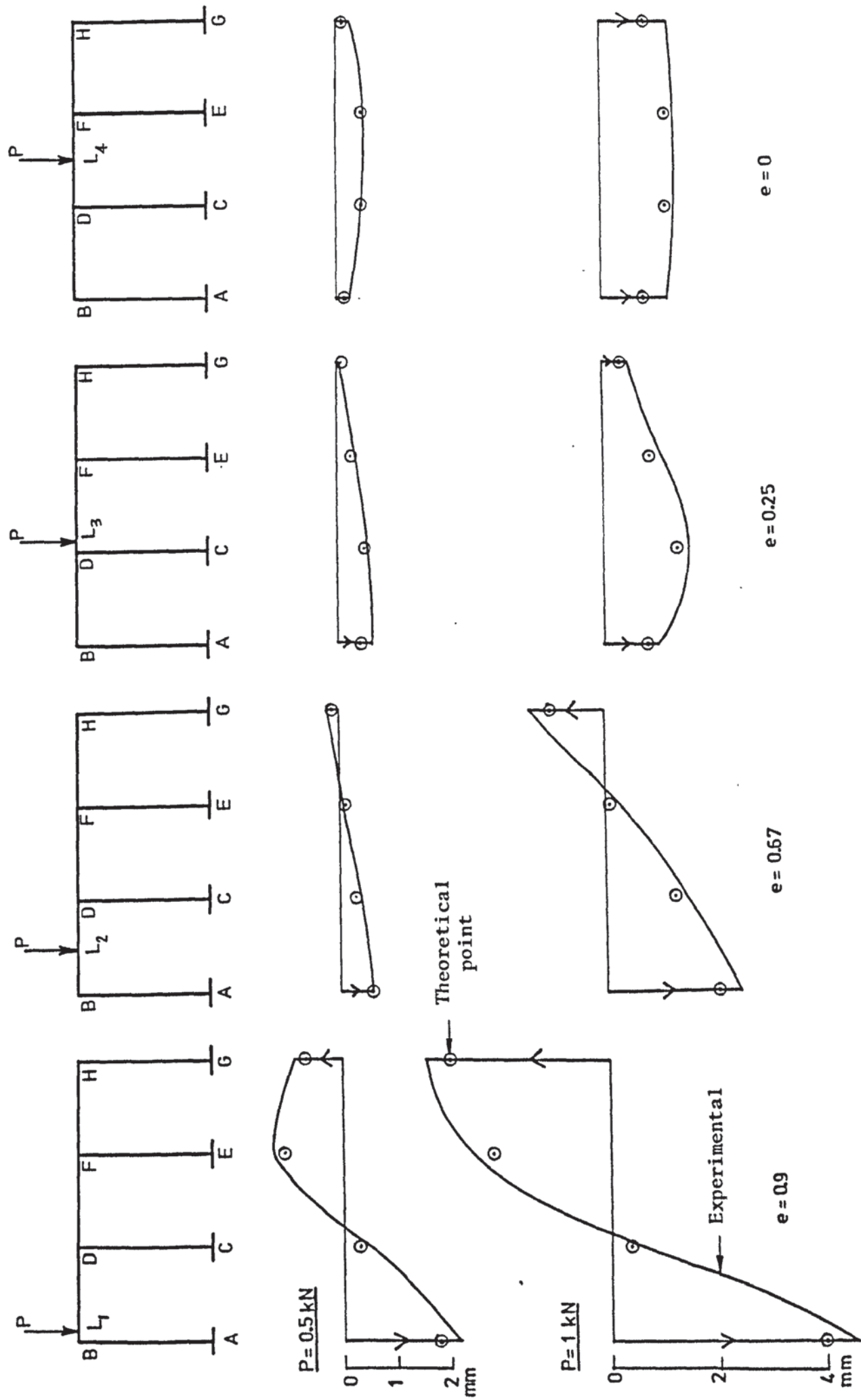


FIGURE 8.58 SETTLEMENT OF FOUNDATION OF MODEL D1 WITH PAD FOOTINGS

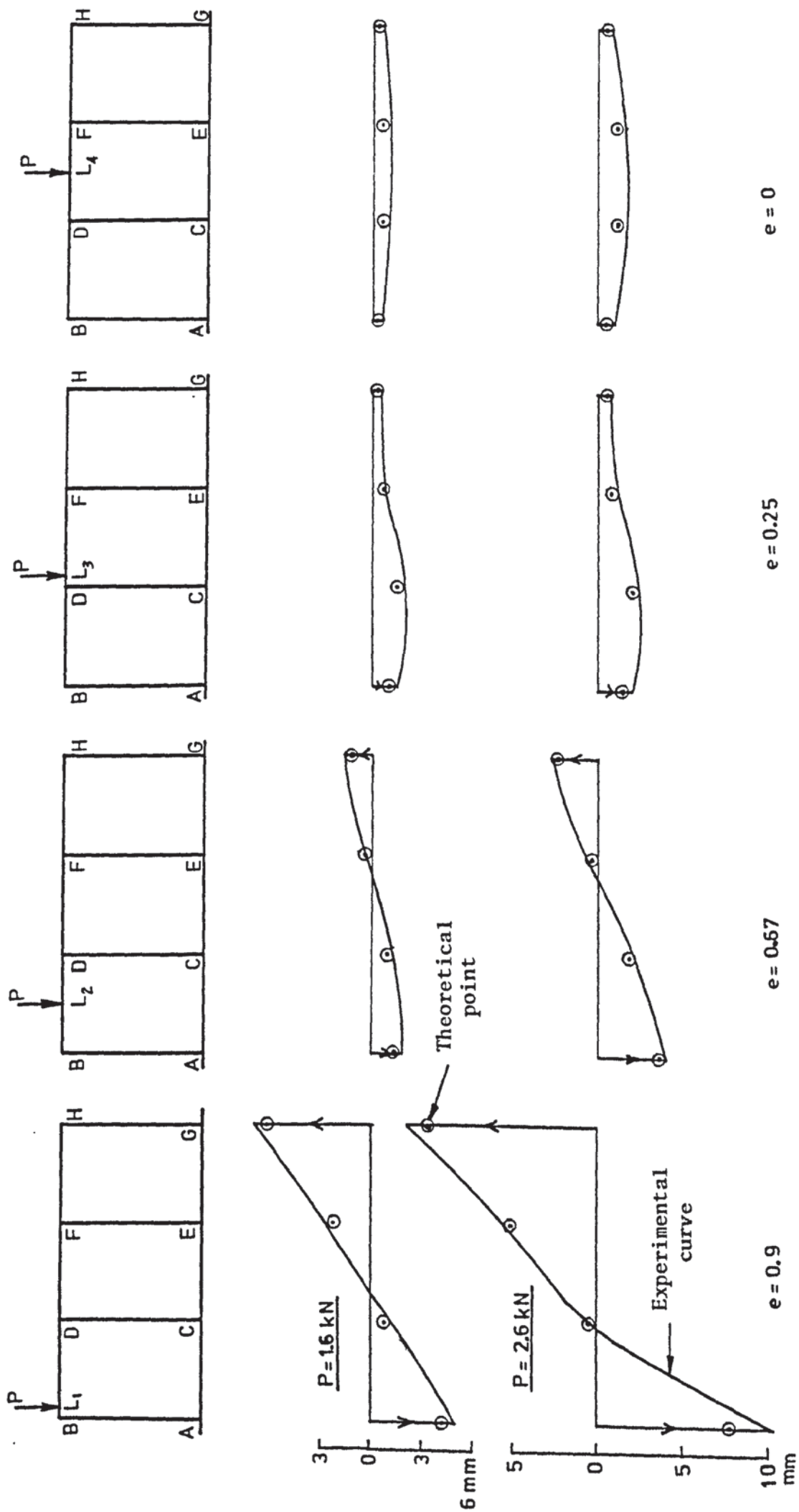


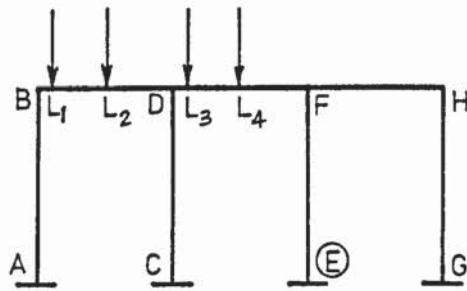
FIGURE 8.59 SETTLEMENTS OF FOUNDATION OF MODEL D2 WITH STRIP FOOTINGS

theoretical values, which show a good agreement with the experimental curves. The maximum error in the case of the strip footings is about 9%. The difference is somewhat higher in pad footings as the values are small and the experimental error is likely to be more. The maximum error in the larger values is in the order of 13%.

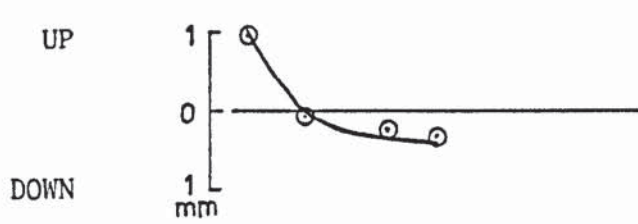
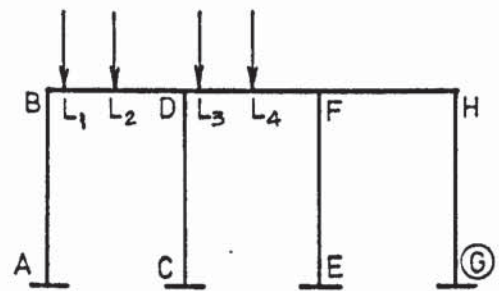
The vertical displacements of E and G are the ones that vary the most with the change in the load position. The variations of the vertical displacements at E and G with the load position are shown in figures (8.60) and (8.61) for the pad and the strip footings respectively. In figure (8.60), for pad footings, point E has a downward settlement when the load is at L_2 , L_3 and L_4 . For strip footings, this point moves upwards when the load is at L_2 . This indicates that the strip footings, being more stiff, suffers a more severe separation from the soil when the frame is loaded eccentrically.

The deflections of points A and G with varying eccentricity are compared for the two types of foundation in figure (8.62). A similar comparison for points C and E is shown in figure (8.63). The firm lines indicate the strip footing case and the dashed lines indicate the pad footings. The diagrams are drawn for an applied load of 1.2 kN. Under symmetrical loading, $e = 0$, the settlements of A and G in figure (8.62) are equal, small and downwards for both footings. The settlement of the pad footings is however some 83% higher than that of the strip footings. As the eccentricity increases the downward settlement of A increases. This increase is more rapid in the case of the pads. At $e = 0.9$, point A in the pad footings settles 244% more than that in the strip. The displacement of point G on the other hand reverses direction at a

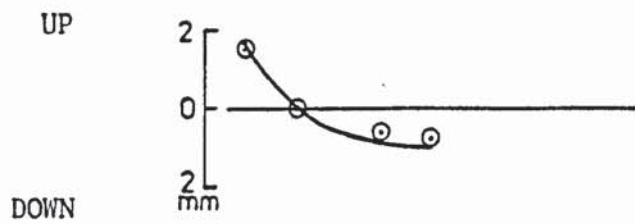
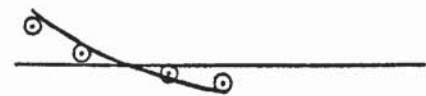
AT POINT E



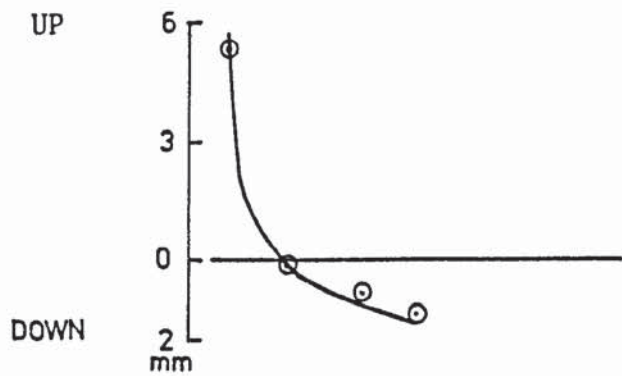
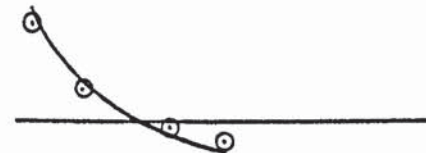
AT POINT G



LOAD
0.4 kN



0.8 kN



1.2 kN

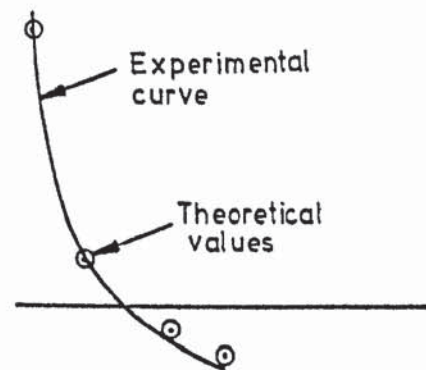
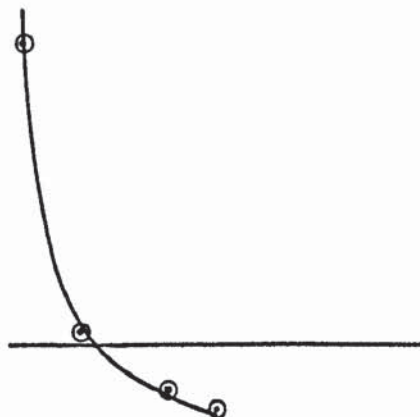
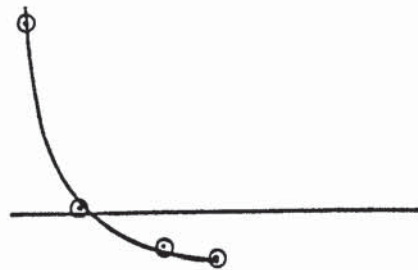
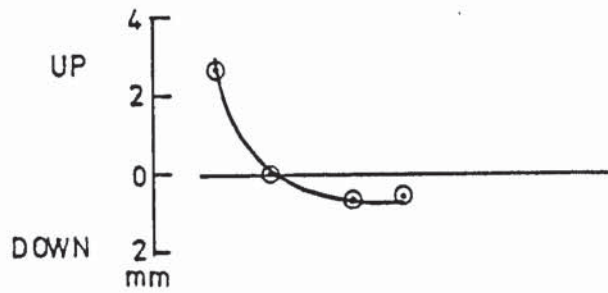
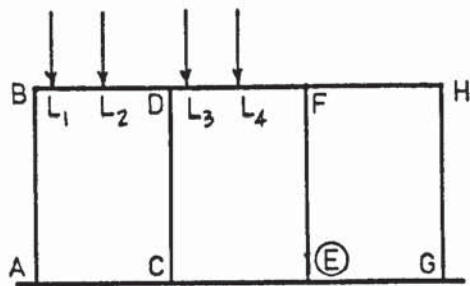
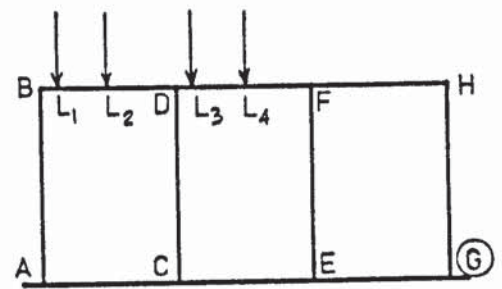


FIGURE 8.60 VARIATION OF SETTLEMENT WITH LOAD POSITION IN MODEL D1 WITH PAD FOOTINGS

AT POINT E

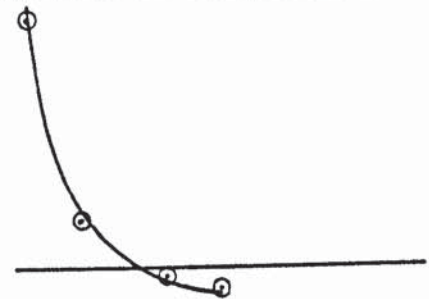


AT POINT G

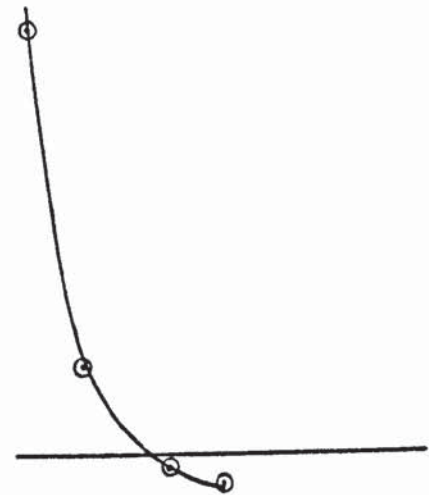


LOAD

2 kN



2.5 kN



3 kN

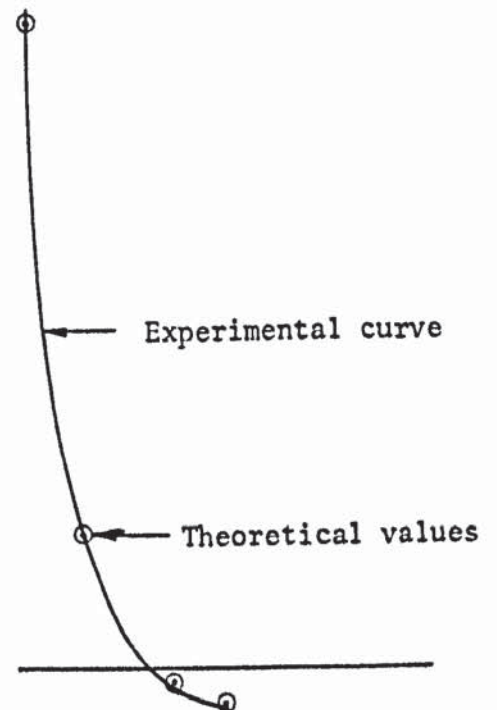


FIGURE 8.61 VARIATION OF SETTLEMENT WITH LOAD POSITION:
MODEL D2, STRIP FOOTINGS

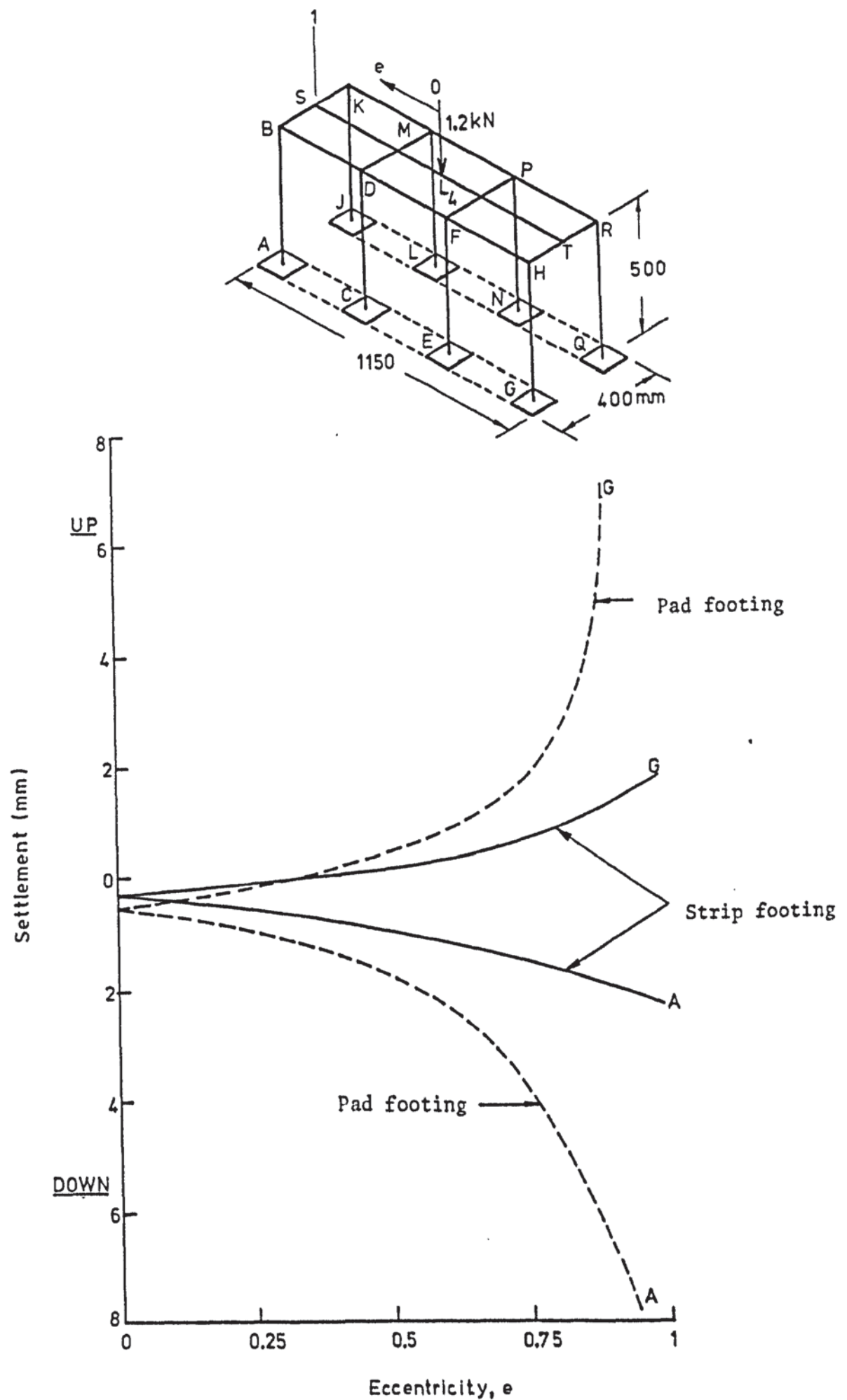


FIGURE 8.62 SETTLEMENTS OF POINTS A AND G OF THE THREE-BAY FRAME AT LOAD = 1.2 kN

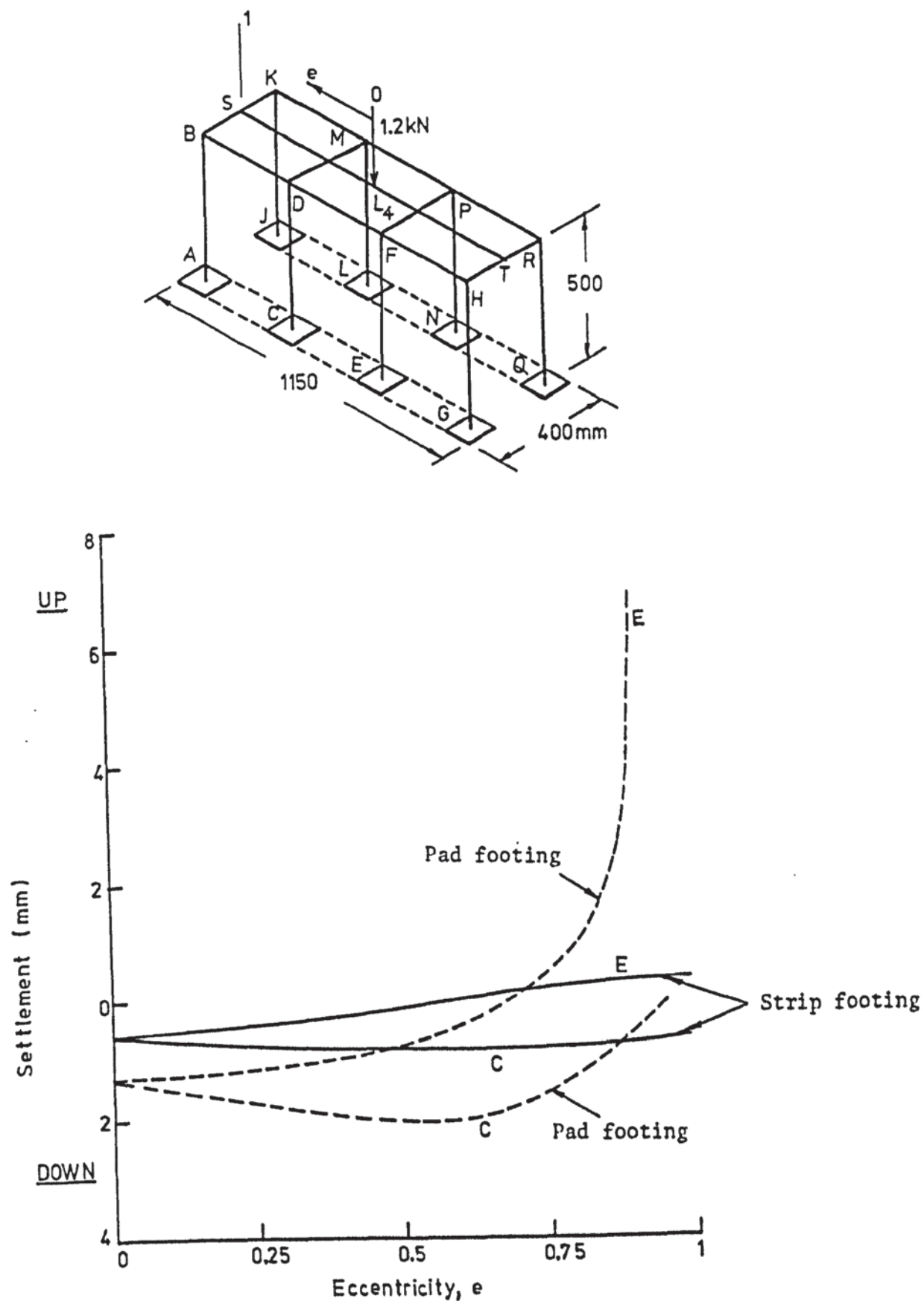


FIGURE 8.63 SETTLEMENTS OF POINTS C AND E OF THE THREE-BAY FRAME AT LOAD = 1.2 kN

value of e between 0.33 and 0.36 and increases rapidly in the upward direction for higher eccentricities. This increase is also more pronounced in the pads than in the strip. The same trend is also noticed in the displacements of points C and E in figure (8.63).

It is observed in figures (8.62) and (8.63) that the pad footings displace more than the strip footings even at $e = 0$ and that these displacements become excessive at high values of e . It is considered that the following are the reason for this:

- (1) The strip footings connect the various column bases and make the structure more rigid. As one column settles, the stiffness of the beams and the strips transmit the forces to the other columns and involve them in reducing the deflections. When pad footings are used the columns are interconnected only by the beam at the top. The system is thus more flexible and the columns act more independently of one another. This reduced interaction between the columns contributes to the increased settlement of the pad footings.
- (2) As the separation of the foundation from the ground takes place, the strip footing arches down still holding the separated columns as part of the structure. These columns continue to contribute stiffness to the structure and interact with the other members in reducing the deflections. In the case of the pad footings, the separated columns hang from the beams and do not contribute to or take part in the deformation of the structure. In fact when the load is in the outer bay ABDC and both footings E and G lift up, the entire portion DFHGE, see figure (8.60), acts as a cantilever without an applied load and do not contribute to the stiffness of the structure. This accounts for the large post-

separation displacements of the pad footings in figures (8.62) and (8.63).

8.6.2 Bending moments

The bending moments in the columns with a load of 1.5 kN acting centrally on the frame are shown in figure (8.64). Line (1) represents the theoretical bending moments for the strip footing case and line (2) shows that for the pad footing case. The moments shown by line (3) were obtained by analysing the frame assuming the column bases to be completely fixed. Both types of footings show a wide variation of the bending moments from the fixed base case. The pad footings rotate almost freely and give very small moments at the column bases. The moments at the top are greatly increased and there is a reversal of the sign in column AB. The difference in the column top moments between this case and the fixed base analysis is 113.8% in AB and 52.1% in CD. In the case of the strip footings the column bases are interconnected and therefore offer resistance to the rotation. Consequently there is an increase in the bending moments both at the base and the top of the columns. There is also a reversal of the sign of the moments in column AB. The maximum difference between these moments and the fixed base moments is 123.4% in AB and 69.2% in CD. The diagrams show that it is wrong to assume the columns, with strip footing, are fixed base.

The variations with the eccentricity of the bending moments at the top of columns AB and GH are shown for a load of 1.5 kN in figures (8.65) and (8.66) respectively. In figure (8.65) the high negative bending moment in the strip footing case reduces after $e = 0.4$ and becomes positive at $e = 0.89$ increasing steadily after-

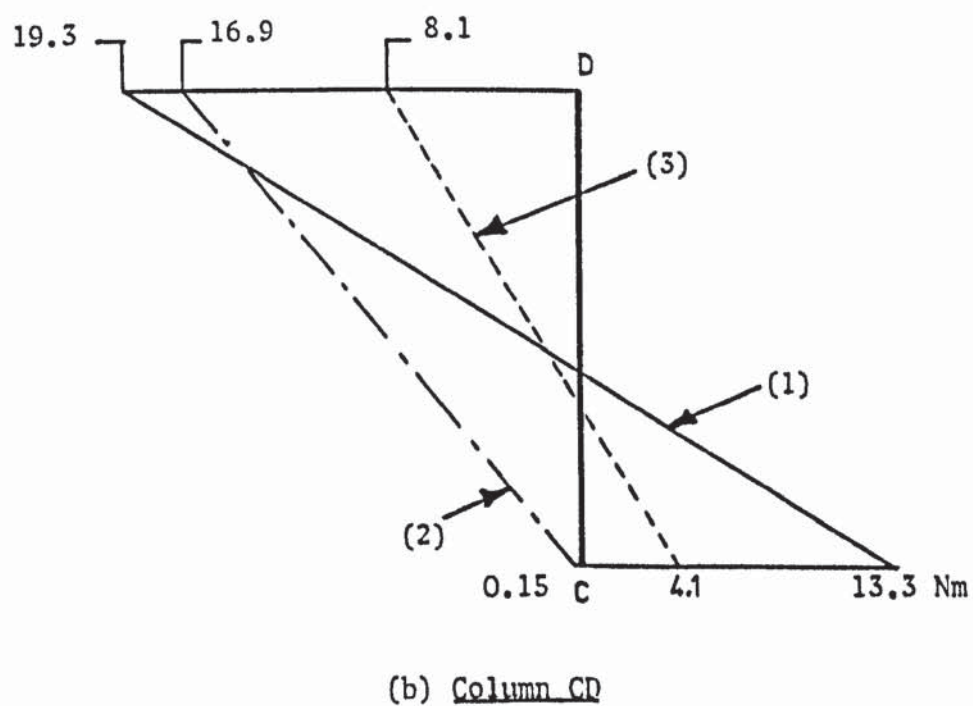
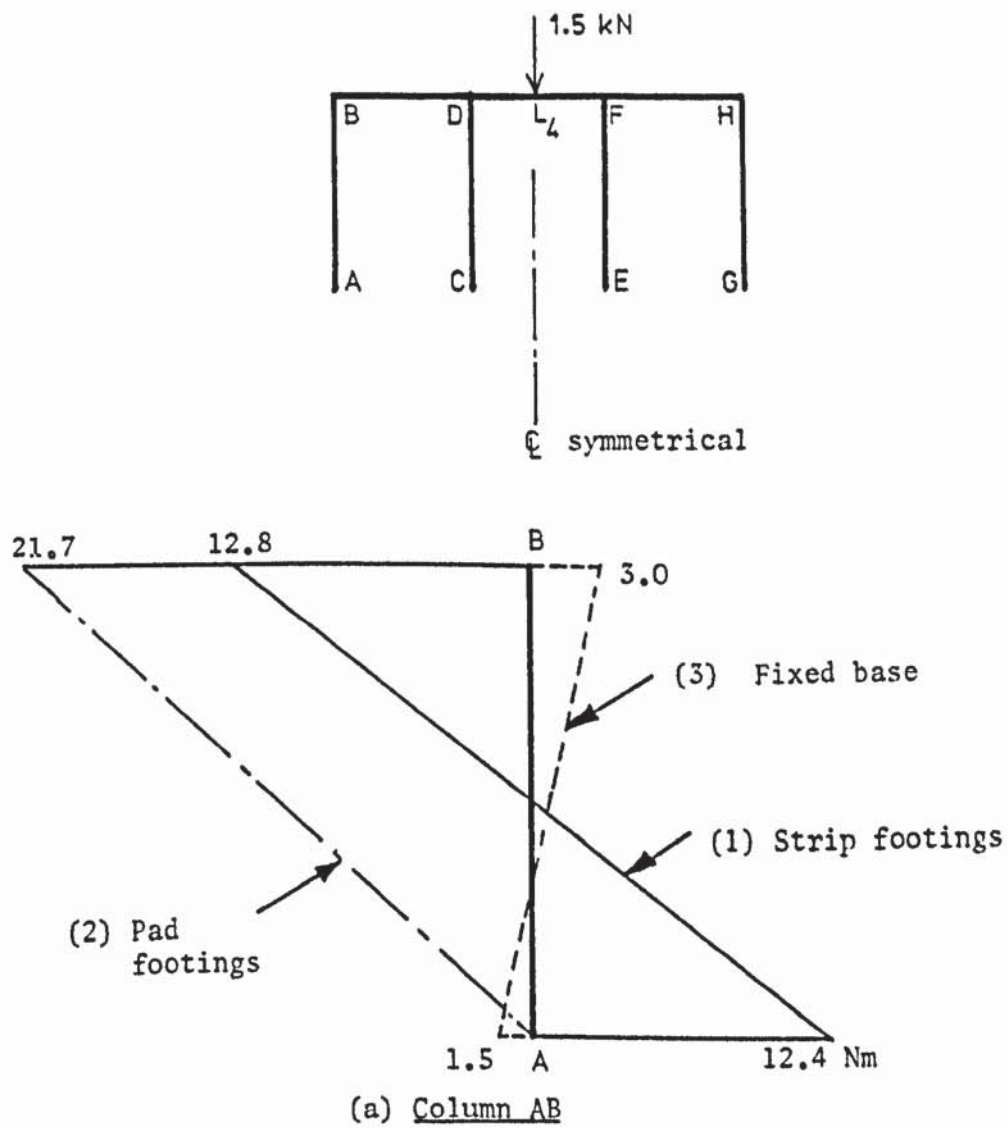


FIGURE 8.64 COMPARISON OF COLUMN BENDING MOMENTS IN THREE-BAY FRAME

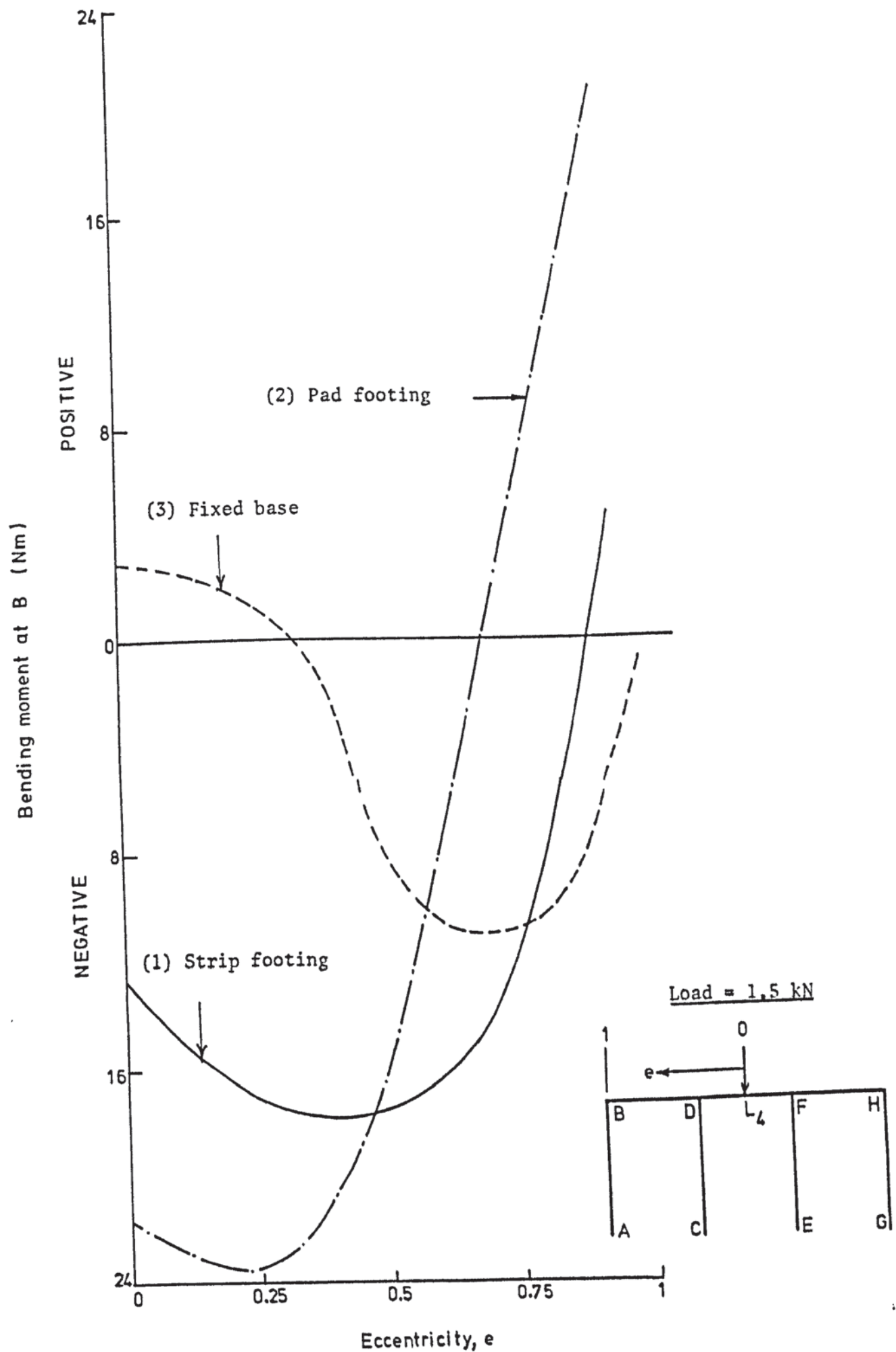


FIGURE 8.65 VARIATION OF BENDING MOMENT WITH ECCENTRICITY AT TOP OF COLUMN AB

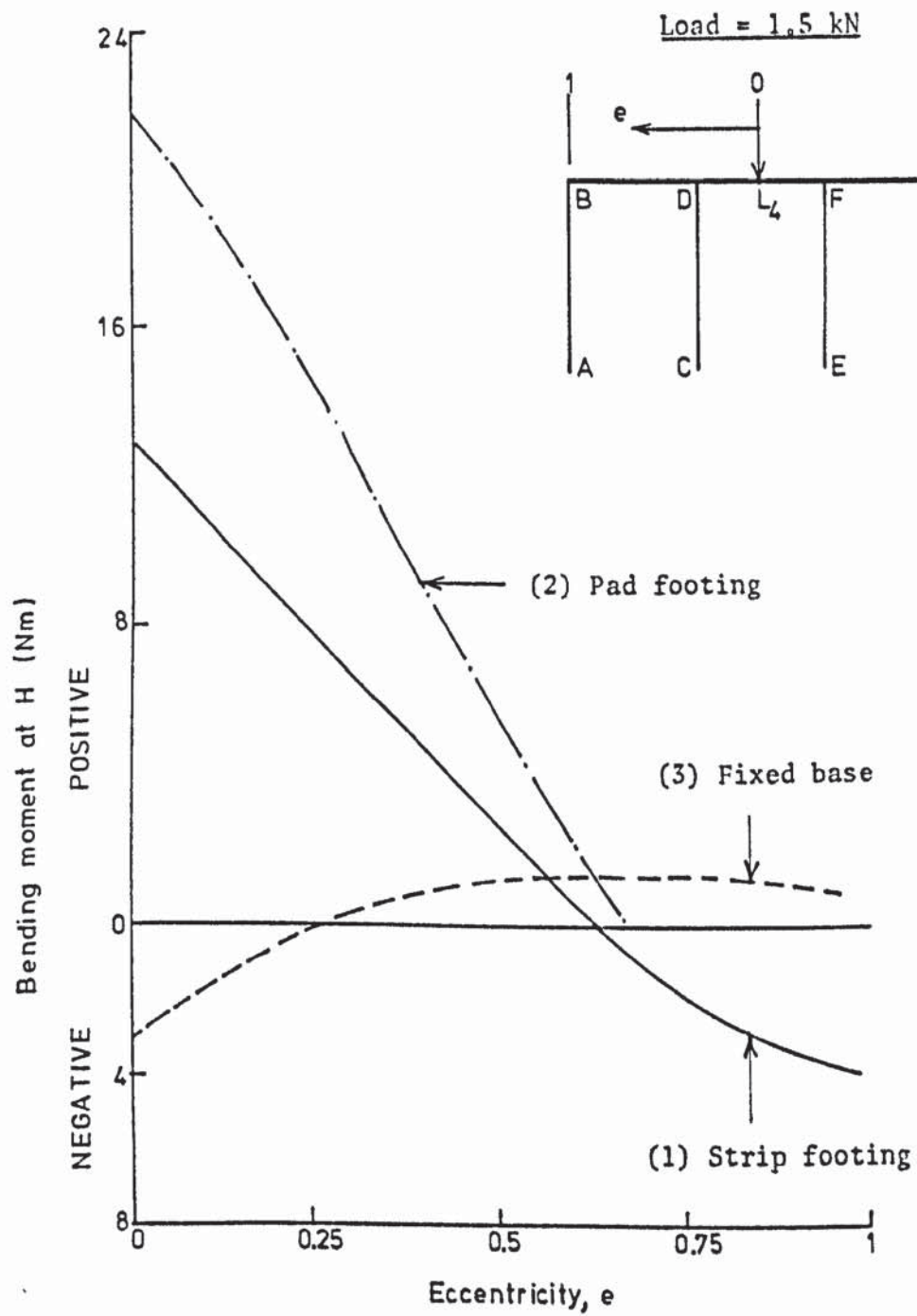


FIGURE 8.66 VARIATION OF BENDING MOMENT WITH ECCENTRICITY AT TOP OF COLUMN GH

wards. The negative moment in the pad footing case starts reducing early at $e = 0.25$ and becomes positive at $e = 0.69$. This is again due to the relative freedom of rotation of the pads. While the fixed base curve initially gives positive moments, it becomes negative at $e = 0.33$. As e approaches unity all three curves become parallel, with the pad footing showing the highest and the fixed base case the lowest moment.

In figure (8.66) the fixed base moment at the top of column GH is opposite in sign to the other two cases, for e less than 0.25. As e increases further in the fixed base case, the axial force in GH becomes tensile due to its tendency to lift up from the support. The bending moment remains almost constant and then reduces when e is close to unity. As was stated, after separation of footing G from the soil at $e = 0.67$, column GH acts as a free cantilever in the case of the pad footings. Therefore, the moment in this column becomes zero. In the strip footing case the column remains an active part of the structure after the separation. The bending moment reverses the sign and continues to increase in magnitude.

8.6.3 Stresses in the soil

The vertical stresses in the soil, obtained analytically, in a vertical section passing through the footings, are shown for a typical case, with $e = 0.25$, in figure (8.67). At a depth of 50 mm below the surface, the stress profiles for the two types of foundation are quite different. High stresses develop directly under the pad footings, reducing rapidly between the pads and diminishing away from the structure. On the other hand, there is a more uniform stress distribution under the strip footing as this distributes the column loads more efficiently. Deeper in the soil however the difference between the two stress profiles reduces to almost zero.

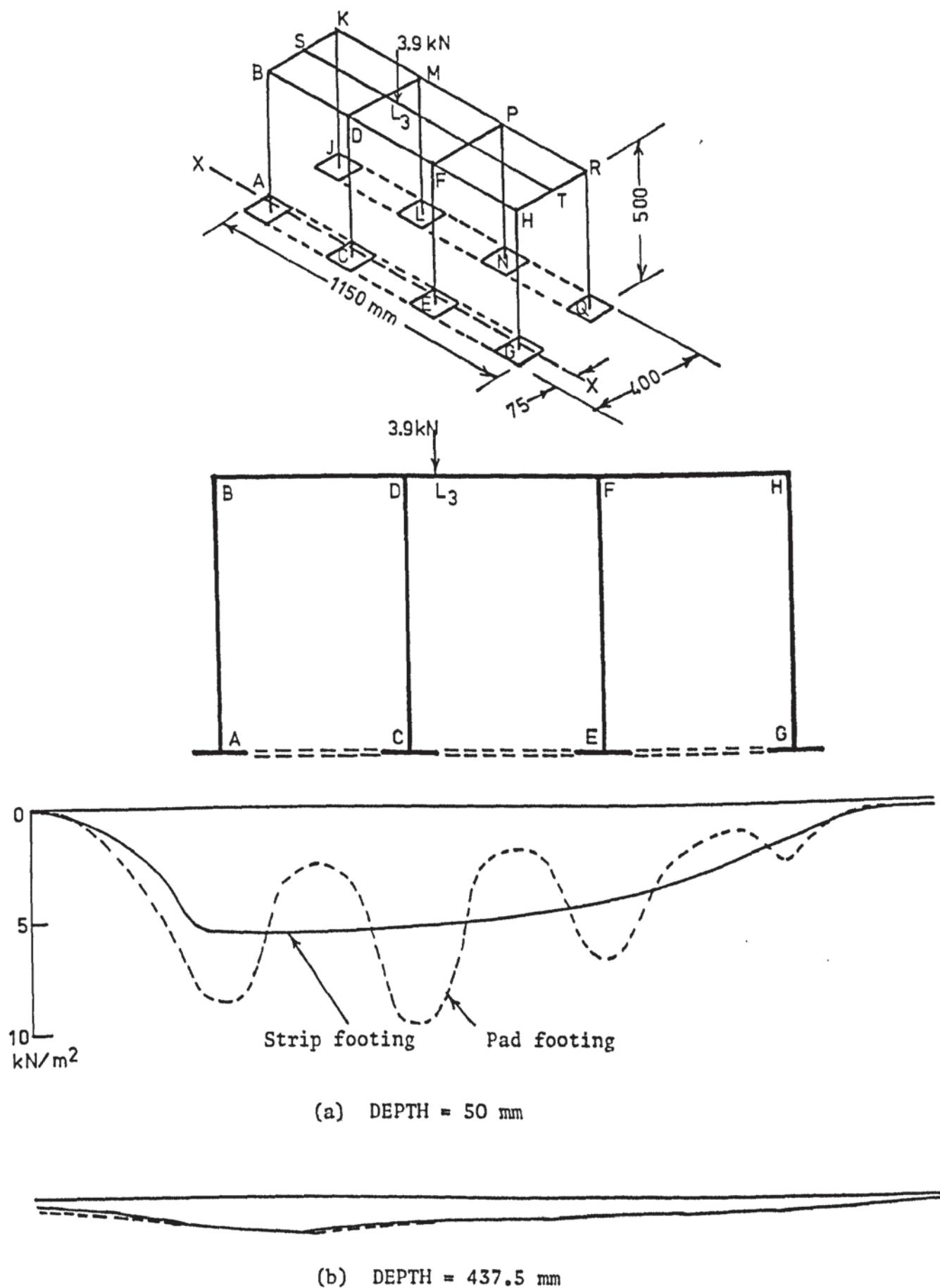


FIGURE 8.67 VERTICAL STRESS DISTRIBUTION UNDER THE THREE-BAY FRAME IN SECTION X-X

CHAPTER 9

INTERACTIVE BEHAVIOUR OF PRACTICAL STRUCTURES

9.1 INTRODUCTION

The method of analysing a complete structure together with its foundation and the supporting soil developed in this thesis has so far been applied to simple frames and model structures. Its usefulness is now tested by analysing complex practical structures. Two such structures, for which an exhaustive interactive analysis would normally be considered either impossible or expensive, were selected for this purpose. The first was a complex of four silos resting on a chalk foundation and the second was a 50-storey space frame resting on a bed of clay. Both are described in this chapter.

9.2 A SILO COMPLEX

Burland and Davidson (1976) published a detailed report of the observed behaviour of a silo complex resting on chalk with non-linear material properties. The structure had concrete columns that developed severe cracks during the filling of the silos. The recordings of settlements of the silo bases and cracking of the columns constituted a useful case history of structure-soil interaction. However, an exhaustive interaction analysis of the silos and their foundations was not performed by Burland and Davidson. The structures were designed and the foundation settlements were calculated on the assumption that each silo acted independently. The purpose here is to present an analysis of the silos together with their foundations and the supporting soil. It is shown that

not only the soil and the structure interact but the loading of one silo influences the others via the soil.

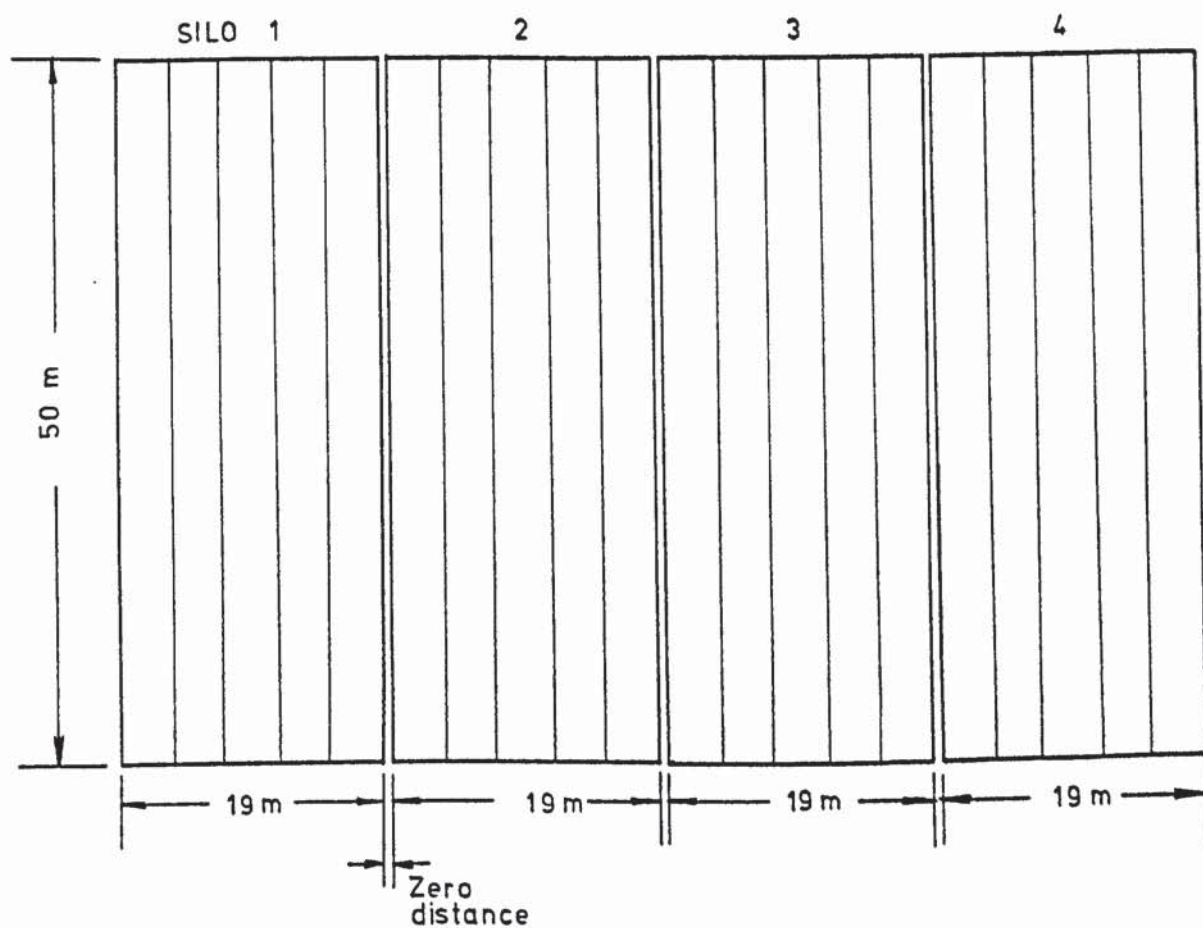
9.2.1 Description of the silo structure

The complex analysed consists of a battery of four polygonal silos placed side by side in a row, as shown in figure (9.1). Each silo has a plan area of 336.5 m^2 and a height of 50 m. They are separated from each other at the base level and throughout the height. The walls of the silos are 230 mm thick and they rest directly on a 1.22 m thick raft, as shown for a typical silo in figure (9.2). The raft has the same area in plan as the silo cross section and the wall is constructed monolithically at its circumference. Each silo contains a 1.065 m thick flat floor elevated 2.5 m from the raft by 32 columns. The floor and the columns are structurally separated from the walls. The diameter of columns 3, 4, 5 and 10, see figure (9.2), is 431 mm while that of the rest is 610 mm.

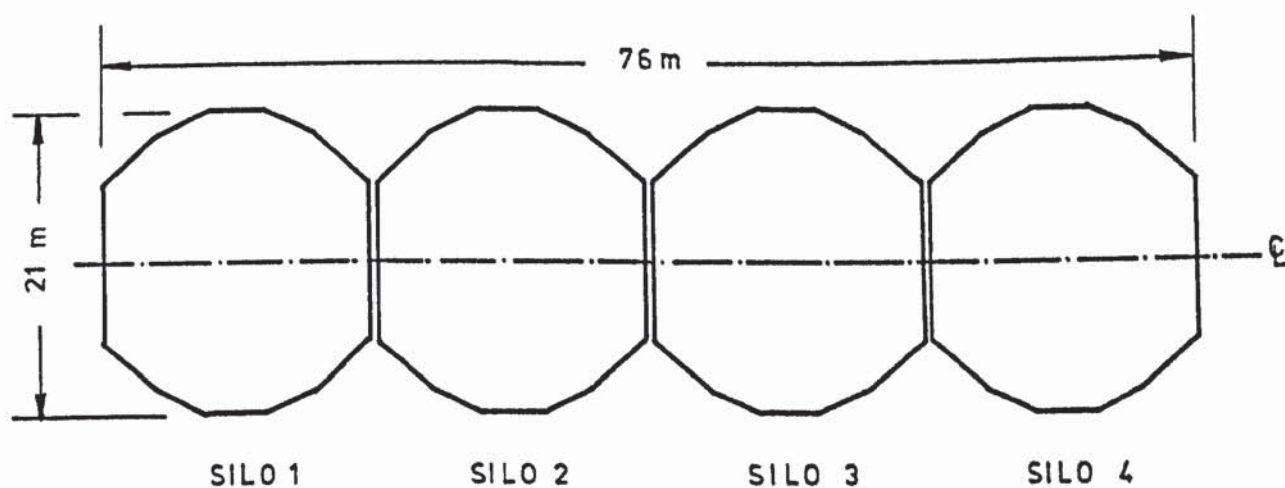
The rafts of the silo were made of reinforced concrete with a nominal cube strength of 25.8 N/mm^2 . This value for the concrete in the columns was 41.3 N/mm^2 . In the present analysis the modulus of elasticity of the material of the raft was assumed to be $27 \times 10^6 \text{ kN/m}^2$ and that for the columns, the floors and the walls was $31 \times 10^6 \text{ kN/m}^2$. In all the cases the value of ν was assumed to be 0.15. The self weight of each silo is 4100 tonnes and the weight of the stored material is 12000 tonnes.

9.2.2 Description of the supporting soil

The boreholes sunk at the site of the silo complex indicated that the ground consisted of chalk overlaid by a shallow layer of



ELEVATION



PLAN

FIGURE 9.1 THE SILO COMPLEX

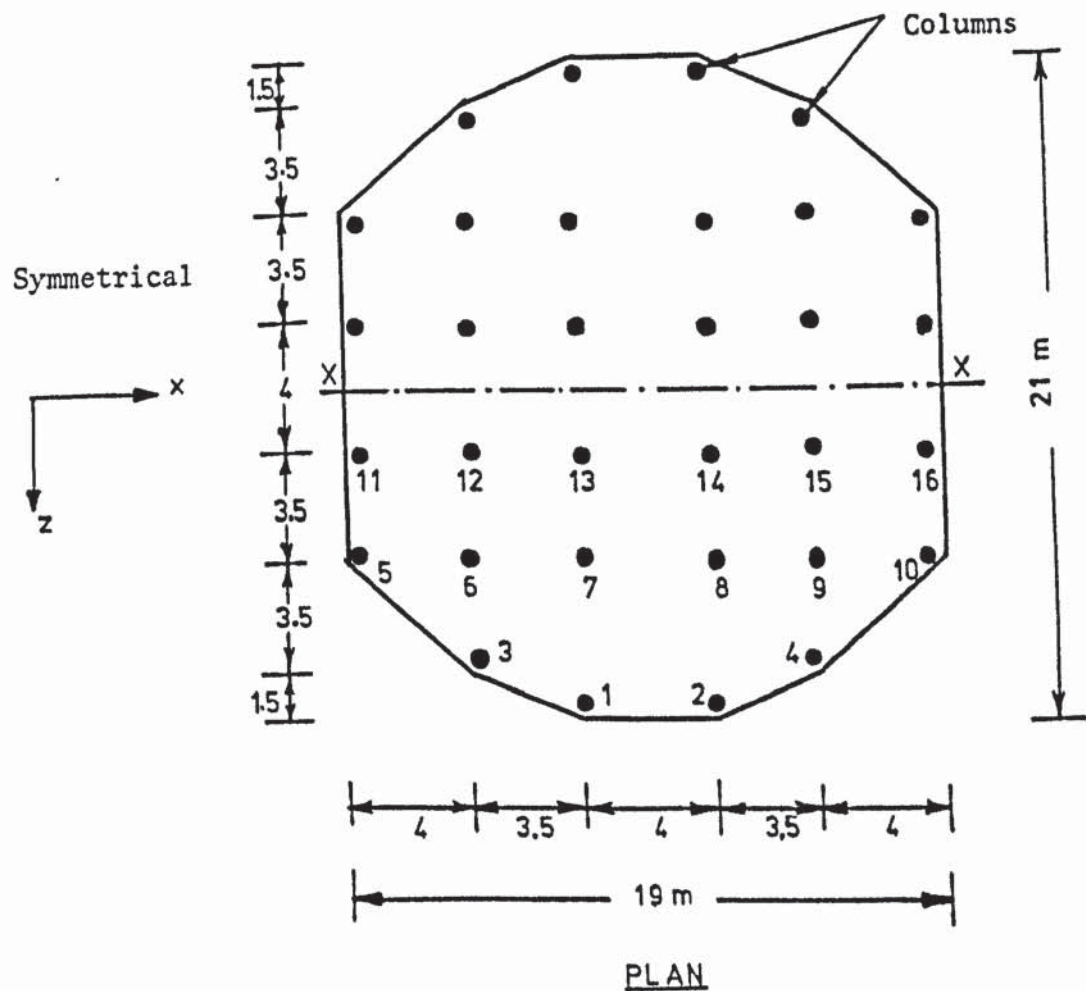
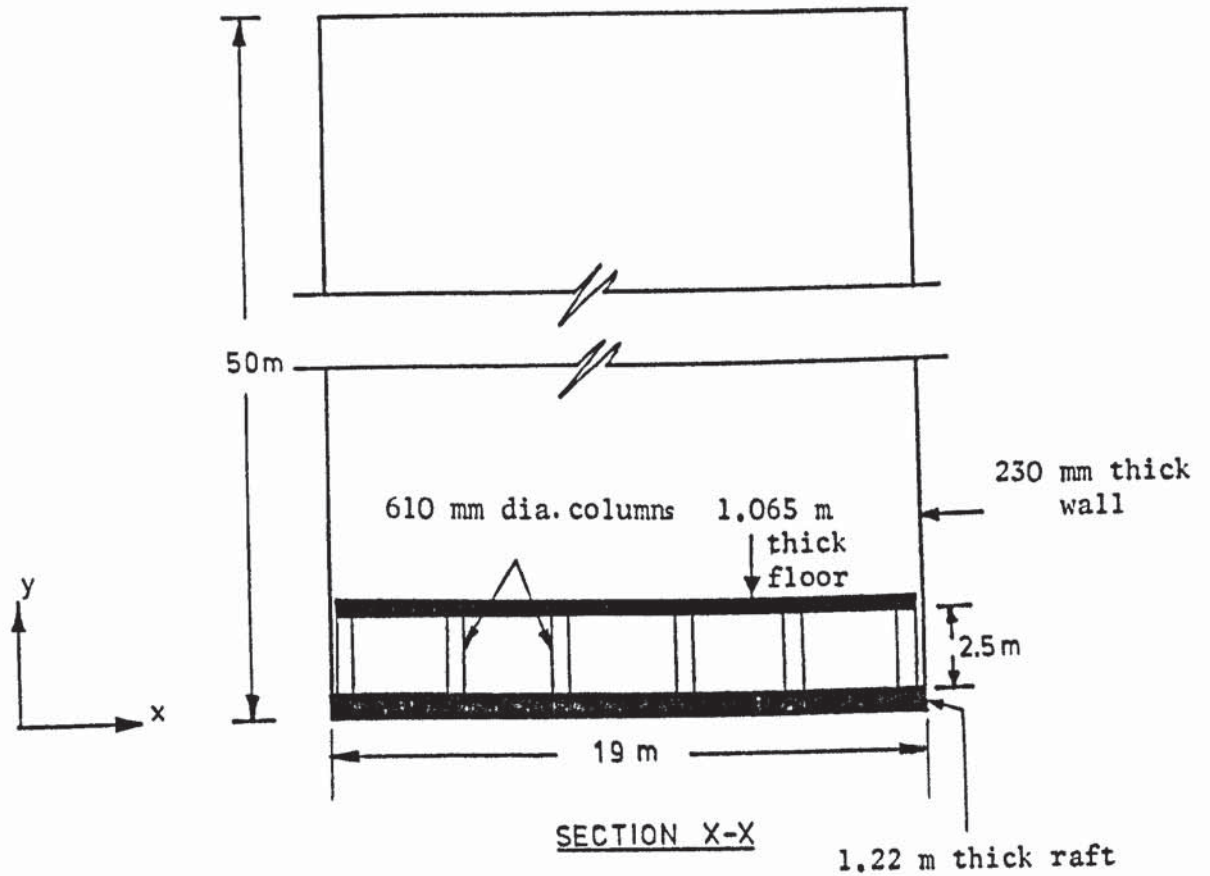


FIGURE 9.2 A TYPICAL SILO

stiff sandy clay with flints and gravel. Plate loading and standard penetration tests were performed on the site to determine the mechanical behaviour of the chalk. In the settlement calculation of the raft, Burland and Davidson assumed a uniform quality of chalk to a great depth. Plate loading tests with different diameter plates yielded different pressure-settlement curves. All of these were approximately bilinear, with the initial modulus of elasticity ranging between 135 and 617 N/mm^2 and the final value between 11 and 20 N/mm^2 . The values of the moduli obtained from the relationship between the average settlement and the average bearing pressure, observed after the silos were constructed, were however different. The values reported for silo 3 are 686 N/mm^2 for the initial and 26 N/mm^2 for the final modulus of elasticity.

A randomly heterogeneous soil can be analysed by the method presented in this Thesis. However, the insufficient data available made the author to assume a uniform quality of chalk. The stress-strain property of the soil was taken from the observed pressure-settlement relationship of silo 3 as reported by Burland and Davidson. The stress-strain curve is shown in figure (9.3), in which the central portion, shown dashed, was approximated by a straight line. This gave a trilinear representation of the stress-strain relationship of the chalk. The value of Poisson's ratio was assumed to be 0.24 which is the same as given by Burland and Davidson.

9.2.3 Finite element idealization of the problem

The silos in the complex were side by side, thus they were interconnected by the ground and interacted with each other. This

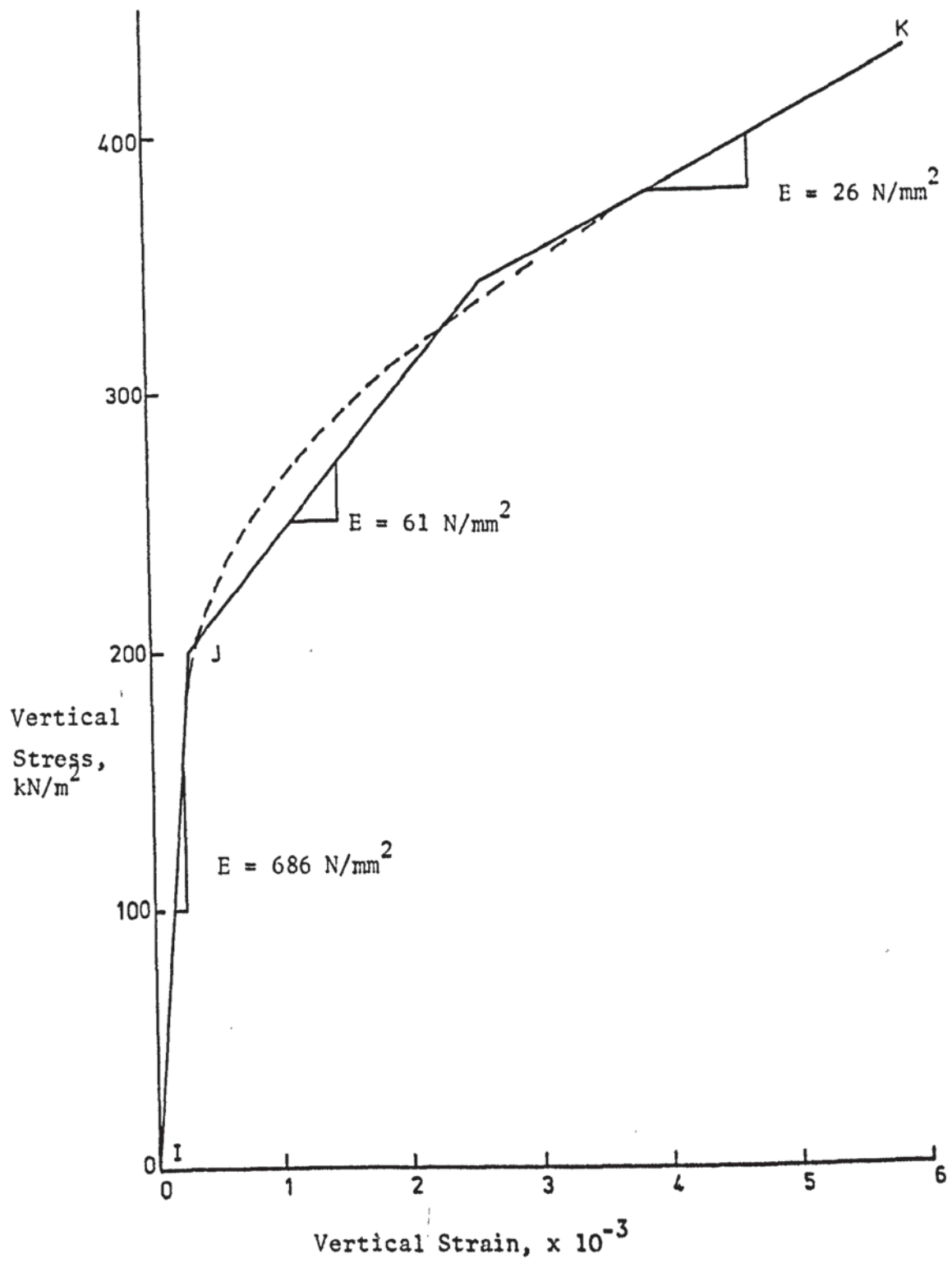
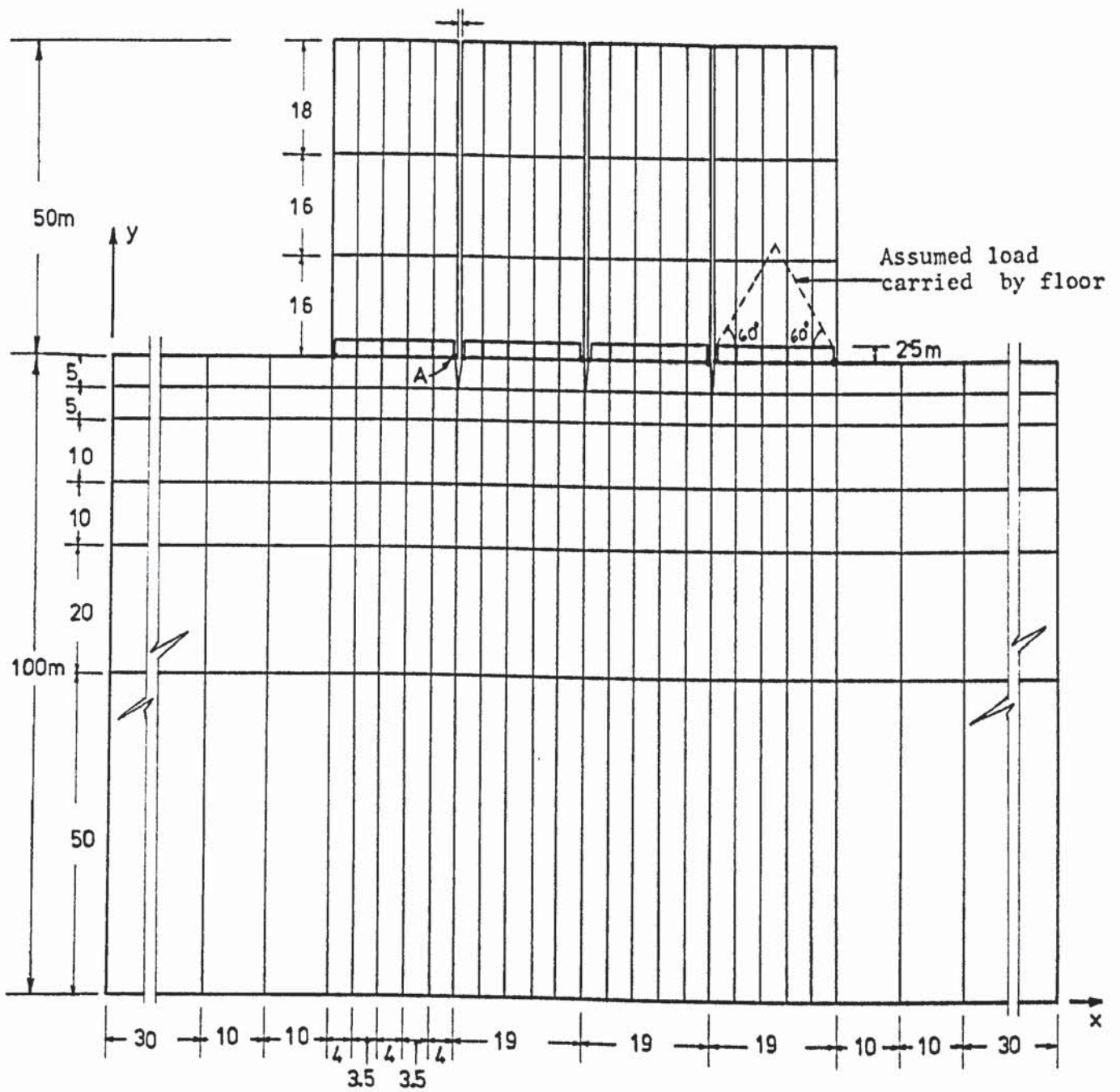


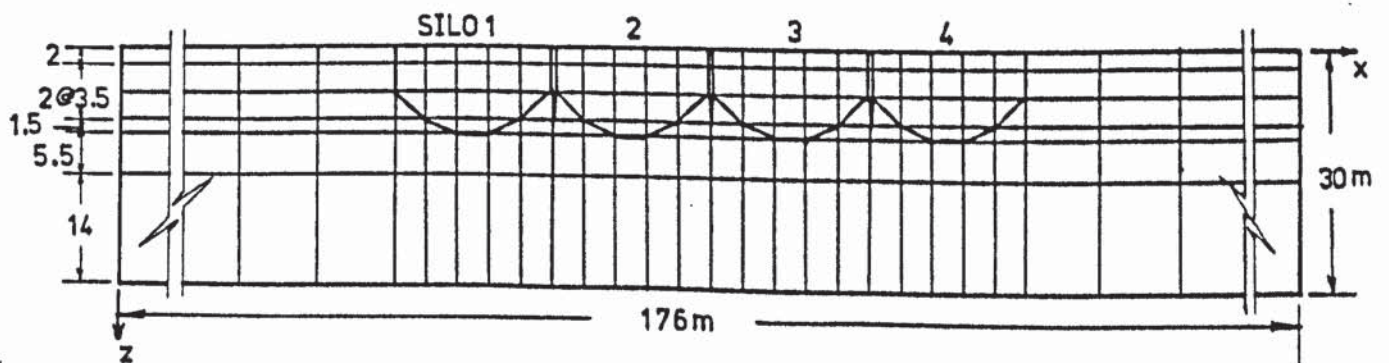
FIGURE 9.3 STRESS-STRAIN DIAGRAM OF CHALK

is in spite of the fact that the silos themselves were entirely separated from each other. The analysis of an individual silo neglecting the influence of the others on its behaviour is thus inadequate. The complete battery of silos together with their supporting soil was therefore considered as an integral system. A three dimensional body of soil under the silos was enclosed by rough rigid planes and included in the analysis. A depth of 100 m below the ground surface, a distance of 50 m on the longitudinal sides and 19.5 m on the lateral sides were considered. Because of symmetry about the vertical plane passing through the longitudinal centre line of the silos, only half of the structure was analysed. The finite element mesh used for this problem is shown in figure (9.4). As the silos and their bases are structurally separated from each other, they were represented as separate structures with a zero distance between them. Joints, such as A in figure (9.4), on the ground surface at the junction of two silos were given two numbers with the same co-ordinates and degrees of freedom. Thus all the joints at the boundary between two silos acted independently and displaced relative to each other. The soil was represented by three dimensional solid elements. The walls, the floors and the rafts were represented by rectangular plate elements while the columns were represented by prismatic members. The cylindrical shape of the walls of the actual silos was approximated by plane rectangular plates as a curved plate element is not included in the program. The finite element mesh consisted of 1580 joints, 252 plates, 64 members and 936 solid elements. The total number of degrees of freedom was 3934 and the number of elements of the stiffness matrix stored by the program was 671,928. The load of the content of the silo was divided between the wall and the floor

Zero distance



ELEVATION



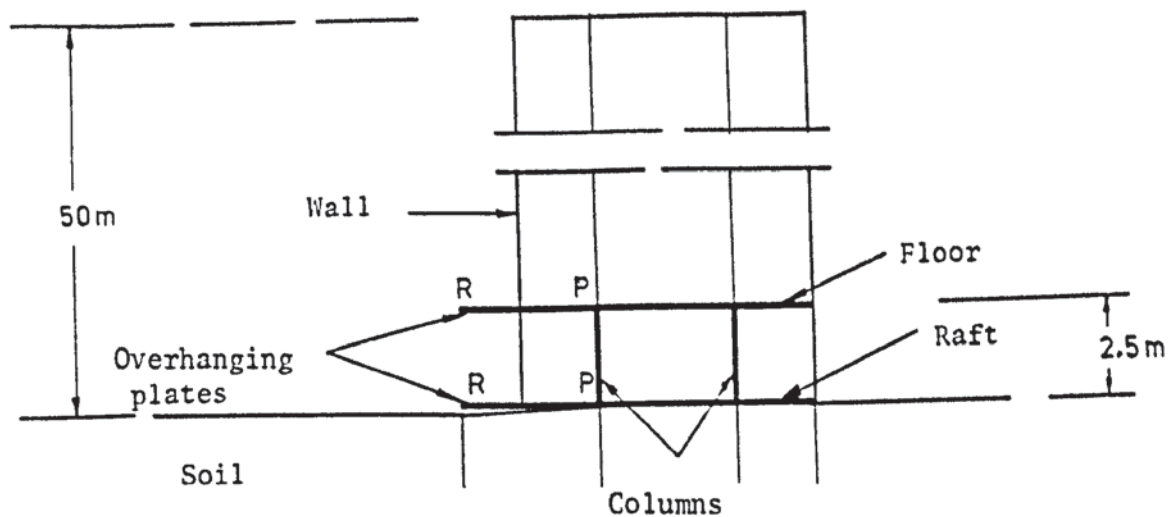
PLAN

FIGURE 9.4 FINITE ELEMENT IDEALIZATION OF SILO PROBLEM

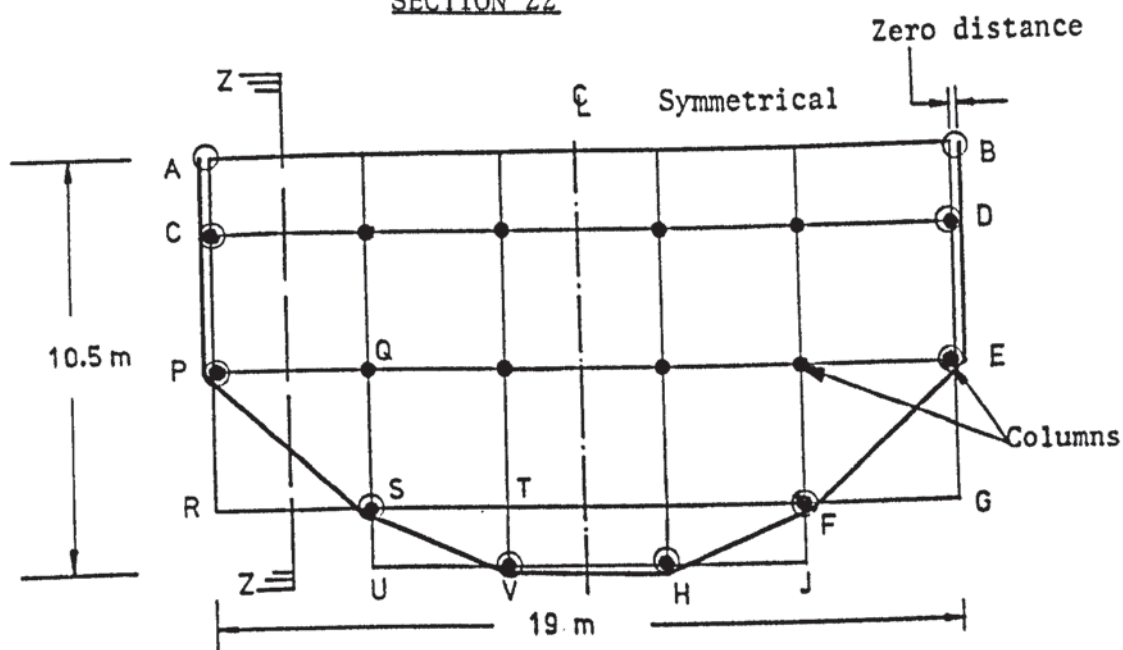
by assuming that the floor carried the material contained in a 60° cone above it. The load was assumed to be uniformly distributed on the floor and was divided among the floor joints. The load carried by the wall was divided among the joints at the top of the wall.

The detailed finite element mesh of a typical silo is shown in figure (9.5). The triangular portions of the floor and the raft such as PQS, P'Q'S', STV and S'T'V' were represented by the rectangular plates PQRS, P'Q'R'S', STUV and S'T'U'V' respectively. The silo itself was represented by the line ACPSVHFEDB, which was connected to the base only at the points A', C', P', S', V', H', F', E', D' and B'. This representation is unlikely to cause an appreciable error as no load was applied at the corners R, U, J and G of the floor. The corners R', U', J' and G' of the raft were separated from the ground by giving them two numbers each. The contribution of the additional triangular portions PRS, SUV, P'R'S' and S'U'V' etc. to the total stiffnesses of the floor and the raft is considered to be negligible.

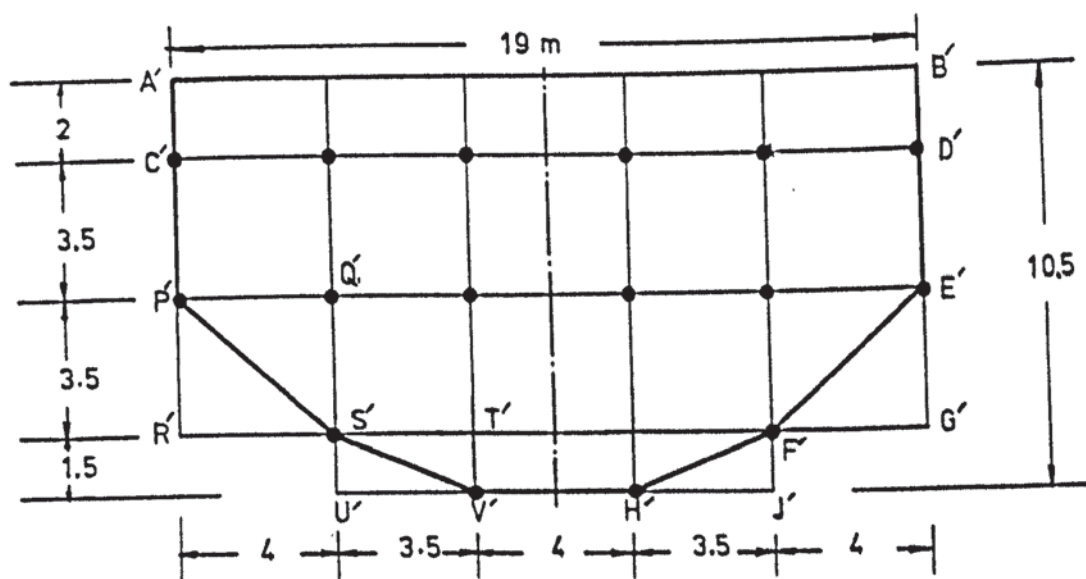
The joints A, C, P, S, V, H, F, E, D and B, shown by small circles in the figure, were on the floor and not connected to the silo wall. Therefore, the entire floor together with the portions PRS, SUV, HJF and FGE intersecting the wall deflected independently of the wall. This was done to keep the floor structurally separated from the wall as it is in the actual silo. At the base level however the joints A', C', P', S', V', H', F', E', D', and B' were connected to the raft, the wall and the soil. This was because the wall and the raft were constructed monolithically in the actual silo.



SECTION ZZ



PLAN AT FLOOR LEVEL



PLAN AT BASE LEVEL

FIGURE 9.5 DETAILED FINITE ELEMENT MESH OF A TYPICAL SILO

9.2.4 The analysis of the silos

The non-linear analysis described in chapter 5 was used for this problem. A uniformly distributed load due to the self weight and the contents was first applied on the rafts assuming them to be infinitely flexible and neglecting the silo structures. The vertical stresses in the soil were calculated for this case by Boussinesq's equations. The properties of the solid elements corresponding to these stresses were taken from figure (9.3). The complete silo structure and the soil were then analysed by the finite element method. The stresses and the elastic moduli were successively modified in each cycle of the analysis until convergence was obtained.

Five different load cases were considered and a separate analysis was carried out for each of these. The load cases are:

- 1 Loads due to the self weight and the contents in silo 1, while the rest were subjected to self weight only. As stated earlier, the contents within a 60° cone above the floor were assumed to be carried by the floor, the rest being taken by the walls. The floor loads were applied at the joints on the floor and the wall loads were applied at the joints along the circumference at the top of the silo.
- 2 Loads on silo 2 only, while the rest were unloaded.
- 3 Silos 1 and 2 loaded simultaneously.
- 4 Silos 1, 2 and 3 loaded simultaneously.
- 5 All the silos loaded simultaneously.

In this manner it became possible to study the behaviour of the structure due to sequential loading. The cases of silos 3 and 4 loaded individually were not analysed and were obtained from

load cases 1 and 2 utilizing symmetry.

9.2.5 Results of the analysis

9.2.5.1 Deflections and settlements

As the loads were applied the silos settled, swayed and distorted circumferentially. The settlement profiles of the silo bases along the longitudinal centre line, with the different silos loaded individually, are shown in figure (9.6). These diagrams indicate that the rafts deflected into domes with the circumference deflecting more than the centre. This also happened in practice and was observed by Burland and Davidson. This observation is significant, because it disagrees with the conventional, non-interactive analysis which suggests that the rafts deflect more at the centre. The domed type of settlement indicates that the bulk of the load was transferred to the soil via the walls and the outer columns.

It is observed in figure (9.6) that when silo 2 or 3 is loaded the two silos on either side settle symmetrically about the centre of the loaded one. When the outer silos are loaded they tilt towards the neighbouring silo. The tilt and the sway of the silos, when the load is in silo 1 only, are shown in figure (9.7). This diagram shows that silos 1 and 2 lean towards each other and in fact their walls overlap. Silo 2 sways to the left in spite of the fact that it was not loaded. The overlapping of the walls at the top of the silos is as much as 183.1 mm. In practice, this means that silos 1 and 2 rest against each other causing stresses in both of them. In the analysis, two neighbouring joints showing such an overlap can be joined together and replaced by a single

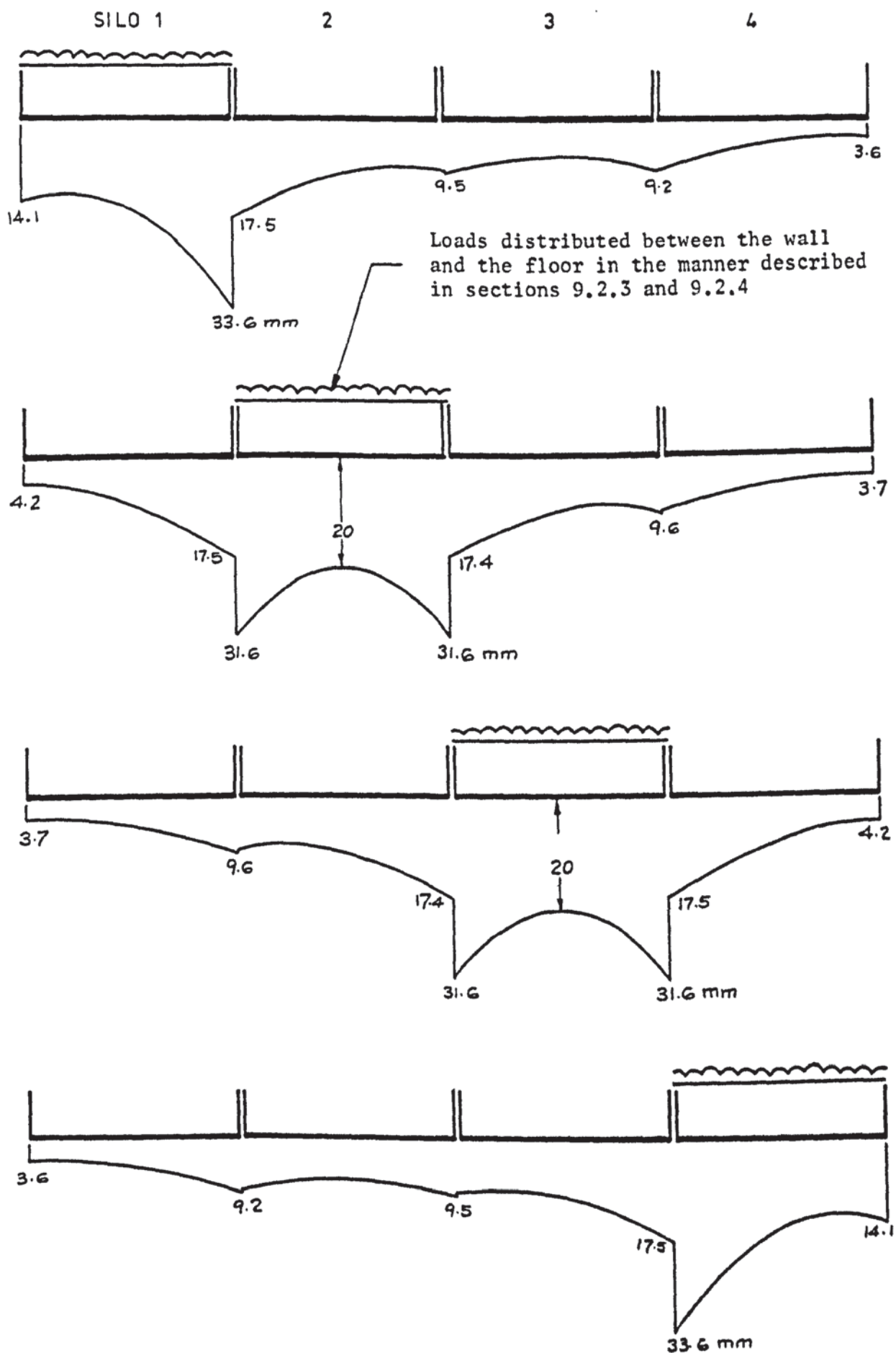


FIGURE 9.6 SETTLEMENT PROFILES WITH INDIVIDUAL SILOS LOADED

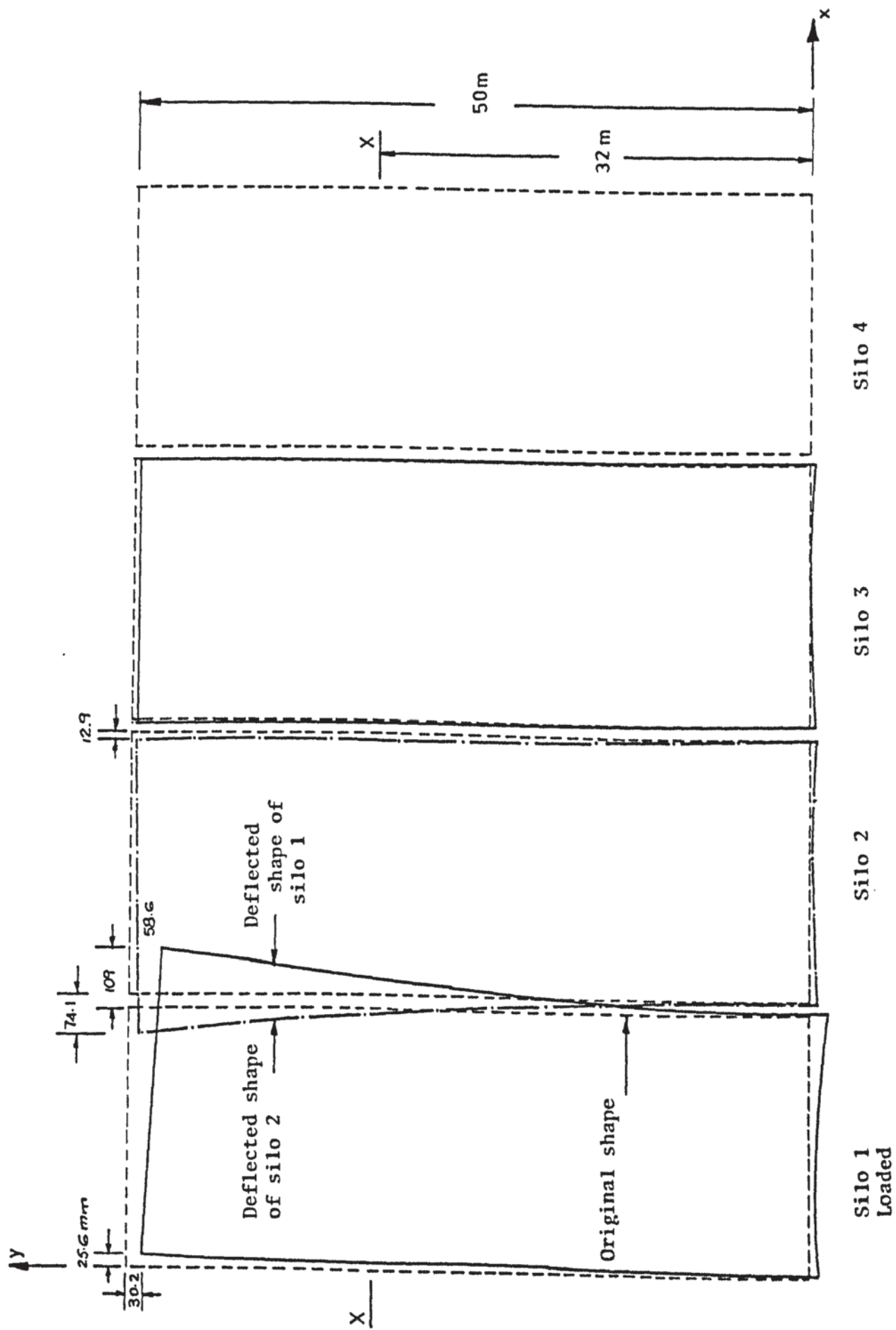


FIGURE 9.7 SWAY AND TILT OF THE SILOS WITH SILO 1 LOADED ONLY

joint. This needs a modification of the computer program for which the author did not find time. The circumferential distortions and the overlapping of the silo cross sections, at the top and at section X-X, 32 m above the base, are shown in figure (9.8). It is noticed that at both levels the cross sections tend to elongate in the longitudinal x direction and contract in the lateral z direction. At the top, the distance between the opposite walls of silo 1 increases by 83.4 mm in the x direction and decreases by 57.2 mm in the z direction. For silo 2, these values are 61.2 mm and 45 mm respectively. The cross sections nearer the base were observed to suffer similar distortions but of a lesser magnitude. At the base, the distortion was found to be negligible.

The settlement profiles in figure (9.6) and the sway and the distortions shown in figures (9.7) and (9.8) indicate that when an individual silo is loaded the neighbouring silos form a group and act together. An unloaded silo comes to the aid of its loaded neighbour and deflects with it. The group as a whole tends to form a sagging settlement profile with the maximum ordinate under the loaded silo and reducing away from it. This can be seen in figure (9.6) when silo 2 or 3 is loaded. In this case the loaded silo settles by 20 mm at the centre and by 31.6 mm at the edges. The neighbouring silos settle by about 17.5 mm at the edges nearer the loaded one and as little as 4.2 mm at the far edge.

Figure (9.9) shows the vertical deflections of the rafts when more than one silo are loaded simultaneously. Curve (1) indicates the value obtained by superimposing the settlements in figure (9.6). Curve (2) shows the settlements obtained by analyses 3, 4 and 5 with a group of silos loaded simultaneously. It is seen in the figure

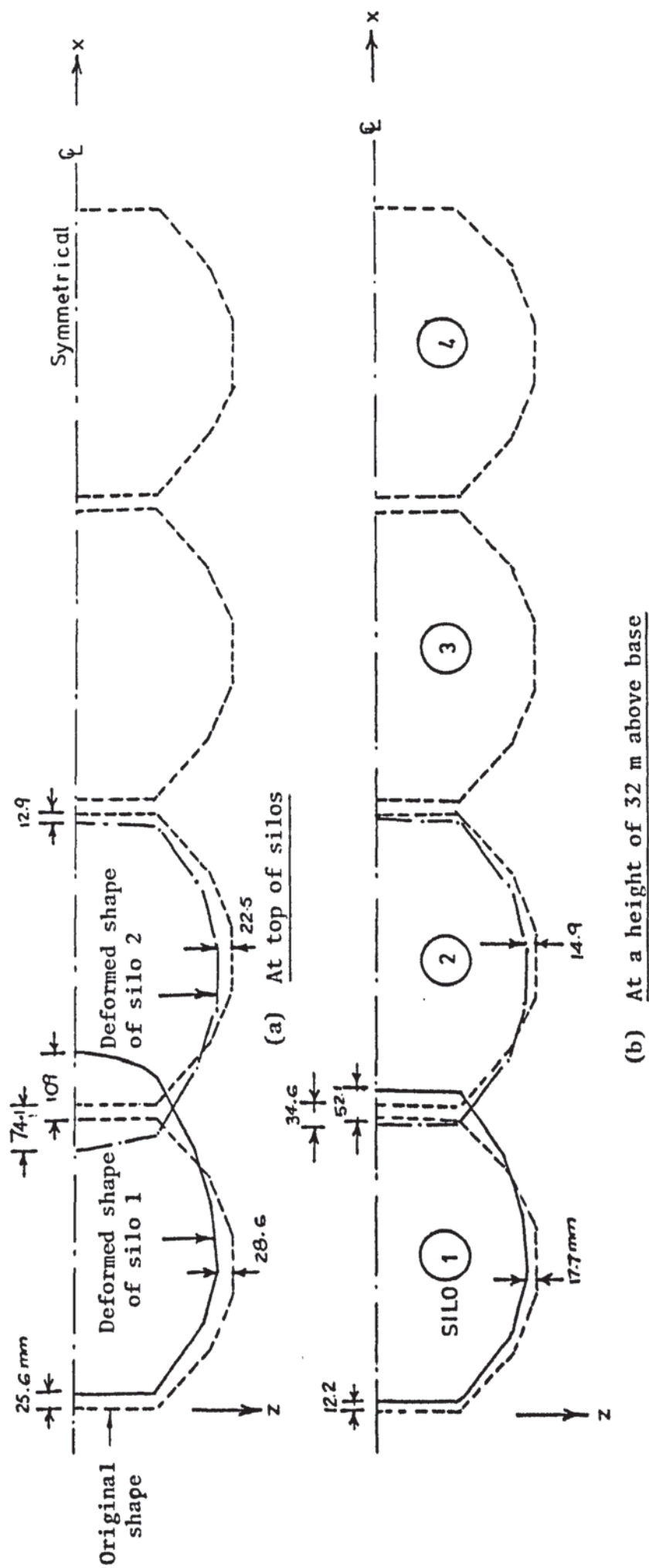


FIGURE 9.8 CIRCUMFERENTIAL DISTORTIONS OF THE SILOS WITH SILO 1 LOADED ONLY

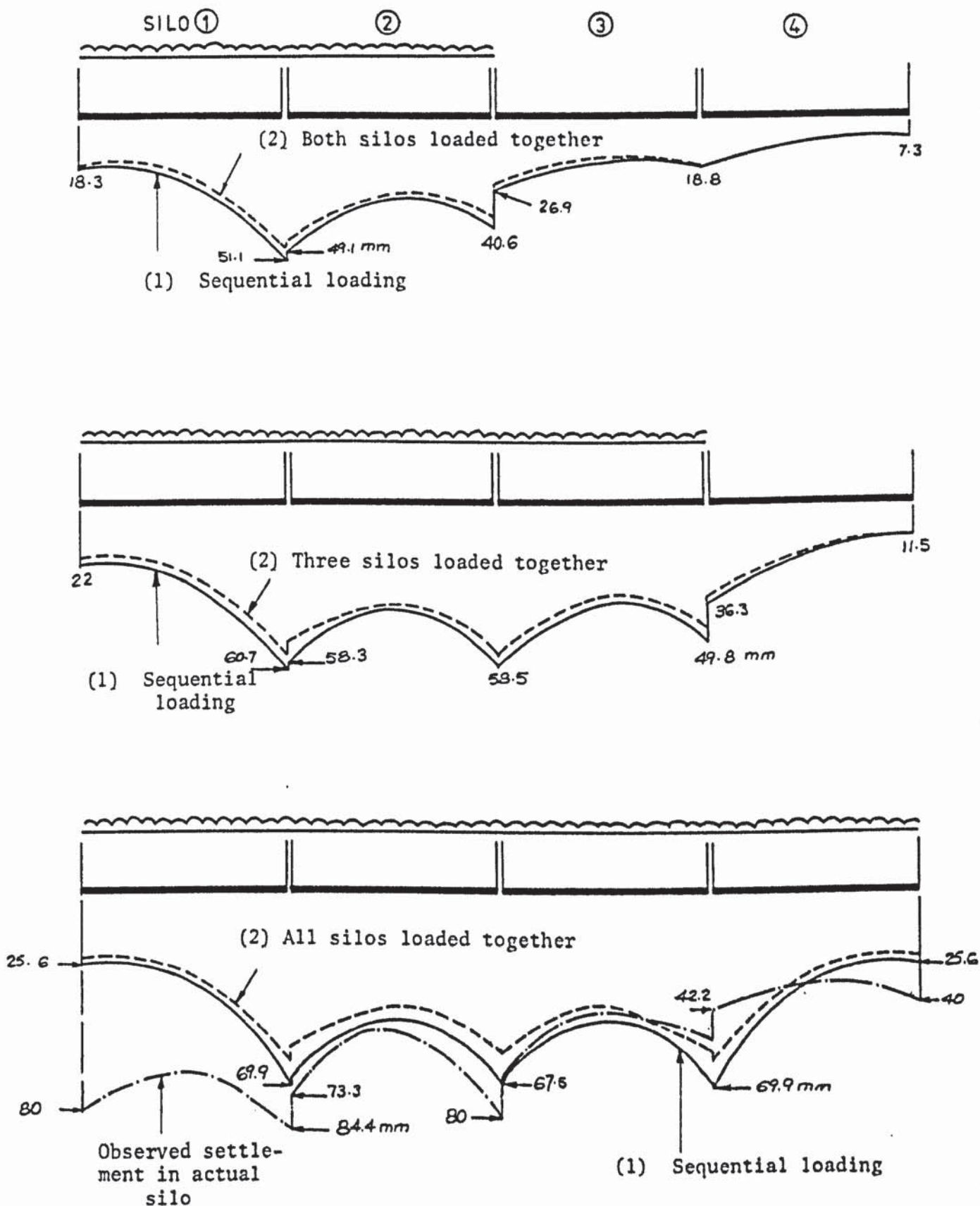


FIGURE 9.9 SETTLEMENT PROFILES WITH SILO GROUPS LOADED IN SUCCESSION AND SIMULTANEOUSLY

that the settlements are higher when the silos are loaded progressively. The difference is more pronounced when the load is applied on all four silos. This indicates that applying the loads on a group of silos simultaneously results in a more favourable stress distribution in the soil. However, the analysis with the silos loaded one after the other is more realistic and gives higher settlements.

The sway and the tilt of the silos when silos 1 and 2 are loaded are shown in figure (9.10). It is seen that silos 1 and 3 lean on silo 2 while the walls of silo 2 itself open up. The relative horizontal displacement between the top of silos 1 and 2 is 371 mm while that between silos 2 and 3 is 173.1 mm. The walls of the three silos press against each other, causing a redistribution of stresses. The deformation of silo 4 for this load case was negligible and is not shown in the figure.

The overlapping and the circumferential distortions of the silos for the same load case are shown in figure (9.11). All the silos are observed to suffer an elongation in the x direction and a contraction in the z direction, with silo 2 suffering the maximum distortion. Its diameter along the x-axis increases by 285.8 mm and that along the z-axis decreases by 224 mm at the top of the structure. At a height of 32 m, these values are 137.2 mm and 145.6 mm respectively. The distortions at lower levels decreased and became negligible at the base.

The sway of the silos for the case when silos 1, 2 and 3 are loaded is shown in figure (9.12). In this case the deflections are significant for all the silos. Silos 2 and 3 open up in the x direction while 1 and 4 lean towards the centre of the group. The

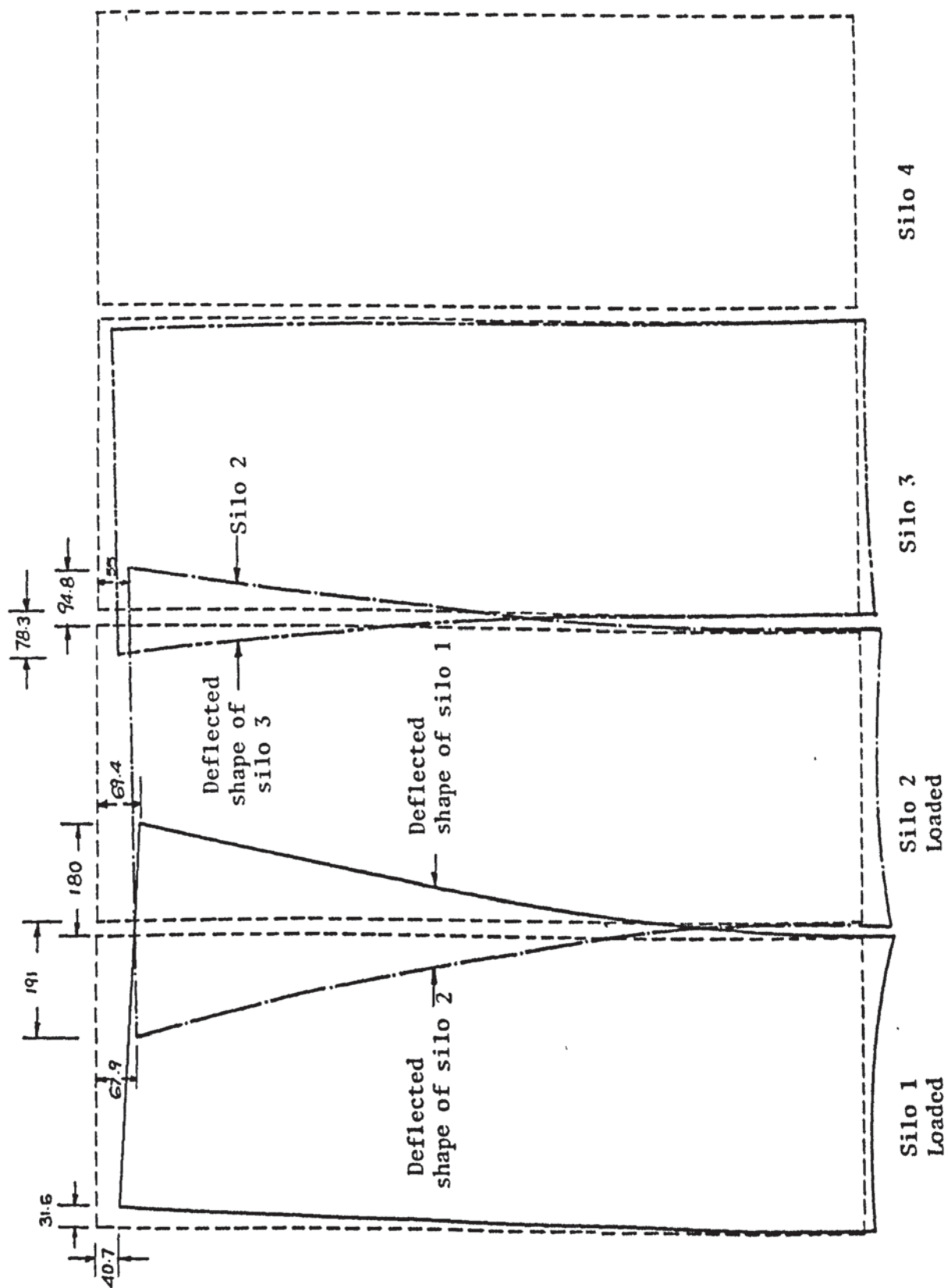
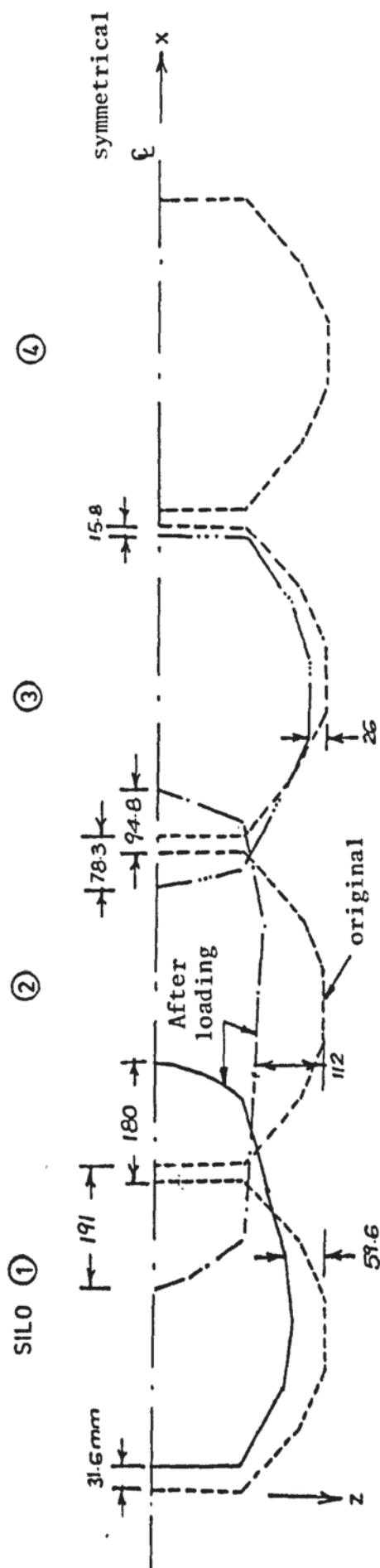
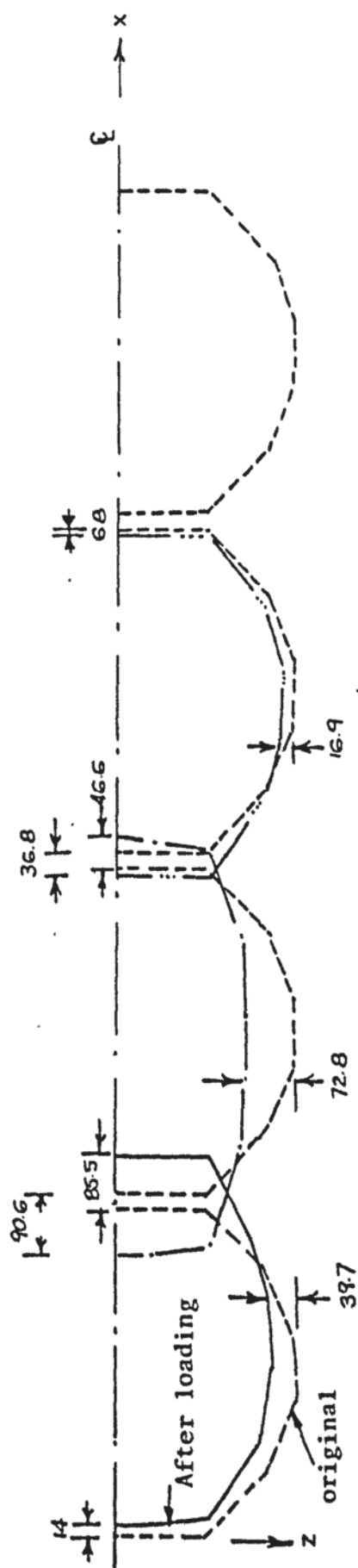


FIGURE 9.10 SWAY AND TILT OF THE SILOS WITH SILOS 1 AND 2 LOADED SIMULTANEOUSLY



(a) At top of silo



(b) At a height of 32 m above base

FIGURE 9.11 CIRCUMFERENTIAL DISTORTIONS OF THE SILOS WITH SILOS 1 AND 2 LOADED SIMULTANEOUSLY

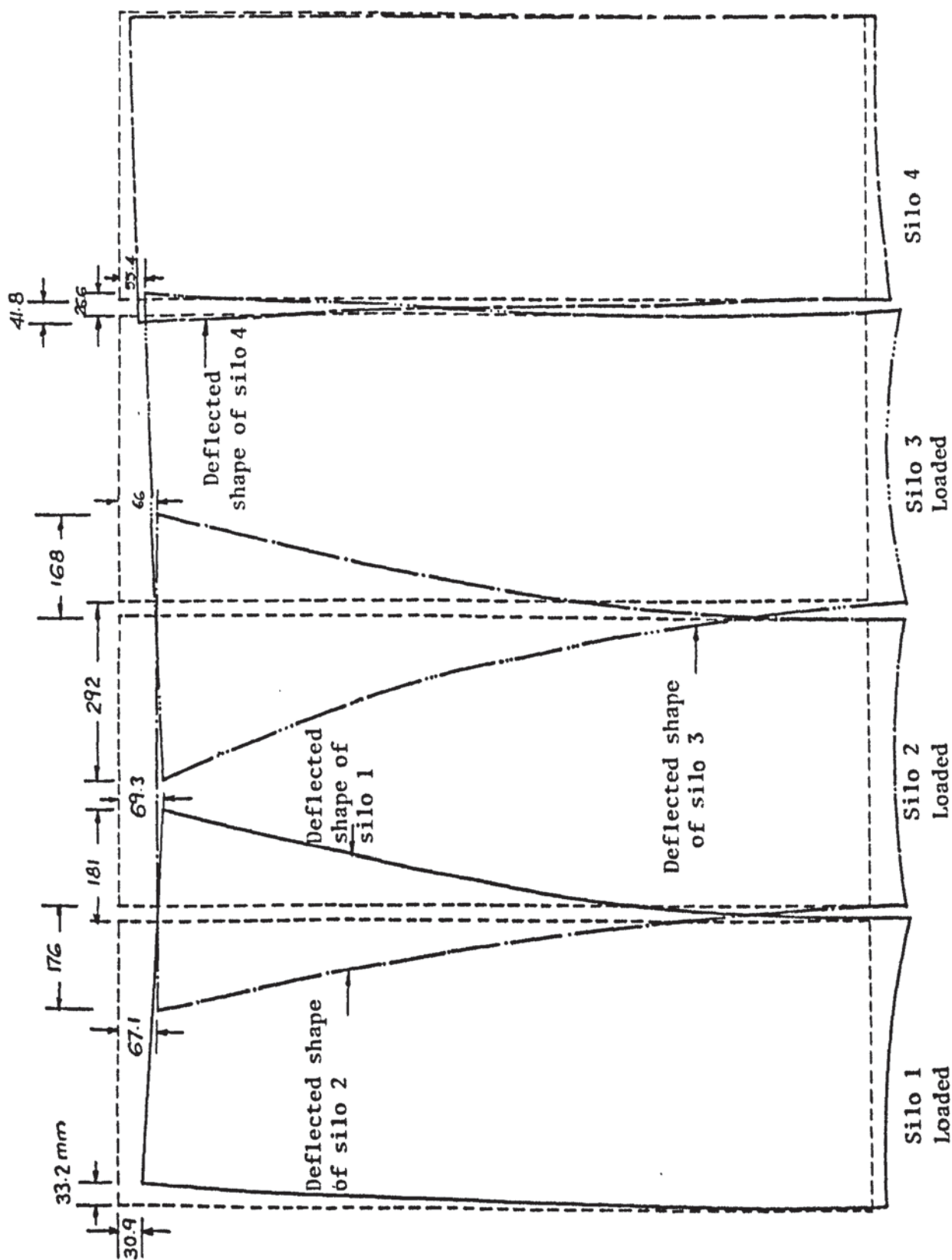


FIGURE 9.12 SWAY AND TILT OF THE SILOS WITH SILOS 1, 2 AND 3 LOADED SIMULTANEOUSLY

overlapping is maximum at the top between silos 2 and 3 which is 460 mm. This overlapping is 357 mm between the walls of silos 1 and 2 and 68.4 mm between silos 3 and 4. It is observed in this figure that while silos 1, 2 and 3 are loaded, the unloaded silo 4 sways towards its neighbour by 41.8 mm at the top. However, when silos 1 and 2 are loaded in figure (9.10), silo 3 sways towards silo 2 by as much as 78.3 mm. This indicates that loading more silos in a group reduces the deformation of the unloaded ones. The cross sectional deformations of the structure with silos 1, 2 and 3 loaded are shown in figure (9.13). It is observed that silo 2 suffers the maximum distortion which is also the case when only silos 1 and 2 are loaded. The increase in its diameter along the x-axis is 344 mm at the top and 165.8 mm at a height of 32 m above the base. The decrease in this distance in the z direction is 266 mm at the top and 174.4 mm at 32 m above the base.

The sway of the structure when all the silos are loaded is shown in figure (9.14). The silos deform symmetrically about the vertical centre line between silos 2 and 3 and therefore only half the structure is shown. The overlapping at the top of the walls is 191.5 mm between silos 1 and 2 and 187.2 mm between silos 2 and 3. The circumferential distortions for the same load case are shown in figure (9.15). In this case also, silo 2 suffers the maximum distortion, in which the diameter along the x-axis increases by 186.4 mm at the top and 89.8 mm at 32 m above the base. The decrease in this distance in the z direction is 144.6 mm and 94.4 mm at the top and at 32 m respectively. These values are lower than the case when silos 1, 2 and 3 are loaded and silos 1 and 2 are loaded as described above. Table (9.1) shows a comparison of the

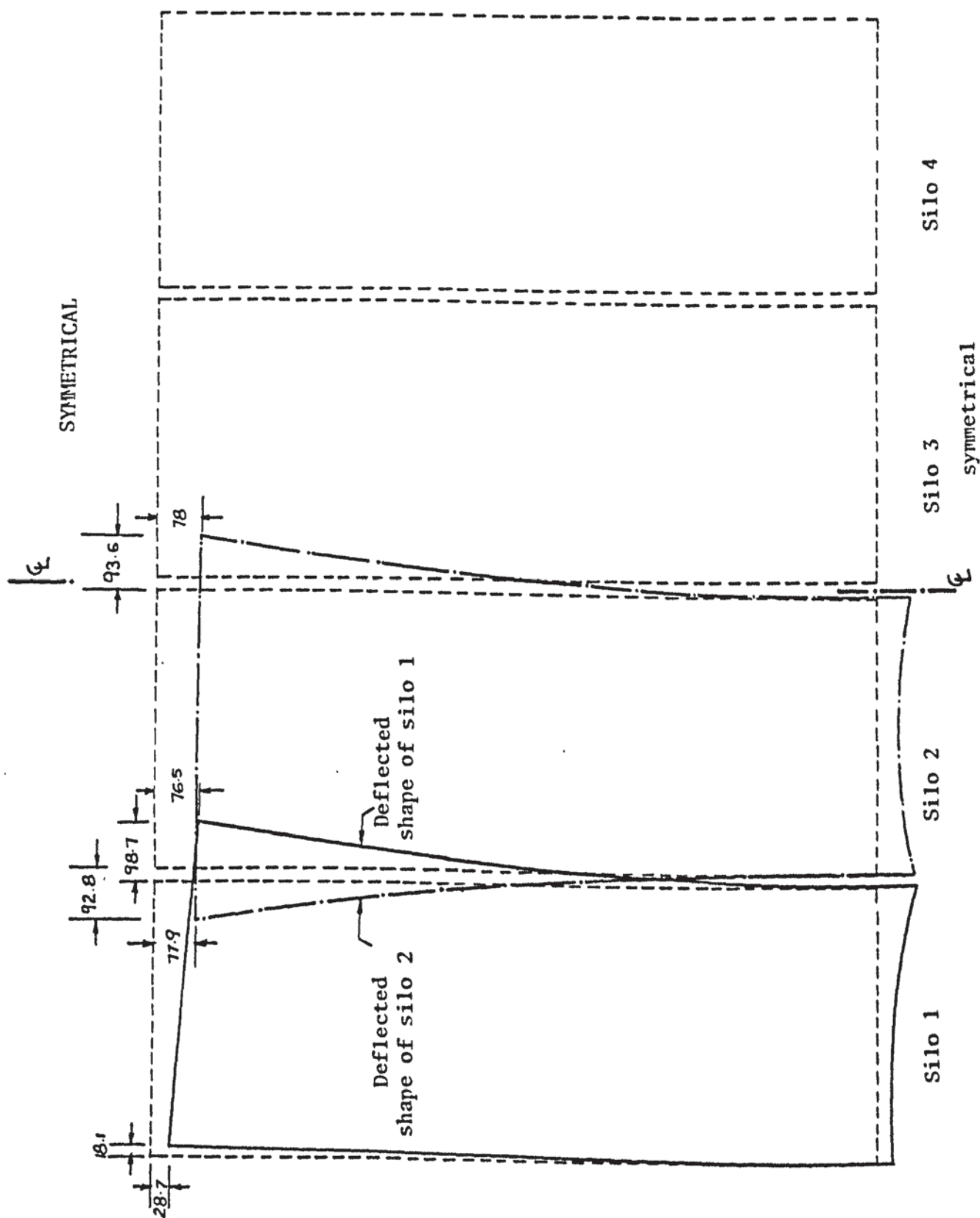
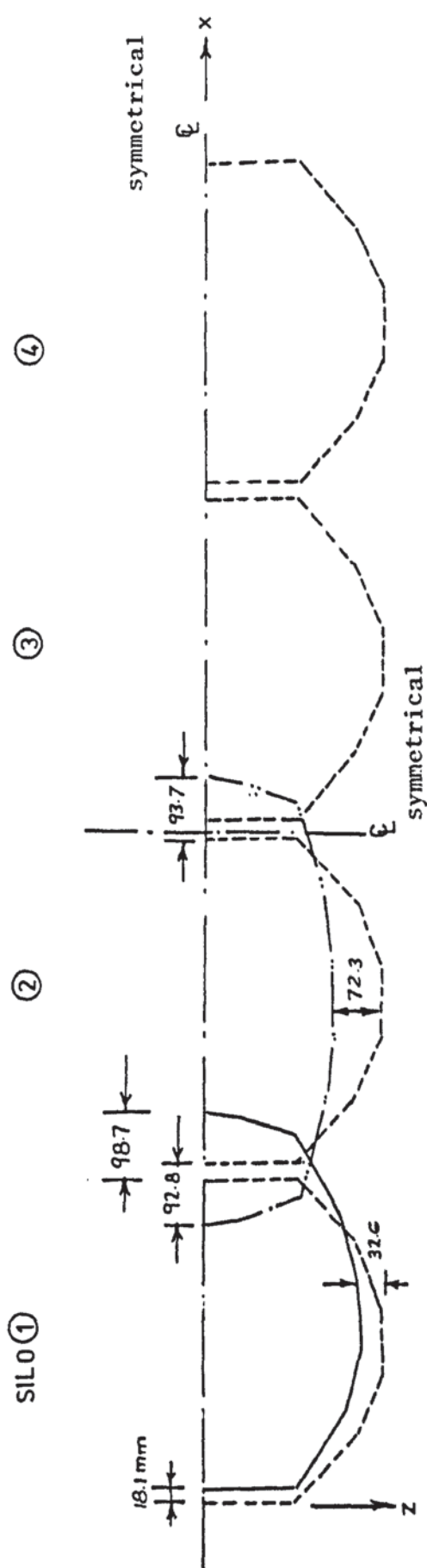
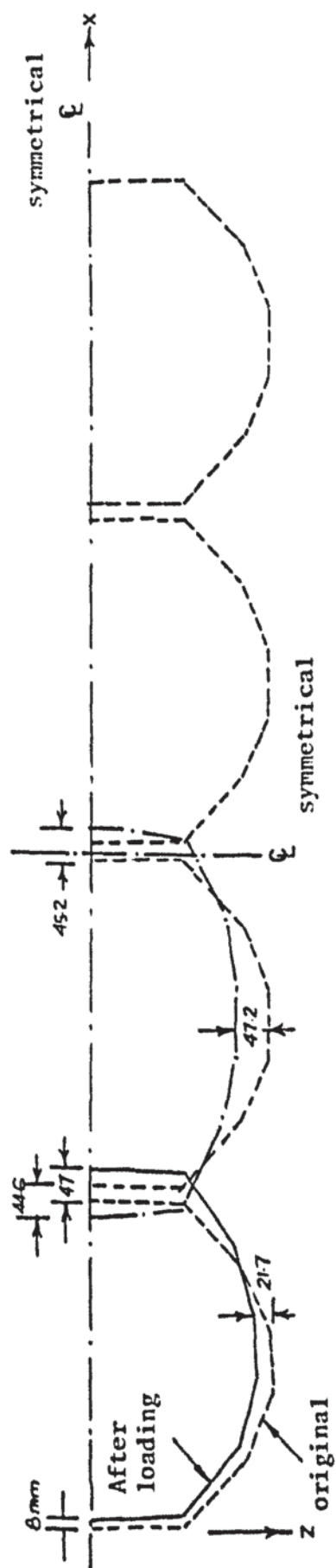


FIGURE 9.14 SWAY AND TILT OF THE SILOS WITH ALL THE SILOS LOADED SIMULTANEOUSLY



(a) At top of silos



(b) At a height of 32 m above base

FIGURE 9.15 CIRCUMFERENTIAL DISTORTIONS OF THE SILOS WITH ALL THE SILOS LOADED SIMULTANEOUSLY

Loaded silos	Overlapping of walls (mm) at the top between silos			Maximum elongation of cross section in x direction (mm)	Maximum contraction of cross section in z direction (mm)
	1 and 2	2 and 3	3 and 4		
1	183.1	-	-	83.4	57.2
1 and 2	371	173.1	-	285.8	224
1,2 and 3	357	46.0	68.4	344	266
1,2,3 and 4	191.5	187.2	191.5	186.4	144.6

TABLE 9.1 OVERLAPPING AND DISTORTIONS OF THE SILOS

overlapping between the silos and the maximum cross sectional distortions for the different load cases. It is clear from this table that the circumferential distortions are the maximum when silos 1, 2 and 3 are loaded. This is also the load case when the columns of the silos reported by Burland and Davidson developed the cracks.

The tilts $\delta p/D$ of the silo bases as obtained by the computer are shown in table (9.2). Here, δp is the differential settlement across the raft along the longitudinal centre line and D is the length of the raft in this direction. The values of the hogging

Loaded silos	Tilt $\delta p/D$				Hogging ratio Δ/D ($\times 10^{-3}$)			
	Silo 1	Silo 2	Silo 3	Silo 4	Silo 1	Silo 2	Silo 3	Silo 4
1 and 2	1/579	1/2235	1/2346	-	0.65	0.79	0.31	0.17
1, 2 and 3	1/491	-	1/2183	1/766	0.68	0.95	0.92	0.32
1,2,3 and 4	1/429	-	-	1/429	0.84	0.96	0.96	0.84

TABLE 9.2 TILT AND HOGGING RATIO OF SILO BASES

ratio Δ/D in the same direction are also shown in the table. Here, Δ is the maximum displacement relative to the line joining two diametrically opposite points on the circumference of the raft. The results show that whereas silo 1 suffers the largest tilt, silo 2 experiences the largest relative deflection Δ . This is in agreement with the values reported by Burland and Davidson for the direction perpendicular to the longitudinal centre line.

The settlements of the rafts obtained by the computer analysis are less than those observed under the actual silos, as shown in figure (9.9). This is considered to be due to the following reasons:

- (1) The representation of the soil properties by a single stress-strain curve based on the average bearing pressure and settlement of silo 3 is inadequate. Visual site investigation by Burland and Davidson after the failure of the silos indicated that the quality of the chalk varied both with depth and in the horizontal directions. A more elaborate soil test data is therefore necessary for a realistic representation of its properties in the analysis.
- (2) The actual silos were filled successively from left to right. Thus as one silo was filled all the settlement due to this load took place. The stresses in the soil under the unloaded silos also increased and their modulus of elasticity decreased. When the next silo was filled the soil underneath was therefore less stiff than its unloaded state. This increased the settlements. This sequence was not truly represented in the present analysis as the other silos were considered unloaded when the load was applied on a particular silo.
- (3) Wind forces on a tall and solid structure like this are important. These are generally neglected in the calculation of long term

settlements because of their short duration and the time-dependency of the soil behaviour. In the paper by Burland and Davidson it is noticed that although the immediate load-dependent settlement was followed by time-dependent settlements, the bulk of this took place during the loading. It was also observed by them that the columns in the structure began to crack by the time the third silo was being loaded. It is therefore considered that the settlement of the chalk was rapid. If this is the case, then it makes it necessary that the effect of wind loads should be included in the analysis. It is therefore evident that the silos should be reanalysed with wind loading which could not be performed by the author for lack of time.

The actual silos were observed to suffer a tilt in the direction perpendicular to the common longitudinal centre line and to lean forward. In the analysis, symmetry about this line was assumed and therefore no such tilt could be reproduced. Site investigation by Burland and Davidson after the failure of the columns indicated that the chalk was weaker under the front edges of the silos than elsewhere. This and the part played by the wind forces are considered to aggravate the lopsided settlement of the silos.

(4) The silos were loaded after being constructed. The initial settlement of the silos due to self weight was not included in the analysis.

(5) The fact that the silos lean against each other causes further settlement of the foundation during a sequential loading and this fact was not included in the analysis.

9.2.5.2 Bending Moments

The columns of the actual silos developed severe cracks as they were being filled. The cracks were first noticed when silos

1, 2 and 3 were loaded. It was shown in table (9.1) that at this load case the silos suffered the maximum distortion of the cross section. The bending moments in the columns supporting the floor were plotted and compared for the various load cases. The highest bending moments were obtained when silos 1, 2 and 3 were loaded. The maximum difference between these moments and those for the case where all the silos were full was as high as 98%. Therefore, the bending moment diagrams are presented here for the case with silos 1, 2 and 3 full. The bending moments about the z-axis in the columns of silo 1 are shown in figure (9.16). The same bending moments in silos 2, 3 and 4 are shown in figures (9.17), (9.18) and (9.19) respectively. In all these diagrams it is observed that the largest M_z occur in columns 11 and 16 at the circumference of the silo. The next largest moments occur in columns 6, 9, 12 and 15 which are approximately midway between the circumference and the centre. These are the columns where the maximum relative rotations of the raft occur. The bending moments in these columns in each silo are given in table (9.3). The moments obtained by analysing a typical silo by assuming the raft to be completely fixed are also shown in the table. These moments are the same in all the silos and are shown in figure (9.20). It is seen from the table that the maximum column bending moments always occur in silo 2 and the minimum in silo 4. This is in direct relation to the magnitude of the relative deflection given in terms of the hogging ratio in table (9.2), in which the maximum value of $\Delta/D = 0.95 \times 10^{-3}$ was recorded for silo 2. The fixed base analysis gives bending moments which are not only extremely low but always opposite in direction to those obtained by the analysis of the complete system.

NOTE: COLUMN NUMBERS ARE INDICATED IN FIGURE (9.2)

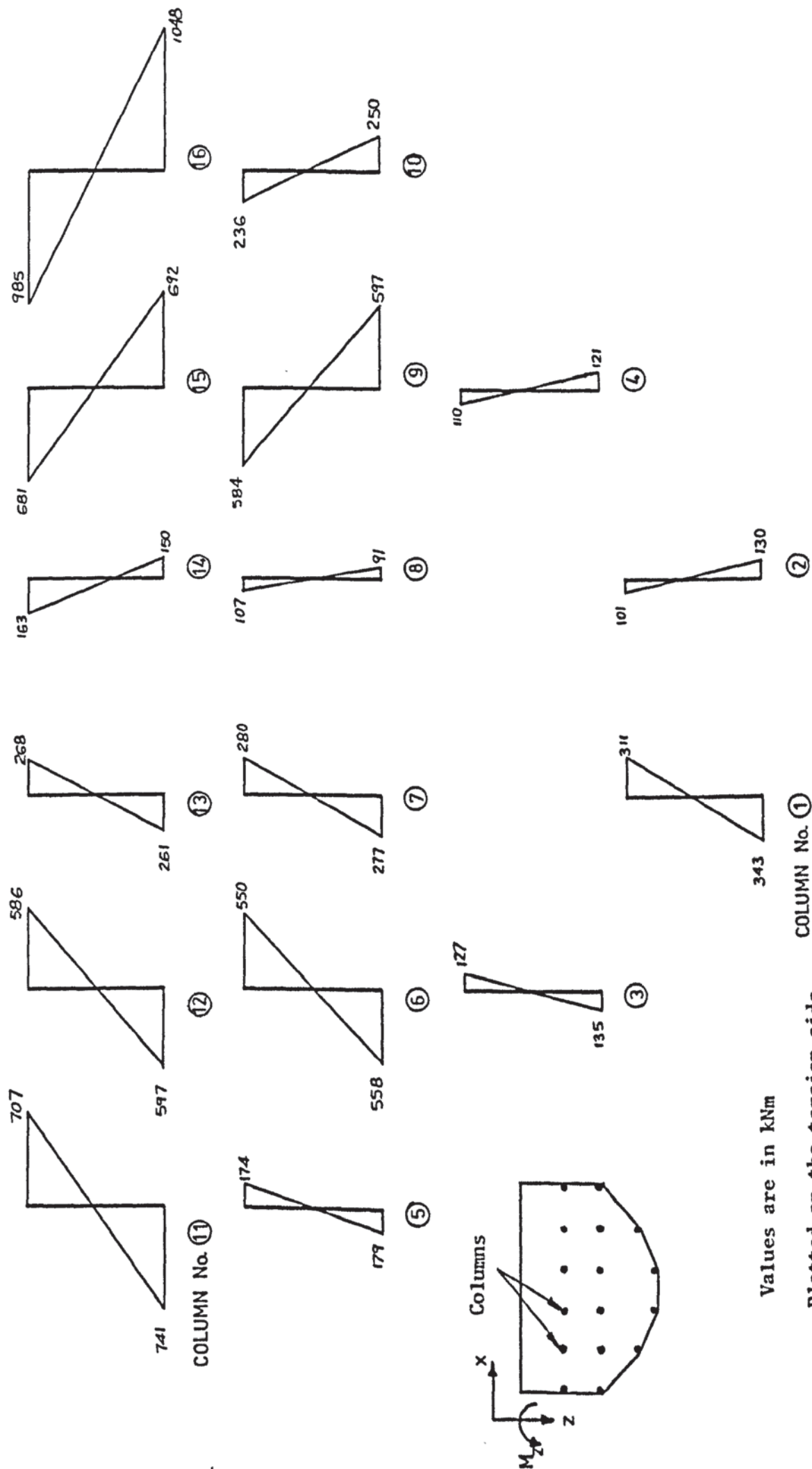


FIGURE 9.16 BENDING MOMENTS M_z IN COLUMNS OF SILO 1 WITH LOADS ON SILOS 1, 2 AND 3

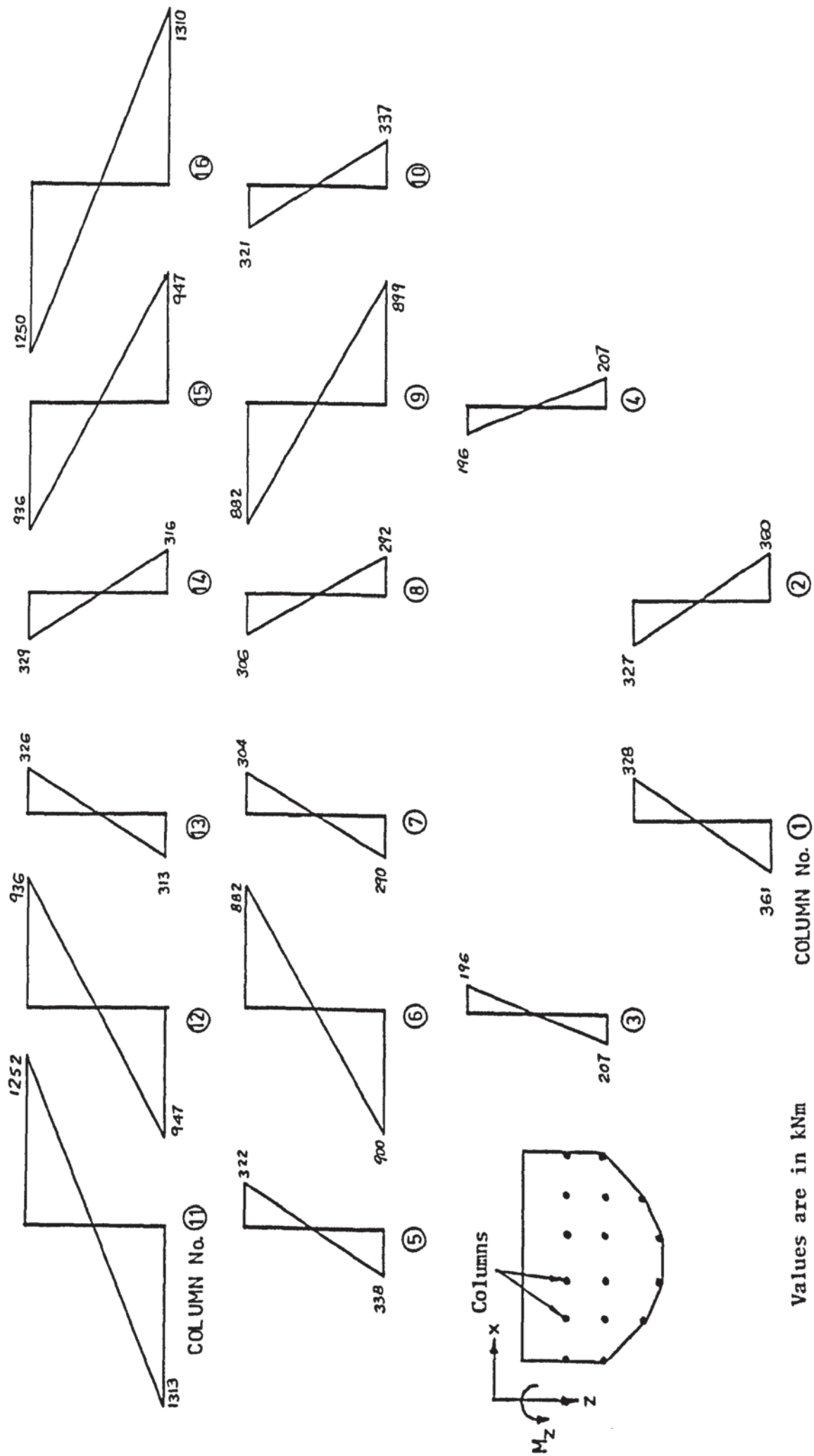


FIGURE 9.17 BENDING MOMENTS M_z IN COLUMNS OF SILLO 2 WITH LOADS ON SILOS 1, 2 AND 3

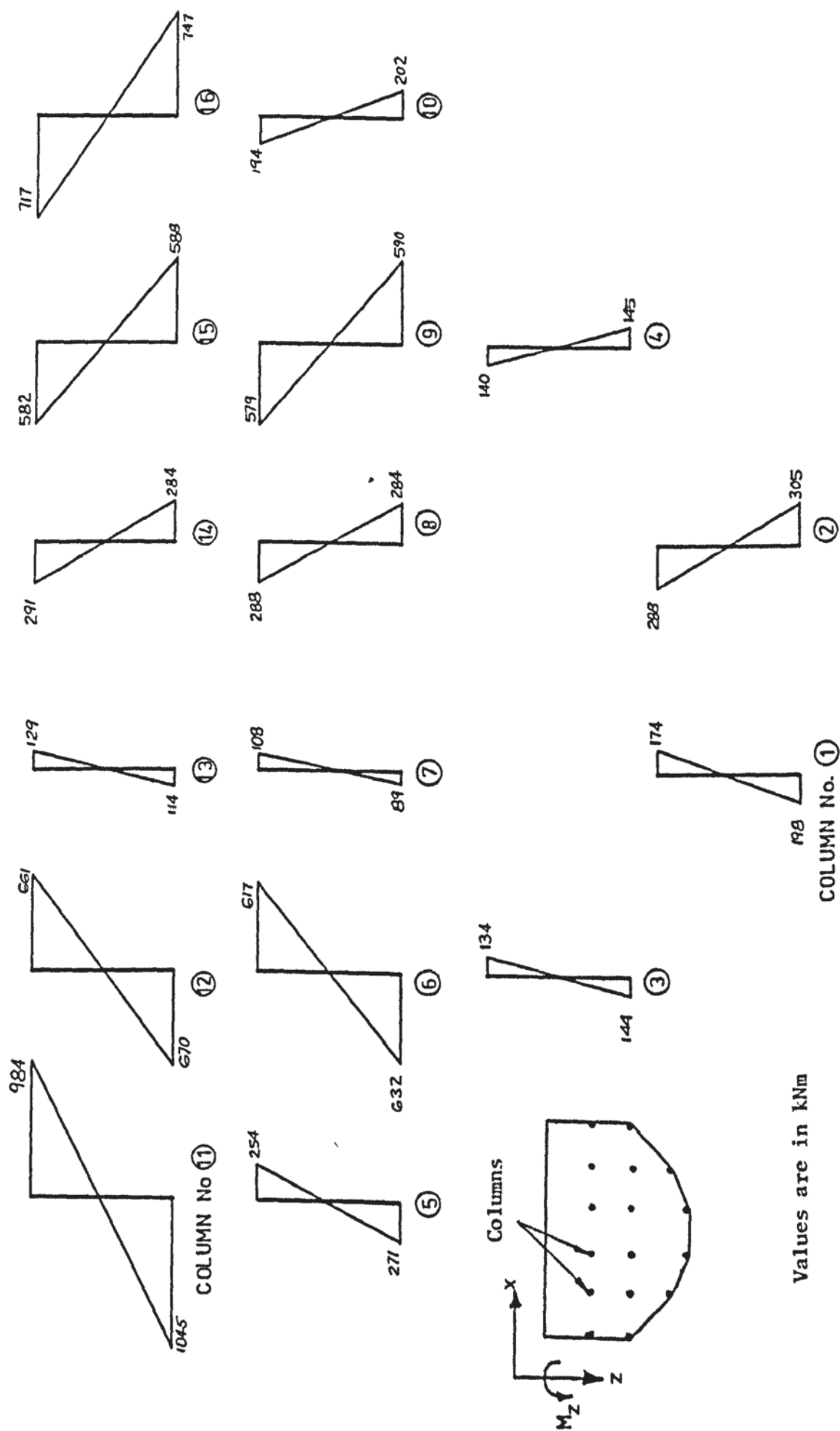


FIGURE 9.18 BENDING MOMENTS M_z IN COLUMNS OF SILLO 3 WITH LOADS ON SILOS 1, 2 AND 3

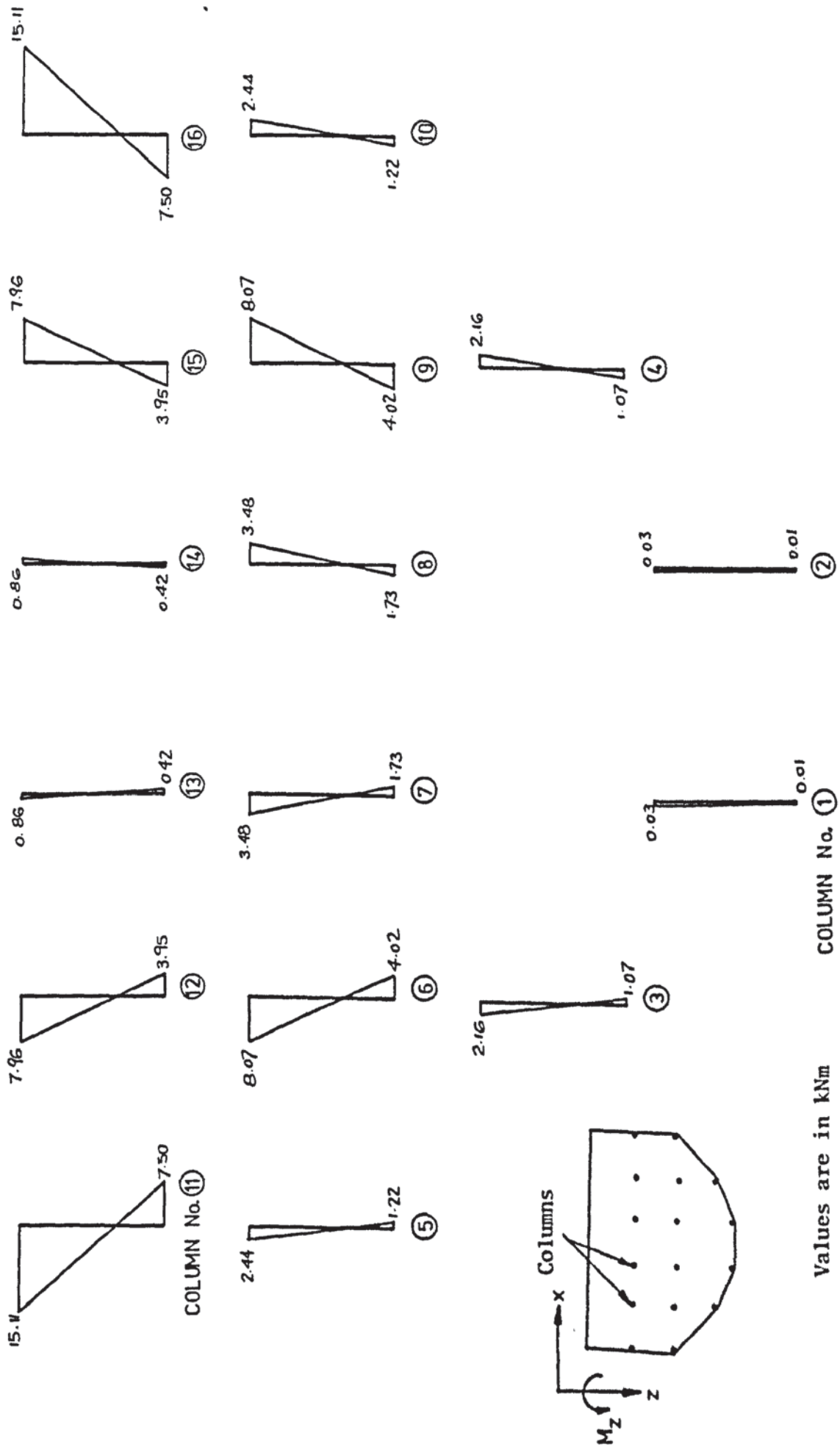


FIGURE 9.20 FIXED BASE BENDING MOMENTS ABOUT z AXIS - THE SAME FOR ALL SILOS

Column No	(1) Bending moments obtained from flexible base analysis (kNm)				(2) Fixed base analysis moments (kNm)	% difference between (1) and (2) for silo 2
	Silo 1	Silo 2	Silo 3	Silo 4		
6 top bot	550 -558	882 -900	617 -632	67 -68	-8.1 4	100.9 100.4
9 top bot	-584 597	-882 899	-579 590	-66 68	8.1 -4	100.9 100.4
11 top bot	707 -741	1252 -1313	984 -1045	67 -66	-15.1 7.5	101.2 100.5
12 top bot	-681 -597	-936 -947	-582 -670	63 -63	-8 4	100.9 100.4
15 top bot	-681 692	-936 947	-582 588	-62 63	8 -4	100.9 100.4
16 top bot	-985 1048	-1250 1310	-717 747	-79 80	15.1 -7.5	101.2 100.6

TABLE 9.3 BENDING MOMENTS IN THE COLUMNS OF THE SILOS

This is partly because of the rotations developed at the column bases as the raft deforms into its domed shape. The percentage difference between the bending moments in silo 2, obtained by analysing the complete system and those obtained by the fixed base analysis is shown in the last column of the table. This difference varies between 100.4% and 101.2%. The inadequacy of the fixed base analysis in predicting the actual bending moments is therefore clearly demonstrated.

The bending moments about the x axis in the columns of silo 1 with silos 1, 2 and 3 loaded are shown in figure (9.21). These

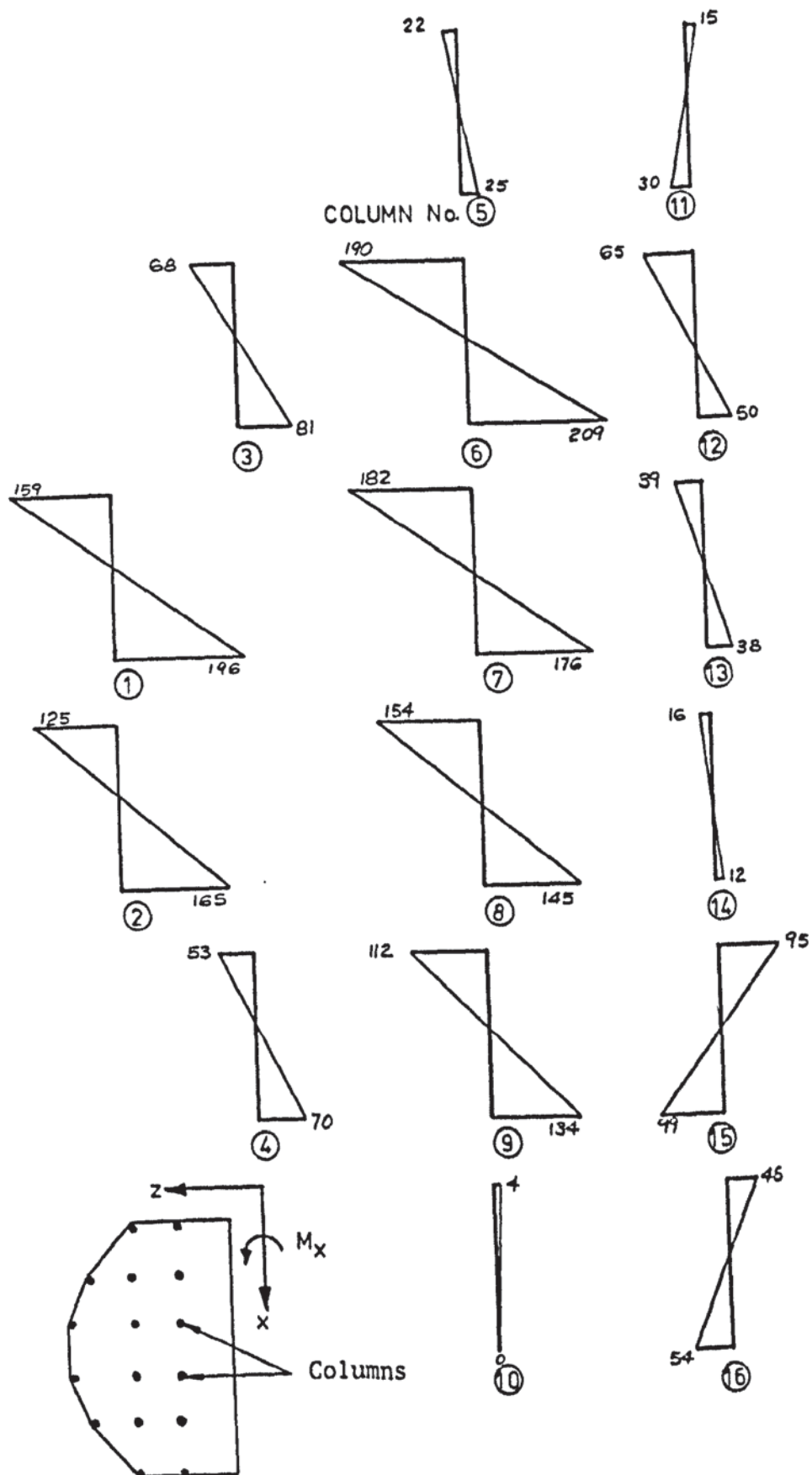


FIGURE 9.21 BENDING MOMENTS M_x IN COLUMNS OF SILLO 1 WITH LOADS ON SILOS 1, 2 AND 3

bending moments in silos 2 and 3 are shown in figures (9.22) and (9.23) respectively. The figures show that the largest M_x bending moments always occur in columns 1 and 2 which are on the circumference. The magnitude of this is a maximum of 212 kNm which occurs in column 2 of silo 3. However, the M_z bending moments in these columns are low compared to the others as shown in figure (9.16) to (9.19). The resultant of M_x and M_z are therefore low in these columns. The resultant bending moment computed as the square root of the sum of the squares of M_x and M_z are shown in table (9.4). This is done for columns 1 and 2 where M_x is high, columns 11 and 16 where M_z is high and columns 6, 9, 12 and 15 where both are high. It is seen that the columns in silo 2 suffer the highest resultant bending moments. The value of this is 1313 kNm in column 11 which is 77% higher than the corresponding moment in silo 1 and 26% higher than that in silo 3. In all the silos the maximum bending moments occur in the circumferential columns 11 and 16. The next highest ones occur in columns 6, 9, 12 and 15 which are approximately halfway between the centre and the circumference of the silos. These are the columns that are reported by Burland and Davidson to have suffered severe cracks. Columns 1 and 2, on the other hand, suffer low resultant bending moments. The cracks in the circumferential columns 1, 2, 5, 10, 11 and 16 were observed to be less severe. High bending moments but minor cracks occurred in columns 11 and 16. It appears, as stated by Burland and Davidson, that these columns were close to the silo wall and came within its zone of influence. The central columns 7, 8, 13 and 14 were near the crown of the domed raft and did not suffer significant rotations

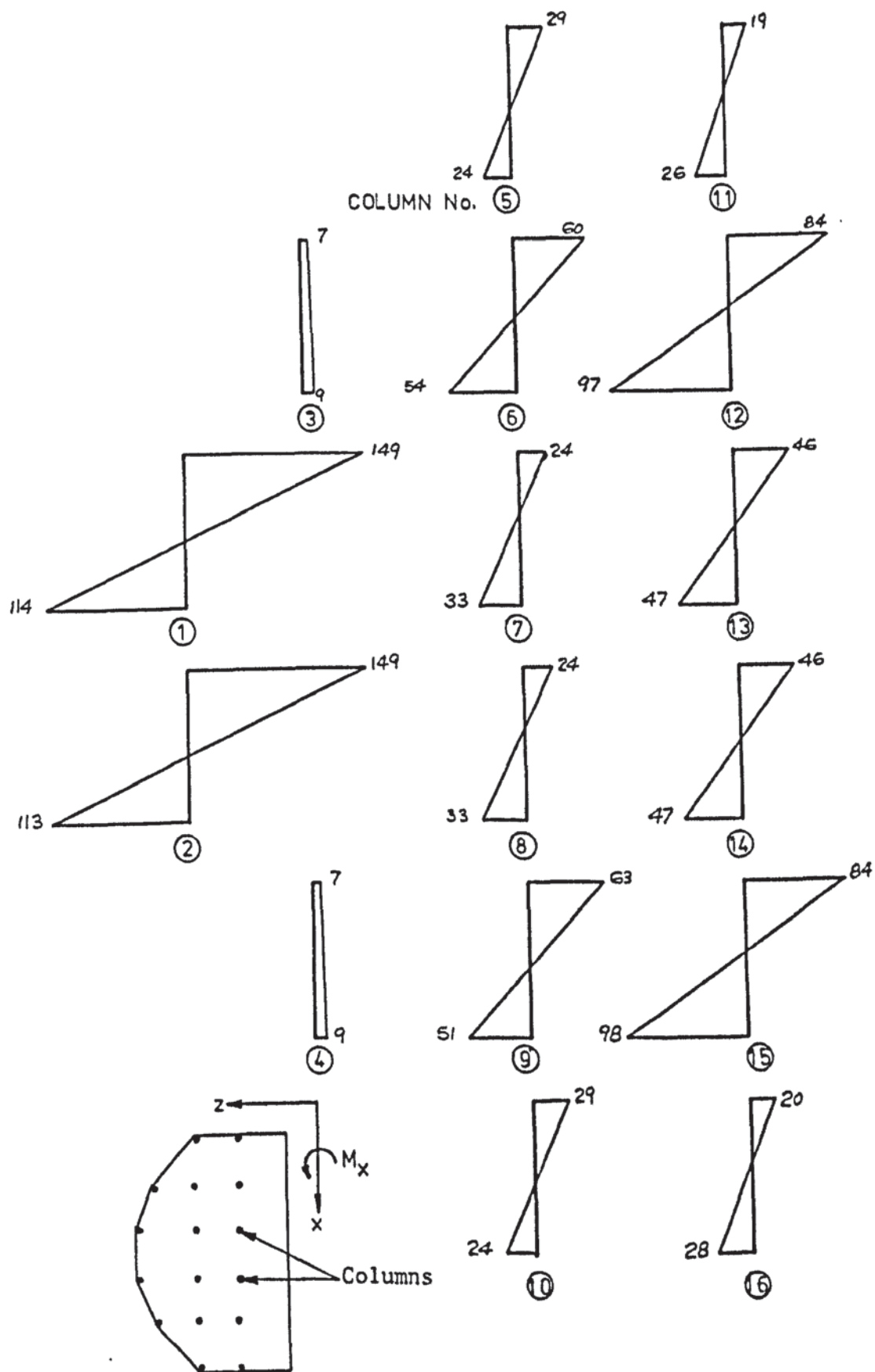
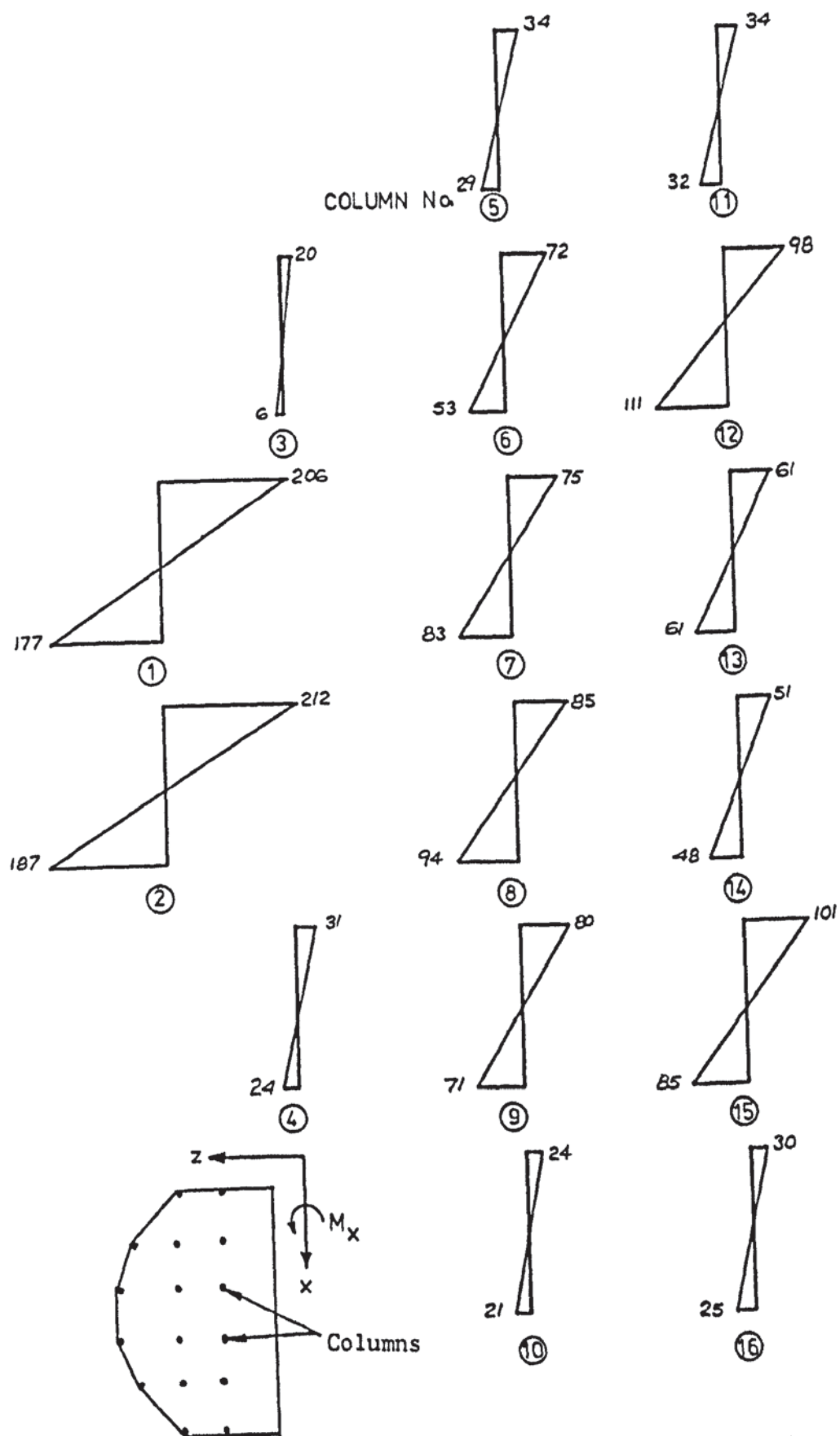


FIGURE 9.22 BENDING MOMENTS M_x IN COLUMNS OF SILLO 2 WITH LOADS ON SILOS 1, 2 AND 3



Column No		Resultant bending moment $M = \sqrt{M_x^2 + M_z^2}$ obtained by flexible base analysis, (kNm)		
		Silo 1	Silo 2	Silo 3
1	top	349	360	270
	Bot	395	379	266
2	top	161	359	358
	bot	210	377	358
6	top	582	884	521
	bot	596	902	643
9	top	565	884	585
	bot	612	900	594
11	top	707	1252	984
	bot	472	1313	1045
12	top	590	940	668
	bot	599	952	594
15	top	688	940	591
	bot	699	952	594
16	top	986	1250	718
	bot	1049	1310	747

TABLE 9.4 RESULTANT BENDING MOMENT IN THE COLUMNS

at the bases. This is why both M_x and M_z are low in them and their cracks were less severe.

The value of M_x obtained by the fixed base analysis are shown in figure (9.24). Again these moments are very low compared to those obtained by the analysis of the complete system. At the top of column 2, the fixed base moment is 45 kNm while that obtained by the flexible base analysis is 212 kNm in silo 1. This again

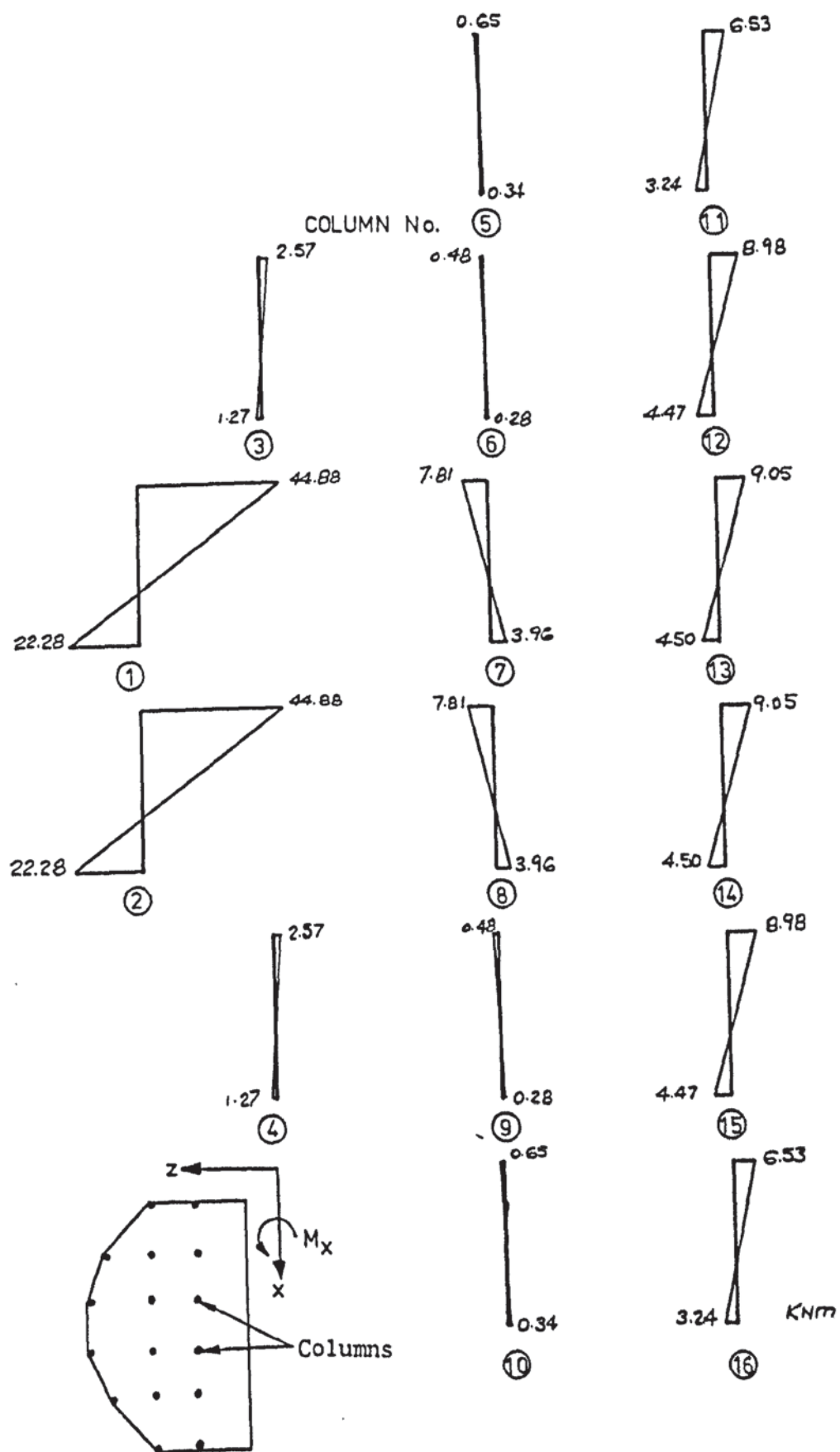


FIGURE 9.24 FIXED BASE BENDING MOMENTS ABOUT x-AXIS:
THE SAME FOR ALL SILOS

shows the inadequacy of the conventional fixed base analysis.

The variation of the bending moments, M_z , in the silo rafts along their longitudinal centre line is shown in figure (9.25). These are for the case when silos 1, 2 and 3 are loaded. The bending moments reflect the hogging deflection profile of the rafts being the highest near the centre and lower at the edges. The maximum moment occurs in silo 2 in which the column moments also were shown to be the highest. The value at the centre is 1505 kNm/m which is 24.5% higher than the maximum moment in silo 1 and 18% higher than that in silo 3. Silo 4 not being loaded its raft suffers negligible bending moments.

9.2.5.3 Stresses in the soil

It was shown in the last two sections that the worst case of the distortions of the silo walls, the deflections of the rafts and the bending moments in the columns occurred when silos 1, 2 and 3 were loaded. The stresses in the soil for this load case are shown in figure (9.26). The solid lines in this figure indicate the variation of the vertical stress obtained by the finite element analysis along the longitudinal centre line of the silos at various depths. The dashed lines show the corresponding stresses calculated from Boussinesq's equations by neglecting the structure. At a depth of 7.5 m the Boussinesq stress distribution is fairly uniform under the silos decreasing rapidly away from them. The stresses obtained by the finite element analysis show a highly non-uniform variation. At greater depths the difference between the two stresses reduce as shown at a depth of 25 m in the figure. Boussinesq stresses are lower by a maximum of 46.4% at this depth.

As stated earlier the bulk of the load of the silo is

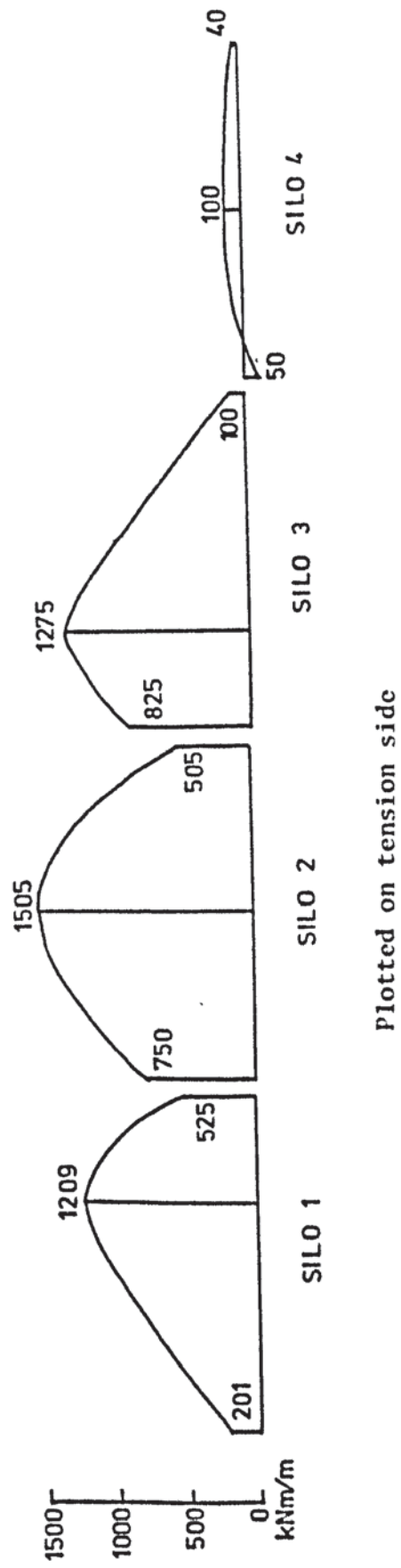


FIGURE 9.25 VARIATION OF BENDING MOMENT M_z IN THE SILO RAFTS WITH SILOS 1, 2 AND 3 LOADED

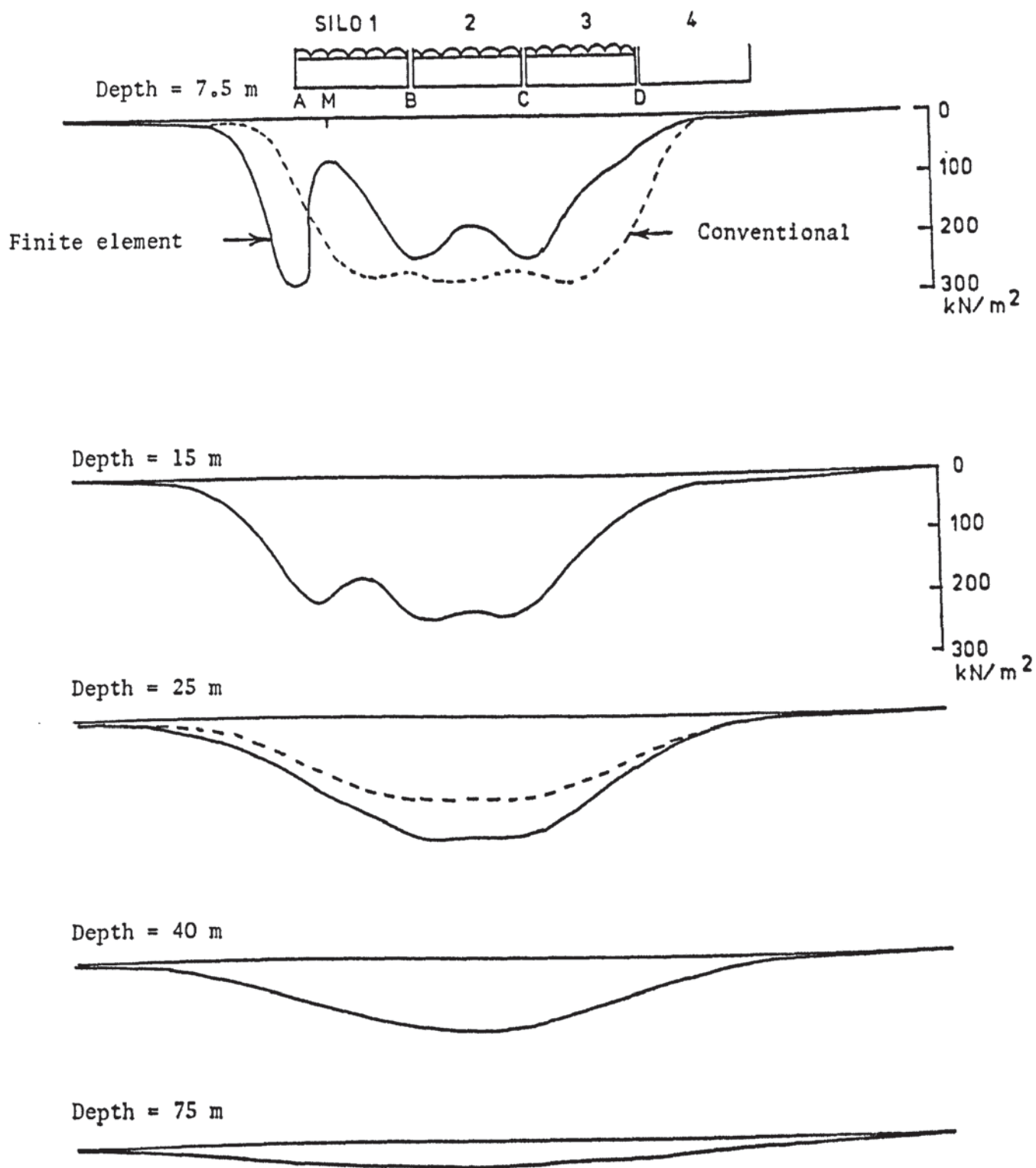


FIGURE 9.26 DISTRIBUTION OF VERTICAL STRESS AT VARIOUS DEPTHS IN THE SOIL WITH SILOS 1, 2 AND 3 LOADED

transferred to the soil via the wall and the outer columns. The finite element stresses are therefore higher at the circumference than at the centre of the rafts at shallow depths. At a depth of 7.5 m the stress under the edge A of silo 1 is 285 kN/m^2 while the minimum stress occurring at the internal point M is only 75 kN/m^2 . This pattern of stress variation conforms with the hogging deflection profile of the rafts. The stress near the surface at end A of silo 1 is higher than that at end B. This is in spite of the fact that the settlement at B is higher, which is considered to be due to the influence of silo 2. As stated before, the group of silos tend to form a sagging settlement profile with the maximum settlement under the central silo. Thus point B being at the edge of silo 2 settles more than point A.

The stresses at the circumference of the rafts exceed the elastic limit of 200 kN/m^2 and are well within the range JK of the stress-strain curve shown in figure (9.3). This indicates that the soil yields beneath the edges of the rafts which aggravates the settlements at the circumference and accounts for the hogging deflection of the rafts.

9.2.6 Conclusion

The stress-strain diagram of the chalk, shown in figure (9.3), indicates that the post-yield stiffness of the soil is very low. As the soil yields under the circumference of a raft the settlement there is aggravated. The stiffness of the structure and the raft resists this settlement and reduces it. It was shown that by including the soil in the analysis the column bending moments increase drastically over the fixed base case. It appears that

the stiffness of the structures and the rafts did reduce the soil settlement sufficiently.

It was shown that loading the silos sequentially caused higher settlements than those obtained by loading them simultaneously. The largest settlements and bending moments were obtained when silos 1, 2 and 3 were loaded. Thus the loading sequence plays an important part in determining the behaviour of the structure. A fixed base analysis neglects this sequence and assumes that loading one silo does not affect the others.

The sway and the distortions of the silos indicated that they leaned against each other. This produced new stresses in the structure which may have been one of the reasons for the development of cracks in the columns. The structure should therefore be reanalysed by connecting the joints when they show an overlapping. This and the analysis with the wind loads could not be performed by the author for lack of time. Nevertheless, it is considered that these should be included in the analysis to obtain a more realistic representation of the problem.

9.3 ANALYSIS OF A 50-STOREY SPACE STRUCTURE

As another example the 50-storey three dimensional structure shown in figure (9.27) was analysed. This was subjected to both vertical and wind loads. A typical internal frame and an external frame are shown in figure (9.28). The members of the frame were selected to give acceptable deflections under fixed support conditions. The external frames were stiffened by some diagonal bracings and shear walls to prevent excessive sway. The shear wall is shown in figure (9.28) marked by the letters F to T. The members

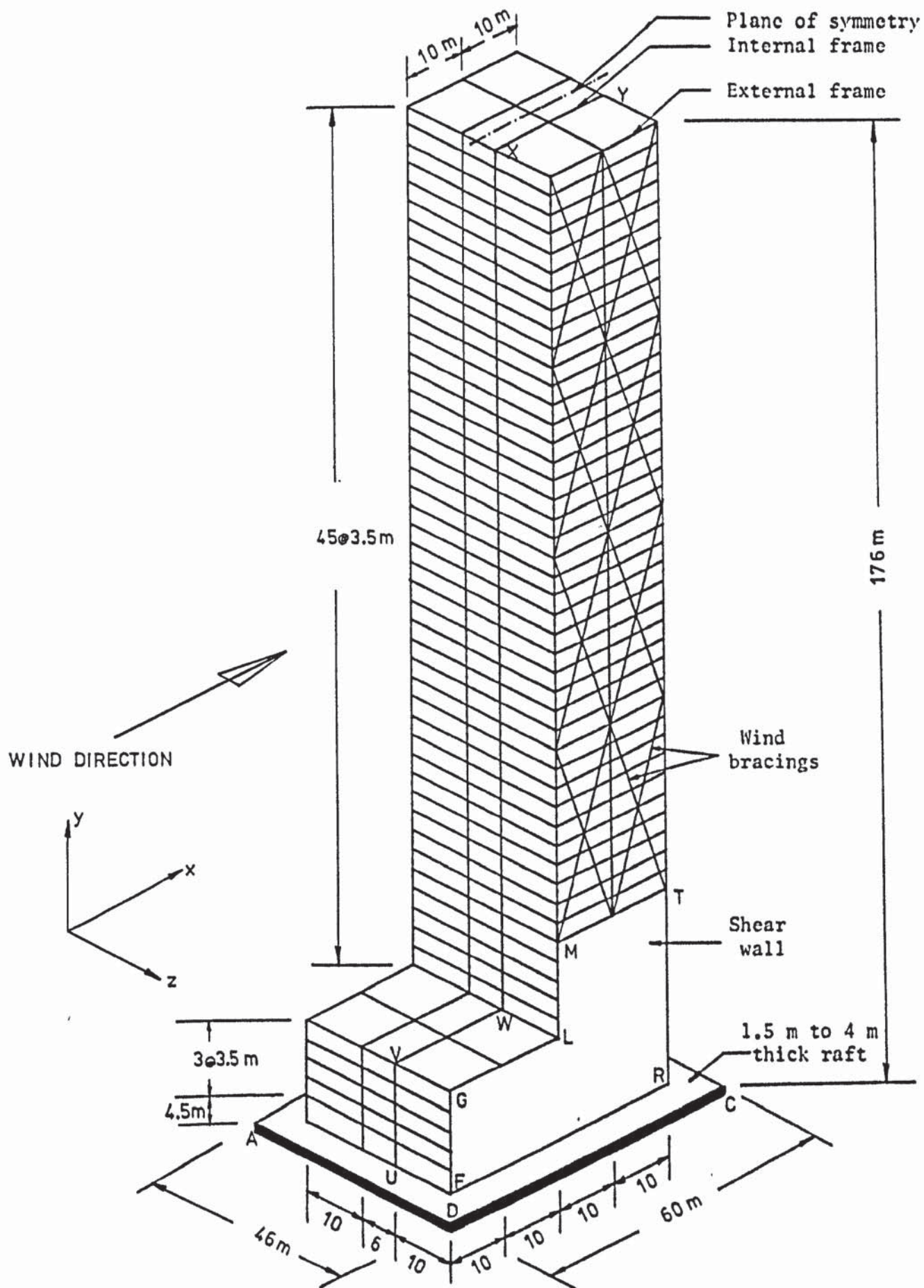
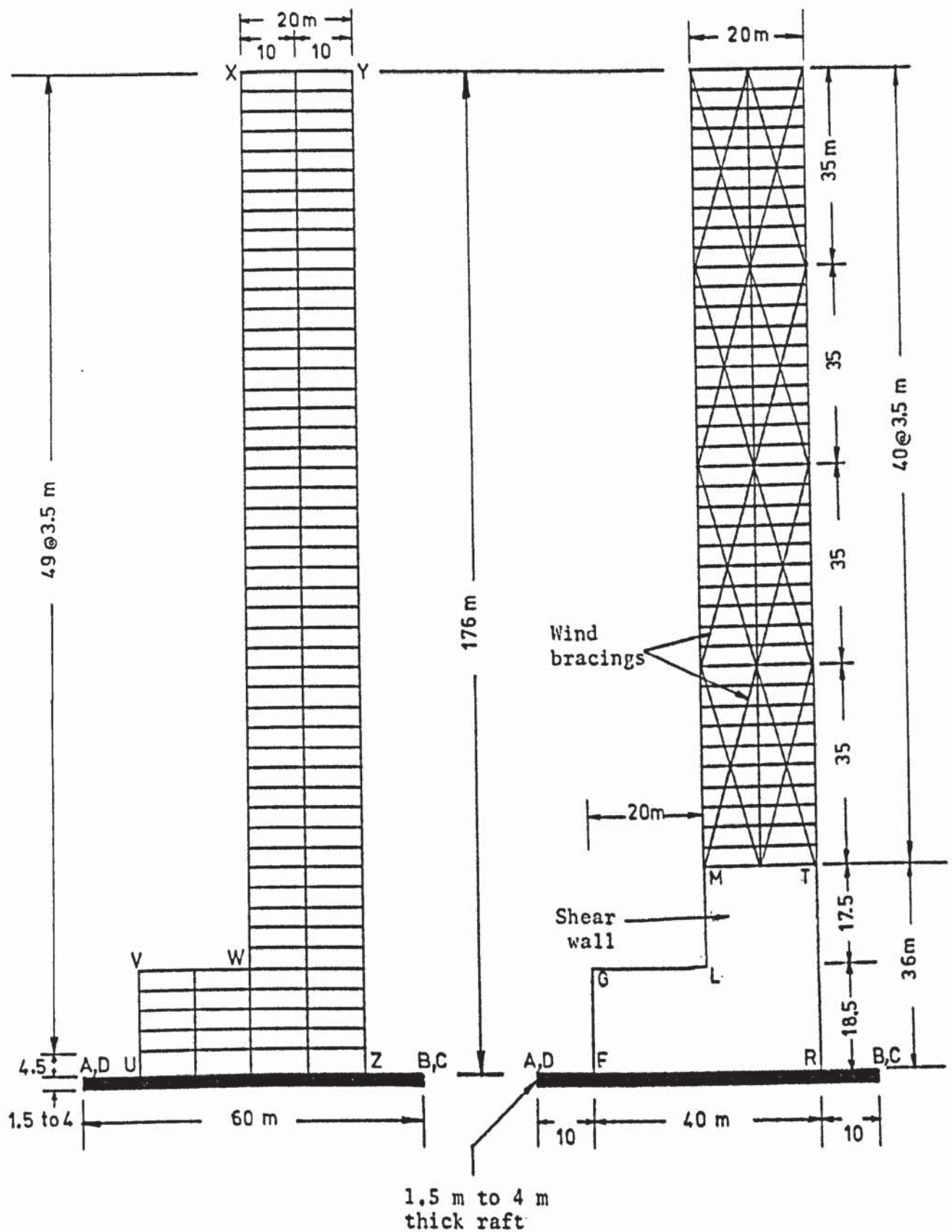


FIGURE 9.27 THE 50-STOrey SPACE STRUCTURE



(a) A typical internal frame

(b) A typical external frame

FIGURE 9.28 AN INTERNAL AND AN EXTERNAL FRAME OF THE 50-STOREY STRUCTURE

were all assumed to be mild steel universal beams and columns. The beam section was kept the same throughout the structure while the column sections were reduced with the height. The T-beam effect between the beams and the slabs was considered and the beam section was increased to account for this. The sectional properties of the frame members are given in table (9.5), in which I_1 and I_2 are the second moments of area about the major and the minor axes respectively. The thickness of the concrete shear wall in the bottom ten storeys was assumed to be 0.5 m.

Member	Floor level	Area (m ²)	I_1 (m ⁴)	I_2 (m ⁴)
Columns	Ground to 10th	0.324	0.11	0.039
	11th to 20th	0.282	0.0825	0.0295
	21st to 30th	0.242	0.055	0.0196
	31st to 40th	0.202	0.0413	0.0147
	41st to 50th	0.162	0.0275	0.0098
Beams and wind bracings in all levels		0.31	0.304	0.0128

TABLE 9.5 SECTION PROPERTIES OF MEMBERS

The structure was supported on a 46 m X 60 m concrete raft ABCD whose thickness was varied between 1.5 m and 4 m. The soil was assumed to be clay supported by a rigid permeable stratum.

The properties of the clay were those used for the examples in chapter 5 and given in table (5.3). The value of Poisson's ratio for the clay was assumed to be 0.33. The thickness of the clay layer was varied between 15 m and 175 m.

9.3.1 Loads on the structure

The dead load was taken as 1.8 kN/m^2 on each floor of the building. The live load, for a general office block, taken from CP3 (Chapter V, Part 1, 1967) was 2.5 kN/m^2 . These vertical loads on the floor were applied as concentrated forces at the joints.

The wind forces recommended in CP3 (Chapter V, Part 2, 1972) depend on the location, topography, building size and height, ground roughness and building life. The code gives a variable wind pressure distribution along the height of the building with the maximum at the top reducing towards the bottom. This pressure is to be used for designing the structural elements utilizing an unyielding base assumption. For foundation design certain reductions in the wind forces are permissible. The reason for this is the generally short duration of the high wind given as the 'basic' wind speed in the code. It was considered that taking 50% of the wind forces given by CP3 for a basic wind speed of 40 m/sec (London) would be adequate. The resulting wind pressure distribution is shown in figure (9.29). This pressure was applied as concentrated horizontal forces at the joints on the windward face of the building.

9.3.2 The finite element analysis

The horizontal extent of soil beyond the raft included in the analysis was 40 m on the side of the structure facing the wind and

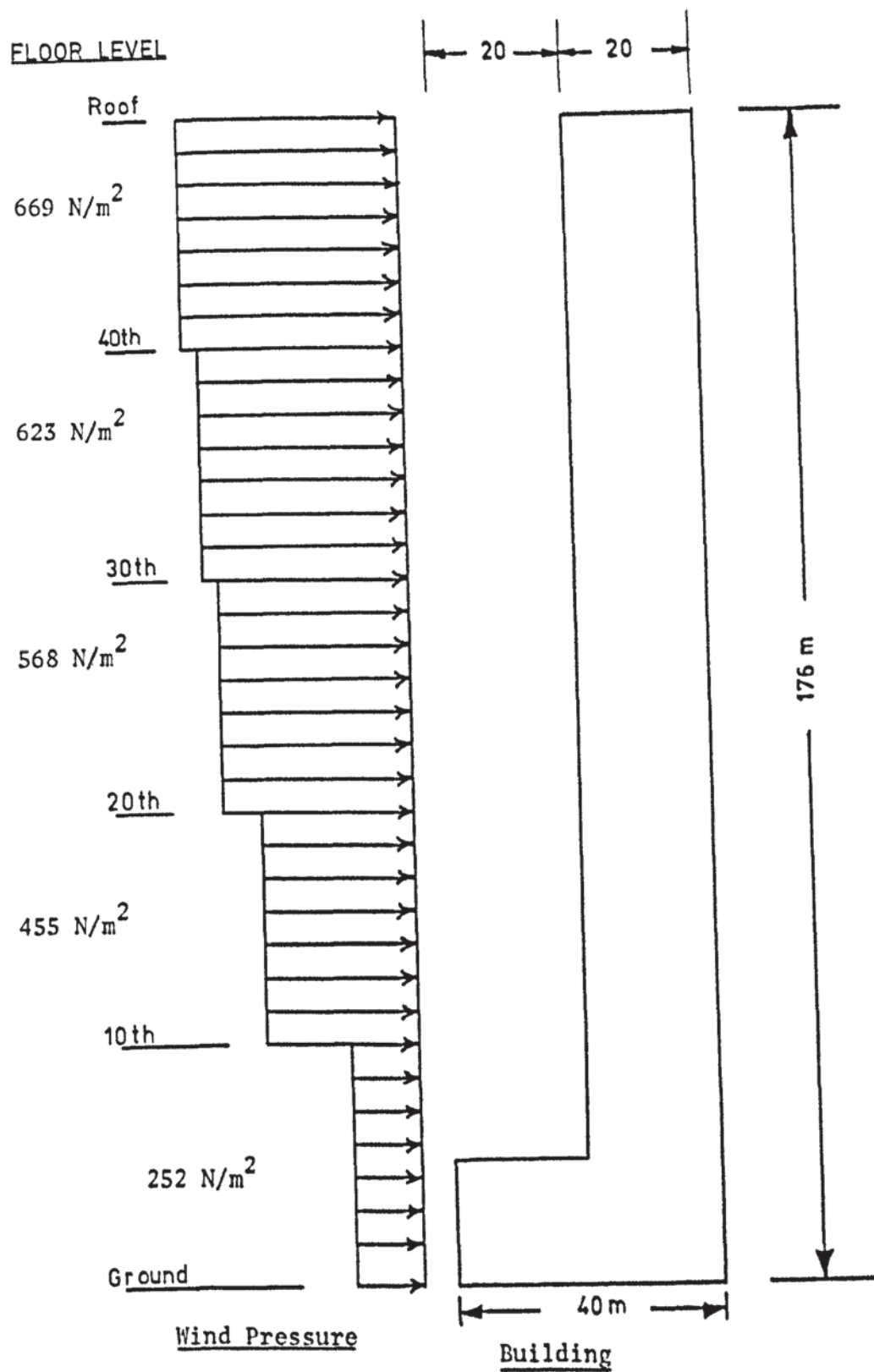


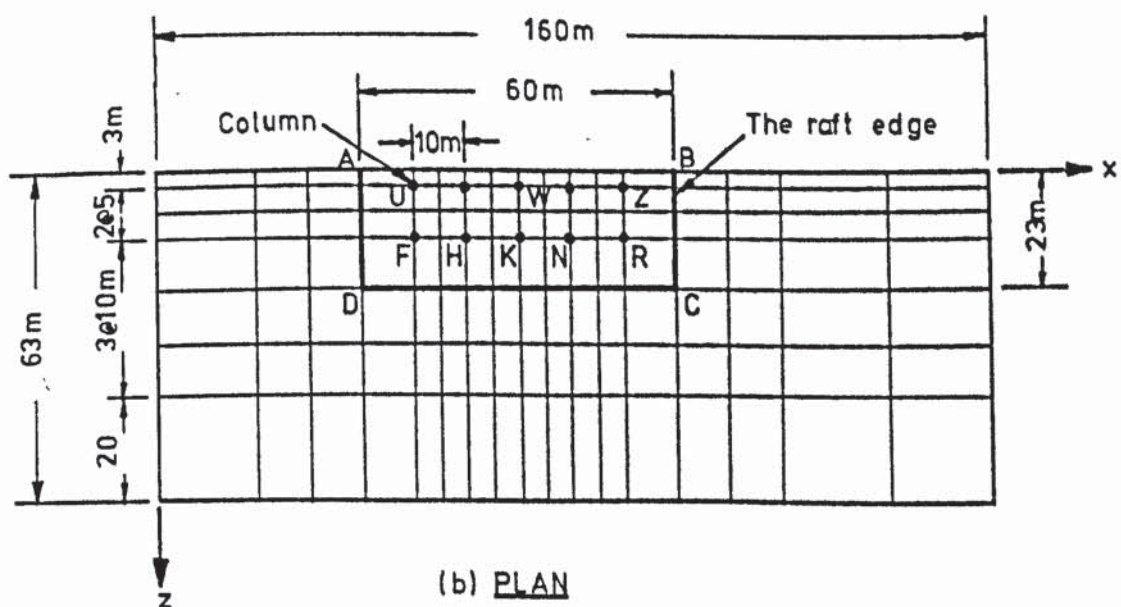
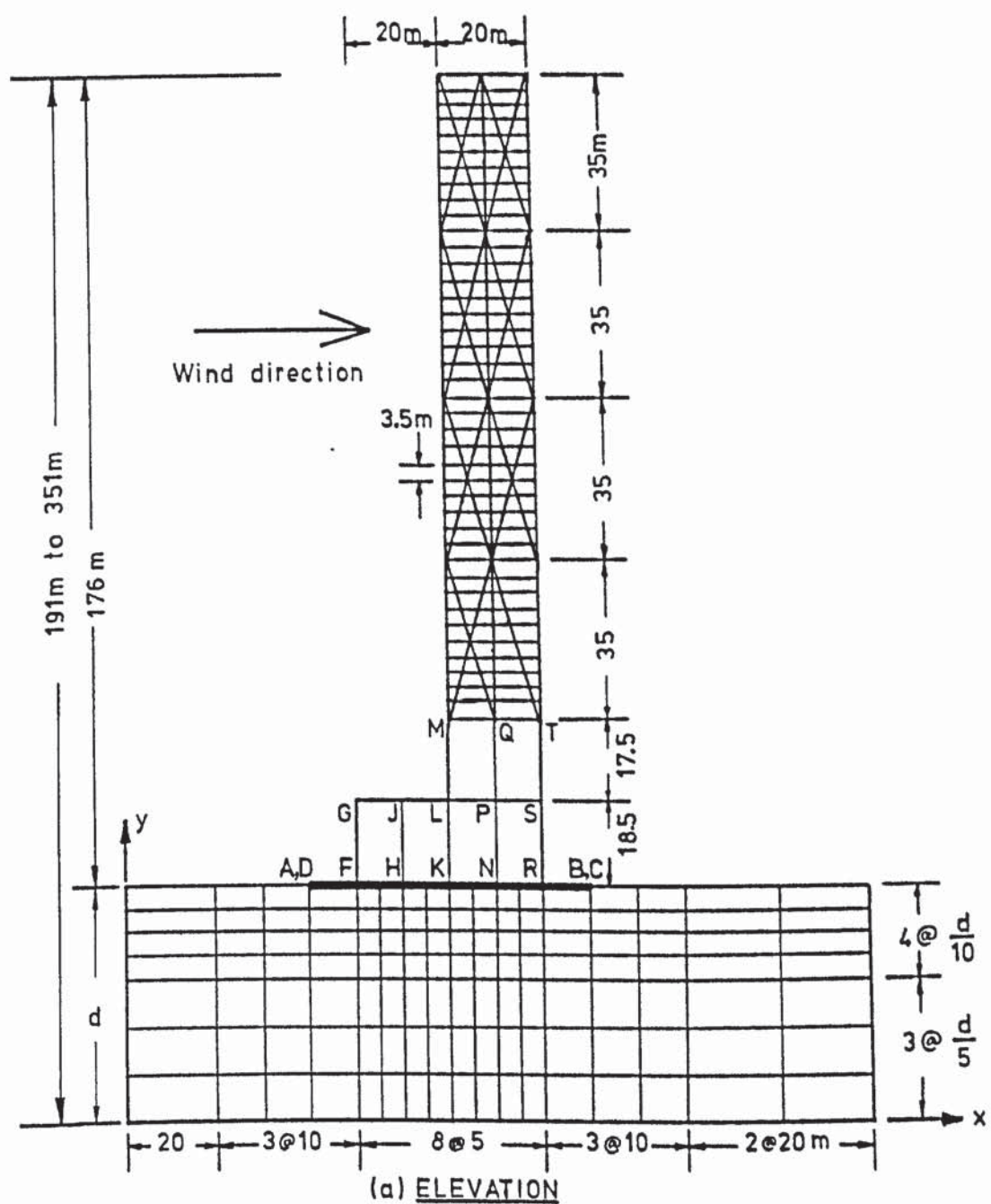
FIGURE 9.29 WIND PRESSURE ON THE FRAME

60 m on the opposite side. On either of the other two sides a distance of 40 m was considered. Because of symmetry about the xy plane, shown in figure (9.27), only half of the structure was analysed.

The finite element mesh is shown in figure (9.30). The depth of the soil was varied between 15 m and 175 m for the various analyses. Each time the pattern and the number of divisions in the vertical direction were kept the same. The detailed dimensions of the finite element mesh are shown in figure (9.31a and b). The raft ABCD in figure (9.31b) was divided into 40 plate elements. The shear wall was represented by 6 plates such as FGJH, HJLK, etc. in figure (9.31a). The beams, the columns and the diagonal bracings were all represented by prismatic members. The model consisted of 1632 joints, 833 solid elements, 46 plates and 876 members with 4419 unknown degrees of freedom.

A total of ten analyses were performed. These are:

- 1 A fixed base analysis with no soil.
- 2 The analysis of the complete structure, the foundation and the soil, with the depth of the clay layer taken as 175 m and the thickness of the raft as 4 m.
- 3 The same as analysis 2 but 25 m deep piles were embedded in the soil. These were assumed to be a group of piles under each column with an equivalent diameter of 0.9 m. The raft was considered to act as pile cap.
- 4 The same as analysis 2 but the depth of clay was reduced to 50 m.
- 5 The same as analysis 4 but with 15 m deep piles.
- 6 The same as analysis 4 but the thickness of the raft was reduced to 1.5 m.



Note: Depth d varies between 15 m and 175 m

FIGURE 9.31 DETAILS OF THE FINITE ELEMENT MESH FOR 50-STOREY STRUCTURE

- 7 The depth of clay was 15 m, the thickness of the raft was 4 m and no pile was used.
- 8 The same as analysis 7 but with 1.5 m thick raft.
- 9 The same as analysis 8 but 9 m deep piles were used.
- 10 The same as analysis 9 with the pile depth increased to 15 m. This was equal to the depth of the clay used in this analysis and therefore the ends of the piles were bearing directly on the rigid stratum underneath. In the analyses with piles, all the surrounding soil elements were connected to them throughout their lengths. The piles themselves were represented by prismatic members.

In the method of chapter 5, the analysis starts with the calculation of the Boussinesq stresses in the soil assuming fixed support reactions. The resultant dead and imposed load acted eccentrically on the raft as the building was subjected to wind forces. It was therefore considered that the final contact pressure distribution under the raft would be non-uniform with the maximum ordinate along the edge BC and the minimum along the edge AD of the raft, see figure (9.31). To speed up convergence, it was initially assumed, that the pressure under the raft was not uniform but varied linearly from 27.3 kN/m^2 at the edge AD to a maximum of 61.9 kN/m^2 at the edge BC.

The Boussinesq stresses due to the above distribution of surface pressure were used to choose the appropriate m_v values for the solid elements from table (5.3). These were then used to carry out the first cycle of the finite element analysis. The m_v values, the displacements, the stresses and the strains were successively modified by using the stresses given by the finite element analyses.

9.3.3 Results of the analyses

9.3.3.1 The deflections of the structure and the raft

A summary of the deflections obtained by the various analyses is given in table (9.6). The sway is the maximum horizontal deflection of the internal frame at the top of the building. The maximum and the minimum settlements of the raft occurred at points B and A, see figure (9.31). The differential settlement is the difference between these two values.

A fixed base analysis gave the sway as $1/1913$. The structure is therefore considered to be stiff in the horizontal direction. When the soil was included in the analysis this sway increased. For the deepest layer of clay (175 m) the ratio of the sway to the height was as high as $1/68$. This was accompanied by a tilt of the raft. The tilt, defined as the ratio of the differential settlement to the length AB of the raft, was as high as $1/71$ for analysis 2 which was considered to be excessive. Analysis 3 with 25 m deep piles was performed to study the effectiveness of the piles in reducing the deflections. The reduction in both the sway and the differential settlement was about 18%. The ratio of sway to height obtained from analysis 3 was $1/83$ and the tilt was $1/87$. It was concluded that the deflections were unacceptable even when piles were used.

In reality, a depth of 175 m of clay is rare and the above analyses were performed to examine the effect of depth of soil on the deflections. The sway and the differential settlement are plotted in figure (9.32) against the depth of the clay. The values were obtained from analyses 1, 2, 4 and 7, see table (9.6). In all these cases the thickness of the raft was 4 m with no piles.

Analysis No	Thickness of clay (m)	Depth of piles (m)	Raft thickness (m)	Sway at top (m)	Differential settlement (m)	Maximum settlement (m)
1	Fixed supports			0.092	0	0
2	175	0	4	2.58	0.841	1.08
3	175	25	4	2.117	0.687	0.92
4	50	0	4	2.355	0.767	0.848
5	50	15	4	2.118	0.689	0.764
6	50	0	1.5	2.486	0.779	0.855
7	15	0	4	1.292	0.353	0.379
8	15	0	1.5	1.42	0.358	0.383
9	15	9	1.5	1.25	0.282	0.318
10	15	15	1.5	0.155	0.009	0.0136

TABLE 9.6 DEFLECTIONS OF THE 50-STOREY STRUCTURE

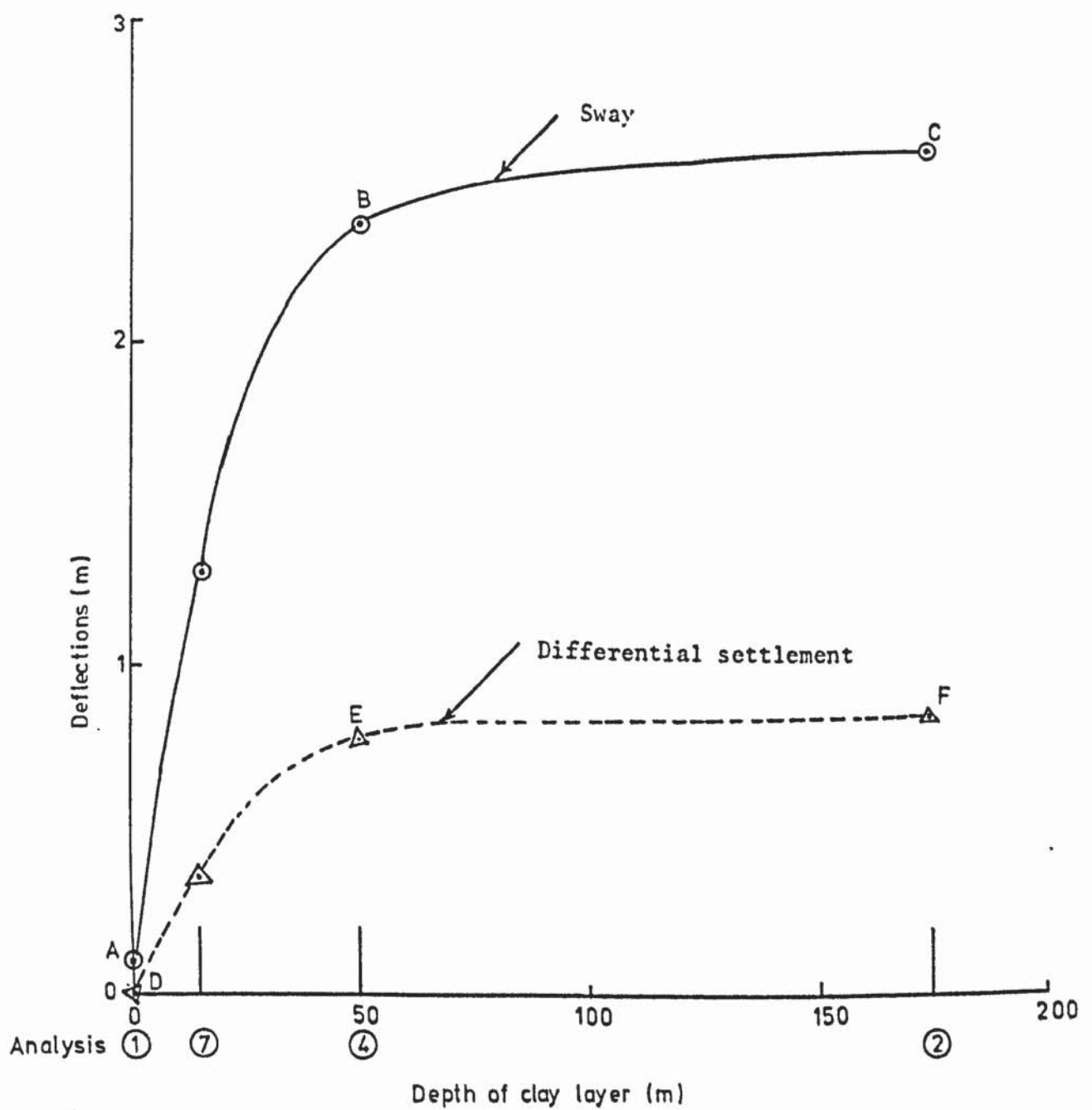


FIGURE 9.32 VARIATION OF SWAY AND DIFFERENTIAL SETTLEMENT WITH DEPTH OF CLAY FOR A RAFT THICKNESS OF 4m AND NO PILES, ANALYSES 1, 2, 4 AND 7

It is observed in figure (9.32) that there is a rapid increase in both the sway and the differential settlement as the depth of the clay increases up to about 50 m. Beyond the points B and E, the portions BC and EF are relatively flat and nearly horizontal indicating that increasing the depth of clay beyond 50 m does not significantly increase the deflections of the structure. As the depth was increased from 50 m to 175 m both the sway and the differential settlement increased by only 9.6%. The reason for this small increase is that the stresses in the soil reduce with the depth. Thus most of the settlement is caused by the compression of the highly stressed top region of the soil and the contribution of the deeper regions with low stress is negligible. This will be explained in greater detail later in the chapter while describing the stresses in the soil.

Analysis 6 with 50 m deep clay, 1.5 m raft and no pile gave a sway of 2.486 m, see table (9.6), which is $1/71$ of the height of the building. It also gave a tilt of $1/77$. Increasing the thickness of the raft to 4 m in analysis 4 reduced the sway by only 5.3% and the differential settlement by 1.5%. As 15 m deep piles were also included, in analysis 5, the sway reduced by 14.8% and the differential settlement by 11.6%. The deflections are however still too high to render the structure usable. This indicates that neither the use of a heavier raft nor the inclusion of the 15 m piles solves the foundation problem of this building when the depth of clay is 50 m.

The depth of clay was then reduced to 15 m for analyses 7 to 10 in which a significant reduction of the deflections was observed. When no pile was used in analyses 7 and 8 the sway reduced by 45%

from the case with 50 m clay for a raft thickness of 4 m and by 43% for a raft thickness of 1.5 m. The reduction in differential settlement for both the rafts was about 54%. The inclusion of the piles in the 15 m clay in analyses 9 and 10 reduced these deflections still further. The sway and the differential settlement are plotted in figure (9.33) against the depth of piles for analysis cases 8, 9 and 10, with 15 m deep soil and 1.5 m thick raft. The portions AB and DE of the curves are flat indicating that the deflections do not reduce significantly as the pile depth is increased upto 9 m, indicating that short piles do not strengthen the foundation. This is because a 15 m deep layer of clay is highly stressed throughout the depth as will be shown later in the chapter.

As the length of the piles was increased further both the sway and the differential settlement decreased rapidly as shown by the portions BC and EF in figure (9.33). When the piles were 15 m long and rested directly on the rigid stratum under the clay layer the sway reduced by 98% of that for the case with no pile and the differential settlement reduced by 97%. The ratio of the sway to the height for this case is only $1/1135$ and the tilt is $1/6667$. These low values are due to the fact that the loads of the structure were transmitted directly to the rigid stratum by the end bearing piles. The piles themselves carried most of the load and the soil did not settle appreciably. It is considered that the use of the piles penetrated down to the rigid stratum gives an acceptable foundation for this structure.

The sway and the settlement of the internal frame UVWXYZ, see figure (9.27) and (9.28), are plotted in figure (9.34). The sway

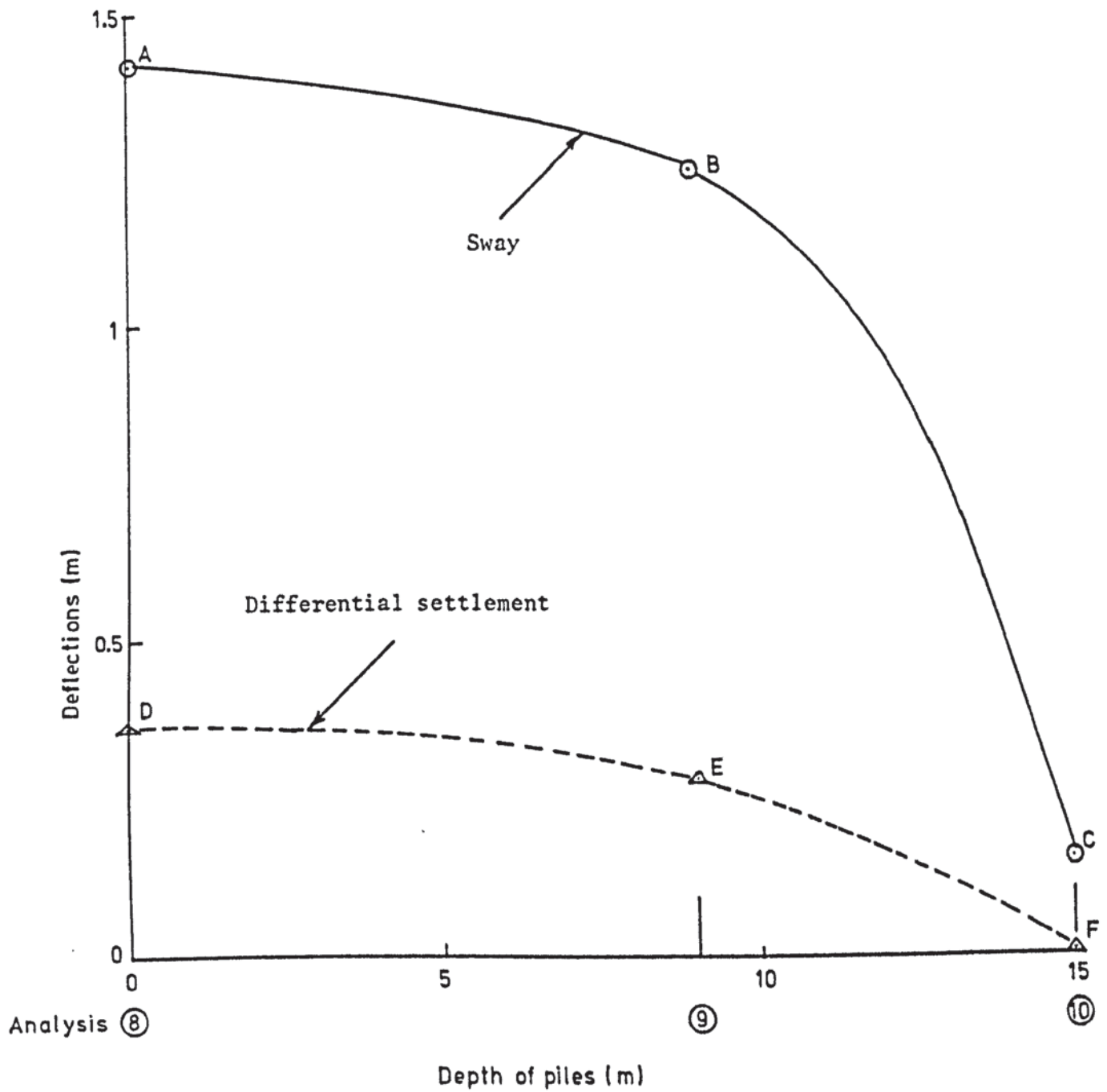


FIGURE 9.33 VARIATION OF SWAY AND DIFFERENTIAL SETTLEMENT WITH DEPTH OF PILES FOR 15 m DEEP CLAY LAYER AND 1.5 m THICK RAFT; ANALYSES 8, 9 AND 10

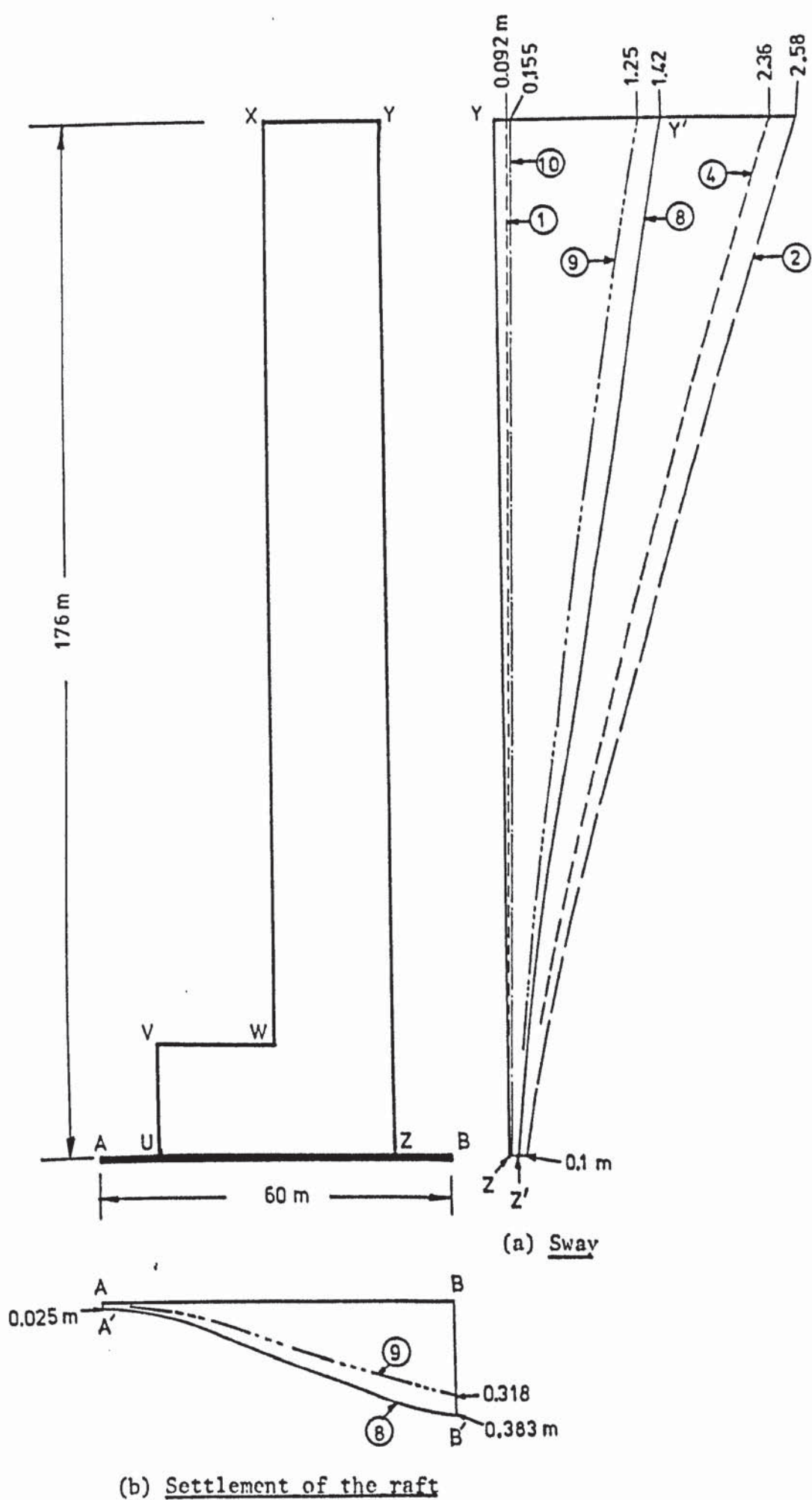


FIGURE 9.34 SWAY AND SETTLEMENT OF INTERNAL FRAME FOR ANALYSIS CASES 1, 2, 4, 8, 9 AND 10

shown in this diagram is the horizontal displacement of the joints on the external column YZ in the frame. It was observed that the axial deformations of the beams were negligible and the horizontal displacements of the other columns were almost the same. The sway diagrams obtained by the various analyses are indicated by the analysis number encircled beside each curve. The settlements of the raft for analyses 8 and 9 are shown in figure (9.34b). In analysis 8, as the raft tilted from the position AB to A'B', the column YZ assumed the new position Y'Z'. This is because the rigidity of the joint Z between the column and the raft and the in plane stiffness of the frame UVWXYZ forced the column to rotate with the raft. Notice too that point Z moves horizontally to Z' which is due to the deformation of the soil. ZZ' was 0.1 m for analysis 2. A conventional analysis neglects this. It is considered that while the building is subjected to wind forces, sway is aggravated by the accompanying differential settlement of the raft. When the differential settlement was reduced to 0.009 m in analysis 10 by using the end bearing piles the sway reduced to only 0.155 m at the top. The resulting sway diagram is almost coincident with the one obtained by analysis 1 assuming fixed supports.

9.3.3.2 The bending moments

The bending moments in the members of the frame obtained by the various analyses were examined by comparing them with those obtained by assuming a fixed base. It was observed that the difference in these moments was in direct proportion with the sway and the differential settlement suffered by the structure. As a

15 m depth of clay is thought to be a practical figure, analysis 8 was singled out for a detailed study of the bending moments.

The redistribution of the bending moments was most significant at the base of the building. At point Z, in column YZ, see figure (9.28), the fixed base bending moment was 325 kNm and the flexible base moment was -5600 kNm showing a reversal of the sign. The difference between these moments reduced rapidly along the height of the building and vanished at the top. The column moments in the bottom 7 floors of the internal frame UVWXYZ, are shown in figure (9.35). In this diagram the solid lines indicate the bending moments obtained by analysis 8 and the dashed lines indicate those obtained by analysis 1 which assumes a fixed base. In the bottom four storeys the fixed base moments are very small while the flexible base ones are very high. In column YZ these moments are opposite in sign in the lower three storeys. In the other columns the maximum difference between the flexible base and the fixed base moments is as high as 92.6%. This occurs at point Z' at the base of the internal column Y'Z', see figure (9.35). Above the 4th floor the difference reduces rapidly and becomes a maximum of only 27.6% at the 6th floor level. From this floor upwards the two bending moments converged rapidly and the difference became negligible. The column bending moments in the top eight floors of the internal frame are shown in figure (9.36).

The bending moments in the beams of the bottom seven floors of frame UVWXYZ are shown in figure (9.37). Again the difference between the flexible base and the fixed base moments is most significant near the base of the building and reduces along the height. In the 1st floor there is a reversal of sign of the

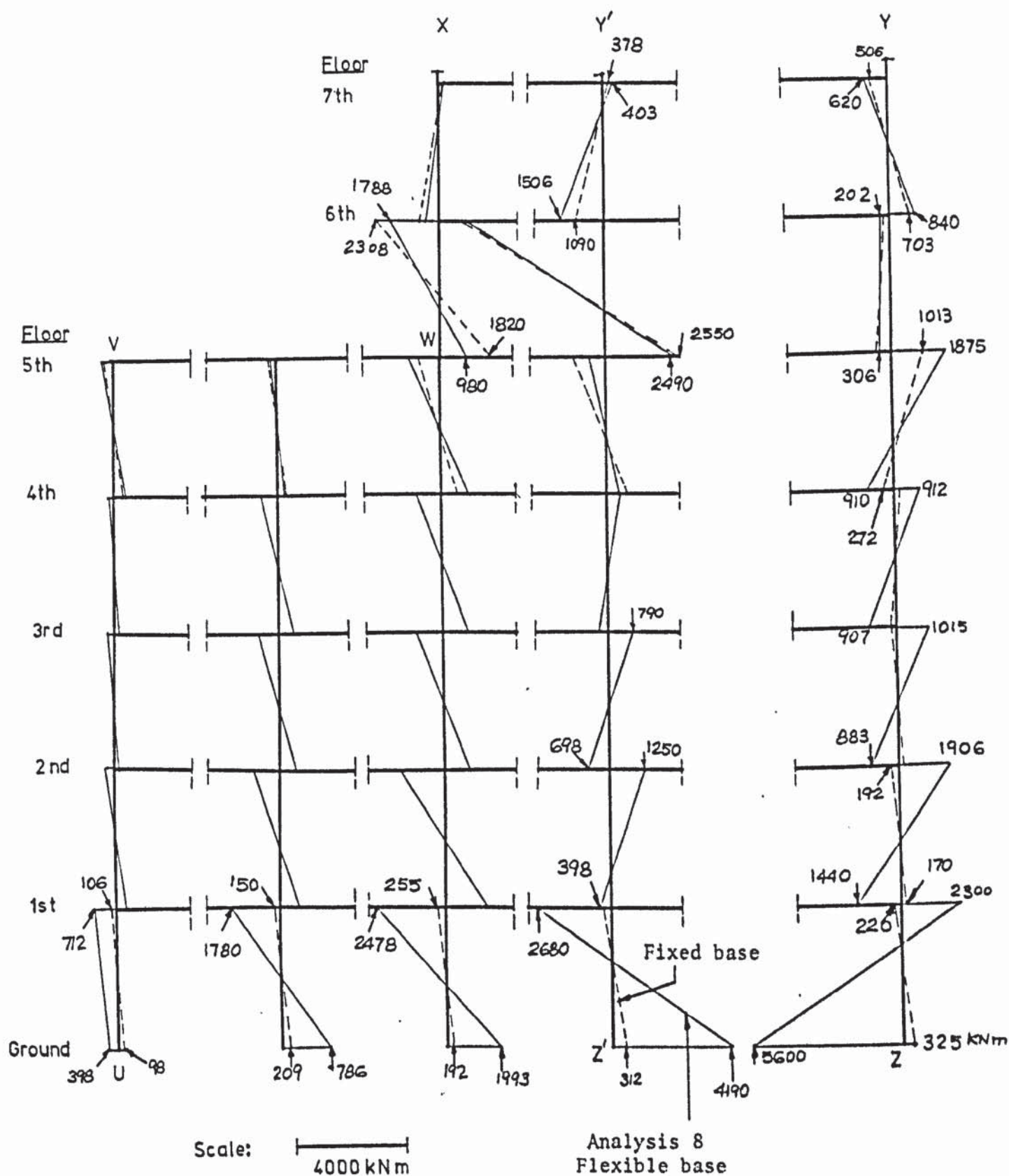


FIGURE 9.35 COLUMN BENDING MOMENTS IN THE BOTTOM 7 FLOORS OF THE INTERNAL FRAME: ANALYSIS CASES 1 AND 8

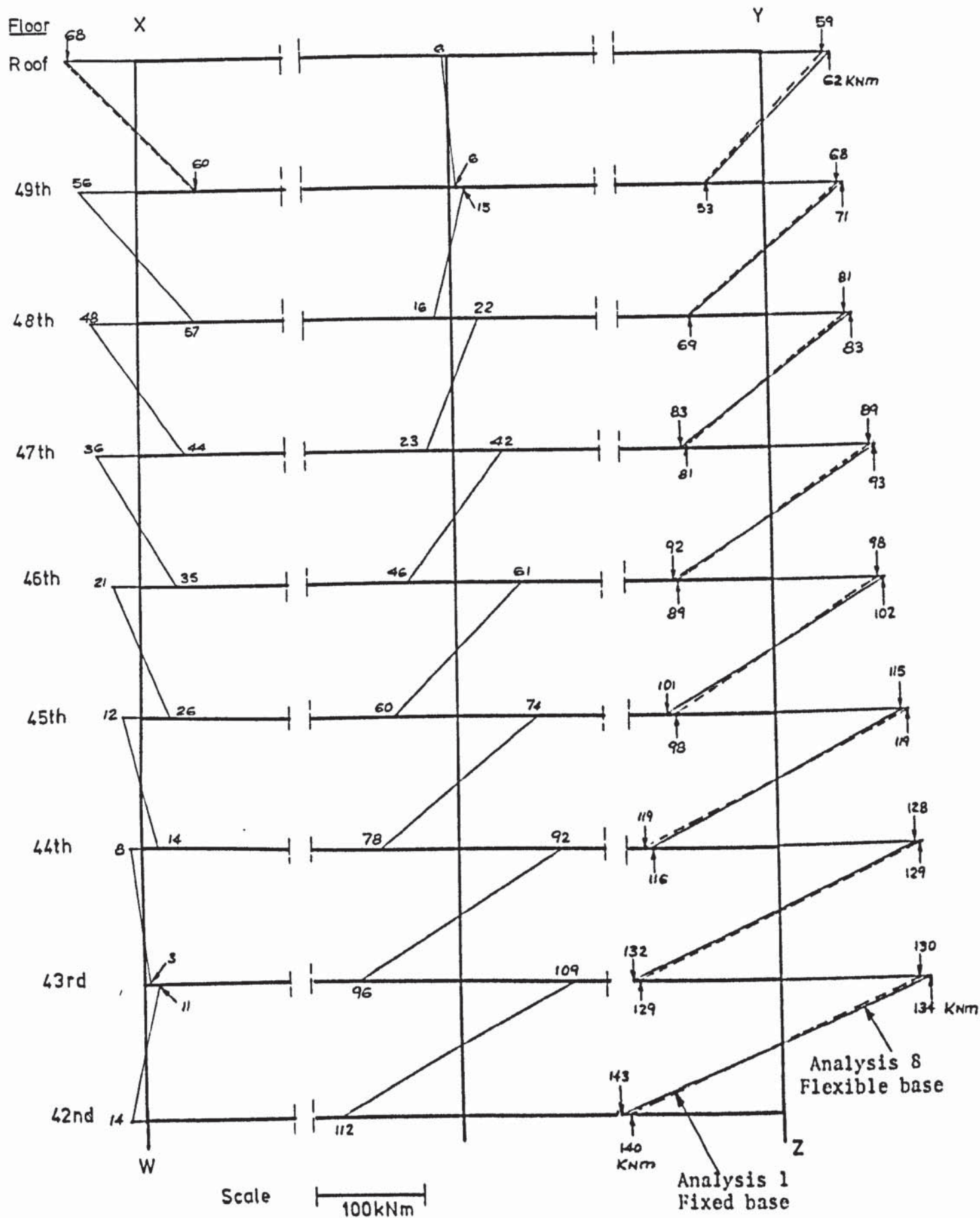


FIGURE 9.36 COLUMN BENDING MOMENTS IN THE TOP 8 FLOORS OF THE INTERNAL FRAME: ANALYSIS CASES 1 AND 8

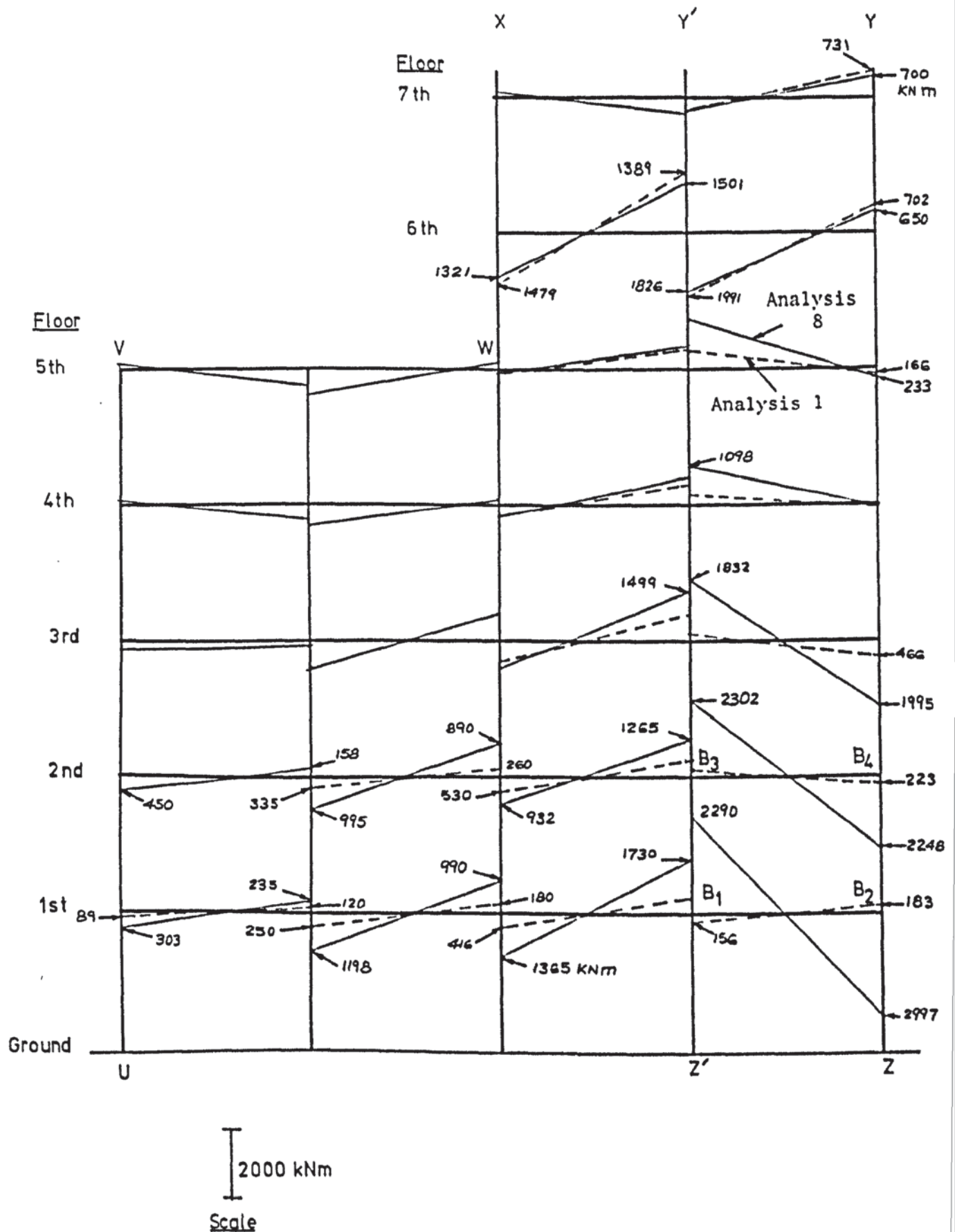


FIGURE 9.37 BEAM BENDING MOMENTS IN THE BOTTOM 7 FLOORS OF THE INTERNAL FRAME: ANALYSIS CASES 1 AND 8

moment in beam B_1B_2 but they become of the same sign in the 2nd floor in B_3B_4 directly above B_1B_2 . The maximum difference of the beam moments in this floor is 89.6% which occurs in B_3B_4 . This maximum difference reduces in the higher floors becoming only 4.4% at the 7th floor. It was observed that by about the 20th floor the difference between the flexible and the fixed base moments reduced to almost zero. The beam bending moments in the top eight floors of frame UVWXYZ are shown in figure (9.38). The fixed base moments were almost the same as the flexible base ones and are shown only at the top of the frame where a difference of only 0.2% is recorded.

The maximum difference between the fixed and the flexible base moments were calculated for all the beams and the columns of the whole structure at each floor level and expressed as a percentage of the flexible base moment. These maximum differences for the beams and the columns are plotted in figure (9.39) against the floor level. There is a sudden change in curvature of both the curves in the figure at about the 5th floor level where the number of bays of the structure reduces from 4 to 2. It is considered that the bottom 5 floors of the building are stiffer and suffer the most by the tilt and the sway of the building.

The rapid dissipation of the difference between the fixed and the flexible base moments in the structure is in agreement with the findings of Litton and Buston (1968) who analysed a symmetrical 5-bay 23-storey plane frame subjected to an applied vertical displacement of each leg in turn. Although the structure considered here is three dimensional and subjected to both sway and differential settlement the influence of these become insignificant in the higher floors.

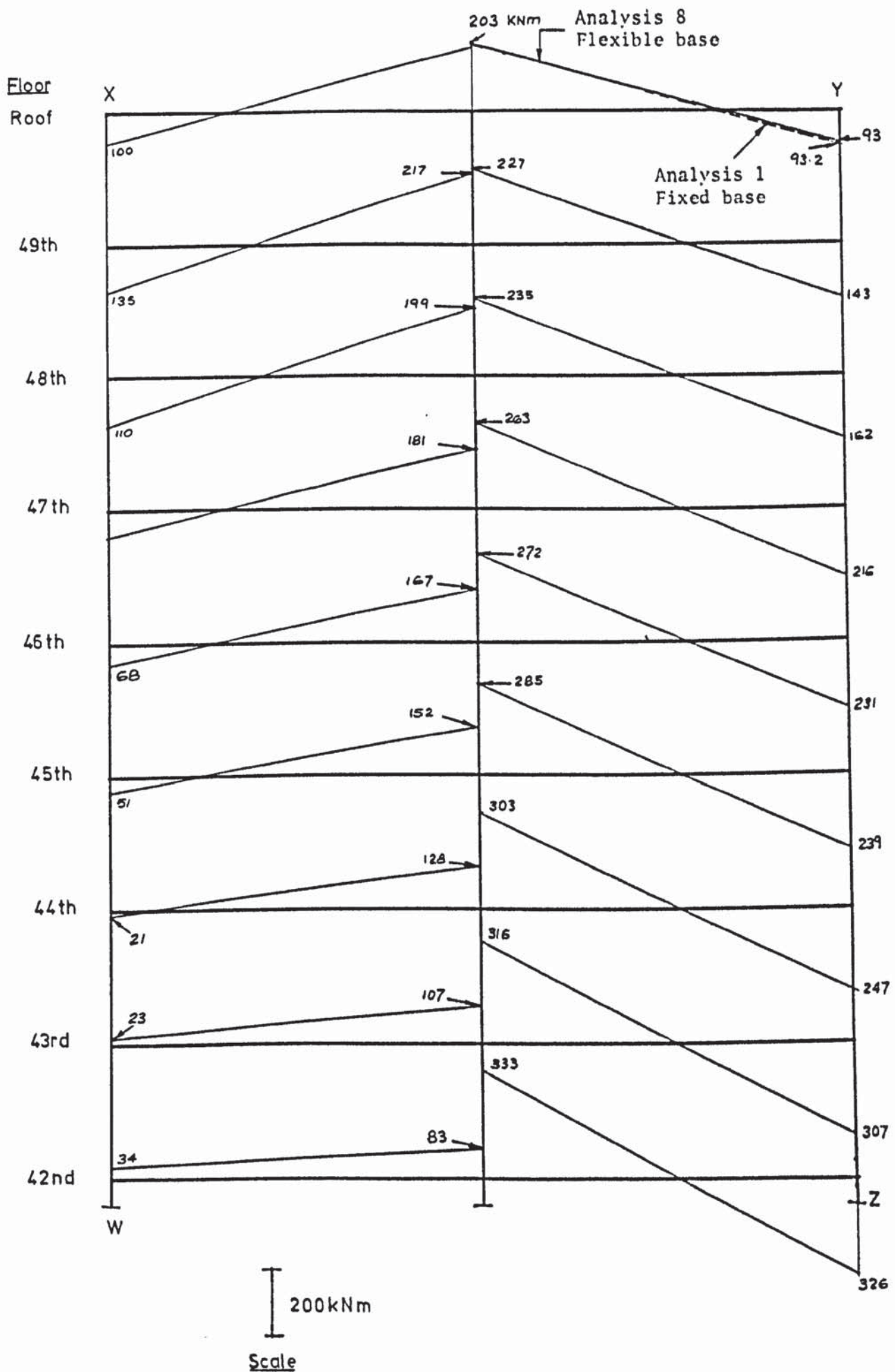


FIGURE 9.38 BEAM BENDING MOMENTS IN THE TOP 8 FLOORS OF THE INTERNAL FRAME: ANALYSIS CASES 1 AND 8

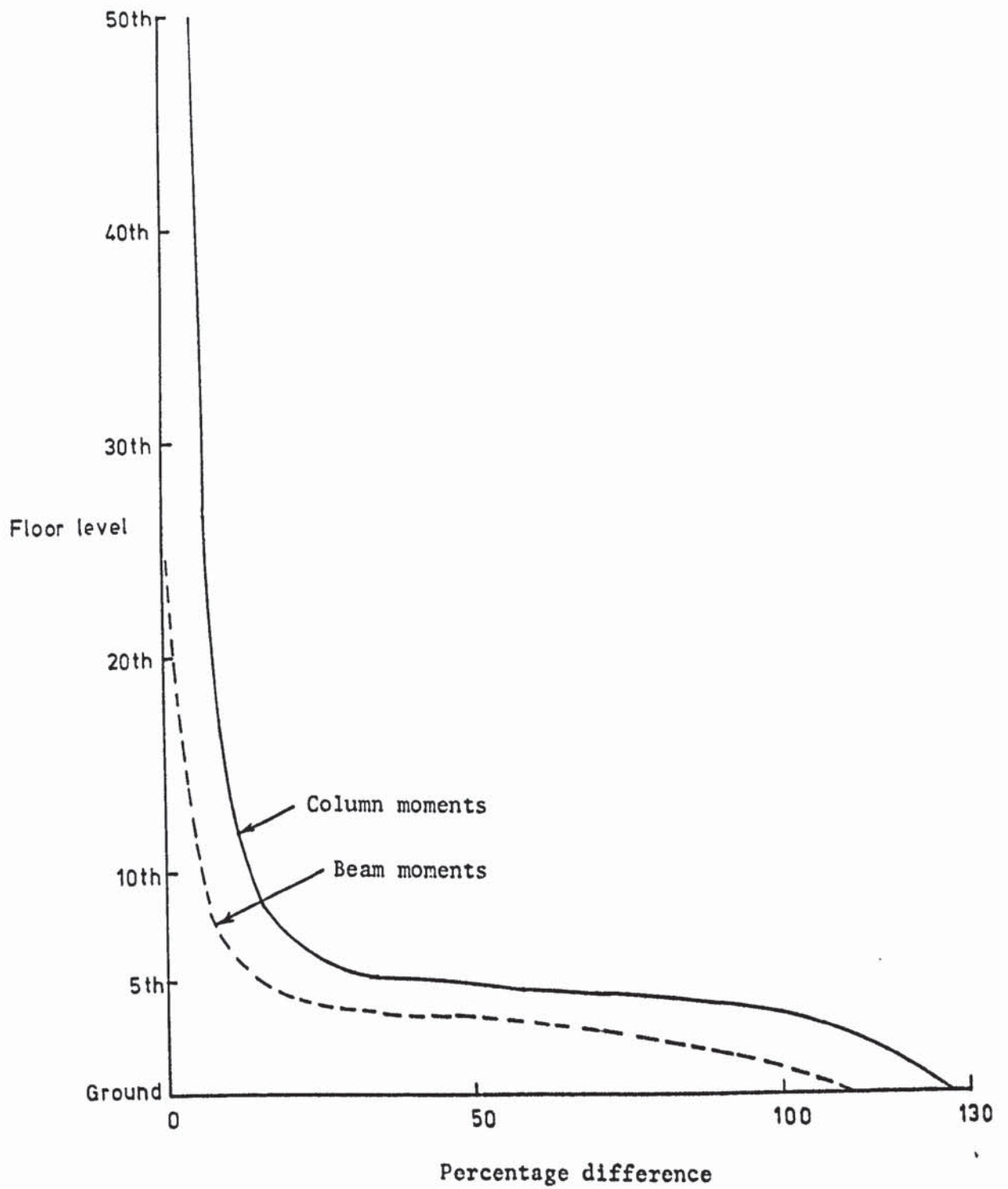


FIGURE 9.39 VARIATION OF THE MAXIMUM DIFFERENCE OF THE FLEXIBLE BASE (ANALYSIS 8) AND THE FIXED BASE MOMENTS ALONG THE HEIGHT

9.3.3.3 Stresses under the structure

The maximum vertical stresses in the soil were directly under the raft and reduced with the depth. The variation of the vertical stress with depth under the column YZ, see figure (9.30), is shown in figure (9.40). Curve (1) in this figure shows the stresses obtained from Boussinesq's equations for the applied surface loads ignoring the structure. Curve (2) shows those obtained by analysis (2) assuming the depth of clay as 175 m, curve (3) represents the stresses from analysis 4 with 50 m clay and curve (4) shows the stresses for a 15 m deep clay in analysis 8. It is observed that the Boussinesq stresses are higher than those given by curves (2) and (3) throughout the depth. However, the stresses reduce with the depth and the difference between curves (1) and (2) become negligible at a depth of about 150 m. Curves (2) and (3) almost coincide, with curve (3) showing about 10% more stress at a depth of 50 m. This is because in the case of curve (3) there is a rigid boundary at this depth which increases the stresses. Below this depth the stresses indicated by curve (2) are small and therefore it is thought that the soil below this depth does not significantly contribute to the total settlement of the 175 m thick layer. In both analysis 2 and analysis 4 the total settlement is caused mainly by the compression of the top 50 m of the soil. Hence these two settlements differed by only 9.6% as shown in section 9.3.3.1. Curve (4), on the other hand, indicates high stresses throughout the 15 m deep layer of soil. At the bottom of this layer the stress is 34% higher than the one obtained for a 50 m deep soil. However, since the depth of the compressible soil is only 15 m in analysis 8 the total

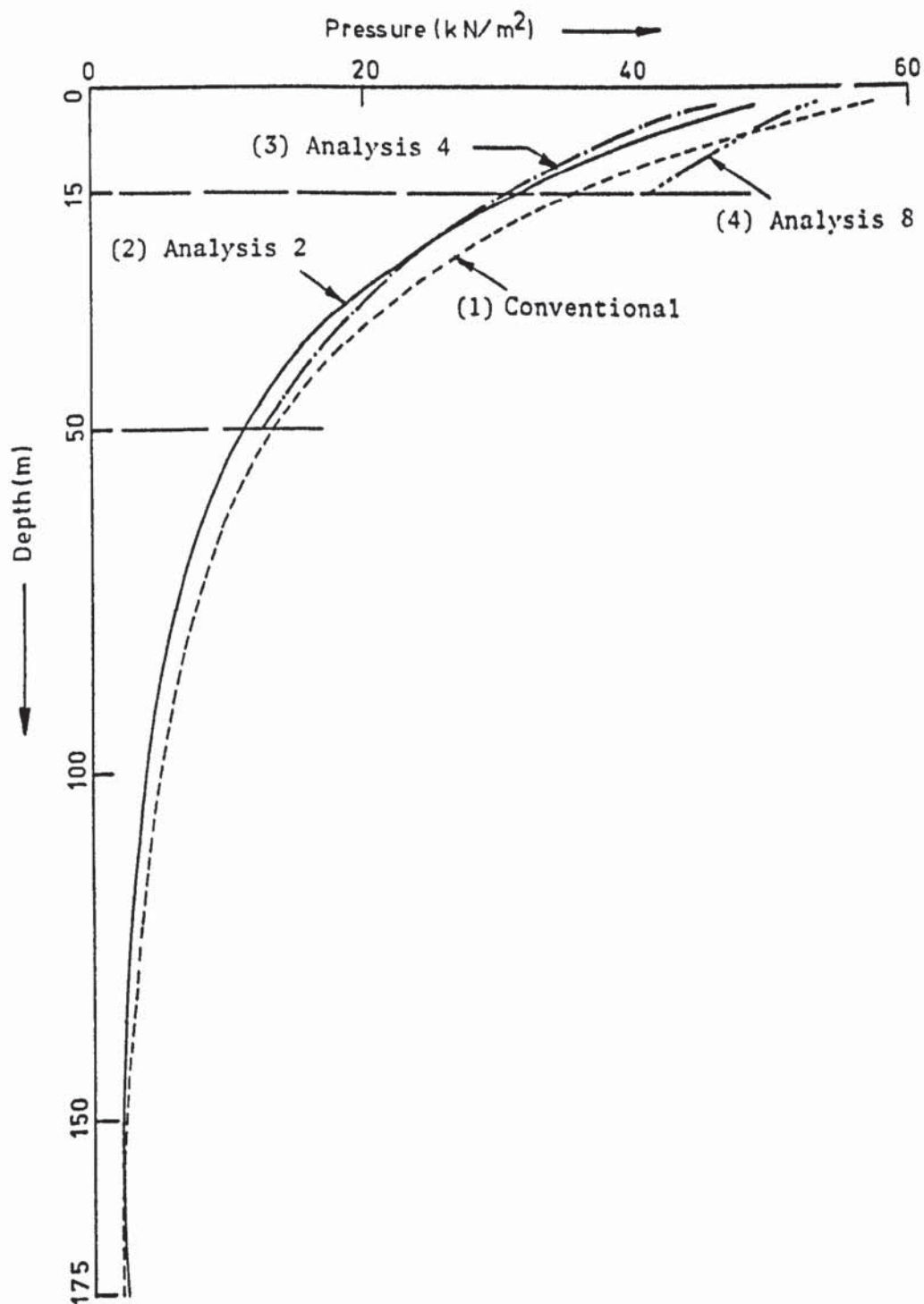


FIGURE 9.40 VARIATION OF VERTICAL PRESSURE WITH DEPTH UNDER COLUMN YZ FOR THE VARIOUS ANALYSES

settlement reduced by 54% from analysis 4 with 50 m clay. This is because of the considerable stresses in the soil between 15 m and 50 m in the case of curve (3) which contributed significantly to the settlement.

When piles were included in the 15 m clay there was a considerable change in the variation of the stresses in the soil. The vertical stress under the column YZ is plotted against the depth in figure (9.41) for a 15 m deep soil with no pile, 9 m piles and 15 m piles. The inclusion of the 9 m piles reduced the stresses by as much as 34% in the top 9 m of the soil. Below 9 m, however, the stresses increased by 20% over the no pile case. Thus while the settlement of the top 9 m of soil reduced due to the presence of the piles, that of the bottom 6 m increased. This is why the settlement of the raft was reduced by only 21% by using the 9 m piles as stated in section 9.3.3.1. When the pile length was increased to 15 m, analysis 10, to penetrate them down to the rigid stratum the load was directly transmitted to this stratum through the piles. The stresses in the soil throughout the depth were negligible as shown by the dashed curve in figure (9.41). As the piles themselves were quite stiff there was a significant reduction in the settlement, which was only about 3% of that with no pile.

The distribution of the vertical stress in the soil in x-direction for analysis 8 is shown in figure (9.42). The stresses are plotted at various depths for the vertical section E-E shown in the top figure. The corresponding Boussinesq stresses obtained by neglecting the structure are shown by the dashed lines. Near the edge AD of the raft, the Boussinesq stress is high with a value of about 30 kN/m^2 ,

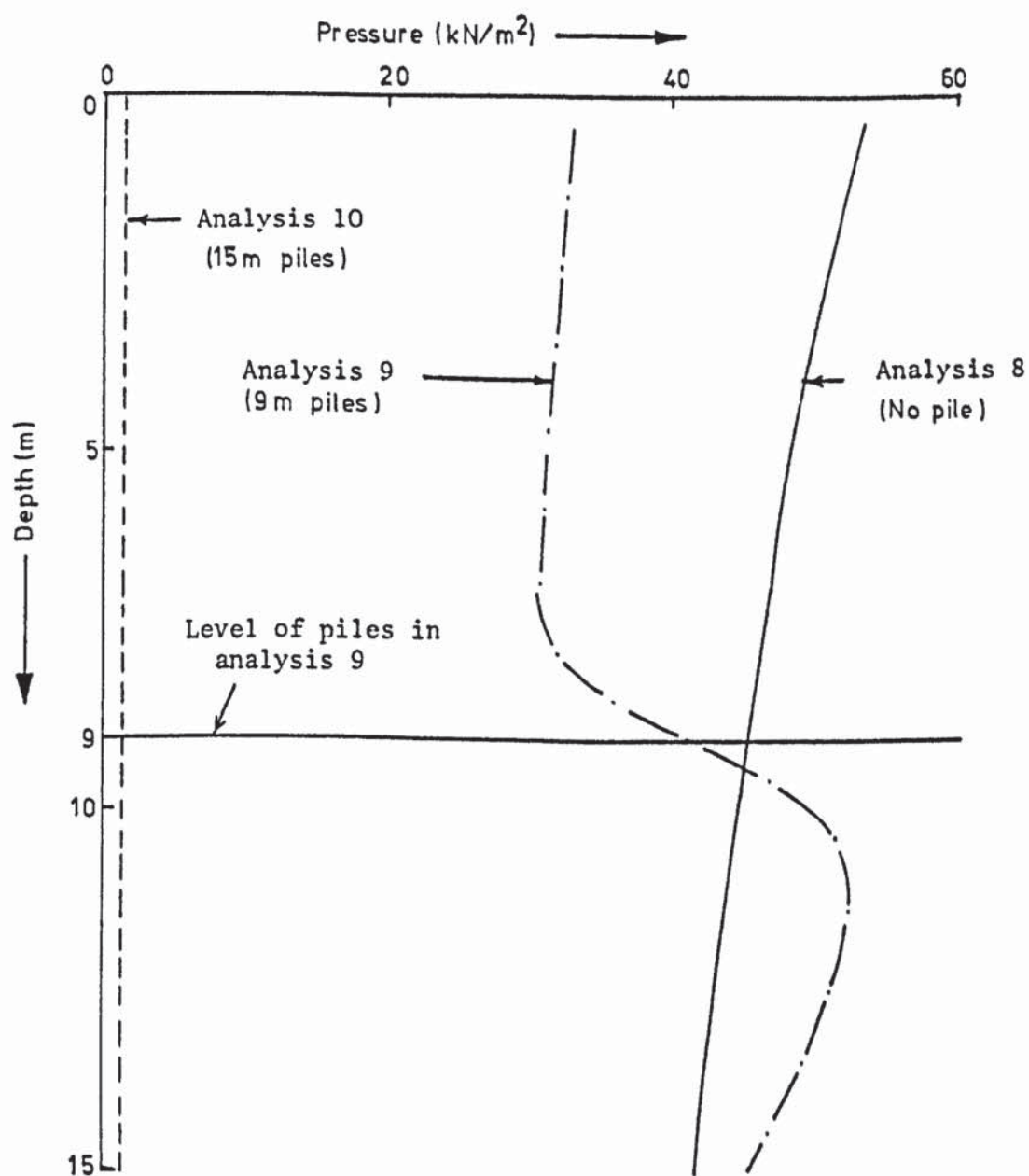


FIGURE 9.41 VARIATION OF VERTICAL PRESSURE WITH DEPTH UNDER COLUMN YZ
FOR 15 m DEEP CLAY : ANALYSIS CASES 8, 9 AND 10

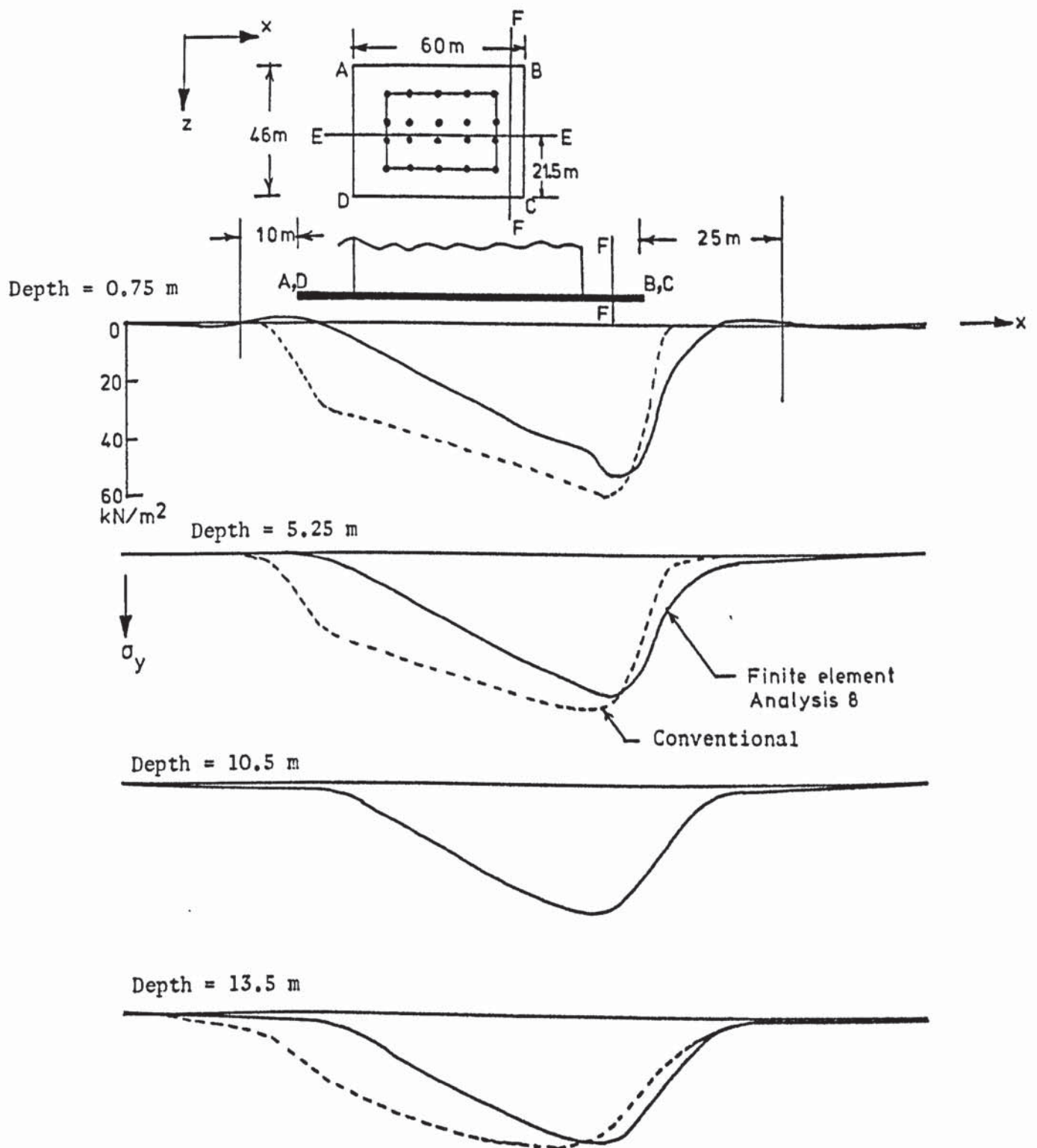


FIGURE 9.42 DISTRIBUTION OF VERTICAL STRESS σ_y IN x-DIRECTION AT SECTION E-E AT VARIOUS DEPTHS : ANALYSIS 8

while that obtained by analysis 8 is almost zero. This is because the Boussinesq stresses were calculated for a linearly varying surface load with an ordinate of 27.3 kN/m^2 at the edge AD and 61.9 kN/m^2 at the edge BC of the raft. As the structure tilted about the edge BC the stresses given by the finite element analysis reduced along AD. At shallow depths, there is a sudden reduction in the stress to the right of BC. This sudden reduction in stresses becomes less marked at the deeper levels. The depth of the layer was only 15 m and therefore the whole thickness was highly stressed. The maximum stress reduced by only 19% at a depth of 13.5 m from the value at 0.75 m.

The curves in figure (9.42) show that the stresses reduced rapidly at points to the left of AD and to the right of BC. This was also observed in the stress distribution in z-direction which is shown in figure (9.43). The stresses are plotted for the vertical section F-F passing through the maximum stress ordinate in figure (9.42). In both figures (9.42) and (9.43) it is noticed that a column of high vertical stress developed directly beneath the raft which diminished rapidly away from it. This indicates that the lateral extent of soil included in the analysis could be reduced. This reduces the number of solid elements in the problem and thus renders the analysis cheaper. It is considered that an extent of 10 m on side AD and 25 m on side BC beyond the raft as shown in figure (9.42) and a distance of 17 m in z-direction beyond the edge CD shown in figure (9.43) would be adequate. The maximum stress on this boundary is only about 4% of the maximum stress under the raft.

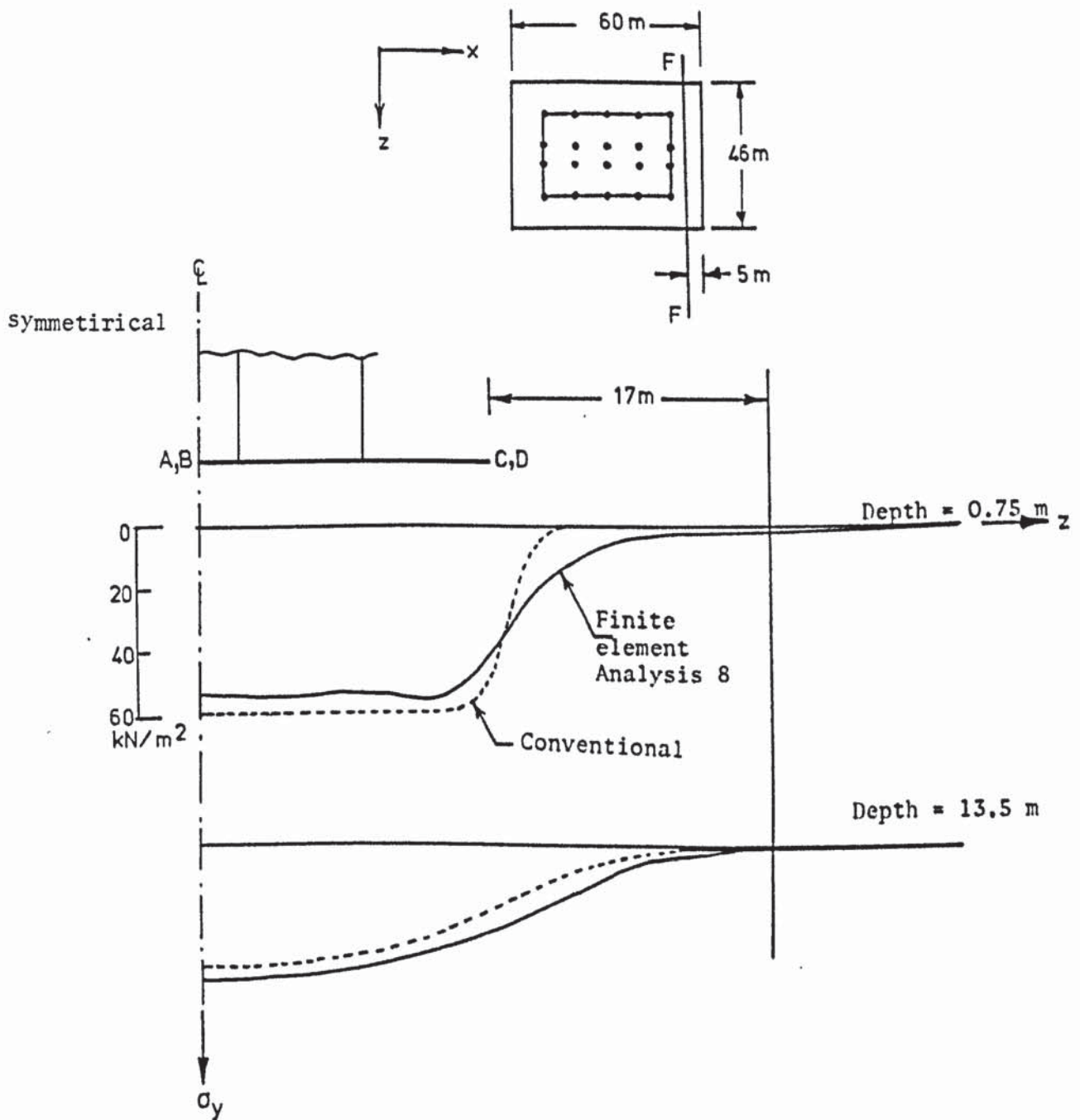


FIGURE 9.43 DISTRIBUTION OF VERTICAL STRESS σ_y IN z -DIRECTION AT SECTION F-F AT VARIOUS DEPTHS: ANALYSIS CASE 8

CHAPTER 10

CONCLUSIONS AND SUGGESTIONS FOR FURTHER WORK

Several features of a realistic interaction problem were listed in chapter 1. One of them is that the non-linear behaviour of the system must not be ignored. In fact it has been demonstrated that the load-bending moment and the load-deflection relationships of a structure are essentially non-linear. This is caused by the non-linear soil properties which must be adequately represented in the analysis.

The spline functions used in chapter 2 to represent the stress-strain curves of the soil were found to be very efficient. These gave an exact fit with the experimental $\tau_{oct}-\gamma_{oct}$ curves. The load-deflection curves obtained by using them compared favourably with the experimental results. An analysis using the hyperbolic representation was found to be inadequate. Although the mathematical formulation of the spline functions is more involved than that of a single polynomial or hyperbola, the procedure can easily be programmed into a computer. In fact, for the soil in the model experiments, this program was run only once and the resulting spline parameters were used repeatedly for the analyses of all the models. It is concluded that not only do these functions give an exact representation of the non-linear soil properties they are also inexpensive to use.

The saving of the computer time has been a major aim in the development of the computer programs. An isoparametric hexahedral and a rectangular paralleliped element were used to represent the soil. It was found that since the former requires numerical

integration, a considerable saving can be achieved by deriving the stiffness matrix of the latter in an explicit form. This was done in chapter 3. Furthermore, by dividing the soil into a limited number of elements of the same dimensions, a finer mesh can be used. This improves the accuracy of the analysis. Using rectangular parallelopiped elements also enabled the data preparation to be automated.

As stated in chapter 1, the tensile weakness of the soil causes cracks within the soil mass and at the boundary between the soil and the foundation. The finite element method was extended in chapter 4 to represent these cracks in a three dimensional structure-soil system. By using dummy joints, the procedure allows physical cracks to take place, propagate as well as close at a later stage of the loading. This method was found to be superior to those that treat the cracks as zones of material weakness, because the actual propagation of the cracks can be followed and their widths calculated. The computer program is made entirely automatic so that the complete crack propagation history is obtained in a single analysis. The program successfully reproduced the cracks observed during the model experiments.

A method of analysing structures resting on clay was proposed in chapter 5, in which the long-term settlements were considered. It was demonstrated that the conventional method of settlement calculation in clay is erroneous in three respects: (i) It ignores the structure, (ii) it ignores Poisson's ratio and (iii) it uses Boussinesq's equations to calculate the stresses in the soil by assuming it to be an elastic continuum. It was shown that even for a plane frame, the stresses in the soil disperse in three directions

and the influence of lateral stresses on the vertical settlements is quite significant. As the value of Poisson's ratio approaches 0.5 the settlements become excessive. Therefore, for such soils one dimensional settlement calculation is grossly inadequate and exhaustive analyses of the type proposed here are warranted.

The large finite element meshes analysed in this thesis required a large computer storage for the stiffness matrix. To solve this problem, two methods of sequential construction of the stiffness matrix have been developed in chapter 6. The first divides the joints in the mesh into groups so that only two consecutive are kept in the core store at any time. The second method, which is a further development to save space, constructs the stiffness matrix one joint at a time. The core requirement for this method is nil as the small temporary storage required is allocated to other arrays after the construction of the stiffness matrix.

In this method however, an element has to be considered several times. Nevertheless, it was found that this method needs only slightly more time than the joint group method. This is because the stiffness terms corresponding to each node of an element are explicitly and separately defined in the program. By using this method, it is possible to obtain finite element analysis of large structure-soil systems without an excessive core or time requirement. In fact the investigation into the cost of running a job proved that the actual commercial cost of analysing large problems is not exorbitant. This is contrary to the belief of the advocates of simplified analysis methods who are often sceptical about the elaborations involved in the finite element approach.

Chapter 8 showed that a good correlation of the experimental

and the theoretical results is obtained by analysing the complete system. The non-linear behaviour of the structure and the separation of its foundation from the soil can be studied only by performing such an analysis.

The stiffness of a structure was found to have a definite influence on the settlements of its foundation. When the stiffness of the tall structure model was reduced, by increasing its base height, the settlements increased. In the three-bay frame there was a reduction in the settlements when the pads were replaced by a pair of strip footings. When a structure is loaded at a point, the unloaded parts contribute to the reduction of its deformations. Therefore, if the soil under one part of a structure is weak, stiffening the structure elsewhere will reduce the deflections.

The sway and the bending moments in the model structures were compared with those obtained by a fixed base analysis. The following conclusions are drawn from this study:

- 1) As the applied loads are vertical, the fixed base sway is negligible in all the models even when the eccentricity of the load is maximum. The actual sway is several hundred times higher than that shown by such an analysis. This is caused by the tilt of the structure due to the differential settlements of the foundations.
- 2) The difference between the fixed base and the flexible base sway increases as the structure becomes more slender and decreases as it spreads in the horizontal direction. At the maximum eccentricity of a load of 2 kN, the sway in the single bay space frame was some 220 times higher than that given by a fixed base analysis. This factor increased to 350 in the tall structure model and reduced to 110 in the case of the three-bay frame resting on strip footings.

- 3) The overall stiffness of the structure reduces the sway. The sway of the three-bay frame with pad footings was about 150 times that given by a fixed base analysis, while this factor was only 110 for strip footings. In the case of the box culvert model, which had a stiff cross-section, the actual sway was only 33 times higher than the fixed base sway.
- 4) The bending moment redistribution due to a flexible foundation medium depends on the geometry and the stiffness of the structure. In both the single-bay and the three-bay framed structures, the bending moments changed throughout the beams and the columns. On the other hand, in the slender tall structure model with a latticed base, the change in the moments was confined only inside the base. While these moments were sometimes opposite in sign and had a magnitude as much as 30 times higher than the fixed base moments, the difference was negligible at the top of the structure. In the cross-sectionally stiff box culvert model the moments were only 2 to 3 times higher than those given by the conventional analysis.
- 5) The magnitude of the bending moments at the base of a structure depends on the type of the foundation. When individual pad footings were used in the single-bay and the three-bay space frames, the column bases were relatively free to rotate and the bending moments were nearly zero under symmetrical loading. On the other hand, when the columns or the walls were interconnected by a combined footing, in the tall structure, the box culvert and the three-bay frame, the magnitudes of the base moments were considerable. In some cases they were opposite in sign to those given by a fixed base analysis and had high values.

The economy in the use of the computer programs was demonstrated

in chapter 9 by analysing two large practical structures. The adequacy of the analysis was proved by reproducing the domed deflected shape of the rafts and the high bending moments in the columns, which were observed in the actual silo. It is concluded that when a series of unconnected structures are constructed side by side they influence each other via the soil. They lean towards each other and become interconnected causing stresses in their members. Such tall and slender silo structures are considered highly susceptible to foundation movements and they warrant an elaborate analysis of the type performed here.

In the analysis of the 50-storey space structure, the depth of the soil was varied. The investigation showed that reducing the depth of soil does not significantly reduce the settlements. It is inferred that most of the settlement is caused by the compression of the top few metres of the soil as the stresses become insignificant at greater depths. The use of a thick raft or of piles that are confined only in the top highly stressed zone of the soil does not appreciably reduce the settlements. The choice of a foundation for such a structure must be based on a study of the type performed here. Such a study gives a direct assessment of the stresses in the structure due to the settlements and the sway caused by various types of foundation.

To increase the applicability of the proposed computer programs certain modifications can be done. A linear interpolation was performed between two neighbouring $\tau_{oct}-\gamma_{oct}$ curves of the soil to obtain the shear modulus for an intermediate value of σ_{octi} . This was found to be adequate for the sand used in the model experiments. However, in a general case, a more realistic representation of the

soil properties may be obtained by the spline interpolation of the three dimensional surface of τ_{oct} , γ_{oct} and σ_{octi} using the bicubic spline functions.

The incremental method was found to underestimate the deflections of a structure for a particular load. A better correlation between the theoretical and the experimental results may be obtained by performing a mixed iterative and incremental analysis. But the use of Newton-Raphson type of iteration in every increment of the load increases the computer time. A restricted number of iterations with a large increment size may however prove to be beneficial.

As mentioned in the thesis, the prismatic member and the plate element subroutines were taken from an existing program and incorporated into the author's computer programs. These subroutines were written in such a way that they could be used easily in conjunction with other isoparametric elements. This resulted in many unnecessary storage and computations and were kept basically unaltered by the author. However, a major alteration of the programming technique will enable these unnecessary operations to be avoided, thus reducing the storage and the time considerably.

For instance, the direction cosines of the members are calculated from the joint co-ordinates whenever the mesh geometry changes due to a crack. At present, this requires the storage of all the joint co-ordinates in a permanent and large array. This can be avoided by calculating the direction cosines and storing them on a disc for future use.

The degrees of freedom of the joints are stored in three different ways in separate permanent arrays. The array IX contains the degrees of freedom in the index form as supplied in the data.

These are then used to construct an array IR containing 6 rows and as many columns as there are joints. Each element of a column contains the numbers 1, 2, 3, 4, 5 or 6 indicating the presence of δ_x , δ_y , δ_z , θ_x , θ_y or θ_z . This array facilitates the calculation of the location of an element in the overall stiffness matrix where a particular contribution from a member or plate should go. Another array DF contains the accumulated degrees of freedom upto and including each joint of the mesh. This is used to locate the rows of the overall stiffness matrix that correspond to a particular joint. Both the arrays IR and DF can be avoided and the same informations can be derived directly from array IX.

The k A matrix of each member, required for the calculation of the forces and the moments, is evaluated in advance and sent to the backing store. These are then repeatedly transferred to the core to calculate the forces after each increment of the load. On the other hand, the DBA matrices of the plates are repeatedly evaluated after each increment and used to calculate the stresses from the nodal displacements. Both of these are time-consuming procedures. The computer time can be reduced considerably by writing explicit expressions for the member forces and the plate stresses in a manner very similar to that described for the solid elements in chapter 3. The programs proposed in this thesis already proved to be capable of analysing large structures and the improvements suggested will improve the efficiency of these programs.

The results obtained bring out new features of the behaviour of various structures resting on soil. However, it is considered that many other structures should be analysed and tested in order to improve our understanding of soil-structure interaction.

The stiffness matrix for a solid soil element can be generalised so that the material property G may vary within the element and hence the soil mass. This may become necessary for two reasons: (1) in a homogeneous soil G varies with depth and (2) G also varies in x and z directions for non-uniform soil. To obtain this generalised stiffness matrix, matrix \underline{D} must be altered so that G is a function of x , y and z . A linear variation of G then requires eight values of G , one at each node. Referring to the solid element in figure (3.3), let the shear modulus at the nodes be G_1, G_2, \dots, G_8 . Along the line 1 to 3, the value of G at a distance y from node 1 is g_{y13} given by:

$$g_{y13} = G_1 + y(G_3 - G_1)/b$$

Similarly along the line 2 to 5, the value of G is

$$g_{y25} = G_2 + y(G_5 - G_2)/b.$$

In the xy plane 1235, the value of G at any point (x, y) is

$$g_{xy1235} = g_{y13} + x(g_{y25} - g_{y13})/a$$

Similarly in the xy plane 4678, the value of G is

$$g_{xy4678} = g_{y46} + x(g_{y78} - g_{y46})/a$$

Finally the value of G at any point (x, y, z) is given by:

$$g_{xyz} = g_{xy1235} + z(g_{xy4678} - g_{xy1235})/c$$

Substituting for g_{xy1235} etc. we obtain

$$\begin{aligned} g_{xyz} = & G_1 + y(G_3 - G_1)/b + x[G_2 + y(G_5 - G_2)/b - \{G_1 + y(G_3 - G_1)/b\}]/a \\ & + z \left[G_4 + y(G_6 - G_4)/b + x[G_7 + y(G_8 - G_7)/b - \{G_4 + y(G_6 - G_4)/b\}]/a - [G_1 + y(G_3 - G_1)/b \right. \\ & \left. + x\{G_2 + y(G_5 - G_2)/b - (G_1 + y(G_3 - G_1)/b)\}/a \right] / c \end{aligned}$$

This expression for g_{xyz} should replace G in \underline{D} matrix given in equation 3.6.1 on page 58.

Similarly if v varies within the solid element, then the value of v at any point $[x, y, z]$ will be given by:

$$v_{xyz} = v_1 + y(v_3 - v_1)/b + x[v_2 + y(v_5 - v_2)/b - \{v_1 + y(v_3 - v_1)/b\}/a + \\ z \left[v_4 + y(v_6 - v_4)/b + x[v_7 + y(v_8 - v_7)/b - \{v_4 + y(v_6 - v_4)/b\}/a - [v_1 + y(v_3 - v_1)/b + x\{v_2 + y(v_5 - v_2)/b - \{v_1 + y(v_3 - v_1)/b\}/a\}] / c \right]$$

It should be pointed out that while it is simple to include a variable G in matrix \underline{D} , the variation of v makes the integration process in equation (3.7) of page 58 rather difficult.

It should be pointed out that the value of v calculated in this thesis assumed that during the triaxial test, both σ_1 and σ_3 are variables. In fact σ_3 is constant and the value of v should be calculated as follows:

Since σ_3 is constant, the axial strain ϵ_1 is $\epsilon_1 = \Delta\sigma_1/E$ where $\Delta\sigma_1$ is the change in the axial stress. The lateral strain ϵ_3 is $\epsilon_3 = -v\Delta\sigma_1/E$. The volumetric strain ϵ_v is $\epsilon_v = 2\epsilon_3 + \epsilon_1 =$

$\Delta\sigma_1 (1-2v)/E = \epsilon_1 (1-2v)$. Thus $v = 0.5 (1 - \epsilon_v/\epsilon_1)$. This indicates that when the volume is expanding and ϵ_1 is compressive, v will be greater than 0.5. This means that with $v < 0.5$, the strain in the soil should not exceed point A in figure (7.13a). For strains larger than point A, the finite element methods proposed in this thesis are not valid. It is therefore suggested that methods should be developed to deal with cases where excessive strains are developed so much so that v exceeds 0.5.

In figure (3.7a) it should be noted that the incremental analysis actually follows the line $Oa'b''$, where $a'b''$ is parallel

to abt. This is one reason why the theoretical approach underestimates the deflection under a given load. One way of overcoming this difficulty is to assume upper and lower bounds of the stress-strain curve. Whenever the stress at a point exceeds a bound the incremental load should be altered to bring the stress within the tolerance imposed.

APPENDIX I

LISTING OF THE SPLINE FORMULATION PROGRAM

The FORTRAN Program listed below is written for running on ICL 1900 series computers. It requires a core storage of about 9000 words for loading and execution.

```
PROGRAM(AZAD)
COMPRESS INTEGER AND LOGICAL
INPUT 1= CK0
OUTPUT 2= LP0
OUTPUT 4=LP1
TRACE 2
END

TRACE 0
MASTER SPLINE
C THIS PROGRAM FORMULATES THE CUBIC SPLINE S(X) FOR A SET OF X AND Y.
C IT CALCULATES DY/DX AND ALSO THE CHORD SLOPE IN THE NEIGHBOURHOOD
C OF GIVEN POINTS FOR COMPARISON. THE OUTPUT OF CHANNEL 2 IS PRINTED
C ON LINE PRINTER. CHANNEL 4 SHOULD BE ASSOCIATED WITH A PERMANENT
C FILE NAME. THE OUTPUT TO THIS FILE WILL CONSIST OF THE DATA REQUIRED
C BY THE MAIN FINITE ELEMENT PROGRAM FOR THE NON-LINEAR ANALYSIS OF
C STRUCTURE-SOIL INTERACTION PROBLEMS.
C
  REAL Y(30),X(30),L(30),LM(57),BET(29,30),CP(10),GT(10,30),XORY(30)
  1,CS(10,30)
  INTEGER SEQ(29)
  READ(1,100) MP,MG
C MP=NO. OF CURVES, MG=NO. OF POINTS WHERE Y & DY/DX ARE TO BE PRINTED.
  READ(1,103) (XORY(I),I=1,MG)
C XORY VALUES SHOULD BE IN ASCENDING ORDER. THESE ARE INTERMEDIATE
C X VALUES WHERE Y, DY/DX ETC ARE TO BE PRINTED.
  READ(1,103) (CP(I),I=1,MP)
C CP(I)=CONFINING PRESSURE OF CURVE NO.1
  WRITE(4,401) MP
  401 FORMAT(I3)
  DO 12 JJ=1,MP
C N IS THE NUMBER OF NODE POINTS
  READ(1,101) N
  N=N-2
  WRITE(4,402) CP(JJ),N
  402 FORMAT(E20.10,I10)
  DO 1 I=1,N+2
  READ(1,102) X(I),Y(I)
C X & Y VALUES AT EACH NODE.
  1 WRITE(4,403) X(I),Y(I)
  403 FORMAT(2E20.10)
  DO 2 I=1,N+1
  2 L(I)=X(I+1)-X(I)
  LM(I)=2*(L(I)+L(I+1))
  SEQ(I)=0
  SEQ(I+1)=1
  DO 3 I=2,N
  LM(2*I-2)=L(I)
  LM(2*I-1)=2*(L(I)+L(I+1))
  3 SEQ(I+1)=2*SEQ(I)-1
  DO 4 I=1,N
  4 BET(I,1)=6.0*(((Y(I+2)-Y(I+1))/L(I+1))-((Y(I+1)-Y(I))/L(I)))
```

```

      NI=N+1
      NA=SEQ(NI)
      CALL SOLUTION(LM,BET,N,NA,1,SEQ,NI)
      WRITE(2,205) JJ,CP(JJ)
205  FORMAT(1H1,'CURVE NUMBER=',I3,/, ' CONFINING PRESSURE=',F10.6,/)
      WRITE(2,201)
201  FORMAT(1H0,'VALUES OF PHI AT NODE POINTS',/, ' NOTE: PHI IS THE SE
      1COND DERIVATIVE OF THE SPLINE FUNCTION',/, ' PHI(1)=PHI(N+2)=0',/,
      210X,'NODE NO.',7X,'PHI')
      DO 5 I=1,N
        IP1=I+1
        5 WRITE(2,202) IP1,BET(I,1)
202  FORMAT(10X,15,2X,E15.6)
      DO 50 I=1,N
        50 WRITE(4,404) BET(I,1)
404  FORMAT(E20.10)
      WRITE(2,203)
203  FORMAT(1H0,'VALUES OF X, Y AND SLOPE AT VARIOUS POINTS ON THIS CU
      IRVE',/, ' POINT',11X,'X',7X,'CORRESPONDING Y ON SPLINE',5X,'MODULU
      2S',11X,'CHORD SLOPE',/)
      ICOUNT=1
      DO 60 KK=1,MG
        XOCT=XORY(KK)
        IJK=1
        61 IF(XOCT.GE.X(N+2)) GO TO 20
        IF(XOCT.LE.X(1)) GO TO 7
        DO 8 I=2,N+2
          IF(XOCT.LE.X(I)) GO TO 9
        8 CONTINUE
        9 J=1
        IF(J-N-1) 0,0,10
        IF(J-2) 0,98,0
        GT(JJ,KK)=(-6*Y(J-1)+6*Y(J)-(3*((X(J)-XOCT)**2)-(L(J-1))**2)*BET(J
        1-2,1)+(3*((XOCT-X(J-1))**2)-(L(J-1))**2)*BET(J-1,1))/(6*L(J-1))
        S=(6*(X(J)-XOCT)*Y(J-1)+6*(XOCT-X(J-1))*Y(J)+((X(J)-XOCT)**3-(L(J
        1-1))**2)*(X(J)-XOCT))*BET(J-2,1)+((XOCT-X(J-1))**3-(L(J-1))**2)*
        2XOCT-X(J-1))*BET(J-1,1))/(6*L(J-1))
        GO TO 6
      10 GT(JJ,KK)=(-6*Y(J-1)+6*Y(J)-(3*((X(J)-XOCT)**2)-(L(J-1))**2)*BET(J
        1-2,1))/(6*L(J-1))
        S=(6*(X(J)-XOCT)*Y(J-1)+6*(XOCT-X(J-1))*Y(J)+((X(J)-XOCT)**3-(L(J
        1-1))**2)*(X(J)-XOCT))*BET(J-2,1))/(6*L(J-1))
        GO TO 6
      98 GT(JJ,KK)=(-6*Y(J-1)+6*Y(J)+((3*(XOCT-X(J-1))**2)-(L(J-1))**2))*
        1BET(J-1,1))/(6*L(J-1))
        S=(6*(X(J)-XOCT)*Y(J-1)+6*(XOCT-X(J-1))*Y(J)+((XOCT-X(J-1))**3-(
        2L(J-1))**2)*(XOCT-X(J-1))*BET(J-1,1))/(6*L(J-1))
        GO TO 6
      7 GT(JJ,KK)=(-6*Y(1)+6*Y(2)-(L(1))**2)*BET(1,1))/(6*L(1))
        S=Y(1)+GT(JJ,KK)*(XOCT-X(1))
        GO TO 6
      20 IF(ICOUNT.NE.1) GO TO 99
        GT(JJ,KK)=(-6*Y(N+1)+6*Y(N+2)+(L(N+1))**2)*BET(N,1))/(6*L(N+1))
        S=Y(N+2)+GT(JJ,KK)*(XOCT-X(N+2))
        ICOUNT=2
        GO TO 6
      99 GT(JJ,KK)=GG
        S=Y(N+2)+GT(JJ,KK)*(XOCT-X(N+2))
        6 IF(IJK-1) 0,0,62
        XOCT=XORY(KK)-0.001
        SS=S
        GG=GT(JJ,KK)
        IJK=IJK+1

```

```

      GO TO 61
62 IF(IJK-2) 0,0,63
      X1=XOCT
      Y1=S
      XOCT=XORY(KK)+0.001
      IJK=IJK+1
      GO TO 61
63 X2=XOCT
      Y2=S
      GT(JJ,KK)=GG
      CS(JJ,KK)=(Y2-Y1)/(X2-X1)
60 WRITE(2,204) KK,XORY(KK),SS,GT(JJ,KK),CS(JJ,KK)
204 FORMAT(13,2E20.6,2E21.6)
100 FORMAT(210)
101 FORMAT(10)
102 FORMAT(2F0.0)
103 FORMAT(5F0.0)
12 CONTINUE
STOP
END

```

```

SUBROUTINE SOLUTION(A,B,N,NA,NRHS,IS,N1)
DIMENSION A(NA),B(N,NRHS),IS(N1),C(2)
INTEGER R,RJ,Q,RI
DO 1 I=1,N
RI=1-IS(I+1)+IS(I)+1
J=RI
6 RJ=J-IS(J+1)+IS(J)+1
R=RJ
IF(RJ.GT.R) R=RJ
IJ=IS(I+1)-1+J
L=J-RI+1
C(L)=A(IJ)
IF(R.GT.J-1) GO TO 2
DO 3 K=R,J-1
JK=IS(J+1)-J+K
M=K-RI+1
3 C(L)=C(L)-C(M)*A(JK)
2 IF(J-1) 0,4,0
JJ=IS(J+1)
A(IJ)=C(L)*A(JJ)
DO 5 Q=1,NRHS
5 B(I,Q)=B(I,Q)-C(L)*B(J,Q)
J=J+1
GO TO 6
4 II=IS(I+1)
A(II)=1.0/C(L)
DO 7 Q=1,NRHS
7 B(J,Q)=B(J,Q)*A(II)
1 CONTINUE
I=N
11 K=1-IS(I+1)+IS(I)+1
IF(K.EQ.1) GO TO 8
10 IK=IS(I+1)-1+K
DO 9 Q=1,NRHS
9 B(K,Q)=B(K,Q)-A(IK)*B(I,Q)
K=K+1
IF(K.LT.1) GO TO 10
8 I=I-1
IF(I.GT.1) GO TO 11
RETURN
END
FINISH

```

APPENDIX II

THE FINITE ELEMENTS

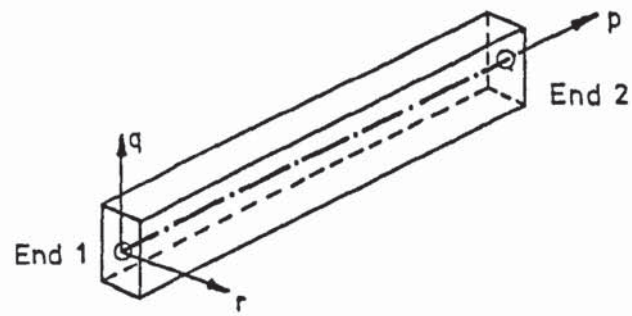
A2.1 SPACE FRAME MEMBER ELEMENT

The element is shown in figure (A2.1) in which the direction of the p-axis is always from end 1 to end 2. Each end of the member can have all three translations and three rotations as shown in figure (A2.1b). The eight possible member forces and moments are shown in figure (A2.1c). These are the axial force p_a , two shear forces S_R and S_Q , torque T and the moments at the two ends about q and r axes M_{Q1} , M_{Q2} , M_{R1} and M_{R2} .

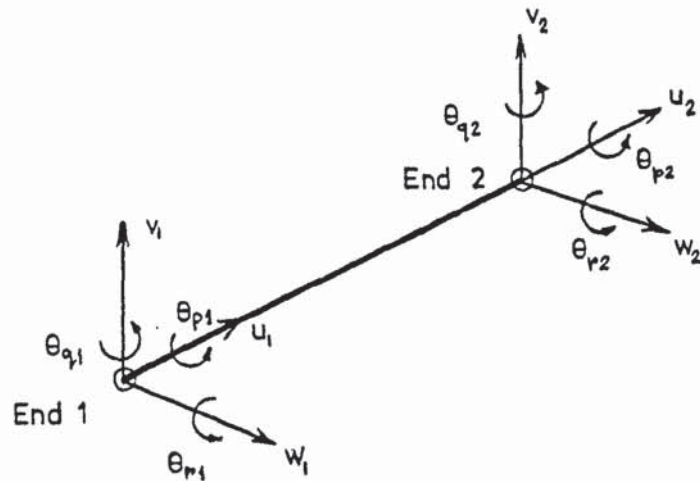
The irregularities due to the non-coincidence of the ends of the member with the specified joints and that of the centroid of the section with the shear centre are taken care of. In figure (A2.2a) i and j are the joints specified at the ends of the member while A and B are the actual centroids of the end sections. PCA and PCB are the distances in p direction of the ends A and B from the joints i and j respectively. QC and RC are the offsets in the q and the r directions of the member axis AB from the line ij. QS and RS in the figure are the distances in q and r directions between the centroid G and the shear centre C of the member cross section, as shown for an angle section in figure (A2.2b).

A2.2 RECTANGULAR PLATE ELEMENT

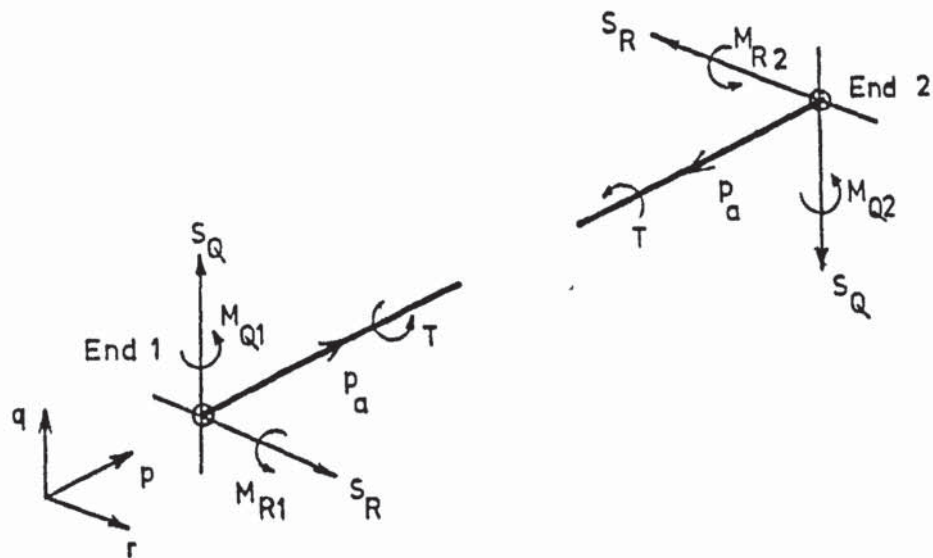
The node numbering and the local axes of the element are shown in figure (A2.3a). Each node can have a maximum of three translations and two rotations as shown in figure (A2.3b). The in-plane rotation of the nodes about the r axis is suppressed. The in-plane displacements u and v and the out of plane freedoms w, θ_p and θ_q are



(a) Reference axes

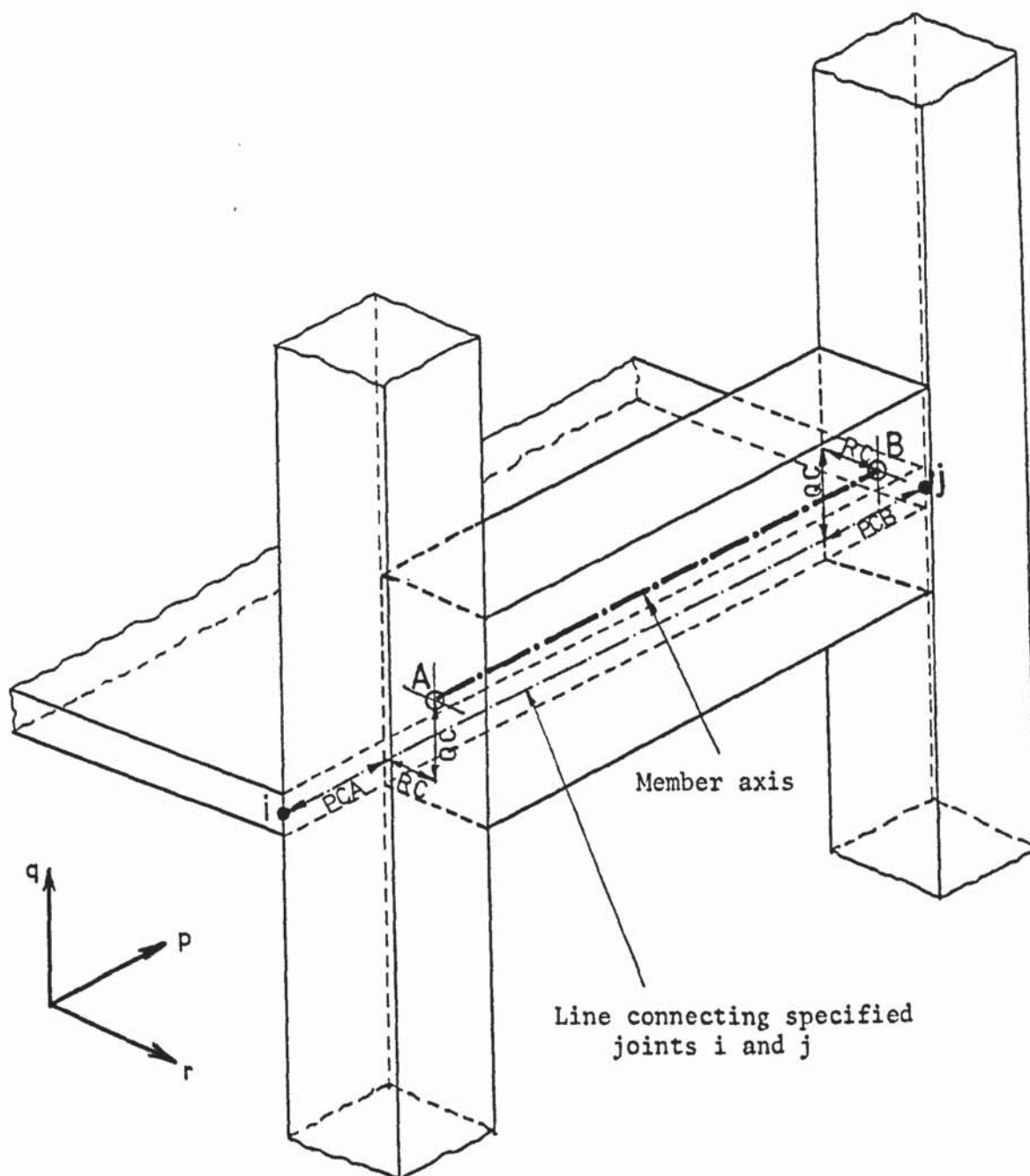


(b) Nodal displacements

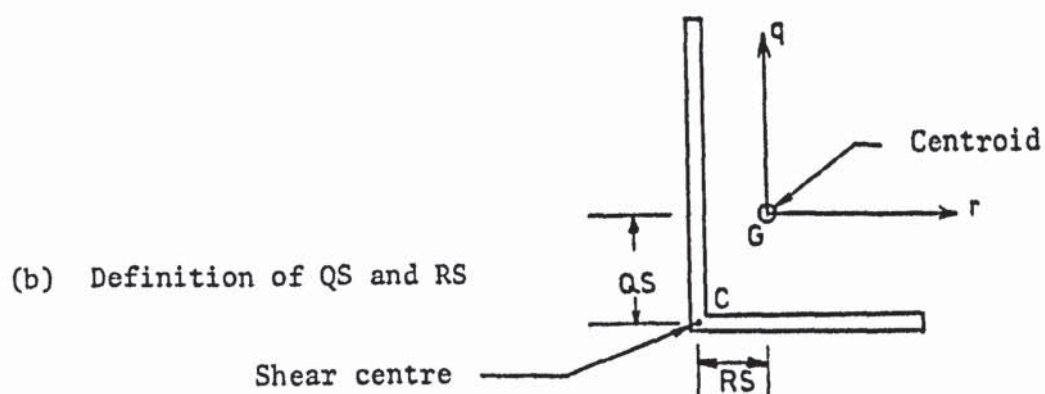


(c) Forces and moments

FIGURE A2.1 SPACE FRAME MEMBER ELEMENT

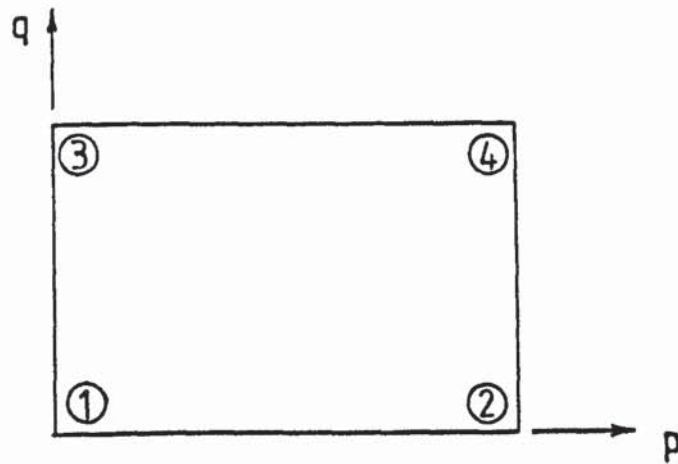


(a) Definition of end irregularities

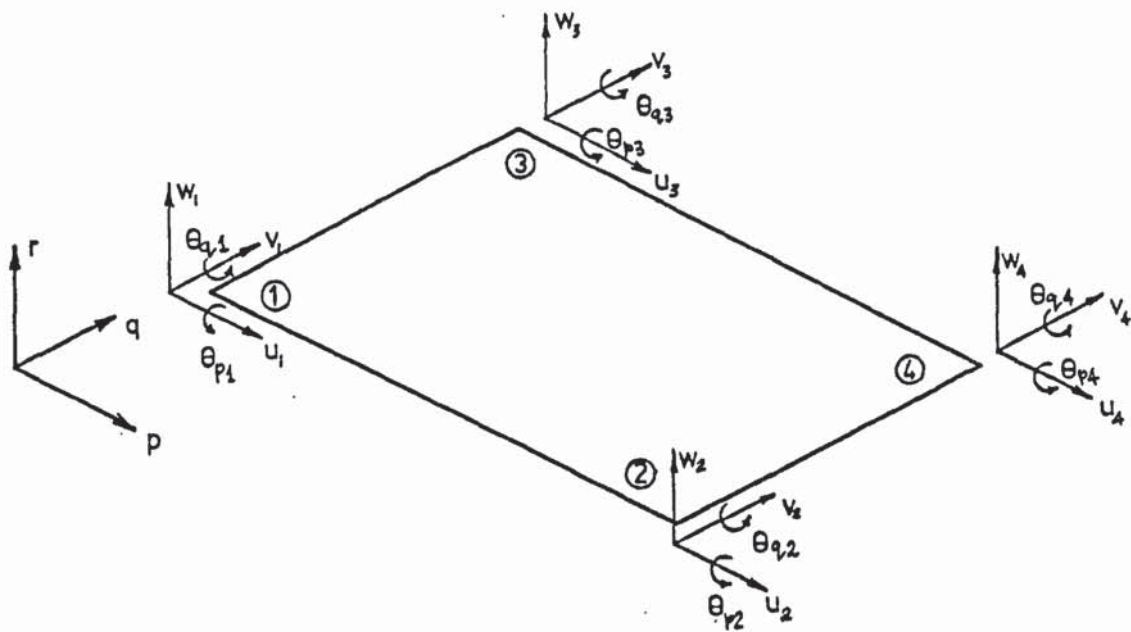


(b) Definition of QS and RS

FIGURE A2.2 END IRREGULARITIES OF THE SPACE MEMBER ELEMENT



(a) Reference axes and node numbering



(b) Nodal displacements

FIGURE A2.3 RECTANGULAR PLATE ELEMENT

formulated separately. The element can be used either as a plane element by suppressing the out of plane displacements or as a bending element by allowing these.

APPENDIX III

ARRAYS AND VARIABLES IN PROGRAMS DESCRIBED IN CHAPTER 6

A	Working space array.
AA	Temporary array of co-ordinates of dividing planes for automatic data generation.
BB	Temporary array of co-ordinates of dividing planes for automatic data generation.
C	Temporary array holding reduction factors during solution.
CC	Same as AA and BB.
DAS	Diagonal address sequence array.
DOSP	Incremental joint displacements matrix.
DSQ	Incremental element stresses.
IB	Array containing the numbers of the first passive block required by each active block.
IC	Last row number of each block.
ICS	Crack state indicator.
INDCRK	Indicator of a crack formed by activating a dummy joint.
INDDOF	Indicator of a crack of any type.
ITS	Number of joints where a check for crack is made.
IX	Array containing the informations for each joint.
IZ	Block size.
JGRP	Array containing the last joint number of each joint group.
JMISS	Temporary array containing the number to be added to each joint of the basic grid for automatic data generation.
LEFT	Number of elements of stiffness array left over from the previous joint or group in a solution block.
LGRP	Solid element numbers belonging to each joint group.
LMGRP	Member element numbers belonging to each joint group.

LMISS	Temporary array containing the number to be added to each solid element of the basic grid for automatic data generation.
LML	Location in the stiffness array of the last element of a joint group.
LPGRP	Plate numbers belonging to each joint group.
MC	Location of the first element of a block in DA10.
NEJG	Number of solid elements belonging to each joint group.
NJG	Total number of joint groups.
NJ1	Last joint number of the first group.
NMJG	Number of members belonging to each joint group.
NOJ	Total number of joints in the finite element mesh.
NPJG	Number of plates belonging to each joint group.
SNQ	Incremental joint stresses array.
TNQ	Total joint stresses array.
TOSP	Total joint displacements matrix.
TQ	Total element stresses array.
TS	Array containing tensile strengths of the joints that are likely to crack.

REFERENCES

- AHLBERG J H, NILSON E N and WALSH J L (1967)
The theory of splines and their applications. Mathematics in science and engineering series, Vol 38, Academic Press, New York.
- ALSHARQI I A (1977)
Finite element analysis of axisymmetric cracked solids. Ph D Thesis, University of Aston in Birmingham.
- BISHOP A W and HENKEL D J (1957)
The measurement of soil properties in the triaxial test. Edward Arnold, London.
- BOROWICKA H (1936)
Influence of rigidity of a circular foundation slab on the distribution of pressures over the contact surface. Proc. 1st Int. Conf. Soil Mech. Found. Eng., 2, pp 144-149.
- BOROWICKA H (1938)
The distribution of pressure under a uniformly loaded elastic strip resting on elastic isotropic ground. Final report, 2nd Congr. Int. Assoc. Bridge and Struct. Eng., p 840.
- BRAY K H M (1973)
Computer analysis of large civil engineering structures. Ph D Thesis, University of Aston in Birmingham.
- BURLAND J B, BROMS B B and deMELLO V F B (1977)
Behaviour of foundations and structures. State of the art report, Proc. 9th Int. Conf. Soil Mech. Found. Eng., Tokyo, 2, pp 495-546.
- BURLAND J B and DAVIDSON W (1976)
A case study of cracking of columns supporting a silo due to differential foundation settlement. Building Research Establishment, Current paper CP42/76.
- BURMISTER D M (1945)
The general theory of stress and displacements in layered soil systems. Journ. Applied Physics, 16, No 2, pp 89-96, No 3, pp 126-127, No 5, pp 296-302.

BURMISTER D M (1956)

Stress and displacement characteristics of a two-layer rigid base soil system: influence diagrams and practical applications. Proc. Highway Research Board, 35, pp 773-814.

CHAMECKI S (1956)

Structural rigidity in calculating settlements. Journ. Soil Mech. Found. Div., Proc. A.S.C.E., 82, SM1, p 1.

CHAMECKI S (1969)

Calculation of progressive settlements of foundations in interaction with structure and soil, (in French). Annales de L'Institut Technique du Bâtiment et des Travaux Publics, Paris, No 261, pp 1320-1334.

CHEUNG Y K and NAG D K (1968)

Plates and beams on elastic foundations - linear and non-linear behaviour. Geotechnique, 18, pp 250-260.

CHEUNG Y K and ZIENKIEWICZ O C (1965)

Plates and tanks on elastic foundations - an application of finite element method. Int. Journ. Solids Struct., 1, pp 451-461.

COATES R C, COUTIE M G and KONG F K (1972)

Structural analysis. Thomas Nelson and Sons Ltd., London.

CROXTON P C L (1974)

The analysis of complete structures consisting of bare frames, shear walls and plate elements. Ph D Thesis, University of Aston in Birmingham.

CUNNELL M D (1974)

The application of finite elements to problems of soil. Ph D Thesis, University of Aston in Birmingham.

DAVIS E H and POULOS H G (1968)

The use of elastic theory for settlement prediction under three dimensional conditions. Geotechnique, 18, pp 67-91.

DESAI C S (1971)

Non-linear analysis using spline functions. Journ. Soil Mech. Found. Div., Proc. A.S.C.E., 97, SM10, pp 1461-1480.

DESAI C S (1972)

Closure of discussion of the above paper. Journ. Soil Mech. Found. Div., Proc. A.S.C.E., 98, SM9, pp 967-971.

De SIMONE (1966)

Suggested design procedures for combined footings and mats. ACI committee report 436, ACI Journal, October, p 1041.

DOMASCHUK L and WADE N H (1969)

A study of bulk and shear moduli of a sand. Journ. Soil Mech. Found. Div., Proc. A.S.C.E., 95, SM2.

DUNCAN J M and CHANG C Y (1970)

Non-linear analysis of stress and strain in soils. Journ. Soil Mech. Found. Div., Proc. A.S.C.E., 96, SM5, pp 1629-1651.

FLETCHER D Q and HERMANN L R (1971)

Elastic foundation representation of continuum. Journ. Eng. Mech. Div., Proc. A.S.C.E., 97, EM1, pp 95-107.

GALLETLY G D (1959)

Circular plates on a "generalized" elastic foundation. Journ. Applied Mech., 26, Trans. A.S.M.E., 81, series E, p 297.

GIBSON R E (1967)

Some results concerning displacements and stresses in a non-homogeneous elastic half-space. Geotechnique, 17, pp 58-67.

GIBSON R E and SILLS G C (1971)

Some results concerning the plane deformation of a non-homogeneous elastic half-space. Stress-strain behaviour of soils, R H G Parry (Ed.), Proc. Roscoe Mem. Symp., Cambridge, pp 564-572.

GIRIJA VALLABHAN C V and JAIN R K (1972)

Octahedral stress approach to analysis of water resources structures. Proc. Symp. Application of finite element method to Geotechnical Eng., C S Desai (Ed.), U S Army Engr. Waterways Expt. Station, Soil Mech. information analysis centre, Vicksburg, Mississippi, III, pp 1185-1213.

GIRIJA VALLABHAN C V and REESE L C (1968)

Finite element method for problems in soil mechanics. Journ. Soil Mech. Found. Div., Proc. A.S.C.E., 94, SM2, pp 473-496.

GIROUD J P (1968)

Settlement of a linearly loaded rectangular area. Journ. Soil Mech. Found. Div., Proc. A.S.C.E., 94, SM4, pp 813-831.

GORBUNOV-POSADOV M I and SEREBRJANYI R V (1961)

Design of structures on elastic foundations. Proc. 5th Int. Conf. Soil Mech. Found. Eng., Paris, 1, pp 643-648.

GRASSHOF H (1957)

Influence of flexural rigidity of superstructure on the distribution of contact pressure and bending moments of an elastic combined footing. Proc. 4th Int. Conf. Soil Mech. Found. Eng., London, 1, pp 300-306.

GREVILLE T N E (1967)

Spline functions, interpolation and numerical quadrature. Mathematical methods for digital computers, II, 2nd Ed., Ralston and Wilf (Eds), John Wiley, pp 156-168.

HETENYI M (1946)

Beams on elastic foundation. University of Michigan Press, Ann Arbor, Michigan.

HETENYI M (1950)

A general solution for the bending of beams on an elastic foundation of arbitrary continuity. Journ. Applied Physics, 21, pp 55-58.

HRENIKOFF A (1941)

Solution of problems of elasticity by the framework method. Journ. Applied Mech., Trans. A.S.M.E., 63, pp A169-A175.

JENNINGS A (1966)

A compact storage scheme for the solution of symmetric linear simultaneous equations. Computer Journ., 9, pp 281-285.

JENNINGS A (1977)

Matrix computation for engineers and scientists. John Wiley & Sons.

JENNINGS A and TUFF A D (1970)

A direct method for the solution of large sparse symmetric simultaneous equations. Large sparse sets of linear equations, Proc. Oxford Conf. Institution of Maths. and its Applications, Oxford, pp 97-105.

- KAMESWARA RAO N S V, DAS Y C and ANANDAKRISHNAN M (1971)
Variational approach to beams on elastic foundations. Journ. Eng. Mech. Div., Proc. A.S.C.E., 97, EM2, pp 271-294.
- KERR A D (1961)
Viscoelastic Winkler foundation with shear interactions. Journ. Eng. Mech. Div., Proc. A.S.C.E., 87, EM3, pp 13-30.
- KERR A D (1964)
Elastic and viscoelastic foundation models. Journ. Applied Mech., 31, Trans. A.S.M.E., pp 491-498.
- KING G J W and CHANDRASEKARAN V S (1974)
Interactive analysis of a rafted multi-storey space frame on an inhomogeneous clay stratum. Proc. Conf. Finite Element Methods in Eng., Univ. N S W, pp 493-509.
- KOMORNIK A and MAZURIK A (1974)
Interaction of superstructure-soil under restrained settling. Canadian Geotechnical Journ., 11, No 4, pp 470-479.
- KONDNER R L (1963)
Hyperbolic stress-strain response: cohesive soils. Journ. Soil Mech. Found. Div., Proc. A.S.C.E., 89, SM1, pp 115-143.
- KONDNER R L and ZELASKO J S (1963a)
A hyperbolic stress-strain formulation for sands. 2nd Pan Am. Conf. Soil Mech. Found. Eng., 1, Brazil, pp 289-324.
- KONDNER R L and ZELASKO J S (1963b)
Void ratio effects on the hyperbolic stress-strain response of a sand. Laboratory shear testing of soils, A.S.T.M., STP361.
- LARNACH W J (1970)
Calculation of settlements of building frames taking account of structural stiffness. Civ. Eng. Public Works Review, September, pp 1040-1043.
- LARNACH W J and WOOD L A (1972)
The effect of soil-structure interaction on settlements. Proc. Int. Symp. Computer aided structural design, Univ. Warwick, Pergamon Ltd., 2, pp G1.1-G1.13.
- LEE I K (1963)
Elastic settlement in footings with a rough interface. Proc. 4th Australia-New Zealand Conf. Soil Mech. Found. Eng., p 225.

LEE I K and BROWN P T (1972)

Structure-foundation interaction analysis. Journ. Struct. Div., Proc. A.S.C.E., 98, ST11, pp 2413-2431.

LEE I K and HARRISON H B (1970)

Structure-foundation interaction theory. Journ. Struct. Div., Proc. A.S.C.E., 96, ST2, pp 177-198.

LEONARDS G A and HARR M E (1959)

Analysis of concrete slabs on ground. Journ. Soil Mech. Found. Eng. Div., Proc. A.S.C.E., 85, SM3, pp 35-58.

LITTLEJOHN G S and MACLEOD I A (1974)

(Editors) Structure-soil interaction in relation to buildings. Report by a special study group, Institution Struct. Engineers, London.

LITTON E and BUSTON J M (1968)

The effect of differential settlement on a large, rigid, steel-framed, multi-storey building. The Structural Engineer, 96, No 11, pp 353-356.

LOVE A E H (1929)

The stress produced in a semi-infinite solid by pressure on part of the boundary. Philosophical transactions, Royal Society of London, 228, series A, pp 377-420.

MAJID K I (1972)

The effect of irregularities on the finite element analysis of civil engineering structures. Proc. Speciality Conf. Finite Element Methods in Civ. Eng., J O McCutcheon, M Saeed Mirza and A A Mufti (Editors), McGill University, Montreal, Quebec, Canada, pp 917-946.

MAJID K I and Al-HASHIMI K (1976)

Failure of brittle materials due to crack propagation. The Structural Engineer, 54, No 5, pp 175-182.

MAJID K I and CRAIG J S (1972)

An incremental finite element analysis of structural interaction with soil of non-linear properties. Proc. Conf. Soil-Structure Interaction, Univ. Birmingham, pp 131-145.

MAJID K I and CUNNELL M D (1976)

A theoretical and experimental investigation into soil-structure interaction. Geotechnique, 26, No 2, pp 331-350.

MAJID K I and WILLIAMSON M (1967)

Linear analysis of complete structures by computers. Proc. Institution of Civil Engineers, London, Part 2, 38, pp 247-266.

McCORMICK C W (1963)

Plane stress analysis. A.S.C.E. Conf. Electronic Computation, Boulder, Colo, Journ. Struct. Div., Proc. A.S.C.E., 89, ST4, pp 37-54.

McHENRY D (1943)

A lattice analogy for the solution of stress problems. Journ. Institution of Civil Engineers, London, 21-22, No 2, pp 59-82.

MEYERHOF G G (1947)

The settlement analysis of building frames. The Structural Engineer, London, 25, pp 369-409.

MEYERHOF G G (1953)

Some recent foundation research and its application to design. The Structural Engineer, London, 31, pp 151-167.

MILOVIC D M and TOURNIER J P (1974)

Stress and deformations in an elastic layer as a result of pressure across a rigid rectangular plate, (in German). Der Bauingenieur, 49, pp 63-66.

MORRIS D (1966)

Interaction of continuous frames and soil media. Journ. Struct. Div., Proc. A.S.C.E., 92, ST5, pp 13-45.

NEWMARK N M (1942)

Influence charts for computation of stresses in elastic soils. Univ. Illinois Eng. Expt. Station, Bulletin No 338.

NGO D and SCORDELIS A C (1967)

Finite element analysis of reinforced concrete beams. A.C.I. Journ, 64, March, pp 152-163.

NILSON A H (1968)

Non-linear analysis of reinforced concrete by the finite element method. A.C.I. Journ., 65, September, pp 757-766.

PECK R B, HANSON W E and THORNBURN T H (1974)

Foundation Engineering, 2nd Ed., John Wiley & Sons Inc., New York.

PHILLIPS D V and ZIENKIEWICZ O C (1967)

Finite element non-linear analysis of concrete structures.
Proc. Institution of Civil Engineers, Part 2, 61, pp 59-88.

PICKETT G and McCORMICK F J (1951)

Circular and rectangular plates under lateral load and supported
on an elastic solid foundation. Proc. 1st U S Nat. Congr.
Applied Mech., Chicago, Ill., A.S.M.E., pp 331-338.

PISTER K S and WILLIAMS M L (1960)

Bending of plates on a viscoelastic foundation. Journ. Eng. Mech.
Div., Proc. A.S.C.E., 86, EM5, pp 31-44.

PONCE V M and BELL J M (1971)

Shear strength of sand at extremely low pressures. Journ.
Soil Mech. Found. Div., Proc. A.S.C.E., 97, SM4, pp 625-638.

POULOS H G (1967a)

The use of the sector method for calculating stress and displace-
ments in an elastic mass. Proc. 5th Australia-New Zealand Conf.
Soil Mech. Found. Eng., pp 198-204.

POULOS H G (1967b)

Stresses and displacements in an elastic layer underlain by a rough
rigid base. Geotechnique, 17, pp 378-410.

POULOS H G and DAVIS E H (1974)

Elastic solutions for soil and rock mechanics. Series in Soil
Eng., T W Lambe and R V Whitman (Eds), John Wiley & Sons, New York.

REISSNER E (1958)

A note on deflections of plates on a viscoelastic foundation.
Journ. Applied Mech., Trans. A.S.M.E., 80, pp 144-145.

RIDDINGTON J R (1975)

Composite behaviour of walls interacting with flexural members.
Ph D Thesis, University of Southampton.

RUSER J R and DAWKINS W P (1972)

3D finite element analysis of soil-structure interaction. Proc.
Symp. Application of finite element method to Geotechnical Eng.,
C.S Desai (Ed), U S Army Engr. Waterways Expt. Station, Soil Mech.
information analysis centre, Vicksburg, Mississippi, III, pp 1117-1144.

SEETHARAMULU K and KUMAR A (1973)

Interaction of foundation beam and soil with frames. Proc. 8th Int. Conf. Soil Mech. Found. Eng., Moscow, Session 2.

SMITH I M (1970)

A finite element approach to elastic soil-structure interaction. Canadian Geotechnical Journ., 7, No 2, pp 95-105.

SOMMER H (1965)

A method for calculating settlements, contact pressures and bending moments in a foundation including the influence of the flexural rigidity of the superstructure. Proc. 6th Int. Conf. Soil Mech. Found. Eng., Montreal, 2, pp 177-201.

SOVINC I (1961)

Stresses and displacements in a limited layer of uniform thickness, resting on a rigid base, and subjected to a uniformly distributed flexible load of rectangular shape. Proc. 5th Int. Conf. Soil Mech. Found. Eng., Paris, 1, pp 823-827.

SPIEGEL M R (1968)

Mathematical handbook of formulas and tables. Schaum's outline series, McGraw-Hill Book Co Limited.

STAFFORD SMITH B and RIDDINGTON J R (1977)

The composite behaviour of elastic wall-beam systems. Proc. Institution of Civil Engineers, Part 2, 63, pp 377-391.

TERZAGHI K (1943)

Theoretical Soil Mechanics. John Wiley & Sons.

TIMOSHENKO S P and GOODIER J N (1970)

Theory of Elasticity, 3rd Ed., McGraw-Hill Book Company.

THORBURN S (1978)

(Editor) Structure-Soil Interaction. State of the art report by an ad hoc committee, Institution of Structural Engineers, London.

TRIKHA D N and EDWARDS A D (1972)

Analysis of concrete box girders before and after cracking. Proc. Institution of Civil Engineers, Part 2, 53, pp 515-528.

TSAI N and WESTMANN R A (1967)

Beam on tensionless foundation. Journ. Eng. Mech. Div., Proc. A.S.C.E., 93, EM5, pp 1-12.

VLASOV V Z and LEONTIEV N N (1966)

Beams, plates and shells on elastic foundations. (Translated from Russian), NASA, TT F-357, U S A.

ZBIROHOWSKI-KOSCIA K F and GUNASEKERA D A (1970)

Foundation settlement and ground reaction calculations using a digital computer. Civil Eng. Public Works Review, 65, p 152.

ZIENKIEWICZ O C (1977)

The Finite Element Method, 3rd Ed, McGraw-Hill Book Co Limited.

ZIENKIEWICZ O C, VALLIAPPAN S and KING J P (1968)

Stress analysis of rocks as a 'no-tension' material. Geotechnique, 18, pp 56-66.